

# REPORT DOCUMENTATION PAGE

Form Approved  
OMB No. 0704-0188

Public reporting burden for this collection of information is estimated to average 1 hour per response, including the time for reviewing instructions, searching existing data sources, gathering and maintaining the data needed, and completing and reviewing the collection of information. Send comments regarding this burden estimate or any other aspect of this collection of information, including suggestions for reducing this burden, to Washington Headquarters Services, Directorate for Information Operations and Reports, 1215 Jefferson Davis Highway, Suite 1204, Arlington, VA 22202-4302, and to the Office of Management and Budget, Paperwork Reduction Project (0704-0188), Washington, DC 20503.

1. AGENCY USE ONLY (Leave Blank)		2. REPORT DATE July 15, 1997		3. REPORT TYPE AND DATES COVERED Technical 7/1/94 - 7/15/97	
4. TITLE AND SUBTITLE Analysis of Three-Dimensional Turbulent Shear Flow Experiments with Respect to Algebraic Modeling Parameters				5. FUNDING NUMBERS  N00014 - 94 - I - 0802	
6. AUTHOR(S)  D. S. Ciochetto and R. L. Simpson					
7. PERFORMING ORGANIZATION NAME(S) AND ADDRESS(ES) Dept. of Aerospace and Ocean Engineering Virginia Polytechnic Institute and State University Blacksburg, VA 24061-0203				8. PERFORMING ORGANIZATION REPORT NUMBER  VPI-AOE-248	
9. SPONSORING/MONITORING AGENCY NAME(S) AND ADDRESS(ES) Office of Naval Research 800 N. Quincy St. Arlington, VA 22217				10. SPONSORING/MONITORING AGENCY REPORT NUMBER	
11. SUPPLEMENTARY NOTES					
<div style="border: 1px solid black; padding: 5px; display: inline-block;"> <b>DISTRIBUTION STATEMENT B</b>  Approved for public release;  Distribution Unlimited </div>					
12a. DISTRIBUTION/AVAILABILITY STATEMENT  Unlimited				12b. DISTRIBUTION CODE	
13. ABSTRACT (Maximum 200 words)  <p>The extension of simple two-dimensional turbulent boundary layer (TBL) concepts to three-dimensional flows has met with limited success due to non-equilibrium effects. Transport equations for some turbulent stresses are proposed to account for the non-equilibrium effects. This study is aimed at developing algebraic relationships among the various Reynolds-averaged terms in these equations to reduce the number of modeled parameters, specifically the triple products. Eleven existing experimental data sets, with a variety of flow geometries, that included all six Reynolds stresses and triple products were acquired from the original authors and re-examined with respect to algebraic parameters. The ratio <math>1/S</math> (<math>S = \overline{v^2}/\tau/\rho</math>) approximates a constant for <math>0.3-0.4 &lt; y/\delta &lt; 0.7-0.8</math> ranging from values of 0.5-0.8 with an overall average of approximately 0.7. At <math>y/\delta=1.0</math>, <math>1/S</math> appears to have a mean value, for the data presented, of approximately 0.3. The <math>B_2</math> parameter (<math>B_2 = \overline{v^3}/[(\overline{uv})^2 + (\overline{vw})^2]^{1/2}</math>) approximates a constant value of <math>0.85 \pm 0.15</math> for <math>0.3 \leq y/\delta \leq 0.7-1.0</math>. It correlates the triple products that appear in the transport equations for the <math>-\overline{vw}</math>, <math>-\overline{uv}</math>, and <math>\overline{v^2}</math> Reynolds stresses. The <math>\overline{v^3}/\overline{vq^2}</math> parameter maintains better correlation than <math>B_2</math> across the TBL over various data sets. It maintains a value of 0.3-0.4 for <math>y/\delta &gt; 0.4</math> and tends to extend farther towards the wall for the upstream stations in a given experiment. The parameters are most useful in the outer portion of the turbulent boundary layer. The parameters presented here reflect the modified physics of three-dimensional turbulent boundary layers and can be useful in future turbulence models.</p>					
14. SUBJECT TERMS  Three-Dimensional Flow, Turbulence Structure				15. NUMBER OF PAGES 443	
				16. PRICE CODE	
17. SECURITY CLASSIFICATION OF REPORT Unclassified	18. SECURITY CLASSIFICATION OF THIS PAGE Unclassified	19. SECURITY CLASSIFICATION OF ABSTRACT Unclassified	20. LIMITATION OF ABSTRACT Unlimited		

## Table of Contents

Abstract	ii
Dedication	iii
Acknowledgements	iv
Table of Contents	v
Nomenclature	viii

### Chapter 1 Introduction

1.1 Overview	1
1.2 Brief History	1
1.3 Brief Review of Turbulence Models	3
1.4 The Relationships Between 2D and 3D TBL Models	5
1.5 Objectives	7
Figures	8

### Chapter 2 Experimental Test Cases

2.1 Introduction and Discussion of Criterion for Experiment Selection	9
2.2 Description of Individual Test Cases	10
2.2.1 The Experimental Juncture Flow of McMahon	10
2.2.2 The 'Infinite' Curved Swept Wings of Baskaran and Bradshaw	13
2.2.3 The Wing-Body Junction of Devenport and Simpson	16
2.2.4 The Axisymmetric Shear Induced Flow of Driver and Johnston	18
2.2.5 The Rotating Disk Experiment of Littell and Eaton	23
2.2.6 The Converging and Diverging Duct Flows of Pompeo	28
2.2.7 The 30° Bend Experiment of Schwarz and Bradshaw	31
2.2.8 Ellipsoid Cylinder Experiment of Barberis and Molton	36
2.2.9 6:1 Prolate Spheroid Experiment of Kreplin and Stäger	38
2.2.10 6:1 Prolate Spheroid Experiment of Chesnakas and Simpson	39
2.2.11 The Wing-Body Junction Experiment of Ölçmen and Simpson	41
2.3 Summary and Observations on the Current State of Experimental Data	45
Tables	47
Figures	55

19970806 061

### Chapter 3 Results and Discussion (Reynolds Stress Parameters)

3.1 The 1/S Parameter	71
3.2 The S Parameter	79
3.3 The Ratio of Reynolds Stress Production, C	79
3.4 Other Algebraic Ratios Involving Reynolds Stresses	80
3.4.1 The ratio $-\overline{vw} / -\overline{uw}$	80
3.4.2 The ratio $\overline{uv} / \overline{vw}$	81
3.4.3 The relationship $(\overline{v^2} / \overline{u^2})^{0.5}$	81
3.4.4 The relationship $\frac{\overline{vw}}{\overline{uw}} \sqrt{\frac{\overline{u^2}}{\overline{v^2}}}$	83
3.5 Nagano and Tagawa parameters	83
3.6 The $a_1$ relationship of Chesnakas	84
3.7 Conclusions	86
Tables	88
Figures	90

### Chapter 4 Results and Discussion (Triple Product Relationships)

4.1 B Parameters	136
4.2 $\overline{vq^2}$ Paramaters	139
4.3 Other Ratios	142
4.4 Insight from Individual Triple Products	143
4.5 Conclusions	145
Figures	146

### Chapter 5 Discussions and Conclusions

5.1 Overview	184
5.2 Discussion of Coordinate System Choice	185
5.3 Discussion of Regions in the Flow	186
5.4 Physical Interpretations	187
5.5 Modeling Issues	192
5.6 Conclusions	194

References	196
------------	-----

## Appendices

A - Uncertainty Analysis	201
B - Additional Figures for Pompeo	204
C - Additional Figures for Schwarz	218
D - Additional Figures for Ölçmen	252
E - Additional Figures for Baskaran	261
F - Additional Figures for Chesnakas	292
G - Additional Figures for Stäger	335
H - Additional Figures for Molton	340
I - Additional Figures for Devenport	360
J - Additional Figures for McMahon	381
K - Additional Figures for Driver	387
L - Additional Figures for Littell	393
M - Nagano & Tagawa Parameters	411
 Vitae	 438

## Notes:

The data as supplied by the original authors is available via the world wide web at the following URL.

<http://www.aoe.vt.edu/~ciochett/pubs/data/>

Information on the author can also be found on the internet at the following URL.

<http://www.aoe.vt.edu/~ciochett/index.html>

The author can be reached through email at;

[ciochett@apollo.aoe.vt.edu](mailto:ciochett@apollo.aoe.vt.edu)

The pictures illustrated on the title page and abstract are plates 157 and 158 from VanDyke (1982) respectively. They are presented to illustrate the complex nature of turbulent boundary layers. The figures employ flow visualization to study the structure of a 2D TBL. The present study focuses on 3D TBLs which are more complex than the boundary layers shown.



## Nomenclature

2D	two-dimensional
3D	three-dimensional
$a_1$	$\left  \frac{\tau}{\rho} \right  / \overline{q^2} = \sqrt{\overline{-uv^2} + \overline{-vw^2}} / (\overline{u^2} + \overline{v^2} + \overline{w^2})$
$B_1$	$\overline{v^3} / \sqrt{\overline{u^2 v^2} + \overline{w^2 v^2}}$
$B_2$	$\overline{v^3} / \sqrt{\overline{uv^2} + \overline{v^2 w^2}}$
C	$\frac{\text{production.}\overline{vw}}{\text{production.}\overline{uw}} = -\left( \overline{v^2} \frac{\partial W}{\partial Y} \right) / -\left( \overline{uv} \frac{\partial W}{\partial Y} + \overline{vw} \frac{\partial U}{\partial Y} \right)$
$C_f$	Friction coefficient
$F_i$	Flatness in $i^{\text{th}}$ component, $\frac{\overline{u_i^4}}{(\overline{u_i^2})^2}$
FA	Flow angle, $\tan^{-1}(W/U)$
FGA	Flow gradient angle, $\tan^{-1}(\frac{\partial W}{\partial Y} / \frac{\partial U}{\partial Y})$
$l_m$	$\frac{\sqrt{\left  \frac{\tau}{\rho} \right }}{\sqrt{\left( \frac{\partial U}{\partial Y} \right)^2 + \left( \frac{\partial W}{\partial Y} \right)^2}} = \frac{(\overline{-uv^2} + \overline{-vw^2})^{1/4}}{\sqrt{\left( \frac{\partial U}{\partial Y} \right)^2 + \left( \frac{\partial W}{\partial Y} \right)^2}}$
N	Anisotropy; $\frac{v_z}{v_x} = \frac{\tan(\text{SSA})}{\tan(\text{FGA})} = \frac{\overline{-vw}}{\frac{\partial W}{\partial Y}} / \frac{\overline{-uv}}{\frac{\partial U}{\partial Y}}$

N-S	Navier-Stokes
$\overline{q^2}$	$\overline{u^2} + \overline{v^2} + \overline{w^2}$
$Re_\theta$	Reynolds number based on Momentum thickness
Rotta's $T, N', N_e$	$T = \tan(SSA - FA) / \tan(FGA - FA)$
S	$\overline{v^2} / \left  \frac{\tau}{\rho} \right $
1/S	$\left  \frac{\tau}{\rho} \right  / \overline{v^2}$
$S_i$	Skewness in $i^{th}$ component, $\frac{\overline{u_i^3}}{(\overline{u_i^2})^{3/2}}$
SSA	Shear stress angle, $\tan^{-1}(\overline{vw}/\overline{uv})$
TBL	turbulent boundary layer
TKE	Turbulent kinetic energy, $\overline{q^2}/2 = (\overline{u^2} + \overline{v^2} + \overline{w^2})/2$
U, V, W	Mean velocities in an orthogonal coordinate system
u, v, w	Fluctuating velocities
$u', v', w'$	Root-mean-square fluctuating velocity, i.e. $u' = \sqrt{\overline{u^2}}$
$\overline{u^2} \quad \overline{v^2} \quad \overline{w^2} \quad \overline{uv} \quad \overline{vw} \quad \overline{uw}$	Reynolds stresses
$\overline{u^2 v}, \overline{uv^2}, \overline{v^3}, \overline{v^2 w}, \overline{vw^2},$ $\overline{u^2 w}, \overline{uw^2}, \overline{uvw}, \overline{u^3}, \overline{w^3}$	Turbulent triple products

$U_e$	Edge velocity
$U_{fs}$	Free stream velocity at the measurement location
$U_{ref}$	Reference velocity of the flow
$u_\tau$	Friction velocity
$\overline{vq^2}$	$(\overline{u^2v} + \overline{v^3} + \overline{w^2v})$
$x,y,z$	Mutually orthogonal coordinate system where x is typically in the direction of the flow or the wind tunnel centerline. Y is normal to the surface and z completes the coordinate system based upon a right hand rule.
$y^+$	Wall coordinate normal to the wall, $y u_\tau / \nu$
$\delta$	Boundary layer thickness
$\tau_w$	Wall shear stress
$\tau $	$\sqrt{(-\rho\overline{uv})^2 + (-\rho\overline{vw})^2}$
$\nu_x$	x-direction eddy viscosity; $\overline{-uv} / \frac{\partial U}{\partial y}$
$\nu_z$	z-direction eddy viscosity; $\overline{-vw} / \frac{\partial W}{\partial y}$

# **Chapter 1      Introduction**

## **1.1 Overview**

Over the past century, a great deal of knowledge concerning turbulence in fluids has been advanced by a number of prolific researchers. The objective of turbulence research is to develop mathematical models that adequately represent the physics of the flow field. These models then can be applied to predicting the forces produced by fluid motion on a body immersed in the fluid. Most of the past research focused on the modeling of flows that are two-dimensional (2D) with respect to the mean velocity. However, most flows of engineering interest are three-dimensional (3D) with respect to the mean velocity. There are many regions in a flow where viscosity is a significant factor and turbulence is encountered. This study focuses on turbulence in wall-bounded shear layers which may be classified as turbulent boundary layers (TBLs). The current study adds to the existing base of knowledge by providing algebraic relationships between terms in some equations used in turbulence modeling.

## **1.2 Brief History**

For continuity, a brief history of fluid turbulence is included. Note that only equations that are relevant to this study are formally presented. For a more detailed account, the reader is referred to Bradshaw (1987 a, b), Rotta (1962), Schetz (1993), Schlichting (1987), Tennekes (1972), Townsend (1976), or a number of other good texts on the theory. The governing equations for the motion of a fluid are the Navier-Stokes equations (N-S) and the continuity equation. They express Newton's second law of motion and the law of mass conservation. Turbulent flow is unsteady flow containing coherent vortical-three dimensional structures of various size and velocity that have limited lifetimes and spatial extent. In 1895 O. Reynolds introduced the concept of treating the actual fluid velocity as the sum of a mean and a fluctuating velocity (Rotta, 1962). Using this Reynolds averaging, statistical concepts could be applied to the understanding of turbulence. When a mean and fluctuating velocity is substituted into the N-S equations for the instantaneous velocity, the resulting equations for the mean velocity are similar to the original N-S equations. The difference is the appearance of averaged products of the fluctuating velocities (with respect to a Cartesian coordinate system) in the momentum equation. These are referred to as

Reynolds stresses and produce more unknown variables than available equations. This restricts an analytical solution for the system of equations. The bulk of turbulence research is focused on the development of models for these terms. Models are empirical, based directly on experimental data, or semi-empirical, a model (or theory) that is developed to capture the physics of the flow and supported by experiments.

Assumptions about certain regions of the flow can simplify the equations. Prandtl in 1904 illustrated that in fluids of small viscosity, the frictional effects are confined to a thin layer near a fluid interface, typically (but not necessarily) a solid boundary or wall. Under the assumption of a thin boundary layer, span-wise and stream-wise derivatives of the Reynolds stresses can be neglected on an order of magnitude comparison. Experimental studies have verified (Rotta, 1962) that the neglected values are in fact small relative to the other quantities of interest. The boundary layer equations are:

the x-direction momentum equation,

$$U \frac{\partial U}{\partial x} + V \frac{\partial U}{\partial y} + W \frac{\partial U}{\partial z} = -\frac{1}{\rho} \frac{\partial P}{\partial x} + \nu \frac{\partial^2 U}{\partial y^2} - \frac{\partial \overline{uv}}{\partial y} \quad (1.1)$$

the z-direction momentum equation,

$$U \frac{\partial W}{\partial x} + V \frac{\partial W}{\partial y} + W \frac{\partial W}{\partial z} = -\frac{1}{\rho} \frac{\partial P}{\partial z} + \nu \frac{\partial^2 W}{\partial y^2} - \frac{\partial \overline{vw}}{\partial y} \quad (1.2)$$

and the continuity equation.

$$\frac{\partial U}{\partial x} + \frac{\partial V}{\partial y} + \frac{\partial W}{\partial z} = 0 \quad (1.3)$$

The y-direction momentum equation reduces to a statement that the static pressure across the boundary layer is constant or  $\partial P / \partial y = 0$ . In order to solve these equations, models for  $\overline{-uv}$  and  $\overline{-vw}$  are needed with respect to the mean velocity gradients and/or other turbulence quantities.

### 1.3 Brief Review of Turbulence Models

As stated previously, turbulence models try to relate the Reynolds stresses ( $\overline{-uv}$  and  $\overline{-vw}$ ) to mean flow or other turbulence parameters. The simplest and earliest models apply the turbulent

eddy viscosity concept. This was first attempted by J. Boussinesq who assumed that a turbulent exchange coefficient  $\nu_\tau$  exists for turbulent flow that defined the Reynolds shearing stress as proportional to the rate of strain, analogous to Newton's law of fluid friction.

$$-\overline{\rho uv} = \rho \nu_\tau \frac{\partial U}{\partial y}$$

or for 3D flow,

$$-\overline{u_i u_j} = \nu_\tau \left( \frac{\partial U_i}{\partial x_j} + \frac{\partial U_j}{\partial x_i} \right) - \frac{2}{3} k \delta_{ij} \quad (1.4)$$

where  $\delta_{ij}$  is the Kronecker delta,  $k$  is the turbulent kinetic energy (TKE) and  $\nu_\tau$  the turbulent eddy viscosity. Turbulence models using the eddy viscosity concept are then classified as to the number or complexity of additional equations that must be solved in addition to equations 1.1 - 1.3. Algebraic models do not employ any transport equations. They simply relate the Reynolds stresses as functions of the mean-flow quantities. An example of an algebraic model is Prandtl's mixing length model,

$$-\overline{\rho uv} = l_m^2 \left| \frac{\partial U}{\partial Y} \right| \frac{\partial U}{\partial Y}$$

or for 3D

$$l_m = \frac{\sqrt{\frac{|\tau|}{\rho}}}{\sqrt{\left(\frac{\partial U}{\partial Y}\right)^2 + \left(\frac{\partial W}{\partial Y}\right)^2}} = \frac{(\overline{-uv^2} + \overline{-vw^2})^{1/4}}{\sqrt{\left(\frac{\partial U}{\partial Y}\right)^2 + \left(\frac{\partial W}{\partial Y}\right)^2}} \quad (1.5)$$

One and two equation models imply that the value of either one or two model parameters is obtained by solving a differential equation describing the transport of that parameter in the flow. The most popular two-equation model is the k- $\epsilon$  model (Schetz, 1993) which uses a partial differential equation for the transport of TKE ( $k$ ) and one for the dissipation rate of TKE ( $\epsilon$ ).

Higher order turbulence models can be developed through the development and use of turbulent transport equations. These equations are obtained by manipulating the N-S equations and applying the Reynolds decomposition. They represent the rate of change of the desired quantity and are sometimes called second moment equations. The equations typically include

convection, diffusion, generation, dissipation and redistribution terms. Some examples of transport equations are;

the transport of  $-\overline{uv}$  stress,

$$\frac{D(-\overline{uv})}{Dt} = \overline{v^2} \frac{\partial U}{\partial y} - \frac{\overline{p'}}{\rho} \left( \frac{\partial u}{\partial y} + \frac{\partial v}{\partial x} \right) + \frac{\partial}{\partial y} \left( \frac{\overline{p' u}}{\rho} + \overline{uv^2} \right) - \nu (\overline{v \nabla^2 u} + \overline{u \nabla^2 v}) \quad (1.6)$$

the transport of  $-\overline{vw}$  stress,

$$\frac{D(-\overline{vw})}{Dt} = \overline{v^2} \frac{\partial W}{\partial y} - \frac{\overline{p'}}{\rho} \left( \frac{\partial w}{\partial y} + \frac{\partial v}{\partial z} \right) + \frac{\partial}{\partial y} \left( \frac{\overline{p' w}}{\rho} + \overline{v^2 w} \right) - \nu (\overline{w \nabla^2 v} + \overline{v \nabla^2 w}) \quad (1.7)$$

and the transport of  $\overline{v^2}$  stress.

$$\frac{1}{2} \frac{D(\overline{v^2})}{Dt} = -\overline{v^2} \frac{\partial V}{\partial y} - \frac{\partial}{\partial y} \left( \frac{\overline{v^3}}{2} \right) - \frac{\overline{v}}{\rho} \frac{\partial p}{\partial y} + \nu (\overline{v \nabla^2 v}) \quad (1.8)$$

These equations introduce several terms which must also be modeled to obtain closure.

Other models also exist which are not related to the eddy viscosity concept or to turbulent transport equations. Townsend (1956, 1st ed.) proposed an algebraic "structural" parameter,  $a_1$ , which assumes proportionality between the Reynolds shear stress and twice the TKE.

$$a_1 = \left| \frac{\tau}{\rho} \right| / \overline{q^2} = -\overline{uv} / (\overline{u^2} + \overline{v^2} + \overline{w^2})$$

or for 3D,

$$a_1 = \sqrt{-\overline{uv^2} + -\overline{vw^2}} / (\overline{u^2} + \overline{v^2} + \overline{w^2}) \quad (1.9)$$

This parameter approximates a constant over a large portion of 2D TBLs and is assumed to be constant in modeling efforts.

## 1.4 The Relationships Between 2D and 3D TBL Models

The turbulence models mentioned, above among many others, have achieved reasonable success in 2D turbulent boundary layers. Some models are applicable with reasonable accuracy generally in 2D flows. Others apply to specific regions of 2D flows or to particular flow geometries or pressure gradient configurations. Over the past few decades, turbulence modeling research for complex 3D flows has focused on the calculation of 3D flows through experimentation and the extension of concepts that were derived for 2D flows. In general this extension of concepts has failed to accurately model the 3D flows. An important consideration in modeling 3D TBLs is the choice of coordinate system or the development of parameters that are independent of coordinate transformation.

In 2D TBLs, the directions of the shear stress vector and the mean velocity gradient vector are necessarily coincident. Turbulence models which extend the eddy viscosity hypothesis from 2D to 3D flows often assume an isotropic eddy viscosity, or more specifically, that the span-wise and stream-wise components are equal. This is generally not the case as has been shown by various 3D experiments including the ones in this study. The anisotropy can be determined by evaluating the ratio of the spanwise eddy viscosity ( $\nu_z$ ) to the streamwise eddy viscosity ( $\nu_x$ ). This is the anisotropy parameter or  $N$ .

$$N = \frac{\nu_z}{\nu_x} = \frac{\tan(SSA)}{\tan(FGA)} = \frac{\overline{-vw}}{\frac{\partial w}{\partial y}} \bigg/ \frac{\overline{-uv}}{\frac{\partial u}{\partial y}} \quad (1.10)$$

For isotropic flow  $N$  should equal one. Deviations from one indicate that the flow is anisotropic and the 2D eddy viscosity concept will fail. The  $N$  parameter is dependent on the choice of coordinate system.

Another indicator of the flow anisotropy, and that structural changes in the flow are the cause of the anisotropy, is the relationship of the flow gradient angle (FGA) to the shear stress angle (SSA). If these angles do not coincide, the flow is anisotropic. For most 3D flows, the shear stress angle lags the flow gradient angle. When this occurs the value of  $N$  is less than one. There are a few cases that report a value of  $N$  that is greater than one (for example the convex curvature case of Baskaran *et. al.*) which indicates that the SSA actually leads the FGA.

In an attempt to model the anisotropy of the flow, Rotta (1977) developed the  $T$  parameter. It is an anisotropy parameter independent of coordinate system choice. He derived it from



transport equations 1.6 and 1.7 approximated for thin shear layers. After some manipulation, he arrived at the following equation:

$$\tan(SSA - FA) = T \cdot \tan(FGA - FA) \quad (1.11)$$

where FA represents the local flow angle. This parameter is sometimes referred to as N (but defined as in eq. 1.11) or N'. Observation of the T parameter in 3D experimental flows illustrate that it does not attain a value of unity either. Combined with the other anisotropy considerations mentioned, it can be stated that 3D TBLs are generally anisotropic and that models that are extensions of the eddy viscosity concept will not accurately model the 3D flow field.

The  $a_1$  structural parameter is independent of coordinate system choice when  $y$  is chosen normal to the surface. For 2D flows, this parameter maintains a fairly constant value of 0.14-0.15 over a fairly extensive region of the TBL. When observed in 3D TBLs, the  $a_1$  structural parameter is changed from the 2D value. This is an indicator that the development of the shear stresses and TKE differ from each other and from their interaction in 2D flows.

Turbulence models must accurately represent the physics of the flow field. There are several differences between 2D and 3D TBLs. A 2D TBL has only one significant rate of strain which is  $\partial U / \partial y$ . Three-dimensional TBLs are characterized by additional rates of strain as well as lateral pressure gradients and the presence of crossflow. A representation of a typical pressure-driven 3D TBL is given in Figure 1.1. (A shear-driven profile is represented in Figure 2.5.b for the experiment of Littell and Eaton) Some physical aspects of the 3D flow that must be accounted for are the transport of Reynolds stresses by the mean flow, the redistribution of the turbulent energy between the various Reynolds stresses by the secondary flows, the effect of lateral pressure gradients on the slower moving fluid near the wall, the modification of sweeps and ejections and their impact on the production of Reynolds stresses in the near wall region. The near wall region can have significant effects on the overall characteristics of the TBL and must not be neglected (Simpson, 1995, 1996). Evidence of these effects have been observed in experiment. For example, Driver and Johnston observed that near the wall the TKE responds to modifications in the rate of strain field slower than the Reynolds shear stresses. Away from the wall neither reacts to change very rapidly. They also inferred that the streamwise vorticity interfered with the turbulence. They showed that existing models fail to predict the flow accurately. They fail to predict a decrease in the  $-\overline{uv}$  stress at the onset of three-dimensionality in the experiment of Driver among other shortcomings.

This modification of the physics of 3D flow fields is represented by lags in various quantities. The development of the Reynolds stresses are seen to lag the modifications to the rate of strain field. The stresses maintain a slow response to directional changes in the strain rate. A decrease is also seen in Reynolds stress from values typical of 2D TBLs. This is due to a lack of production through the additional strain rates, modification of the boundary conditions and the response to these changes, and the redistribution of the turbulence energy through the pressure-rate-of-strain terms of the transport equations.

Turbulence modeling efforts for 3-D flow situations that are currently employed rarely account for the lags in the flow. This indicates a need for a set of equations that can account for lags in the flow structure. Simpson (1995) proposed the use of equations 1.1 - 1.3 and 1.6 - 1.8 as the minimum set of equations necessary to account for these lags in the various parameters.

## 1.5 Objectives

The research presented here focused on the development and evaluation of algebraic parameters to aid in the modeling of complex three-dimensional turbulent boundary layers. A main objective was the development of useful relationships involving the turbulent triple products appearing in the transport equations for the turbulent shear stresses (equations 1.6-1.8). Other algebraic parameters involving only the Reynolds stresses, sometimes introduced in former publications, were also evaluated with respect to the data sets considered in this study and compared to the prior results. A diverse selection of experimental data from several previous investigations with different types of three-dimensionality was used.

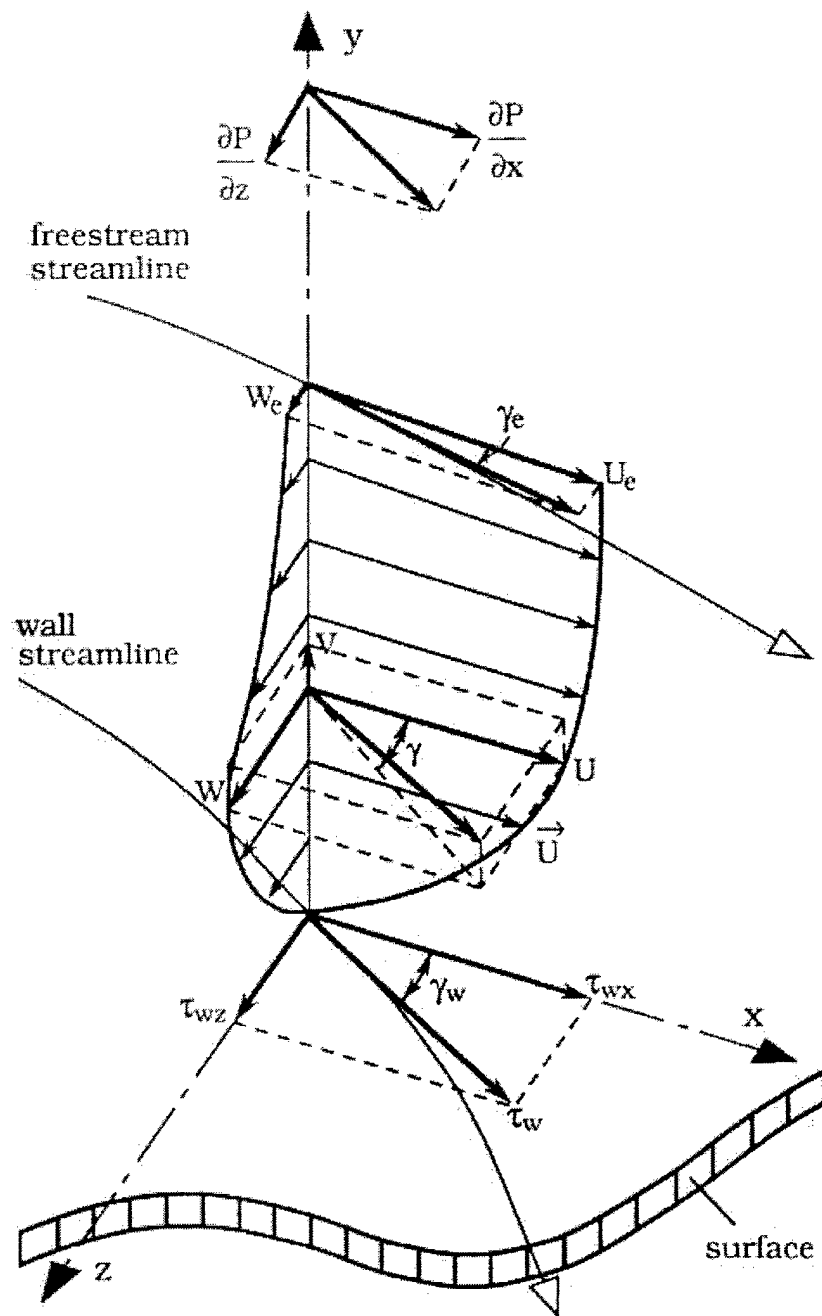


Figure 1.1 The representation of a typical wall-bounded pressure-driven turbulent boundary layer. (Figure 1.1 from Pompeo, 1992)

## Chapter 2 Experimental Test Cases

### 2.1 Introduction and Discussion of Criteria for Experiment Selection

There have been several experiments performed on three-dimensional (3D) turbulent boundary layers (TBLs) with various geometries and regions of interest. Reviews by Johnston (1976), Fernholz and Vagt (1981), van den Berg (1987), Anderson (1987), Littell and Eaton (1991), Pompeo (1992), and Schwarz and Bradshaw (1992) illustrate the range of experiments that were performed and exist in the literature base. These previous experiments documented the Reynolds stress tensor, or most of its components, in primarily the outer layer. Recent advances in measurement and sensor technology have permitted the investigation of regions of the flow down to  $y^+ \approx 3$  in 3D TBLs (Simpson, 1995). These, and other, advances have allowed for the determination of the  $\overline{vw}$  Reynolds shear stress and higher order fluctuating velocity products with less uncertainty than previously possible. The determination of the turbulent triple products allows the evaluation of several terms in the Reynolds-averaged transport equations for the turbulent kinetic energy (TKE) and the individual Reynolds stresses. The current study focuses on the examination of existing experimental data sets with regards to several beneficial algebraic relationships. Parameters not previously examined for the data sets were evaluated. Emphasis was placed on experiments that reported values of the triple products. Another primary goal was the development of algebraic parameters to relate the triple products appearing in the set of transport equations outlined in chapter one.

The experimental data sets chosen for this study were scrutinized using the realizability conditions of Schumann (1977). These conditions must be satisfied by a turbulence model to guarantee realizable solutions for any realizable initial and boundary conditions. There are three conditions that were checked for the Reynolds stress components at every point for every data set. The first requires non-negative energies, i.e., the terms on the diagonal of the Reynolds stress tensor can not assume a negative value. The second condition requires that the cross-correlation between any two fluctuating velocity components be bounded by the magnitude of the autocorrelations. This can be seen as, the correlation coefficient formed by the desired Reynolds shear stress squared, normalized by the normal stresses that form it, being less than unity.

$$\left(\overline{u_{ij}}\right)^2 \leq \overline{u_{ii}} \cdot \overline{u_{jj}} \quad \text{or} \quad \frac{\left(\overline{u_{ij}}\right)^2}{\overline{u_{ii}} \cdot \overline{u_{jj}}} \leq 1 \quad \text{where } i \neq j$$

The third condition requires that the determinant of the Reynolds stress tensor is greater than or equal to zero. It is a statement that the three cross-correlations can not attain arbitrary values. All of the data used in this study met the three conditions outlined above. Three data points from the McMahon *et. al.* data set did not meet the realizability conditions and were discarded from the study. Several data points from the Devenport and Simpson (1990) data set also failed these conditions and were discarded.

## **2.2 Description of Individual Test Cases**

A summary of the data sets that were examined is presented in Table 2.1 with a brief description of several important characteristics of the experiment. The remainder of this chapter is dedicated to a description of these experiments, the important results and observations that were illustrated by the authors, and observations and comments arrived at during this study that concern the previous commentary. In particular, discussion of the results of each experiment will focus on the anisotropy of the flow and the parameters outlined in chapter one.

### **2.2.1 The Experimental Juncture Flow of McMahon**

McMahon, Hubbart, and Kubendran (1982) obtained three mean velocities and the full Reynolds stress tensor in a juncture flow. The juncture was formed by a body of constant thickness with a 3:2 elliptical leading edge mounted normal to a flat plate and parallel to the approaching flow (figure 2.1). The juncture flow is similar to the wing-body junction flows studied by Devenport and Simpson (1990), Ölçmen and Simpson (1995), and Dechow (1977). A horseshoe vortex is formed as the approaching flow separates and forms a vortex sheet that wraps around the body. A schematic illustrating the general characteristics of this flow is shown in Figure 2.1.a. Hot-wire anemometers were used to make measurements in planes at two stream-wise locations, 165 mm and 902 mm downstream of the leading edge of the plate.

Prandtl's secondary flow of the first kind (Bradshaw, 1987a, b) occurs when a shear layer is skewed about an axis parallel to the plane of the mean shear, resulting in a component of mean stream-wise vorticity. The vortex lines in the approaching flow which are initially perpendicular to

the mean flow are bent by the streamlines that become curved due to presence of the plate. This results in stream-wise vorticity.

The facility employed was a large-scale low-speed open jet tunnel at the Georgia Institute of Technology in the United States. The test section is illustrated in Figure 2.1.b. The open jet tunnel was chosen to reduce the effects of blockage and adverse pressure gradients due to the development of wall boundary layers. The free-stream turbulence intensity near the exit of the test section was 0.5%. The body consisted of 3:2 elliptical nose mated to a plate of constant thickness of 57.9 mm. The body was 1.22 m in length, 609.6 mm high, and was mounted perpendicularly to the floor of the test section. It was aligned with the wind tunnel axis to within  $\pm 0.5^\circ$ . To insure turbulent flow, a roughness element was attached 24.5 mm downstream of the leading edge and had a width of 6.35 mm. The hot-wires were constructed to minimize the blockage but induced stream-wise vorticity production. Two needle supports projected through the floor of the test section and were connected by the wire (figure 2.1.c). The actuator was located beneath the floor of the tunnel test section. One straight wire and one slant wire ( $45^\circ$ ) were used individually. The experimental rig was arranged such that the probe could be rotated about an axis through the center of the probe. The straight wire was able to measure to 0.51 mm away from the wall, but the slant wire could only move to 2.29 mm above the wall.

The uncertainty in the flow angle was reported to be  $\pm 1^\circ$ . The uncertainty in the y and z locations were  $\pm 0.051$  mm and  $\pm 0.10$  mm respectively. The data for the velocity components were not obtained simultaneously. The two wires were used sequentially with the slant wire oriented parallel to the desired measurement plane in two orientations  $180^\circ$  from each other. The uncertainty in the tunnel flow velocity was  $\pm 0.5\%$ . Data was reported in a (local free-stream) laboratory coordinate system. They measured the data in a coordinate system that was aligned with the local flow angle (s-y-n system). This meant that the probes were aligned to the local flow angle for each y-location of each profile. The experiment was performed at a free-stream velocity of 15.24 m/s, corresponding to a Reynolds number of 984,000 /m. The turbulent boundary layer without the plate installed was 22.9 mm thick at the location where the leading edge would be.

They reported three mean velocities and six Reynolds stresses for each profile. They verified the existence of the secondary flow by mapping the mean velocity in the y-z planes at the two x locations. They showed the existence of the horseshoe vortex in these planes. The vortex was confined to a region extending from the body to 51 mm away at 165 mm downstream from the leading edge. At 902 mm downstream from the leading edge, a smaller vortex was observed very near the body exhibiting rotation in the opposite sense, clockwise looking downstream, from the main vortex. They showed that the main vortex diffuses and moves slightly away from the body at

the downstream location. They determined that the core of the vortex was located at  $z = 32$  mm and  $y = 8.9$  mm for the upstream station and  $z = 44$  mm and  $y = 17.8$  mm at the downstream station. They suggested that the strong secondary flow was contained within a narrow region near the body surface. In a comparison with other similar studies, they indicated that weaker junction vortices tended to remain closer to the body. They also mentioned that the weaker vortex from the previous study tended to be closer to the wall at the upstream station decreasing in height as it moved downstream, whereas their stronger vortex moved farther away from the wall as it progressed downstream. The maximum difference in the flow angle across the layer for the upstream station was approximately  $12^\circ$  and occurred at the core of the vortex. For the downstream plane, the maximum difference in the local flow angle was approximately  $4^\circ$  and appeared outboard of the vortex core. This flow was different from the traditional concept of a boundary layer flow, specifically in the fact that it had a significant velocity component normal to the wall, which is assumed to be small in the boundary layer assumptions. This major difference should be accounted for when this flow is compared and contrasted to the other experiments that were investigated in this study.

They plotted the local mean flow angle as a function of  $y$  for a few stations to illustrate flow angle as a function of  $x$ ,  $z$ , and  $y$ . They presented plots of the mean velocities and the Reynolds stresses. They illustrated the fact that high momentum fluid was transported by the secondary flow towards the wall near the body and that low momentum fluid was ejected from the floor away from the body. They noted that the turbulence quantities, when compared to the values for undisturbed 2D TBLs (in a local free-stream coordinate system), were redistributed by the secondary flow. The  $u'$  normal stress indicated an equilibrium in the wall layer, by a collapse of the profiles onto each other for each measurement plane, and was augmented near the core at the upstream station. The  $v'$  and  $w'$  normal stresses tended to be reduced between the body and vortex core and increased in the region away from the secondary flow. These effects were more pronounced at the upstream station. The Reynolds shear stresses were reported to be transported by the mean flow. They were small near the surface and  $\overline{uv}$  was reported as negative in the downstream plane. Significant values of  $\overline{uw}$  were reported for this flow. The Reynolds shear stresses were highly distorted near the vortex core. The stations furthest outboard from the body were effectively in a 2D TBL and were considered so for comparison. The wall shear was not determined, nor were any triple products. The boundary layer thickness ( $\delta$ ) was not reported for this experiment. A few points in this flow did not meet the realizability conditions of Schumann and were discarded from the results of the present study.

### 2.2.2 The 'Infinite' Curved Swept Wings of Baskaran and Bradshaw

Baskaran, Pontikis, and Bradshaw (1990) obtained mean flow and turbulence data in curved ducts that were constructed to simulate the pressure gradients on curved infinite swept wings. Two test cases were examined, one with convex curvature and one with concave curvature. Their experiment was part of a series of experiments concerning "complex three-dimensional flows" at Imperial College in England. It complimented an 'infinite' wing experiment performed at the Netherlands NLR by van den Berg *et. al.* (1975) and Elsenaar and Boelsma (1974). Previous studies have shown that the effects of convex and concave curvature are different. Concave curvature tends to increase turbulent mixing and produce Taylor-Görtler roll cells. Convex curvature tends to suppress turbulent activity. Strong surface curvature causes large changes in the turbulence structure across the entire boundary layer including the near wall region. They predicted the curvature effects in the present case to be seen in the outer layer where the large-scale eddies exist. They did not attempt to measure the near-wall region but expressed the need for future experiments of this general configuration to determine the effects of convex and concave curvature on the near-wall flow structure.

Their results illustrated only a small modification of the turbulence structure for the combined effects of mild surface curvature, either convex or concave, and mean flow three-dimensionality. The increased cross flow in the concave case tended to reduce the Taylor -Görtler vortices that were observed in the earlier two-dimensional experiments. The convex case coupled with cross flow reduced the turbulence data less drastically than was expected. Both of these effects considered individually tend to reduce the turbulence intensity. The experiment illustrated that the combined processes can not be treated as a simple linear superposition of the effects and are characterized by a highly non-linear coupling.

The experimental setup consisted of two different test sections that were independently attached to the exit of a blower tunnel. Both had an initially flat entrance section followed by a 35° swept section where the curvature existed (see Fig. 2.2.a for concave curvature and Fig 2.2.b for convex curvature). At the entrance to the curved section was a 6 mm suction slot swept at 35° to simulate the leading edge of a swept wing. A 50 mm wide section of sandpaper located immediately after the slot was included to enhance transition and to thicken the boundary layer. The boundary layer thickness ( $\delta$ ) and momentum thickness Reynolds number at the end of the flat section were 20 mm and 4000 respectively. The radius of curvature ( $\rho$ ) was 2540 mm to give approximately the same  $\delta/\rho$  ratio as the previous studies. They defined this ratio to be the



'curvature parameter' which was 0.008 at the start of the curvature. They adjusted the sidewall geometry to generate 'infinite' swept flow conditions which was verified by span-wise static pressure profiles at several stream-wise locations. The skin friction coefficient for the concave experiment, illustrated in detail by Baskaran and Bradshaw (1987), indicated that the cross flow from the wall on the negative  $z$  side did not reach the region where the measurements were made. This indicated that there was no influence on the measurements from any cross flow originating in the wall region. It also showed that the near wall region measurements would be lacking the cross flow component of the experimental objectives. The flexible roof was adjusted such that the chord-wise (axial) pressure gradient was similar to the previous 'infinite' swept flat wing experiments.

They defined the  $x$ -axis of a tunnel coordinate system to be aligned with the centerline of the initially straight section with  $y$  normal to the surface and  $z$  completing a right handed system. The  $x$ -axis maintained this initial direction throughout the test section and differed from the centerline of the test section. The flow angle at the edge of the boundary layer, with respect to the  $x$ -axis in this tunnel coordinate system, reached a maximum turning angle of approximately  $11.5^\circ$  for the concave curvature and  $10^\circ$  for the convex curvature as reported by Baskaran *et. al.* (1990). This could be classified as a weakly skewed flow that was in a state of development due to a continual increase in the external flow angle. The free-stream velocity for these test cases was nominally 33 m/s which corresponded to  $U_{ref}/\nu = 2.2 \times 10^6$  (Re/m). The effective chord length was 2 m.

For the concave case, the surface shear stress vector's direction was measured by using a three-hole surface yaw meter with a diameter of 0.7 mm in non-null mode. The magnitude of the surface shear stress vector was measured with a Preston tube with a 1.1 mm diameter. The Preston tube was aligned with the direction of the shear stress vector as measured above. The calibration used for the Preston tube assumed that the 2D law-of-the-wall holds for 3D flow. The mean flow measurements across the boundary layer were performed using a three-hole probe with a 0.89 mm diameter in non-null mode. For the convex case, the magnitude of the shear stress vector was measured with a Preston tube with the same diameter as above and a three-hole probe as described above. Both were aligned with the surface flow direction. The same three-hole probe was then nulled in the boundary layer to measure the mean velocities. They then obtained the surface flow direction by extrapolating the cross flow-angle profiles towards the wall. Turbulence data were obtained through the use of crossed hot-wire probes which were statically calibrated before each profile. The tests were conducted with the axis of the probe parallel to the tunnel axis. They measured all six components of the Reynolds stress tensor, all ten triple products, and the fourth order moments of the normal fluctuating velocities. The  $v$  and  $w$  fluctuating correlations

were determined by rotating the probe to planes at  $\pm 45^\circ$  such that a velocity vector containing both  $v$  and  $w$  was measured. The  $-\overline{vw}$  shear stress and the triple products involving these fluctuating velocities were "deduced as sums and differences of the quantities corresponding to these two planes," (Baskaran and Bradshaw, 1987). At each roll angle, 20,000 samples were acquired at a rate of 200 Hz. They report the uncertainty in the measured quantities, at the station with the maximum cross flow with respect to the probe, to be 5% for the normal stress components, 15% for  $-\overline{uv}$ , and 30% for  $-\overline{vw}$  and  $-\overline{uw}$ . The uncertainties were reported in detail in Baskaran and Bradshaw (1987). They reported that the flow angles near the wall for the concave case were overestimated by as much as  $2^\circ$  due to the interference of the flow by the probe in close proximity to the wall. The flow angles near the wall for the convex case are overestimated as well but they do not quantify the uncertainty.

For the concave case, the locations of the stations and the mean flow parameters as measured by the three-hole probe are detailed in Table 2.2.a. The mean flow profiles were presented in a wall coordinate system. A displacement correction of 15% of the probe diameter was applied to the wall distance. A 1.1 mm diameter Preston tube was used to measure the wall skin friction magnitude. This assumed that a law-of-the-wall holds for three-dimensional flow. They cite Fernholz and Vagt (1981) and Pierce and Zimmerman (1973) as verifying that the law-of-the-wall carried over into the three-dimensional flow case from the two dimensional flow case, however Ölçmen and Simpson (1992) illustrated that this was not necessarily the case. The friction velocity was obtained by plotting the resultant mean velocity on a Clauser chart. The direction of the friction velocity was inferred from the law-of-the-wall through the use of an iterative procedure. The results are given in Table 2.2.b for the various stations.

They calculated the integral parameters based on relationships that were illustrated by Cooke and Hall (1962). They are based on a potential velocity rather than an edge velocity but for this case the potential velocity and the edge velocity are very close. The integral parameters for the concave case are given in Table 2.2.c.

They presented Reynolds stress profiles normalized on  $U_{ref}$  verses  $y$  in millimeters in the tunnel coordinate system. They appeared to be consistent with previous experiments but differed a bit from the results of Bradshaw and Pontikos (1985). They claimed that the profiles of  $-\overline{vw}$  at the last two stations are unreliable. The data for the axial skin friction tends to agree with calculations that were made using a model based on two-dimensional characteristics.

The mean flow parameters and station locations for the convex curvature flow case are tabulated in Table 2.2.d. Mean flow profiles were created as described in the discussion of the concave case. They plotted the Reynolds stresses as described above and which tended to agree

with previous experiments. The integral parameters for the convex case are given in Table 2.2.e. The triple product profiles were presented in a previous papers by Baskaran and Bradshaw (1987) for the concave curvature and Baskaran, Pontikis, and Bradshaw (1987) for the convex case.

They plotted the  $a_1$  structural parameter for both cases against  $y/\delta$ . The concave case exposed  $a_1$  to be less than the accepted two-dimensional value of 0.15 with the values near the wall and towards the free-stream attaining lower values for each station. The convex case had values of  $a_1$  that were greater than 0.15 and illustrated a significant amount of scatter in the parameter. The values towards the free-stream also tend to be reduced as the region of entrainment is approached. They plotted transport velocities for TKE and  $-\overline{uv}$  shear stress which were defined as;

$$V_q \equiv \frac{\overline{u^2 v} + \overline{v^3} + \overline{w^2 v}}{\overline{q^2}} \quad (2.1)$$

and

$$V_{uv} \equiv \frac{\overline{uv^2}}{\overline{uv}} \quad (2.2)$$

These transport velocities were plotted against  $y$  in mm and did not correlate very well with each other. It appears that if  $y$  were non-dimensionalized on  $\delta$ , they may have correlated better. They calculated and plotted the anisotropy factor,  $N$ , in local free-stream coordinates. As was seen in many 3D flow cases, this parameter did not maintain a value of unity which implied that an eddy viscosity turbulence model would not apply for modeling this flow. The convex curvature case produced values of  $N$  that were greater than unity and highly scattered across the boundary layer. The concave case tended to be reduced from unity except near the outer edge of the layer where the values began to increase. It was seen that the shear stress lags behind the velocity gradient vector for the concave experiment ( $N < 1$ ) while the shear stress lead the velocity gradient vector for the convex flow case ( $N > 1$ ). They concluded that more experiments involving curvature are needed especially with measurements made in the near-wall region.

### 2.2.3 The Wing-Body Junction of Devenport and Simpson

Devenport and Simpson (1992) performed a detailed survey of the time-averaged and time-dependent properties of an idealized wing-body junction flow. This flow was similar to the juncture flow of McMahon *et. al.*. An appendage-body flow is formed when a boundary layer over

a surface encounters a body protruding from the surface. The upstream time-averaged vorticity was initially oriented in the span-wise direction. A horseshoe shaped vortex with dual legs of stream-wise vorticity was formed about the body where, according to the vortex theorems of fluid mechanics, each leg attained vorticity of the opposite direction. Strong pressure gradients were imposed on the approaching flow in the nose region of the appendage. An airfoil shape, commonly used in applications, was used for the wing. It produced regions of strong flow acceleration between the nose and maximum thickness, and an adverse pressure gradient region towards the trailing edge.

The wing was a 3:2 elliptical nose (major axis aligned to the chord) with a NACA 0020 tail joined at the maximum thickness. The maximum thickness was 7.17 cm, the chord was 30.5 cm, and the height was 22.9 cm (figure 2.3.a). The boundary layer tunnel at Virginia Polytechnic and State University was used for the experiment. It is an open-circuit tunnel powered by a centrifugal blower. The flow passed through a honeycomb, several screens, and a 4:1 contraction before entering the test section. The free-stream turbulence intensity in the tunnel was 0.2% at 27 m/s. The test section was 8 m long and 0.91 m wide and is depicted in Figure 2.3.b. A throat (an additional 1.5:1 contraction) was located 1.63 m downstream of the entrance. In the absence of the wing, the stream-wise pressure gradient was nearly zero. The flow was tripped by the 0.63 cm blunt leading edge of the floor at the leading edge of the test section. Previous work in this 2D flow showed that the statistical and spectral properties of this boundary layer to be similar to equilibrium boundary layers studied by other scientists. Velocity and pressure spectra showed no preferred frequencies. The wing was mounted 1.39 m downstream of the throat with no sweep or angle of incidence. A gap was left between the upper wall and wing to prevent the formation of a second horseshoe vortex on the ceiling. Blockage effects were accounted for by removing plexiglas inserts from the sidewalls.

The data was presented in a right handed coordinate system defined in Figure 2.3.a. The reference velocity was the approach main stream velocity measured at the throat by a pitot-static probe. Measurements were made at three different momentum thickness Reynolds numbers of 2500, 4500, and 6700 based on the reference velocity. The momentum thickness was determined at  $2.15T$  ( $T \equiv$  wing thickness = 71.7 mm) upstream of the wing leading edge. The flow on the wing was tripped to reduce unsteadiness and non-uniformity in the flow over the wing. A 1 mm diameter wire located 28.2 mm downstream of the wing leading edge in the x-direction was used to trip the flow for most of the cases of this experiment. Planes 5, 8, and 10 (see Fig. 2.3c) were tripped with 120 grit sandpaper 6.35 mm wide. Oil-flow visualizations were performed on the wing and the floor. The streaks indicated the direction of the time-averaged wall shear stress which

should be in the direction of the limiting streamlines at the surface. Extensive pressure measurements were made on the floor and wing. Hot-wire surveys were used to determine the mean velocity and three terms of the Reynolds stress tensor. The region of interest was the region surrounding the nose of the wing excluding the zone immediately ahead of the wing. The data used in the present study was obtained by Devenport with a LDV system.

A three-component laser doppler velocimeter system was employed to measure the mean velocities and Reynolds stresses in six planes about the wing. The location of the planes and individual profile points are described in Figure 2.3.c. A Coherent argon-ion laser was used at a wavelength of 514.5 nm and produced a power of 1.5 W. The beam was Bragg shifted to produce four beams of equal intensity shifted by 0, -15, 21.5, and 6.5 MHz. Three sets of transmitting optics were used individually to determine a pair of velocity components. Two sets of beams enter the tunnel through a plexiglas floor, while the third (UV plane) enters from the sidewall. The flow was seeded with dioctyl phthalate smoke produced by an aerosol generator. It was introduced to the flow at the leading edge of the test section. The receiving optics were situated to observe the measurement volume from the sidewall of the tunnel at about 20° downstream of the transmitting optics. The measurement volume for each of the three systems was different. The output signal was processed with a fast-sweep-rate sampling spectrum analyser. This prevented the determination of the Reynolds shear stresses by simple multiplication, so the mean square values corresponding to the difference of velocity components were used to calculate these stresses. The data was corrected for velocity gradient broadening and transit time broadening. The uncertainty in the measured values is reproduced in Table 2.3.

#### **2.2.4 The Axisymmetric Shear Induced Flow of Driver and Johnston**

Driver and Johnston (1990) performed experiments over an axisymmetric cylinder aligned with the direction of the flow. The cylinder incorporated a spinning section which could be adjusted to various rotational rates and was used to establish a 3D shear induced flow field. The walls of the test section were adjusted for separate experiments to establish varying degrees of adverse pressure gradient or zero pressure gradient. The primary objectives of the study were: to find correlations between the degree of mean flow three-dimensionality and the lag and decrease in the Reynolds stresses that is seen for 3D TBLs, to determine if a 3D TBL is more prone to separation due to adverse pressure gradient than a 2D TBL, and to determine the effect of the drop in Reynolds stress on the boundary layers ability to resist separation. The primary measurement

region was just beyond the spinning section where the flow was relaxing from a shear induced 3D TBL towards a 2D TBL.

The experimental facility that was used allowed the effects of the magnitude of shear (three-dimensionality) and adverse pressure gradient to be examined independently or in combination. As the flow progressed along the cylinder, it evolved through several different states. The flow approaching the spinning portion of the cylinder was initially a 2D TBL aligned with the mean flow. Over the upstream portion of the rotating cylinder, only the near wall fluid was affected and was a region of 3D flow. It reached a collateral state by the end of the cylinder where the entire boundary layer fluid was moving in the direction of the wall flow and the flow is essentially 2D in this wall collateral direction. At the downstream edge of the spinning cylinder, a new boundary condition is imposed, the wall was no longer spinning, and the lateral flow near the wall became retarded resulting in a classical 3D TBL. After some distance downstream, the flow field reached a 2D state aligned with the mean flow once again. Figure 2.4.a depicts a graphical description of these regions in the flow. The length of the regions mentioned above all depended upon the specific set of boundary conditions of a particular experiment.

Several different wall velocities and adverse pressure gradients were examined to determine a set of experiments with the maximum effects on the turbulence of both transverse strain-rate and adverse pressure gradient. For pressure gradient variation, they had four separate cases that were designated with letters. Case A had parallel walls with  $dP/dx = 0$ . For case B, the side walls diverged and mild suction was applied at  $x = -180$  mm (mild  $dP/dx$ ). In case C, the side walls diverged with strong suction applied at  $x = -180$  mm (strong  $dP/dx$ ). And in case D, the side walls diverged with strong suction at  $x = -4$  mm (strong  $dP/dx$ ). The stream-wise pressure gradient in the upstream half of the test section was zero due to the divergence of the walls to allow for boundary layer growth. The downstream half had adjustable top and bottom walls and several sets of rigid side walls to vary the adverse pressure gradient. The rigid side walls had three geometries; the zero pressure gradient configuration, a set that diverged 1060 mm downstream of the entrance to the test section (corresponding to the junction between the spinning and stationary cylinders), and one that began diverging at 833 mm downstream of the entrance to cause an adverse pressure gradient on the spinning cylinder which grew to a maximum at the end of the spinning cylinder. Boundary layer suction was applied to all four walls 38 mm upstream of the start of the wall divergence and removed the inner third of the boundary layer. This resulted in approximately a 10% mass flow removal and caused an additional adverse pressure gradient. In case B, suction was too small to prevent separation in the corners of the diverging section. In case C, corner separation was avoided but separation occurred on the body at  $x = 50$  mm reattaching at

225 mm. Case D had an identical sidewall diffuser shape as in case C and the boundary layer is nearly detached by 225 mm. The pressure at the boundary layer edge,  $\delta$ , was determined by LDV measurements and Bernoulli's equation. Static pressure outside the boundary layer was nearly equal to the pressure measured on the cylinder's surface. For all cases, the pressure gradient began upstream of the wall divergence. The pressure distributions were nearly the same for spinning and non-spinning cases. With the cylinder spinning, case C remains attached. Four spin rates ( $W_s/U_r$ ) were considered 0/30, 15/30, 30/30, and 30/15 equal to 0, 0.5, 1.0, and 2.0 and were denoted as S0, S1/2, S1, and S2 respectively.  $W_s$  corresponds to the transverse velocity on the surface of the rotating cylinder and  $U_r$  corresponds to the upstream free-stream velocity. Figure 2.4.b illustrates a typical experimental setup. Case D focused the pressure gradient on the truly 3D part of the flow, the other cases turned it on the upstream part of the test section. Pressure gradient effects on 3D flow field can be observed by comparing cases A.S1, B.S1, C.S1, and D.S1. Effects of transverse strain are not easily distinguished. Comparison between spinning and non-spinning cases are obscured by curvature and rotational effects. The spinning cases caused the boundary layer to grow at a faster rate due to a destabilization rate generated by a normal pressure gradient. This generated different upstream boundary conditions and downstream differences that were not generated by the turbulence. However, the upstream boundary conditions of D.S1, C.S1, and B.S0 were nearly the same and can be compared to determine the differences between the spinning and non-spinning cases. Case D.S1 was the most useful experiment, where two extra strain rates,  $\partial W/\partial y$  and  $\partial U/\partial x$ , are imposed at the same location in the flow field. Case A.S1 is also very useful in that it serves as a baseline case. They disregard case B.S1 based on a poor momentum integral balance due to the separation in the corners being unbalanced. Cases C.S0 and D.S0 separated at  $x = 50$  and  $x = 300$  mm respectively.

The test section and measurement techniques were devised to produce the least amount of flow interference and uncertainty in the measurements. The spinning and non-spinning cylindrical sections were equal in diameter to within  $\pm 0.04$  mm ( $y^+ < 4$ ) and the vibration was minimized to less than  $\pm 0.03$  mm ( $y^+ < 3$ ). The flow was determined to be reasonably axisymmetric. Primary measurements were obtained on the downstream stationary section where the flow was a 3D TBL relaxing to a 2D state. Two 51 mm sandpaper trips were attached to the stationary cylinder upstream of the spinning section at 230 mm and 305 mm upstream of the spinning section. Nominal  $U_{fs}$  were 15 m/s and 30 m/s with 1% and 0.6% turbulence intensities respectively. The spinning section of the cylinder was 914 mm long and was rotated at circumferential speeds of 0, 15, and 30 m/s. The boundary layer thickness,  $\delta$ , at the end of the spinning section for  $W_s = U_s = 30$  m/s was 27 mm and for  $W_s = 0$  and  $U_s = 30$ , it was 18 mm. This produced a  $Re_\theta$  of 6000 and

4000 for these two conditions. The maximum pressure gradient was at  $x = 0$  mm. Probes were avoided due to the fact that in an adverse pressure gradient case, the wake of the probe can affect the upstream flow. Surface pressure was obtained with 0.3 mm diameter static pressure taps in the stationary cylinder. The accuracy in  $C_p$  was better than  $\pm 0.01$  based on repeat runs. Surface pressure on the rotating portion was obtained by attaching static pressure tubes to the surface while the cylinder was not spinning. Surface skin friction was measured with a two beam laser-interferometer oil-flow technique (no correction was applied to correct for the effect of an adverse pressure gradient effects on the oil since it was determined to be negligible). The oil thickness was 10  $\mu\text{m}$  and the major source of error was assumed to be generated by scratches in the finish on the order of 1  $\mu\text{m}$ . The uncertainty in  $C_f$  was estimated to be  $\pm 10\%$  of the measured value. Preston pitot tube measurements were made to determine the skin friction where there was no significant crossflow. An oil flow visualization was performed and determined the surface flow direction to within  $\pm 1.5^\circ$ . All three components of velocity were determined through the use of a three color LDV system (Blue, 488 nm, Green, 514.5 nm, violet, 476 nm) where one beam of each color was Bragg shifted by 40 MHz and the beam angles were generally  $8^\circ$ . The receiving optics was placed in a direction  $30^\circ$  off of forward scatter mode. Velocity bias corrections were used to obtain mean  $U$ ,  $V$ , and  $W$  to  $\pm 0.3$  m/s (1% FS) and  $\overline{u^2}$ ,  $\overline{v^2}$ , and  $\overline{w^2}$  to  $\pm 10\%$  of local values. Reynolds shear stress values were determined with an accuracy of  $\pm 5\%$  of the rms values when multiplied to form the proper product ( $u_i' u_j'$ ). Triple product quantities have an accuracy of  $\pm 4\%$  of  $u_i' u_j' u_k'$ . Pressure fluctuations induced by the fan were less than  $\pm 1\%$  of the dynamic pressure at 25 Hz. It should be noted that skin friction for case B was obtained in off design conditions and should be used qualitatively only. Data were obtained for distances from the wall of  $y^+ > 20$  through the edge of the boundary layer.

At the upstream stations the flow behaved like a 2D TBL traveling in a  $-45^\circ$  direction. The turbulent kinetic energy decayed as the flow progresses downstream due to the removal of the production caused by the wall. The absence of the transverse strain removed the direct production of  $\overline{w^2}$ . The  $\overline{v^2}$  normal stress magnitude dropped too since its growth is related to redistribution by the pressure-rate-of-strain terms. Therefore in this flow,  $\overline{u^2}$  was the only Reynolds normal stress left being produced and the others fed off of it causing its reduction. The  $-\overline{uv}$  Reynolds shear stress decayed downstream but it does not directly depend on the transverse strain as for the TKE. Its level can drop as a result of a decrease in  $\overline{v^2}$ . It decayed to levels lower than observed in 2D flows which was assumed to be caused by three-dimensionality. They employed an axial momentum equation to ascertain the importance of the various terms. In doing so, they ignored the laminar viscous stress. The Reynolds stress terms were large only near the wall in comparison to



the convection and pressure gradient terms. Near the wall, the stress acts to balance the pressure gradient and re-energize the mean flow. Away from the wall, the small amounts of shear stress added to pressure forces in extracting flow momentum. Outer layer momentum was transferred to the inner layer and maintained forward motion of the flow near the wall, decelerating the outer flow. (note: in a zero pressure gradient flow the stress would act to retard the flow across the entire layer.) Transverse momentum was lost in the wall region due to Reynolds stresses being produced by the stationary wall. The imposition of an adverse pressure gradient did not affect the direction of the shear stress angle while the flow gradient angle was turned, evidence that the stresses maintain a slow response to directional changes in the strain rate. The imposition of the adverse pressure gradient caused the mean flow angle and the strain rate angle to turn in different directions.

As inferred from the above discussion, the flow behaved anisotropically as seen in other 3D TBL experiments. Driver made his observations of the Reynolds stresses and flow angles in a local free-stream coordinate system. The Reynolds shear stress development was seen to lag the modifications to the rate of strain field. This was observed in qualitative examination of the shear stress development as compared to the mean flow development and also by a direct comparison of the shear stress angles to the flow gradient angles. This implies that a constant turbulent eddy viscosity concept breaks down for this flow and that  $N$  is less than the 2D value of unity. The mixing length, formulated to include the span-wise values of strain and shear stress magnitude, was observed to be lower than the typical 2D values of  $0.09 \delta$ , for the outer layer. This reduction does not seem to exhibit consistent behavior when a number of 3D experiments are compared. A reduction in the shear stresses was seen in the near wall region. This reduction tended to be diffused outward into the boundary layer for downstream stations and adverse pressure gradients tended to increase the magnitude of the reduction. The  $a_1$  structural parameter, which is normally 0.14 - 0.15 and approximately constant across most of a 2D TBL, was reduced by 30%. Adverse pressure gradients are known to reduce this parameter, so part of the decrease was credited to this condition, but the total reduction was due to the combined effects of transverse strain and pressure gradient. Considering that the mixing length was effected greater in the outer layer and  $a_1$  in the inner layer, they inferred that near the wall Reynolds stress adjusts rapidly to the new strain field while the turbulent kinetic energy does not. While, away from the wall neither adjust quickly. They attempted to correlate  $2a_1$  with several parameters, a recommended parameter being the value of  $a_1$  at  $0.1 y/\delta$ . The problem with this correlation being that it does not apply to the flow across the entire boundary layer, but rather is tailored for the flow dynamics about that location. The parameters that they examined seemed to fail to accurately correlate the behavior of  $a_1$ . They

inferred that the stream-wise mean vorticity is somehow interfering with the turbulence. They proposed a model for  $a_1$  that under predicts it across the boundary layer, but they claim that  $a_1$  is more sensitive in the inner layer and this model will not effect the outer layer prediction sufficiently.

They evaluated the behavior of transport equations and several turbulence models for this flow. To evaluate the transport equation for TKE, they used the experimental data, along a path of constant stream function beginning at  $y^+ \simeq 100$  and  $x = -457$ , for all of the terms except the dissipation term which was inferred as the difference of the others. This analysis showed that, in the upstream section, the production and dissipation were nearly equal and opposite. The production of TKE was greatly enhanced by the additional rate of strain from the spinning cylinder. They inferred from this analysis that the TKE evolved relatively slow in comparison to the rates of production and dissipation and imposed a near equilibrium state on the turbulence. The Reynolds stress transport equations were determined similarly but the pressure rate of strain terms were grouped with the dissipation and calculated as the difference from all of the other terms. This term (pressure strain) was nearly equal to the production of the  $\overline{uv}$  stress. The convection and diffusion terms were small relative to the production term for all cases. The transport equation for the  $\overline{vw}$  stress showed that production was the largest term and tended to decay with distance downstream. The convection term was negative indicating a net decay of  $\overline{vw}$  stress as the flow progresses downstream. The convection term was relatively large in comparison to the production term as well.

They performed various calculations with several turbulence models and compared the results to their experimental data. All of the models failed to predict the drop in the  $-\overline{uv}$  stress with the onset of three-dimensionality. This reflects an inherent error in the models with respect to the actual physics of the flow. The models under predicted the  $\overline{vw}$  stress in the outer layer and over predicted it in the inner layer. The TKE was generally under predicted in the entire flow, which is a classical flaw in turbulence models for  $k-\epsilon$  models and is suspected to be caused by errors in the dissipation rate equation. They report that the mixing length models worked the worst of all the models tested. They claimed that even in models where anisotropy is taken into account, the pressure rate of strain models are suspected to be in error.

### 2.2.5 The Rotating Disk Experiment of Littell and Eaton

Littell and Eaton (1991) performed an experiment over a smooth flat disk at various rotational rates in a quiescent ambient atmosphere. This established a truly shear driven flow in

the absence of any pressure gradients. The experimental setup allowed them to vary the amount of shear influencing the boundary layer by simply varying the rotational rate of the disk. Near the disk, the fluid close to the surface felt a centrifugal force proportional to the tangential velocity at that location. This force flung the fluid mass near the disk outward tangentially and new fluid was entrained from above the disk. Figure 2.5.a illustrates the streamlines over the rotating disk. This setup is different from traditional 3D TBL experiments, but it provides a simple test case for comparison with calculations. The configuration eliminated the effects of pressure gradients on the three-dimensionality of the flow field. The boundary layer profile of this flow is shown in Figure 2.5.b. Their main objective was to determine the flow dynamics of an 'infinite rotating disk' and detail the turbulence structure.

The disk was 15 mm thick, 1 m in diameter and lapped to provide a surface deviation better than 10  $\mu$ inches. The disk was situated on a stand which was isolated from the drive motor (figure 2.5.c). Additional measures were provided to dampen vibrations that were transmitted through the drive train. It was determined that the maximum operating speed was 1500 RPM. A test cell was constructed about the experimental apparatus for safety in case the disk would have exploded or been separated from its foundation (figure 2.5.d). The test cell also provided additional temperature control and protection from particular contaminants in the flow. The disk was positioned within an apron, 1/3 of the radius, that extended the flat surface of the disk to isolate the flow above the disk from the flow below the disk. A topless box that could be raised or lowered was attached under the table to additionally separate the flow on the lower surface of the disk from the flow in the room. Vanes were added to the apron to direct the fluid exiting the test zone in a radial direction and remove its angular momentum. This caused the flow in the test cell to assume a toroidal shape as seen by particles injected for flow visualization. A traverse was constructed that mounted to a frame, independent of the drive stand, to minimize the vibrations in the probes. This allowed probes to be lowered to the surface of the disk from above (figure 2.5.c). A gooseneck probe stem was employed to allow rotation of the probe while maintaining the same measurement location. A computer was used to control the disk speed, the traverse, and to acquire and store the data. The traverse allowed the probe to be aligned with the mean flow at each location. It had a vertical resolution of 1.6  $\mu$ m.

Several different probes were used to examine this flow. First, they used a three-hole pressure, Conrad, probe in non-nulling mode. This meant that they calibrated the probe to determine the angle of the flow with respect to the probe axis. Measurements with this probe gave an uncertainty of  $\pm 0.2$  m/s. It was used throughout the flow to investigate the laminar region of the flow near the center of the disk and in the region where the flow had transitioned to fully

turbulent. They used hot-wire anemometers to explore the turbulence structure of the flow. A straight wire was used in the inner region, near the disk center, to examine the laminar part of the flow for comparison with theory. Crosswire hot-wire probes were used to determine the turbulence characteristics in the turbulent regime of the flow. The probes were rotated in  $45^\circ$  increments about the probe stem axis to determine the three mean velocity components, six Reynolds stresses, and ten triple products. For each measurement location, 10,000 samples were acquired at 100 Hz. The probe stem was aligned with the mean flow for the data acquired with these probes. The uncertainties in the Reynolds stress components is given in Table 2.4.a. The probes were calibrated before the final set of data was obtained for each measurement station.

For the turbulence data, nine separate experiments for three different radii and eight different rotational rates are reported. Their study focused on the outer layer and the measurements spanned from  $y/\delta = 0.1$  to beyond the edge of the boundary layer. The various velocities were non-dimensionalized on the momentum thickness due to the fact that the boundary layer thickness was extremely difficult to determine in the absence of an external mean flow. Several of the flow characteristics are listed in Table 2.4.b. The friction velocity,  $u_\tau$ , was determined from a fit to the law-of-the-wall. This provided profiles that seemed to scale on the conventional 2D law-of-the-wall for the U component of the mean velocity as well as the total velocity vector magnitude. The value of the skin friction was also determined from log law fit for each profile. The normal Reynolds stresses were roughly similar in relative magnitudes to those seen in other TBLs. Twice the TKE was seen to be constant with increasing Reynolds number where in other flows, this parameter was seen to decrease with increasing three-dimensionality. By observation of the  $-\overline{uv}$  shear stress, they determined that there is no constant stress layer in this flow. They did not observe a peak in this stress away from the wall as typically seen in other 3D TBLs. The behavior of this stress suggested the existence of major structural differences in this flow. The other shear stresses behaved similarly to what was seen in other 3D TBLs.

They compared various structural parameters between their experiment and five other 3D TBL experiments. The maximum difference in the flow angle was  $11^\circ$  which implies weak 3D effects when compared to the range of available 3D experimental data sets. The ratio of the Reynolds stresses in the plane parallel to the wall to those normal to the wall illustrates the boundary layers preference for stream-wise velocity fluctuations over wall normal fluctuations. An increase in this value points to a decrease in eddy coherence (Littell and Eaton, 1991). The previous experiments showed a monotonic decrease in this parameter as the measurements move away from the wall. However, the present experiment illustrated a peak in this parameter in the outer layer that seemed to decrease and move outward with Reynolds number at a given radius.

The  $a_1$  structural parameter exhibited behavior that was different from any of the other flows that were examined. In the other flows,  $a_1$  is seen to be depressed near the wall with the decrease diffusing outwards downstream. For the disk flow, it reached its maximum (approximately 0.15) nearest the wall and then decreased nearly linearly to the edge of the boundary layer. The shear stress angle was seen to slightly lag the flow gradient angle. Since this lag was so small they could not clearly discern the anisotropy from this type of analysis. The value of the invariant anisotropy factor,  $N_e$  or Rotta's  $T$  parameter, was near unity throughout this boundary layer. This is indicative of a flow that is slowly turning or has had ample time to adjust to the imposition of the crossflow. It was seen by calculations that an isotropic eddy viscosity performed well for this type of flow. If a Coriolis force were acting to redistribute the Reynolds stresses among the various tensor components, the  $u$  and  $w$  fluctuations would have been negatively correlated. This was not the case and the Coriolis effects were determined to be small and did not cause the structural changes in this boundary layer. They suspected that the outer region of this boundary layer was dominated by inviscid irrotational motions as supported by other studies (Littell and Eaton, 1991).

They use the anisotropy invariant map (Reynolds, 1989) illustrated that all of the turbulent data for this flow fell near the axisymmetric expansion line. This is another Realizability test for experimental data or for turbulence models to determine if they produce geometrically realizable states of turbulence. In the outer regions of the boundary layer, the one component state was approached which indicated that most of the energy in the flow was concentrated in a direction parallel to the wall. Also from this analysis, they were able to determine that at the points nearest to the wall, the turbulence was not yet wall dominated.

They investigated the Prandtl mixing length concept formulated such that it was invariant to a coordinate system transformation about an axis normal to the wall (equation 1.5). They compared it to the near wall value of  $l = 0.41y$  and the data are seen to approach this line, but the data were not obtained near enough to the wall for an overlap between the data and the theory. The other data sets are seen to follow this near wall prediction well but deviate from the accepted value of  $0.09\delta$  in the outer layer. Each experiment has a different amount of decrease in the outer region. The disk flow data was decreased less (by approximately only 15%) than the other data sets reported.

They calculated a dissipation length scale which was the ratio of the turbulent kinetic energy to the isotropic dissipation rate,  $L_{EK} = k^{3/2}/\epsilon$ . Here  $\epsilon$  is the isotropic dissipation of TKE. They calculated this length scale and a similar scale with the magnitude of the Reynolds shear stress in the numerator,  $L_{\epsilon\tau}$ , by using a similar model length scale equation with the  $\overline{v^2}$  in the

numerator. The model only seemed to predict the scale  $L_{EK}$  well. This analysis indicated that the dissipation rate was similar to a 2D TBL with the same TKE distribution.

They evaluated the Reynolds stress transport for this data set also. Derivatives with respect to the tangential direction are zero due to axisymmetry and were removed from the equations. The dissipation terms were evaluated as the difference of the other terms. In doing so, they included the fluctuating pressure terms (Pressure Diffusion and Pressure Strain) in the differenced term. The viscous diffusion term was reasoned to be small and was simply neglected. No uncertainties were evaluated for this analysis and it was to serve as a qualitative representation. For the  $-\overline{uv}$  stress in this flow, the production was concentrated much nearer to the wall than a 2D TBL. This also indicated that the outer layer was dominated by inactive motion. Numerical simulations have shown a peak in the turbulent diffusion near  $y/\delta = 0.5$  which were slightly perceivable in the data. The deficiency was attributed to the inability to measure the pressure diffusion terms which attain increased importance in the outer layer. The Coriolis forces were seen to be a one way redistribution of stress from  $-\overline{uv}$  to  $-\overline{vw}$ . The production and dissipation were seen to dominate the transport of the  $-\overline{uv}$  stress. The evolution of the  $-\overline{vw}$  stress was more effected by the Coriolis effect and the rotation than the  $-\overline{uv}$  stress. Due to rotational effects in this flow and coordinate system, a particle with a  $-w$  fluctuation develops a  $+u$  fluctuation (due to the Coriolis effects). A peak was seen in the various terms where  $-\overline{vw}$  changes sign. The rotation tended to cut down on the turbulent transfer of momentum and allowed for a steep velocity gradient near the wall. They also evaluated the transport of  $(2 * TKE)$ . The rotation terms analytically dropped out of this equation which shows that the total TKE budget was not altered by the rotation. This analysis showed the dissipation to be under predicted and for the production to drop off sooner near the wall in comparison to other 3D TBLs.

They summarized that the disk flow is dominated by the near wall region and that inactive motions and reduced entrainment were more prevalent than in 2D TBLs. They were unable to determine the cause of the reduced level of Reynolds shear stress in the disk flow. They hypothesized that the turbulence in a 3D TBL is less efficient at extracting energy from the mean flow field. They also performed a series of two-point measurements in an attempt to determine the structure of the turbulent eddies and other coherent structures. They determined that the log layer structures described by Robinson (1991), the vortical arches with one quasi-stream-wise leg trailing behind, were possible in this flow. However, they were modified in that if the leg fell on the side of the arch towards the disk center, it could product ejections but not strong sweeps. A leg lying on the outboard side of the arch could produce strong sweeps but no ejections. A detailed

description of the analysis is not included due to the difference in the analysis from the focus of the current study.

### 2.2.6 The Converging and Diverging Duct Flows of Pompeo

Pompeo (1992) studied turbulent boundary layers generated in three duct geometries: a 2D duct, a laterally converging duct, and a laterally diverging duct. The blower tunnel had 2D flow characteristics at the inlet and exit to the test section. There were small pressure fluctuations in the flow due to the blower. The test section was designed around a movable table to facilitate the adjustment and precision of the measurement locations and provided a large degree of computer control for the instrumentation. This required that the tunnel be positioned at a  $3^\circ$  angle of incidence to the floor of the test section (figure 2.6.a). The location of the origin of the tunnel coordinate system was at 850 mm downstream of this deflection. They determined that a typical 2D TBL had developed by this point exhibiting no traces of the deflection. No trip was used and transition occurred about 2 m upstream of the deflection. This resulted in a free-stream turbulence intensity of 0.1% at the entrance of the test section and  $\delta = 17$  mm at  $x = 0$ . They measured the stream-wise pressure gradient ( $dU_e/dx$ ) and determined the flow acceleration to be 4% which indicates a weak adverse stream-wise pressure gradient. The reference dynamic pressure ( $P_{ref}$ ), measured at (0,80 mm, 0), was 1000 Pa for all of the experiments. The reference free-stream velocity was  $\approx 42$  m/s for all test cases. The Reynolds number based on momentum thickness ( $Re_\theta$ ) ranged from 4000-4700 (at  $x = 0$  mm) to 25,000 (at  $x = 2500$  mm) in the converging nozzle.

The 2D nozzle (figure 2.6.b) was used to check the wind tunnel and to compare the measuring techniques. It was designed such that the distance from the floor to the roof was increased along the x-direction to account for the growth of the boundary layers on the four surfaces. This resulted in a nearly constant free-stream velocity (acceleration of the flow is mentioned above). The data supplied for the 2D nozzle were corrupted. All of the stations report exactly the same numbers as the first station. Therefore, the data for this nozzle were not used in the present survey.

The converging duct was designed to generate a potential flow with uniform velocity far upstream, far downstream, and along the centerline with a specified  $\partial W/\partial z$  along the centerline. A potential calculation was performed according to theory by Lamb (see Pompeo, 1992) which consisted of a vertical array of sources and a horizontal array of sinks located in a parallel flow (see Figure 2.6.c for the calculation coordinate system). The tunnel walls were determined by

defining streamlines to give a certain inlet and exit area. The  $\partial W/\partial z$  strain rate was specified to be  $-0.015 \text{ s}^{-1}$  at  $x = -500 \text{ mm}$  and  $x = 2500 \text{ mm}$  (experimental tunnel coordinates, Figure 2.6.b) and  $-31.434 \text{ s}^{-1}$  at  $x = 1000 \text{ mm}$ . The cross sections were approximated as rectangles with a constant cross-sectional area where the width was reduced and the height increased along the centerline (see Figure 2.6.c for tunnel geometry). The growth of the boundary layer was not considered in the calculation and resulted in the flow acceleration mentioned above. This meant that they had to measure the flow in great detail to provide a solid test case for comparison with calculations. This duct provided a flow with converging streamlines and tended to increase  $\delta$  as predicted by the additional term in the continuity equation. The flow was initially 2D, became 3D, and relaxed again to 2D conditions.

A diverging test case was created by simply rotating the converging duct  $180^\circ$  about a vertical axis. This case had diverging streamlines which tended to reduce  $\delta$  and affected the turbulence structure through additional vortex stretching in the  $z$ -direction. This resulted in a small deceleration of the flow comparable to the acceleration of the converging duct.

To match the tunnel outlet to the various test ducts, several curved connection ducts were designed. The origin of the experimental tunnel coordinates was  $500 \text{ mm}$  downstream of the location where the connection duct and the test duct were joined (fig 2.6.b). This caused a greater initial acceleration of the diverging test case due to a smaller initial  $x$ -dimension.

Several measurement techniques were evaluated for use in this flow. Single-hole, three-hole, and five-hole pitot tubes of various diameter were used to determine the mean velocity vector, static pressure, and skin friction (using a Preston algorithm). The  $y$  location of each measurement was accurate to within  $\pm 0.01 \text{ mm}$  and the yaw measurement had uncertainties of  $\pm 0.5^\circ$  near the wall and  $\pm 0.2^\circ$  in the outer region. The Preston tube skin friction measurements were determined to be  $\pm 1\%$  uncertain. The use of each type of pitot tube is described in the data supplied with the report (Pompeo, 1992). The skin friction along the centerline of the test section was determined with a skin-friction balance. It could be used off of the centerline, but they relied on the Preston tube measurements in these regions. The uncertainty in the skin friction measurement was about  $\pm 0.03 \text{ N/m}^2$ . Rotatable cross-wire hot-wire probes were used to determine the turbulence characteristics of this flow. Pompeo experimented with several different wire configurations using from one to four wires. They determined that a rotatable cross-wire method would produce the least amount of uncertainty. To reduce the measurement errors due to finite differences in probe geometry, they took advantage of the symmetry of the tunnel and made measurements at locations exactly on opposite sides of the centerline for a given  $x$ -location using the same probe. All of the Reynolds stress components and triple products were determined by rolling the probe about its



stem axis to four different roll angles. The angles were determined to  $\pm 0.6^\circ$ . The probe was not aligned with the mean flow direction but was calibrated in a 3D flow field for several yaw angles and later matched to the proper calibration from the measurement of the mean velocity direction by the three-hole pitot probe (the non-nulling measurement technique). They were able to measure turbulence characteristics down to  $3 \pm 0.05$  mm away from the wall which corresponded to  $y/\delta \geq 0.1$ . They report uncertainties of  $< 10\%$  for the Reynolds stresses and  $< 2\%$  for the mean velocities measured by the pitot tubes but do not report uncertainty in the triple product measurements.

The focus of this experiment was on the centerline where the only additional three-dimensionality was the  $\partial W/\partial z$  rate of strain. In this plane, the  $\overline{uw}$  and  $\overline{vw}$  Reynolds shear stresses should be zero. However in the data that accompanies the Pompeo (1992) report, they report  $\overline{uw}$  shear stresses on the order of 20% of the  $-\overline{uv}$  shear stress. It is assumed that these values are the result of experimental uncertainties and that no  $\overline{vw}$  shear stresses existed in the plane of the centerline.

They calculate the characteristic boundary layer thicknesses from the pitot tube data. The boundary layer thickness,  $\delta$ , was determined as the  $y$  location where  $U = 0.995 U_e$ . Also the displacement thickness ( $\delta^*$ ), the momentum thickness ( $\theta$ ), and the energy thickness ( $\delta_3$ ) were calculated but not reported. They reported that calculation of the skin friction with the Ludwig and Tillman equation systematically overestimated the measured values by  $\simeq 8\%$ . The Preston tubes in the 3D flow were aligned with the tunnel axis and it was assumed that their yaw characteristics varied as a Cosine function. They determined  $\tau_{wx}$  to within 2% and calculated  $\tau_{wz}$  as  $\tau_{wz} = \tau_{wx} \tan(\gamma_w)$  where  $\gamma_w$  was determined by the three-hole probe at  $y = 0.2$  mm. Comparison with the skin-friction balance yielded differences of  $< 2.5\%$ .

Along the centerline, the level of the turbulent stresses was greater than the 2D values for the diverging case and lower than the 2D values for the converging case. The hierarchy of normal stresses,  $\overline{u^2} > \overline{w^2} > \overline{v^2}$ , was observed in all cases. They determined the eddy viscosity and mixing length values along the centerline. The converging case showed that both parameters were lower than expected for a 2D flow. There were smaller differences for the mixing length than for the eddy viscosity. There was very little indication of the flow relaxing to a 2D state from these parameters. For the diverging case, both of the parameters increase from 2D values initially and then relax to values comparable to 2D experiments.

The stations away from the centerline were skewed by a mild span-wise pressure gradient. The normal Reynolds stresses did not illustrate any variation in the span-wise direction and the value of  $-\overline{uv}$  was nearly constant. The  $\overline{uw}$  and  $\overline{vw}$  shear stresses increased away from the

centerline. The maximum difference between the wall stress angle and the local free-stream angle is  $8^\circ$  for the converging and  $5^\circ$  for the diverging flow. The shear stress angle slightly lagged the flow gradient angle for most of the flow but an opposite trend was observed for some regions of the flow. The anisotropy parameter,  $N$ , was  $< 1$  with a minimum at 0.6 for both 3D cases. It tended more towards unity near the wall and attained higher values near the maximum yaw angle. The span-wise variation of the turbulent eddy viscosity was small. The  $a_1$  structural parameter was approximately constant at 0.14 across the layer for both the converging and diverging cases. They claimed that the velocity distributions for this experiment agreed with the logarithmic law-of-the-wall as seen in 2D flows. They also report the calculation of a correlation coefficient for the  $-\overline{uv}$  Reynolds stress (Pompeo *et. al.*, 1993) but do not present the results.

### 2.2.7 The $30^\circ$ Bend Experiment of Schwarz and Bradshaw

Schwarz and Bradshaw (1992) examined the turbulence structure in a pressure driven  $30^\circ$  bend downstream of an initially 2D mean flow. The experiment focused on the outer layer flow and was accompanied by an experiment by Flack and Johnston (1993) in a water tunnel with a  $30^\circ$  bend to examine the near wall flow. The flow downstream of the bend gradually relaxed to a 2D TBL in the absence of a span-wise pressure gradient. This allowed a study of two distinct regions of the flow, crossflow development and crossflow decay. The focus of this study was to examine the physics and the modeling of this flow field.

The experimental facility was an open-circuit low-speed blower tunnel with a 762 mm by 762 mm cross sectional working section. Figure 2.7 shows the test section and the measurement stations. The turbulence intensity in the tunnel was approximately 0.3%. A wire (1.6 mm in diameter) was used to trip the flow at the exit of the 7:1 contraction ( $x = 0$  mm). To a first approximation, the pressure along the centerline was constant. Crossflow from the fluid in the outside half of the tunnel which experienced adverse pressure gradients however imposed some stream-wise pressure gradient effects on the centerline. The Reynolds number based on length of the working section was approximately  $6 \times 10^6$ . Tests were performed at a constant reference velocity of 27 m/s corresponding to a reference dynamic pressure of 1.75 inches of water measured at a distance 108 mm upstream of the exit to the contraction. By the entrance to the bend, the boundary layer thickness had reached about 30 mm which resulted in a momentum thickness Reynolds number of 6000. The tunnel was run at room temperature and atmospheric pressure.

The data acquisition system that they used was computer-controlled. It consisted of the data transducers and the traverse mechanism. Static pressure in the floor was measured by 161 static pressure taps that were flush in the floor arranged in 23 rows of 7. The pressure was determined from an inclined tube manometer to  $\pm 1\%$  of the reading. Surface shear stress was indirectly determined by using a Preston tube and Patel's calibration. They assumed that the law-of-the-wall was valid across the diameter of the Preston tube. A three-hole pressure probe was used to explore the mean velocity field. The tube was aligned with the tunnel centerline and then the yaw angle and magnitude of the mean velocity were determined by a polynomial fit to calibration curves from the free-stream flow field. A correction for wall proximity effects was applied to the near wall stations. Turbulence statistics were obtained through the use of cross-wire hot-wire anemometers. Before each measurement session, the wires were calibrated in the free-stream to determine a calibration. Turbulence measurements were taken in the plane of the wires placed at four different roll angles. At each probe position, 20,480 samples were obtained at a sampling rate of 1000 Hz. Each boundary layer traverse contained approximately 35 points. Three mean velocities, six Reynolds stresses, ten triple products, and the three normal components of the fourth order products were obtained. The probe was placed at 4.5 mm away from the wall at its closest location which corresponded to  $y/\delta \geq 0.1$ . The hot-wire probe was aligned with the mean flow direction as determined by the three-hole probe at each measurement location. The surface flow direction was determined from an oil-flow visualization. This illustrated that the surface flow turned through an angle greater than  $30^\circ$  demonstrating the effect of the span-wise pressure gradient. The surface flow angles were then measured with a protractor and was repeatable to within  $\pm 1^\circ$ . The uncertainties in the hot-wire measurements are given in Table 2.5.a.

They performed measurements at 22 stations along the centerline of the duct and at 14 stations located off of the centerline adjacent to 7 of the centerline stations. A graphical description of the test section with the measurement locations labeled is shown in Figure 2.7. A slight favorable axial pressure gradient developed in the downstream section due to the growth of the boundary layer. The span-wise pressure gradient reached its maximum at about station 10. The direction of the flow near the wall increased rapidly at the beginning of the bend and continued to increase throughout the bend reaching a maximum value of  $20^\circ$  relative to the local tunnel centerline. Downstream of the bend, the angle slowly decayed to approximately  $12^\circ$ . The maximum cross flow occurred at the end of the bend which corresponded to station 12. The maximum difference between the wall-stress angle and the free-stream angle at this location was approximately  $24^\circ$ . The mean  $V$  velocity was determined from the  $U$  and  $W$  three-hole measurements and a  $1/5$  power law. It was determined to be negligible for all analysis prior to the

calculation of the transport equations. The mean velocity profiles normalized on the edge velocity magnitude showed a good collapse from station to station which implied the absence of a pressure gradient. Their velocity profiles matched the law-of-the-wall up to  $y^+ \simeq 250$ . They determined several integral length scales for all of the stations. The boundary layer thickness was defined as the height where  $U/U_e = 0.99$ . The boundary layer thickness grew from 20 mm at the entrance to the test section to about 53 mm at the last measurement location. Some of the integral length scales are reproduced in Table 2.5.b. There was distinct evidence that the flow near the wall was effected prior to the outer layer fluid in this experiment.

Turbulence characteristics showed that  $\overline{u^2}$ ,  $\overline{v^2}$ ,  $\overline{w^2}$ , and  $-\overline{uv}$  attained a maximum closest to the wall and then decayed toward zero as the edge of the boundary layer was approached. These Reynolds stresses seem to continually increase until station 12 where they begin to decrease once again to values comparable to the upstream ones. All three normal stresses increased;  $\overline{u^2}$  and  $\overline{w^2}$  were directly produced and the increase in  $\overline{v^2}$  resulted from a redistribution of the former two normal stresses by the pressure-rate-of-strain terms. The increase in  $-\overline{uv}$  was tied to the increase in the  $\overline{v^2}$  normal stress that is present in the production term for the  $-\overline{uv}$  stress. The  $\overline{vw}$  and  $\overline{uw}$  stresses changed sign at  $y/\delta \simeq 0.3-0.4$  with the earlier stations changing sign at the lower values of this range. A few of the upstream stations did not change sign but just gradually increased across the layer and then decreased as the boundary layer edge is approached, similar to the other stations. The increase in these two shear stresses was much less than the previous stresses and harder to distinguish. The TKE also peaked near the wall and then decreased towards zero as the non-turbulent free-stream was approached. It also increased up through the bend reaching a maximum at the exit of the bend. A peak in TKE developed near  $y/\delta = 0.3$  which persisted into regions where the crossflow rapidly decayed. This showed that the Reynolds averaged structure responded to the three-dimensionality slower than the mean flow for this experiment and illustrated the importance of history effects and their proper modeling in turbulence calculations. The  $\partial W/\partial y$  rate of strain that was added by the 3D section of the tunnel provided the major contribution to the increased production of TKE in this region. The profiles of the  $-\overline{uv}$  stress were very similar to the  $|\tau/\rho|$  profiles since it was the major contributor.

The structural turbulence parameter  $a_1$  was calculated for each station. It was decreased slightly, in comparison to the reduction seen in other 3D TBLs, from the nominal 2D value of 0.15. The average reduction was approximately 20% for  $y/\delta < 0.3$  and 5% elsewhere. They presented the hypothesis that part of the reason why a different reduction is seen from experiment to experiment was due to varying adverse pressure gradients. In the presence of an adverse pressure gradient, the  $\overline{u^2}$  and  $\overline{w^2}$  normal stresses tend to be increased near the wall while the  $-\overline{uv}$  shear

stress is not affected which tends to decrease the value of  $a_1$ . At the downstream locations, an increase in the value of  $a_1$ , beyond 0.15, was observed. They determined that the shear stresses developed slower than the normal stresses (TKE) which was the cause for the reduction in the  $a_1$  structural parameter. They presented results for another structural parameter, the ratio of  $(\overline{u^2} + \overline{w^2})$  to  $\overline{v^2}$  which indicates the preference for velocity fluctuations in a plane parallel to the wall over the fluctuations normal to the wall (see previous comments on the Driver and Johnston flow). This parameter was largest near the wall and decreased slightly as the boundary layer edge was approached. It approached a value of 2 in the region beyond the boundary layer edge which would be its value in purely isotropic turbulence. It was approximately constant over the region  $0.2 < y/\delta < 0.7$  except for the downstream stations that saw a reduction of the parameter in this region. An analysis of the flow gradient angle and the shear stress angle showed that these vectors were initially aligned in the upstream region where the flow was two dimensional and a lag of the shear stress vector with respect to the flow gradient vector became clear at station 10 in the flow. The vectors became more aligned at station 13, but lag effects are still clear in the regions of the flow closer to the wall. The calculation of a coordinate invariant anisotropy factor showed that this factor reduced as low as 0.6 in the crossflow development region and then recovered towards a value of unity downstream. They report values of this parameter for various other flows. They reported that in some experiments, it can be as large as 1.6 and in others as small as 0.1. This experiment ranged similar to the experiment of Littell and Eaton (1991) from 0.6-1.2. This parameter does not appear to maintain a constant value over any region of this flow or exhibit a definite functional dependence.

They calculated and presented an anisotropy invariant map. This was established by expressing the anisotropy tensor in principal coordinates and then applying the desired turbulence conditions (Schwarz and Bradshaw, 1992). This showed that in the 2D region, the anisotropy was greatest near the wall and then approached an isotropic state as the free-stream was approached. This trend was also seen in the 3D region of this flow.

They measured the triple products to compare the terms in the Reynolds stress transport equations. The  $\overline{u^2v}$  and  $\overline{uv^2}$  triple products show similar behavior but are nearly opposite in sign. The  $\overline{v^2w}$  and  $\overline{vw^2}$  triple products are smaller than but similar to the  $\overline{u^2w}$  and  $\overline{uw^2}$  triple product. The terms appearing in the stress transport equations are  $\overline{uv^2}$  and  $\overline{v^2w}$ . The  $\overline{v^2w}$  product has more error involved due to the small magnitude of its products as well as error induced by the two roll angles of the probe that were necessary to determine this product.

They also calculated several vertical transport velocities that implied the effect of the turbulence in transporting the specific quantity in the normal to wall ( $y$ ) direction. The first of

these represented the transport of TKE by the turbulence (equation 2.1). As  $\delta$  is reached, both the top and bottom of this ratio approach zero causing an increase in the uncertainty of this parameter in that region of the flow. The results for the upstream sections show that the TKE near the wall is transported upward by the turbulence. In the bend section of the flow, TKE was transported towards the wall in the near wall regions and in the outer layer, the transport away from the wall was increased with respect to the values seen upstream. This transport velocity maintained a linear region between  $0.2 < y/\delta < 0.7$  but the slope varied from station to station. They formulated a transport velocity for the three Reynolds shear stresses as well (i.e.  $V_{uv} = \overline{uv^2} / \overline{uv} \dots$ ). The  $V_{uv}$  velocity maintains significant correlation from station to station in the region  $0.3$  ( $0.4$  for the downstream stations)  $< y/\delta < 1.0$  and is approximately a linear function of  $y/\delta$ . The  $V_{vw}$  transport velocity is scattered as is the  $V_{uw}$  velocity. The  $V_{uw}$  velocity becomes negative at  $y/\delta < 0.3-0.4$  and is highly scattered in the region closer to the wall. The flatness and skewness (of  $v$ ) are seen to collapse well when non-dimensionalized on the boundary layer thickness. The flatness maintains a constant value near 3 from  $y/\delta = 0.6$  down to the closest measurement location to the wall. This indicates a gaussian distribution of the fluctuating  $v$  velocity component. The region above  $y/\delta = 0.6$  was suspected to be affected by the intermittancy of the boundary layer edge.

They evaluated the various terms of the turbulent transport equations. For the TKE transport equation, they combined the contribution of the pressure fluctuations to the diffusion term with the dissipation term and calculated it as the difference of the rest of the terms from unity. For the stress transport equations, see their discussion in chapter five of Schwarz and Bradshaw (1992) since it is too lengthy to describe here. For TKE, the production and dissipation were nearly equal in the inner layer of the upstream stations and production was largest near the wall. A major difference between the 2D and 3D stations was the increased importance of the advection and turbulent transport terms. They also discussed the transport equations for the three normal stresses which will not be discussed here. The transport of  $-\overline{uv}$  stress showed that the production was the dominant term and the advection and turbulent transport terms became more significant in the 3D regions of the flow. The  $-\overline{vw}$  transport equation revealed a net destruction of this stress due to the right hand turning of the flow. The production (destruction) term was again seen to be dominant with the pressure-strain redistribution term offsetting it. The main changes to the turbulence transport due to the imposition of the span-wise pressure gradient were the increased production and dissipation accompanied by a greater turbulent diffusion. The largest effects were seen in the  $-\overline{vw}$  and  $-\overline{uw}$  stress transport.

### 2.2.8 Ellipsoid Cylinder Experiment of Barberis and Molton

Barberis and Molton (1993) studied the separated flow over a half axisymmetric prolate ellipsoid with a cylindrical extension that terminated in a flat base oriented at  $45^\circ$  to the longitudinal model axis. The major axis of the ellipsoid was 800 mm and the minor axis was 200 mm. The length of the model was 1600 mm along the center of the model, longitudinal body axis (figure 2.8). They performed an extensive study of the flow over this body at several different angles of attack ( $0^\circ$ ,  $10^\circ$ ,  $20^\circ$ ,  $25^\circ$ ,  $30^\circ$ ,  $35^\circ$ , and  $40^\circ$ ) and several different tunnel velocities (10 m/s-90 m/s). The data represented within this report are for an upstream velocity of 50 m/s at  $20^\circ$  angle of attack. This corresponded to a Reynolds number based on model length of  $5.6 \times 10^6$ .

They focused their study on the boundary layer evolution in the regions of separation and on the evolution of a detached primary vortex. They employed several different techniques to detail this flow. They performed surface flow visualizations, surface pressure measurements, three-hole pressure probe measurements in the boundary layer, and three-component LDV measurements. Preliminary flow visualizations in a water tunnel were performed to determine the optimum shape and dimensions for the experiment. Two separate models were constructed to facilitate the tests. One was used for the pressure measurements (both surface and flow field) and the other was used for oil-flow visualizations and LDV measurements. The model used for pressure measurements had a line of 46 surface pressure holes located along a meridian line and had an internal traversing mechanism for the three-hole "cobra" pressure probes (figure 2.8.b). With this model, the whole section could be rotated to measure the pressure at several circumferential angles and the three-hole probe could be traversed in a plane tangent to the body. The other model was solid and the LDV system was external to the model. They defined a body axis that began at the nose of the model and pointed rearward along the centerline of the model ( $XG^1$ ), the other two axes were in a plane orthogonal to this longitudinal axis (figure 2.8.c). (The parameters calculated for the current study take the origin of the X-axis at the nose of the body with positive x pointing towards the aft end of the model). The three-hole probes were able to determine the local stagnation pressure and the local velocity vector in the plane parallel to the surface of the body at that location. The probe was not able to determine the component of velocity that was normal to the wall (assuming that is small in comparison to the U and W velocities). They used a three color (Green 514.5 nm, Blue 488 nm, and violet 476.5 nm) three component LDV system which was able to make measurements in both forward and backward scatter modes of operation. It produced a probe volume of 350  $\mu\text{m}$  with a fringe distance of 15

$\mu\text{m}$ . Two beams of each color were used where one beam was Bragg shifted to determine the direction of the measured velocity component.

The pressure measurements were made over as much of the body as possible in  $1^\circ$  circumferential increments (figure 2.8.b). Use of the three-hole probe was limited up to the region where the vortex was beginning to develop (due to the growth of large  $V$  velocities). Operation of the LDV system in the forward scatter mode was limited to the vertical plane of symmetry of the model (darkest region in Figure 2.8.b). Measurements near the wall were more difficult in backscatter mode due to the lower signal to noise ratio from the reduction in light intensity reflected from the particles and the reflection of laser light from the surface of the model when the probe volume was positioned close to the wall. The backscatter mode was only used in the downstream investigation where the vortex was clearly detached. The LDV system determined three mean velocities and all six components of the Reynolds stress tensor. No triple product data were supplied for this data set. Also, there was no information on the wall skin friction presented.

Near the nose of the model, a separation was observed that caused a sudden transition of the flow from laminar to turbulent. The surface flow patterns between the two angles of attack are similar (figure 2.8.d). It was noted that the secondary separation line formed closer to the leeward plane at  $30^\circ$  compared to the  $20^\circ$  case. The surface pressure distributions were different between the two angles of attack. The vortex at  $30^\circ$  was determined to be more intense than at  $20^\circ$ . The separation lines can be seen on the oil flow visualizations. For the forward scatter mode they performed eleven cross sections in planes normal to the longitudinal axis. In each cross section, boundary layer traverses were performed at five circumferential angles ( $\phi = 190^\circ, 180^\circ, 175^\circ, 170^\circ$ , and  $165^\circ$ ). They saw two regions of the flow, where the flow converged towards the plane of symmetry in the outer zone and where the flow diverged away from the plane of symmetry in an inner zone. They are separated by the location where the mean normal velocity,  $V$ , is zero. They observed a second peak in the  $-\overline{uv}$  turbulent shear stress profiles not typically seen in TBLs (however this phenomena was observed in Ölçmen and Simpson, 1995). They presented a comparison between the flow gradient angle and the shear stress angle for  $\phi = 170^\circ$ . The two vectors were aligned, to within the measurement uncertainties, up to  $XG^1 = 800 \text{ mm}$  where they began to illustrate the anisotropy of the flow in this region.



### 2.2.9 6:1 Prolate Spheroid Experiment of Kreplin and Stäger

Kreplin and Stäger (1993) investigated the turbulent flow about a 6:1 prolate spheroid oriented at angles of attack ranging from  $0^\circ$  to  $30^\circ$  for various Reynolds numbers. The data used here is for a  $10^\circ$  angle of attack with a 30 m/s free-stream velocity and transition to turbulent flow fixed at  $x/L = 0.2$ . The model and streamlines are indicated in Figure 2.9. The model was 2.4 m in length with the probe traversing mechanism mounted within the model such that the instrumentation could be rotated with the model. The Reynolds number based on model length was  $4.8 \times 10^6$ . They measured surface pressures, local wall shear stresses, mean velocities with three-hole pressure probes, and turbulence data with hot-wire probes.

The hot-wire data were obtained at four separate planes normal to the longitudinal axis of the body ( $x/L = 0.48, 0.56, 0.64, 0.73$ ) and at eleven circumferential angles ( $\phi = 0^\circ, 30^\circ, 60^\circ, 90^\circ, 120^\circ, 130^\circ, 140^\circ, 150^\circ, 160^\circ, 170^\circ, \text{ and } 180^\circ$ ). They employed a four sensor hot-wire probe of the Kovasznay type to determine three mean velocities, six Reynolds stresses, and all ten triple products. The effective measuring volume for hot-wires in this configuration was about  $1 \text{ mm}^3$ . They made no corrections to compensate for velocity gradients across the measurement volume during the measurements; however Pompeo (1992) determined these gradients to be the major source of error in a four-wire hot-wire scheme. The mean velocities were corrected later for errors associated with mean velocity gradients. A test of the four sensor probe in a classical flat plate boundary layer illustrated good agreement with the data of Klebanoff (1954) for the normal stresses and the  $-\overline{uv}$  stress. However the  $\overline{uw}$  and  $\overline{vw}$  stresses were slightly different from zero. Data from the 3D case in the plane of symmetry also indicated non-zero  $\overline{uw}$  and  $\overline{vw}$  shear stresses. In the 3D flow near the wall they measured comparably large values of the  $\overline{vw}$  shear stress and state that those values should be disregarded due to the large velocity gradients in the near wall region of the flow. The data sampling rate was 1 kHz taken over an elapsed time of 16 seconds for each probe position.

They note that the streamlines converged on the lee side of the model causing a growth in the boundary layer thickness. They detailed the region where the flow separates from the body and a flow reversal occurs with respect to the meridian lines. They also noted the development of a vortical structure within the boundary layer within the four measured planes. They did not see the development of a second peak in the  $-\overline{uv}$  turbulent shear stresses as pronounced as Molton (1993) did over their ellipsoid-cylinder model. This may be due to the difference in model geometry in the aft region of the particular bodies. This data did indicate an increase in the  $\overline{u^2}$  and  $\overline{w^2}$  normal stresses which is expected in a flow with adverse pressure gradients.

They present plots for  $\phi = 120^\circ, 130^\circ, 140^\circ, 150^\circ, 160^\circ$ , and  $180^\circ$  of the flow gradient angle and shear stress angle as functions of  $y/\delta$ . The plots indicate that the shear stress vector lags the flow gradient vector. As the wall is approached, the angles approach each other. They also show that  $N$  is less than one indicating the flows anisotropy. The data describe no observable trend from station to station in  $N$ , however the values tend to decrease more as the leeward plane of symmetry is approached. The mixing length tended to converge to the expected 2D value ( $l_m = 0.41 y$ ) as the wall was approached but was reduced from the 2D value ( $0.09\delta$ ) by 25%-50% in the outer region of the flow. The  $a_1$  structural parameter was also shown to be less than the 2D value of 0.15. The decrease illustrates no trend and tends to illustrate scattered values, however the values closer to the wall are greater than those away from the wall.

### 2.2.10 6:1 Prolate Spheroid Experiment of Chesnakas and Simpson

Chesnakas and Simpson (1994) studied the three-dimensional turbulent boundary layer about a 6:1 prolate spheroid at a  $10^\circ$  angle of attack (figure 2.10.a). The objective of this study was to determine the complete velocity vector, the Reynolds stress tensor, and triple products throughout the boundary layer and in the cross-flow separation region on the model. The model was 1.37 m long and could be rotated circumferentially about a sting located at the aft end of the model. The experiments were conducted at a nominal free-stream velocity of 50 m/s which resulted in a Reynolds number based on length of  $4.2 \times 10^6$ . The turbulence intensity in the wind tunnel was on the order of 0.05%. The flow was tripped at  $x/L = 0.2$  to stabilize the location of the transition from laminar to turbulent flow.

The measurements for this particular study were performed with a two color (green 514.5 nm and blue 488.0 nm) three-velocity-component LDV system. Two of the green beams are Bragg shifted at different frequencies (-27 MHz and 40 MHz) and one blue beam is Bragg shifted (40 MHz) in order to determine the direction of the particle passing through the probe volume. The transmission and collection optics were mounted within the model to a traverse that moved ( $\pm 2.5$  cm) in a radial direction orthogonal to the longitudinal body axis (figure 2.10.b). A thin Plexiglas window was installed flush with the surface skin of the model through which the measurements were made such that the flow was virtually undisturbed by the instrumentation. This configuration allowed accurate measurements from the boundary layer edge down to  $y^+ \simeq 7$ . The five beams intersect in a probe volume that is 55  $\mu\text{m}$  in diameter with a 5  $\mu\text{m}$  fringe spacing. The data from the three individual velocity signals was obtained in coincidence mode. The data rate varied from

30 samples/second near the wall to 150 samples/second at the edge of the boundary layer and 16,384 samples were obtained at each point.

Data were obtained at five axial locations;  $x/L = 0.4, 0.6, 0.752, 0.762, 0.772$ . For  $x/L = 0.4$  and  $0.6$ , boundary layer profiles were obtained starting at  $0.01$  cm from the surface out to  $2.5$  cm for  $\phi = 90^\circ$  to  $180^\circ$  in  $10^\circ$  increments. At  $x/L$  of  $0.752$  and  $0.762$ , profiles were taken at  $\phi = 120^\circ, 123^\circ$ , and  $125^\circ$ . At  $x/L = 0.772$ , profiles were taken at  $\phi = 105^\circ$  to  $130^\circ$  in  $5^\circ$  increments. An earlier study determined that the primary separation at  $x/L = 0.772$  was located at  $\phi = 123^\circ$ . The focus of this study was to make detailed measurements about this location. A previous study determined the wall flow angles through an oil flow visualization.

The uncertainty in the normal Reynolds stresses was estimated to be  $\pm 2\%$  of  $u_{ii}$  and in the shear stresses to be  $\pm 3\%$  of  $(u_i u_i * u_j u_j + 2 [u_i u_j]^2)^{1/2}$ . The uncertainty in the location of the measurement volume in the radial direction was  $\pm 10$   $\mu\text{m}$ . To obtain data for different circumferential locations, the entire model was rotated at the sting to within  $\pm 1^\circ$ . Measurements were corrected for gradient broadening effects and velocity bias. The skin friction was calculated, assuming a collateral wall region existed, by using points in the collateral wall region in Spalding's wall law. This wall law was also used to determine the error in the initial position of the probe volume with respect to the wall. The boundary layer thickness was calculated as the point where  $U(y)$  became 99% of the maximum value in the profile. They stated a 10% uncertainty in the value of  $\delta$  due to the difficulty in determining an edge velocity. It should be used only as a reference due to the high uncertainty.

There is no reverse flow in this experiment as was seen in the experiment of Stäger (1993) which was performed under similar conditions. They did not observe the second peak in  $-\overline{uv}$  stress away from the wall as reported in Molton (1993). They observed the differences in the flow gradient angle, the shear stress angle, and the flow angle. The shear stress vector lagged the flow gradient angle for this flow. This was true for the entire boundary layer even down to the wall where the flow gradient angle approaches the flow angle. They noted the reduction in the  $a_1$  structural parameter and present an attempt to correlate the three-dimensionality to the reduction. This correlation was examined as part of the current study with other data sets and will be discussed in the results section.

### 2.2.11 The Wing-Body Junction Experiment of Ölçmen and Simpson

Ölçmen and Simpson (1995) performed an experiment on a 3D pressure driven TBL that was created by a 3:2 elliptical-nose NACA 0020 tail wing mounted perpendicularly to a flat plate. The experimental stations were located along a line following the direction of the mean velocity vector component parallel to the wall at a  $y$  location where the  $\overline{u^2}$  normal stress attained a maximum. The flow along this line was influenced by a strong crossflow pressure gradient that changed sign for the downstream stations. The first station was chosen to be a sufficient distance from the horse shoe vortex such that the governing equations were not violated but to maintain the maximum amount of span-wise pressure gradient. The upstream stations were then determined as discussed above. The study was focused on obtaining accurate near-wall data ( $y^+ > 3$ ) and the determination of the triple velocity products for use with Reynolds stress transport equation models. The main goal of the study was the investigation of the flow features along the  $x$ - $z$  path described above.

The experiment was performed in the Virginia Tech Aerospace and Ocean Engineering Department low speed boundary layer tunnel. The inlet boundary layer flow was tripped by a 0.63 cm blunt leading edge (the tunnel floor) to insure that the flow was turbulent downstream of the inlet. The test section was designed such that any blockage induced pressure gradients around the wing were minimized. The model, described above, had a chord length of 30.5 cm and a maximum thickness of 7.17 cm. The nominal reference velocity was 27.5 m/s and the Reynolds number based on momentum thickness was 5940 at a location on the tunnel centerline 0.75 chord lengths upstream of the nose of the model. The boundary conditions and upstream boundary layer characteristics were established at this location. The turbulence intensity in the tunnel free-stream was 0.1%. The potential core was uniform to within 0.5% in the span-wise direction and 1% in the vertical direction. The tunnel test section was 8 m in length and 0.91 m in width. All tests were conducted at an ambient temperature of  $25 \pm 1.0^\circ \text{C}$ . The model, experimental test stations, and the surface flow structure are detailed in Figure 2.11.a. The stations used in this study are located on the starboard side of the model and were obtained with the LDV system described below.

The experiment determined time-mean static pressure, skin friction magnitude, three mean velocities, six Reynolds stresses, and ten turbulent triple products. The skin friction magnitude was determined by a separate study by using an oil-flow skin-friction interferometry technique where the oil thickness was less than 100  $\mu\text{m}$  at the time of the measurements. The wall shear stress direction is inferred from the LDV measured mean flow vector nearest the wall. The pressure measurements were made on the wall with a J- type Scanivalve and conventional inclined

manometers. The stagnation and reference static pressures were measured with a Pitot-static tube located 1.55 m downstream of the tunnel entrance. A single hot-wire technique was employed to determine the path of maximum normal stress and to compare results with the LDV data obtained. The hot-wire was primarily used on the port side of the model and was able to determine  $U$ ,  $W$ ,  $\overline{u^2}$ ,  $\overline{w^2}$ , and  $-\overline{uw}$  and assumed that the  $V$ -components were negligible. This assumption was determined to hold away from the primary horse shoe vortex.

The main measurements were made with a three-velocity-component LDV system that was a subsystem of a five component LDV system. It used two colors (green, 514.5 nm, and blue, 488.0 nm) and three Bragg shifts to distinguish the three velocity components and the direction of the particle through the probe volume. The green beams were shifted by 0, -50, and 30 MHz and the blue beams were shifted by 0 and -50 MHz. The resulting fringe spacing was 4.73  $\mu\text{m}$  for the green beams and 4.8  $\mu\text{m}$  for the blue beams. The transmitting optics were positioned below a glass floor such that the three probe volumes overlapped and measured three mutually orthogonal velocity components. The transmitting and receiving optics were mounted on an actuator that translated the entire system normal to the wall. The overlap of the five transmitting beams and the focus of the receiving optics resulted in a probe volume that was approximately 30  $\mu\text{m}$  in diameter. Micron-sized light scattering particles were injected at the entrance of the tunnel just prior to the trip. Data were acquired in coincidence mode at validation ratios of 95% or greater which helped to minimize the noise. At each measurement point, 30,000 samples were acquired at rates that varied from 50 samples/second near the wall to 200-400 samples/second away from it. The data were corrected for velocity-bias and gradient-broadening.

The flow about the wing was determined to be symmetrical by consideration of the wall pressure measurements, the oil-flow visualization, and the hot-wire measurements made on both sides of the wing. The LDV data were taken at seven stations on the starboard side of the wing as shown in Figure 2.11.a and information on these stations is given in Table 2.6. The LDV data was presented in local free-stream coordinates and other coordinate systems were compared and contrasted for several other flow parameters that were investigated. The free-stream direction was taken as the point in each profile that was farthest away from the wall in the potential core of the tunnel. The uncertainty in the mean velocities normalized on  $U_{\text{ref}}$  were  $\pm 0.003$ ,  $\pm 0.001$ , and  $\pm 0.002$  for  $U/U_{\text{ref}}$ ,  $V/U_{\text{ref}}$ , and  $W/U_{\text{ref}}$  respectively. For the fluctuating velocity components,  $u'/U_{\text{ref}}$  had an uncertainty of  $\pm 0.001$ ,  $v'/U_{\text{ref}}$  had an uncertainty of  $\pm 0.0009$  except nearest the wall, and the  $w'/U_{\text{ref}}$  uncertainty was  $\pm 0.0008$ . For the Reynolds shear stresses,  $-\overline{uv}/U_{\text{ref}}^2$  had an uncertainty of  $\pm 0.00008$ ,  $-\overline{vw}/U_{\text{ref}}^2$  had an uncertainty of  $\pm 0.00002$ , and the uncertainty in the  $-\overline{uw}/U_{\text{ref}}^2$  stress was  $\pm 0.00004$ .

They examined several parameters to determine the Reynolds averaged flow structure and anisotropy of the flow field. Table 5 in Ölçmen and Simpson (1995) gives several integral length scales and their definitions for the seven LDV stations. Comparisons of the flow angle (FA), flow gradient angle (FGA), and the shear stress angle (SSA) illustrate the development of the stress and rate of strain field. The SSA lagged the FGA for this flow illustrating that the stresses reacted slower to the imposed three-dimensional changes than the rate-of-strain field. Uncertainties in the FA, FGA, and SSA were  $\pm 0.25^\circ$ ,  $\pm 1^\circ$ , and  $\pm 2.6^\circ$  respectively. The flow angle showed wall collateral regions for  $y^+ < 10$ . The maximum flow angle occurred near station four where the lateral pressure gradient changes sign and then decreased to the point where the free-stream angle was similar to the wall-stress angle. At all stations, the FGA approached the FA below  $y^+$  of 10 as is expected for a wall collateral region.

The anisotropy factor,  $N$ , was evaluated for this flow in a number of different coordinate systems. In general, they reported  $N$  to decrease and even to assume negative values. In a search for regions and a coordinate system where  $N$  was a constant, they report that the normal stress coordinate system appeared to correlate the values better away from the wall and the wall stress coordinate system to produce more constant values of  $N$  near the wall. Data from other data sets was employed to determine the best coordinate system in which to represent  $N$ . They recommend that the wall stress coordinate system be used and that it produces a value of  $N$  that is approximately constant at 0.6.

They calculated the mixing length and compared it to a model equation of Cebeci and Smith. The experimental data falls below the model values as was seen in the other 3D TBL experiments. However for this experiment, the outer layer did not decrease as much from the accepted 2D value of 0.98 as seen in the previous experiments and the stations appeared fairly well correlated. The TKE when normalized on  $U_{\text{ref}}^2$  was seen to increase to almost twice its upstream value for stations 5, 6, and 7. This was seen to be caused by increases in the  $\overline{u^2}$  stress. From  $80 < y^+ < 300$ , a region existed where the value of TKE was approximately constant for all of the stations. The structural parameter  $a_1$  was investigated and seen to decrease from the typical 2D value of 0.15 which indicated a reduction in the shear stress. Nearest the wall, this reduction was more severe as  $a_1$  appeared to approach zero. There appears to be little correlation for  $a_1$  from station to station above  $y^+ > 20$ .

They present a new parameter to aid in the search for turbulence models for complex turbulent shear flows. This is the ratio of the  $\overline{v^2}$  normal stress to the magnitude of the shear stresses in a plane parallel to the wall,  $|\tau/\rho|$ . This parameter is invariant to coordinate system rotation about an axis that is normal to the wall. Near the wall,  $\overline{v^2}/|\tau/\rho|$  (defined to be  $S$ , Simpson,

1995) must be zero and vary linearly as a function of  $y$  to satisfy the fluctuating mass continuity equation (Rotta, 1962). This parameter was determined to be approximately constant for each station at a value of approximately 2 in the region from  $y^+ > 100$  to the outer layer. Below  $y^+ \simeq 100$ ,  $S$  decreases towards zero. In the outer layer, the inverse of the above ratio or  $1/S \equiv \tau/\rho/\overline{v^2}$ , should approach zero due to the lack of production of shear stress by the irrotational free-stream fluctuations. They also present values of this parameter for other data sets (see Figure 13 of Ölçmen and Simpson, 1995, for a description of particular experiments and stations) which illustrated an average value of 1.6 for  $S$  in the region mentioned above and constant for any given station. The analysis also determined that  $1/S$  was approximately 0.6 and constant for these experiments.

The ratio of the  $-\overline{vw}$  stress to the  $-\overline{uw}$  stress was determined to act as a function of  $y^+$  near the wall in wall stress coordinates. They claimed that the ratio varies in a semi-logarithmic fashion up to  $y^+ = 500$ . The slope of this region was reported to differ from flow to flow but always approximates a constant.

The ratio of the rate of production of  $-\overline{vw}$  shear stress to the rate of production of  $-\overline{uw}$  shear stress was nearly constant over a range of  $y$  for a given station. The ratio was derived to be;

$$C = \frac{\text{prod.} \overline{vw}}{\text{prod.} \overline{uw}} = \frac{-\left(\overline{v^2} \frac{\partial W}{\partial Y}\right)}{-\left(\overline{uv} \frac{\partial W}{\partial Y} + \overline{vw} \frac{\partial U}{\partial Y}\right)} = \frac{\overline{v^2} \text{Tan}(FGA)}{\overline{uv} \text{Tan}(FGA) + \overline{vw}} \quad (2.3)$$

which reduces to;

$$C_{2D} = \frac{\overline{v^2}}{\overline{uv}} = -\frac{\overline{v^2}}{\left| \frac{\tau}{\rho} \right|} \quad (2.4)$$

for 2D flows. This was seen to be similar to the  $S$  parameter, the difference being the  $-\overline{vw}$  shear stress in the magnitude of the shear stresses term. For several different flows, they illustrated that  $C$  maintained a constant value over  $100 < y^+ < 1000$  for a given station. Many of the stations seemed to be near a value of -1.

They expressed the concern that even though the  $-\overline{uw}$  shear stress is neglected in the Reynolds-averaged Navier-Stokes equations with the boundary-layer approximations, it reaches values that can be twice as large as  $-\overline{uv}$  and may be important. They determined that the overlap of the inner-region and the outer-region scaling became less valid in this 3D TBL and that the

semi-logarithmic law-of-the-wall did not hold. An essential difference between this flow and other existing pressure driven TBL experiments is the sudden reversal of the span-wise pressure gradient. This caused an increase in the  $\overline{u^2}$  normal stress and a sign change in the  $-\overline{vw}$  and  $-\overline{uw}$  shear stresses. They recommended that the wall stress coordinate system best illustrated the physics of the flow.

## 2.3 Summary and Observations on the Current State of Experimental Data

The data sets that were examined in this study support the general consensus that 3D TBLs can not be effectively modeled by the adaptation of existing 2D turbulence models to the 3D cases. This is supported by the fact that the flow is anisotropic in regards to the turbulent eddy viscosity modeling concept. The physics governing the 3D flow field show signs that it differs from the 2D cases. This is evident in the behavior of the Reynolds stress magnitude, the TKE, and the lag of the turbulence field with respect to the mean flow field. Littell and Eaton (1991) performed two point correlations and compared to the observations of Robinson (1991) on the coherent structures found in the flow field. The coherent structures were determined to differ, however they described how the structures of Robinson may be modified to include the presence of span-wise shear. This illustrates that the basic structures seen in 2D flows are modified with the addition of a span-wise shear.

Analysis of the turbulence field for the several cases provides evidence of the change in the physics of 3D flow when compared to 2D flow. There is a redistribution of the Reynolds stresses in 3D flows. The normal stresses tend to maintain the same ratios with respect to each other when viewed in a local free-stream coordinate system. However, the production of the TKE is different near the wall where the skewed flow is adding to its generation and the pressure-rate-of-strain terms are modifying its diffusion into other regions of the flow. The Reynolds shear stresses are seen to be reduced near the wall. This reduction then diffuses outward into the shear layer. This can also be seen by the Reynolds stress development lagging the mean flow development. That is, the fluctuating flow field responds slower than the mean field to directional changes in the flow. This indicates the great importance of history effects in the physics of modeling 3D TBLs. The stream-wise shear stress is seen to be reduced from typical 2D values as 3D flow fields degenerate back into 2D flows. The shear stress also seems to develop slower than the normal stress field. Which introduces another lag into the physics that must be modeled. A simple analysis of the various characteristic angles in the flow illustrates the lag of the fluctuating quantities to the mean



quantities. The shear stress angle generally lags the mean flow gradient angle. This is different for the convex curvature case of Baskaran and Bradshaw (1990) where the shear stress angle is seen to lead the flow gradient angle. Even the flows that are mildly 3D show signs of a change in the physics, while the most common modeling parameters tend to be similar to their values when observed in 2D turbulent flows.

A number of structural parameters are used to describe turbulent flow among the various geometries. The  $a_1$  structural parameter is seen to be reduced from its approximately constant 2D value of 0.15. For the experiments examined in this study,  $a_1$  illustrated a decrease from 0.15 for all of the wall bounded flows excluding the convex curvature case of Baskaran and Bradshaw. It was also greater for the flows with data taken in the horseshoe vortex of a wing-body junction experiment and in the separated vortex region of the flow over the ellipsoid cylinder (Barberis and Molton). These later experiments have significant flow normal to the surface and therefore differ greatly from the traditional wall bounded shear flow. The  $a_1$  parameter was observed to be affected by three-dimensionality greater closer to the wall.

The ratio of eddy viscosity,  $N$ , and Rotta's  $T$  parameter would be equal to unity across the layer if the eddy viscosity were isotropic. For the data sets examined, these parameters are reduced from unity which indicates that the eddy viscosity is anisotropic with the magnitude in the span-wise direction generally less than the magnitude in the stream-wise direction. These parameters are also seen to attain values greater than unity for some stations of these experiments. The anisotropy seems to be greatest near the wall. Prandtl's mixing length, when calculated for 3D flow fields, tends to be less than the 2D values and is effected greater in the outer layer. Transport velocities that are formed for certain quantities can illustrate characteristics of the physics of the flow, but do not tend to correlate well enough to use as a modeling parameter.

From the existing data, it can be seen that, future turbulence models must be able to account for a change in the physics of the 3D flow field. They must be able to account for the lag in the fluctuating quantities with respect to the mean flow quantities. They must also be able to account for the reductions in shear stress that are seen in 3D flows and the apparent lag of the development of the shear stress field with respect to the normal stress field. A better understanding of the pressure-rate-of strain terms and methods of modeling them is also needed to develop better 3D turbulence models. The importance of the near wall flow on the behavior in the outer regions is hinted at by the data in this study. More investigations of the near wall flow are needed to detail the important physical processes that are occurring in this region of the flow field.

**Table 2.1.** Summary of the experiments examined in the present study.

Notation; TP - triple product, RS - Reynolds stress.

Author	Flow Description	Data Reported	Apparatus
McMahon, Hubbart, and Kubendran (1982)	The horseshoe vortex region of a wing body juncture flow between a flat plate and a 3:2 elliptical nose wing of constant thickness. $U_{ref}=15.24$ m/s	3 mean velocities and 6 RS for 2 Y-Z planes along the body. $y > 2.3$ mm.	Hot wires that protruded through the floor and test wall (flat plate) of the test section.
Baskaran and Bradshaw (1987)	Flow in curved ducts simulating flow on 'infinite' swept curved wings of convex and concave curvature. $U_{ref}=33$ m/s	3 mean velocities, 6 RS, 10 TP and the 3 normal 4th order products. $y^+ > 300$ .	Cross wire hot wire probes, 3 hole pitot probe, 3 hole surface yawmeter, Preston tube.
Driver and Johnston (1990)	Axial flow, on a cylinder downstream of a rotating section, subjected to different pressure gradients. $U_{ref}=15$ m/s and 30 m/s	3 mean velocities, 6 RS, 10 TP, surface static pressures, $\tau_w$ , and $\beta_w$ . $y^+ > 20$ .	3 component LDV, wall static pressure taps, laser - interferometer, oil flow visualizations, surface pitot tube.
Littell and Eaton (1991)	The boundary layer over a smooth flat rotating disk with a constant angular speed.	3 mean velocities, 6 RS, and 10 TP. $y/\delta \geq 0.1$ .	3 hole pitot tube, cross - wire hot - wire probes.
Devenport and Simpson (1992)	Flow in the horseshoe vortex region of a 3:2 elliptical nose NACA 0020 tail wing normal to a flat plate. $U_{ref}=27$ m/s	3 mean velocities and 6 RS. $y > 0.14$ mm.	Hot - wire probes and a LDV system in 3 different planes.
Pompeo (1992)	Flow in a converging duct of constant area focusing on the plane of the centerline. With the duct reversed, diverging duct flow was examined. $U_{ref}=42$ m/s	3 mean velocities, 6 RS, 10 TP, friction coeff's, and surface pressures. $y/\delta \geq 0.1$ .	Static pressure taps, (1, 2, 3, 5) multi-hole pitot tubes, single and cross-wire hot-wires, skin friction balance and Preston tubes.

**Table 2.1. (Cont.)** Summary of the experiments examined in the present study.  
Notation; TP - triple product, RS - Reynolds stress.

Author	Flow Description	Data Reported	Apparatus
Schwarz and Bradshaw (1992)	Flow in a 30° constant area bend over a flat wall with an axial pressure gradient $\approx$ zero. $U_{ref}=27$ m/s	3 mean velocities, 6 RS, 10 TP, surface static pressure, $\tau_w$ , and $\beta_w$ .  $y/\delta \geq 0.1$ .	Preston tube, static pressure taps, 3 hole pitot probe, cross - wire hot-wires, oil-flow.
Barberis and Molton (1993)	Flow over an ellipsoid cylinder body at $U_{fs} = 50$ m/s and $\alpha = 20^\circ$ .	3 mean velocities and 6 Reynolds stresses.  $y/\delta > 0.1$ .	3 component LDV, surface pressure taps, oil-flow, 3 hole pitot tube.
Kreplin and Stäger (1993)	Flow over a 6:1 prolate spheroid at $\alpha = 10^\circ$ and $U_{fs} = 30$ m/s.	3 mean velocities, 6 RS, 10 TP, $\tau_w$ , and P surface.  $y/\delta > 0.1$ .	3 hole pressure probes, 4 sensor Kovasznay type hot-wire probes.
Chesnakas and Simpson (1994)	Flow over a 6:1 prolate spheroid at $\alpha = 10^\circ$ and $U_{fs} = 50$ m/s.	3 mean velocities, 6 RS, 9 TP, $\tau_w$ , and $\beta_w$ .  $y^+ > 7$ .	3 component LDV, fit to Spalding's wall law in the collateral zone.
Ölçmen and Simpson (1995)	Flow along a line of maximum normal stress, in the Devenport wing body junction flow, away from the vortex. $U_{ref}=27$ m/s	3 mean velocities, 6 RS, 10 TP, 15 quadruple products, $\tau_w$ , and $\beta_w$ .  $y^+ > 3$ .	3 component LDV, oil-flow visualizations.

**Table 2.2.a**, the experiment of Baskaran and Bradshaw. Mean flow parameters for the concave flow case of Baskaran and Bradshaw as measured by the 3 hole yaw meter.  
(extracted from a RAE report obtained through communication with P. Bradshaw)

Station	x (mm)	z (mm)	$U_{ref}$ (m/s)	$\delta$ (mm)	$Q_e$ (m/s)	$\phi_e$ (deg.)
1	591	303	32.671	15.103	32.968	-1.13
2	921	-127	32.596	23.25	31.366	1.21
3	921	102	32.55	20.846	31.423	0.67
4	921	254	32.628	22.967	31.763	1.62
5	1229	150	32.352	41.109	28.473	5.89
6	1229	279	32.582	38.96	28.342	6.88
7	1229	381	32.62	43.04	28.518	7.1
8	1533	260	32.6	56.685	27.057	10.64
9	1839	387	32.734	70.746	26.515	10.29

**Table 2.2.b**, the experiment of Baskaran and Bradshaw. Wall streamline angles and friction velocities for the concave case. (The second  $Q^+$  and  $U^+$  were measured with the Preston Tube)  
(extracted from a RAE report obtained through communication with P. Bradshaw)

Station	x (mm)	z (mm)	$\phi_w$ (deg.)	$Q^+$	$Q^+$	$U^+$
1	591	303	-3.75	1.250	1.323	1.321
2	921	-127				
3	921	102				
4	921	254	4.65	1.101	1.161	1.156
5	1229	150				
6	1229	279				
7	1229	381	17.25	0.878	0.924	0.857
8	1533	260	19.85	0.869	0.885	0.792
9	1839	387	18.00	0.845	0.885	0.817

**Table 2.2.c**, the experiment of Baskaran and Bradshaw. Integral parameters for the concave curvature flow case. (Table 1 of Baskaran *et. al.*, 1990)

$x_n$ (mm)	$\delta_{11}^*$ (mm)	$\delta_{22}^*$ (mm)	$\theta_{11}$ (mm)	$\theta_{22}$ (mm)	$H_{11}$	$H_{22}$
591	2.62	-0.024	1.71		1.53	
921	4.12	-0.391	2.767	-0.01	1.49	
1229	8.58	-2.414	5.604	-0.228	1.53	10.61
1533	11.33	-4.124	7.46	-0.428	1.52	9.64
1839	12.96	-4.864	9.087	-0.456	1.43	10.67

**Table 2.2.d**, the experiment of Baskaran and Bradshaw. Mean flow parameters for the convex flow case as determined by the 3-hole probe.  
(extracted from a RAE report obtained through communication with P. Bradshaw)

Station	$x_n$ (mm)	$z_n$ (mm)	$U_{ref}$ (m/s)	$\delta$ (mm)	$Q_e$ (m/s)	$\phi_e$ (deg)
3	513	150	33.87	14.829	33.68	0.0
6	927	150	32.8	22.34	32.26	1.14
8	1232	150	33.57	37.43	28.18	6.16
10	1535	150	34.1	52.89	26.71	9.09
11	1713	150	33.93	59.39	26.34	10.2

**Table 2.2.e**, the experiment of Baskaran and Bradshaw. Integral parameters for the convex case calculated in free stream coordinates. (table 2 from Baskaran et. al., 1990)

$x_n$ (mm)	$\delta^*_{11}$ (mm)	$\delta^*_{22}$ (mm)	$\theta_{11}$ (mm)	$\theta_{22}$ (mm)	$H_{11}$	$H_{22}$
584	2.48	-0.008	1.59		1.56	
867	3.99	0.163	2.55	-0.003	1.57	
1201	9.61	-2.16	5.6	-0.198	1.72	10.93
1477	15.71	-4.13	8.65	-0.473	1.82	8.74
1642	16.94	-5.34	9.96	-0.72	1.7	7.42

**Table 2.3**, the experiment of Devenport and Simpson. The stated experimental uncertainties. (Table F - 1 from Devenport and Simpson, 1990).

Value of:	Plane 1	Plane 3	Plane 4	Plane 5
$X / T$	$-2.0 \text{ e } -1$	$-4.6 \text{ e } -2$	$4.6 \text{ e } -1$	$3.8 \text{ e } -1$
$Y / T$	$1.9 \text{ e } -2$	$1.6 \text{ e } -2$	$9.6 \text{ e } -3$	$1.8 \text{ e } -1$
$Z / T$	0	$-5.2 \text{ e } -1$	$-5.1 \text{ e } -1$	$-9.6 \text{ e } -1$
$U / U_{\text{ref}}$	$-3.4 \text{ e } -1$	$2.8 \text{ e } -1$	$1.1 \text{ e } 0$	$9.5 \text{ e } -1$
$W / U_{\text{ref}}$	$7.1 \text{ e } -3$	$-6.6 \text{ e } -1$	$-5.4 \text{ e } -1$	$-2.3 \text{ e } -1$
$\overline{u^2} / U_{\text{ref}}^2$	$5.2 \text{ e } -2$	$3.9 \text{ e } -2$	$2.3 \text{ e } -3$	$3.6 \text{ e } -3$
$-\overline{uv} / U_{\text{ref}}^2$	$7.0 \text{ e } -3$	$4.5 \text{ e } -3$	$-2.4 \text{ e } -4$	$-1.2 \text{ e } -3$
Uncertainty in:				
$U / U_{\text{ref}}$	$2.5 \text{ e } -2$	$3.5 \text{ e } -2$	$3.7 \text{ e } -2$	$3.6 \text{ e } -2$
$V / U_{\text{ref}}$	$2.5 \text{ e } -2$	$3.5 \text{ e } -2$	$3.5 \text{ e } -2$	$3.5 \text{ e } -2$
$W / U_{\text{ref}}$	$2.5 \text{ e } -2$	$3.6 \text{ e } -2$	$3.6 \text{ e } -2$	$3.5 \text{ e } -2$
$\overline{u^2} / U_{\text{ref}}^2$	$1.6 \text{ e } -3$	$1.3 \text{ e } -3$	$1.4 \text{ e } -4$	$1.9 \text{ e } -4$
$\overline{v^2} / U_{\text{ref}}^2$	$7.5 \text{ e } -4$	$4.4 \text{ e } -4$	$1.5 \text{ e } -4$	$1.4 \text{ e } -4$
$\overline{w^2} / U_{\text{ref}}^2$	$4.3 \text{ e } -4$	$1.0 \text{ e } -3$	$3.0 \text{ e } -4$	$2.0 \text{ e } -4$
$-\overline{uv} / U_{\text{ref}}^2$	$1.3 \text{ e } -3$	$1.1 \text{ e } -3$	$1.5 \text{ e } -4$	$2.0 \text{ e } -4$
$-\overline{uw} / U_{\text{ref}}^2$	-	$9.2 \text{ e } -4$	$2.2 \text{ e } -4$	$2.1 \text{ e } -4$
$-\overline{vw} / U_{\text{ref}}^2$	-	$9.6 \text{ e } -4$	$2.2 \text{ e } -4$	$1.5 \text{ e } -4$

**Table 2.4.a.** the experiment of Littell and Eaton. The uncertainty in the hot - wire measurements of Littell and Eaton (Table 2.1 from Littell and Eaton, 1991)

Quantity	Uncertainty (aligned)	Error from 5° Misalignment	% of Quantity
$U$	3%	1%	$U$
$\overline{u^2}$	5%	4%	$\overline{u^2}$
$\overline{v^2}$	5%	4%	$\overline{u^2}$
$\overline{w^2}$	5%	4%	$\overline{u^2}$
$\overline{uv}$	10%	7.5%	$\overline{uv}$
$\overline{vw}$	15%	8.5%	$\overline{uv}$
$\overline{uw}$	10%	7.5%	$\overline{uv}$

**Table 2.4.b,** the experiment of Littell and Eaton. Various parameters for the seven turbulent stations of Littell and Eaton (Extracted from Table 3.1 in Littell and Eaton, 1991) Note that  $\delta_{99}$  is defined differently than  $U/U_e = 0.99$ , refer to Littell and Eaton (1991) for specifics.

Radius (m)	Re	$U_\infty$ (m/s)	$\delta_{99}$ (mm)	$\theta$ (mm)	$Re_\theta$	H	$u_\tau$ (m/s)	$v/u_\tau$ ( $\mu\text{m}$ )
0.235	400000	26.13	11.60	0.978	1657	1.342	1.206	12.8
0.356	650000	28.22	19.22	1.457	2662	1.290	1.255	12.3
"	940000	41.01	20.05	1.456	3839	1.269	1.750	8.9
0.421	650000	23.72	21.04	1.712	2645	1.298	1.051	14.6
"	1000000	36.72	20.61	1.641	3903	1.282	1.556	9.9
"	1300000	48.14	20.39	1.594	4969	1.270	1.997	7.7
"	1600000	59.12	21.38	1.612	6066	1.267	2.386	6.6

**Table 2.5.a.**, the experiment of Schwarz and Bradshaw. The uncertainty in the hot - wire measurements of Schwarz and Bradshaw (Table 2 -1) from Schwarz and Bradshaw, 1992)

Quantity	Uncertainty (aligned)	Error from 5° Misalignment	% of Quantity
U	3%	1%	U
$\overline{u^2}$	5%	4%	$\overline{u^2}$
$\overline{v^2}$	5%	4%	$\overline{u^2}$
$\overline{w^2}$	5%	4%	$\overline{u^2}$
$\overline{uv}$	10%	7.5%	$\overline{uv}$
$\overline{vw}$	15%	8.5%	$\overline{uv}$
$\overline{uw}$	10%	7.5%	$\overline{uv}$

**Table 2.5.b.**, the experiment of Schwarz and Bradshaw. Integral flow parameters from Schwarz and Bradshaw. (Excerpt from Table 3-1 Schwarz and Bradshaw, 1992)

Station	X (mm)	$\delta_{99}$ (mm)	$C_f \times 10^6$	$\delta^*$ (mm)	$\theta$ (mm)	$Re_\theta$
0	826	20.92	3039	3.31	2.42	4101
1	978	23.02	2880	3.71	2.70	4584
2	1130	25.70	2709	4.23	3.08	5249
3	1283	28.49	2567	4.97	3.55	6076
4	1435	31.22	2514	5.27	3.81	6496
5	1511	32.15	2499	5.27	3.82	6463
6	1676	32.22	2720	5.27	3.80	6571
7	1775	30.91	2622	5.25	3.77	6438
8	1875	32.65	2521	5.57	3.96	6671
9	1975	33.72	2534	5.78	4.11	6929
10	2075	35.25	2598	6.04	4.29	7274
11	2174	36.95	2555	6.34	4.51	7647
12	2338	39.15	2481	6.78	4.81	8217
13	2415	39.97	2498	6.83	4.88	8351
14	2491	41.10	2502	7.03	5.03	8638
15	2567	42.23	2590	6.99	5.06	8761
16	2643	42.67	2663	6.81	5.02	8860
17	2796	44.58	2654	6.89	5.13	9047
18	2948	46.16	2628	6.89	5.17	9062
19	3100	47.81	2867	6.70	5.12	8985
20	3329	50.60	2969	6.44	5.01	8843
21	3634	53.22	2884	6.27	4.90	8588



**Table 2.6** Data for the LDV stations of the wing body junction experiment of Ölçmen and Simpson (1995). (Extracted from Table 4 in Ölçmen and Simpson, 1995.)

Station	X (in.)	Z (in.)	$U_{ref}$ (m/s)	$U_e$ (m/s)	$\beta_{fs}$ (deg.)
0	-4.49	-1.32	27.6	26.4	-1.68
1	-3.50	-1.45	27.5	24.9	-2.64
2	-2.29	-1.75	27.5	24.8	-4.81
3	-1.33	-2.04	27.5	25.3	-8.63
4	-0.47	-2.58	27.5	27.3	-9.45
5	0.26	-2.94	27.5	29.5	7.71
6	1.19	-3.30	27.5	30.5	-5.09
7	2.17	-3.53	27.5	31.0	-2.71

Station	$\beta_w$ (deg.)	$u_\tau$ (m/s)	$v$ ( $m^2/s \times 10^5$ )	$P_{day}$ (mb)	$T_{day}$ ( $^{\circ}C$ )
0	-6.1	0.87	1.68	938	25.4
1	-11.5	0.864	1.65	949	24.6
2	-24.0	0.865	1.65	949	24.3
3	-33.7	0.957	1.65	947	23.5
4	-30.6	1.11	1.65	946	24
5	-19.7	1.15	1.67	940	24.5
6	-7.17	1.16	1.68	934	25
7	-3.50	1.20	1.68	934	24.7

## FIGURES

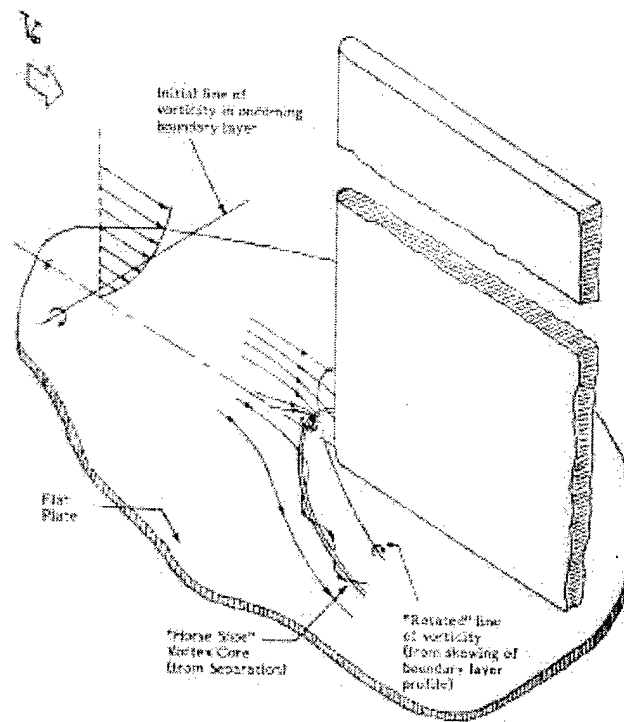


Figure 2.1.a The experiment of McMahon *et. al.* The physical description of a juncture flow as examined by McMahon *et. al.* (Figure 1 from McMahon *et. al.*, 1982)

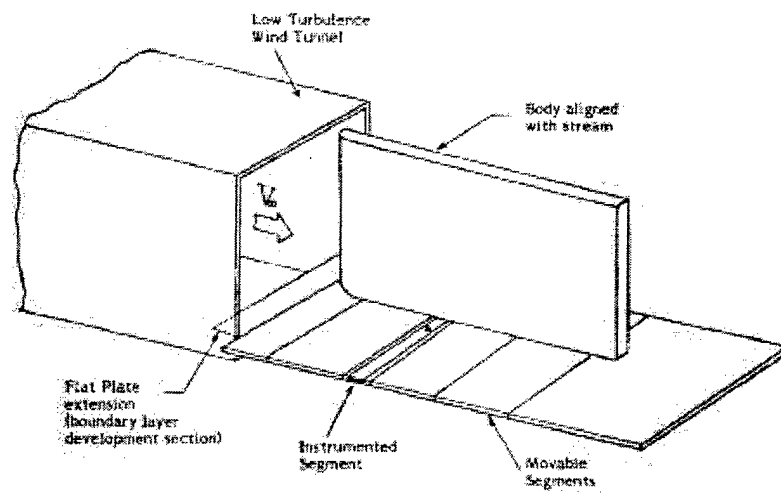


Figure 2.1.b The experiment of McMahon *et. al.* The tunnel exit, model, and test section. (Figure 2 from McMahon *et. al.*, 1982)

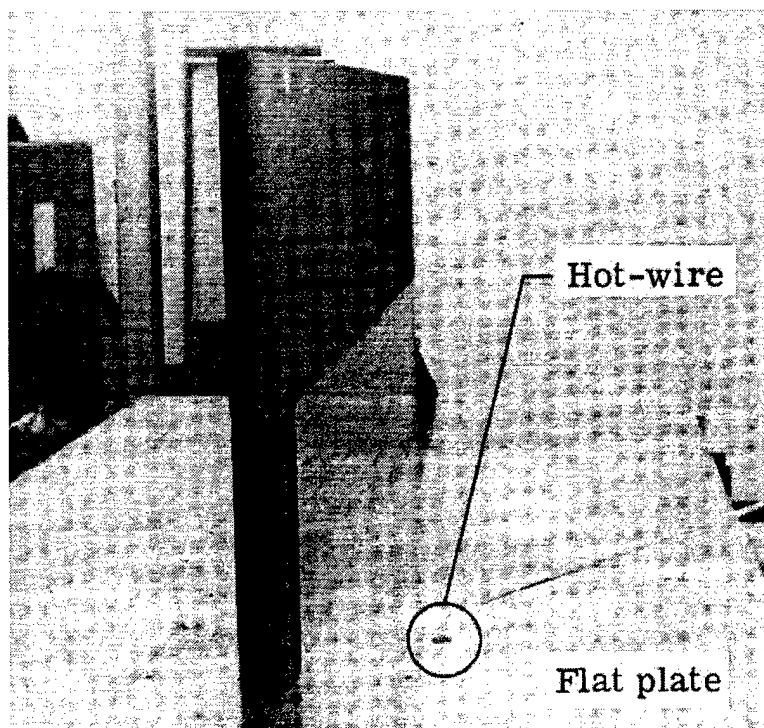


Figure 2.1.c The experiment of McMahon *et. al.* Looking downstream from the tunnel exit at the model and hot-wire probe *in situ*. (Figure 3 from McMahon *et. al.*, 1982)

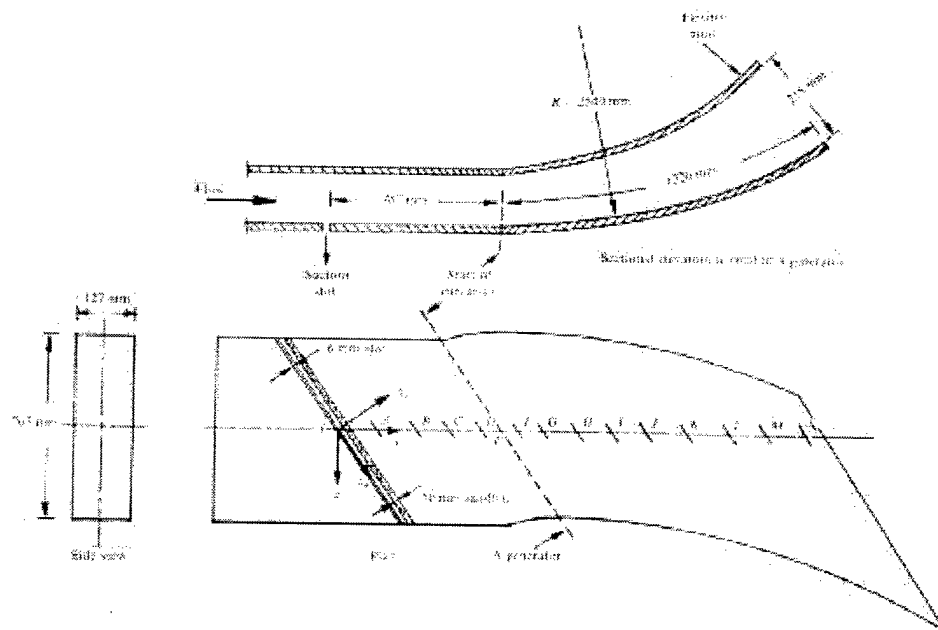


Figure 2.2.a The 'infinite' swept curved wing experiment of Baskaran and Bradshaw (1990), for the concave curvature case. (fig. 1(a) from Baskaran *et. al.*, 1990).

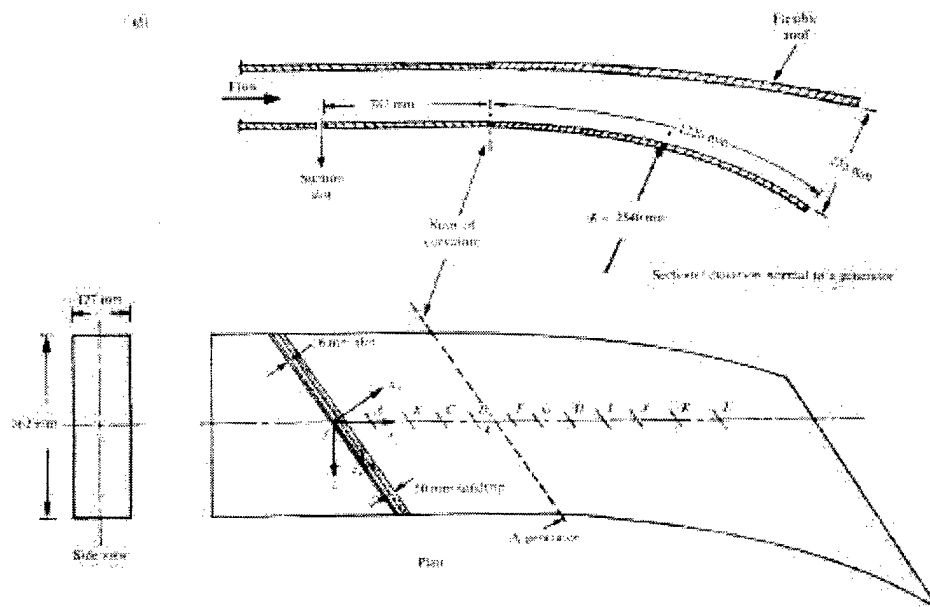


Figure 2.2.b The 'infinite' swept curved wing experiment of Baskaran and Bradshaw (1990) for the convex curvature case. (fig. 1(b) from Baskaran *et. al.*, 1990).

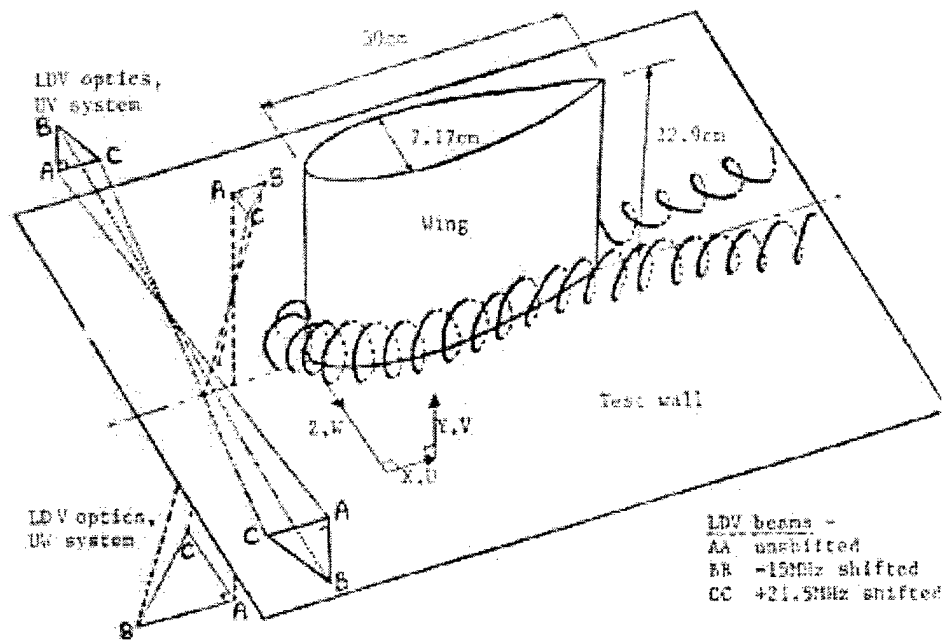


Figure 2.3.a A description of the wing-body experiment of Devenport and Simpson.  
(Figure A-1 from Devenport and Simpson, 1990)

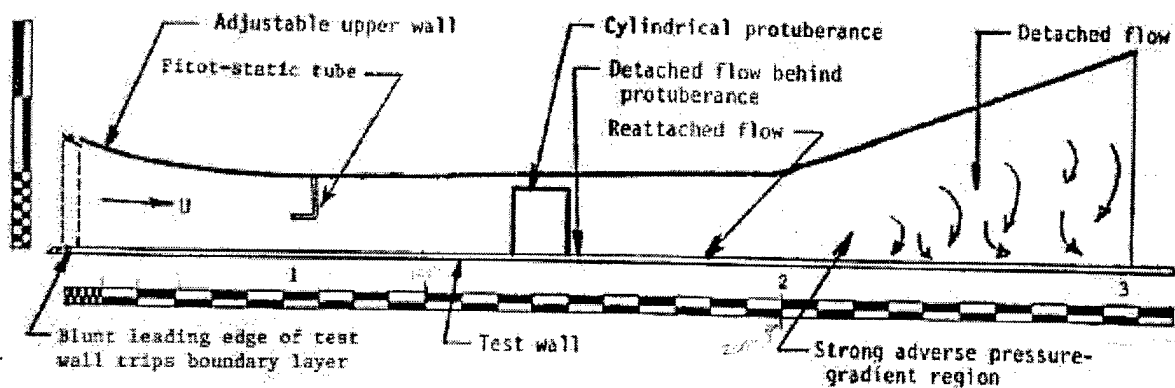


Figure 2.3.b The test section of the boundary layer wind tunnel used for the experiment of Devenport and Simpson. The major scale divisions are 10". (Figure A.1-2 from Devenport and Simpson, 1990)

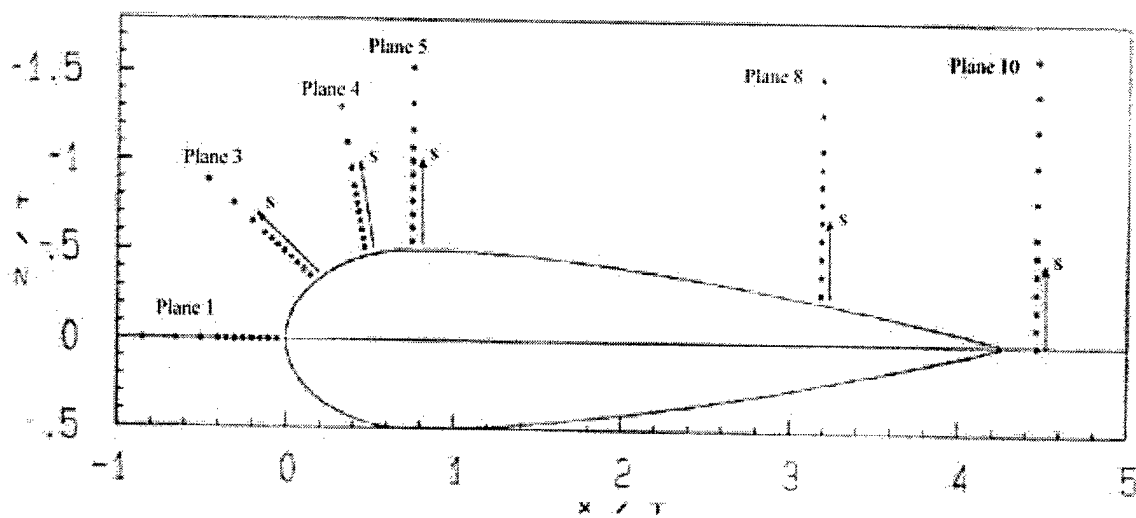


Figure 2.3.c A description of the measurement planes used for the experiment of Devenport and Simpson. (Figure F-1 from Devenport and Simpson, 1990)

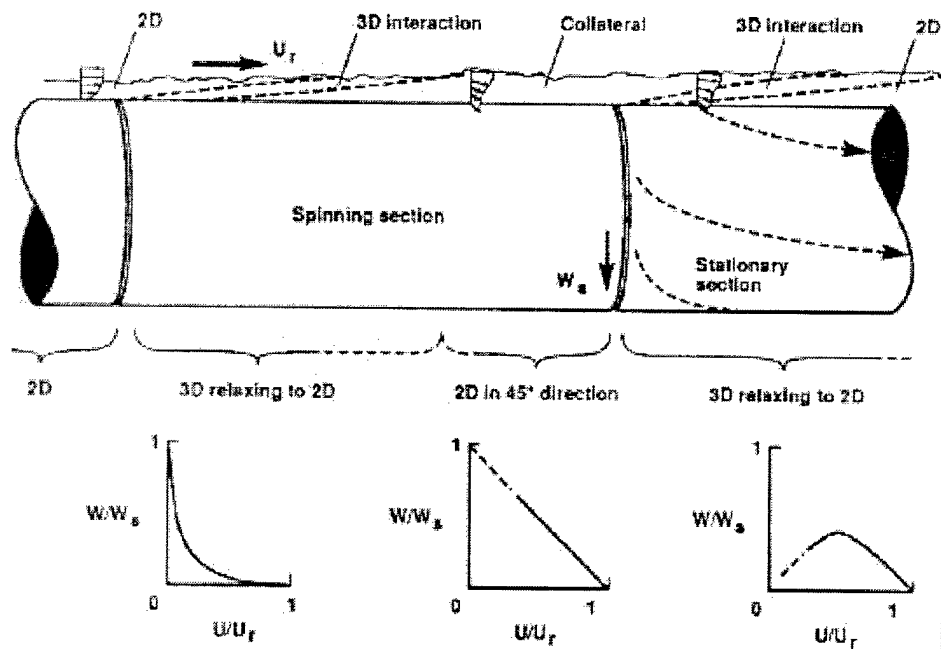


Figure 2.4.a The shear induced experiment of Driver and Johnston. Description of the regions of the flow at various axial locations on the cylinder. (Figure 2.1 from Driver and Johnston, 1991)

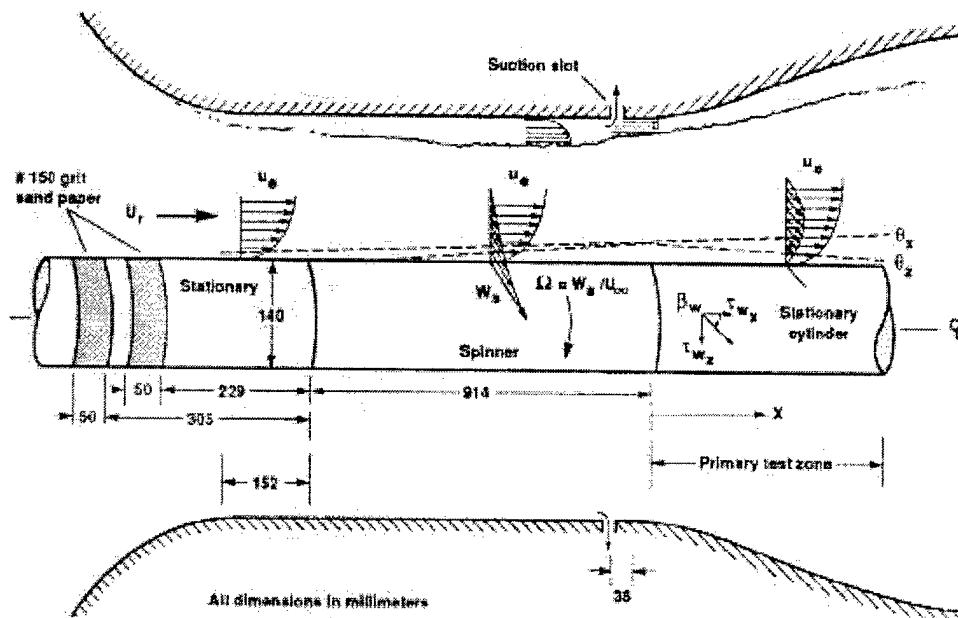


Figure 2.4.b The shear induced experiment of Driver and Johnston. Schematic of the test section and boundary layer behavior over the cylinder. (Figure 2.4 from Driver and Johnston, 1991)

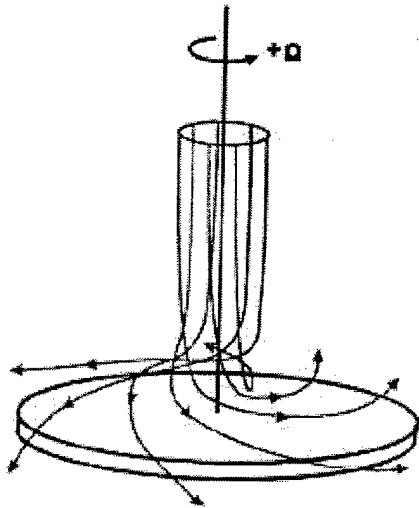


Figure 2.5.a The experiment of Littell and Eaton.  
The streamline pattern over the spinning disk.  
(Figure 1.1 from Littell and Eaton, 1991)

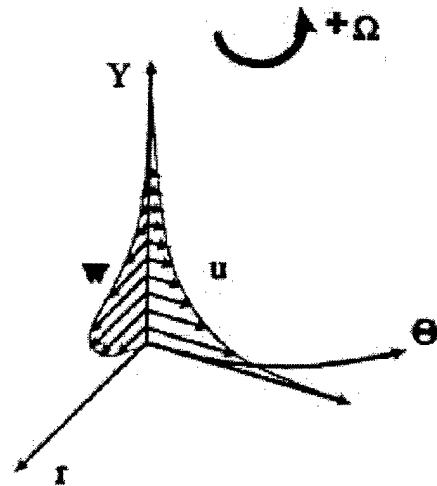


Figure 2.5.b The experiment of Littell and Eaton.  
The 3D TBL created by the shear driven disk flow.  
(Figure 1.2 of Littell and Eaton, 1991)

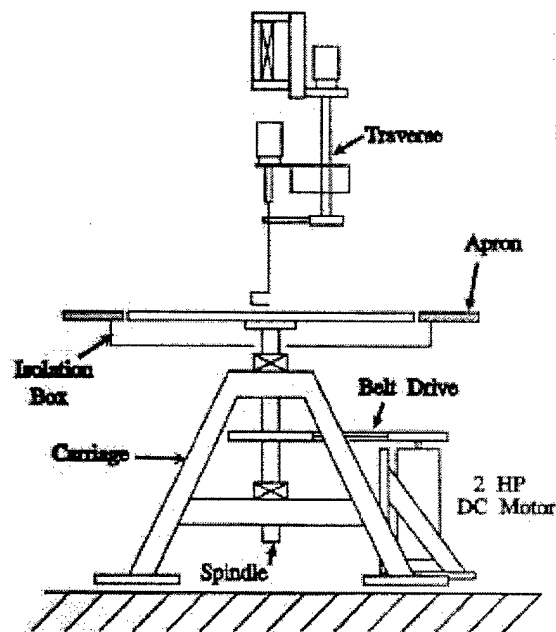


Figure 2.5.c The experiment of Littell and Eaton. The table, frame, measurement traverse and drive apparatus (Figure 1.3 from Littell and Eaton, 1991)



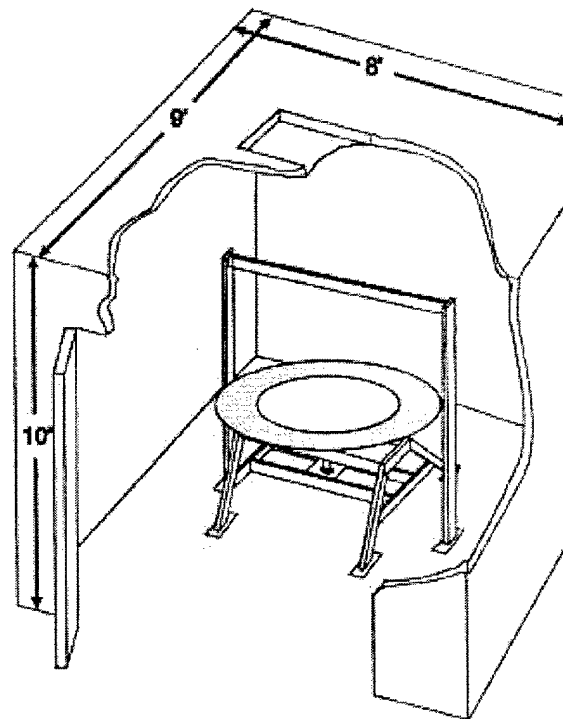


Figure 2.5.d The experiment of Littell and Eaton. The experimental test cell used to contain the experimental apparatus. (Figure 1.4 from Littell and Eaton, 1991)

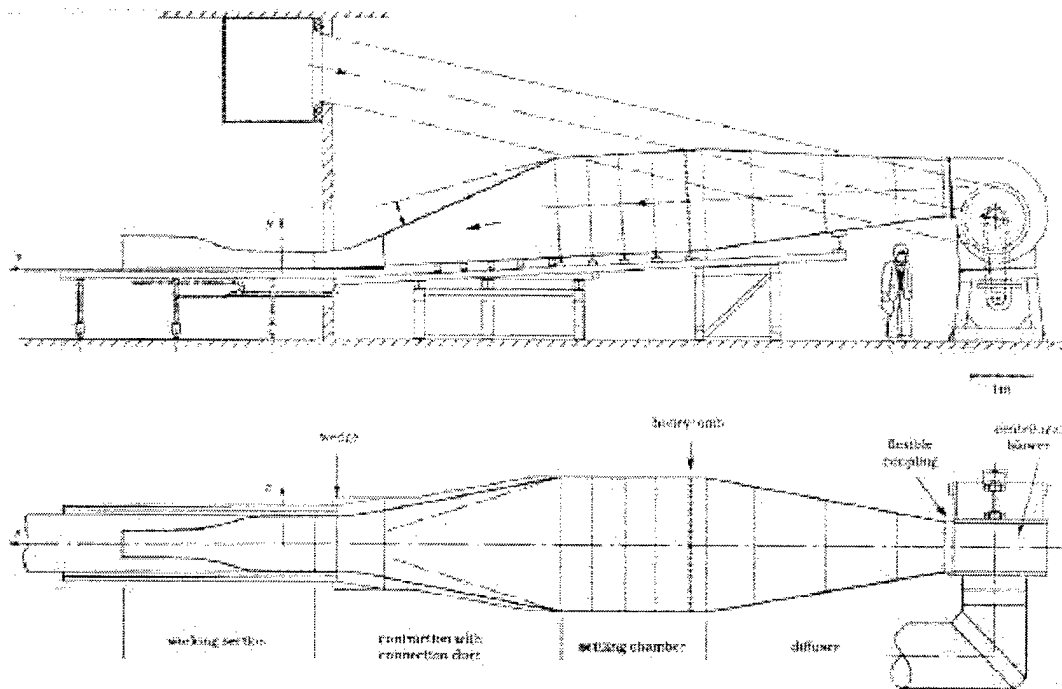


Figure 2.6.a Experimental setup of Pompeo (1992). The wind tunnel arrangement used for this experiment. (Fig 2.1 from Pompeo, 1992)

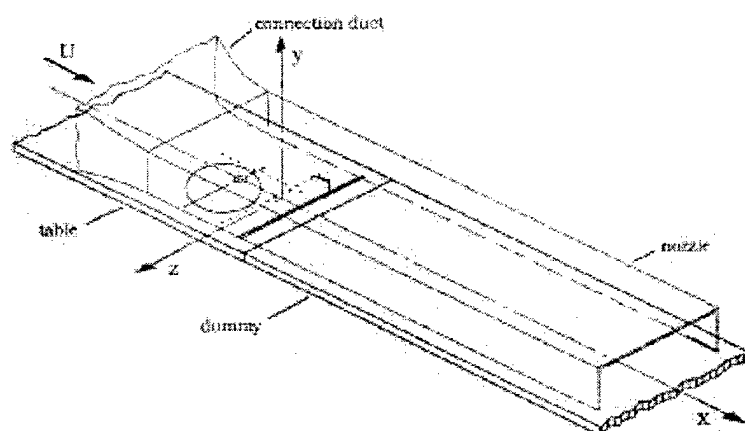


Figure 2.6.b Two dimensional nozzle and definition of the coordinate system used in for Pompeo (1992). (Fig 2.2 from Pompeo, 1992)

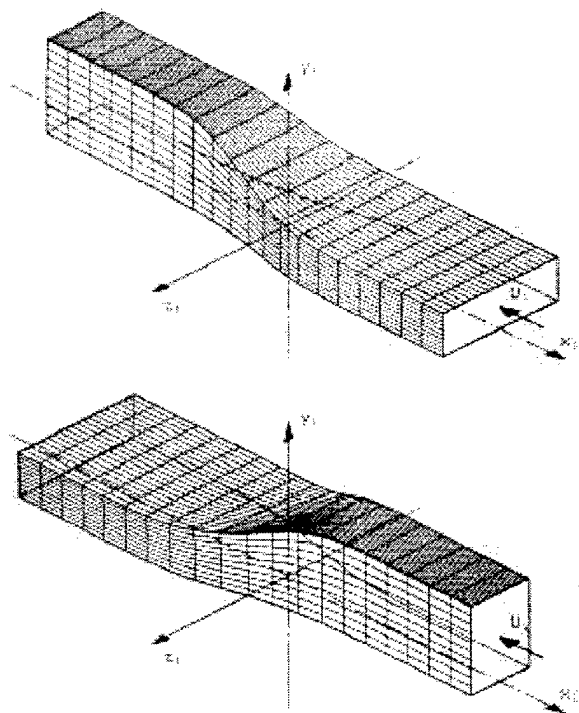


Figure 2.6.c Three dimensional nozzle that was created for the experiment of Pompeo (1992). The coordinate system shown was used for the potential calculation to determine the nozzle geometry. (Fig 2.6 from Pompeo, 1992)

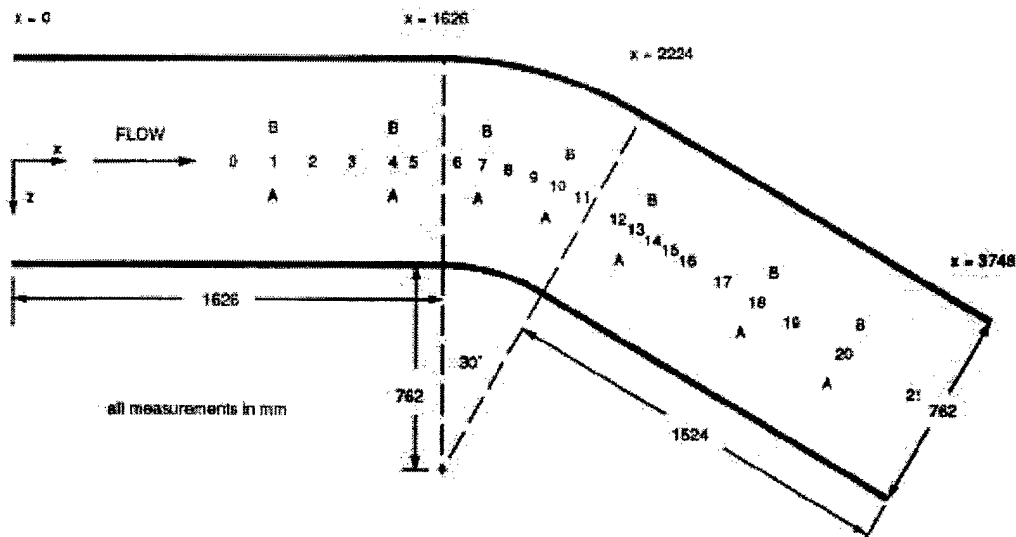


Figure 2.7 The experiment of Schwarz and Bradshaw. The experimental test section and measurement stations used by Schwarz and Bradshaw. (Figure 2.4 from Schwarz and Bradshaw, 1992)

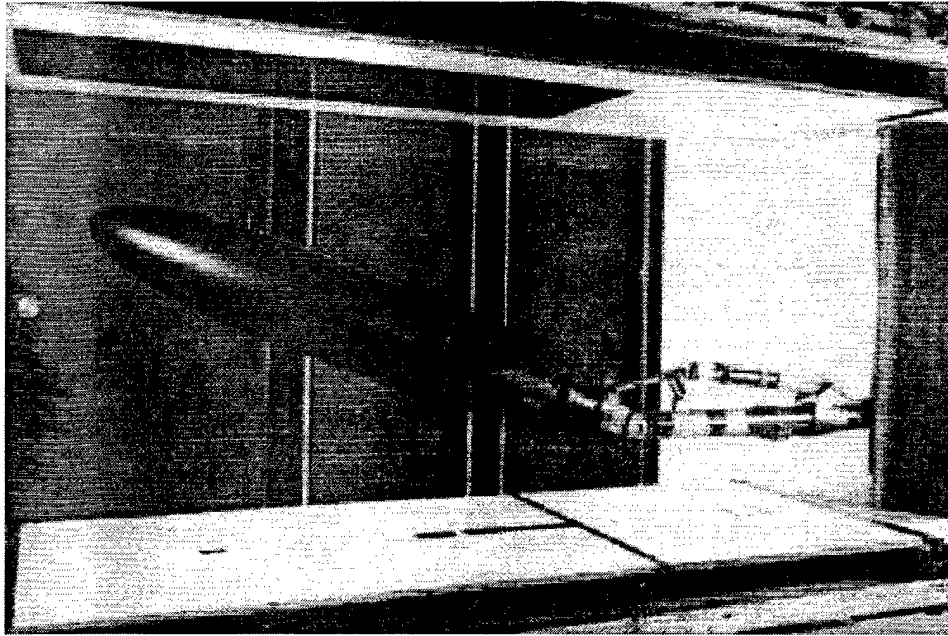


Figure 2.8.a The Experiment of Molton. The ellipsoid cylinder model mounted in the wind tunnel. (Figure 1 from Molton, 1993)

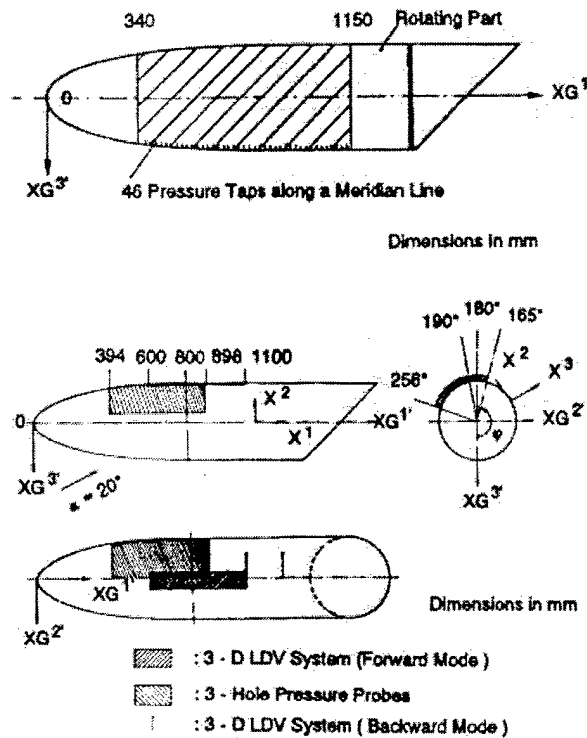


Figure 2.8.b The Experiment of Molton. The measurement regions and definition of coordinate systems used for the ellipsoid cylinder. (Figure 7, 8 from Molton, 1993)

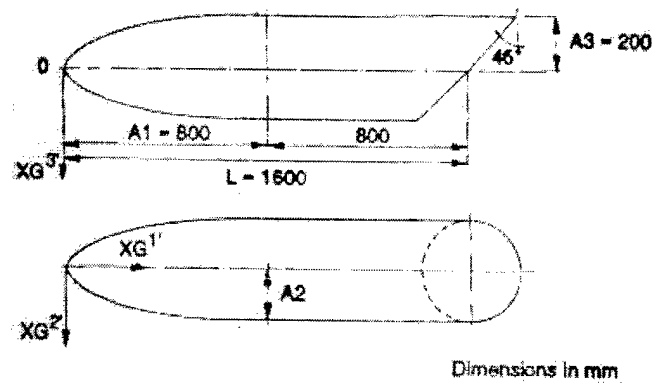


Figure 2.8.c The Experiment of Molton. The ellipsoid cylinder model's dimensions. (Figure 2 from Molton, 1993)

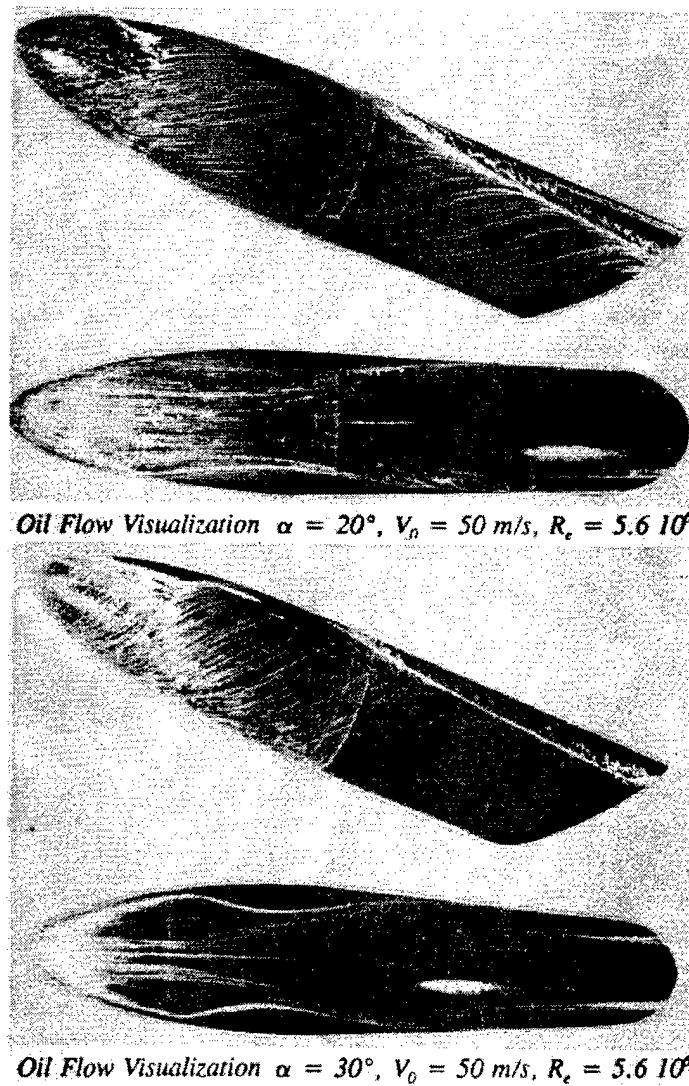


Figure 2.8.d The Experiment of Molton. Oil flow visualizations of the model at two angles of attack. (Figure 9 from Molton, 1993)

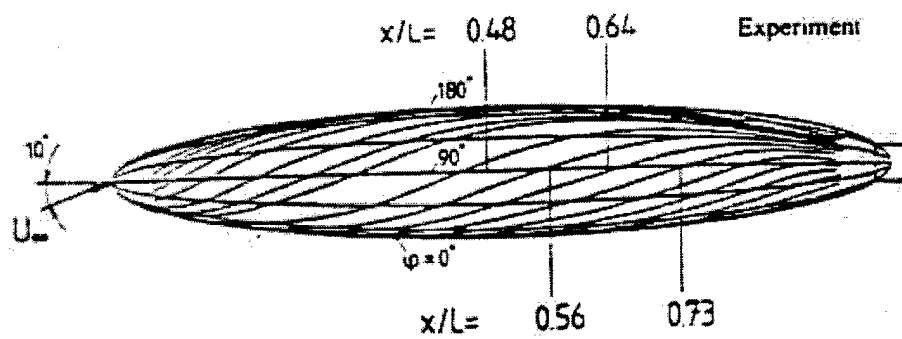


Figure 2.9 The experimental setup and streamlines for the 6:1 prolate spheroid of the Stäger (1993) experiment. (Fig 3 from Kreplin, 1993)

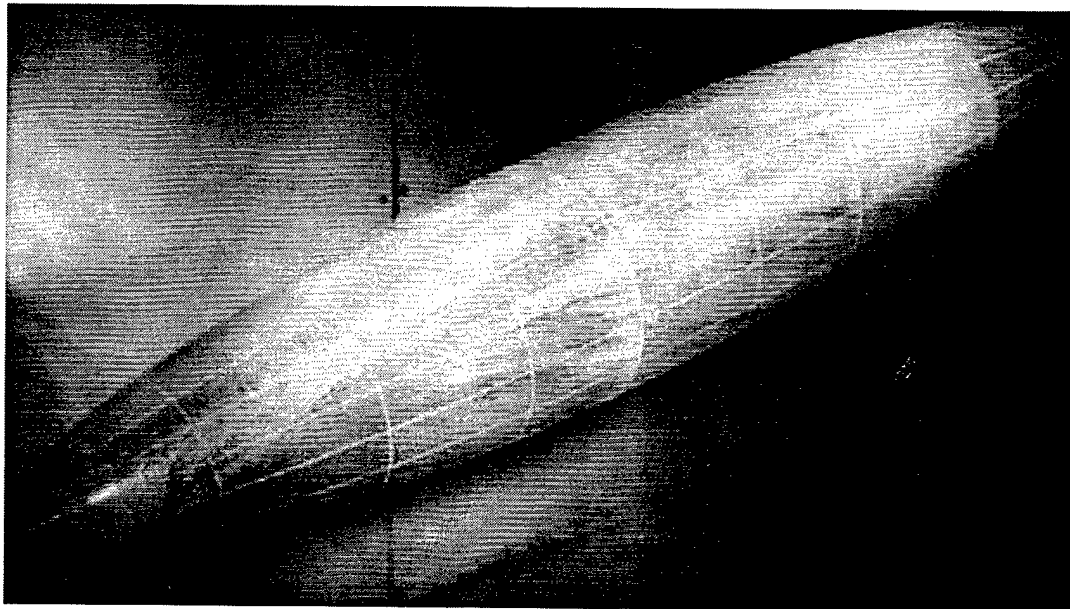


Figure 2.10.a The experiment of Chesnakas and Simpson. The 6:1 prolate spheroid mounted at  $10^\circ$  angle of attack in the wind tunnel. Oil flow illustrates surface skin friction lines. (Figure A.2 from Chesnakas *et. al.*, 1994)

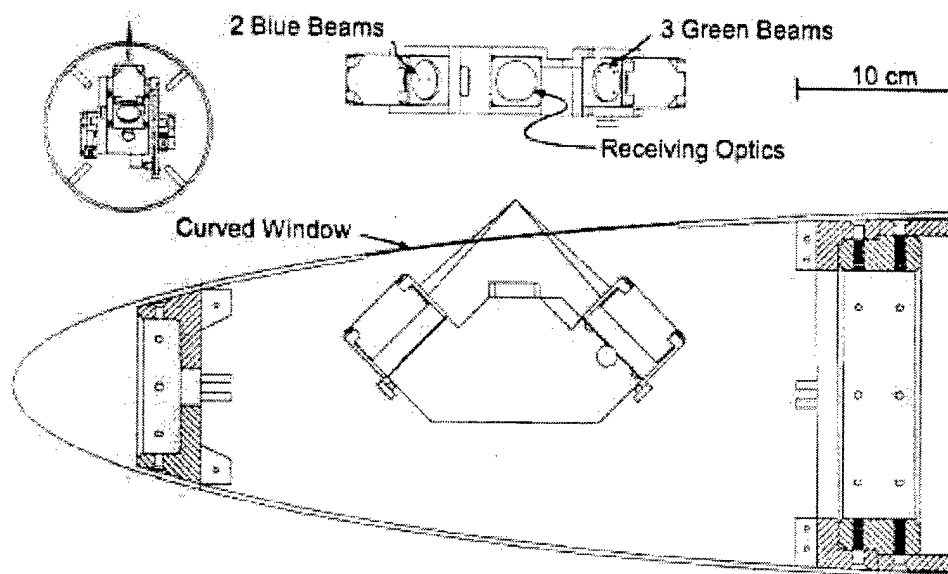


Figure 2.10.b The experiment of Chesnakas and Simpson. A view illustrating the probe positioned within the model. Figure 2 from Chesnakas *et. al.*, 1994)



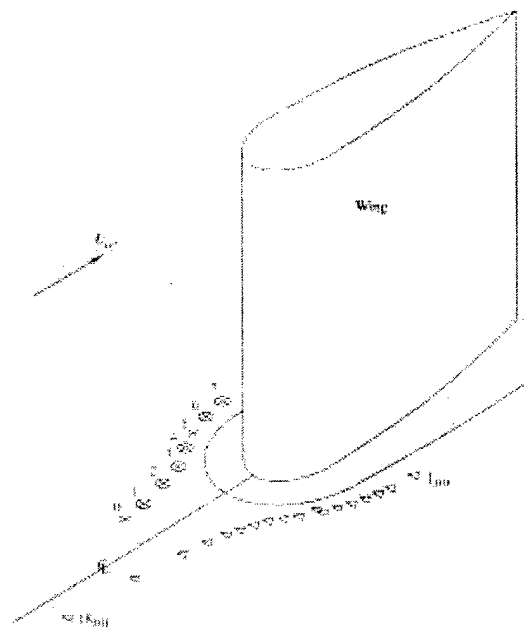


Figure 2.11.a, the experiment of Olcmen and Simpson. A characture of the wing-body junction flow illustrating the measurement stations. The LDV data was obtained on the starboard side of the model. (figure 2(a) from Olcmen and Simpson, 1995)

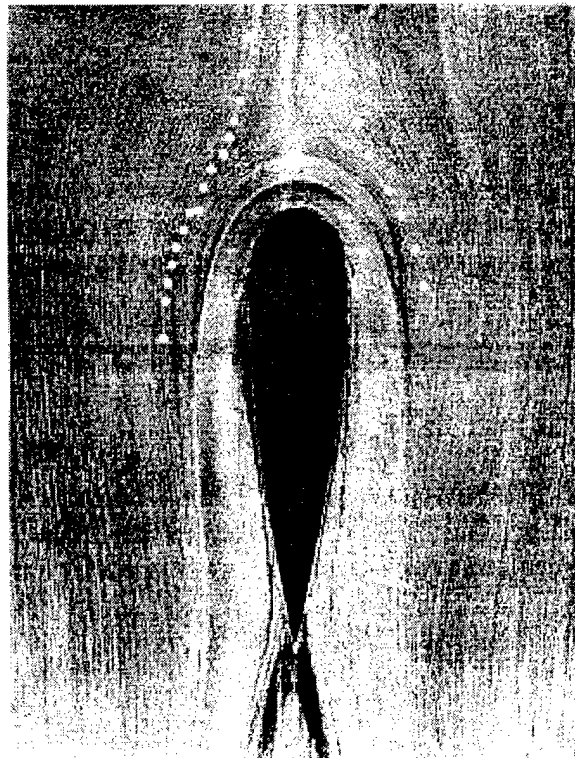


Figure 2.11.b, the experiment of Olcmen and Simpson. An oil-flow visualization of the flow indicating the average wall streamlines and measurement stations. (figure 2(b) from Olcmen and Simpson, 1995)

## Chapter 3 Results and Discussion (Reynolds Stress Parameters)

In Chapter 2, the experiments were presented in chronological order. In the remaining chapters, the presentation of results is arranged based upon the complexity of the flows. This will present an evolution of the parameters through various flow geometries. The organization of flows for the discussion is outlined in Table 3.1. Plots that directly support the discussion are presented at the end of this chapter. Several additional figures, constructed as part of this study, are presented in Appendices B-L. Table 3.1 matches each experimental case to an appendix where the additional figures reside. These plots were significant to this thesis but only briefly mentioned in the text. The uncertainties were estimated, according to the rules of error propagation (Taylor, 1982), from the uncertainties in each individual Reynolds stress component or triple product as reported by the original authors. The uncertainties are included in the discussion to support the conclusions of the current study. An account of the uncertainty analysis is given in Appendix A. For simplicity, throughout the remainder of this chapter, the experiments will be referred to by a single name; McMahon for McMahon *et. al.* (1982), Baskaran for Baskaran and Bradshaw (1987), Driver for Driver and Johnston (1990), Littell for Littell and Eaton (1991), Devenport for Devenport and Simpson (1992), Schwarz for Schwarz and Bradshaw (1992), Molton for Barberis and Molton (1993), Stäger for Kreplin and Stäger (1993), Chesnakas for Chesnakas and Simpson (1994), and Ölçmen for Ölçmen and Simpson (1995). These identifiers are listed in Table 3.1.

The first section of the results will focus on the discussion of parameters formed from terms in the Reynolds stress tensor. The parameters presented are for experimental data sets, and stations within these data sets, for which they were never calculated or presented in previous publications.

### 3.1 The 1/S Parameter

The algebraic relationship expressed as the magnitude of the Reynolds shear stress in a plane parallel to the wall,  $|\tau/\rho|$ , over  $\overline{v^2}$  was determined to approximate a constant value over a significant portion of wall bounded shear layers (Ölçmen and Simpson, 1995). Simpson (1995) defined this parameter to be  $1/S$  and it will be called so throughout the remainder of this discussion. Ölçmen and Simpson (1995) examined the behavior of this parameter for some stations from nine separate experimental data sets. (The various data sets used in the Ölçmen and

Simpson, 1995, examination reside in a *Journal of Fluids Engineering* data bank, see Ölgmen and Simpson, 1992.) For their LDV data in the wing-body junction, they found that  $1/S$  maintained an approximately constant value over the range  $0.03 < y/\delta < 0.6$ . The value that the parameter maintained differed from station to station ranging from values of 0.4 to 0.6 with most of the values near 0.5. The other data sets approximated a constant to values near  $y/\delta$  of 0.7-0.8 and ranged from values of 0.4-0.75 with a heavy concentration about 0.6. At  $y/\delta = 1.0$ ,  $1/S$  appears to have a mean value, for the data presented, of approximately 0.3. This value of  $1/S$  near  $\delta$  is observed in several of the other experiments described below as well.

The bounds of the  $1/S$  relationship can be qualitatively described as follows. As the outer edge of the boundary layer is approached, the amount of Reynolds stress produced by the rotational motion is reduced, due to the turbulent-non-turbulent interface, and the velocity fluctuations approach the values of the turbulence intensity in the freestream, which are small. As the turbulent-non-turbulent interface is approached, intermittency considerations indicate that the irrotational fluctuations should decay as a function of  $y^{-4}$  (Simpson, 1995). At the edge of the boundary layer, global  $v$  velocity fluctuations are produced by the pressure fluctuations as described by the Poisson equation (Simpson, 1995). These effects cause the reduction of  $1/S$  in the outer layer ( $y/\delta > 0.8$ ). At the wall, the fluctuating velocities must be zero and  $1/S$  must vary linearly with  $y$  near the wall ( $y^+ < 3$ ) as can be seen by an analysis of the functional behavior of the fluctuating velocities in the mass continuity equation. This parameter is attractive for inclusion in a modeling scheme since it is invariant to a rotation about an axis normal to the surface. Also due to the fact that  $v' \equiv (\overline{v'^2})^{1/2}$  should act as an important turbulence velocity scale. The importance of  $v'$  is emphasized near the wall where the ejections and sweeps, contributing to the majority of the turbulence production, are strongly related to  $v'$  (Simpson, 1995).

The current study attempts to illustrate variations in the  $S$  parameters over a variety of complex 3D flow geometries and to describe behavior based on common 3D flow features. It extends the study of Ölgmen and Simpson (1995) to data sets and stations that were not previously examined. Uncertainties are discussed where they were able to be determined. The majority of data that were obtained for the current study did not measure the flow very near the wall. For these studies, the data represents the outer layer for  $y/\delta > 0.1$ . For this reason, the  $1/S$  parameter was the focus of this study rather than its reciprocal  $S$ , which was applied in the near wall region in the Ölgmen and Simpson (1995) study. The  $S$  parameter will be presented and discussed, where applicable, following a detailed discussion of the  $1/S$  parameter for each flow case represented in Table 3.1. The stations of McMahon are described in Figure 3.1.

The experiment of Pompeo illustrates the effects of an additional rate of strain for the stations on the centerline and effects of either converging or diverging duct flows. Figure 3.2 details the behavior of  $1/S$  for the experiment of Pompeo. Within the uncertainty of  $\pm 22\%$  estimated for  $1/S$  in this experiment,  $1/S$  maintains fairly constant values for individual stations over the range  $0.1 < y/\delta < 0.7$ . A mean value in this range can be estimated as  $1/S \approx 0.72$  which includes all of the stations. The stations that are on the centerline of the duct tend to maintain a slightly higher value (0.75) than the stations off the centerline (0.68) where additional 3D TBL effects are present. There appears to be no preference for either converging or diverging flow at the off centerline stations. The centerline stations indicate slightly lower values of  $1/S$  for the Converging configuration and the diverging case appears to maintain more precision of the values. As the freestream is approached,  $y/\delta > 0.7$ ,  $1/S$  behaves somewhat linearly and passes through a mean value of 0.3 at  $y = \delta$ .

The experiment of Schwarz provides a test case with crossflow development and decay in a  $30^\circ$  bend with a minimal adverse streamwise pressure gradient. Figure 3.3 contains the results for  $1/S$  calculated for both the upstream development and downstream decay regions. The value of  $1/S$  was estimated to be  $\pm 25\%$  uncertain for this experiment. Station 0 is in the 2D TBL region before the imposition of the spanwise pressure gradient. The values for the upstream stations are slightly decreasing with increasing  $y$  but the slope is slight enough to approximate  $1/S$  by a constant value near 0.7 for  $0.1 < y/\delta < 0.7$ . As the freestream is approached,  $1/S$  appears to decrease in a somewhat linear fashion to a value slightly greater than 0.3 at  $y = \delta$ . Station 12 experiences the maximum amount of crossflow in this experiment. For it,  $1/S$  has the most constant value of 0.7 over the range  $0.1 < y/\delta < 0.7$ . Beyond station 12, the crossflow begins to decay. As this happens, the values of  $1/S$  tend to decrease from 0.7 towards 0.6. For the decay region of the flow,  $1/S$  better approximates a constant value for each individual station, however a definite trend of a lower value is discernible for the decay region. This tends to follow the behavior of the Reynolds stresses for this flow. The flow is decaying back to a 2D TBL, however the turbulence field does not recover as quickly as the mean flow, and  $1/S$  seems to reflect this behavior. Even though, this trend seems clear, the values of  $1/S$  are all quite similar for this experiment and the apparent lag is not significant when the uncertainty is accounted for.

The Ölçmen experiment was discussed above but will be summarized again here for continuity. The  $1/S$  parameter is presented again in Figure 3.4. In the outer layer, above  $y^+$  of 70,  $1/S$  approximated a constant value near 0.5 then trailed off as the boundary layer edge was approached. There was greater scatter from station to station for this flow in comparison to the Chesnakas flow, but a brief review of Chapter 2 will illustrate the increased complexity of the

Ölçmen experiment. The setup and measurement strategy presents a more complex 3D TBL than investigated for some other experiments. Despite the complexities of the flow, the  $1/S$  parameter can still be considered as a constant for individual stations for the region mentioned above. This experiment attained measurements very near the wall. Below  $y^+$  of 100,  $1/S$  begins to increase reaching a maximum value near  $y^+=10$ . For the Ölçmen flow, the stations do not collapse onto the same line nor do they achieve similar maxima. This is attributed to the complexity of the flow and the lag in the near wall fluid to react to changes in the pressure field. However they exhibit a similar functional dependence and approach zero after attaining their maxima. Ölçmen and Ciochetto also performed experiments on a zero pressure gradient flat wall TBL to investigate the dependence of the near wall flow on Reynolds number. This investigation, for similar conditions as the experiment above, resulted in  $1/S$  maintaining a slightly greater value, 0.6, and decreasing continuously to 0.5 as the boundary layer edge was approached. As seen in Figure 3.5, this was lower than  $1/S$  for the 2D data of Klebanoff. Across  $0.2 < y/\delta < 0.6$ , the Klebanoff data is nearer to the 0.7 value of  $1/S$  seen in the previous experiments.

The experiment of Baskaran illustrates the effects of convex and concave curvature for the case of an 'infinite' swept wing. The results for  $1/S$  are given in Figure 3.6, the case of concave curvature is given in Figure 3.6.a and that of convex curvature is given in Figure 3.6.b. The parameter  $1/S$  for the individual stations of the experiment appears to approximate constant values for the range  $0.1 < y/\delta < 0.8$  with a mean value of 0.8. For  $y/\delta > 0.8$ ,  $1/S$  decays approximately linearly as the boundary layer edge is approached. At  $y = \delta$ ,  $1/S$  passes through a mean value of 0.3. For the concave curvature, the only noticeable effect of curvature is seen in station 9 which is furthest downstream. At station 9, the value of  $1/S$  is remarkably constant with a mean value of 0.6 over the range of  $y/\delta$  mentioned previously. The convex curvature case does not indicate strong effects due to curvature. The values for  $1/S$  in the downstream direction fluctuate between values of 0.6 to 1.0 over the range of  $y/\delta$  indicated previously. The uncertainty in  $1/S$  for this experiment was estimated to be  $\pm 45\%$  (Appendix A) based on reported uncertainties in  $\overline{vw}$  of  $\pm 30\%$ . Thus it appears that curvature does not have a strong effect on the behavior of the  $1/S$  parameter.

When  $1/S$  is compared to the  $a_1$  structural parameter with similar full scale values, they appear to be qualitatively similar for this experiment. An example of this similarity is exhibited in the additional figures for Baskaran in Appendix E.

The experiment of Chesnakas used a 6:1 prolate spheroid model that was similar to the Stäger experiment at the same angle of attack with similar freestream conditions. It did differ in experimental techniques. The Chesnakas velocity data was obtained via a LDV system rather than

with hot wire sensors. When viewed as a function of  $y/\delta$  (Figure 3.7),  $1/S$  approximated a constant value of 0.6 for  $y/\delta > 0.1$  or 0.2. The value varied slightly towards the aft end of the model tending to decrease slightly overall and more noticeably towards the edge of the boundary layer. This decrease can be qualitatively observed in the Stäger data as well. The decrease may be due to an increase in the  $v$  velocity fluctuations relative to the magnitude of the shear stress as the flow separates. Increased scatter is observed in the downstream regions too. The behavior of  $1/S$  in the near wall region can be emphasized with a semi-log plot. Figure 3.8 illustrates  $1/S$  as a function of the wall length scale  $y^+$ . This shows  $1/S$  increasing as the wall is approached. For near wall data,  $1/S$  remains relatively well correlated. Comparison with the near wall data of Ölçmen shows similarity in the behavior of  $1/S$  as the wall is approached.

The experiment of Stäger is similar to the Molton and Chesnakas experiments. There is significant scatter in the calculated values of  $1/S$  (Figure 3.9). However, upon closer observation, individual stations can be observed to approximate constant values that differ from station to station. This is more obvious in the upstream measurement planes. A mean value of approximately 0.6 appears to prevail for this experiment. One discernible trend is that the value of  $1/S$  increases as  $\phi$  progresses from  $0^\circ$  to  $180^\circ$ , from the windward to the leeward side of the model. The value of  $1/S$  on the windward side tends to maintain a value of 0.4. The uncertainty in the data prevents further observations to be made.

The experiment of Molton combines effects from several of the flows that have already been discussed. On the leeward side of the model, the streamlines are converging as the case of Pompeo. Also on the rearward section of the model, the flow separates and contains vortical structures (Fig. 3.10) similar to the McMahon and Devenport experiments. It also is similar to the experiments of Chesnakas and Stäger on 6:1 prolate spheroid body. Figure 3.11 has the results of their data taken in the region on the model where forward scatter LDV techniques were used. On the leeward side of the model,  $\phi = 0^\circ$ ,  $1/S$  acts as a decreasing function of  $y$ . The peak value of 0.9 occurs near  $y/\delta = 0.1$  and decreases to 0.3 at  $y = \delta$ . For angles about the body,  $1/S$  acts as a decreasing function of  $y$  but in not as severe a fashion as for  $\phi = 0^\circ$ . As the measurements progress towards the windward side of the body, the peak value near the wall tends to be reduced and approach a more constant value across the boundary layer. An unexplained feature of this flow is an apparent asymmetry between the  $\phi = 170^\circ$  and  $\phi = 190^\circ$  measurement stations at equal angular spacing from the leeward side of the model. For  $\phi = 190^\circ$ ,  $1/S$  maintains a more constant value with a mean value near 0.5. The data obtained in back scatter mode, on the aft portion of the model, were in the separated flow further away from the body (Figure 3.12). Here the uncertainty in the measurements was greater and  $1/S$  can be seen to approximate a more constant value over  $y$

than in the forward measurement region. Some features of  $1/S$  can be observed that are consistent with the observations from the McMahon and Devenport flows. In the presence of a vortex,  $1/S$  becomes reduced from typical upstream values between the surface and the vortex core. This is illustrated by the reduction of  $1/S$  at  $x = 1100$  mm where the separation has not yet fully occurred and the separation vortex is yet weak. Severe effects on  $1/S$  are seen at  $x = 1300$  mm where the value of  $1/S$  peaks near  $\phi = 150^\circ$  where the vortex core occurs. This is opposite of the behavior under the vortex in the McMahon and Devenport flows. This seems to indicate that the vortex is transporting TKE or velocity fluctuations away from the surface near the vortex core and towards the surface near the wall.

Comparison of  $1/S$  with the  $a_1$  structural parameter shows that qualitatively, the parameters behave similarly. These results are presented in appendix H. However in this experiment,  $a_1$  tends to be slightly more scattered than  $1/S$  on the aft portion of the model.  $a_1$  exhibits similar peaks and reductions as discussed above for  $1/S$ .

The experiment of Driver illustrates the behavior of  $1/S$  in a flow that is relaxing from a shear driven state with the application of various adverse pressure gradients. Figure 3.13 presents the results for the  $1/S$  parameter for the experiment of Driver. The results for all of the data of Driver are presented here, however, as pointed out in Chapter 2, Driver recommends specific cases to illustrate the effects of adverse pressure gradient and rate of strain. Regardless of these considerations, the  $1/S$  parameter appears to approximate a constant value for individual stations over the range of  $0.1 < y/\delta < 0.8$ . The  $x$ -locations of the individual stations are documented in Table 3.2 which indicates the position of the measurement with respect to the beginning of the stationary cylinder. In Figure 3.13 a horizontal line across the station list indicates where the transition from rotating to stationary cylinder occurs. This is where the flow transitions from a 2D shear-driven collateral flow to the relaxing 3D flow. The values of  $1/S$  that are over the rotating cylinder tend to maintain greater values than the stations that are in the relaxation zone of the experiment. For the cases with no shear-induced motion, (BS0, CS0, and DS0) the values of  $1/S$  behave similarly from station to station for the range  $0.2 < y/\delta < 0.8$ . One noticeable difference between the regions before and after  $x = 0$  in the behavior of  $1/S$  is a significant decrease upstream of  $x = 0$  for  $y/\delta < 0.2$ .

To examine the effect of adverse pressure gradient on  $1/S$  for this experiment, consider the cases AS1, BS1, CS1, and DS1. All of these cases involve a shear-induced flow with the same surface velocity with respect to the reference velocity. Case AS1 is a zero adverse pressure gradient case and case DS1 has the most severe adverse pressure gradient imposed. Considering case AS1 as a reference state,  $1/S$  tends to have less variation with  $y$  near the wall as greater

adverse pressure gradients are applied. Thus it would appear that an increased pressure gradient tends to stabilize the  $1/S$  parameter near the wall. The uncertainty in the  $1/S$  parameter was determined to be  $\pm 19\%$  for these experiments. Effects of the regions of active skewing v. relaxation regions on  $1/S$  can be seen in this data. No appreciable effects of pressure gradient can be discerned. Comparing cases BS0, CS1, and DS1, which had similar upstream boundary conditions, it can be inferred that the addition of skewing to the flow tends to reduce the scatter in the  $1/S$  parameter. Average values of  $1/S$  for this experiment could be estimated at 0.7 over the rotating cylinder and 0.6 in the downstream section.

The experiment of Littell is another example of a shear driven flow. The results are illustrated in Figure 3.14. For  $0.1 < y/\delta < 0.6$ ,  $1/S$  approximates a fairly constant mean value of 0.7 for the various radii and rotational speeds investigated. The uncertainty on  $1/S$  for this experiment is estimated to be  $\pm 25\%$ . There appears to be no significant effects caused by variation of radial location or disk speed. The ambient flow for this experiment had zero velocity and as  $y$  increased, the velocity and its fluctuations tended to zero. This was a unique feature in comparison to the other flows in this study. This is also the reason for the increased scatter in the parameters with increasing  $y$ . The other parameters that were investigated for the Littell experiment all tended to decrease linearly with increasing  $y$ , see later discussion, however the  $1/S$  parameter tended to maintain a similar behavior as in the previous experiments, which points to the robustness of this parameter for a variety of different flow situations.

The experiment of Devenport was similar to that of McMahon. The results from the current calculations are presented in Figure 3.15 for the various planes of data that were obtained. The values of  $1/S$  for this data were not very constant, even for individual stations. There were several unrealizable data points that were removed from this data set before calculation of  $1/S$ . Also the flow is different from the other data sets previously examined as it is not a true boundary layer flow. The only general trend that can be observed in this experiment is a reduction in  $1/S$  near the body close to the wall region. This appears consistent with the results from the McMahon experiment. The scatter in the results here prevent further comment.

The data of McMahon were obtained in the junction vortex of a wall appendage flow as described in Chapter 2. This flow differs greatly from the traditional concept of a wall-bounded shear flow since, in the vortex region, significant values of the wall normal velocity can exist. A description of the definition of the experimental stations of the McMahon data that were used for the present study is given in Figure 3.1. This figure also indicates the location of the core of the vortex which is useful when considering the behavior of the relationships presented in this study.



Recall from Chapter 2 that the outermost stations, U14 and D15 were considered by McMahon to be in the 2D region of the flow.

Overall,  $1/S$  appears to be rather scattered for this flow. However, some observations may be made when one considers certain regions of the flow independently. The results for  $1/S$  from the upstream plane of data is given in Figure 3.16. Near the body and close to the wall stations U1-U4 exhibit the closest behavior to the approximately constant regions of the previous experiments. Here,  $1/S$  has a mean value near 0.55 before beginning to decrease for  $y > 0.015$  m. As the vortex core is approached, the  $v$  fluctuating velocity increases and dominates the  $1/S$  relationship, which is seen in the reduction of  $1/S$  near the wall for U5-U13. The region above  $y = 0.015$  m for the stations outboard of U8 illustrate an increase in the scatter in this parameter, the cause of which is unknown. A larger reduction in  $1/S$  is observed for the stations outboard of the vortex core where the flow near the wall is directed in the positive  $z$  direction. The worst correlation of  $1/S$  between the stations is observed in the regions farthest away from a surface. Station U14 appears to approach a constant value across the boundary layer, at a value of 0.25, which is lower than typical values observed in other experiments. The results for the downstream plane are illustrated in Figure 3.17. At this location, the vortex has diffused away from the wall and the body. Here,  $1/S$  illustrates a different behavior in the outer region of the flow. It is more scattered and does not appear to tend toward zero as the freestream is approached. Near the wall and the body, stations D1-D3 appear to maintain a mean value near 0.5. This becomes reduced as the core of the vortex is attained. In the downstream plane,  $1/S$  in the outboard region tends to be more correlated from station to station than in the upstream plane. This is assumed to be a result of a reduction in the vorticity as the junction vortex becomes more diffused. The outboard stations reach a minimum value of  $1/S$  below the core and do not exhibit a region where  $1/S$  is sufficiently constant. The deviant behavior of station D15 could not be accounted for.

The  $a_1$  structural parameter was calculated for the stations of this experiment and is presented in appendix J. A qualitative comparison between  $1/S$  and  $a_1$  may be made between these plots. In general, the behavior of the two relationships is similar for the different regions of the flow. It is observed that the outboard stations attain a greater value for  $a_1$  as the freestream is approached. Otherwise, the behavior of these two relationships are similar for this experiment.

### 3.2 The S Parameter

The algebraic ratio  $S$ , defined as  $\overline{v^2}$  over  $|\tau/\rho|$ , was presented by Ölçmen and Simpson (1995) for selected stations of nine different experimental data sets (Figure 3.18a). The individual experiments appeared to approximate a constant value as a function of  $y^+$ . The value varied between experiments and had an average value of 1.6. They report that  $S$  was greater in 3D TBLs than in 2D TBLs due to less correlation between the  $u$  and  $v$  fluctuating velocities. Simpson (1995) refers to the use of  $S$  in the inner layer for proposed modeling efforts. Since the reciprocal  $1/S$  was presented for all of the experiments in this report,  $S$  was examined only where insight into the near wall behavior could be obtained. Figure 3.18b illustrates  $S$  for the seven stations of the Ölçmen flow. It is included here for comparison to the other test cases. For the experiment of Chesnakas,  $S$  values approximated an increasing function of  $y^+$  that had a value near 0.3 at  $y^+ = 10$  and increased to a value near 2.0 at the edge of the TBL (Figure 3.19). For each longitudinal location,  $S$  had little scatter among the different circumferential angles. The scatter tended to increase with the downstream stations. For the Driver flow, near wall data was obtained, but  $y$  could not be scaled on wall variables due to off-design test conditions for the reported data. Due to this,  $S$  was not computed for the Driver flow. The other flows in the study focused on the outer layer.

### 3.3 The Ratio of Reynolds Stress Production, $C$

Ölçmen and Simpson (1995) also introduced a parameter,  $C$ , that represents the ratio of the production of the  $-\overline{vw}$  to the  $-\overline{uw}$  Reynolds shear stresses (see section 2.2.11). They reported that  $C$  was nearly constant for a given station over a range of  $y$  in the wall stress coordinate system. They reported that this behavior persisted between  $100 < y^+ < 1000$ . As part of the current examination, the ratio  $C$  was examined for the eleven different data sets in different coordinate systems. Unfortunately the data in the present study produced values of  $C$  that were too scattered to verify this result presented in Ölçmen and Simpson (1995). To calculate  $C$ , the gradients of  $W$  and  $U$  needed to be computed. It is believed that the experimental uncertainties tainted the results of the gradient calculation and caused high degrees of artificial scatter in the results. The plots of  $C$  are included in the respective appendices.

### 3.4 Other Algebraic Ratios Involving Reynolds Stresses

#### 3.4.1 The ratio $-\overline{vw} / -\overline{uw}$

Ölçmen and Simpson (1995) reported the behavior of the  $-\overline{vw}$  and  $-\overline{uw}$  stresses as "closely related" in a wall-stress coordinate system. They pointed out that, in the boundary layer equations, the  $\overline{uw}$  Reynolds stress is considered a higher-order term and often neglected. Also that the  $\overline{uw}$  stress can be as great or greater than the  $\overline{vw}$  stress. Thus the influence of  $\overline{uw}$  may be of importance. However this ratio is not a good candidate for modeling efforts as it depends on the choice of coordinate systems.

The present study included an examination of this ratio for the eleven data sets that were investigated. Ölçmen and Simpson (1995) found that in wall-stress coordinates for pressure driven flows, that this ratio varied semi-logarithmically and correlated with  $y^+$  for  $y^+ < 500$ . The data of Chesnakas support the observation of Ölçmen and Simpson (see the Appendices for specific plots for this ratio). The ratio is zero near the wall and then is a decreasing function of  $y^+$  up to  $y^+$  of 500 where it becomes uncorrelated. This correlation appears to break down for the plane of data furthest downstream in the Chesnakas experiment. The values of  $y^+$  could not be determined directly for all of the flows included in the present study so the data were compared on  $y/\delta$ . Since this is simply a different scaling for the  $y$  variable, the similarities in the ratio should be apparent. The scale factors for the  $y$  variable at each  $x, z$  location are constants for a given profile. Thus the difference in a plot of a parameter between two different scales is a slightly different slope due to the expansion or contraction of the  $y$  coordinate scale, the inherent behavior of the parameter is preserved. For Schwarz, this ratio attained its largest positive value with the data nearest the wall then decreased towards the outer layer. It was uncorrelated in the crossflow development phase of the flow but well correlated in the crossflow decay region of the flow. Pompeo's experiment illustrated different behavior for this ratio in the converging and diverging test sections. For the diverging case, the data closest the wall produced the largest value of the ratio which decayed towards zero. The converging case illustrated a large positive value of this ratio near the wall which tended toward zero. The spinning disk of Littell produced a value of this ratio that achieved a large negative value nearest the wall and tended toward zero as the velocity reduced towards the free atmosphere. These last results differed from the behavior observed by Ölçmen and Simpson but the ratio still appeared to act as a function of  $y$ . The results of the present study confirm the observation that the  $\overline{uw}$  Reynolds stress can be of similar magnitude as the  $\overline{vw}$  stress in 3D TBLs.

### 3.4.2 The ratio $\overline{uv} / \overline{vw}$

The ratio of  $\overline{uv}$  to  $\overline{vw}$  was computed for some of the flows in this study. The results were similar to the ratio  $\overline{vw} / \overline{uw}$  but tended to collapse from station to station with less correlation. The degree of scatter in these results were greater than the previous ratio. The value in presenting these results is minimal so they are just mentioned here. Figures of results are presented in appendix B - L where appropriate.

### 3.4.3 The relationship $(\overline{v^2} / \overline{u^2})^{0.5}$

Parameters similar to Nagano and Tagawa (1993) were derived for 3D flow by Ölçmen (1995) and put to test as part of this study. These are presented in the next section. In discussion of these parameters, it was determined that for these parameters to maintain a constant value, the square root of the ratio of  $\overline{v^2}$  to  $\overline{u^2}$  should approximate a constant across the regions where these parameters could be considered constant. Therefore, the square root of the ratio of  $\overline{v^2}$  to  $\overline{u^2}$  was calculated and examined for each of the flow cases in this study.

The Pompeo data (Figure 3.20) indicate that this ratio is somewhat constant across the TBL for their experimental setup. It increases slightly from 0.58 to 0.68 across the range  $0.1 < y/\delta < 0.8$ . As their apparatus produced little streamwise pressure gradient, this is consistent with the value of 0.6 from the Driver data with no pressure gradient (Figure 3.24). The lateral strain rate or spanwise pressure gradient did not appear to affect this ratio.

The data of Schwarz, Figure 3.21, support the observations made in the previous experiment and the experiment of Driver. For the upstream stations in the 30° bend, this ratio is approximately constant at a value of 0.6 then increases beyond  $y/\delta$  of 0.7-0.8. The downstream section showed the parameter to increase to values near 0.7 as the flow progressed. The majority of their test section had zero streamwise pressure gradient, but the latter part of their test section was subjected to a slight adverse pressure gradient which is reflected in the behavior of this parameter. This ratio seems to be extremely sensitive to slight changes in streamwise pressure gradient.

The data of Ölçmen (Figure 3.22) show a similar functional dependence on  $y^+$  as the Chesnakas flow (Figure 3.23) but tend to be less correlated from station to station. The lack of

correlation is again attributed to the complexity of the flow (see section 2.2.11). The main feature to be observed in this data is the lack of the constant region for this parameter. For  $y^+ > 100$ , the ratio is an increasing function of  $y^+$  with different slopes for different stations. A great degree of influence from the inner layer fluid is suspected for this flow case.

For the Chesnakas data, this ratio is presented on a logarithmic scale to accent the near wall behavior (Figure 3.23). The degree of correlation for each station for this parameter is high throughout this entire flow. The value approaches zero close to the wall (at  $y^+$  of 10 it is 0.15) and increases as a function of  $y^+$ . Near  $y^+ = 100$ , the parameter begins to approximate a constant value, 0.65-0.7 for this flow. In the outer layer, the parameter becomes less correlated.

The data of Driver produced good correlation of this ratio from station to station, but had variations for the different flow cases, Figure 3.24. This indicates an influence of pressure gradient on this parameter. All flow cases tended to exhibit a similar functional dependence. Nearest the wall, the value rose sharply from zero to a somewhat constant value near  $y/\delta = 0.1$  (0.2 for cases with pressure gradient applied). The section where it approximated a constant value persisted up to  $y/\delta$  of 0.7-0.8 where it began to increase as the boundary layer edge was approached. For cases with no pressure gradient applied, the parameter reached an average value of 0.6 by  $y/\delta = 0.1$ . It tended to be better correlated among the stations nearer the wall and had increased scatter in the outer region. The cases with a pressure gradient had a somewhat linear dependence between  $0.03 < y/\delta < 0.2$  that began at a value of 0.55 and reached a value of 0.8 which it approximately maintained to the point where it began to increase in the outer layer. In comparison to the non-pressure gradient cases, the pressure gradient cases tended to have less correlation near the wall but greater correlation in the outer layer. The effects of shear appear minimal based on this experiment.

The data of Littell are interesting in the reversal of functional dependence with height of this parameter, Figure 3.25. It attains its greatest value nearest the wall and then seems to decrease linearly with  $y/\delta$ . The degree of correlation is less than observed in the Driver data. This seems to imply that the  $v$  velocity fluctuation is greater with respect to the  $u$  velocity fluctuation in the presence of a mean flow independent of its proximity to a solid surface. The values begin near 0.6 at  $y/\delta$  of 0.1 and decrease to 0.4 at  $y/\delta$  of 0.7, the outer layer is too scattered to discern any information from.

The experiment of McMahon presented the least amount of correlation for this parameter, assumed to be due to the uncertainty in the data. The upstream data plane (Figure 3.26) shows the parameter to initially increase, attain a maxima, level out or decrease, then increase throughout the remainder of the boundary layer. It is difficult to compare the location of these features as a non-

dimensionalized function of distance from the wall as neither  $\delta$  or  $u_\tau$  was able to be determined from the information presented in the data report. The downstream plane of data (Figure 3.27) showed this parameter to be an increasing function of  $y$  with significant scatter. Values in the middle of the layer tended to range from 0.8-1.0.

#### 3.4.4 The relationship $\frac{\overline{vw}}{\overline{uw}} \sqrt{\frac{\overline{u^2}}{\overline{v^2}}}$

The inverse of this parameter multiplied by the  $\overline{vw} / \overline{uw}$  shear stress ratio was investigated for a few cases directly, but can be inferred from the plots of the individual components of this parameter as reported elsewhere in this report. The data of Baskaran produced results that had a degree of correlation such that no conclusive observations were able to be made. The data of Littell showed a trend in this parameter similar to the behavior of the ratio  $-\overline{vw} / -\overline{uw}$  for this flow. The results are presented in Figure 3.28. It had values near -0.6 to -0.7 nearest the wall and tended to increase as the boundary layer was traversed reaching values near zero at  $\delta$ . For the experiment of McMahon, the results are similar to the square root of the ratio of  $\overline{v^2}$  to  $\overline{u^2}$  for that flow, Figure 3.26 and Figure 3.27. The results of this parameter are presented in Figure 3.29 and Figure 3.30. There are a few modifications, the values change and the functional dependence is modified near the wall for the upstream plane and away from the wall for the downstream plane. The values nearest the wall are negative (-0.3) and the initial maxima that was observed is now gone. For the downstream plane, the outer layer values do not tend to increase as the boundary layer edge is approached, they either level off or decrease. Other results are presented in the appendices.

### 3.5 Nagano and Tagawa parameters

Following the derivation of several parameters for 2D TBLs by Nagano and Tagawa (1990, 1991), Ölçmen (1995) derived their equivalent for 3D TBLs. He tested these parameters on his wing-body junction data. As part of the present study, these parameters were examined for various data sets. The definitions of the parameters as used in this study follow;

$$I: \quad \frac{\overline{uv^2}}{\overline{v^2} \sqrt{\overline{u^2}}} = - \frac{\overline{u^2 v}}{\overline{u^2} \sqrt{\overline{v^2}}} \quad (3.1)$$

$$\text{II: } \frac{\overline{v^3}}{(\overline{v^2})^{\frac{3}{2}}} = B \frac{\overline{u^2 v}}{\overline{u^2} \sqrt{\overline{v^2}}} \quad B = -1.33. \quad (3.2)$$

$$\text{III: } \frac{\overline{vw^2}}{\overline{w^2} \sqrt{\overline{v^2}}} = \frac{1}{3} \frac{\overline{u^3}}{(\overline{u^2})^{\frac{3}{2}}} + \frac{1}{B} \frac{\overline{v^3}}{(\overline{v^2})^{\frac{3}{2}}} - \frac{\overline{uw^2}}{\overline{w^2} \sqrt{\overline{u^2}}} \quad (3.3)$$

They are referred to as correlation I, II, and III in the plots and text. To examine the characteristics of these equations, designation of the left hand and right hand sides of the equations as LHS? and RHS? respectively was applied, where the ? is replaced by the appropriate correlation number; I, II, or III. The results are presented in appendix M. For the data of Pompeo, these correlations do not appear to hold. When formulated as RHS-LHS of any correlation, the values across the boundary layer are not zero. They are closest to zero nearest the wall but differ greatly towards  $\delta$  and also differ for the converging and diverging test cases. The ratio LHS/RHS should be near  $\pm 1$  which is seen to not be the case. The data of Schwarz also do not support these relationships across the entire layer. However, for  $y/\delta < 0.3$  it appears that they may hold. The difference RHS-LHS shows that all three correlations are near zero for all of the stations in this flow. The interpretation is slightly confused by the results of the ratio LHS/RHS since nearest the wall data is the farthest from  $\pm 1$ , and the data in the outer layer all seems to collapse to a value of -1. The Chesnakas data does not approximate a constant value across the boundary layer for these correlations. It is flatter in the region  $40 < y^+ < 400$ , but the uncertainty bounds on the experiment do not support a constant relationship. As separation is approached, the correlations exhibit more scatter from station to station.

### 3.6 The $a_1$ relationship of Chesnakas

Chesnakas and Simpson (1994) illustrate the reduction in the  $a_1$  parameter as discussed in Chapter 1 for many flow cases. They state that this reduction in  $a_1$  for 3D flows does not attain a common value from experiment to experiment and from station to station in some cases. They use the data of the 6:1 prolate spheroid experiment to develop and propose a scaling to account for this reduction. The scaling is stated to be correlated with the three-dimensionality of the flow, as

suggested by their data set. As part of the current study, this scaling was examined for some other 3D TBLs.

The correlation was implied when they plotted the value of  $a_1$  at a mid-profile location v. a non-dimensional representation of the three-dimensionality (Figure 3.31a). The value of  $a_1$  used was chosen from locations of  $y^+ < 200$  in a somewhat arbitrary fashion. It was chosen to be near the beginning of the log-layer. The non-dimensional three-dimensionality parameter was  $\Delta\beta/Re_\theta$ , where  $\Delta\beta$  is the maximum change in flow angle across the boundary layer (radians). They fit the following curve to the data,

$$a_1 = a_{1_0} \cdot \sec h \left( 18,800 \frac{\Delta\beta}{Re_q} \right) \quad (3.4)$$

where  $a_{1_0} = 0.145$ , is the value for  $a_1$  with no 3D effects. This fit requires that  $a_1$  approach zero with increasing three-dimensionality. Also they note that the value for  $a_1$  calculated does not apply throughout the entire boundary layer. Flack and Johnston (1994) stated that  $a_1$  must vary with  $y^+$  near the wall and approach 0 at the wall. They proposed a curve fit for  $a_1$  for their data near the wall,

$$y^+ = ma_1 + e^{Bc} \left[ e^{ca_1} - 1 - ca_1 - \frac{(ca_1)^2}{2} \right] \quad (3.5)$$

where  $m=150$ ,  $c=33$ , and  $B=0.02$ . Chesnakas reported that this scaling did not work with the prolate spheroid data and the DNS data of Spalart (1988). Based on the prolate spheroid data, Chesnakas suggested the following scaling to describe the behavior of  $a_1$ .

$$a_1 = a_{1_0} \cdot \sec h \left( 18,180 \frac{\Delta\beta}{Re_q} \right) \tanh \left( \frac{y^+}{25} \right) \quad (3.6)$$

The results that Chesnakas and Simpson (1994) obtained are shown in Figure 3.31b.

The scaling was tested for the Schwarz flow. The results are presented in Figure 3.32a. As illustrated, the correlation does not collapse from station to station and does not show much more approximation to a constant than  $a_1$  itself. Figure 3.32b shows the values of  $a_1$  used verses the three-dimensionality parameter. It shows that the effects seen in the prolate spheroid flow are



not present here. That is  $a_1$  does not decrease to the same degree with the addition of crossflow. One reason this may differ is the lack of near wall data, however the choice of  $a_1$  was relatively close to the beginning of the log-layer. The experiment of Ölçmen was also used to test this scaling. The results are presented in Figure 3.33. The investigation of the choice of flow angle difference was examined here. The normalized  $a_1$  correlates best when the difference between the flow angle at the particular  $y^+$  and the wall flow angle is used. The other flow angle differences indicated in the figures do not correlate the data from station to station well enough to draw any conclusions other than the near wall scaling appears to behave logarithmically not linearly as predicted by Flack and Johnston (1994).

It was observed previously, as noted in Chapters 1 and 2, that the value of  $a_1$  does not always behave similarly for different 3D flows. Sometimes the value can increase from the expected 2D value, as in the convex flow geometry as Baskaran (1987), but generally it will decrease. Other 3D effects, such as in Pompeo, the divergence from the 2D value is minimal. The good correlation illustrated in Chesnakas and Simpson (1994) is most likely a result of the curve fit being generated from their data. Thus it will be weighted to favor those particular results. The present study shows that a function requiring  $a_1$  to always decrease with increasing three-dimensionality will not apply to the most general case including all 3D TBLs. If  $a_1$  is to be used as a modeling parameter for 3D flows, more work is needed in determining the effects of three-dimensionality on it.

### 3.7 Conclusions

Parameters and correlations were presented in this chapter that directly related to the Reynolds stresses. Various complimentary parameters and ratios are presented in the early sections of the appendices as well. The  $1/S$  parameter was the best behaved parameter to aid in the modeling effort. It relates the  $-\overline{uv}$ ,  $-\overline{vw}$ , and  $\overline{v^2}$  Reynolds stresses. It provides a relationship for these three Reynolds stresses that is independent of coordinate system when chosen with  $y$  normal to the wall. The parameter approximates a fairly constant value over the inner region of the flow,  $0.3 < y/\delta < 0.8$  for each station. The values from station to station and flow to flow do not tend to vary much either, 0.55 - 0.85. The  $1/S$  parameter is similar in form and behavior to the  $a_1$  parameter which relates the  $-\overline{uv}$ ,  $-\overline{vw}$ ,  $\overline{u^2}$ ,  $\overline{v^2}$ , and  $\overline{w^2}$  Reynolds stresses. Some advantages are that  $1/S$  uses fewer variables reducing the number of overall equations required. Another benefit that was illustrated by this study was that the  $1/S$  parameter approximated a constant behavior for

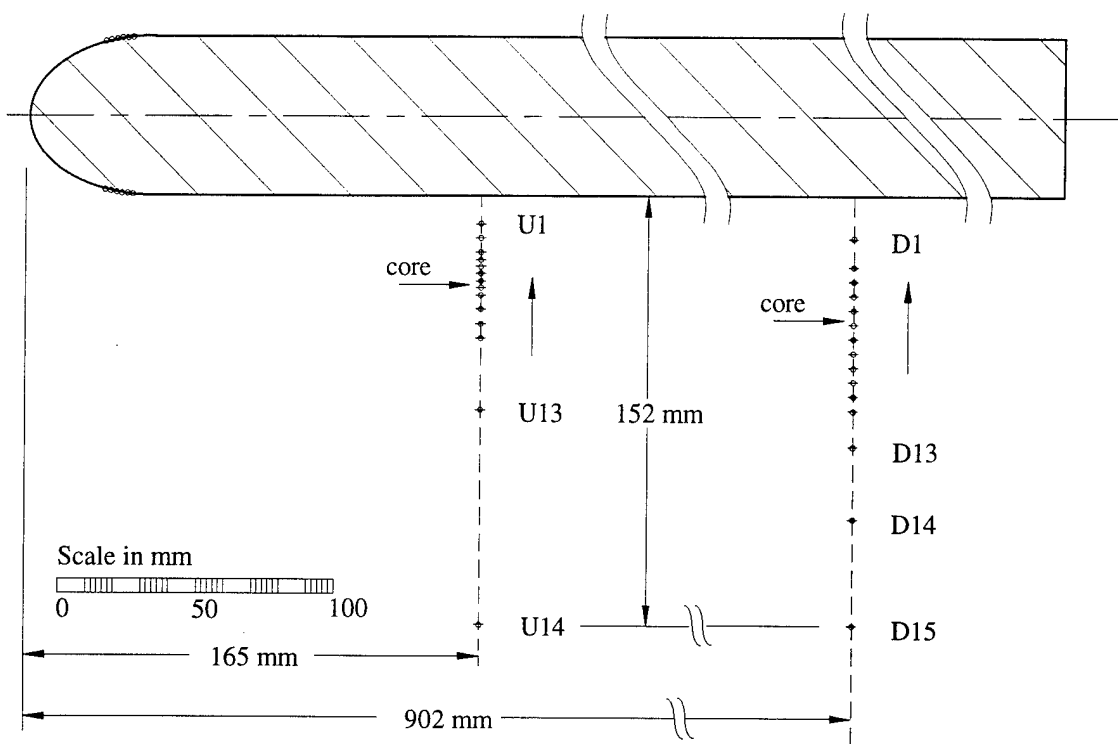
the region mentioned above for the purely shear driven flow of Littell where  $a_1$  was continually decreasing. The  $1/S$  parameter would be useful in complimenting modeling efforts to relate the three Reynolds stresses in its approximately range. Other parameters were presented that have good correlation from station to station but maintain a functional dependence on the  $y$  variable. These may be useful as well for modeling efforts, but the functional form was not sought or estimated here. It was also see that the  $C$  parameter and the  $a_1$  correlations of Ölcmen and Chesnakas worked well for their particular flows but did not correlate for the flows presented in the present study.

Table 3.1 The order of geometrical (or flow) complexity for discussion of the test cases.

Experimental Test Case	Characteristics	Appendix	Identifier	
Pompeo (1992)	plane of symmetry flow with an added centerline spanwise rate-of-strain	B	Pompeo	Pressure-driven TBL with mild streamwise pressure gradient effects
Schwarz and Bradshaw (1992)	mild pressure-driven flow with no imbedded streamwise vortices	C	Schwarz	
Ölçmen and Simpson (1995)	stronger pressure-driven flow with no embedded streamwise vortices	D	Ölçmen	
Baskaran and Bradshaw (1987)	pressure-driven flow with streamwise curvature and no embedded streamwise vortices	E	Baskaran	
Chesnakas and Simpson (1994)	pressure-driven flow generated by a body in the free-stream	F	Chesnakas	Pressure driven 3D TBL approaching separation
Kreplin and Stäger (1993)	same geometry as Chesnakas but the data was taken with different measurement techniques	G	Stäger	
Barberis and Molton (1993)	body at angle of attack with separation	H	Molton	
Driver and Johnston (1990)	relaxing spanwise shear-induced flow with external free stream	I	Driver	3D TBL generated by surface shear
Littell and Eaton (1991)	shear-driven flow with no external free-stream	J	Littell	
Devenport and Simpson (1992)	large vertical velocity in the vortices in addition to the free-stream	K	Devenport	Wing-body junction flows
McMahon, Hubbart, and Kubendran (1982)	large vertical velocity in the vortices in addition to the free-stream	L	McMahon	

Table 3.2 X-Locations for the experimental stations of Driver.

Case/ Station	AS1 x (mm)	BS0 x (mm)	BS1 x (mm)	CS0 x (mm)	CS1 x (mm)	DS0 x (mm)	DS1 x (mm)
X1	-330.2	-457.2	-457.2	-457.2	-457.2	-457.2	-457.2
X2	-152.4	-330.2	-330.2	-330.2	-330.2	-152.4	-152.4
X3	-12.7	-228.6	-228.6	-228.6	-228.6	-76.2	-76.2
X4	6.3	-152.4	-152.4	-152.4	-152.4	-12.7	-12.7
X5	12.7	-76.2	-76.2	-76.2	-76.2	0.0	0.0
X6	25.4	-12.7	101.6	-12.7	-12.7	12.7	12.7
X7	50.8	12.7	152.4	12.7	12.7	25.4	25.4
X8	101.6	152.4	228.6			48.3	48.3
X9	152.4	228.6	304.8	50.8	50.8	101.6	101.6
X10	228.6	304.8		101.6	101.6	152.4	152.4
X11	304.8			152.4		228.6	228.6
X12	457.2			228.6	228.6	304.8	304.8



Upwind Plane	x = 165 mm	Downwind Plane	x = 902 mm
Station	z (mm)	Station	z (mm)
U14	152.4	D15	152.4
U13	76.2	D14	114.3
U12	50.8	D13	88.9
U11	45.7	D12	76.2
U10	40.6	D11	71.1
U9	35.6	D10	66.0
U8	33.0	D9	61.0
U7	30.5	D8	55.9
U6	27.9	D7	50.8
U5	25.4	D6	45.7
U4	22.9	D5	40.6
U3	20.3	D4	35.6
U2	15.2	D3	30.5
U1	10.2	D2	25.4
		D1	15.2

Figure 3.1 Location of the Stations for the Data of McMahon

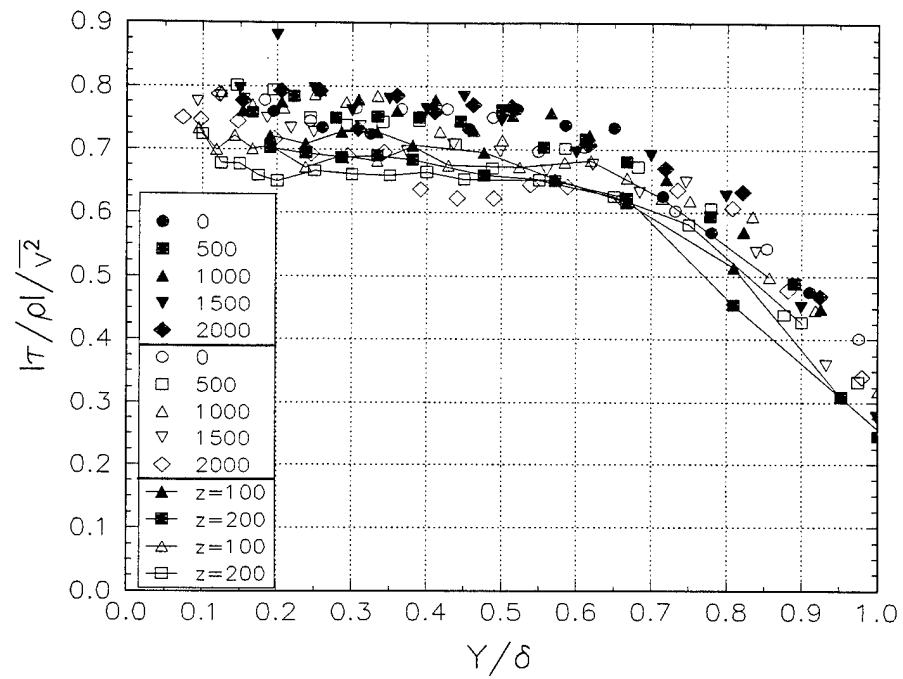


Figure 3.2  $1/S$  for the Pompeo data. Centerline stations (symbols only) have the x location shown in mm. Off centerline stations (lines) were at  $x = 1000$  mm, the z location is shown in mm. Closed and open symbols are for the diverging and converging duct, respectively.

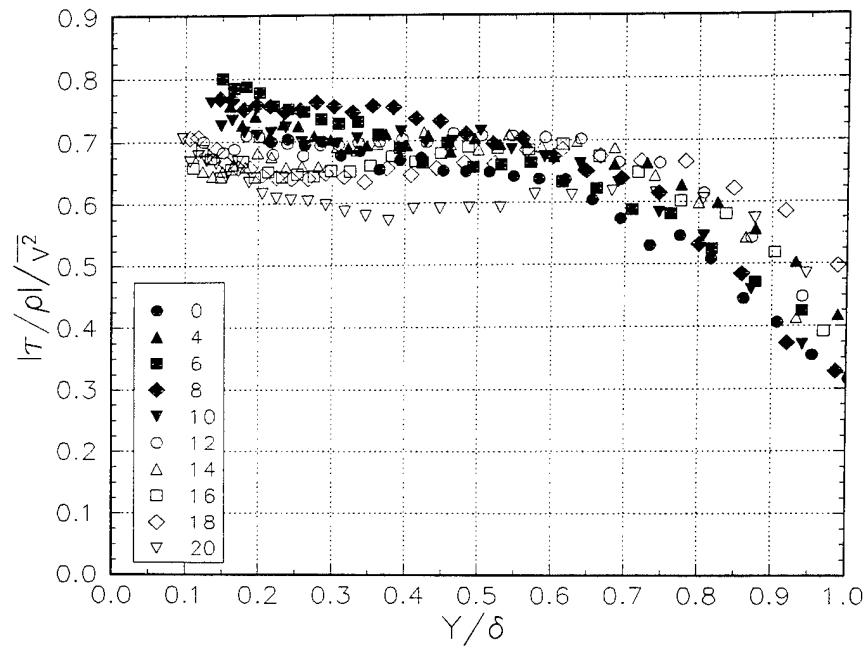


Figure 3.3  $1/S$  for the Schwarz 30° bend flow. Crossflow development region and decay region are the closed and open symbols, respectively.

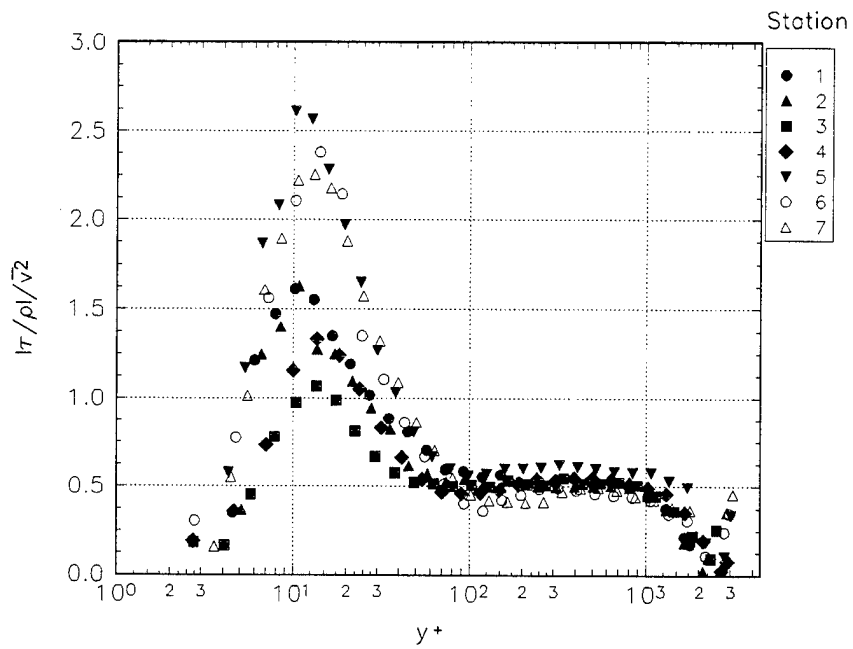


Figure 3.4  $1/S$  for the experiment of Ölçmen

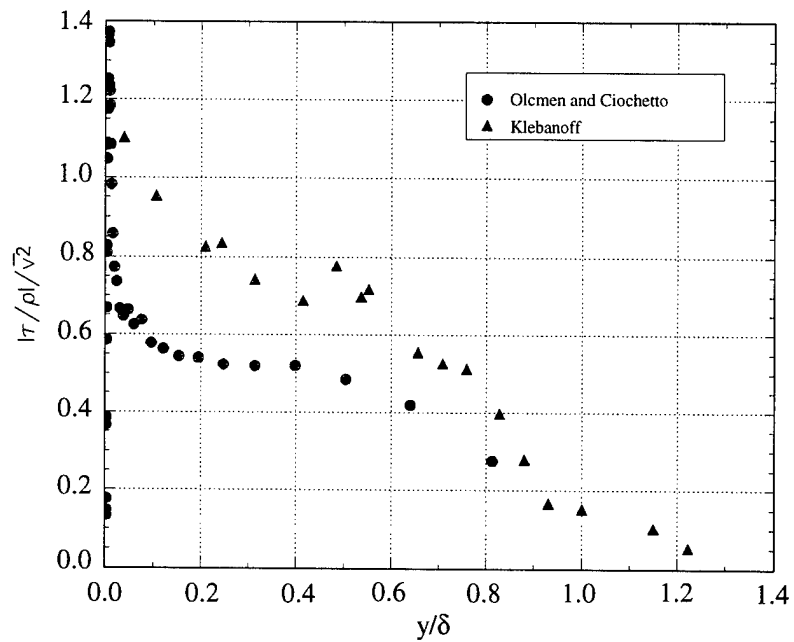


Figure 3.5  $1/S$  for 2D zero pressure gradient flat plate TBLs.



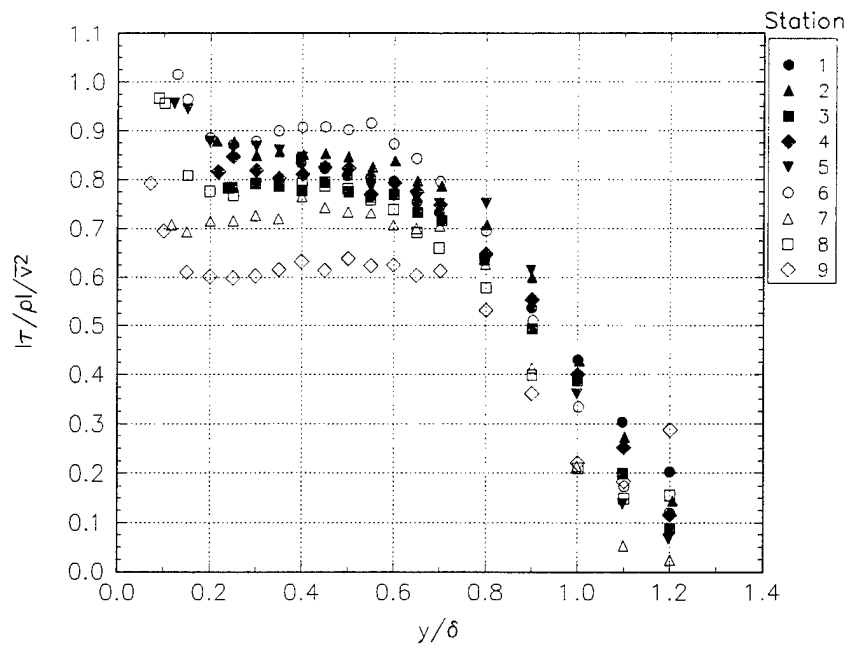


Figure 3.6.a  $1/S$  for the concave test case of Baskaran

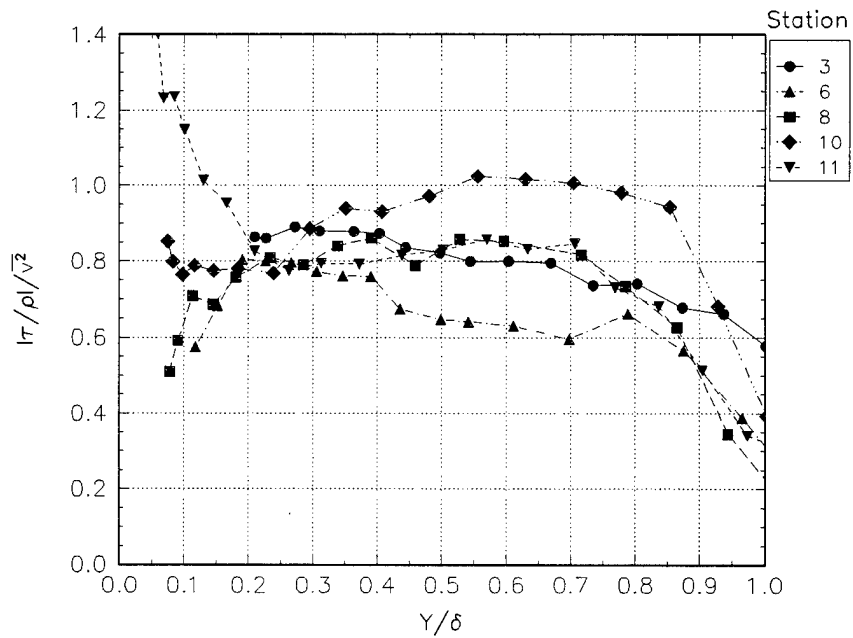


Figure 3.6.b  $1/S$  for the convex test case of Baskaran

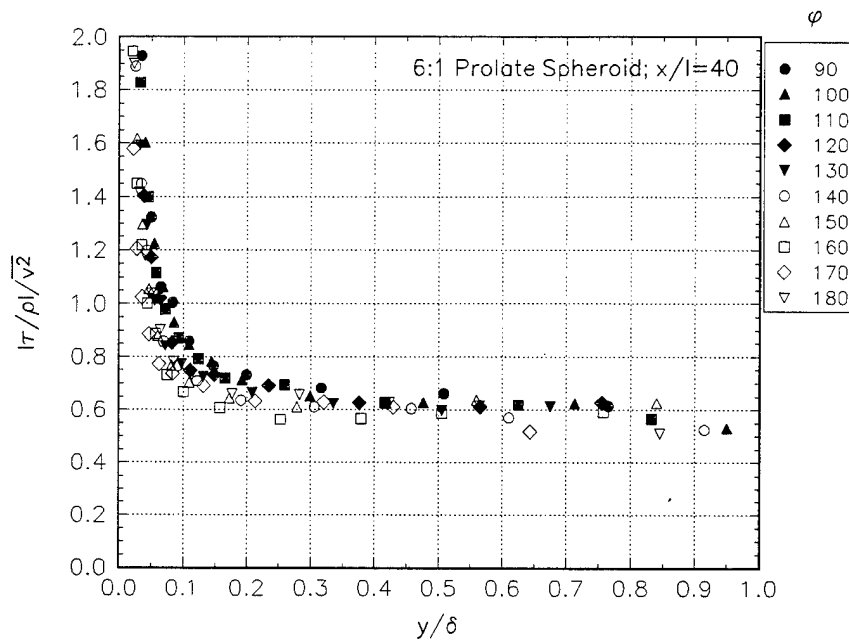


Figure 3.7.a  $1/S$  for Chesnakas at  $x/L = 0.40$

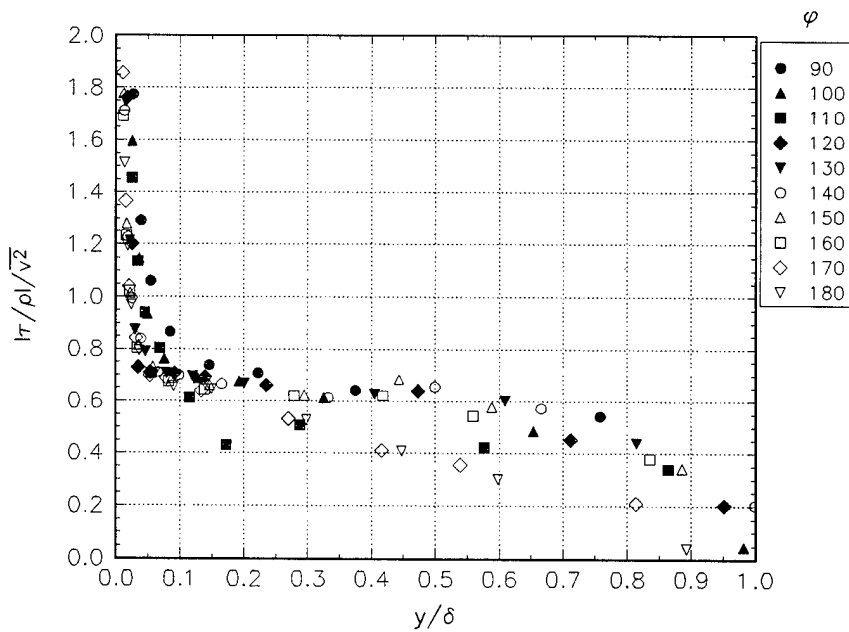


Figure 3.7.b  $1/S$  for Chesnakas at  $x/L = 0.60$

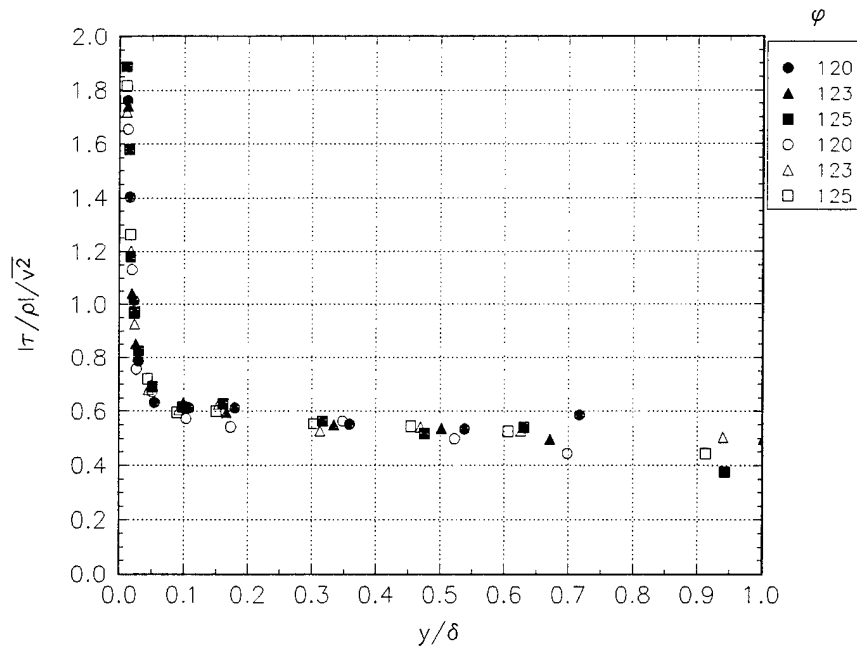


Figure 3.7.c  $1/S$  for the  $x/L=0.75$  (closed symbols) and  $x/L=0.76$  (open symbols) of Chesnakas

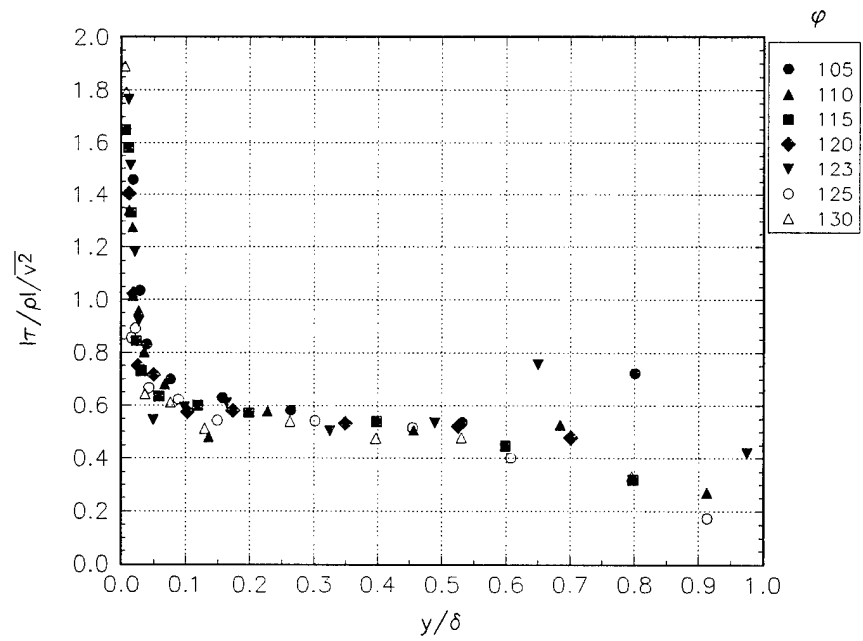


Figure 3.7.d  $1/S$  for Chesnakas at  $x/L = 0.77$

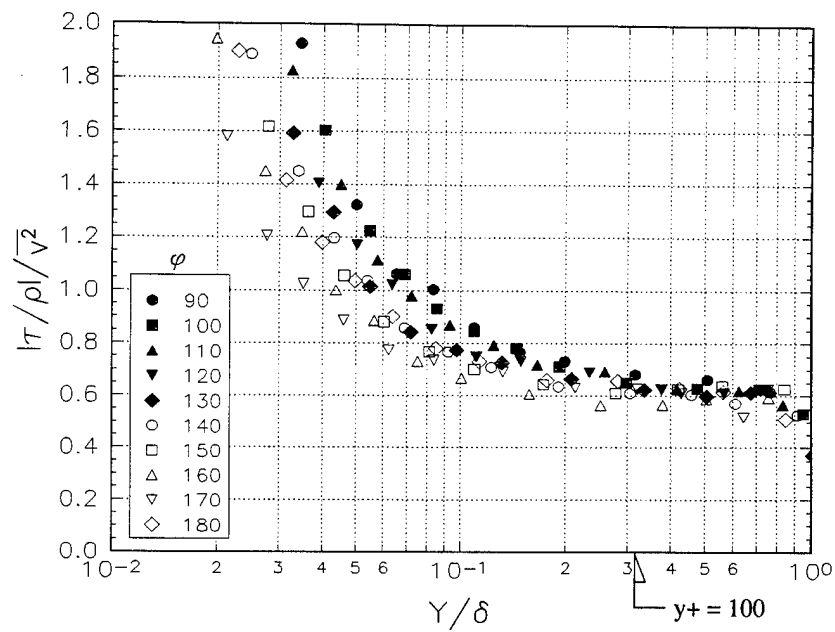


Figure 3.8  $1/S$  for Chesnakas and Simpson,  $\alpha = 10^\circ$  at  $x/L = 0.4$ .

The peripheral angle from the windward side ( $\phi$ ) is indicated.

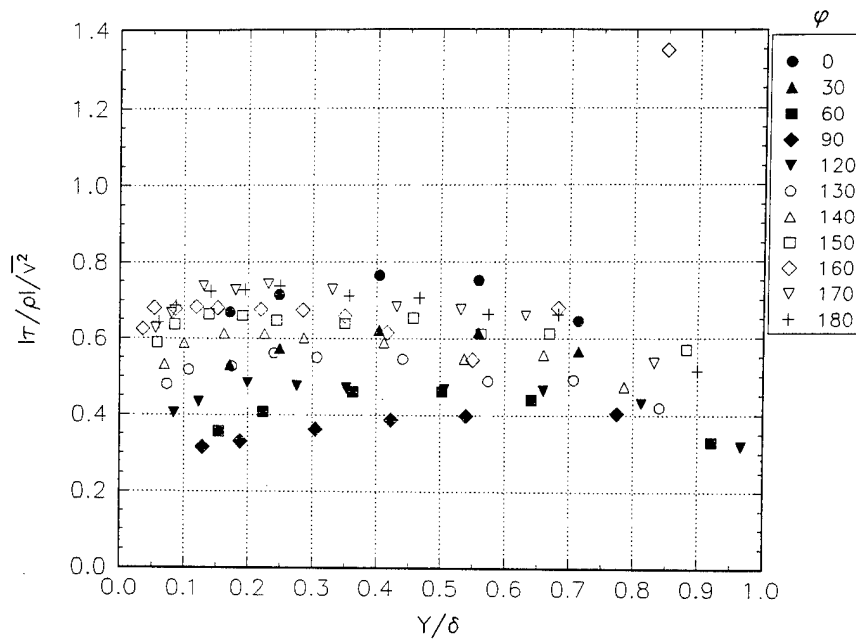


Figure 3.9.a  $1/S$  for Stäger at  $x/L = 0.48$

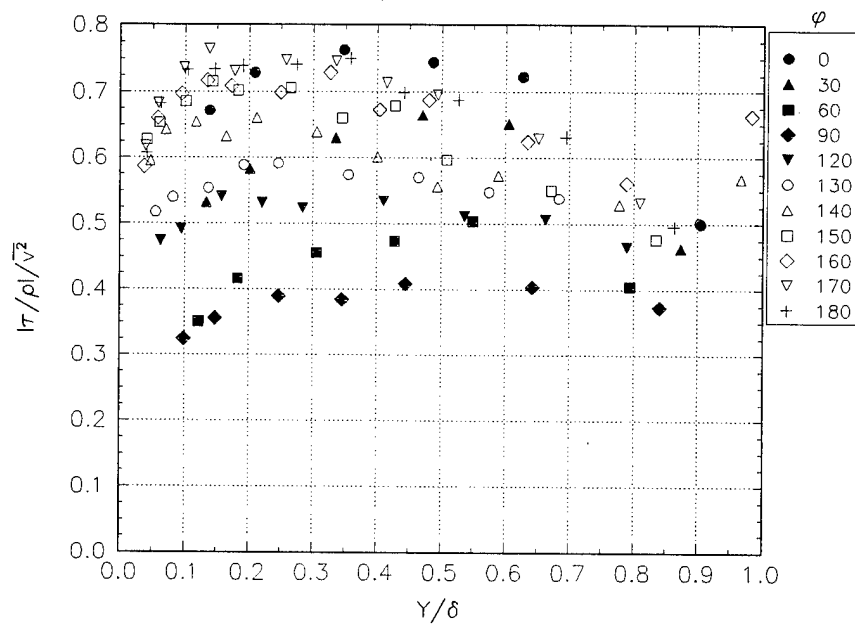


Figure 3.9.b  $1/S$  for Stäger at  $x/L = 0.56$

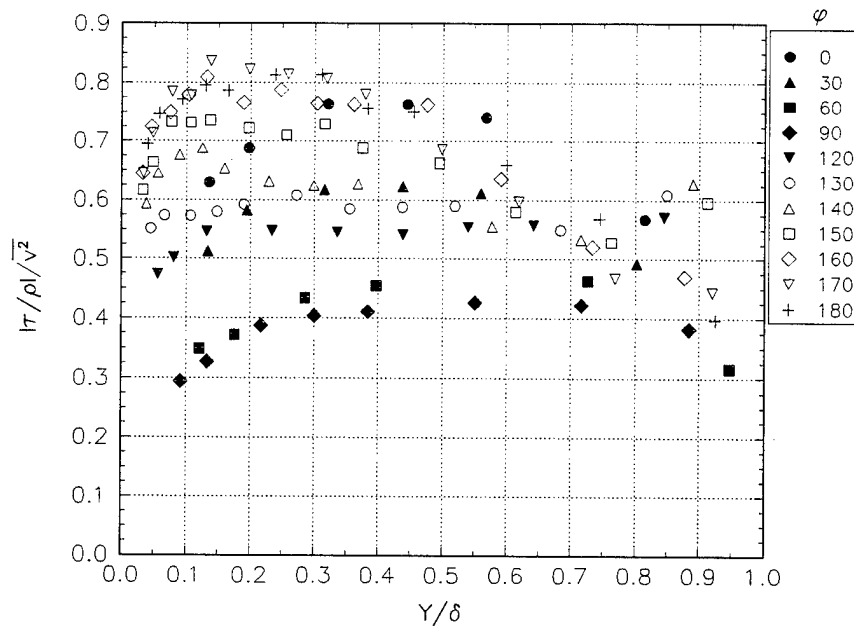


Figure 3.9.c  $1/S$  for Stäger at  $x/L = 0.64$

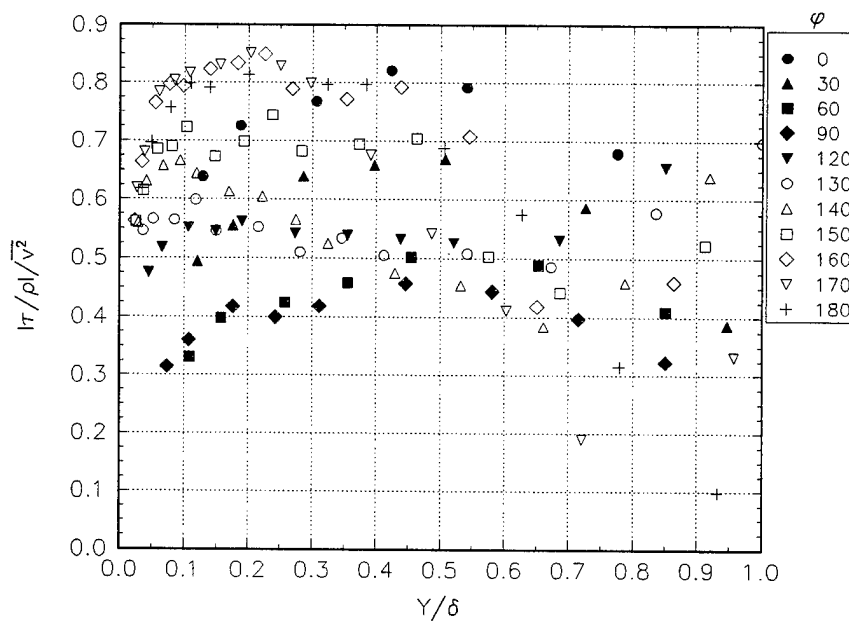


Figure 3.9.d  $1/S$  for Stäger at  $x/L = 0.73$

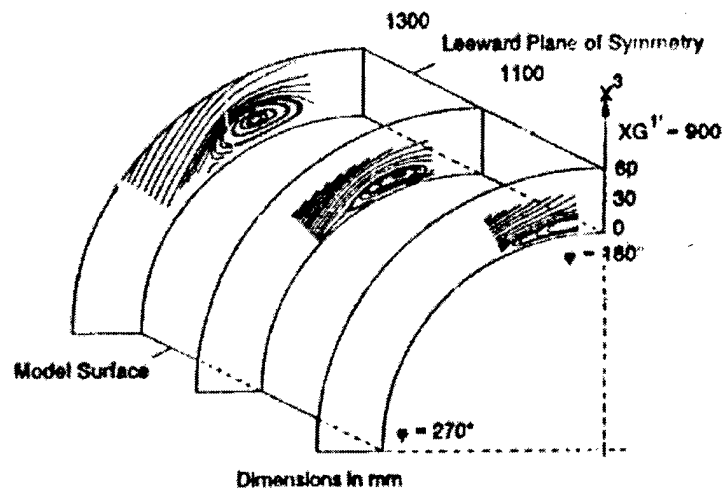


Figure 3.10 a description of the rearward section of the experiment of Molton.  
The longitudinal vortices are illustrated. (fig. 20 from Barberis and Molton, 1993)

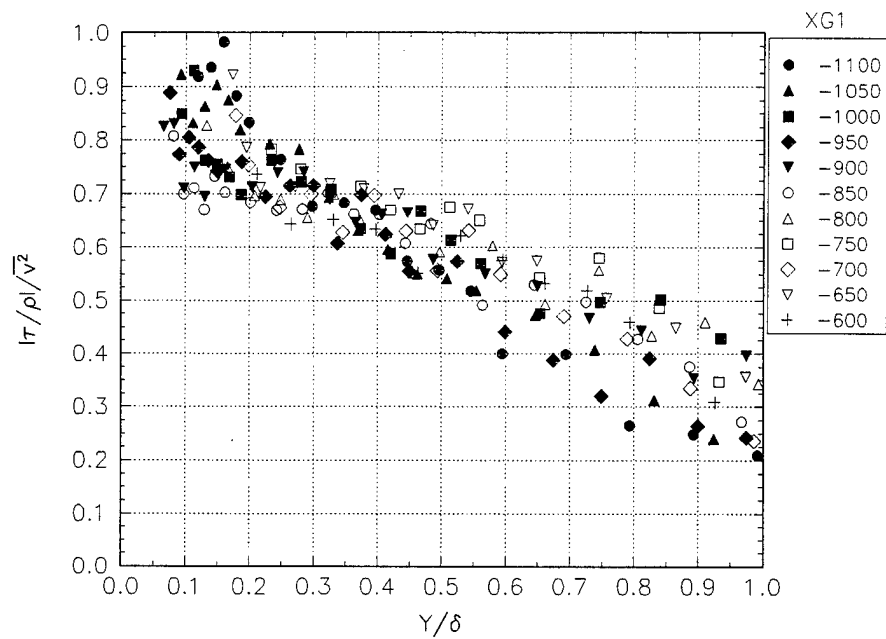


Figure 3.11.a  $1/S$  for the windward plane of symmetry ( $\phi=0$ ) for the experiment of Molton. The x-location (XG1) is given in mm.

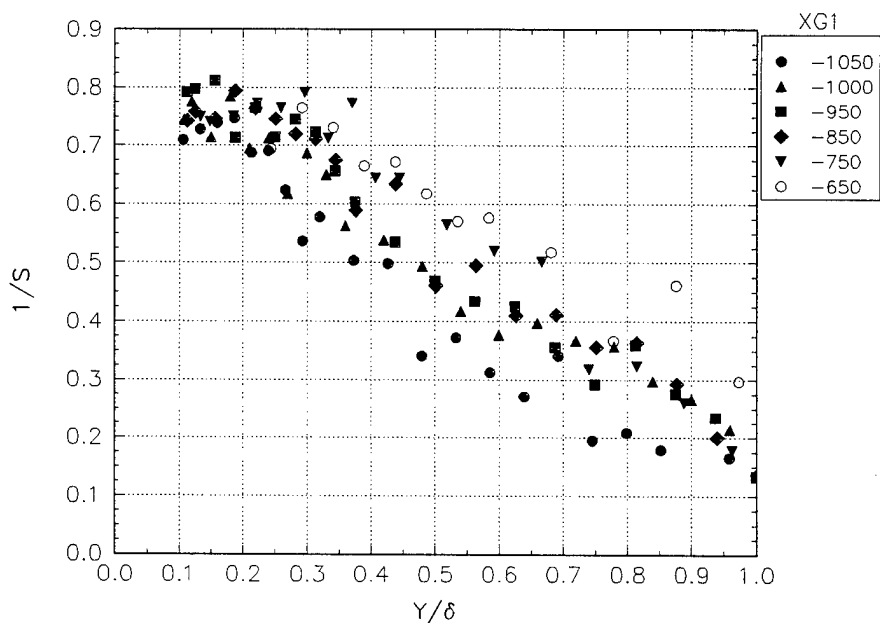


Figure 3.11.b  $1/S$  for the experiment of Molton for  $\phi = -5$ . The x-location (XG1) is given in mm.



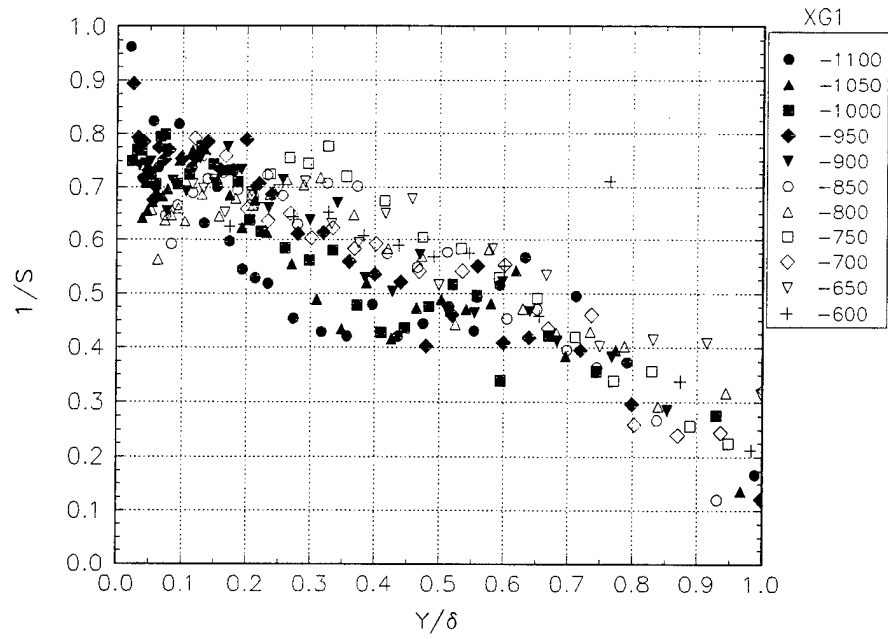


Figure 3.11.c  $1/S$  for the experiment of Molton for  $\phi = -10$  The x-location (XG1) is given in mm.

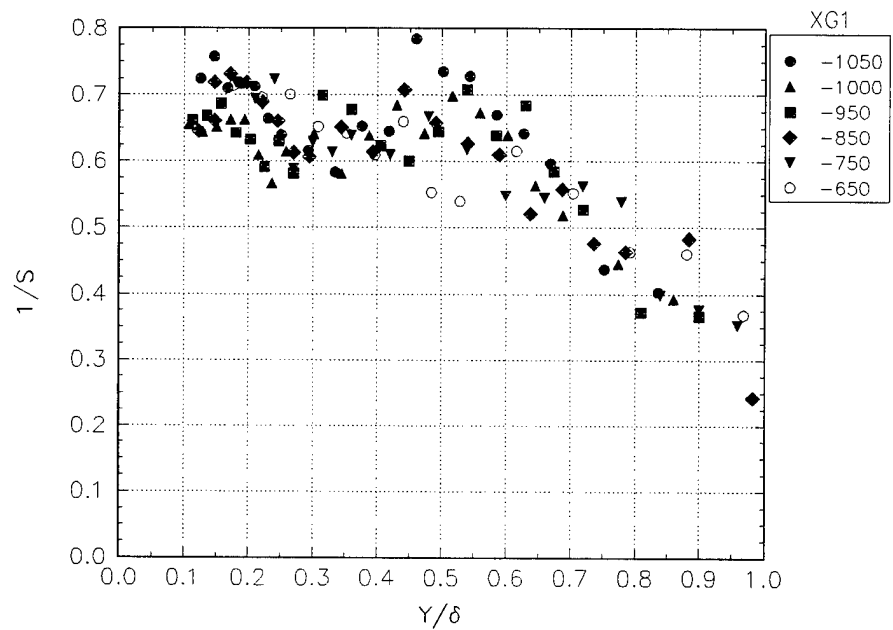


Figure 3.11.d  $1/S$  for the experiment of Molton for  $\phi = -15$  The x-location (XG1) is given in mm.

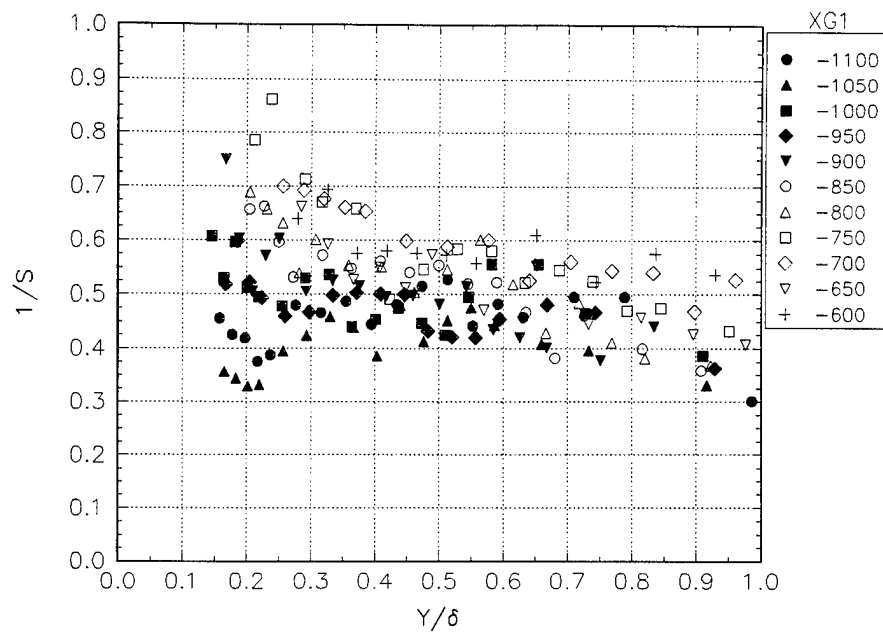


Figure 3.11.e  $1/S$  for the experiment of Molton for  $\phi = 10$ . The x-location ( $XG1$ ) is given in mm.

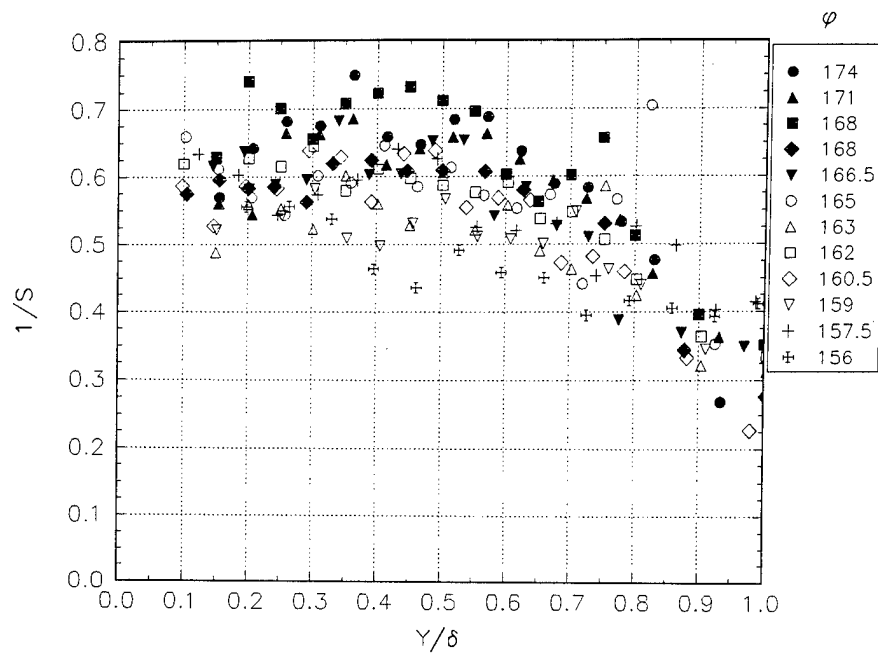


Figure 3.12.a  $1/S$  for the experiment of Molton for  $x=900$  mm for the data taken in backscatter mode.

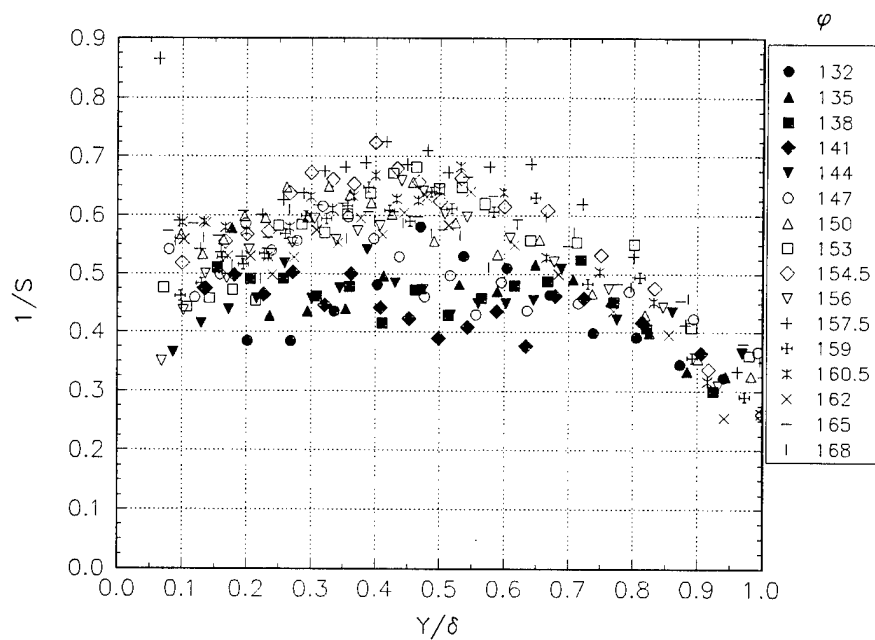


Figure 3.12.b  $1/S$  for the experiment of Molton for  $x=1100$  mm for the data taken in backscatter mode.

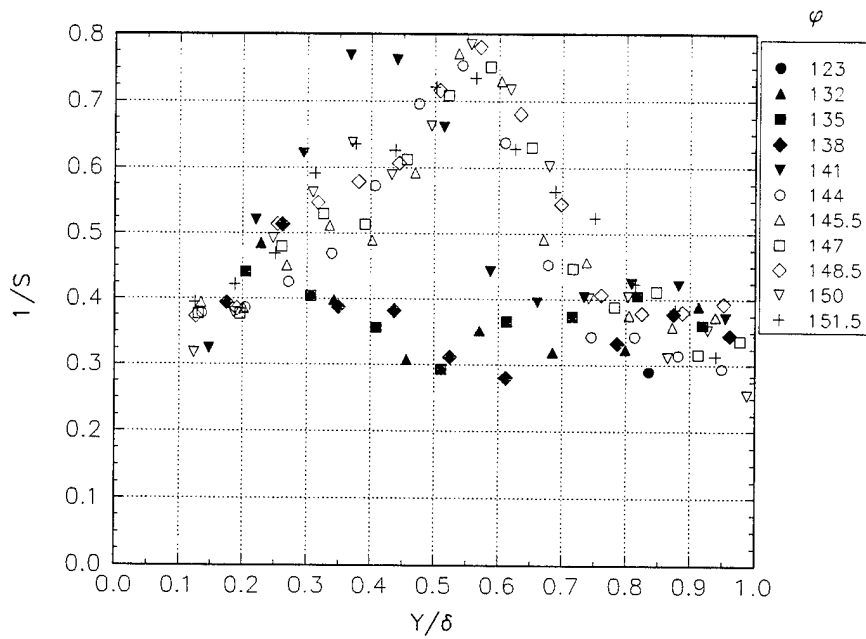


Figure 3.12.c  $1/S$  for the experiment of Molton for  $x=1300$  mm for the data taken in backscatter mode.

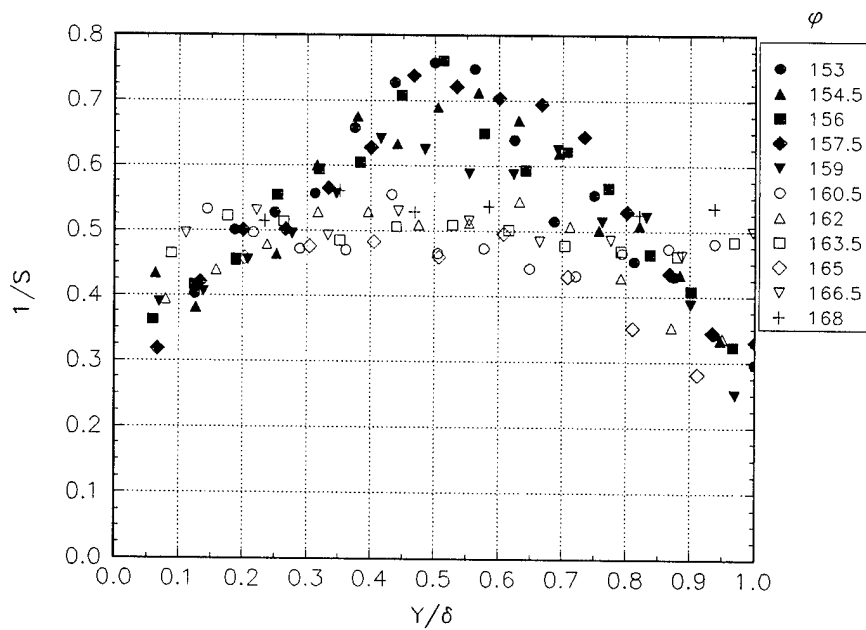


Figure 3.12.d  $1/S$  for the experiment of Molton for  $x=1300$  mm for the data taken in backscatter mode.

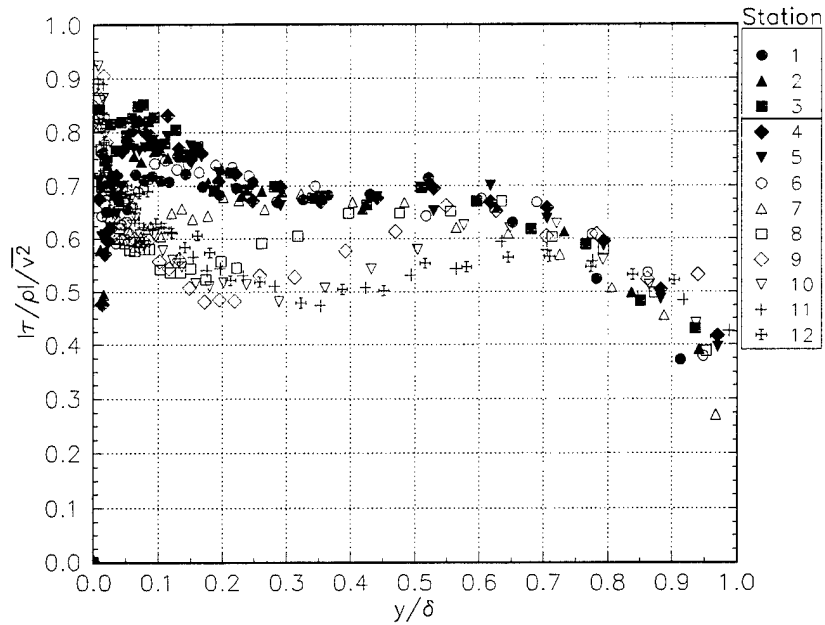


Figure 3.13a.  $1/S$  for stations of case AS1 of Driver and Johnston: Axisymmetric flow without an adverse pressure gradient, relaxing from an upstream shear-driven condition.

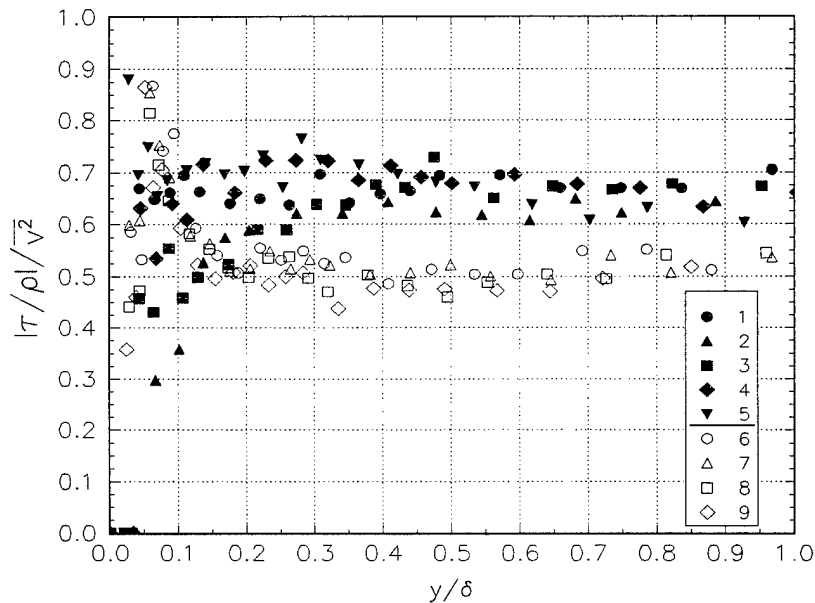


Figure 3.13b.  $1/S$  for stations of case BS1 of Driver and Johnston: an axisymmetric flow with a mild adverse pressure gradient, relaxing from an upstream shear-driven condition.

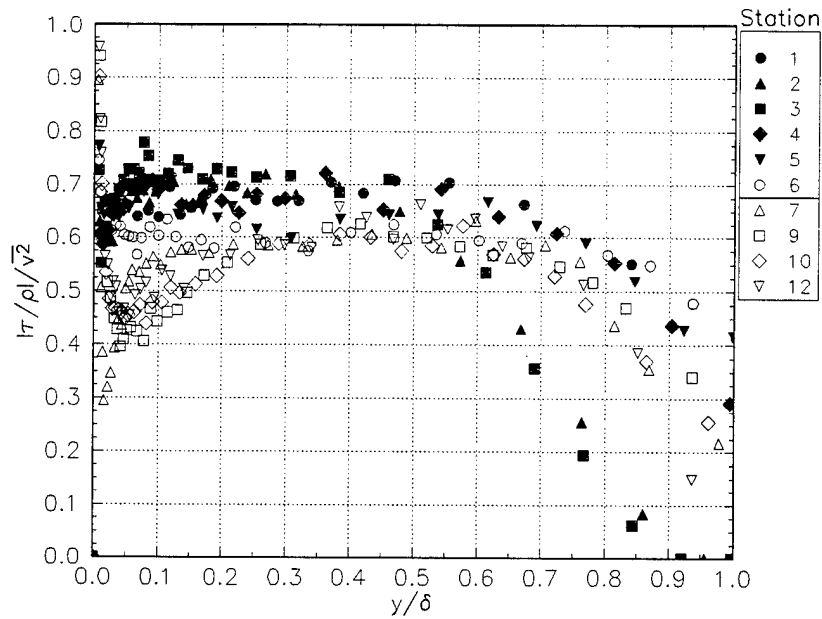


Figure 3.13c.  $1/S$  for stations of case CS1 of Driver and Johnston: an axisymmetric flow with a strong adverse pressure gradient, relaxing from an upstream shear-driven condition.

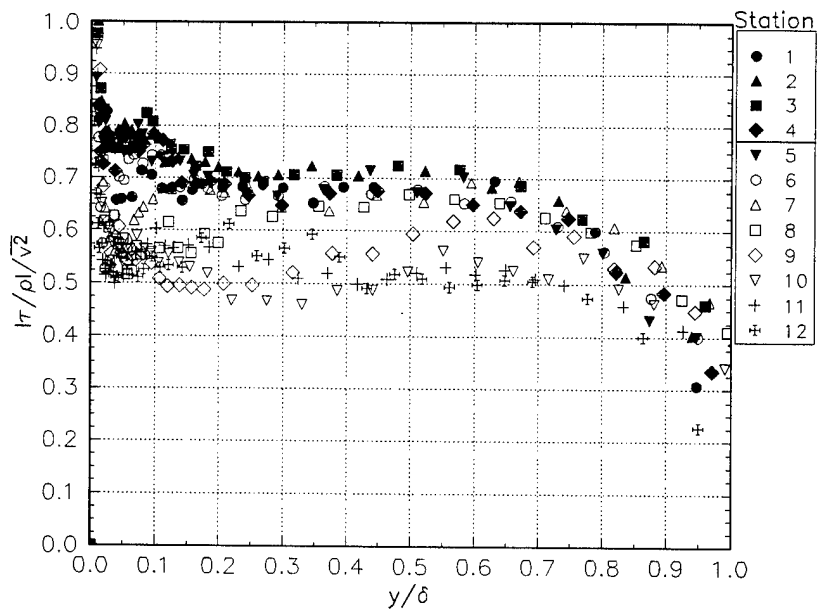


Figure 3.13d.  $1/S$  for stations of case DS1 of Driver and Johnston: Axisymmetric flow with a strong adverse pressure gradient, relaxing from an upstream shear-driven condition.

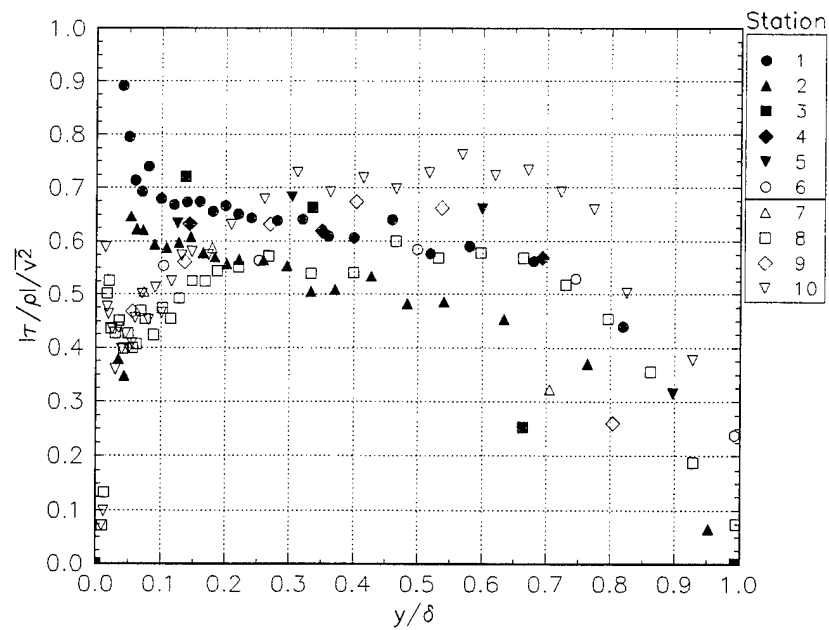


Figure 3.13e.  $1/S$  for stations of case BS0 of Driver and Johnston.  
Axisymmetric flow with a mild adverse pressure gradient but no shear.

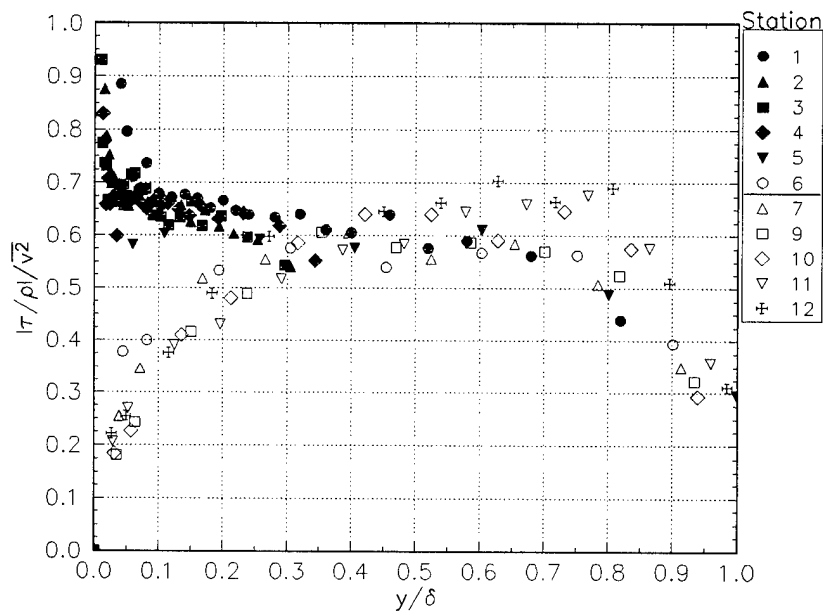


Figure 3.13f.  $1/S$  for stations of case CS0 of Driver and Johnston.  
Axisymmetric flow with a mild adverse pressure gradient but no shear.

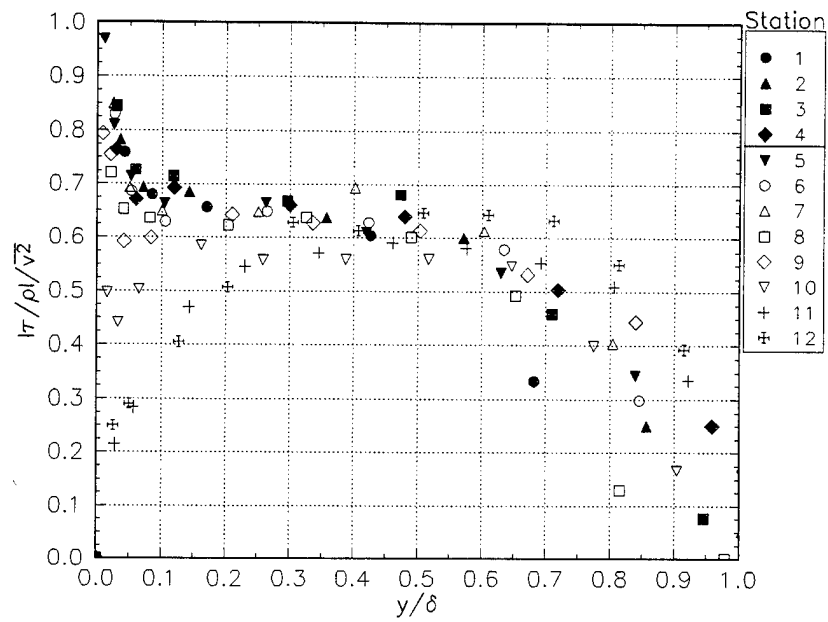


Figure 3.13g.  $1/S$  for stations of case DS0 of Driver and Johnston.  
Axisymmetric flow with a mild adverse pressure gradient but no shear.



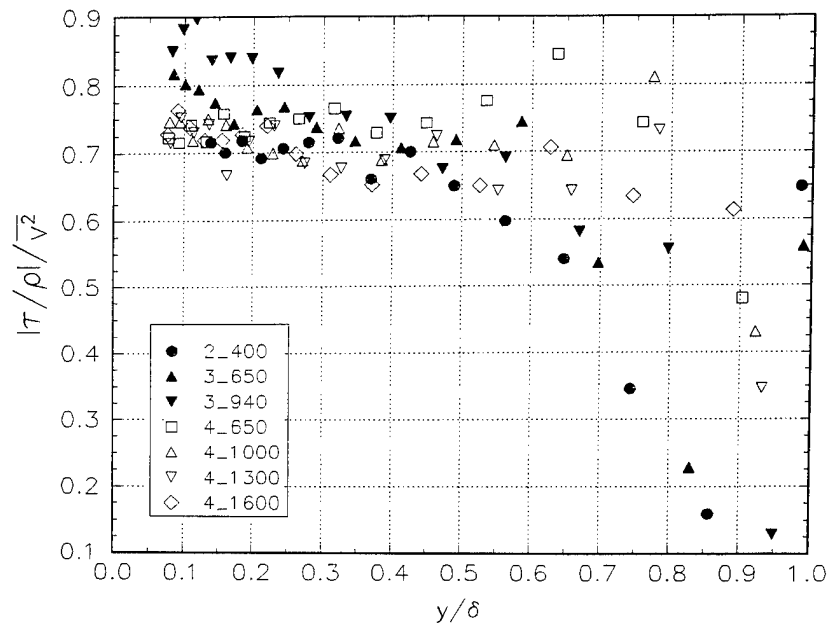


Figure 3.14.  $1/S$  for Littell and Eaton. This is a purely shear driven flow with a stationary atmosphere above the rotating disk. Stations are indicated by radius and Reynolds number ( $\times 10^4$ ). The number 2\_, 3\_, or 4\_ represent a radius of 0.235 m, 0.356 m, or 0.421 m respectively. *i.e.* Reynolds number designation \_100 implies 100e4 or 1,000,000 ...

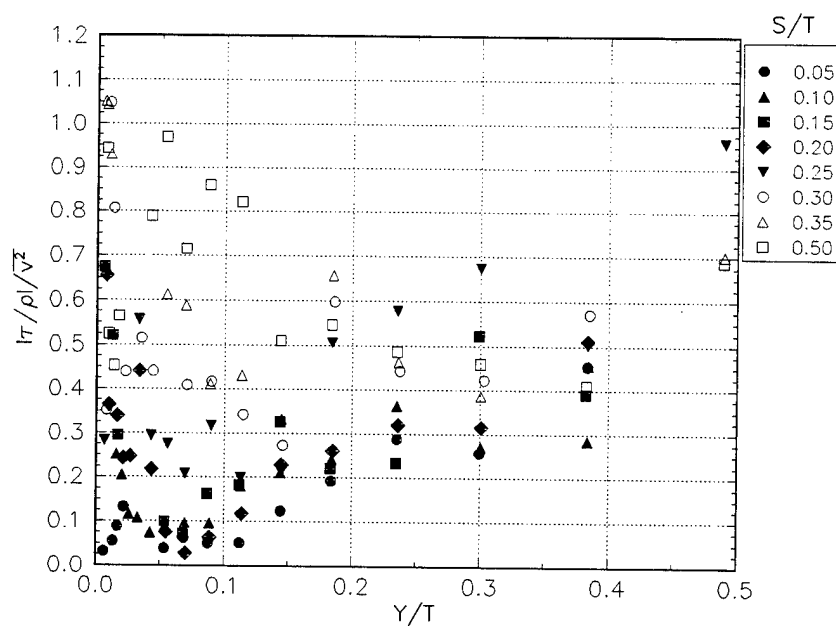


Figure 3.15a. The  $1/S$  parameter for the plane 3 of the wing-body junction flow of Devenport.

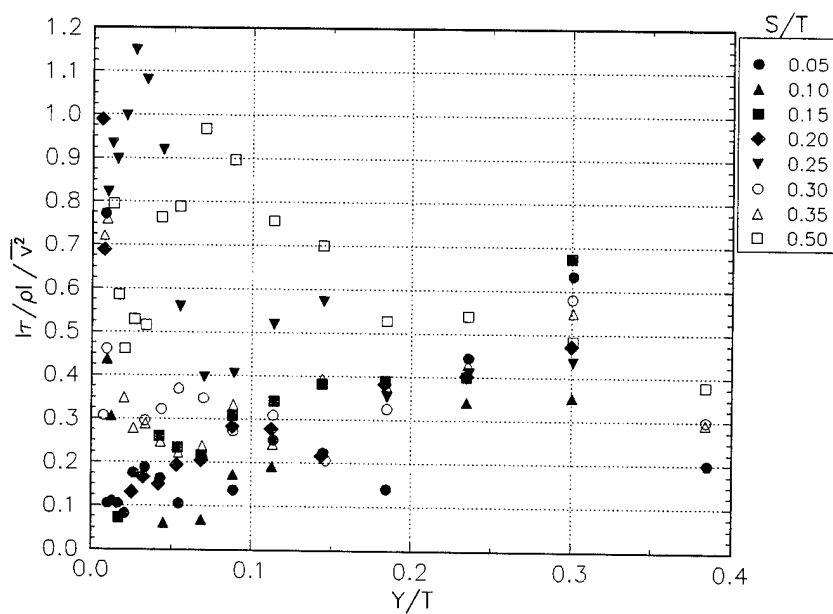


Figure 3.15b. The  $1/S$  parameter for the plane 4 of the wing-body junction flow of Devenport.

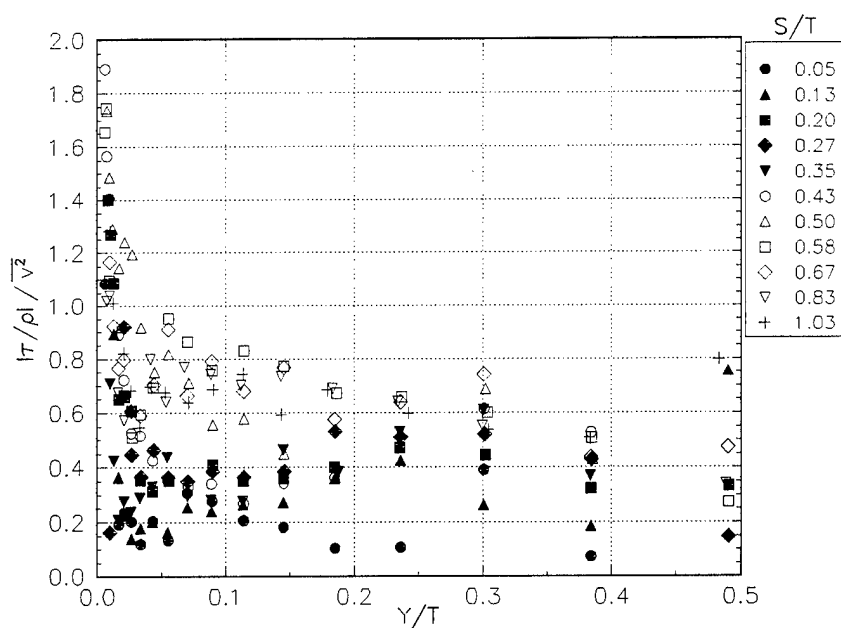


Figure 3.15c. The 1/S parameter for the plane 5 of the wing-body junction flow of Devenport.

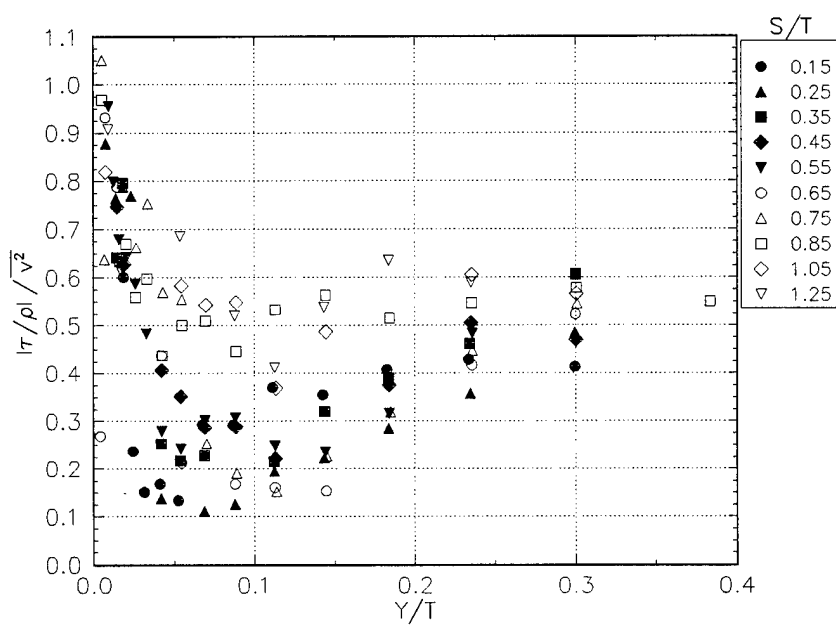


Figure 3.15d. The 1/S parameter for the plane 8 of the wing-body junction flow of Devenport.

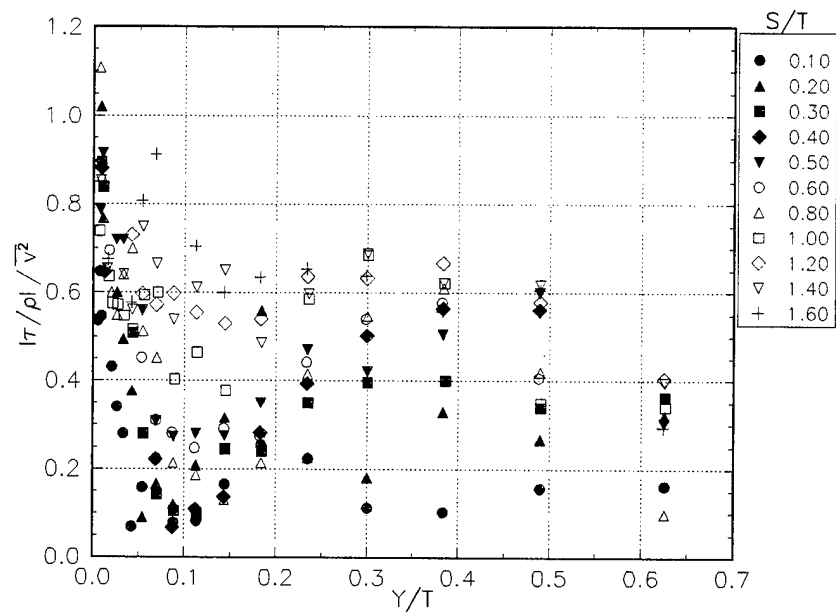


Figure 3.15e. The 1/S parameter for the plane 10 of the wing-body junction flow of Devenport.

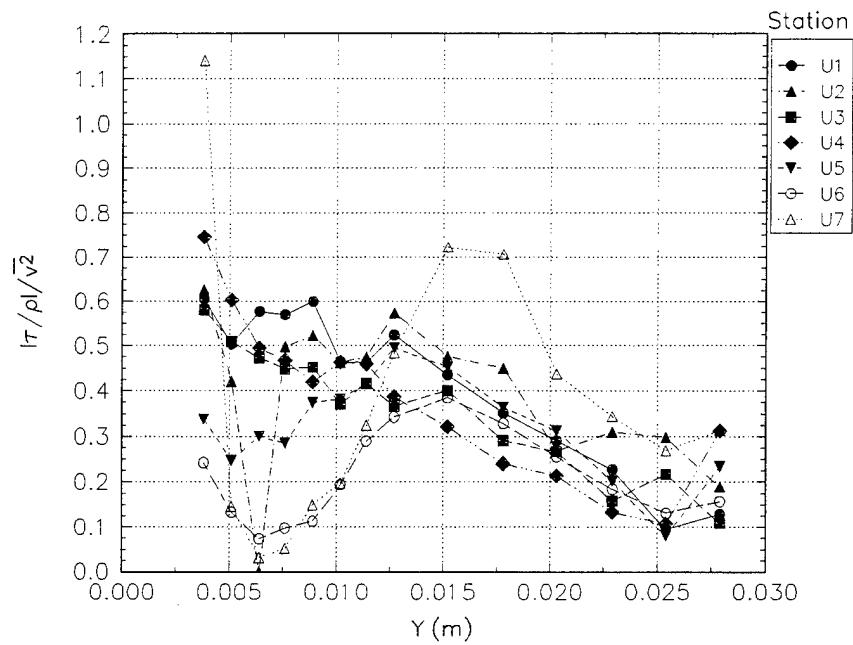


Figure 3.16.a 1/S for the inboard, upstream stations of McMahon.

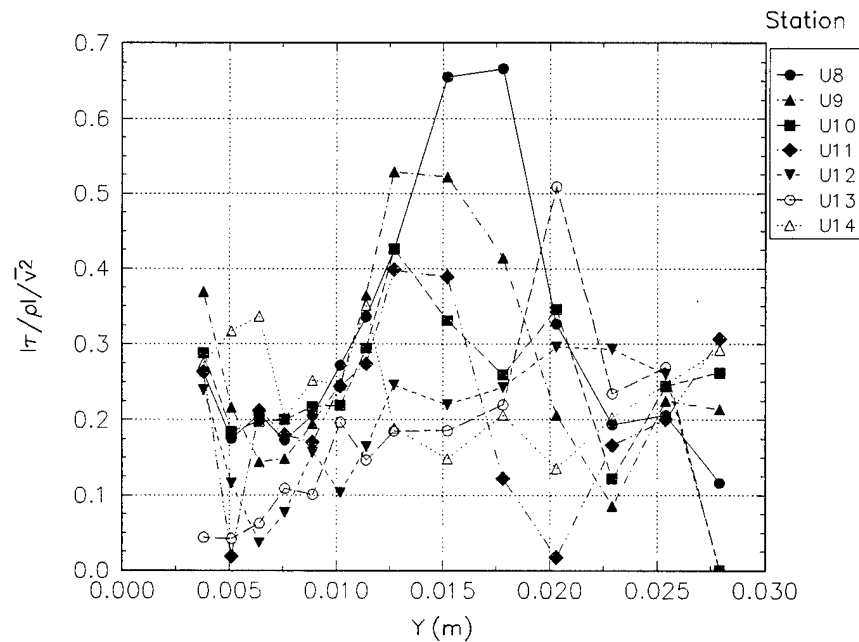


Figure 3.16.b 1/S for the outboard, upstream stations of McMahon.

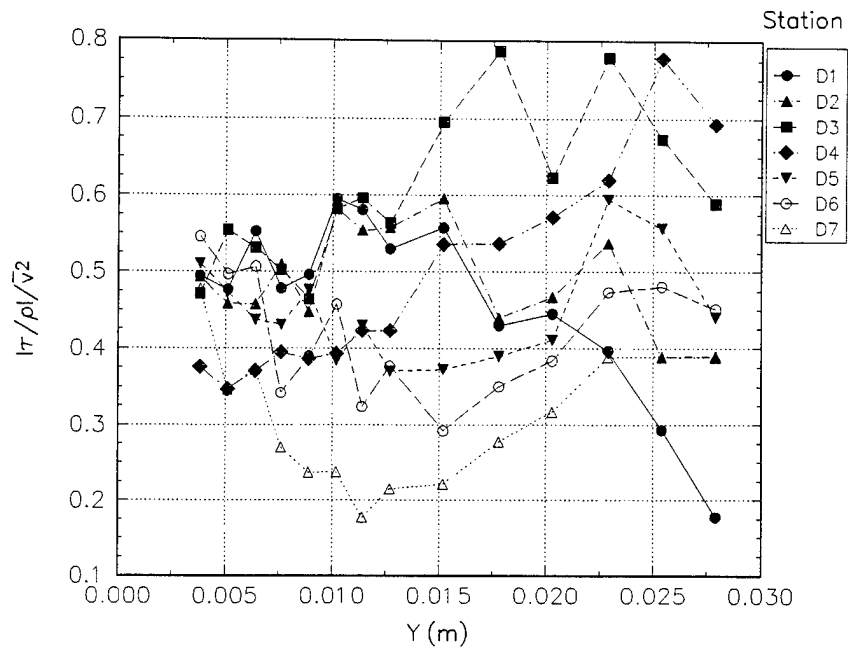


Figure 3.17.a 1/S for the inboard, downstream stations of McMahon.

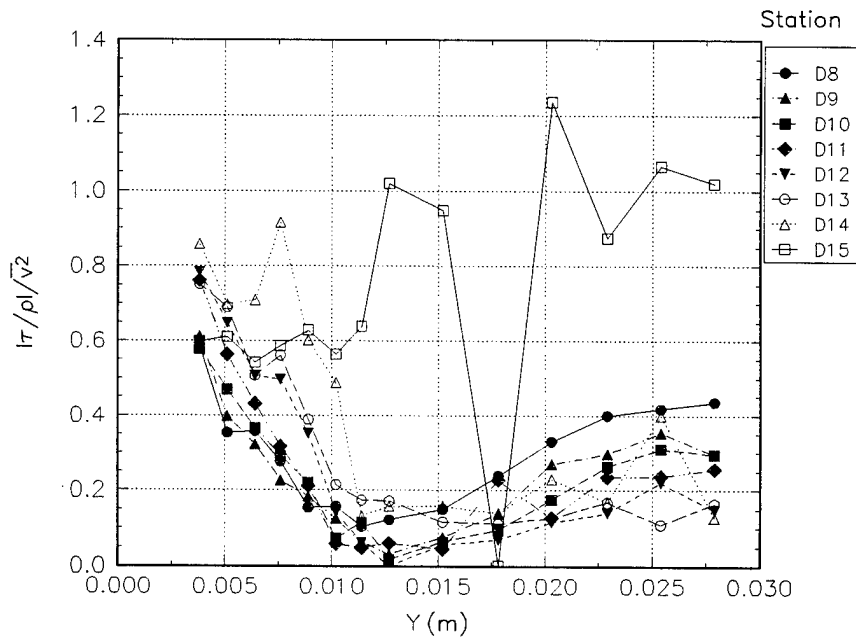


Figure 3.17.b 1/S for the outboard, downstream stations of McMahon.

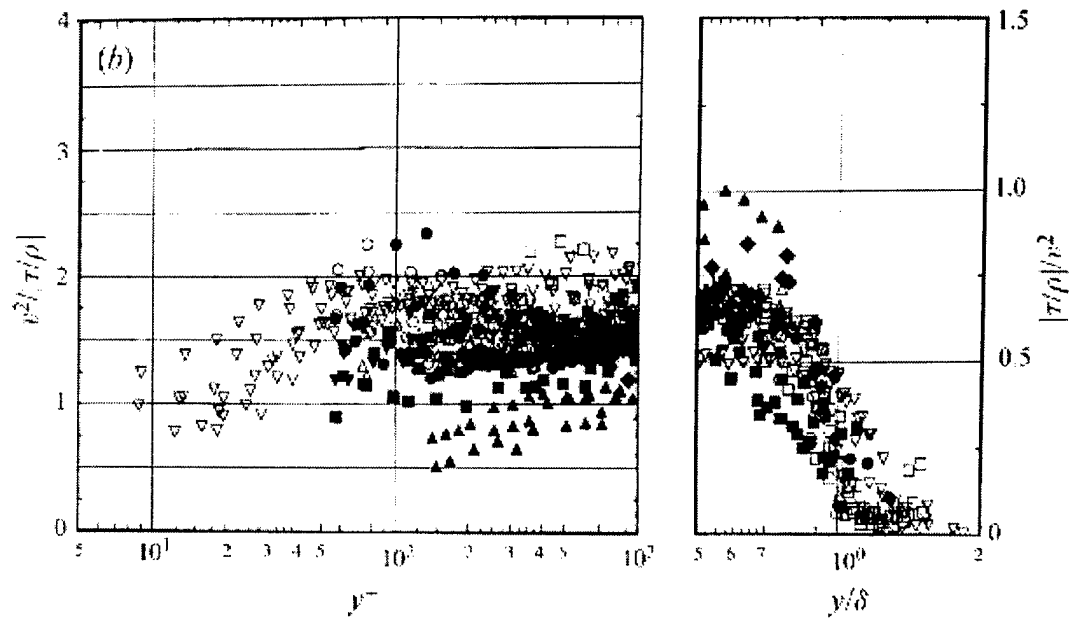


Figure 3.18a Figure 13 from Ölçmen and Simpson (1995) S (left) and 1/S (right) are illustrated for select stations from 9 data sets.

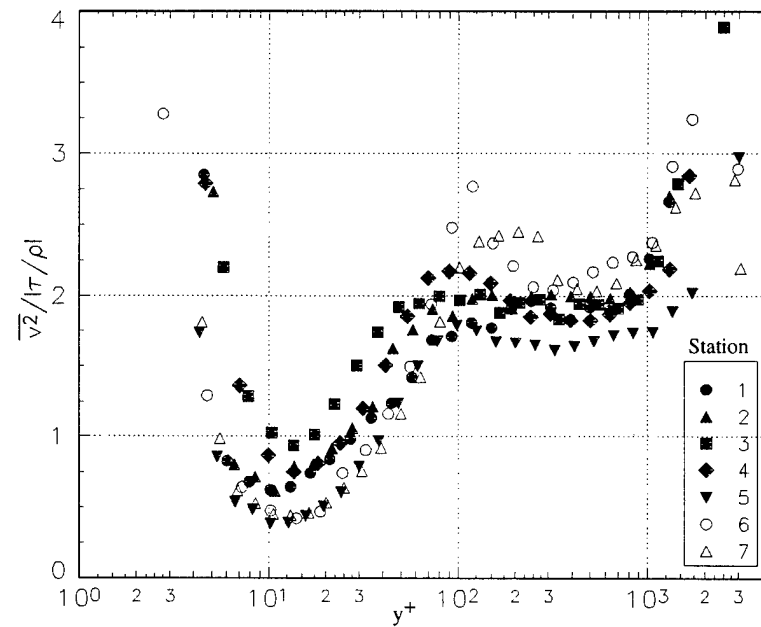


Fig 3.18b S for the Ölçmen flow.

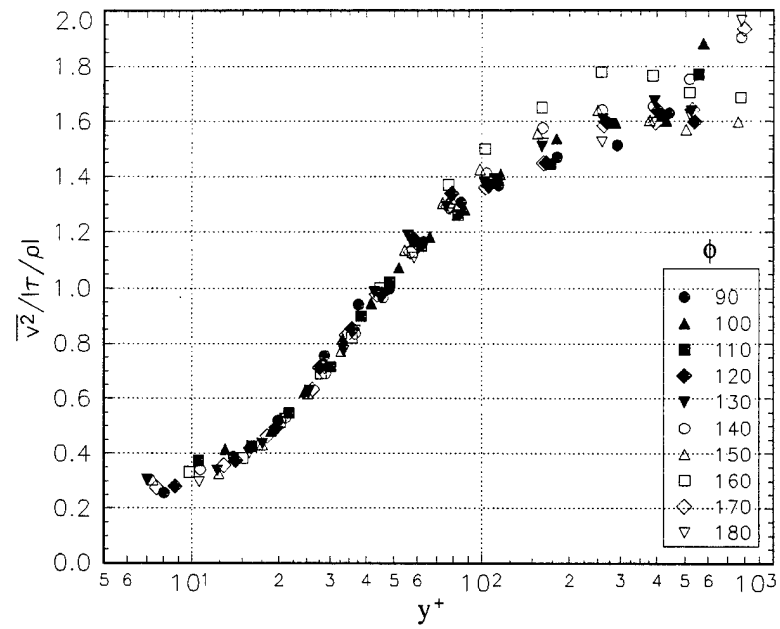


Figure 3.19a The S parameter for the 6:1 prolate spheroid flow of Chesnakas.  $x/L = 0.40$

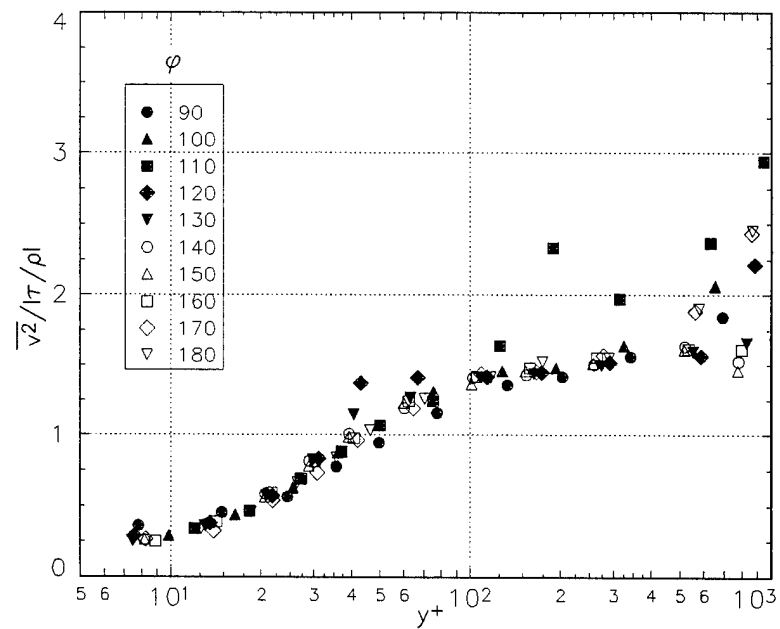


Figure 3.19b The S parameter for the 6:1 prolate spheroid flow of Chesnakas.  $x/L = 0.60$



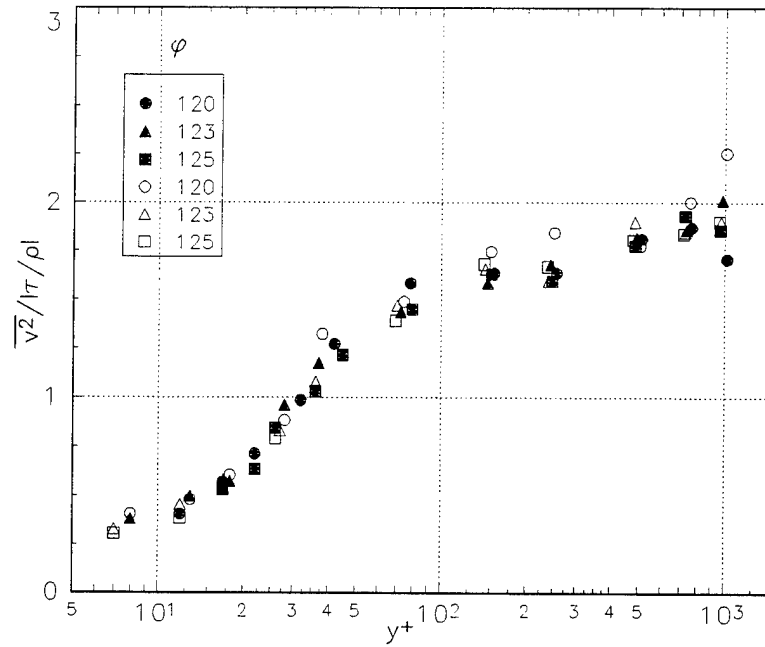


Figure 3.19c The S parameter for the 6:1 prolate spheroid flow of Chesnakas.  $x/L = 0.75$  (closed symbols) and  $x/L = 0.76$  (open symbols)

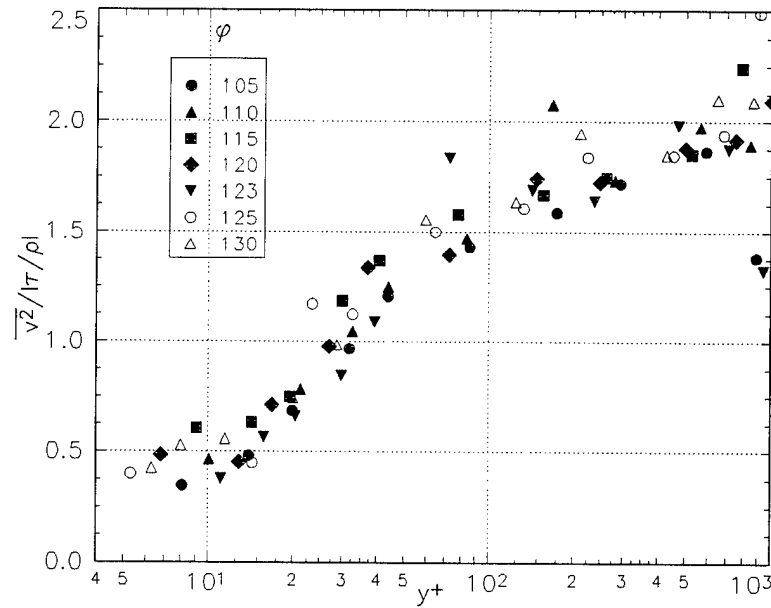


Figure 3.19d The S parameter for the 6:1 prolate spheroid flow of Chesnakas.  $x/L = 0.77$

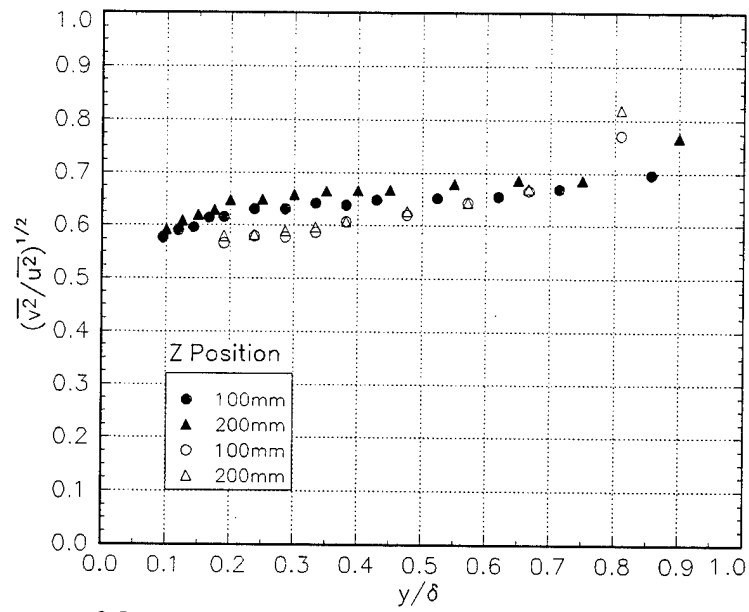


Figure 3.20  $\left(\overline{v^2}/\overline{u^2}\right)^{0.5}$  for Pompeio.  $x=1000\text{mm}$ , the open symbols represent the converging duct and the closed symbols represent the diverging duct. This was calculated in wall stress coordinates.

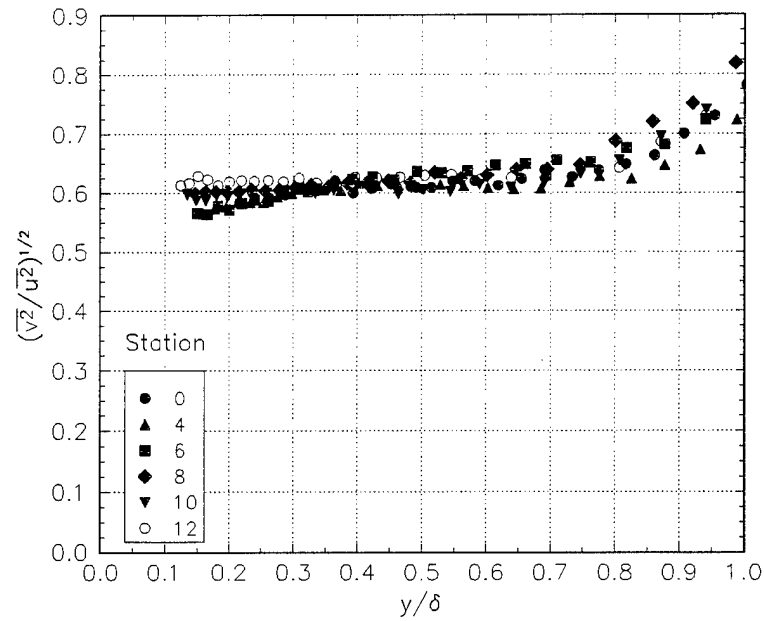


Figure 3.21a  $(\overline{v^2} / \overline{u^2})^{0.5}$  calculated in wall stress coordinates

for the crossflow development region of the experiment of Schwarz.

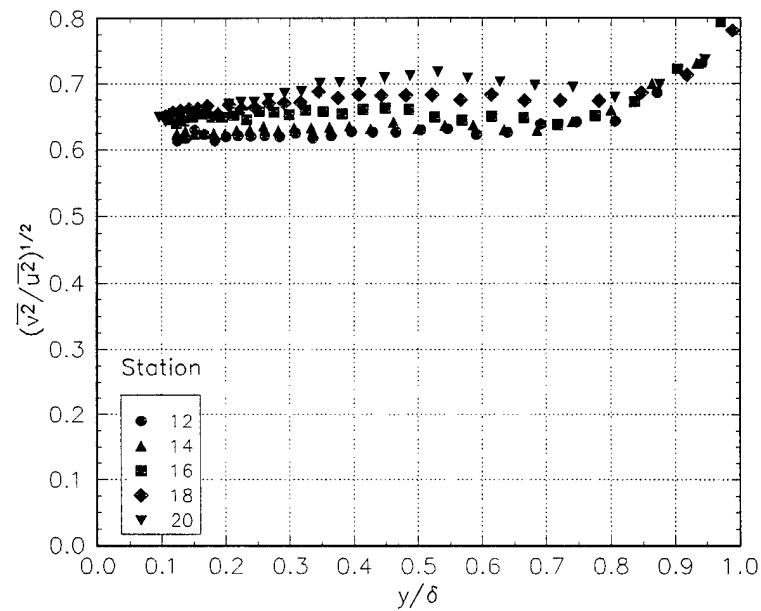


Figure 3.21b  $(\overline{v^2} / \overline{u^2})^{0.5}$  calculated in wall stress coordinates

for the crossflow decay region of the experiment of Schwarz.

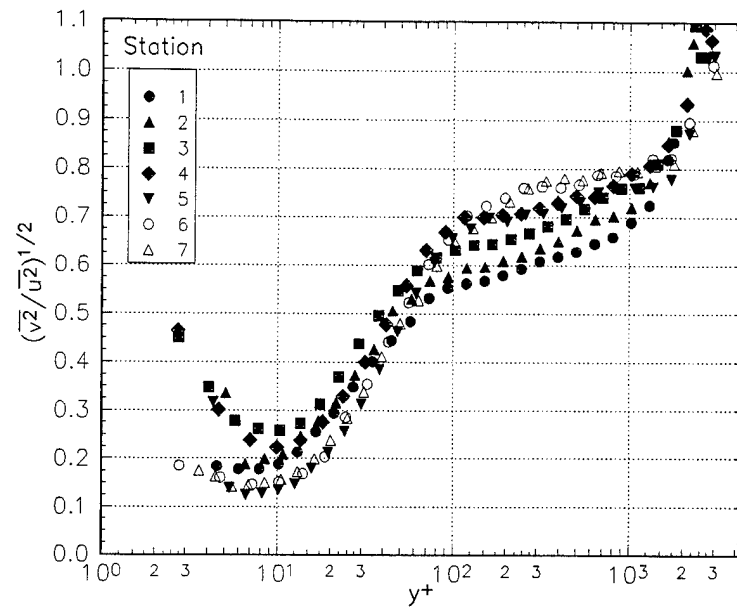


Figure 3.22  $(\overline{v^2} / \overline{u^2})^{0.5}$  calculated in wall stress coordinates for the experiment of Ölçmen.

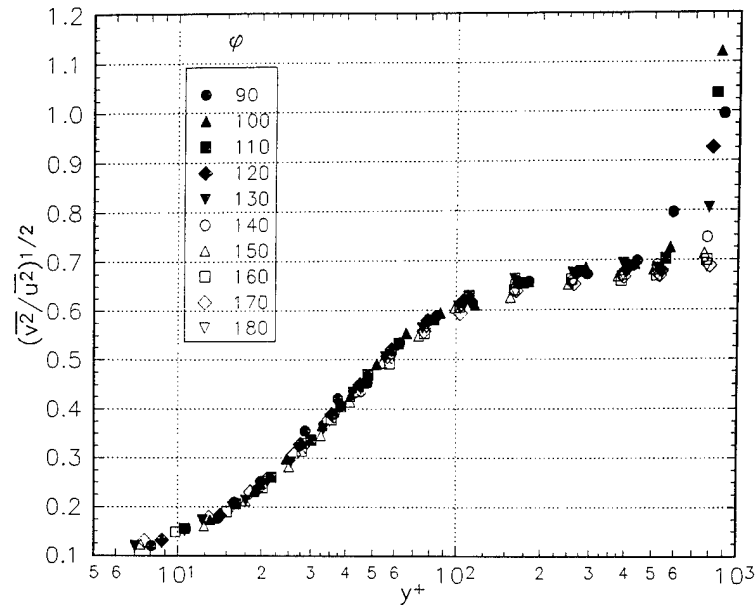


Figure 3.23a  $(\overline{v^2}/\overline{u^2})^{0.5}$  calculated in free-stream coordinates for the experiment of Chesnakas. This is for  $x/L = 0.40$  on the 6:1 prolate spheroid.

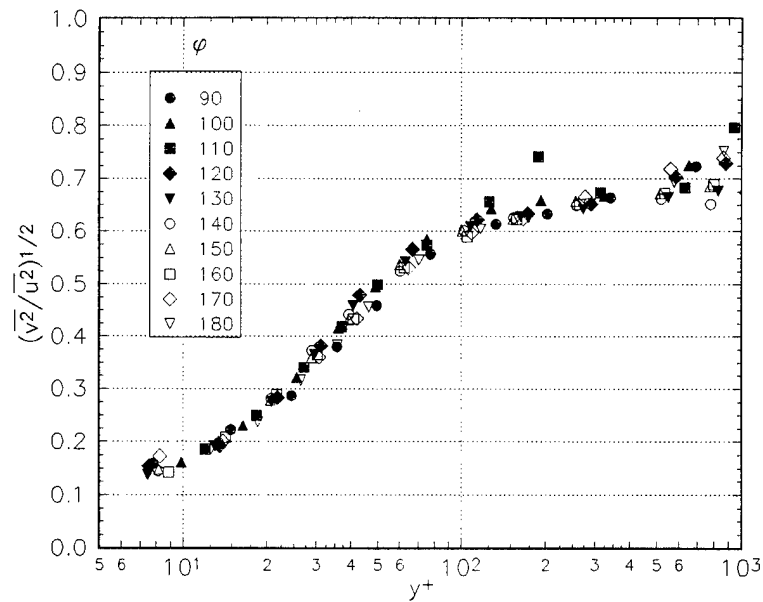


Figure 3.23b  $(\overline{v^2}/\overline{u^2})^{0.5}$  calculated in free-stream coordinates for the experiment of Chesnakas. This is for  $x/L = 0.60$  on the 6:1 prolate spheroid.

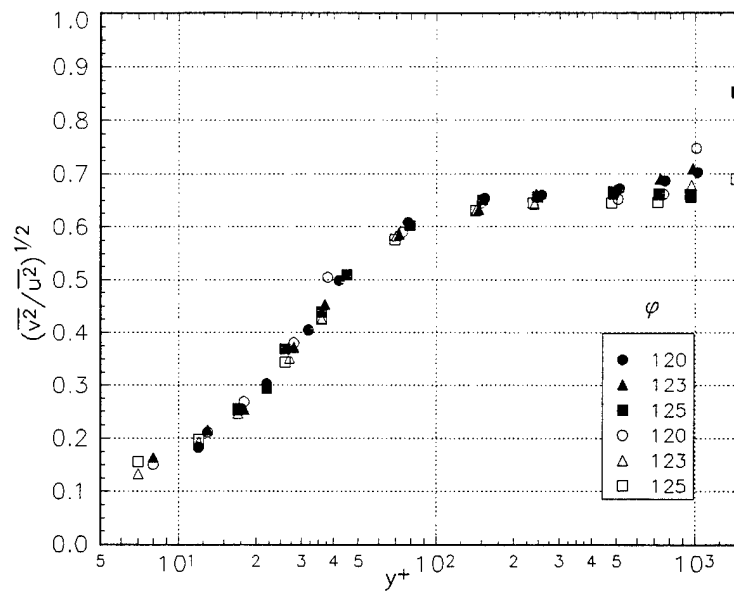


Figure 3.23c  $\left(\overline{v^2} / \overline{u^2}\right)^{0.5}$  calculated in free-stream coordinates for the experiment of Chesnakas. Closed symbols are for  $x/L = 0.75$  and open symbols are for  $x/L = 0.76$

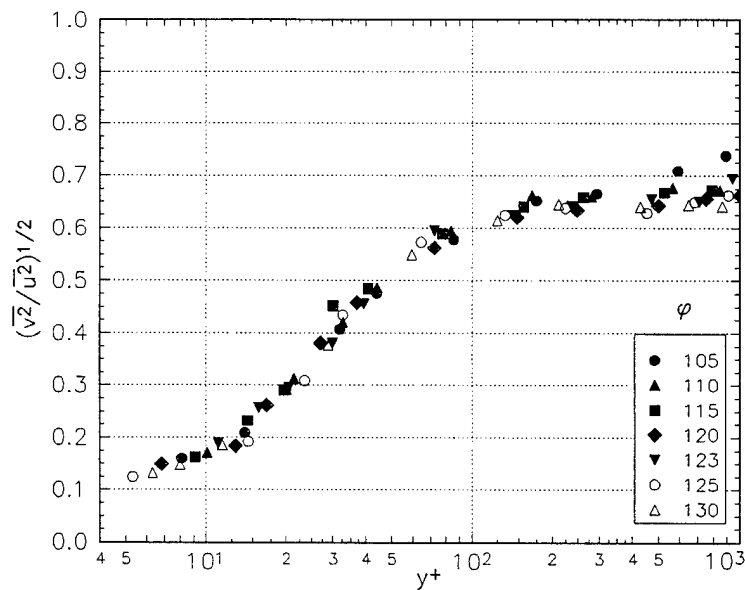


Figure 3.23d  $\left(\overline{v^2} / \overline{u^2}\right)^{0.5}$  calculated in free-stream coordinates for the experiment of Chesnakas. This is for  $x/L = 0.77$  on the 6:1 prolate spheroid.

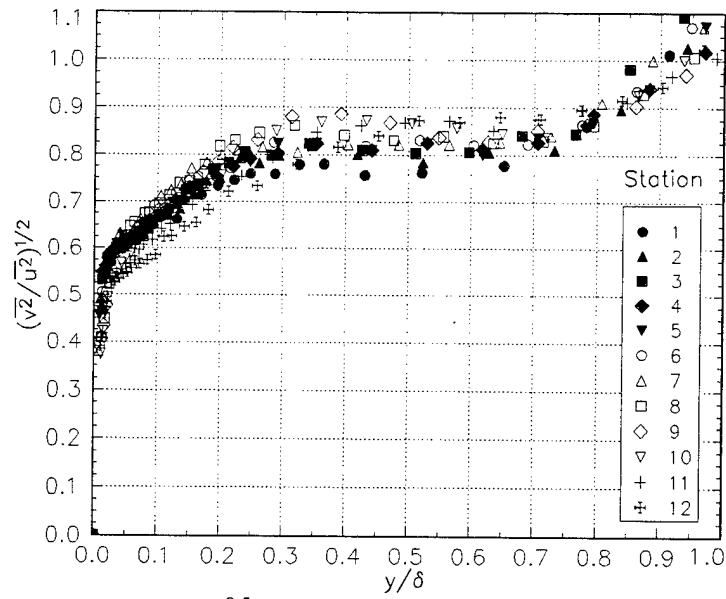


Figure 3.24a  $(\overline{v^2}/\overline{u^2})^{0.5}$  for experiment of Driver. This is case AS1.

The flow is relaxing from a shear induced state without a streamwise adverse pressure gradient. Stations 1-3 are above the rotating cylinder.

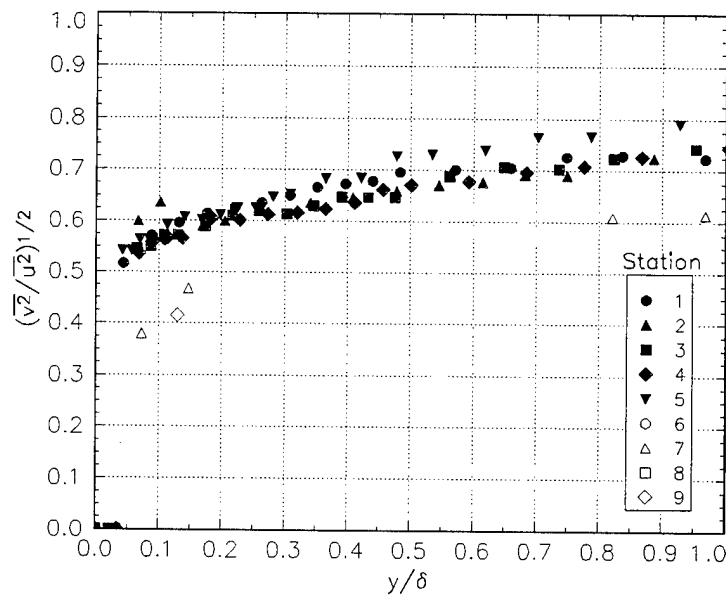


Figure 3.24b  $(\overline{v^2}/\overline{u^2})^{0.5}$  for experiment of Driver. This is case BS1.

The flow is relaxing from a shear induced state with a mild streamwise adverse pressure gradient. Stations 1-5 are above the rotating cylinder.

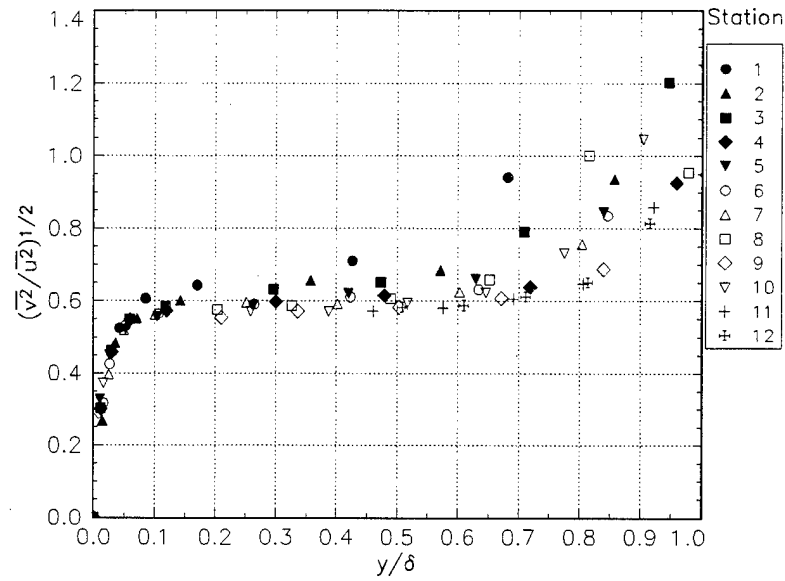


Figure 3.24c  $\left(\overline{v^2}/\overline{u^2}\right)^{0.5}$  for experiment of Driver. This is case DS0.

The flow has no shear but a strong streamwise adverse pressure gradient.

Stations 1-4 are above the rotating cylinder.

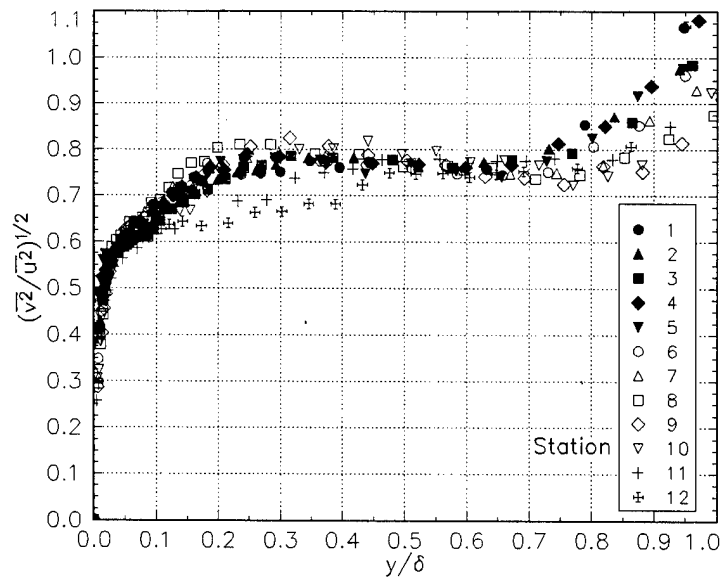


Figure 3.24d  $\left(\overline{v^2}/\overline{u^2}\right)^{0.5}$  for experiment of Driver. This is case DS1.

The flow is relaxing from a shear induced state with a strong streamwise adverse pressure gradient. Stations 1-4 are above the rotating cylinder.



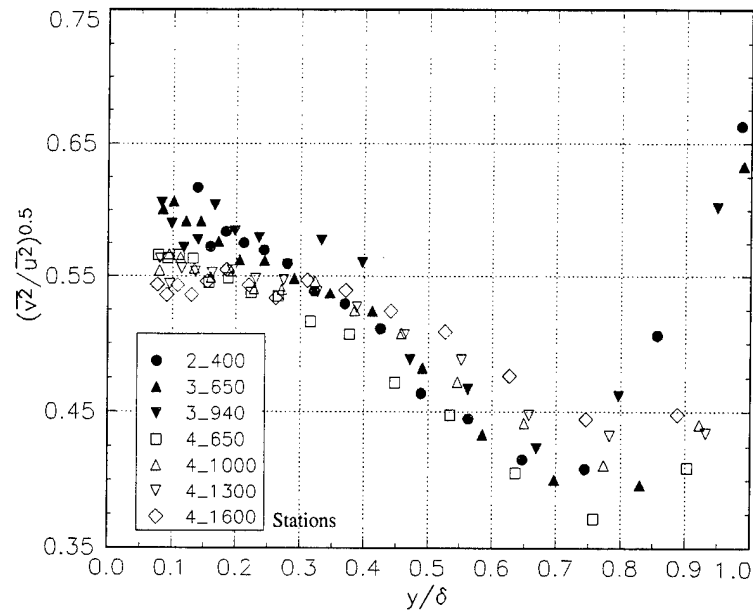


Figure 3.25  $\left(\overline{v^2} / \overline{u^2}\right)^{0.5}$  for the shear-driven flow of Littell. Stations are indicated by radius and Reynolds number ( $\times 10^4$ ). The number 2\_, 3\_, or 4\_, represent a radius of 0.235 m, 0.356 m, or 0.421 m respectively. *i.e.* Reynolds number designation \_100 implies 100e4 or 1,000,000 ...

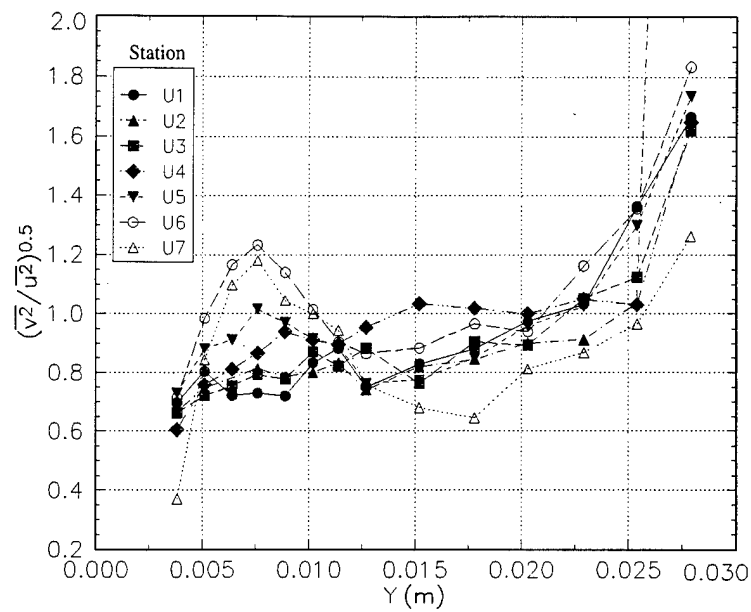


Figure 3.26a  $(\overline{v^2}/\overline{u^2})^{0.5}$  for the inboard upstream plane of McMahon.

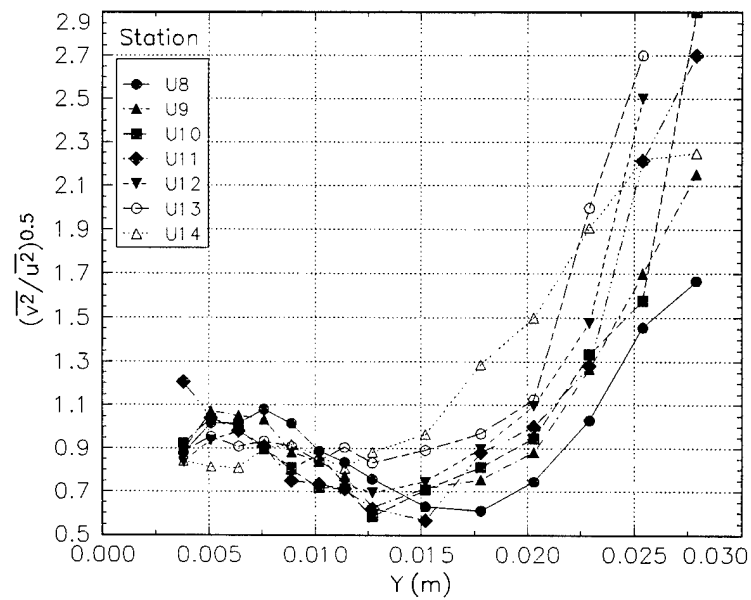


Figure 3.26b  $(\overline{v^2}/\overline{u^2})^{0.5}$  for the outboard upstream plane of McMahon.

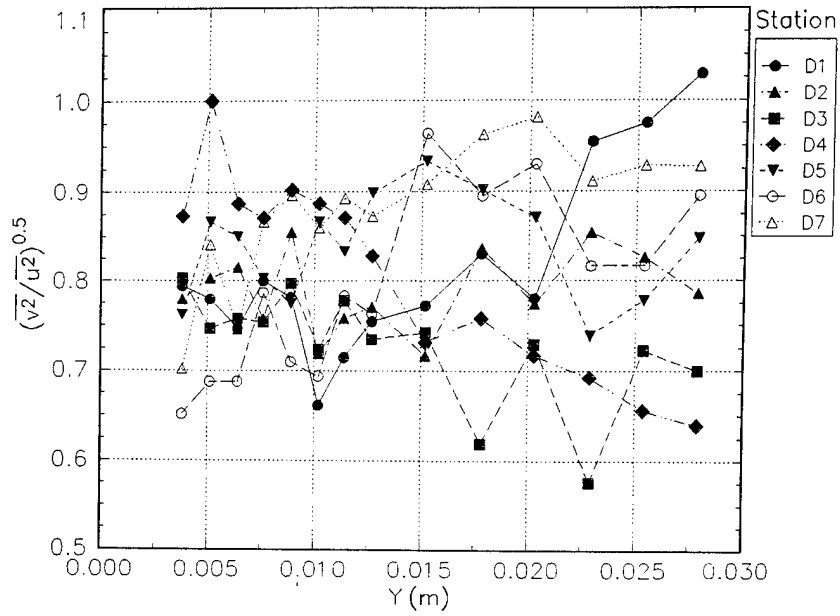


Figure 3.27a  $\left(\overline{v^2}/\overline{u^2}\right)^{0.5}$  for the inboard downstream plane of McMahon.

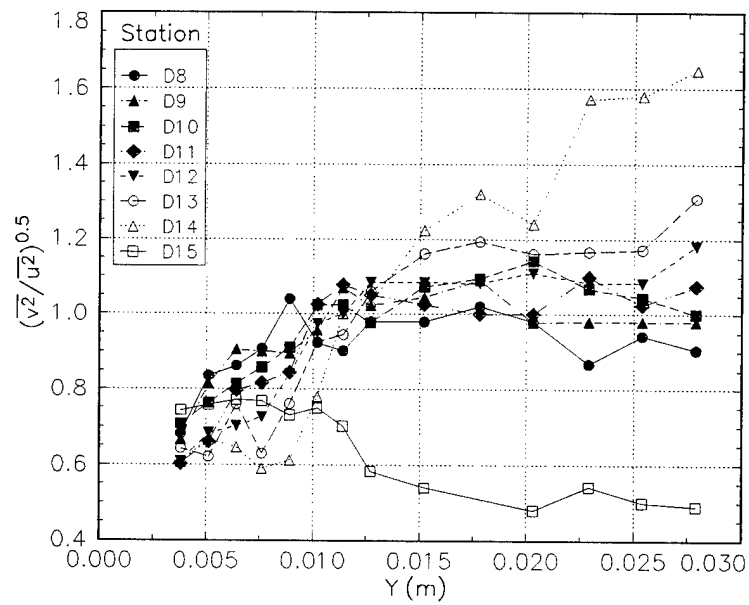


Figure 3.27b  $\left(\overline{v^2}/\overline{u^2}\right)^{0.5}$  for the outboard downstream plane of McMahon.

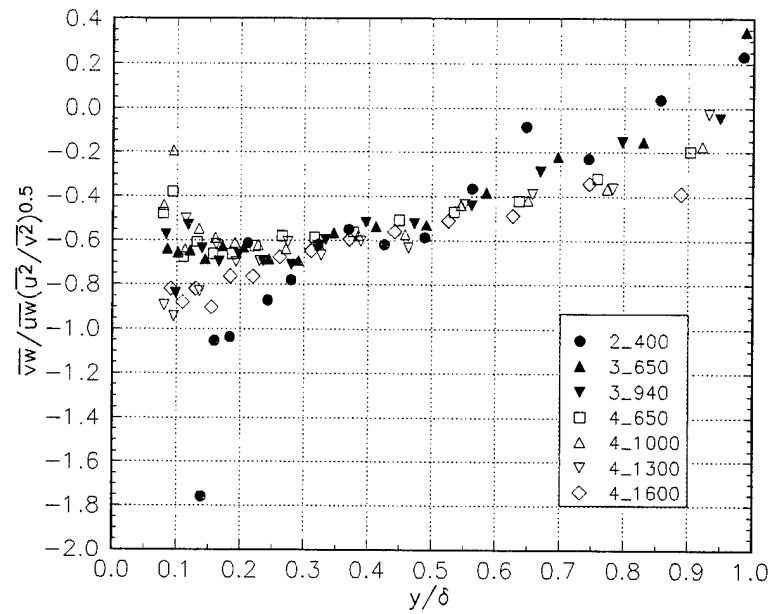


Figure 3.28  $\frac{\overline{v_w}}{\overline{u_w}} \sqrt{\frac{u^2}{v^2}}$  for the shear-driven flow of Littell. Stations are indicated by radius and Reynolds number ( $\times 10^4$ ). The number 2\_, 3\_, or 4\_, represent a radius of 0.235 m, 0.356 m, or 0.421 m respectively. *i.e.* Reynolds number designation \_100 implies 100e4 or 1,000,000 ...

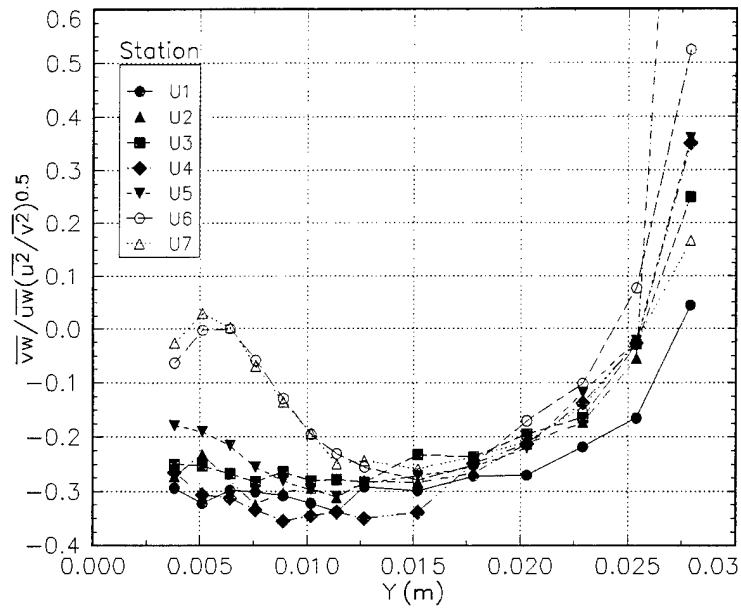


Figure 3.29a  $\frac{\overline{vw}}{\overline{uw}} \sqrt{\frac{\overline{u^2}}{\overline{v^2}}}$  for the upstream inboard stations of McMahon.

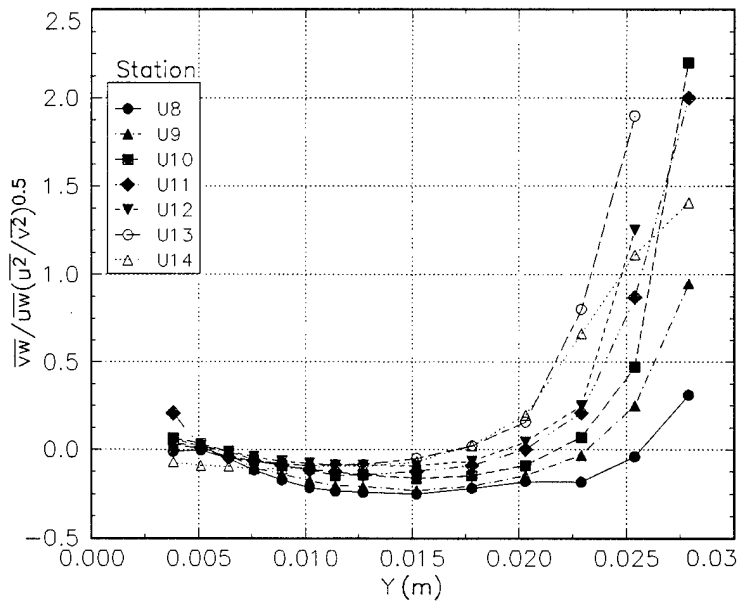


Figure 3.29b  $\frac{\overline{vw}}{\overline{uw}} \sqrt{\frac{\overline{u^2}}{\overline{v^2}}}$  for the upstream outboard stations of McMahon.

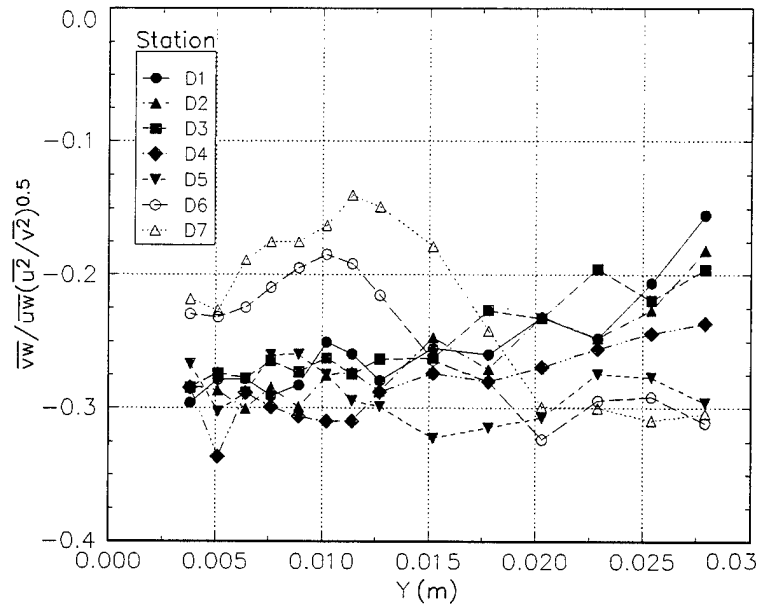


Figure 3.30a  $\frac{\overline{vw}}{\overline{uw}} \sqrt{\frac{u^2}{v^2}}$  for the downstream inboard stations of McMahon.

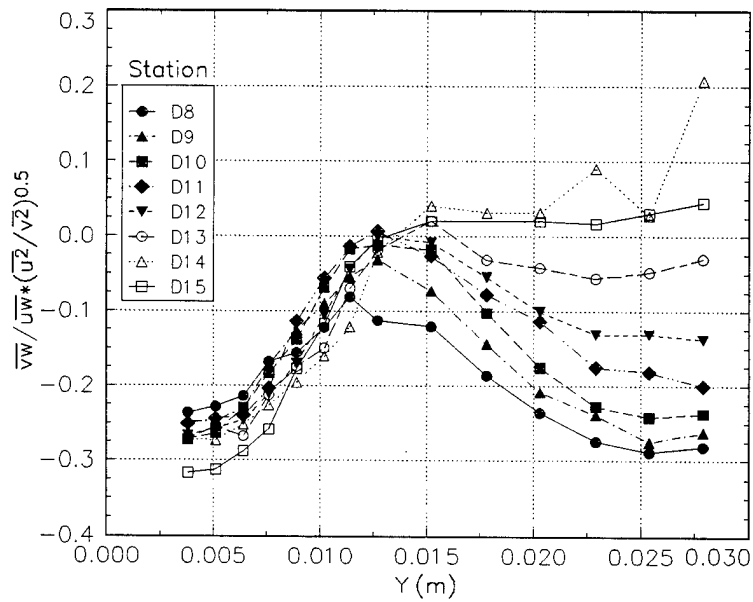


Figure 3.30b  $\frac{\overline{vw}}{\overline{uw}} \sqrt{\frac{u^2}{v^2}}$  for the downstream outboard stations of McMahon.

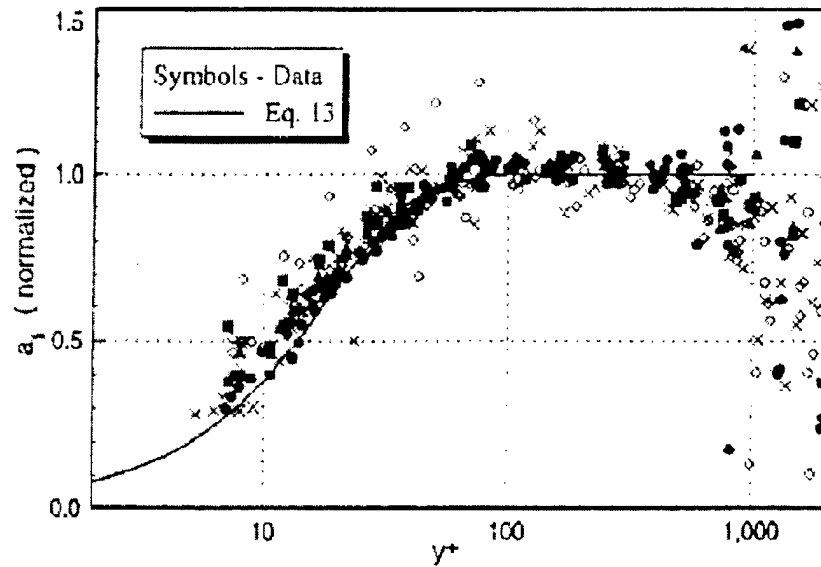


Figure 3.31a Figure 19 from Chesnakas and Simpson (1994). The values of  $a_1$  are normalized on the value of  $a_1$  as computed from equation 3.4.

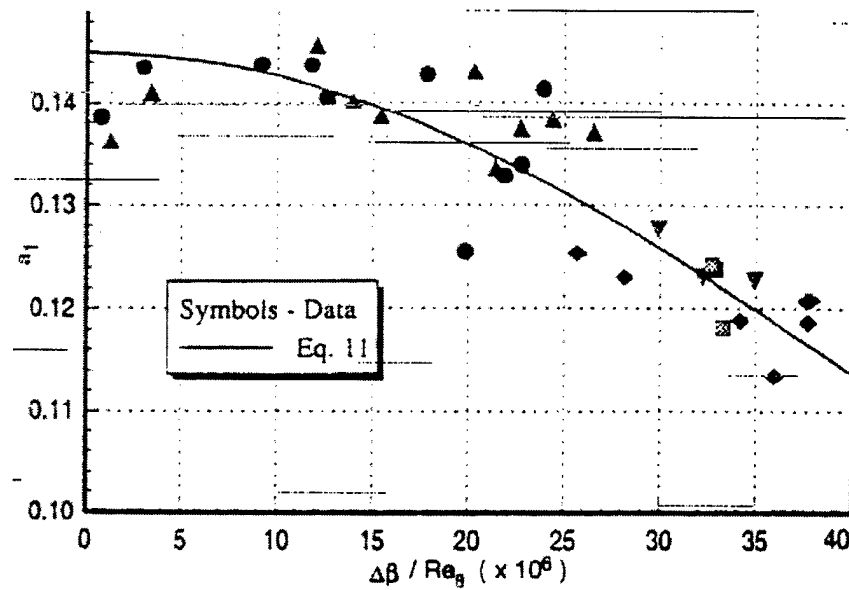


Figure 3.31b Figure 18 from Chesnakas and Simpson (1994). The mid-layer values of  $a_1$ , that were chosen, v. the three-dimensionality parameter. The line represents equation 3.4.

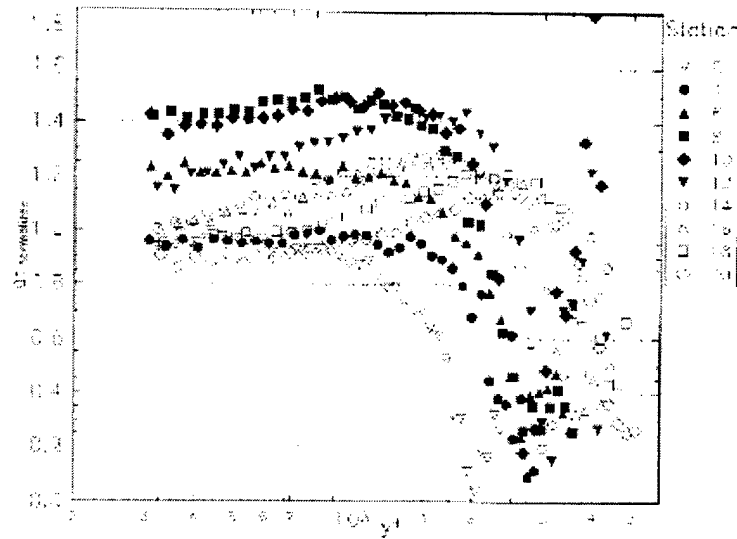


Figure 3.32a The  $a_1$  scaling relationship of Chesnakas and Simpson (1994) for the experiment of Schwarz. The values of  $a_1$  are normalized on the value of  $a_1$  computed from equation 3.4. Stations 0-12 represent crossflow development and 12-20 crossflow decay.

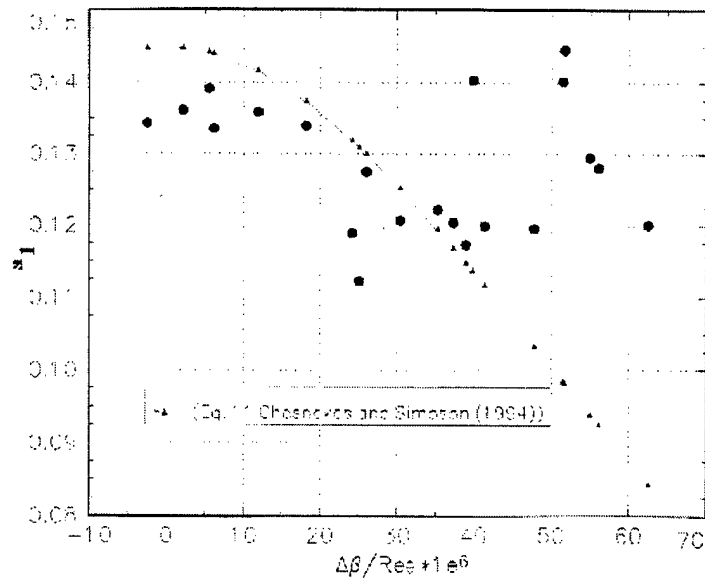


Figure 3.32b The values of  $a_1$ , that were chosen, v. the three-dimensionality parameter proposed by Chesnakas and Simpson (1994) for experiment of Schwarz. The line represents the curve fit of Chesnakas, equation 3.4.



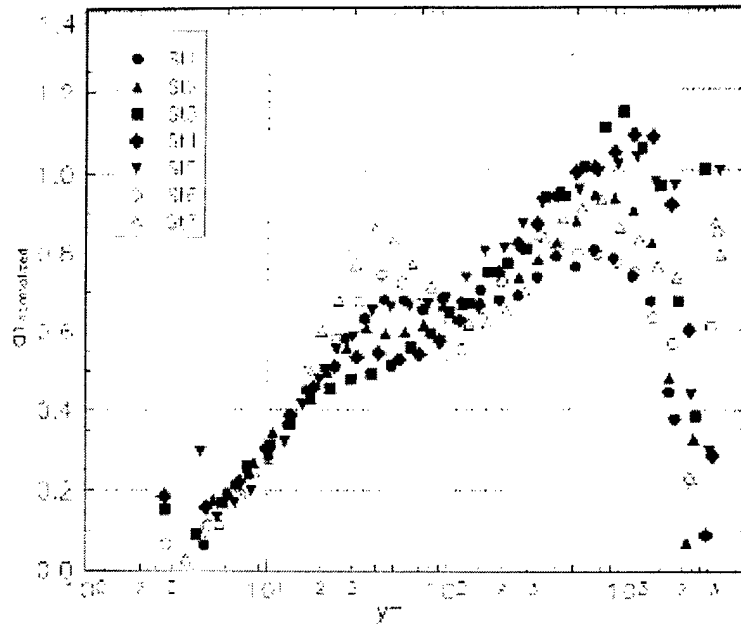


Figure 3.33a The  $a_1$  scaling relationship of Chesnakas and Simpson (1994) for the experiment of Ölçmen. The values of  $a_1$  are normalized on the value of  $a_1$  computed from equation 3.4.  $\Delta\beta$  used here is  $\beta_{local} - \beta_{wall}$

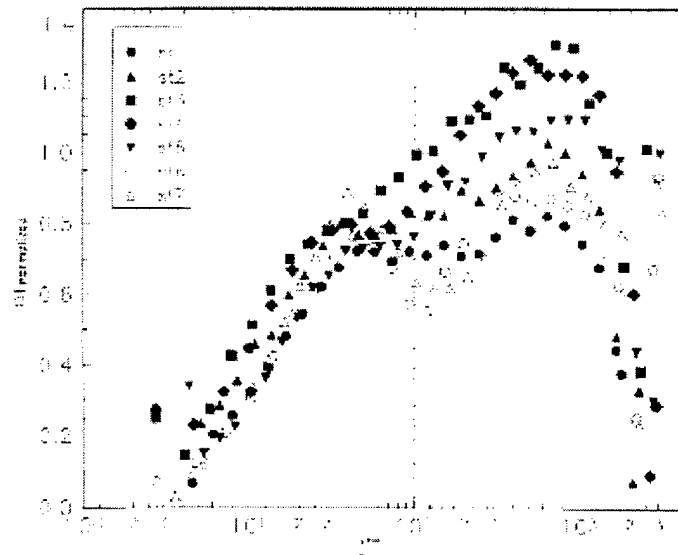


Figure 3.33b The  $a_1$  scaling relationship of Chesnakas and Simpson (1994) for the experiment of Ölçmen. The values of  $a_1$  are normalized on the value of  $a_1$  computed from equation 3.4.  $\Delta\beta$  used here is  $\beta_{fs} - \beta_{wall}$

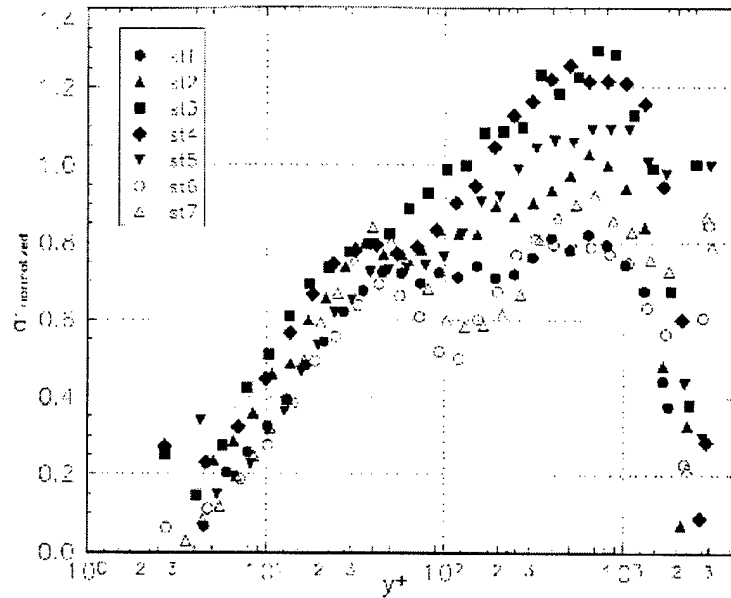


Figure 3.33c The  $a_1$  scaling relationship of Chesnakas and Simpson (1994) for the experiment of Ölçmen. The values of  $a_1$  are normalized on the value of  $a_1$  computed from equation 3.4.  $\Delta\beta$  used here is  $\beta_{\max} - \beta_{\text{wall}}$

## Chapter 4 Results and Discussion (Triple Product Relationships)

This chapter focuses on the discussion of parameters formed from triple products of turbulent fluctuating velocities. The chapter follows the conventions adopted and described in the opening paragraph of chapter 3. Results are presented in an order based upon the complexity of the flows and experimental data sets are called by the name of one of the authors in the study. Appendices B-L contain additional figures that were not directly relevant to the discussion. This organization is detailed in Table 3.1.

The main focus of deriving algebraic modeling parameters involving the triple products was discussed in chapter 1. Simpson (1995) proposed the use of equations 1.1 - 1.3 and 1.6 - 1.8 as the minimum set of equations necessary to account for the lags observed in turbulent flows. The turbulent transport equations, equation 1.6 - 1.8, involve the turbulent triple products;  $\overline{uv^2}$ ,  $\overline{v^2w}$ , and  $\overline{v^3}$ . Relationships involving these triple products are the focus of the present study.

These triple products were normalized on several different quantities to search for any common behavior between flows or stations. This portion of the research did not produce any significant results. The quantities did not produce linear or constant results and were not correlated very well between stations. It appears that the normalizing parameters chosen had a significant weighting effect on the individual triple products. Several plots are included in the appendices to illustrate the results. These primary results led to the examination of ratios and eventually combinations of the triple products. The work was progressive and sample results are included in appendices B-L.

### 4.1 B Parameters

The first set of triple product parameters that will be discussed were defined as the B family of parameters. The first of these was  $B_1$  and is given by the relationship:

$$B_1 \equiv \overline{v^3} / \sqrt{\overline{uv^2}^2 + \overline{w^2v}^2} \quad (4.1)$$

In the appendices, several figures will appear with this  $B_1$  parameter. It is dependent on the choice of coordinate system and due to an early misconception, it does not involve the desired triple products. A similar parameter was devised that includes the triple products of interest to a

modeling effort that employs equations 1.1 - 1.3 and 1.6 - 1.8. For simplicity in discussion and in presentation of the results in figures, this ratio was defined to be  $B_2$  and is the following ratio:

$$B_2 \equiv \overline{v^3} / \sqrt{\overline{uv^2}^2 + \overline{v^2w}^2} \quad (4.2)$$

A benefit for this triple product configuration is its independence of coordinate system choice.

The study illustrated that the two  $B$  parameters exhibited similar behavior for the same stations of the same flows. In some cases, the  $B_2$  parameter had better correlation and was chosen to represent this particular combination of the triple products. For more details on the characteristics of the  $B_1$  parameter, refer to appendices B-G and K-L.

Overall,  $B_2$  approximates a constant function from  $0.3 \leq y/\delta \leq 1.0$  of 0.7 - 1.0 for the experiments presented in this study. An exception to this is the experiment of Littell which will be discussed later in this section. Below  $y/\delta \simeq 0.3$ ,  $B_2$  becomes scattered. This scatter is due to the triple products passing through zero, or an inflection point, and changing sign at different locations as will be illustrated in section 4.4. Near the wall, the uncertainty in the measurements increases and the individual triple products are more scattered themselves.

For the experiment of Pompeo,  $B_2$  maintained a value near 0.7 for  $y/\delta > 0.3$ , (figure 4.1). Below this value of  $y/\delta$ ,  $B_2$  generally increases in value and is less correlated. This illustrates that imposed lateral strain does not have much of an effect on  $B_2$ . As the boundary layer edge is approached,  $B_2$  tends to be more scattered. Like the  $1/S$  parameter, the triple products are approaching zero or the constant value that they attain in the free stream. The rate of change of the triple products may differ leading to less correlation in the triple product parameters.

In the 30° bend of Schwarz,  $B_2$  approximates a constant value for all of the stations for  $y/\delta > 0.4$  as illustrated in Figure 4.2. When the flow is divided into regions of crossflow development and decay, as in Figures 4.2b and 4.2c, greater insight into the behavior is obtained. For the development region,  $B_2 \simeq 0.8$  beginning at  $y/\delta = 0.3$ . Closer to the wall, a small portion of the data illustrates  $B_2 \simeq -0.25$  while a significant share of the data remains near 0.8. For the crossflow decay region the value of  $B_2$  is closer to 1.0 for  $y/\delta > 0.4$ . Below  $y/\delta = 0.4$  the parameter is not correlated well. The only significant observation in the near wall region for this part of the flow is that a significant portion of the data for  $B_2$  are near -0.5. It appears that in the decay region, the flow is relaxing from the 3D generating spanwise pressure gradients and is less likely for parameters to correlate well in the absence of turbulence production.

For the wing-body junction flow of Ölçmen,  $B_2 \approx 1.0$  for  $y/\delta > 0.4$  as seen in Figure 4.3a. The majority of the data in this experiment is in the near wall region. With  $y$  normalized on wall variables (figure 4.3b),  $B_2$  appears to illustrate several regions with independent behavior. For  $y^+ > 1000$  ( $y/\delta > 0.4$ )  $B_2$  maintains a value of 1.0. The value of  $B_2$  generally decreases and is characterized by increased scatter for  $100 < y^+ < 1000$  ( $0.06 < y/\delta < 0.4$ ). It then becomes fairly well correlated and decreases logarithmically for  $30 < y^+ < 100$  from 1.0 to -0.5. Viewed on a log scale against  $y/\delta$ ,  $B_2$  has less degree of correlation than when  $y$  is scaled on wall variables for the near wall regions. As  $B_2$  approaches the wall, it recovers quickly from -0.5 at the end of the linear region and approximates a value of 0.0. The scatter in the parameter for this experiment seems greater than previous, however one must recall that previously we have not been able to view the near wall behavior. The behavior may be explained better after viewing more near wall data. The individual triple products will also illuminate more details of this flow.

The complex curvature flows of Baskaran produce values of  $B_2$  that approximate a constant value across the boundary layer. However the value of  $B_2$  for the concave curvature case varies from station to station. Again the region of good correlation is for  $y/\delta > 0.4$ . The results for the concave curvature are presented in Figure 4.4a. The stations earlier in the test section maintain a value near 0.65 (stations 1-4). Station 5 generates a value of  $B_2$  near 1.2, while stations 6 and 7, which share the same  $x$ -location show values of  $B_2$  of 0.8. Station 8 and 9 also maintain values near 0.8 - 0.9. It is hard to determine what effect of the three-dimensionality is causing the observed behavior due to the combination of effects at station 5 in this duct. The stations of the convex curvature case share the same  $z$ -coordinate while the  $x$ -location progresses downstream. The downstream stations have the approximation to a constant value of  $B_2$  persisting closer to the wall than the downstream stations. The results are presented in Figure 4.4b. All of the stations maintain a value of  $B_2$  near 0.7 for this duct for  $y/\delta > 0.5$ . Investigation of the triple products individually will illustrate the progressive change in the constant behavior location of  $B_2$  with  $y$ .

The behavior of  $B_2$  for the Chesnakas flow is illustrated in Figure 4.5. When  $y$  is scaled on outer variables,  $B_2$  is well correlated and decreases slightly from  $0.2 < y/\delta < 1.0$  in a linear fashion. This is for  $x/L = 4$ , the other downstream planes are similar but are less correlated. This study emphasized the near wall region of the TBL and  $B_2$  is examined on a logarithmic plot and with  $y$  scales on wall variables to examine its behavior closer to the wall. All of the data seem to become less correlated for  $100 < y^+ < 300$  then approximate a linearly decreasing function from  $B_2 = 1.0$  ( $y^+ = 100$ ) to  $B_2 = -1.0$  ( $y^+ = 30$ ). Below  $y^+ = 30$ , the data is scattered but a slight trend to return to  $B_2 = 0.0$  may be observed. Also, a minima in  $B_2$  may be inferred between  $20 < y^+ < 30$ .

In general, the parameter becomes more scattered with the downstream stations, or as the adverse pressure gradient increases.

The similar 6:1 prolate spheroid of Stäger yields similar trends to the Chesnakas data but with greater scatter in the results. The results for  $B_2$  are presented in Figure 4.6. An estimated average value, if one were to approximate  $B_2$  as a constant for this flow, would be 0.6 over the range  $y/\delta > 0.4$ . The degree of scatter here prevents further insight.

Figure 4.7 illustrates  $B_2$  for the cases of the Driver experiment where the flow is relaxing from a shear-driven state. For  $y/\delta > 0.2$ ,  $B_2$  approximates a constant value near 0.8. The varying adverse pressure gradient does not appear to have a significant effect on this parameter. The progressive degree of scatter seen in the Baskaran and Chesnakas flows is not observed here. Therefore it is assumed that the  $B_2$  parameter is approximately constant for flows with adverse pressure gradients with values near non-adverse pressure gradient flows. It appears that lateral and longitudinal wall curvature causes  $B_2$  to lose its correlation. The near wall behavior of  $B_2$  for the experiment of Driver is similar to that reported previously. The scatter is increased for  $100 < y^+ < 300$  and then it has a linear decrease on a log scale. The flows without shear tend to have more scatter than the shear induced 3D cases. It appears that the effects that generate three-dimensionality tend to stabilize the  $B_2$  parameter.

For the experiment of Littell, a pure shear driven flow with quiescent atmosphere,  $B_2$  behaves differently from the other flows investigated here. Like many of the other parameters that were investigated for this flow,  $B_2$  attains its maximum value near the spinning wall and exhibits a linear decrease over the boundary layer. It is fairly correlated from station to station when  $y$  is scaled on  $\delta$ . The results are illustrated in Figure 4.8. (Recall how the  $1/S$  parameter did not exhibit the linear decrease over the boundary layer, an indication of its robust character.)

## 4.2 $\overline{vq^2}$ Parameters

Another class of parameters that were devised employed the algebraic sum  $\overline{vq^2}$ , or:

$$\overline{vq^2} \equiv (\overline{u^2v} + \overline{v^3} + \overline{w^2v}) \quad (4.3)$$

This parameter was examined for the flows in this study. As mentioned earlier, several normalizing factors were employed with the  $\overline{vq^2}$  parameter to make a dimensionless ratio. It was

determined that the best way to present this factor was to use the ratio of  $\overline{v^3}$  to  $\overline{vq^2}$ . The parameter exhibited similar behavior to the  $B_2$  parameter, however in some cases, it presented a better correlation. For the discussion this ratio will be referred to as the normalized  $\overline{vq^2}$  parameter.

The experiment of Pompeo has this parameter as approximately constant at 0.3 for  $y/\delta > 0.4$ . There is less scatter closer to the wall than seen previously in  $B_2$ . The results for Pompeo are presented in Figure 4.9.

The experiment of Schwarz shows this parameter to correlate very well for  $y/\delta > 0.4$  in the developing flow and for  $y/\delta > 0.5$  in the decaying flow. The results for the Schwarz flow are represented in Figure 4.10. The values are approximately constant at 0.35. There is significant scatter in the parameter at  $y$  values less than these and no conclusions can be drawn there. The decay region shows a tendency for this parameter to tend to infinity near  $y/\delta = 0.4$ . This is where the denominator goes to a value near zero as will be seen in the plots of the individual triple products.

The wing-body junction flow of Ölçmen shows similar behavior (figure 4.11). For  $y/\delta > 0.4$  there is good correlation of this parameter at an approximately constant value of 0.35. Viewed with  $y$  scaled on wall variables, it exhibits similar behavior as  $B_2$ . It has a region of increased scatter for  $100 < y^+ < 300$  and then a linear decrease on a log scale from  $30 < y^+ < 100$ , and finally a return to a constant value near 0.0 as the wall is approached. The correlation in this parameter is better than  $B_2$  for this flow.

The behavior of the normalized  $\overline{vq^2}$  parameter for the experiment of Baskaran is again better correlated than  $B_2$  as illustrated in Figure 4.12. The region where it can be approximated as a constant value extends further towards the wall than  $B_2$  for the individual stations. The values for the individual stations are approximately constant for  $y/\delta > 0.4$  and range from 0.3 - 0.4. This approximation to a constant value may extend further towards the wall, but the uncertainty in the measurements does not permit further conclusions to be drawn. The values are a bit better for the concave curvature case than the convex curvature case. The results for the convex curvature case exhibit a few decreases in the value near  $y/\delta = 0.5$  but is still better correlated from station to station than the  $B_2$  parameter. The values appear to increase slightly with increased three dimensionality for the convex case but the uncertainty masks conclusive evidence of such a trend.

Figure 4.13 shows the normalized  $\overline{vq^2}$  parameter for the experiment of Chesnakas. It exhibits similar behavior to the  $B_2$  parameter but it appears to be better correlated from station to station and better approximate a constant in the outer layer. For  $y^+ > 200$  at  $x/L = 0.40$  it

maintains a value near 0.35 before becoming scattered beyond  $\delta$ . Closer to the wall a region of logarithmic behavior (linear on a log scale) occurs for  $30 < y^+ < 100$ . It then goes to  $-\infty$ . Nearest the wall a value of 0.2 is approached. As the flow approaches separation, the parameter becomes more scattered, but not as much as  $B_2$ . At  $x/L = 0.60$ , the stations still approximate the behavior seen at  $x/L = 0.40$  but with a bit more scatter. In the downstream planes, due to scatter, the only conclusion that may be inferred is that this parameter as well as  $B_2$  can not be applied to separating flows.

Stäger's prolate spheroid showed a similar response to the onset of separation, however it was not as pronounced as for the Chesnakas flow as seen in Figure 4.14. This is slightly due to the vertical scaling on  $\delta$  rather than wall variables. But overall, it is better correlated for the Stäger flow than the Chesnakas flow. The  $x/L = 0.48, 0.56$ , and  $0.64$  data planes illustrate the normalized  $\overline{vq^2}$  parameter to approximate a constant value of 0.3 for  $y/\delta > 0.3$ . The scatter in the data for  $y/\delta < 0.4$  increases with the onset of separation, but the station to station correlation mentioned above remains intact. The  $x/L = 0.73$  data plane shows less correlation in this parameter, yet it still seems to approximate a constant of 0.3 for the outer layer. Overall, the normalized  $\overline{vq^2}$  parameter makes a better approximation to a constant and from station to station than  $B_2$  for this flow. It is unknown why such a discrepancy exists between this data set and that of Chesnakas.

The adverse pressure gradient flow of Driver illustrated that the normalized  $\overline{vq^2}$  parameter becomes less correlated with greater adverse pressure gradients. It also illustrates that the effects of shear or three-dimensionality appear to produce a stabilizing effect on this parameter. Figure 4.15 contains the results. For  $y/\delta > 0.4$  this parameter approximates a constant value of 0.4 with increasing station to station scatter for increased adverse pressure gradient. Also the constant value is not approximated for the flow cases lacking the shear induced three dimensionality. On a qualitative level, this parameter exhibits a better approximation to a constant value and station to station correlation than the  $B_2$  parameter for the experiments of Driver. The near wall behavior illustrates a linear decrease for  $0.1 < y/\delta < 0.3$  and then an asymptotic approach towards zero.

The shear flow experiment of Littell does not produce a normalized  $\overline{vq^2}$  parameter that is constant across the boundary layer. It does exhibit a linear decrease that is correlated from station to station. Over the range  $0.1 < y/\delta < 0.8$ , it drops linearly from 0.3 to 0.2. It exhibits similar behavior as the  $B_2$  parameter for this flow. The results are given in Figure 4.16.



### 4.3 Other Ratios

The normalized  $\overline{vq^2}$  and  $B_2$  parameters exhibit good turbulence modeling parameter behavior for flows that incorporate triple products within the modeling equations. They approximate constant values for a large portion of the outer region of the boundary layer for various flows and from station to station. They also exhibit predictable behavior for other seemingly distinct regions of the various experiments. They are invariant to a rotation about an axis normal to the adjacent surface. In the discussion above it was seen that the normalized  $\overline{vq^2}$  parameter appeared to correlate better than the  $B_2$  parameter. This is an important observation since  $B_2$  utilizes the triple products that are required for a model using the equations presented in chapter 1. Based on this, a parameter similar to the  $\overline{vq^2}$  parameter but utilizing the proper triple products was sought. As a first step the relationships between the  $\overline{u^2v}$ ,  $\overline{uv^2}$ ,  $\overline{v^2w}$ , and  $\overline{vw^2}$  triple products were examined. The specific results are presented in the respective appendices and the overall results are discussed here. In general, the ratio of  $\overline{uv^2}$  to  $\overline{u^2v}$  was fairly well correlated for the outer region of the boundary layer at a value near -0.7. Some flows exhibited a bit more scatter than others. The ratio of  $\overline{vw^2}$  to  $\overline{v^2w}$  was also negative but it was very small and less correlated. Based upon these observations, the following parameter was devised.

$$\frac{\overline{v^3}}{(\overline{v^3} - \overline{v^2w} - \overline{uv^2})} \quad (4.4)$$

Results for this parameter in the various flows is presented in Figure 4.17 through Figure 4.22. The behavior of this parameter is similar to the  $\overline{vq^2}$  parameter but a bit less correlated from station to station within a given experiment. Also the approximation to constant values does not extend towards the wall with the same value as the  $\overline{vq^2}$  parameter does. It behaves more like the  $B_2$  parameter as the wall is approached. That is a jump in the parameter is observed where the denominator approaches zero then appears to maintain a new yet constant value. The regions of logarithmic decrease as discussed in the Ölçmen and Chesnakas flows is observed for the near wall regions. Overall the correlation of this parameter is similar to that of  $B_2$  but worse than the normalized  $\overline{vq^2}$  parameter. It exhibits similar behavior in the presence of shear and adverse pressure gradients as mentioned for the  $\overline{vq^2}$  parameter.

The inverse of equation 4.4 is,

$$\frac{(\overline{v^3} - \overline{v^2 w} - \overline{uv^2})}{\overline{v^3}} = 1 - \frac{\overline{v^2 w}}{\overline{v^3}} - \frac{\overline{uv^2}}{\overline{v^3}} \quad (4.5)$$

which may seem trivial because the  $\overline{v^2 w}$  term is generally small and  $\overline{v^3}$  would dominate the relationship. However when viewed independently, the terms in equation 4.5 do not correlate well across the boundary layer. Plots of these ratios are presented in the respective appendices. They illustrate the poor correlation of the individual terms in comparison to the relationship given in equation 4.4. Therefore it is recommended that the parameter remains in the form of equation 4.4 if it were to be used in a turbulence modeling effort.

#### 4.4 Insight from Individual Triple Products

The parameters presented above appear to approximate a constant value or behave predictably over regions of the 3D TBL. It is natural to wonder what is causing such behavior and this section is dedicated to investigating this point further. Since the parameters are simple algebraic ratios, an investigation of the individual triple products of interest should generate insight into the behavior of these parameters. Plots of the individual triple products of interest were generated for each station of the experiments that were examined. The bulk of these reside in their respective appendix. Some figures that are representative of the bulk are presented in Figure 4.23 through Figure 4.28. These will be discussed presently.

The triple products of interest as pointed out in chapter 1 are;  $\overline{uv^2}$ ,  $\overline{v^3}$ , and  $\overline{v^2 w}$ . Figure 4.23 and 4.24 illustrate these triple products for the experiment of Pompeo. For the converging duct, the  $\overline{v^2 w}$  triple product is quite small compared to  $\overline{uv^2}$  and  $\overline{v^3}$ . Also it is shown that  $\overline{uv^2}$  nearly mirrors  $\overline{v^3}$  across the entire boundary layer with increased scatter in the profile as the wall is approached. The diverging duct illustrates that  $\overline{v^2 w}$  is significant for this case particularly as the wall is approached. The  $\overline{v^3}$  triple product exhibits similar behavior as  $\overline{v^2 w}$  but is smaller in magnitude. As the denominator of  $B_2$  is the magnitude of  $\overline{uv^2}$  and  $\overline{v^2 w}$  combined, it is seen why the  $B_2$  parameter becomes more scattered and generally increased with the approach of the wall. Also these figures show that the  $\overline{v^2 w}$  triple product can not readily be ignored in the parameter. It attains significant values and appears to contribute to the parameters that were introduced above.

Figure 4.25 for the experiment of Schwarz illustrates some more features observed with the parameters. Figure 4.25a is for station 8 which is in the developing 3D region of this

experiment. Figure 4.25b is for station 14 in the crossflow decay region of the duct. The behavior of the triple products still follows the discussion presented for the Pompeo experiment where  $\overline{v^2 w}$  is typically small and  $\overline{uv^2}$  and  $\overline{v^3}$  mirror each other. What may be observed in this experiment is the region of the experiment closer to the wall where the triple products approach and pass through zero. By comparison with the plots presented earlier for the  $B_2$  and  $\overline{vq^2}$  parameters, one can discern that this region of decrease is where the parameter becomes scattered. As the flow progresses downstream, this interface progresses to a greater  $y$  location in the boundary layer. As was seen in the parameters, this progression is generally halted near  $y/\delta = 0.4$ . Another observation for the Schwarz flow is that relative to the magnitude of  $\overline{uv^2}$  and  $\overline{v^3}$ ,  $\overline{v^2 w}$  appears to get smaller with the downstream stations.

Figure 4.26 and 4.27 present the triple products for the Baskaran experiment. This flow shows that  $\overline{v^2 w}$  has a magnitude similar to  $\overline{v^3}$  which still mirrors  $\overline{uv^2}$  and thus can not be ignored in a parameter that is to apply to a variety of experimental geometries. It supports the observation in the Schwarz experiment that as the flow progresses downstream, the point where the triple products approach and pass through zero moves farther away from the wall. This flow exhibits a better behavior of the triple products after this zero crossing. This coherency can be observed in the  $B_2$  and  $\overline{vq^2}$  parameters as they recover to a value or attempt to maintain the value seen in the outer layer (normalized  $\overline{vq^2}$ ).

The final triple product relation presented in the body is for the experiment of Littell as represented by Figure 4.28. This is presented as the parameters were distinctly different for the Littell experiment. The triple products are greatest near the wall and decay to zero as the quiescent atmosphere is reached. This is different from the other boundary layer flows that achieved their greatest fluctuating velocities and Reynolds stresses in the outer layer and were bounded by larger regions where the fluctuating velocities were approaching zero. For the rotating disk shear flow presented here, the region where the fluctuating velocities would approach zero near the disk is much smaller and the effects of the outer flow (quiescent atmosphere) would be extended over a greater region. This appears to be why the Reynolds averaged triple products have such a sharp decrease across this boundary layer. This behavior is why this experiment generates parameters so different from the other flows. However once again it must be noted that the  $1/S$  parameter behaved similarly to the other 3D TBLs presented in this study which in light of the triple product examination is remarkable.

## Conclusions

This chapter focused on the discussion of the major results of the investigation into algebraic parameters formed from the turbulent triple products. Ratios were presented that may aid in the modeling effort. In particular, the  $B_2$  parameter illustrates a relationship between the three triple products that appear in equations 1.6 - 1.8 that is reproducible from station to station and to some degree from flow to flow. Overall  $B_2$  approximated a constant value of 0.7 to 1.0 for a flow across  $0.3 < y/\delta < 1.0$ . For  $y/\delta < 0.3$ ,  $B_2$  becomes scattered due to the individual triple products becoming small and passing through zero. Some of this effect is also due to an increased uncertainty in the velocity components as the wall was approached due to the measurement techniques employed. For the triple product relationships, the results for the shear driven experiment of Littell differed from the others.

This and other relationships that were presented were well behaved in the outer region of the turbulent boundary layer then became scattered as the wall was approached. Analysis of the triple products revealed that for the outer layer, the triple products maintain relatively significant values. Near  $y/\delta$  of 0.4, the triple products begin to diminish and pass through zero. They regain an appreciable value for some of the flows in this study, while they remain small for others. The results presented here appear to distinguish definite regions of the turbulent boundary layers that were investigated. The finer points of these conclusions are explored in Chapter 5.

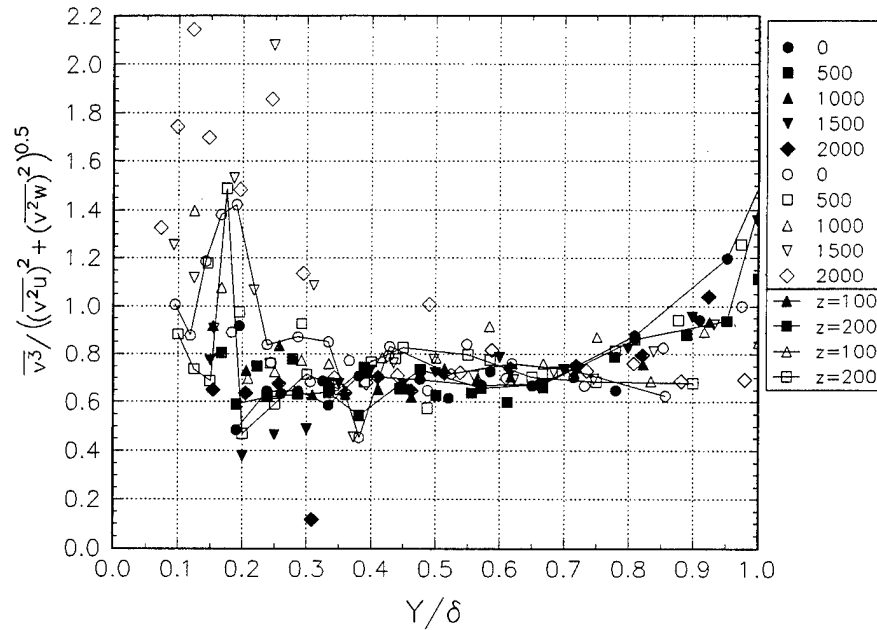


Figure 4.1a  $B_2$  for Pompeo. Centerline stations (symbols only) have the  $x$  location shown in mm. Off centerline stations (lines) were at  $x = 1000$  mm, the  $z$  location is shown in mm. Closed and open symbols are for the diverging and converging duct, respectively.

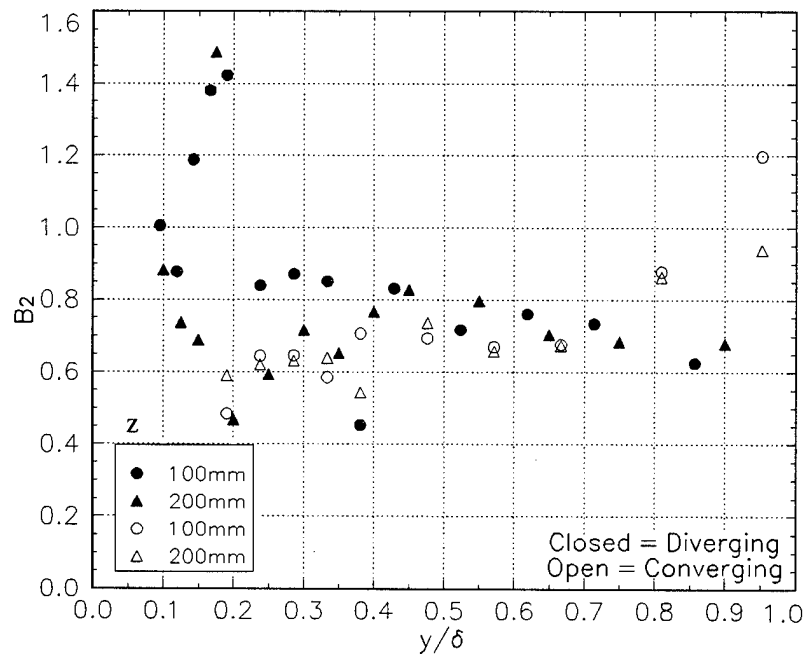


Fig 4.1b  $B_2$  for the experiment of Pompeo. Stations are at  $x=1000$ mm.

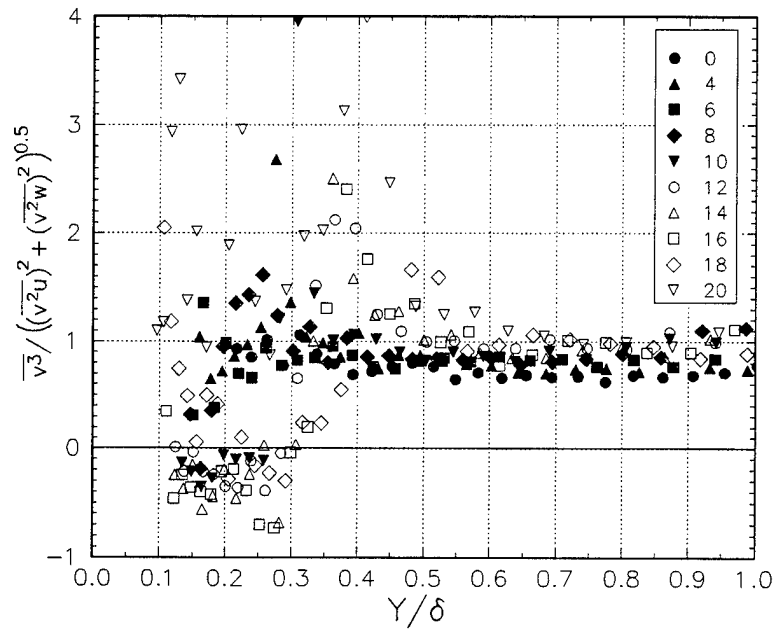


Figure 4.2a  $B_2$  for the Schwarz 30° bend flow. Crossflow development region and decay region are the closed and open symbols, respectively.

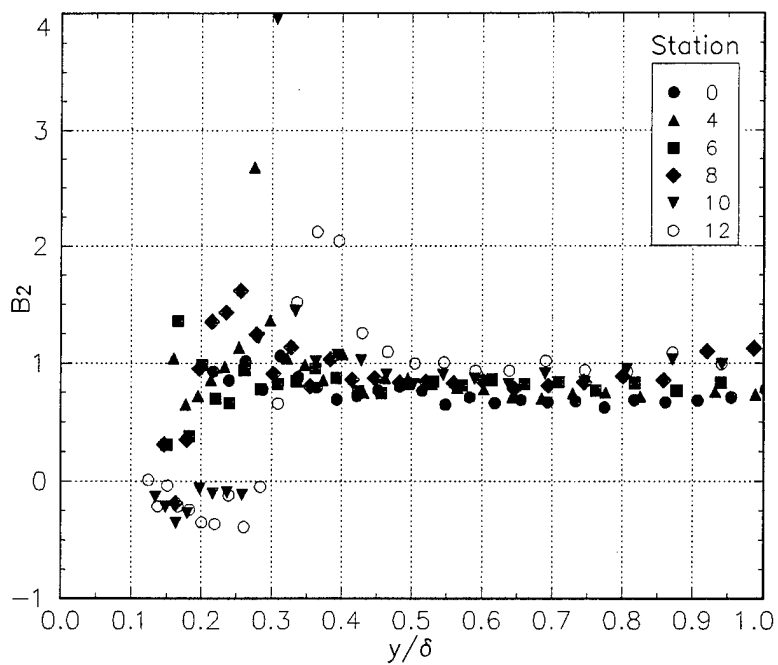


Figure 4.2b  $B_2$  for the crossflow development region of Schwarz.

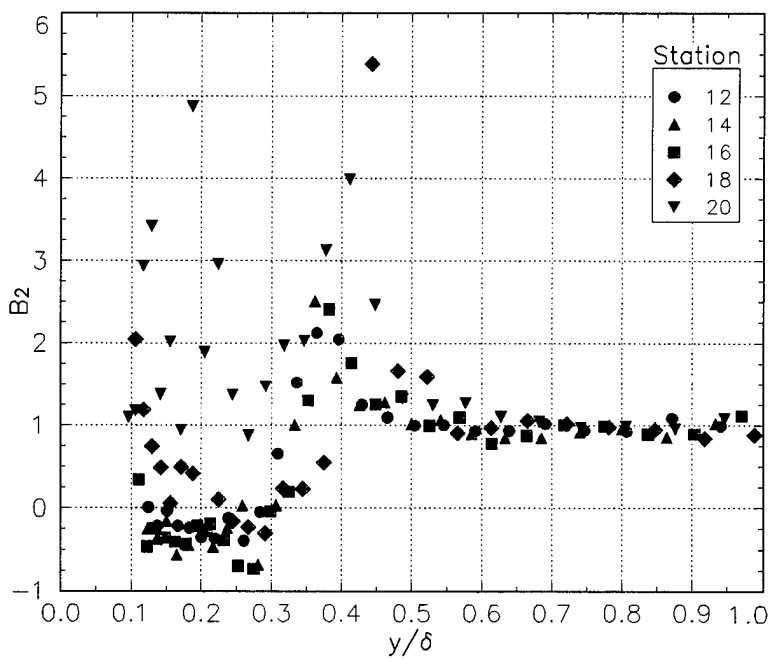


Figure 4.2c  $B_2$  for the crossflow decay region of Schwarz.

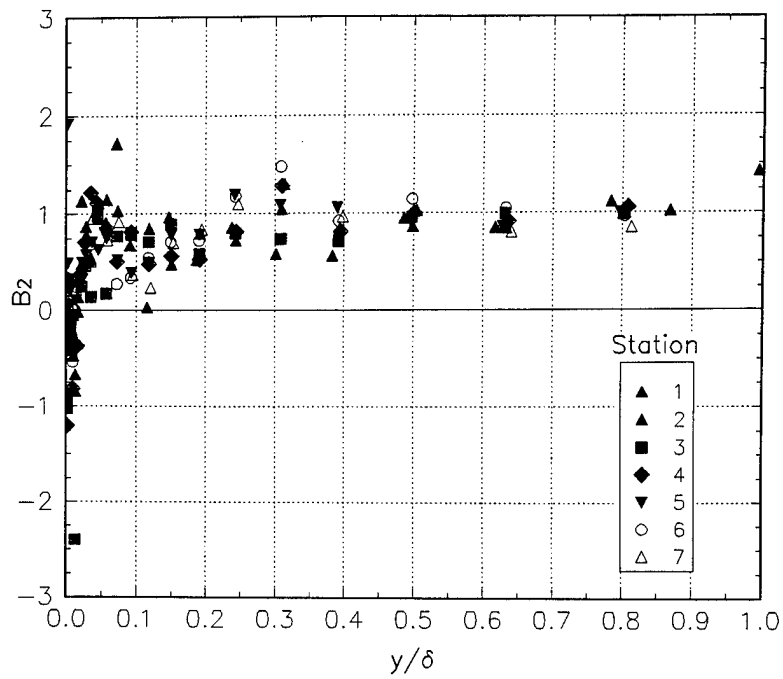


Figure 4.3a  $B_2$  for the wing-body junction flow of Ölçmen.

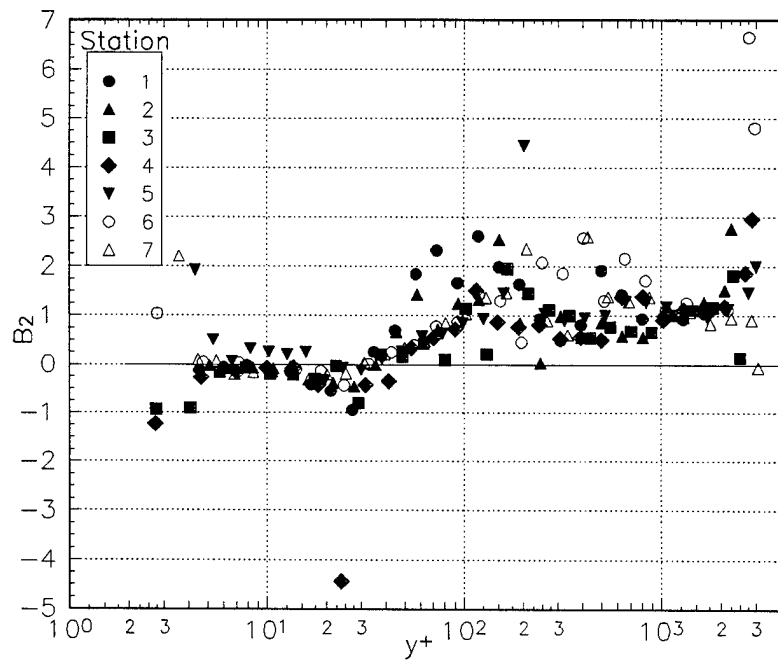


Figure 4.3b  $B_2$  of Ölçmen plotted against wall coordinates.



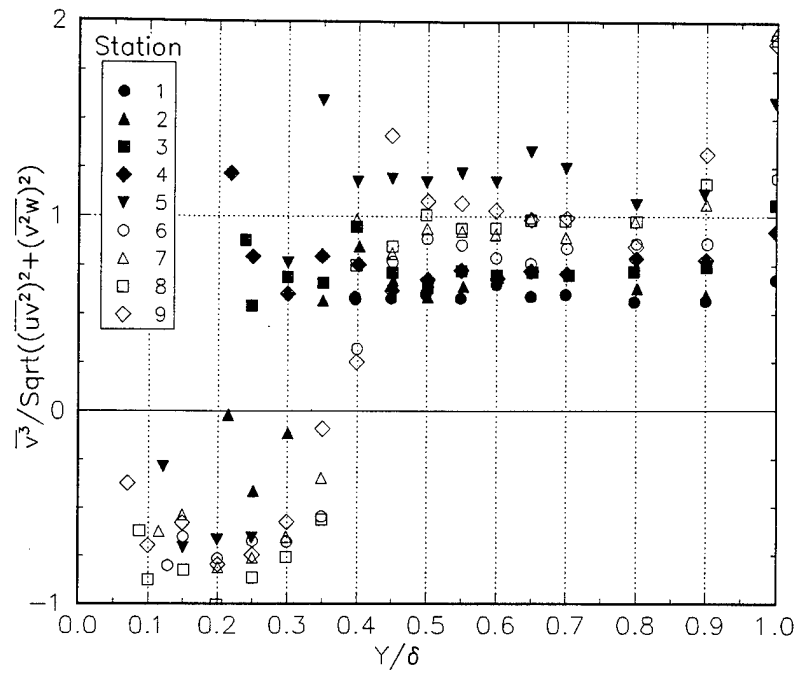


Figure 4.4a  $B_2$  for the Concave curvature case of Baskaran.

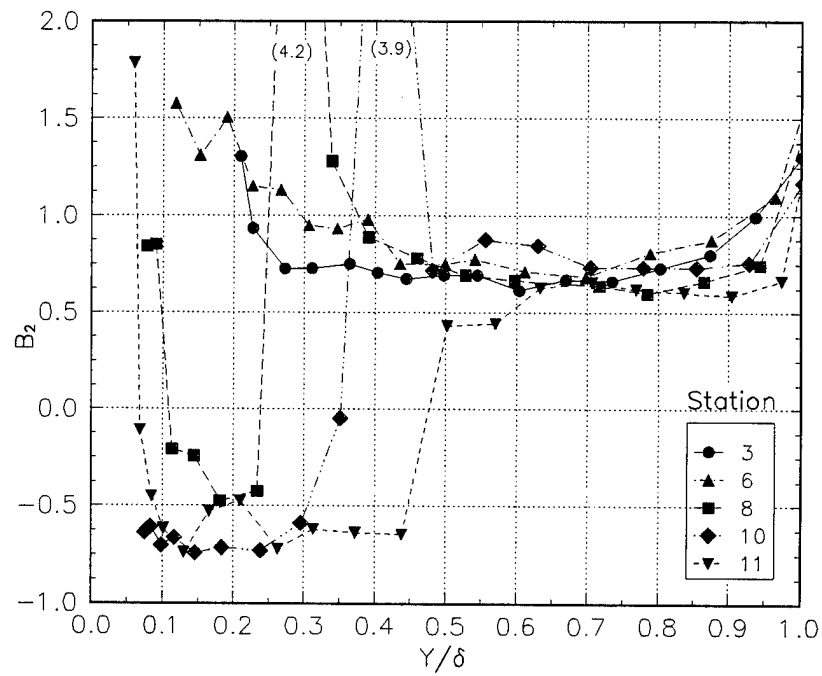


Figure 4.4b  $B_2$  for the Convex curvature case of Baskaran.

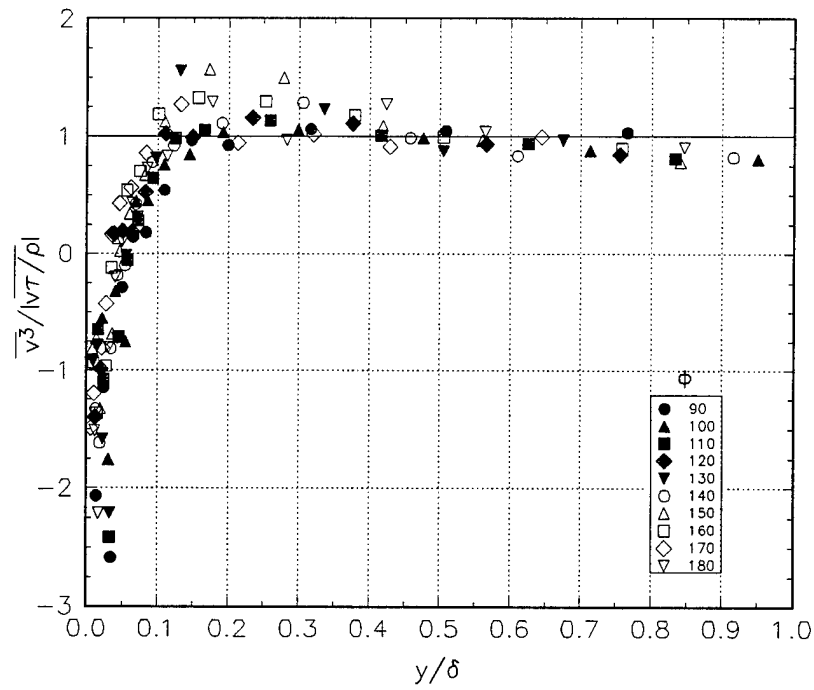


Figure 4.5a  $B_2$  for the 6:1 prolate spheroid of Chesnakas.  $x/L = 0.4$  and  $\alpha = 10^\circ$ . The peripheral angle from the windward side ( $\phi$ ) is indicated.

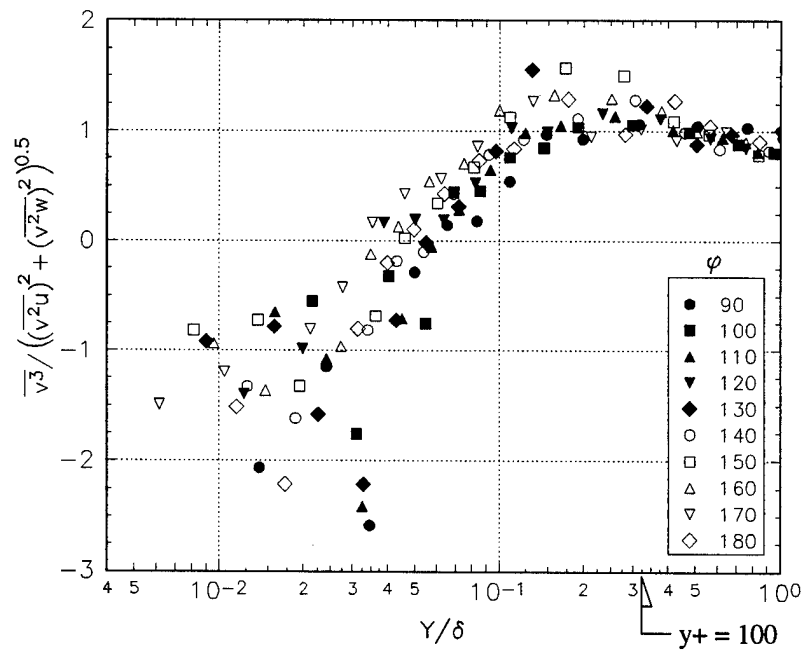


Figure 4.5b  $B_2$  for the 6:1 prolate spheroid of Chesnakas  $x/L = 0.4$ .

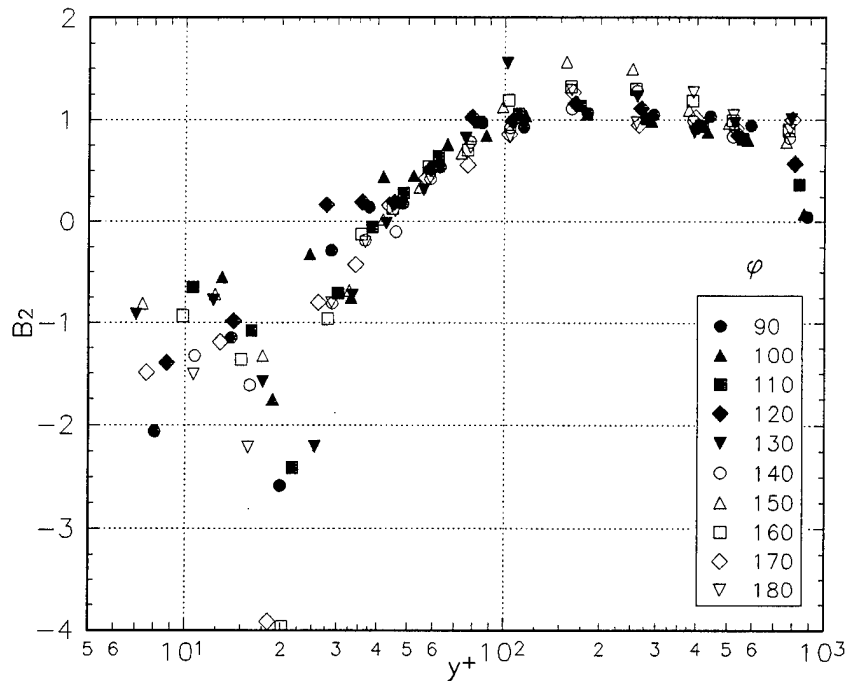


Figure 4.5c  $B_2$  for the 6:1 prolate spheroid of Chesnakas.  $x/L = 0.4$

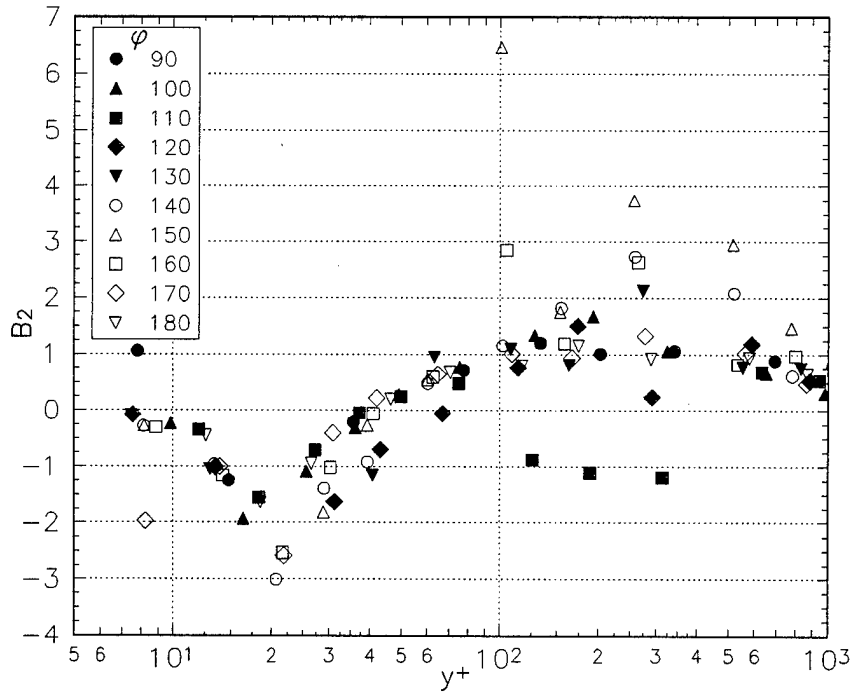


Figure 4.5d  $B_2$  for the 6:1 prolate spheroid of Chesnakas.  $x/L = 0.6$

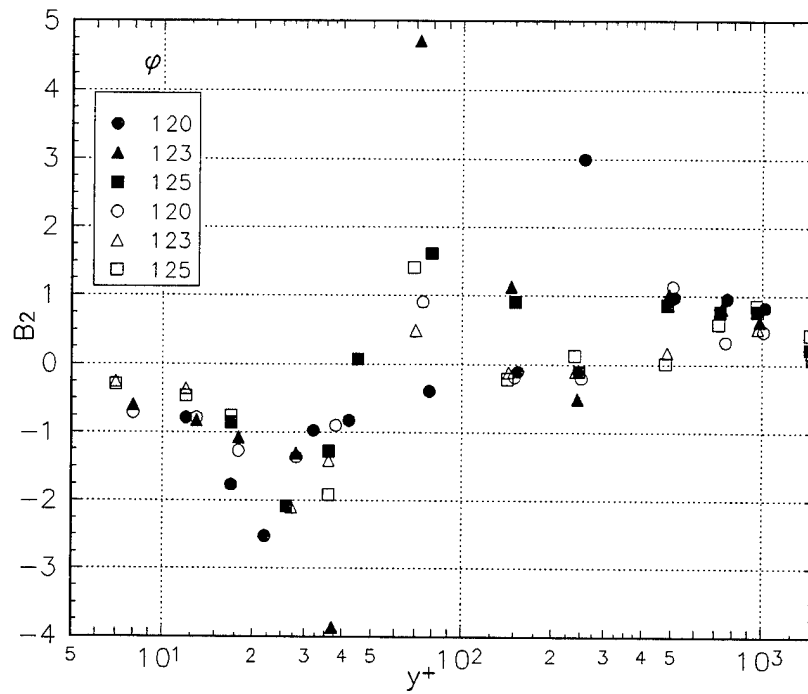


Figure 4.5e  $B_2$  for the 6:1 prolate spheroid of Chesnakas. Closed symbols are for  $x/L = 0.75$  and open symbols for  $x/L = 0.76$ .

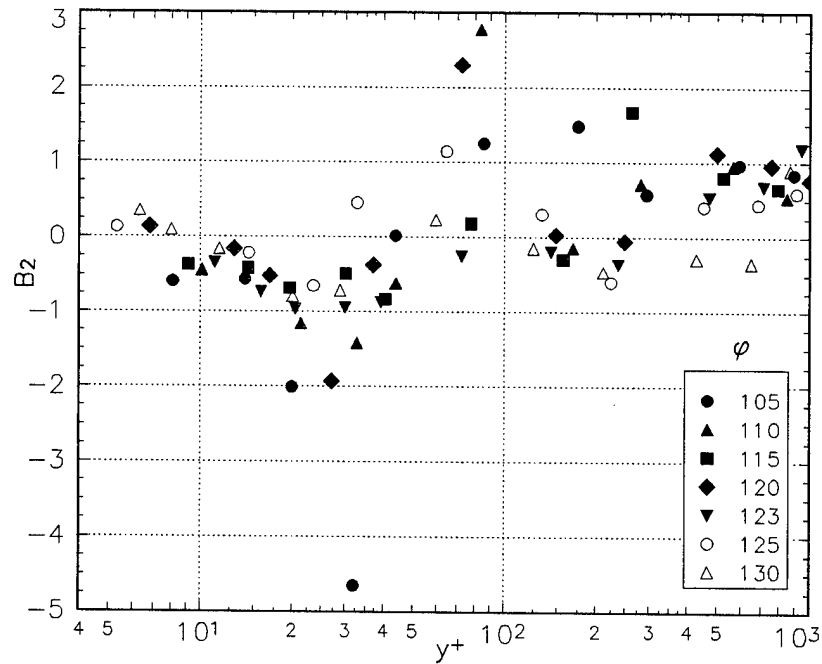


Figure 4.5f  $B_2$  for the 6:1 prolate spheroid of Chesnakas.  $x/L = 0.77$

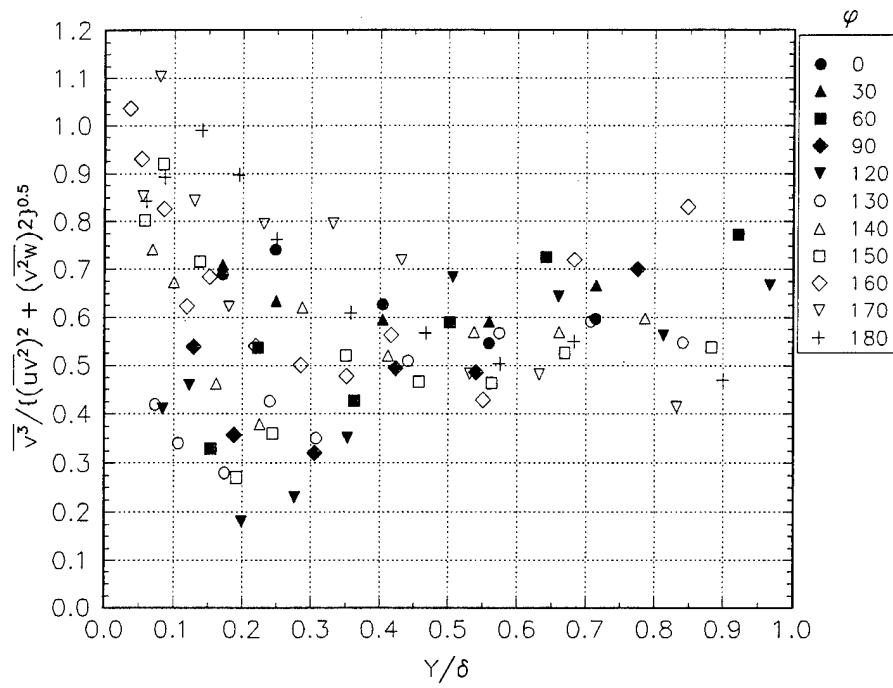


Figure 4.6a  $B_2$  for the 6:1 prolate spheroid of Stäger.  $x/L = 0.48$

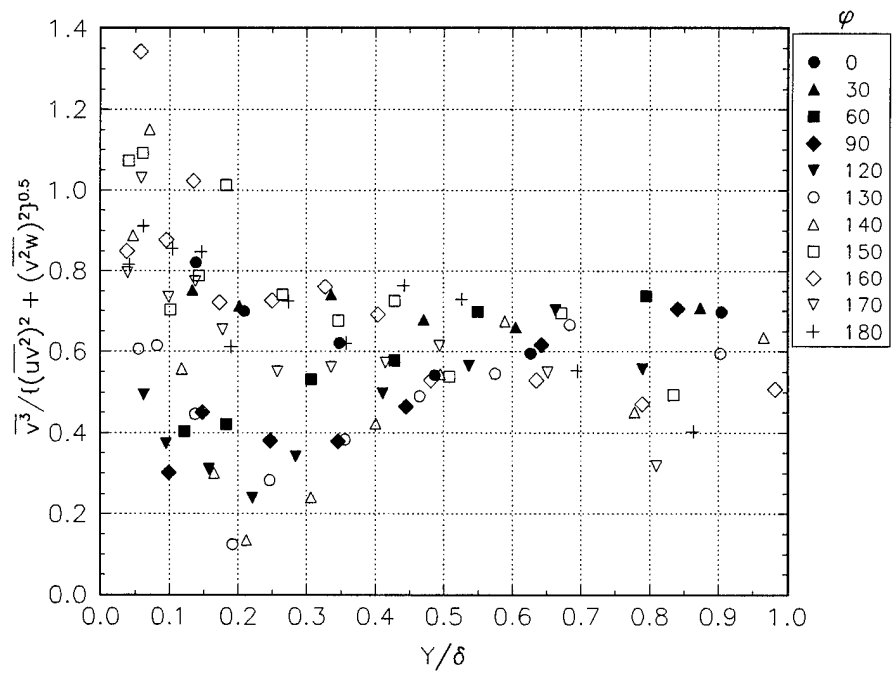


Figure 4.6b  $B_2$  for the 6:1 prolate spheroid of Stäger.  $x/L = 0.56$

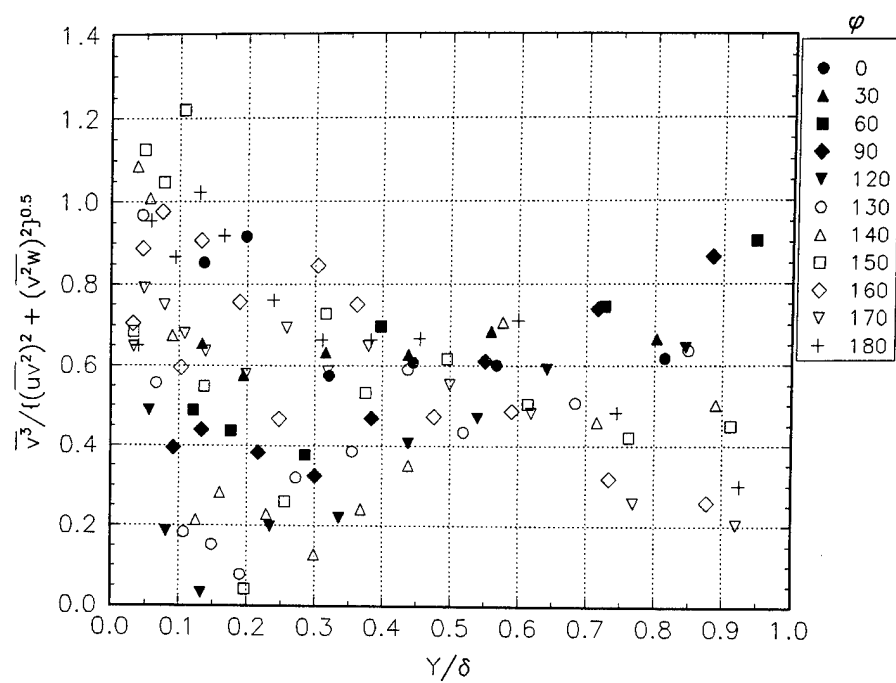


Figure 4.6c  $B_2$  for the 6:1 prolate spheroid of Stäger.  $x/L = 0.64$

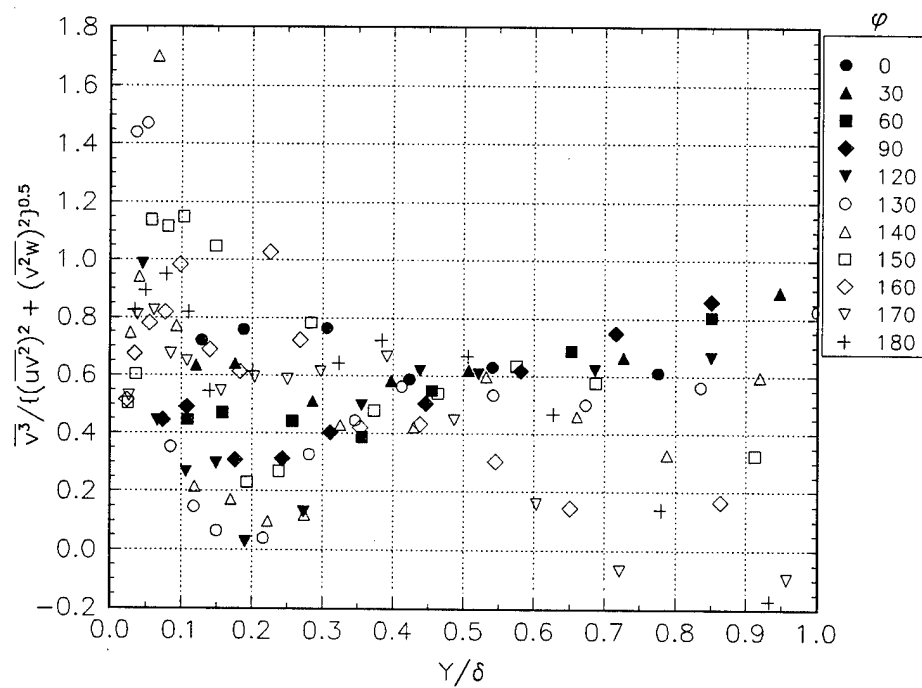


Figure 4.6d  $B_2$  for the 6:1 prolate spheroid of Stäger.  $x/L = 0.73$

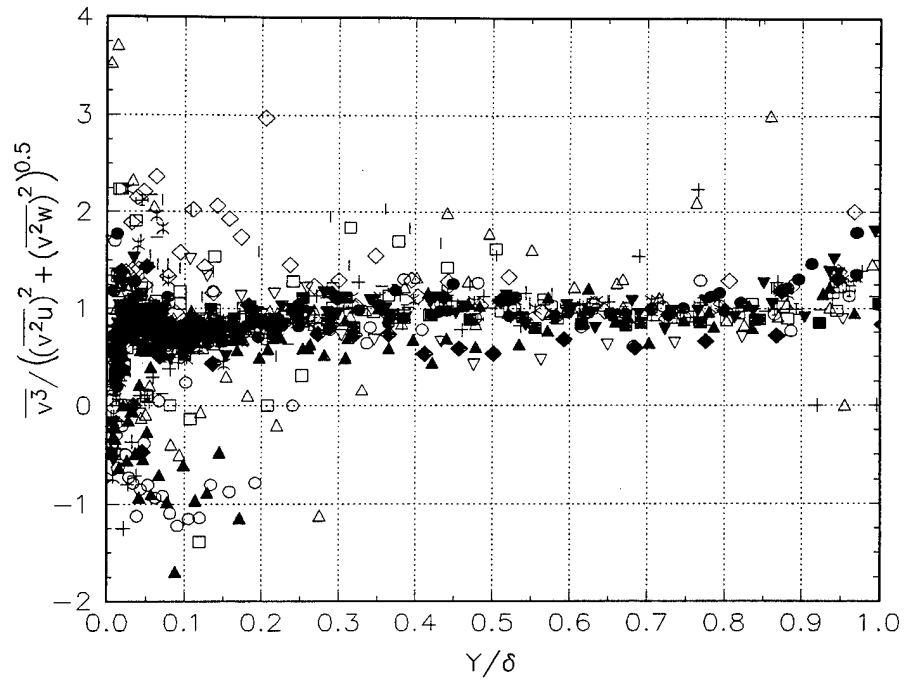


Figure 4.7.  $B_2$  for the experiment of Driver. The stations shown are cases AS1, BS1, CS1, and DS1 excluding stations 6-9 for case BS1. Flows are relaxing from a shear-driven state with varying adverse pressure gradients.

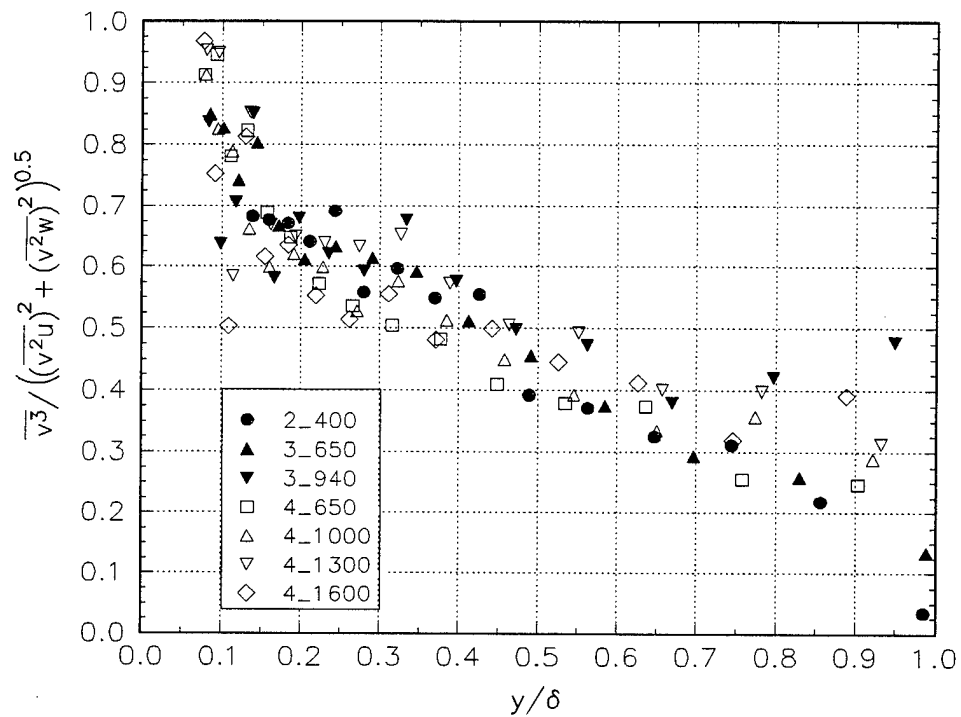


Figure 4.8  $B_2$  for the experiment of Littell. This is a purely shear driven flow with a stationary atmosphere above the rotating disk. Stations are indicated by radius and Reynolds number ( $\times 10^4$ ). The number 2\_, 3\_, or 4\_ represent a radius of 0.235 m, 0.356 m, or 0.421 m respectively. *i.e.* Reynolds number designation \_100 implies 100e4 or 1,000,000 ...



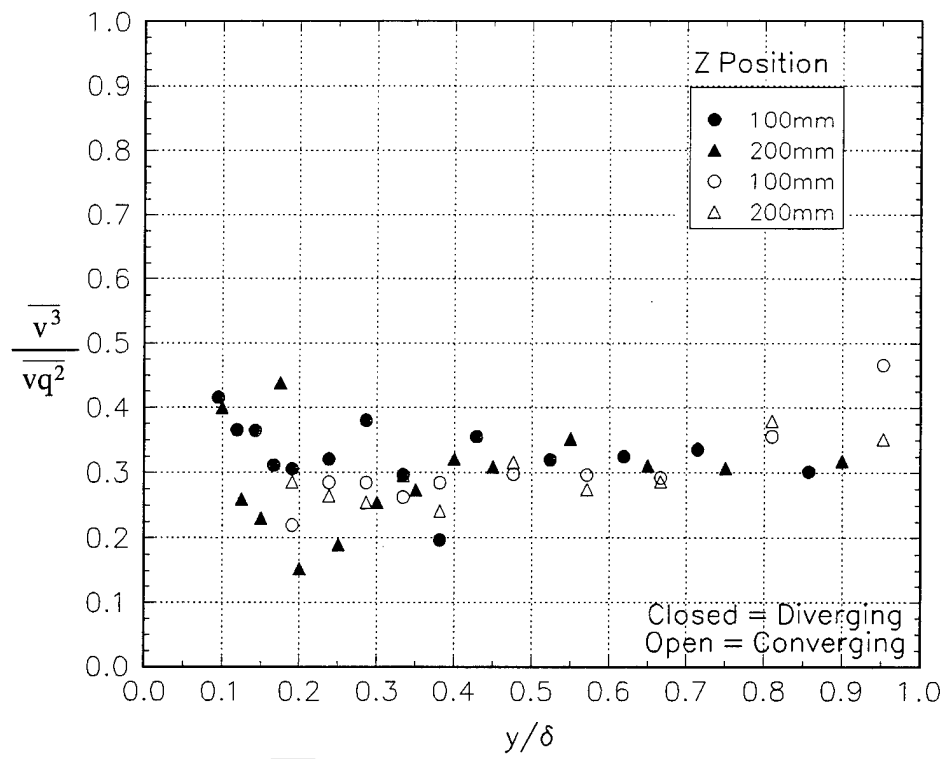


Figure 4.9 The normalized  $\overline{vq^2}$  parameter for Pompeio. Stations are at  $x = 1000$  mm, open symbols represent the converging duct and closed symbols represent the diverging duct.

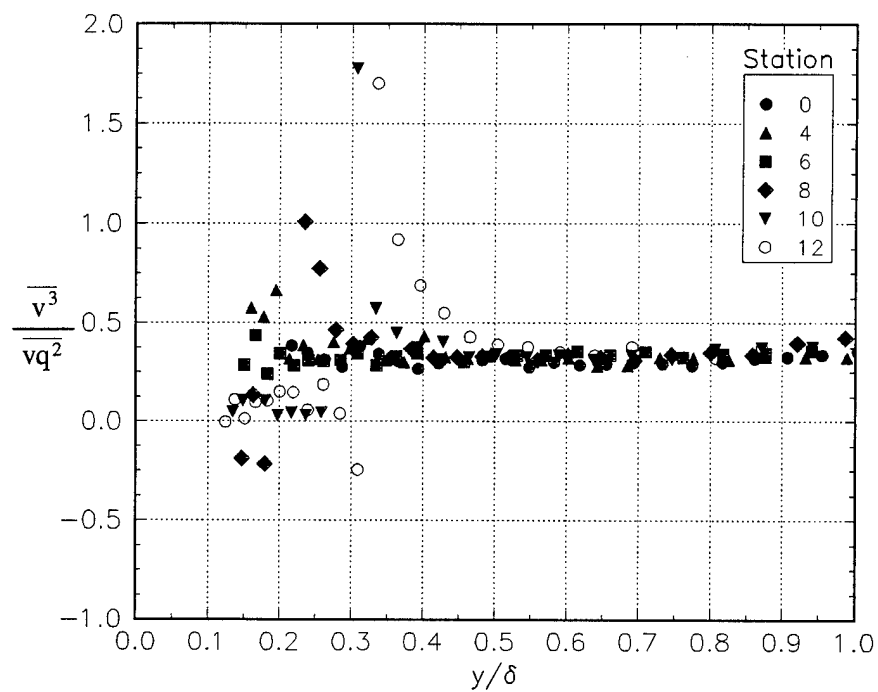


Figure 4.10a The normalized  $\overline{vq^2}$  parameter in the development region of Schwarz.

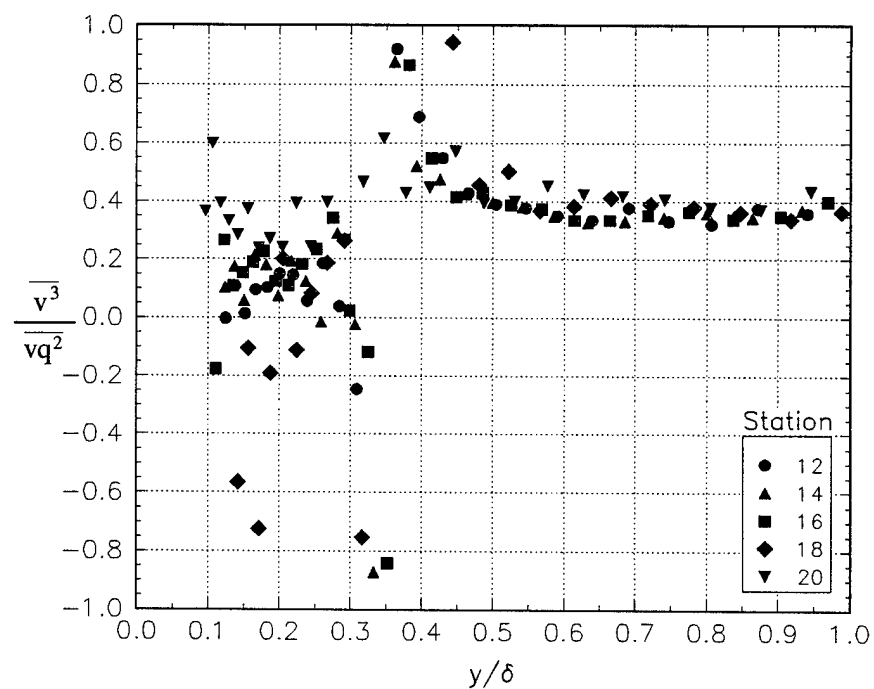


Figure 4.10b The normalized  $\overline{vq^2}$  parameter for the crossflow decay region of Schwarz.

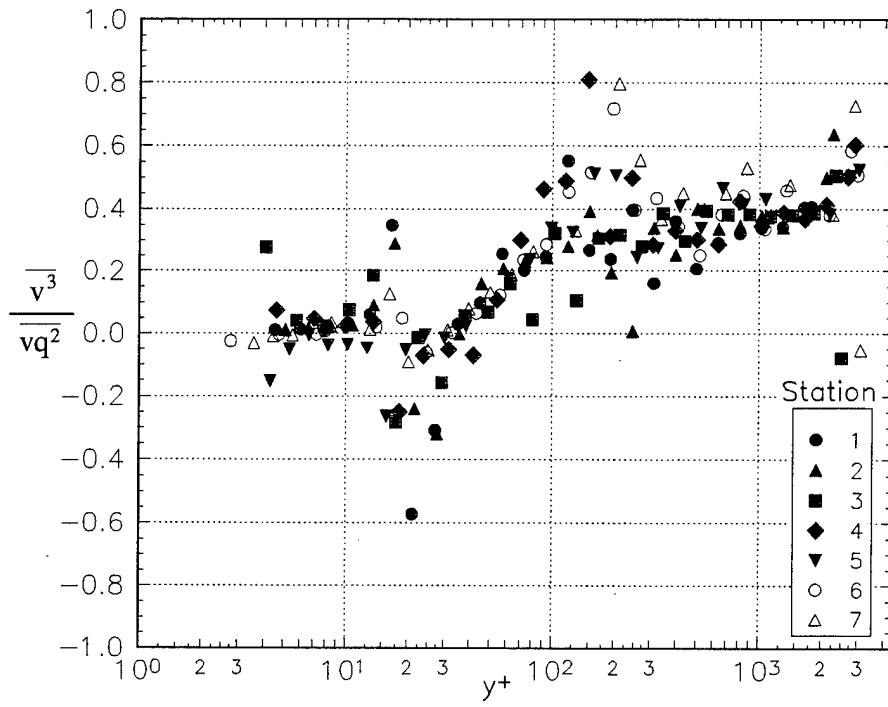


Figure 4.11 The normalized  $\overline{vq^2}$  parameter for the experiment of Ölçmen

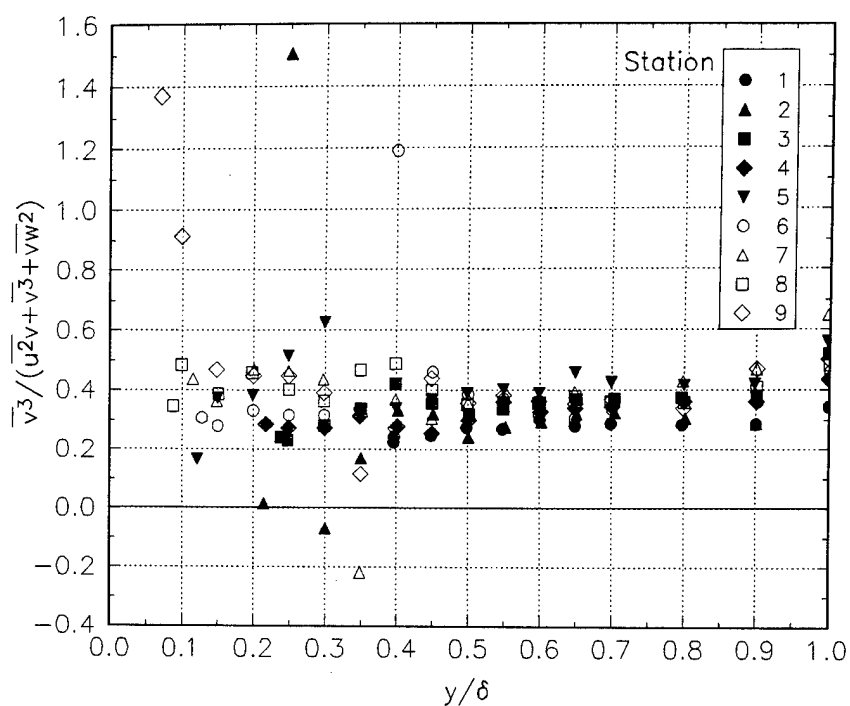


Figure 4.12a The normalized  $\overline{vq^2}$  parameter for the concave curvature case of Baskaran.

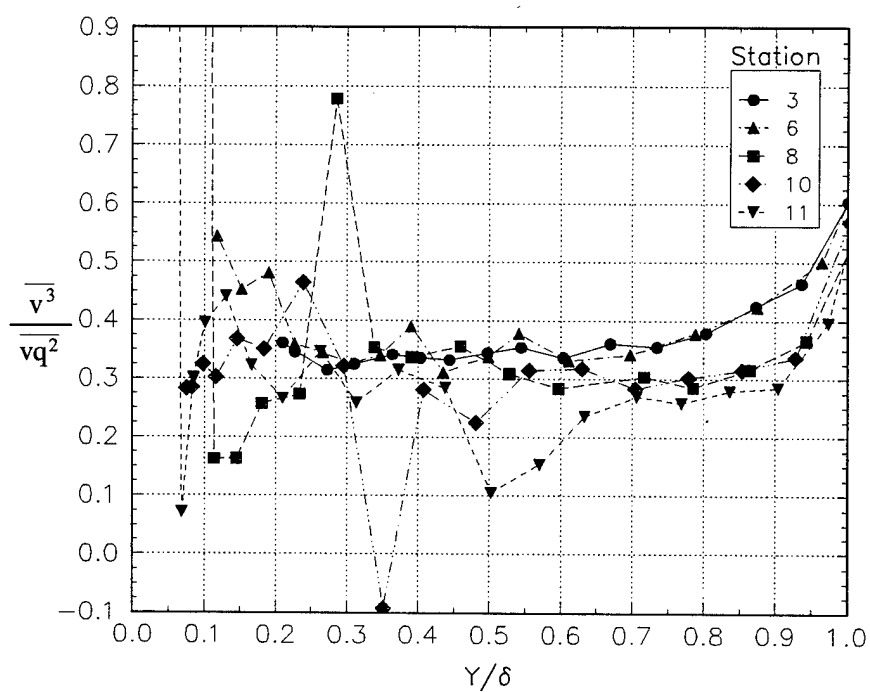


Figure 4.12b The normalized  $\overline{vq^2}$  parameter for the convex curvature case of Baskaran.

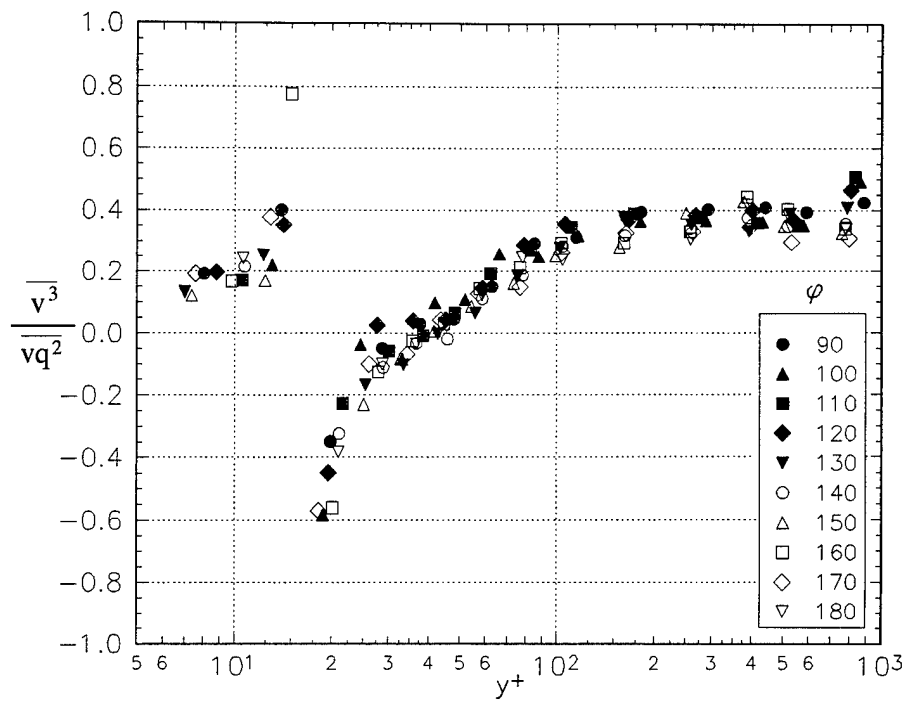


Figure 4.13a The normalized  $\overline{vq^2}$  parameter for the experiment of Chesnakas.  $x/L = 0.4$

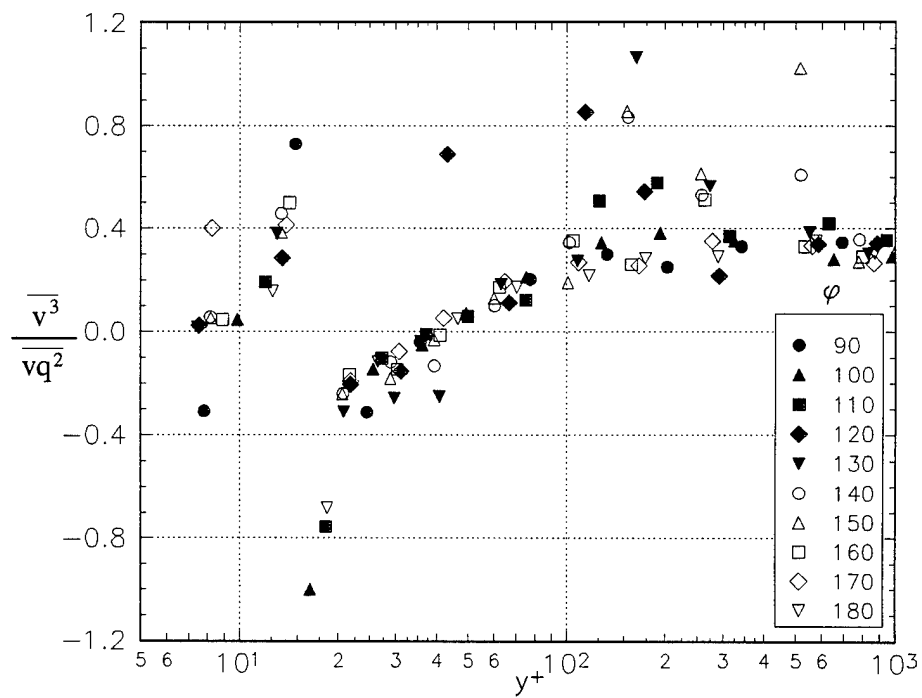


Figure 4.13b The normalized  $\overline{vq^2}$  parameter for the experiment of Chesnakas.  $x/L = 0.6$

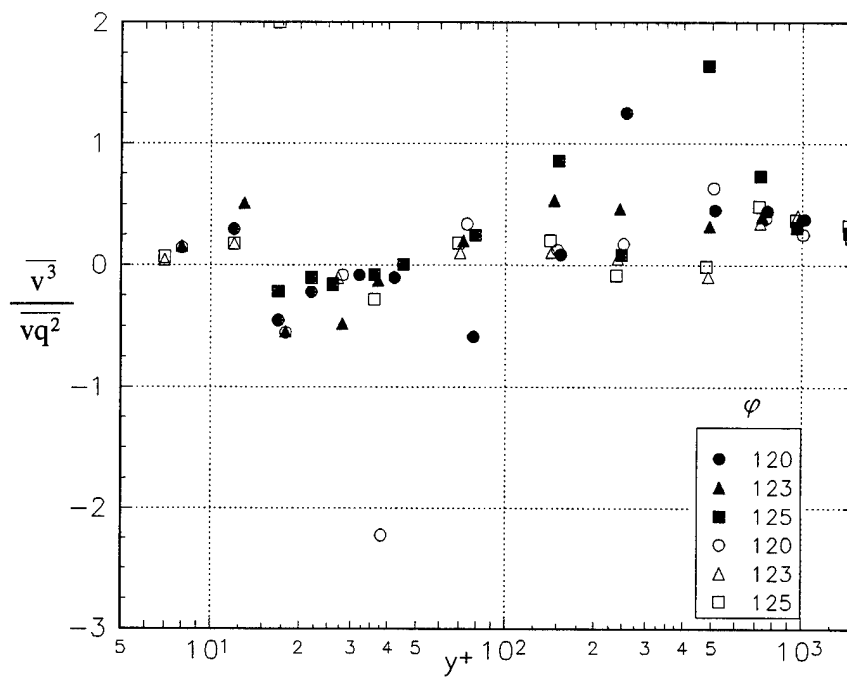


Figure 4.13c The normalized  $\overline{vq^2}$  parameter for the experiment of Chesnakas. Closed symbols represent  $x/L = 0.75$  and open symbol represent  $x/L = 0.76$

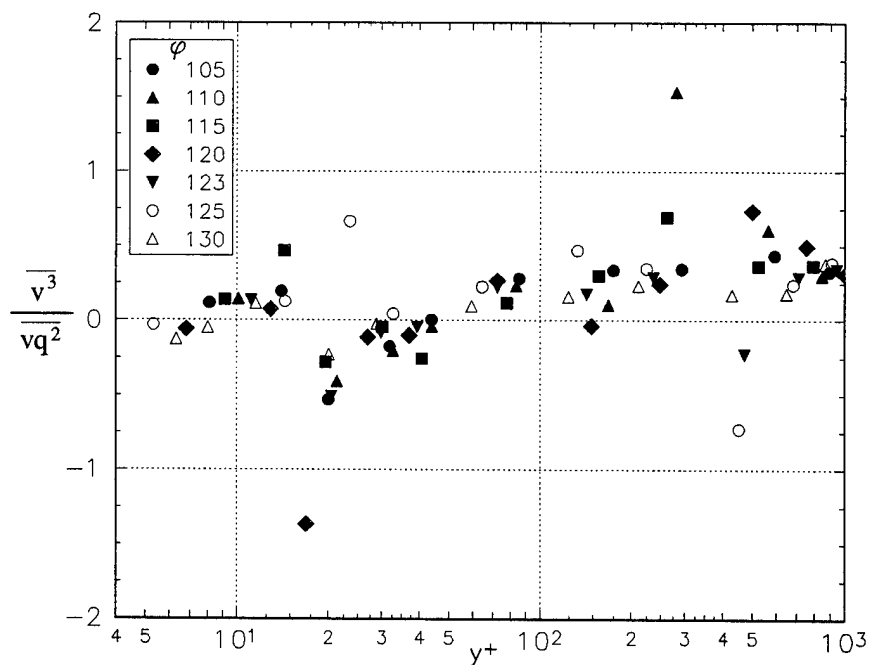


Figure 4.13d The normalized  $\overline{vq^2}$  parameter for the experiment of Chesnakas.  $x/L = 0.77$

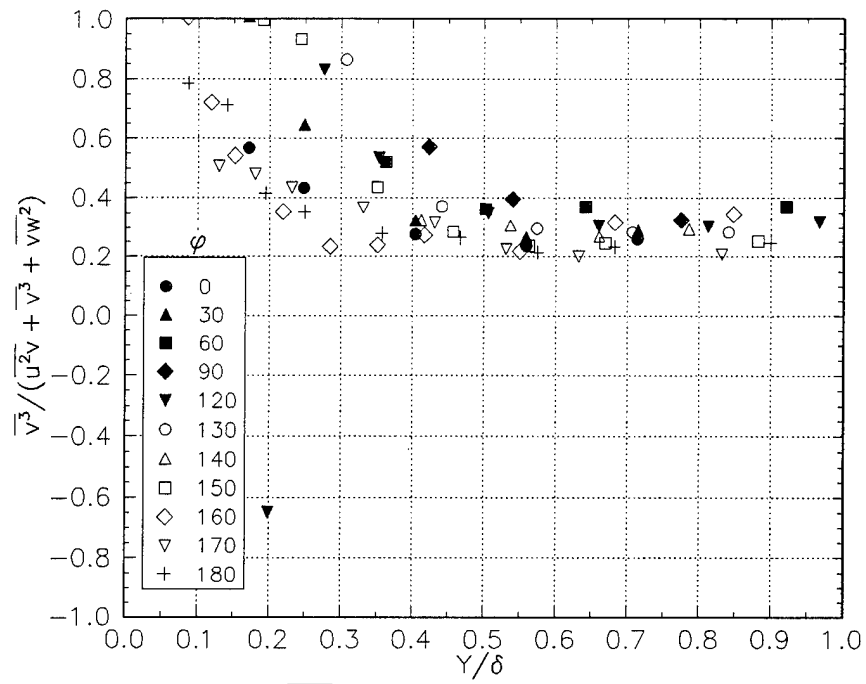


Figure 4.14a The normalized  $\overline{vq^2}$  parameter for the experiment of Stäger.  $x/L = 0.48$

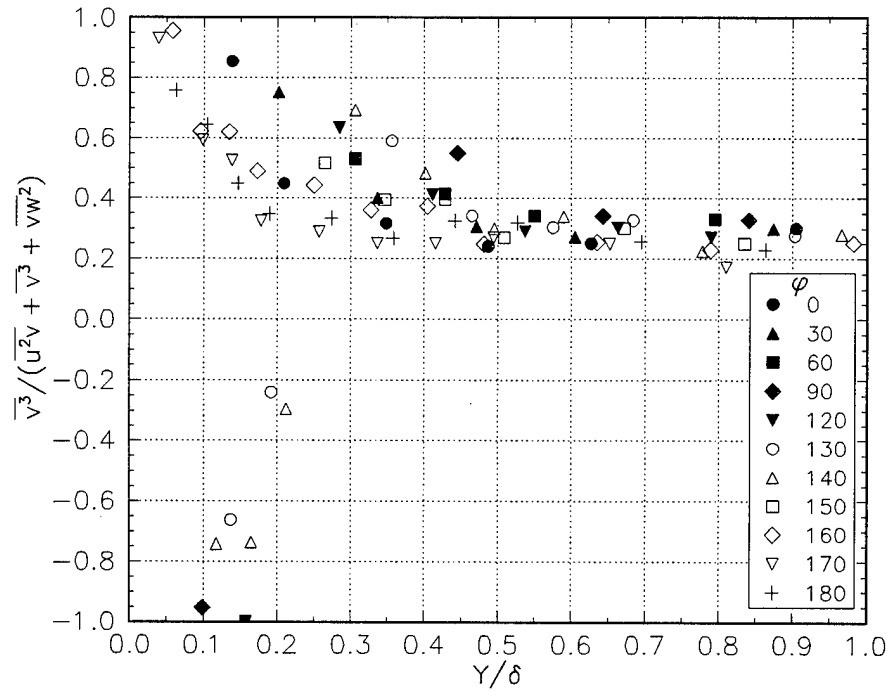


Figure 4.14b The normalized  $\overline{vq^2}$  parameter for the experiment of Stäger.  $x/L = 0.56$

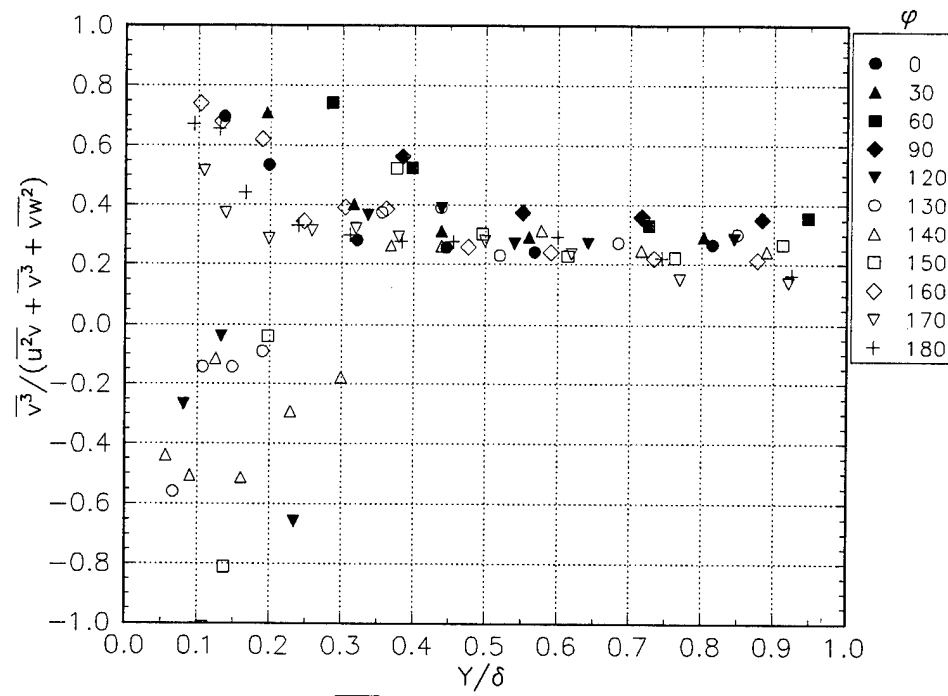


Figure 4.14c The normalized  $\overline{vq^2}$  parameter for the experiment of Stäger.  $x/L = 0.64$

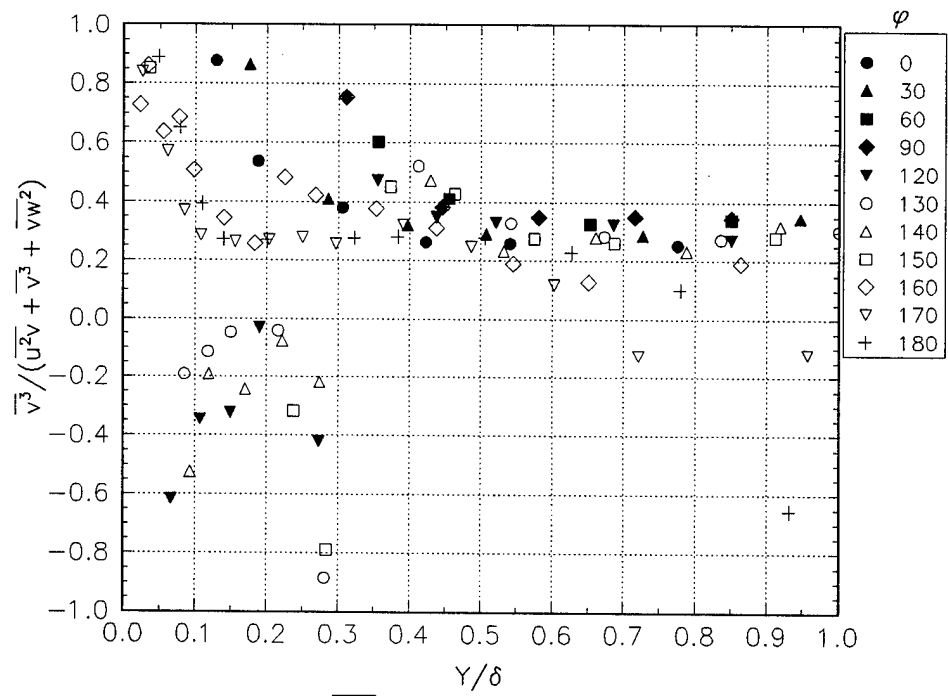


Figure 4.14d The normalized  $\overline{vq^2}$  parameter for the experiment of Stäger.  $x/L = 0.73$



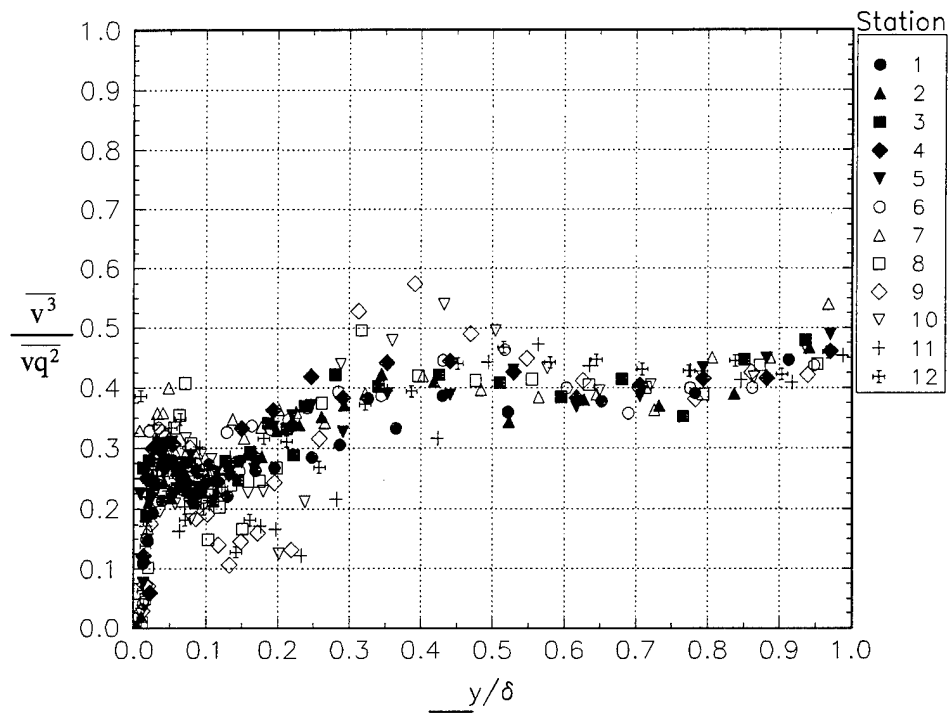


Figure 4.15a The normalized  $vq^2$  parameter for case AS1 of Driver.

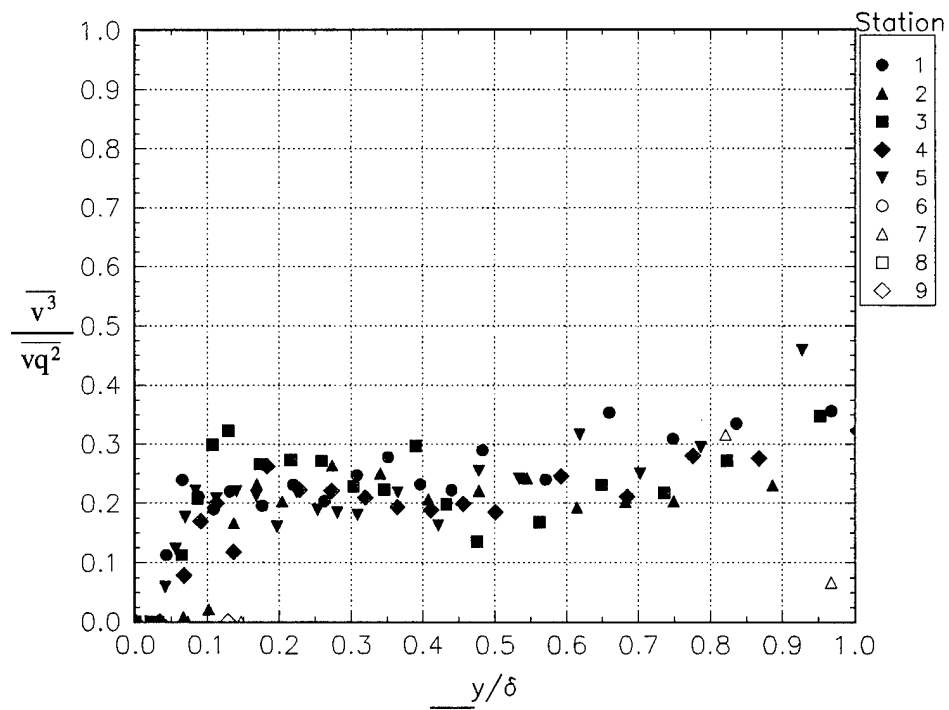


Figure 4.15b The normalized  $vq^2$  parameter for case BS1 of Driver.

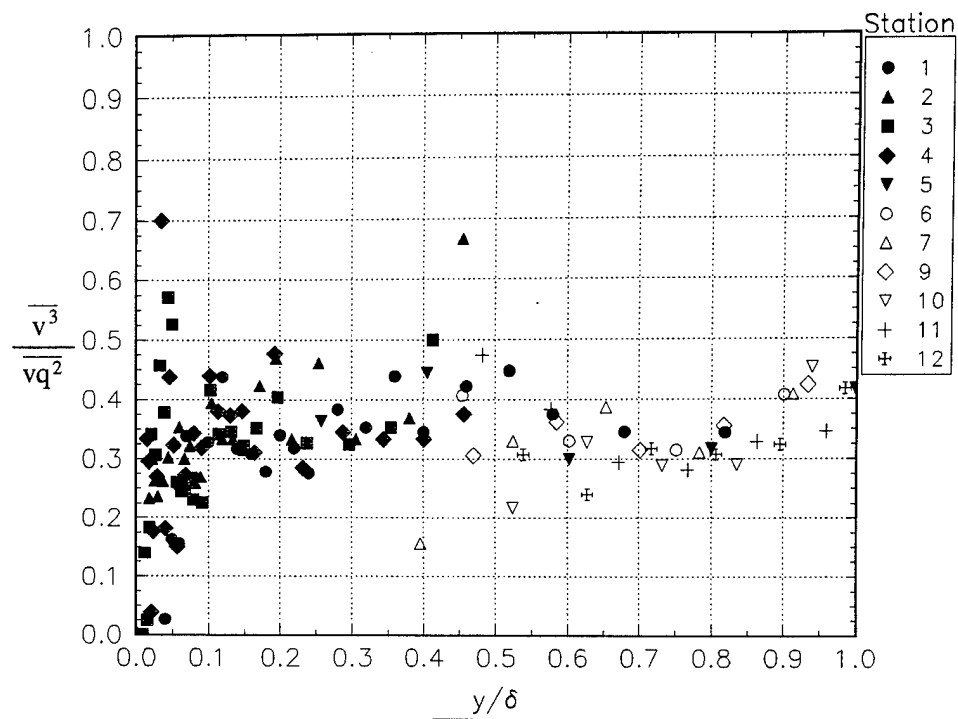


Figure 4.15c The normalized  $vq^2$  parameter for case CS0 of Driver.

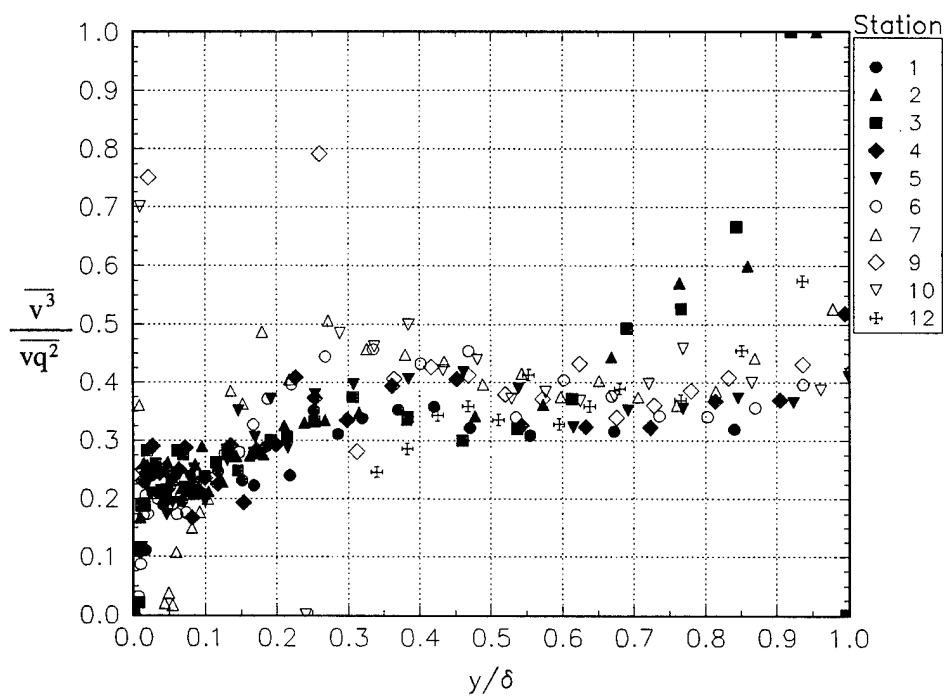


Figure 4.15d The normalized  $vq^2$  parameter for case CS1 of Driver.

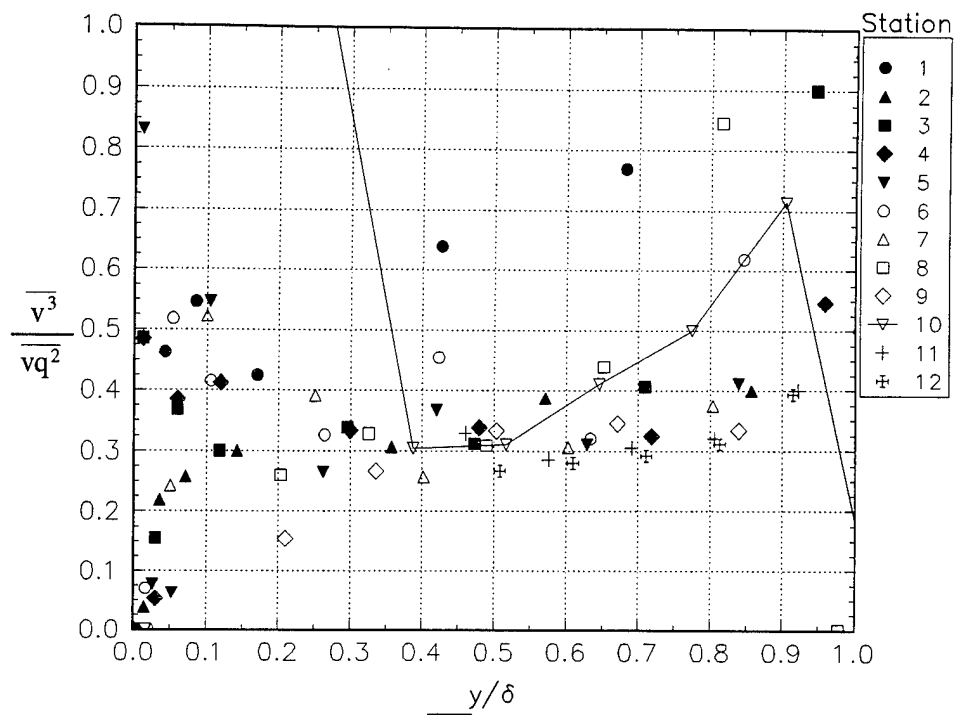


Figure 4.15e The normalized  $\overline{vq^2}$  parameter for case DS0 of Driver.

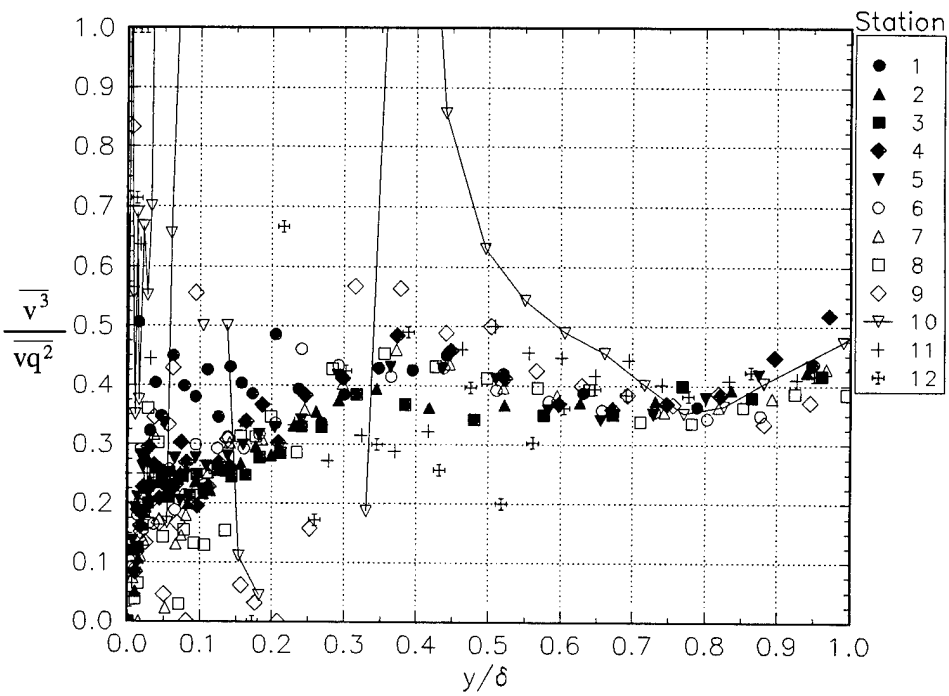


Figure 4.15f The normalized  $\overline{vq^2}$  parameter for case DS1 of Driver.

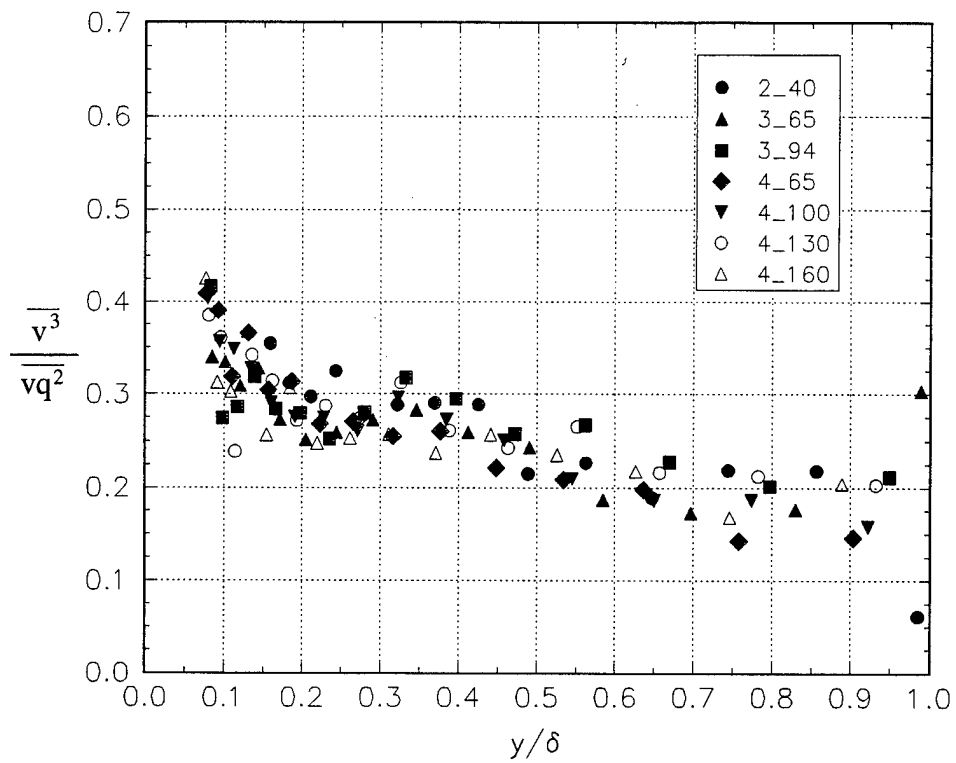


Figure 4.16 The normalized  $\overline{vq^2}$  parameter for the experiment of Littell. Stations are indicated by radius and Reynolds number ( $\times 10^4$ ). The number 2\_, 3\_, or 4\_ represent a radius of 0.235 m, 0.356 m, or 0.421 m respectively. *i.e.* Reynolds number designation \_100 implies 100e4 or 1,000,000 ...

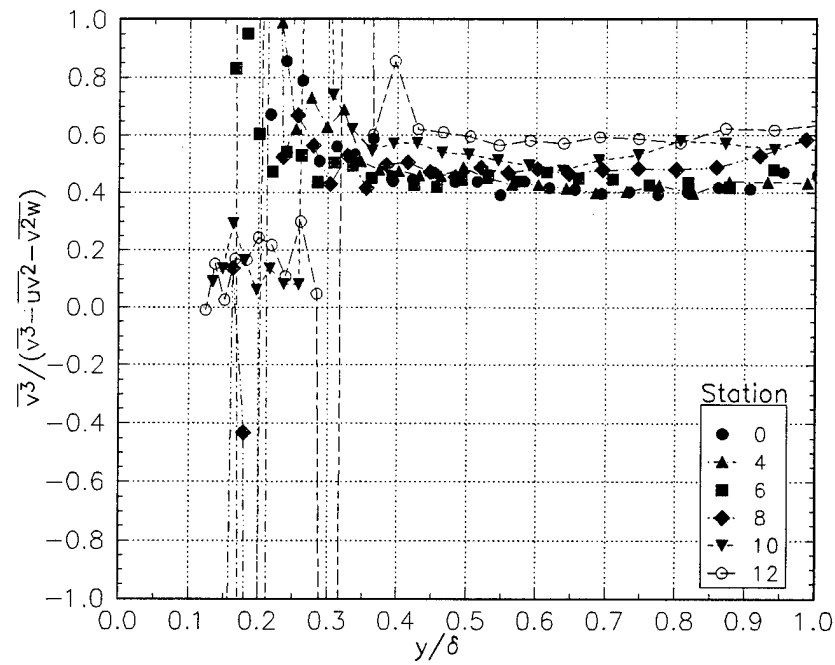


Figure 4.17a The crossflow development region of Schwarz.

Data are presented in free-stream coordinates.

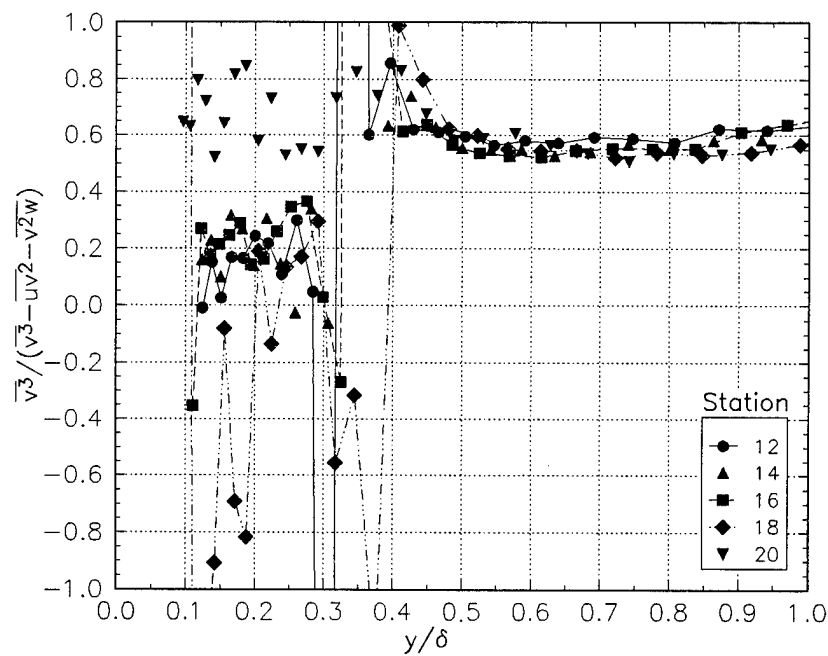


Figure 4.17b The crossflow decay region of Schwarz.

Data are presented in free-stream coordinates.

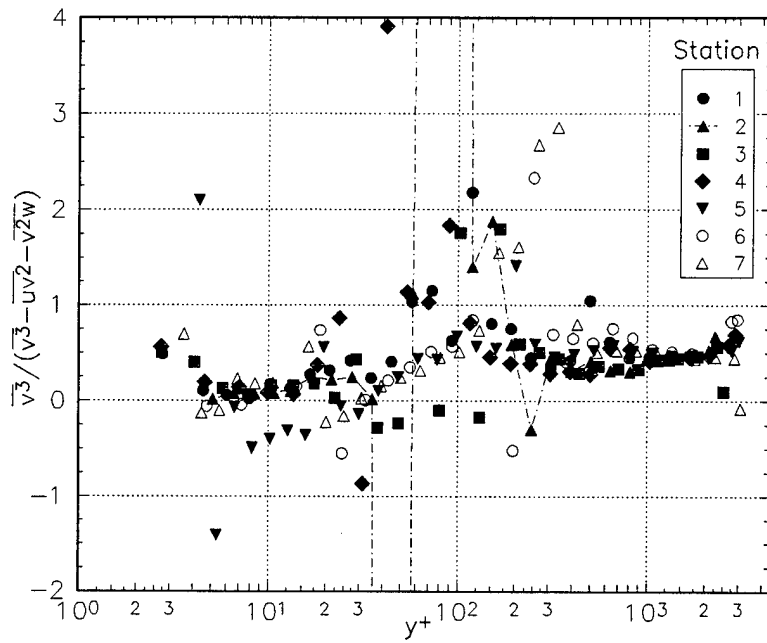


Figure 4.18a The wing-body junction flow of Ölçmen.

Data are presented in free-stream coordinates.

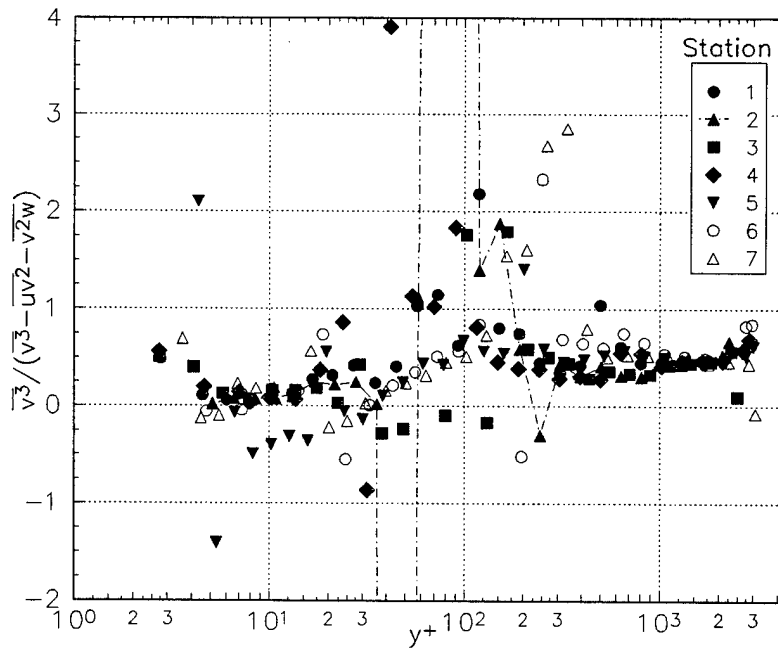


Figure 4.18b The wing-body junction flow of Ölçmen.

Data are presented in wall-stress coordinates.

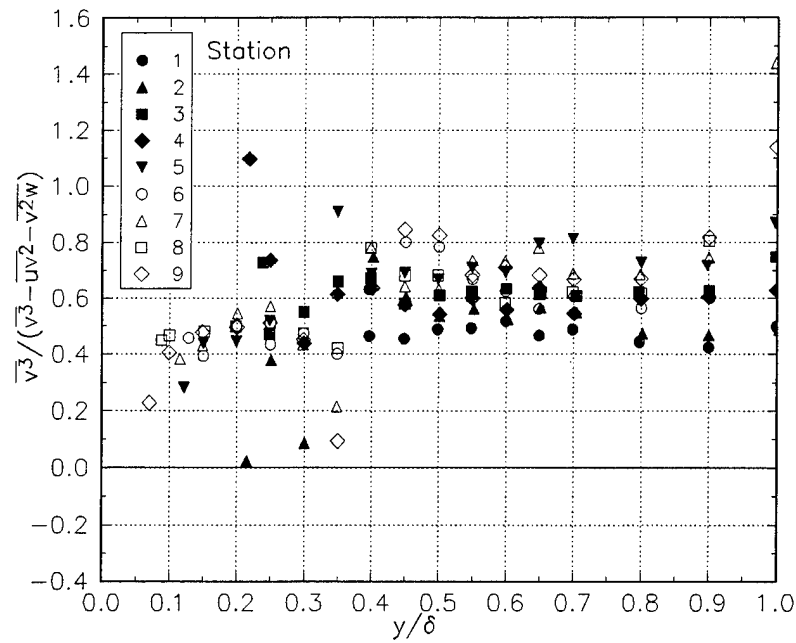


Figure 4.19a The concave curvature case of Baskaran.  
Data are presented in local free-stream coordinates.

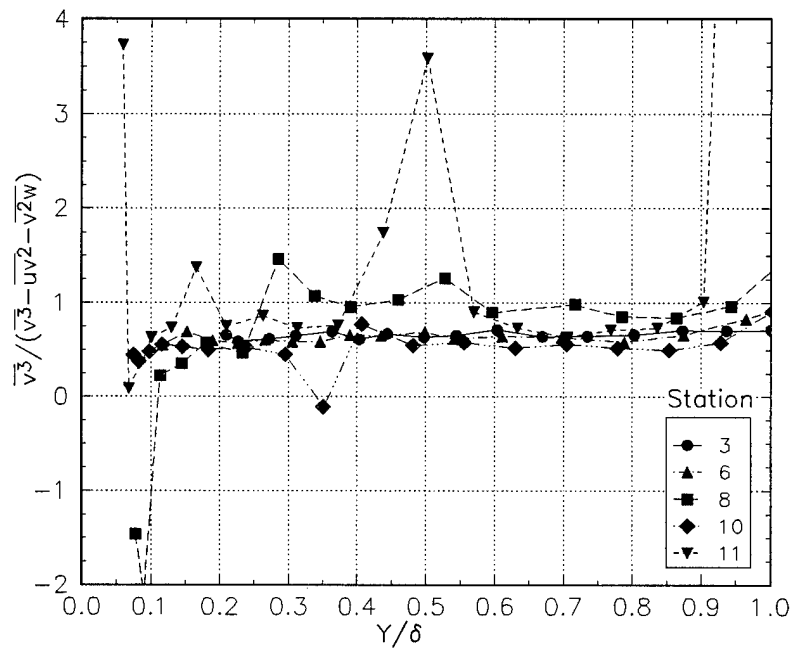


Figure 4.19b The convex curvature case of Baskaran.  
Data are presented in tunnel coordinates.

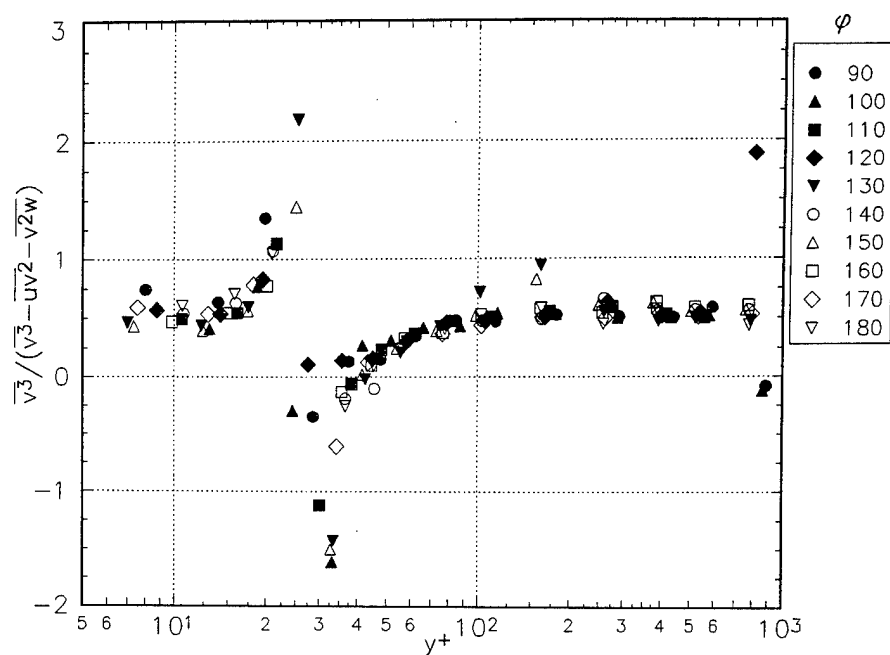


Figure 4.20a Data for the 6:1 prolate spheroid of Chesnakas  
for  $x/L = 0.4$  presented in local freestream coordinates

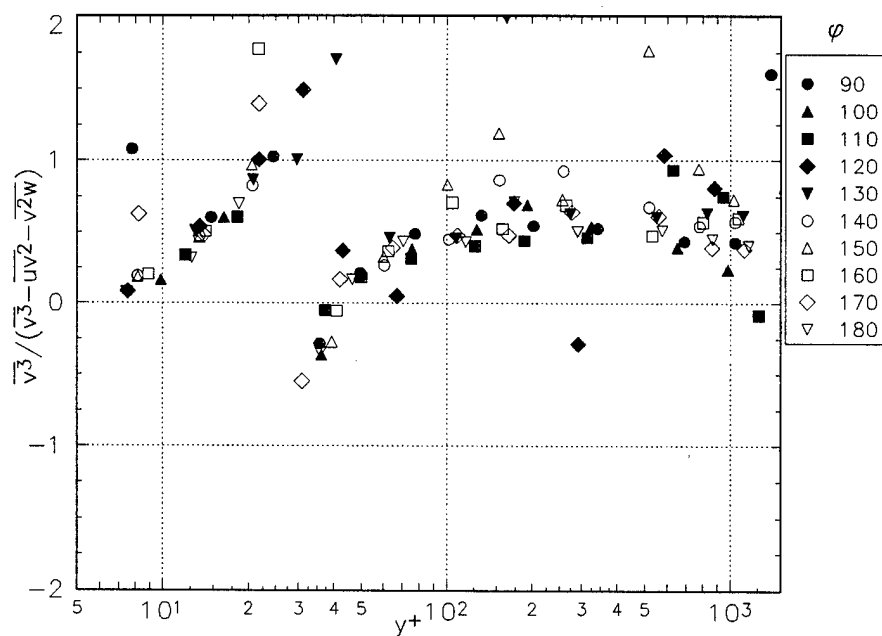


Figure 4.20b Data for the 6:1 prolate spheroid of Chesnakas  
for  $x/L = 0.6$  presented in local freestream coordinates



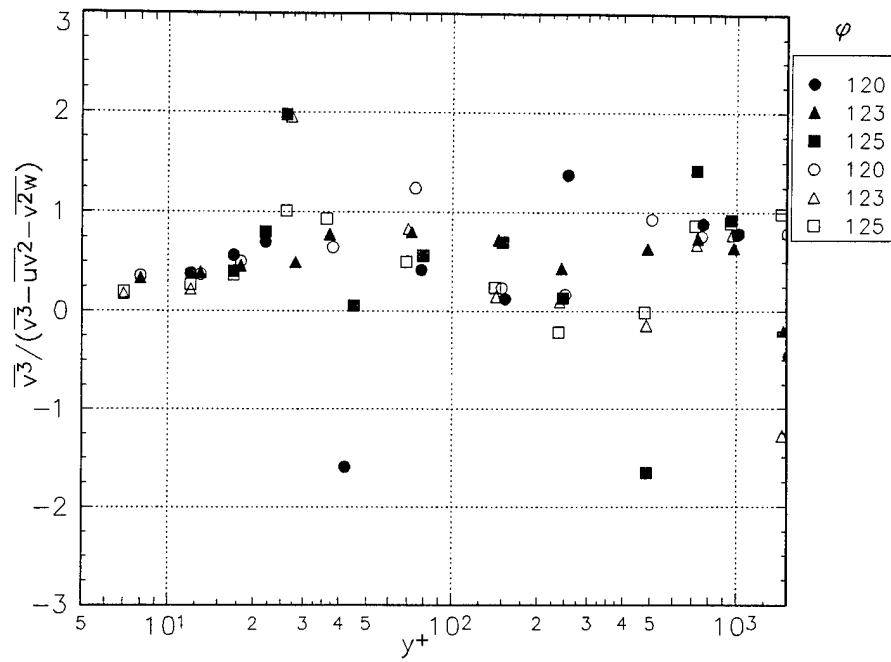


Figure 4.20c Data for the 6:1 prolate spheroid of Chesnakas presented in local freestream coordinates. Closed symbols are for  $x/L = 0.75$  and open symbols represent  $x/L = 0.76$ .

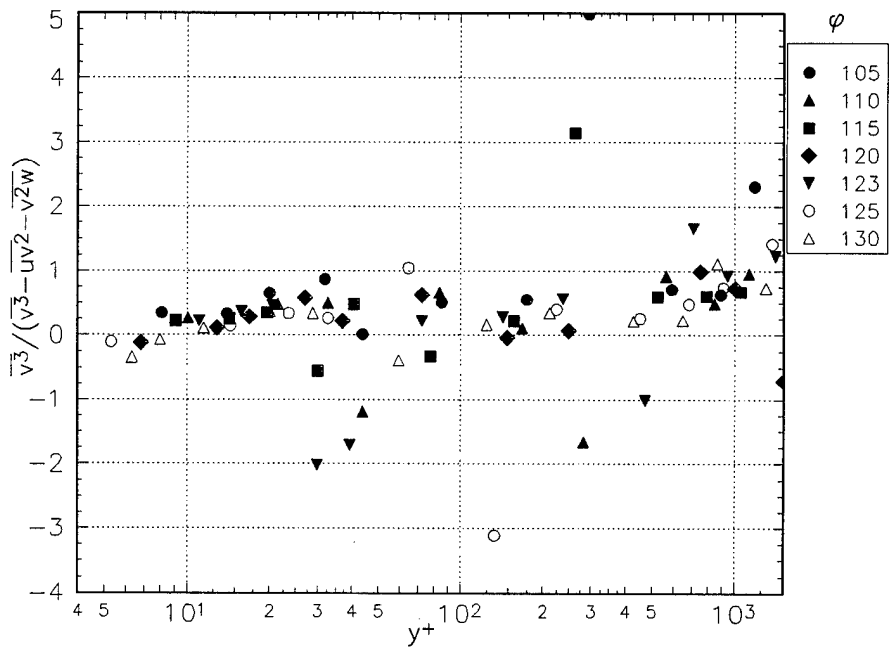


Figure 4.20d Data for the 6:1 prolate spheroid of Chesnakas for  $x/L = 0.77$  presented in local freestream coordinates

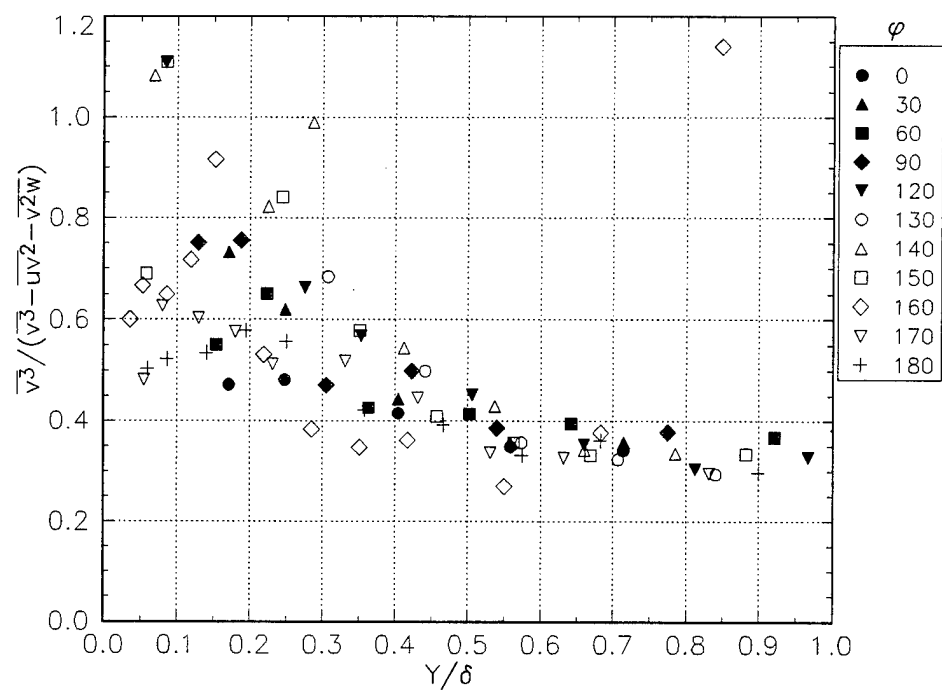


Figure 4.21a Data for the 6:1 prolate spheroid of Stäger at  $x/L = 0.4$  in tunnel coordinates.

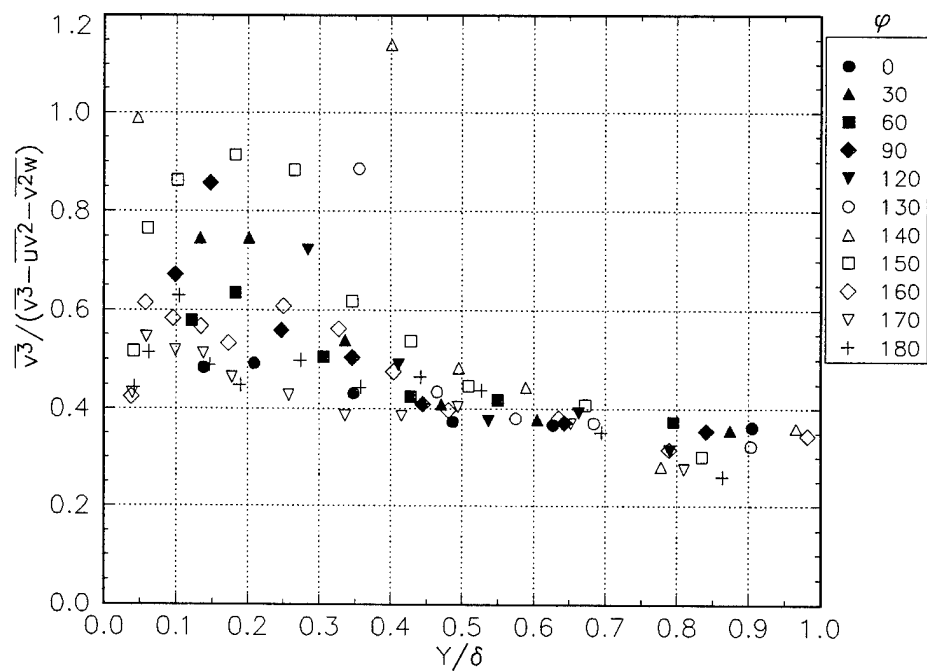


Figure 4.21b Data for the 6:1 prolate spheroid of Stäger at  $x/L = 0.56$  in tunnel coordinates.

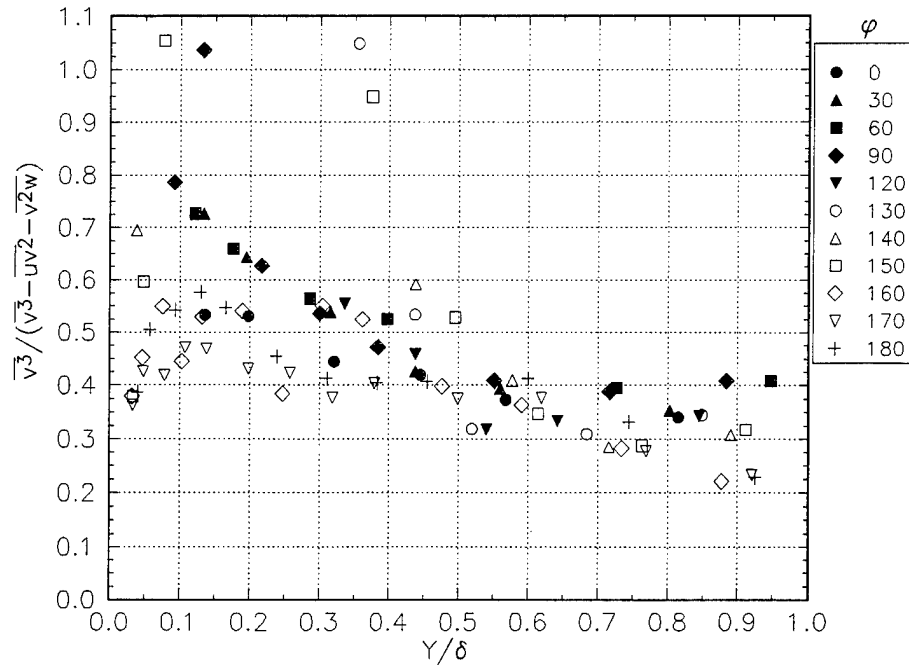


Figure 4.21c Data for the 6:1 prolate spheroid of Stäger at  $x/L = 0.64$  in tunnel coordinates.

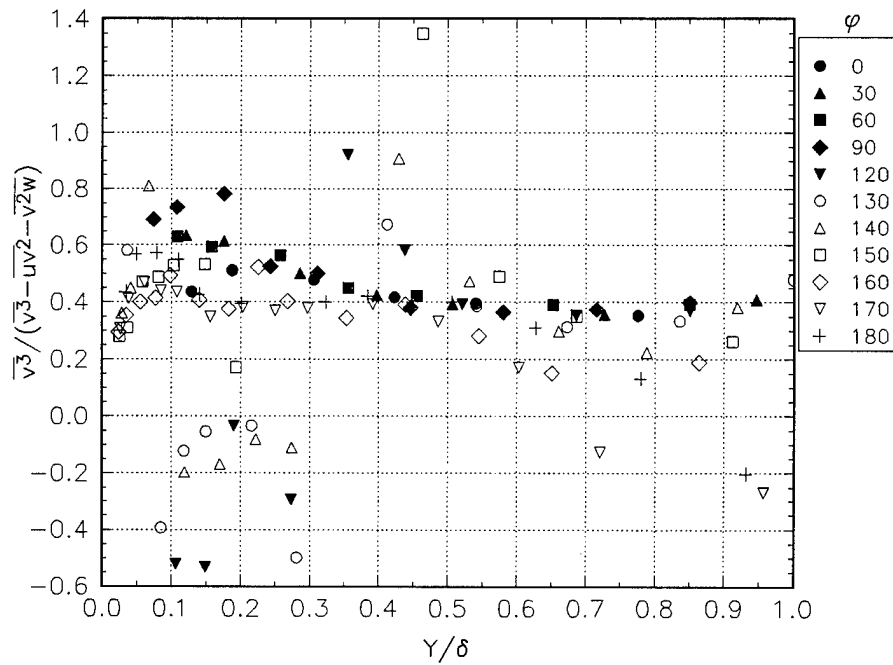


Figure 4.21d Data for the 6:1 prolate spheroid of Stäger at  $x/L = 0.73$  in tunnel coordinates.

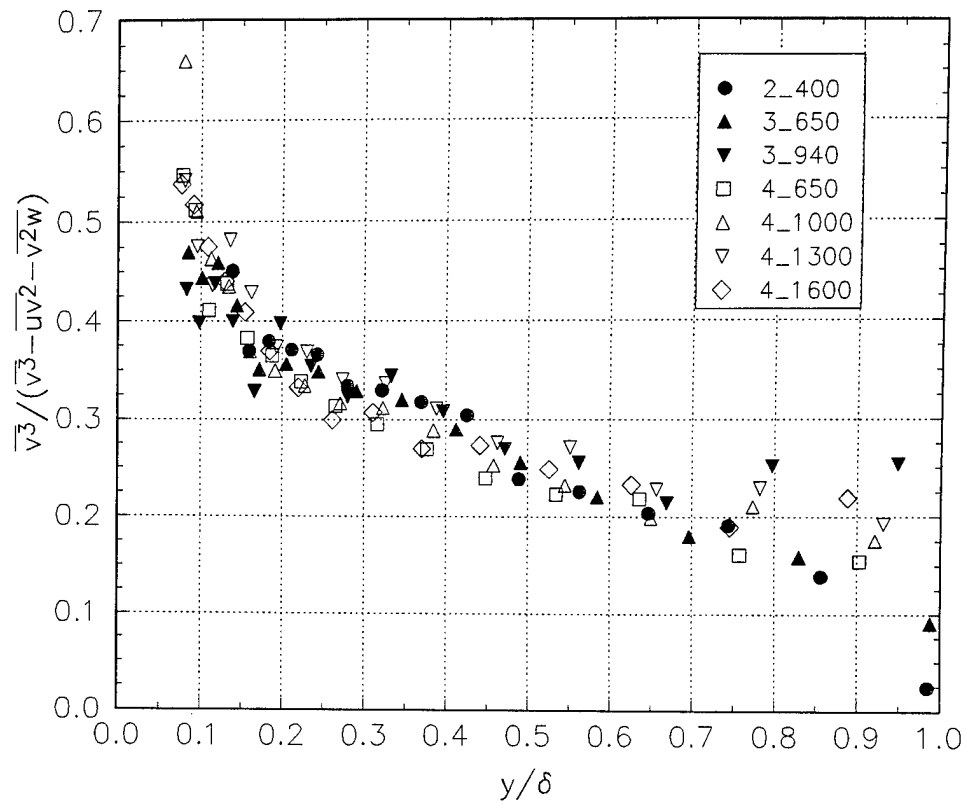


Figure 4.22 The shear induced experiment of Littell. Stations are indicated by radius and Reynolds number ( $\times 10^4$ ). The number 2\_, 3\_, or 4\_ represent a radius of 0.235 m, 0.356 m, or 0.421 m respectively. (i.e. Reynolds number designation \_100 implies  $100 \times 10^4$  or 1,000,000 ...)

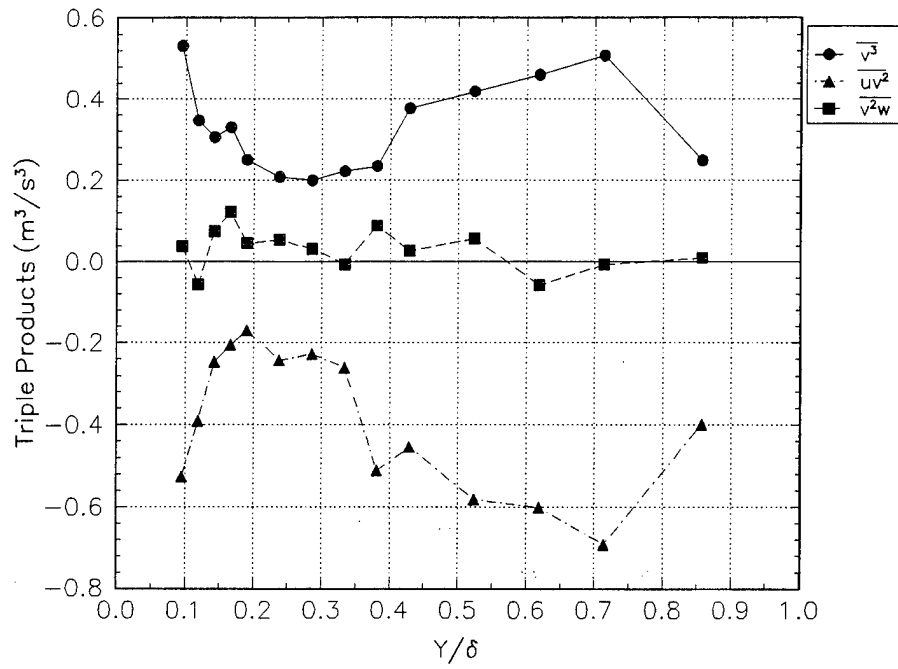


Figure 4.23a Some triple products in wall-stress coordinates from  $z = 100$  mm in the converging duct of Pompeo.

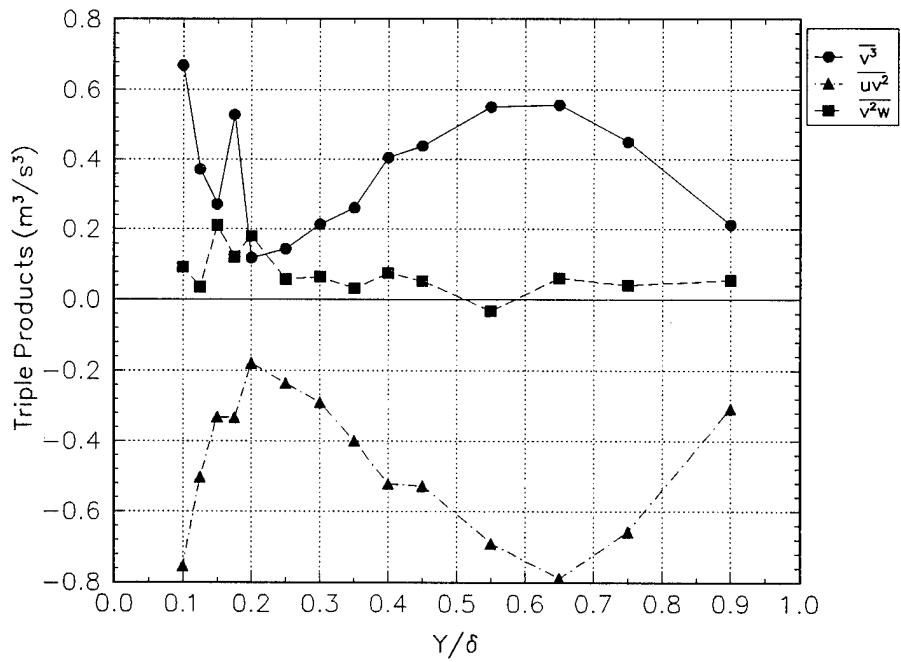


Figure 4.23b Some triple products in wall-stress coordinates from  $z = 200$  mm in the converging duct of Pompeo.

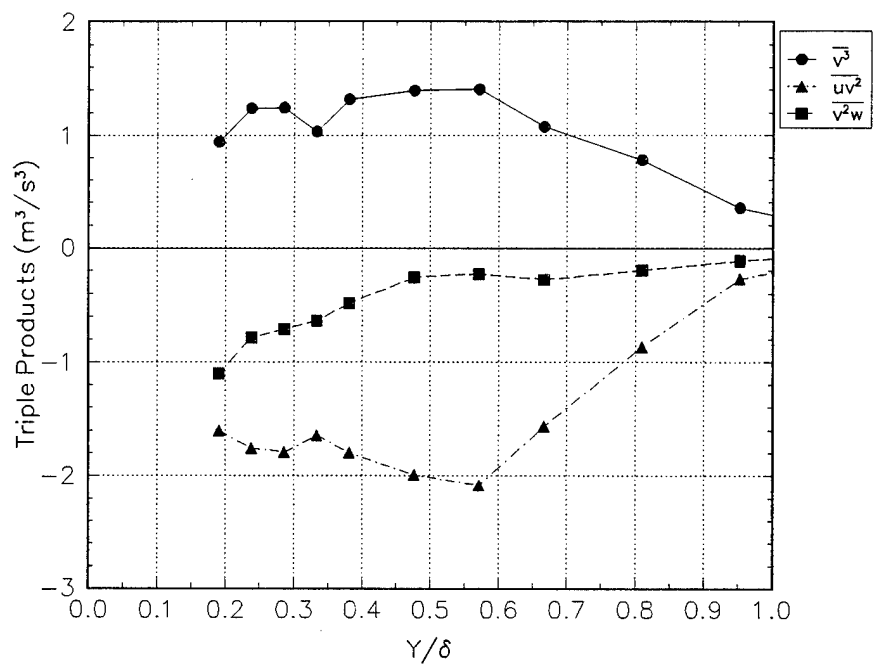


Figure 4.24a Some triple products in wall-stress coordinates from  $z = 100$  mm in the diverging duct of Pompeo.

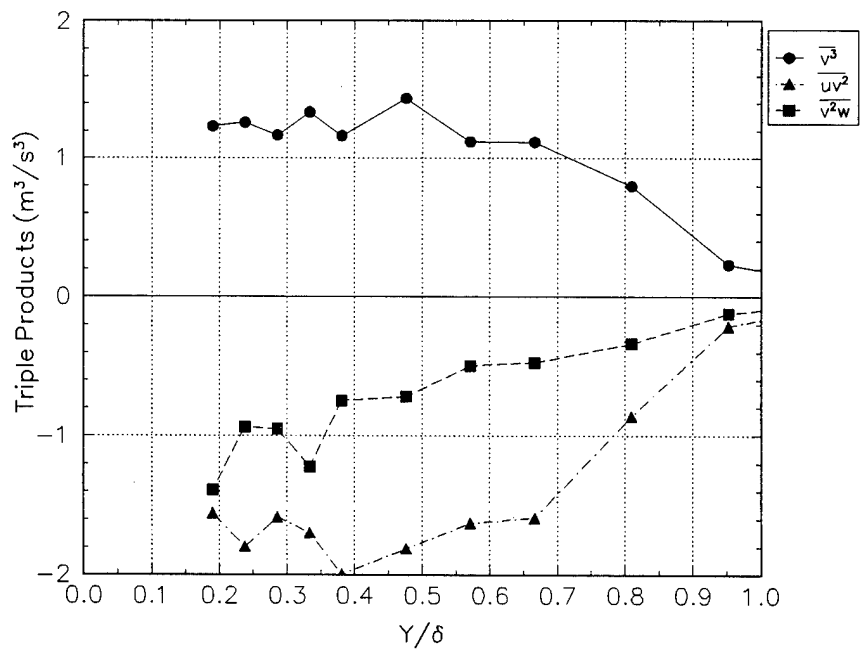


Figure 4.24a Some triple products in wall-stress coordinates from  $z = 200$  mm in the diverging duct of Pompeo.

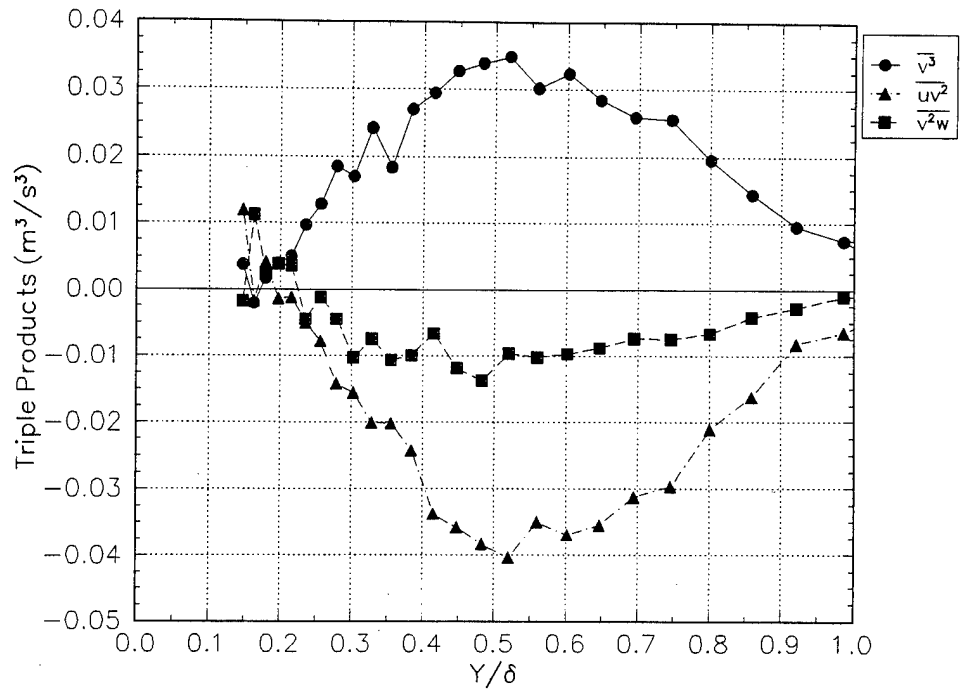


Figure 4.25a. Some triple products in wall-stress coordinates from station 8 of Schwarz.

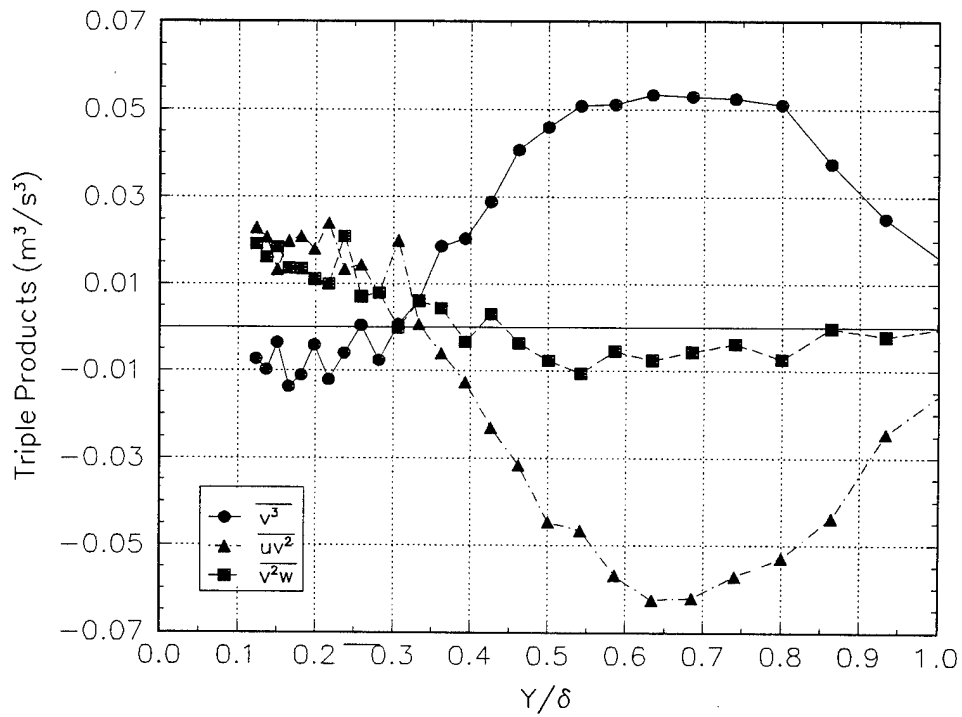


Figure 4.25b. Some triple products in wall-stress coordinates from station 14 of Schwarz.

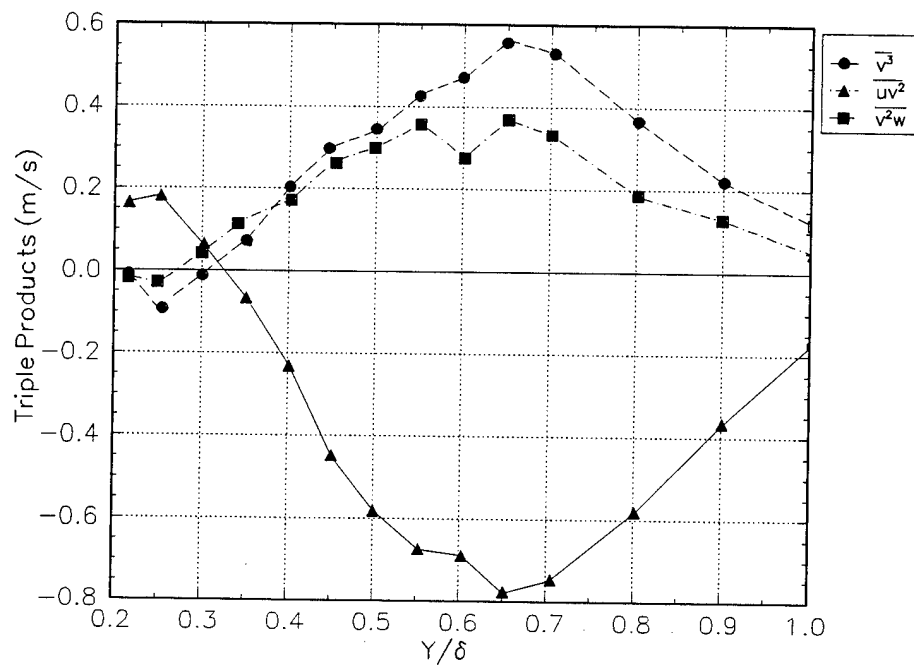


Figure 4.26a. Some triple products in local freestream coordinates from station 2 of the concave curvature duct of Baskaran.

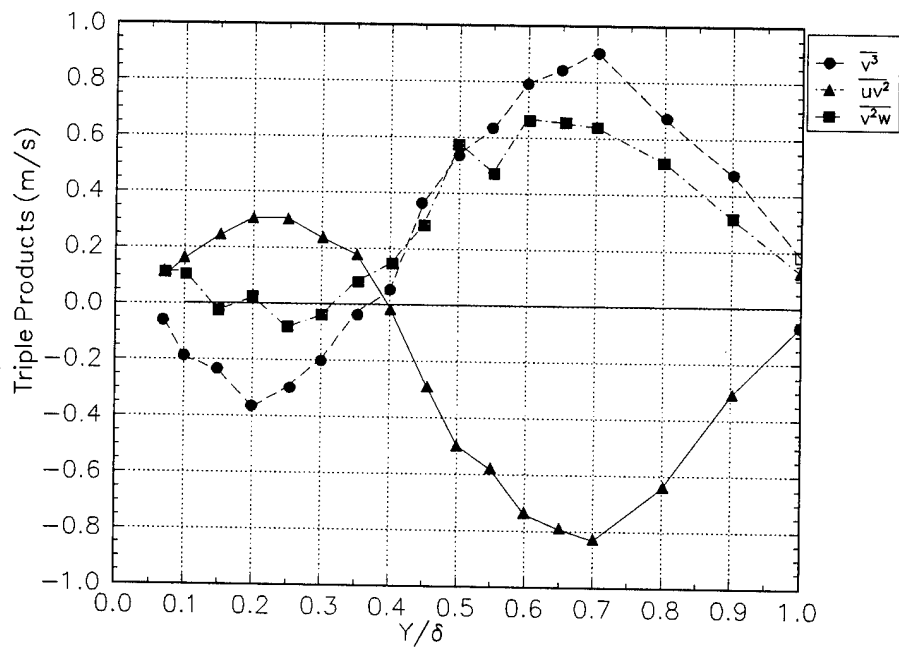


Figure 4.26b. Some triple products in local freestream coordinates from station 9 of the concave curvature duct of Baskaran.



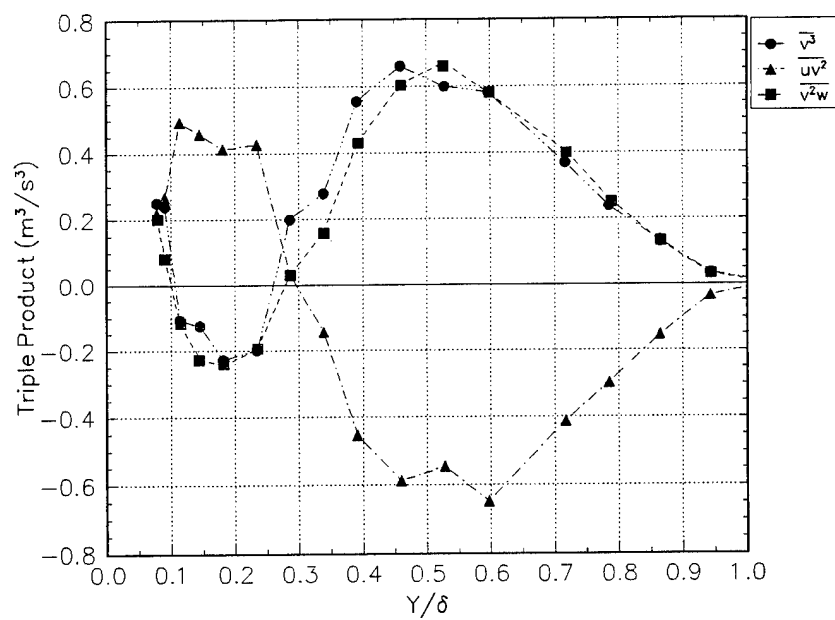


Figure 4.27 Some triple products in local freestream coordinates from station 8 of the convex curvature duct of Baskaran.

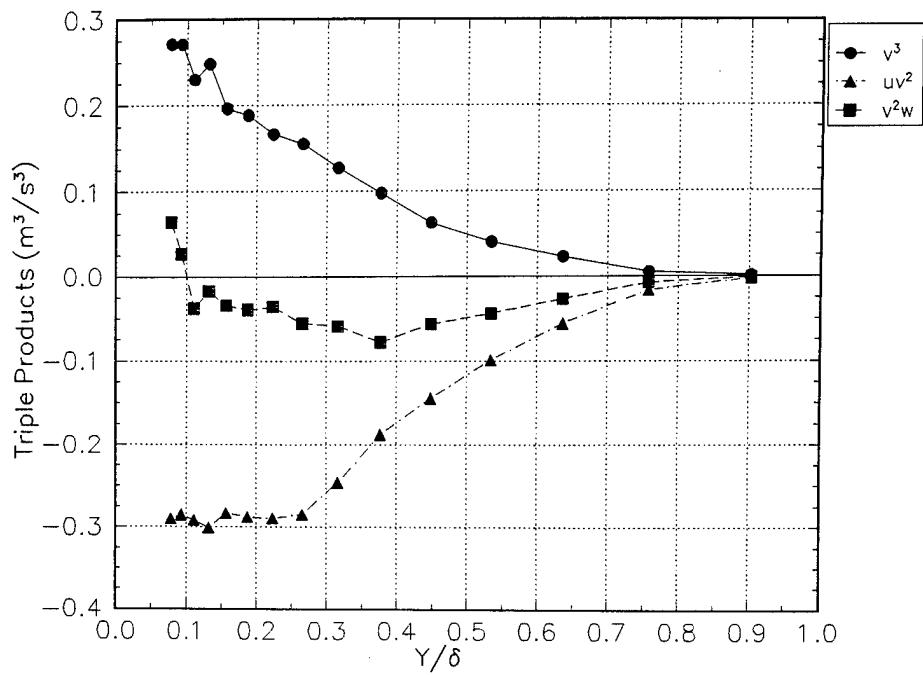


Figure 4.28. Some triple products from the spinning disk of Littell at a radius of 0.421 m and  $Re = 650,000$ .

## Chapter 5 Discussions and Conclusions

### 5.1 Overview

An extensive review of existing three-dimensional data sets and experiments was performed for the present study. Eleven data sets encompassing several different test geometries were examined in relation to algebraic turbulence modeling parameters. Several turbulence models employed in 3D TBLs are simple extensions of 2D TBL modeling concepts based on the existence of an isotropic eddy viscosity ratio. As discussed in Chapter 1 and Chapter 2, many experiments clearly illustrate that, in general, an isotropic eddy viscosity ratio does not exist. The magnitude of the eddy viscosity in the chosen x-direction,  $\nu_x$ , rarely equals the magnitude of  $\nu_z$ . Various parameters such as Rotta's T and the anisotropy parameter, N, illustrate the anisotropy of 3D TBLs. Analysis of the Reynolds stress angle and mean flow angle for individual data sets show that these quantities tend to lag (or lead, as in the convex flow case of Baskaran and Bradshaw, 1987) each other. Thus, if greater accuracy is desired, new modeling concepts are needed for fluid flows characterized by three-dimensionality to either augment or replace existing models.

A set of differential equations is required for a given calculation to account for the lags in the various quantities. In Chapter 1, a set of six equations (1.1-1.3 and 1.6-1.8) including the continuity equation, x and z-direction momentum equations, and the transport equations for the  $\overline{v^2}$ ,  $\overline{uv}$ , and  $\overline{vw}$  Reynolds stresses were suggested. To utilize these equations in a turbulence model, it is necessary to derive relations for the various terms or combinations of them. The focus of the present study is to develop algebraic turbulence modeling parameters for use with these six model equations. The present goal is not to develop a complete model, however some modeling issues will be discussed later to outline their expected use. Depending on the degree of accuracy desired, the isotropic eddy viscosity concept may work just fine (Johnston and Flack, 1996). The higher order modeling scheme suggested here is not suggested to completely replace eddy viscosity models but rather as an alternative modeling concept when greater accuracy is desired.

There are several desirable traits of turbulence modeling parameters. They must exhibit some form of predictable behavior. It is desirable for a modeling parameter to apply over a variety of flow geometries and conditions. It is desired that the parameter represent some aspect of the physics of the flow. Robinson (1991, 1992) outlined the coherent structures that are assumed responsible for the sweeps and ejections that produce the majority of the Reynolds stresses in a TBL. Littell and Eaton (1991) examined some two-point velocity correlations in an attempt to extend the concepts of Robinson to 3D TBLs. They concluded that the structures were basically the same but are modified by the crossflow to contain an asymmetry. These types of physical phenomena are integral to the development of the velocity field and to the transfer of energy from

the object in motion and should be represented in an empirical or semi-empirical turbulence parameter. These concepts will be explored further in the physical insight section. The designation of a coordinate system for a calculation or measurement is always an issue; it is desirable to use modeling parameters that are invariant to coordinate system choice. A parameter must correlate well from station to station or for the entire flow condition. If not, they must be predictable with the onset of modifications to the flow such as with increased adverse pressure gradient, lateral strain, lateral pressure gradient, crossflow modifications, or Reynolds number effects. Finally simple models help to reduce the number of calculations that are required for the numerical computation of flows containing a large number of grid points or complex geometries.

Parameters were examined in this study that exhibit many of the desired traits mentioned above. As seen in Chapter 3 and Chapter 4, some parameters are presented here that approximate a constant value across the outer part of the boundary layer or a portion thereof. This approximation to a constant value was not only from station to station in the respective flows, but a high degree of similarity existed in the value attained for each from experiment to experiment as well. Many are invariant to choice of coordinate system and are simply formulated. The parameters should aid the effort of modeling the dynamical nature of complex 3D TBLs.

## 5.2 Discussion of Coordinate System Choice

As mentioned previously, the choice of coordinate system for a measurement or calculation is important. The various choices of coordinate system can be explained as illustrated in Figure 1.1. The wall-stress coordinate system is oriented such that the x-axis is coincident with the direction of the shear stress vector at the wall. The local free-stream coordinate system has a x-axis aligned with the mean velocity vector at the boundary layer edge. And tunnel coordinate systems are designated by the individual experiments. The y-axis for all of the surface-bounded coordinate systems is normal to the wall and the z-axis is aligned to form a mutually orthogonal right-handed coordinate system.

The Reynolds stresses form a second order tensor and the turbulent triple products a third order tensor. A tensor rotation program was employed to rotate the data about the y-axis based on the respective angle between the coordinate system in which the data was presented and the desired coordinate system. Simpson (1995) indicates that a careful study of coordinate systems seems to indicate that several parameters are better correlated when observed in wall-stress coordinates. The parameters developed in this study, with a coordinate system dependency, were examined in local-free-stream and wall-stress coordinate systems where possible.

The parameters based solely on Reynolds stresses, and approximating a constant value or weak function of  $y$ , were in general less correlated than the  $S$  parameters for the experiments examined here. They appeared to exhibit a similar magnitude of scatter for either coordinate system that was investigated. Based on the results of this study, no coordinate system dependent ratios involving only Reynolds stresses are recommended for use in turbulence models. However the results generated for several parameters are included in the appendices for consideration by other parties.

The results for the triple product parameters illustrated an insignificant difference in the individual parameters. The difference in the  $B_1$  parameter was approximately 1% between the wall-stress and local free-stream coordinate systems. The normalized  $\nu TKE$  parameter exhibited a similar robust behavior between coordinate systems. The normalized triple product ratios, exhibited in the appendices, appeared to show differences in station to station correlation with coordinate system rotation. However the preference for coordinate system appeared to be specific to the ratio formed and no system could be designated as the better choice for the results presented in this study. The  $B_1$  parameter also exhibited values very similar to  $B_2$  but tended to have greater overall scatter and more points that differed greatly from its average behavior. Thus  $B_2$  is the  $B$  class parameter recommended for the use in turbulence modeling with the transport equations.

### 5.3 Discussion of Regions in the Flow

From experiments with data closer to the wall than  $y/\delta$  of 0.15 or  $y^+$  of 200, it appears that distinct regions of the 3D TBL appear. This observation is supported by the plots of the individual triple products of interest. Many of the parameters that were presented in this study maintained a fairly constant value across the outer part of the boundary layer, for  $y/\delta > 0.4$ . For 2D TBLs, this is the region where entrainment is prominent (see the discussion of the intermittency factor by Klebanoff, 1955) and large scale structures dominate the flow. In this outer region, the parameters generally scale better on outer variables.

Many of the data sets illustrated that with increased three-dimensionality (or possibly just downstream distance) that the region where a particular parameter approximated a constant progressed outward from the wall. This is seen most clearly by the individual plots of the triple products as pointed out in section 4.4 of Chapter 4. It is not clear what physical mechanism is causing this progression, but it does indicate the growth of a distinct region in the flow where the physics is changing. Speculation on the modification of the flow physics is presented later. This region marks the lower limit to the useful value of each parameter.

With the experiments of Driver, Chesnakas, and Ölçmen the near wall data appeared to illustrate other distinct regions of physical behavior as the wall was approached. The triple product plots for these experiments (section 4.4) were similar to the experiments that contained only outer layer data. They illustrated large values of the significant triple products in the outer layer which decreased and passed through zero near  $y/\delta = 0.4$ . These data sets also showed the behavior of the triple products nearer to the wall. The plots of the parameters scaled on wall variables appeared to illustrate regions of predictable behavior as they approached the wall. The region between  $100 < y^+ < 500$  is a region of scatter or low correlation of the parameters. For  $30 < y^+ < 100$  the parameters tend to become correlated again for all of the stations and within the various flows. Observation of the triple product plots shows that in this range of  $y$ ,  $\overline{uv^2}$  attains a significant value and exhibits more of a functional behavior rather than being scattered. Near  $y^+ \text{ of } 30$ , some parameters become less correlated again while others approach  $\pm\infty$ . Then nearest the wall the parameters appear to approach a new constant value. It should be noted that for the 2D cases nearest the wall,  $\overline{uv^2}$  again achieves a significant value while  $\overline{v^3}$  and  $\overline{v^2w}$  remain close to zero.

All of the points mentioned in this section seem to indicate several distinct regions in the 3D TBL that appear to be evolving with increasing downstream distance or three-dimensionality. The evolution of the regions appears to depend more on the growth of the boundary layer with downstream distance. Evidence for this exists in the experiments where the three-dimensionality is decaying (or turned off), such as the decay region of the Schwarz flow. For this region of this flow, the trend of the region where the parameter correlates well continues to progress away from the wall even though the crossflow is decaying. More experiments are needed to better determine these regions that are evident in 3D TBLs and the physical mechanisms that are generating them.

## 5.4 Physical Interpretations

An understanding of the physical processes that generate the observed behavior is greatly desired. However, this is a difficult task. The Reynolds averaging of the fluctuating velocities into statistical quantities is helpful for characterizing the flow, but this statistical view of turbulent flows tends to smooth over the details and events. Most of the experiments examined in this study generated single point statistics. These measurements of the flow tend to make any direct physical interpretation difficult. With a combination of experimental techniques and theory, a restricted view of the physics can however be inferred. A few such hypothesis will be presented here.

One of the first steps of understanding the physics beneath the statistics is to characterize the degree of three-dimensionality. This task is more difficult than it appears when all of the

different methods of generating three-dimensionality are considered. As mentioned previously, the application of a spanwise pressure gradient or spanwise surface shear are the two main methods of generation of crossflow. There are also other flows that deviate from 2D by the addition of additional rate of strains in the z-direction such as in the experiment of Pompeo (1992). One method of describing the three-dimensionality is to characterize the degree of crossflow as suggested by Driver and Johnston (1990). This involves indicating the angle difference between the flow in the free-stream and the flow at the wall for a given location. This is good way to characterize the three-dimensionality but it does not account for flows where a pressure gradient reversal may have occurred and the total angle across the boundary layer will not reveal the pressure gradient distribution across the boundary layer as compared to a mildly skewed boundary layer. This characterization also fails to correlate the 3D effects imposed on algebraic modeling parameters as illustrated by Johnston (1996). Another means to characterize the three-dimensionality of a flow may be to employ the streamwise and spanwise pressure gradients to compare flow characteristics. Reynolds numbers based on momentum thickness have also been used.

A ratio of Reynolds averaged products such as  $\overline{v^2 w}$  to  $\overline{uv^2}$  or  $\overline{vw}$  to  $\overline{uv}$  may be useful in characterizing the degree of three-dimensionality. Upon observing the  $\overline{v^2 w}$  and  $\overline{uv^2}$  triple products for the varying flow geometries used in this study, one would arrive at the conclusion that such a ratio is probably useless. The  $\overline{v^2 w}$  triple product tends to change little for each flow, that is if it is small upstream, it tends to be small downstream for the rest of the flow or onset of three-dimensionality. It was typically small, but can attain large values as observed in the experiment of Baskaran and Bradshaw (1987) and the diverging duct flow of Pompeo (1992). Meanwhile the  $\overline{uv^2}$  triple product tends to change with downstream location. Considering these observations, it can be concluded that their ratio would not be an effective measure of three-dimensionality. It would decrease with downstream stations but does not seem to increase with greater crossflow. Similarly, as can be seen in Appendix C for the additional figures for Schwarz and Bradshaw (1993), the simple ratio of  $\overline{vw}$  to  $\overline{uv}$  does not change predictably with increased three-dimensionality. One observation from this experiment though is that some sort of deviation or correlation parameter across the boundary layer for this ratio may be an indicator of flow three-dimensionality. But this correlation parameter concept was not explored here and no conclusion can be made about the speculated effectiveness. The development of a parameter or set of parameters that can accurately describe the modification to the flow physics as a TBL progresses from 2D to 3D may be able to correlate existing parameters, such as  $a_1$ , and model the enhanced physics.

As was noted above and in the discussion of the parameters in Chapter 3 and Chapter 4, there tends to be a region of constant behavior for the parameters investigated in the outer part of

the boundary layer. This corresponds roughly to  $y/\delta > 0.4$ . The Reynolds stress parameters begin to decrease near  $y/\delta$  of 0.8 while the triple product parameters tend to maintain their correlation through the edge of the boundary layer. Investigation of the individual triple products illustrate that in this region the triple products maintain significant values compared to nearer the wall. The investigation of Chapter 4 also illustrated that a combination of the triple products applied more universally to a number of flow geometries. Near  $y/\delta$  of 0.4 the triple products decrease in magnitude and pass through zero (this location is not unique, in fact it tends to be the outer limit for the experiments examined). This was discovered to not be an effect of the increasing uncertainty of the hot-wire anemometer measurements as similar behavior is observed for the LDV measurements. The region where this decrease is observed tends to progress outward from the wall with downstream distance. There appears to be a slight increase of this zero crossing point with increased three-dimensionality. As the  $y$  variable was non-dimensionalized on the boundary layer thickness, this region did not simply grow in direct proportion with downstream boundary layer growth. The near-wall region developed (progressed outward) faster than the boundary layer growth.

The region above  $y/\delta = 0.4$  for 2D TBLs is where large structures dominate the flow characteristics. They are entraining the free-stream fluid, with greater velocity and energy, and imparting vorticity to it through the viscous interaction of the shear stresses. Evidence for these 2D observations exist in the discussion of the intermittency in the work of Klebanoff (1955) and in various flow visualization experiments such as illustrated on the cover page of this report. The application of a wall shear force or spanwise pressure gradient has a greater effect on the near wall fluid. This fluid is moving slower and therefore exposed to the tangential force for a greater amount of time. While the near wall fluid is turned, as seen by the flow angles, across a 3D TBL, the outer layer fluid is convected further in the original direction. Thus the flow at a given point originates from different upstream spanwise locations. The fluid convects with it a history of the upstream structures and their effects on the turbulence. The extent and dynamics of free-stream fluid entrainment is probably modified for 3D TBLs. There are no experimental studies that focus on this modification so no direct conclusions of this suspect variation can be drawn. The applied three-dimensionality may cause the large structures, as seen in the photo on the cover page, to roll over and engulf free-stream fluid in an asymmetric manner. Any modifications to events in the outer layer will tend to have less of an effect on the inner layer fluid at a point as the outer layer structures are convected downstream faster than the near wall fluid. With this reasoning, the near wall fluid at a point is effected even more by the upstream outer layer structure as it folds and mixes with the nearer wall fluid.

The region where the parameters presented in this report exhibit good behavior is believed to coincide with this outer layer region of entrained high energy fluid. The velocity fluctuations



decrease as the free-stream is approached. Their respective rates of decrease may differ. Thus, coupled with the small values and experimental uncertainties, it seems that the probability for existence of an algebraic ratio near the free-stream is low. The Reynolds stress ratios appear to decline from their constant approximation near  $y/\delta = 0.7 - 0.8$ . After Klebanoff (1955) the mean location of the turbulent non-turbulent interface is at  $y/\delta = 0.78$  for a smooth 2D TBL and  $y/\delta = 0.82$  for a rough 2D TBL (Rotta, 1962). This mean location of the turbulent interface has not been detailed by any experimental research but is suspected to coincide with the region where the Reynolds stress parameters presented in this report begin to decline. It appears that some of the triple product ratios presented here maintain their correlation as they approach the free-stream and its level of turbulence intensity. The upstream history of the outer layer flow seems to be expressed in this outer region as illustrated in the good outer layer correlation of the algebraic parameters presented in this report.

The observed region where the individual triple products approach zero near the wall appears as a distinct boundary where the outer and inner flows meet. If this is the case, then the interface where the histories of the flows mix is marked by a decrease in mean velocity fluctuations. This may mean an actual decrease in the velocity fluctuations, which seems unlikely with regard to the presumed degree of small scale structure at that location in the TBL, or that a symmetry of fluctuations is attained at that location (similar to the fact that in 2D TBLs a w fluctuating velocity exists but is averaged out due to symmetry). The location of this interface may be discovered to be an important length scale for 3D TBLs that is not present in 2D TBLs. However more research is needed to ascertain the nature of the physics of this region of the TBL.

Robinson (1991, 1992) compiled the most accepted description of the coherent vortical structures in the various regions of a 2D TBL. The inner region is dominated by quasi-streamwise vortical structures that are spaced laterally at  $z^+ = 100$ , with a typical length of 1000 viscous units and a minimum diameter of 12 viscous units. Streaks observed in flow visualization experiments in the wall layer are evidence that these vortices have passed. If a quasi-streamwise vortical structure becomes tilted, it can produce sweeps or ejections of fluid. These downward sweeping events and outward ejection events are hypothesized to be the major source of Reynolds stress production. Evidence for these events can be seen through the quadrant analysis of Wilmarth and Lu (1972). This region of the flow is assumed to produce the majority of the Reynolds stresses in the TBL. From this region, the Reynolds stresses are convected to other parts of the flow. The pressure rate-of-strain terms also tend to redistribute the Reynolds stresses and turbulent kinetic energy (TKE). In the conceptual model outlined by Robinson (1991, 1992), the outer layer flow is dominated by large arch shaped vortical structures that are responsible for the bulges of turbulent fluid that extend towards the free-stream. Sweeps and ejections occur for different parts of this symmetrical structure. Arches with one trailing leg shorter can occur as well, but the overall

resulting sweeps and ejections occur in a symmetrical manner according to the definition of a 2D TBL.

Few studies have been performed to describe the modifications of the coherent vortical structure model when a flow becomes three-dimensional. Some observations can be outlined that may illuminate the issues facing parameters formed for 3D TBLs. Fleming and Simpson (1994) performed an experimental study that illustrated that the spanwise streak spacing decreased for 3D TBLs from 100 viscous wall units to 85-100 viscous wall units. This decrease in streak spacing was observed by Flack and Johnston (1995) as well. Fleming and Simpson (1994) also discovered a reduction in the oscillation of streaks for 3D sections of the wall-layer. The streaks in the 3D section tended to remain aligned better with the flow. It has been reported that a reduction in the number of sweep and ejection events occurs for increased three-dimensionality (Eaton, 1995). Ha and Simpson (1993) showed that the length scales of the low frequency structures decreased with increased three-dimensionality. Their study indicated that the quasi-streamwise vortical structures tended to be skewed in a direction between the shear stress vector and the mean velocity vector and were convected in this direction. Littell and Eaton (1991) performed two-point velocity correlations on the disk flow to educe the nature of the coherent structures in their experiment. They concluded that symmetric structures do not exist in 3D TBLs. Rather the head section and a tail on only one side comprised a vortical structure in the outer layer. The position relative to the crossflow direction and head tended to determine whether the event produced was a sweep or an ejection. They too concluded that sweep and ejection events are fewer for 3D TBLs.

Effects of the coherent structures are suspected to influence the various regions of 3D TBLs that were outlined earlier in section 5.3. The overlap region mentioned in the discussion of the outer layer above tends to occur at the outer part of the log-law region of the TBL. Some of the hot-wire anemometer and LDV experiments that reach into the wall-layer appear to show evidence for regions of organized motions that produce significant values of the triple products. This recovery of the triple products near the wall, and coincidentally the associated parameter hints at the flow structure in these regions ( $30 < y^+ < 100$ ) becoming more organized and efficient at the production of coherent velocity fluctuations. The region between  $100 < y^+ < 500$  is characterized by scatter and is the overlap region of the outer and inner flow. The structures here are assumed to be less coherent and be less efficient at producing velocity fluctuations. It may be that this mixing layer of the convected upstream structures and the locally produced near-wall turbulence is dominated by small scale turbulence approaching the scales necessary for local isotropy. Locally isotropic turbulence would show no preference for direction and hence the three-dimensionality would fade for this region. The outer flow is being convected downstream faster than the near wall-fluid while the more viscous inner region is being turned (by the applied wall shear and/or pressure gradients) and extracting energy from the outer flow. One hypothesis may be that the

skewing of near-wall structures and interaction with the outer layer fluid causes the inner-layer vortical structures to release their turbulent kinetic energy before they are able to develop to the strength that they may have achieved for a 2D TBL. This would tend to produce weaker sweep and ejection events with smaller time scales. Evidence for this exists in the comments on the Littell and Eaton (1991) flow above where the number of events are reduced and in the results of Ha and Simpson (1993) where the structures were shown to be skewed from the mean velocity vector. The hypothesis of Eaton (1995) can also be explained by structures with a shorter lifetime. Instead of the traced fluid element passing through the center of the vortex with low vertical velocity, the structure dissipates and the significant force on the element is the inertial force of the crossflow in the lateral direction. This is not exactly true as we are comparing a mean quantity with a short lived coherent structure, but it can serve as a model to a greater understanding of the physical processes that affect a 3D TBL. The results from the DNS study of Senstad and Moin (1992) also seem to support this model. Their results indicated that the modification of three-dimensionality causes the fluid of an ejection to originate at a location farther from the wall which causes a smaller velocity difference. This could indicate that the vortical structure responsible for the ejection had a shorter life time than in a similar 2D TBL. Again it must be stated that little direct evidence exists and the concepts presented here are merely hypotheses to be explored in further research.

As the sweeps and ejections are hypothesized to be the major contributor to the production of Reynolds stresses, it is obvious that the fluctuating  $v$  velocity is an important modeling parameter to capture the physics of the flow. Examination of the parameters presented in this study may hint at some trends in the physics of the TBL. For instance, consider the  $B_2$  parameter. The denominator is positive definite. Therefore when  $B_2$  exhibits behavior that is negative, it indicates that the mean motion of the  $v$  fluctuating velocity is skewed negatively. This occurs in the data sets of Schwarz, Ölçmen, Baskaran, Chesnakas, and Driver. The negative regions tend to be near the wall and further downstream. Along this reasoning, one would suspect that ejections were dominant in these regions of the flow. Other evidence of this were not sought for the present study but are being included in a journal paper to be submitted to *Physics of Fluids*. Evidence of the enhanced physics of 3D TBLs along the lines of this study are to be presented there as well.

## 5.5 Modeling Issues

The focus of the present study was not to present a new complete turbulence model, nor was it to outline a complete modeling scheme. The main focus was to generate useful relationships between the triple product and Reynolds stresses that were deemed useful to future modeling

efforts. However a brief discussion will be included here to suggest how the information presented in this report may be of use in a model.

The first point that needs clarification is that the parameters presented here are not suggested to replace existing modeling concepts, rather to compliment and to augment them. The regions in which these parameters are correlated tend to correlate quite well. In these regions, they typically approximate a constant value. Such parameters are highly desired for simple turbulence modeling efforts. However they do not present a universally constant function of  $y$ . There are slight variations from flow to flow that are discernible yet the trends fall within the experimental uncertainties such that the assumption of similar behavior for a number of 3D TBL flows would generate little uncertainty. Care must be taken if they are to be used to apply them to the proper region of the boundary layer.

Examination of equations 1.1-1.3 and 1.6-1.8 demonstrate the requirements of a turbulence model that employs this recommended set of equations. The independent variables are the  $x$ ,  $y$ , and  $z$  spatial coordinates. The dependent variables are  $U$ ,  $V$ ,  $W$ ,  $-\overline{vw}$ ,  $-\overline{uv}$ ,  $\overline{v^2}$ ,  $\overline{v^3}$ ,  $\overline{uv^2}$ ,  $\overline{v^2w}$ , and four pressure rate-of-strain terms. The flows to be modeled are incompressible so the density,  $\rho$ , and kinematic viscosity,  $\nu$ , would be constant and obtained from upstream conditions. The mean static pressure,  $P$ , is not a function of  $y$  and can be computed from an inviscid calculation of the flow away from the boundary layer. Without considering the pressure rate-of-strain terms, there are nine variables for six equations.

To close a model, three relationships are required between the dependent variables. The  $S$  parameter relates  $\overline{v^2}$  to  $-\overline{vw}$  and  $-\overline{uv}$ . The  $B_2$  parameter and equation 4.4 can be used to relate the triple products to each other and would produce nine relationships for nine variables. There seem to be a few problems with this. The relationships for the same three triple products can be manipulated into a form that appears similar. This may imply that there is a degenerative case for the parameters presented and it may not be wise to use more than one of the relationships. With this reasoning, another relationship would be required such as the skewness of the  $v$  fluctuating velocity. It is obvious that models for the pressure rate-of-strain terms must be developed as well.

For greater accuracy, other relationships must be generated for a calculation for the region of  $y^+ < 100$ . The parameters presented here appear to apply well for  $y/\delta > 0.4$ . In light of the lack of experimental data close to the wall, a need for more experiments detailing this region is illustrated. Experiments in the near-wall region would also serve to enhance the general understanding of the physical processes that are modifying 3D TBLs.

## 5.6 Conclusions

Parameters were developed to aid in the modeling of 3D TBLs. The  $S = \overline{v^2} / \tau / \rho$  parameter correlates fairly well from station to station within a flow and between experiments. The ratio  $1/S$  approximates a constant for  $0.3-0.4 < y/\delta < 0.7-0.8$  ranging from values of 0.5-0.8 with an overall average of approximately 0.7. At  $y/\delta=1.0$ ,  $1/S$  appears to have a mean value, for the data presented, of approximately 0.3. The parameter appears to be mildly affected by different 3D effects, however the effects were of the order of the uncertainty in the experiments. Such effects include a noticeable decrease in the crossflow decay region of the Schwarz experiment, a slight rise at the aft end of the models of Stäger and Chesnakas, and a lower value in the decay region of Driver. It did however maintain consistent values for the Baskaran experiments and the experiment of Littell. All of the other parameters investigated for the experiment of Littell had completely different behavior from the other 3D experiments, only  $1/S$  exhibited behavior consistent with all of the other 3D TBLs. The experiments in the horseshoe vortex region of the wing-body junction failed to produce good behavior of the  $1/S$  parameter. This is surmised to result from the significant wall-normal component of velocity and fluctuating velocity. It should be mentioned that the square root of the ratio of  $\overline{v^2}$  to  $\overline{u^2}$  was well correlated and seemed to exhibit predictable behavior between flows. It was not however a constant value but a function of  $y/\delta$ .

The algebraic parameters describing the turbulent triple products were less sensitive to three-dimensional effects than  $1/S$ . They also maintained a constant value for the outer part of the 3D TBL. The  $B_2$  parameter is invariant to coordinate system. This parameter tends to approximate a constant value of  $0.85 \pm 0.15$  for  $0.3 \leq y/\delta \leq 0.7-1.0$ . The values for each station are a very good approximation to a constant in this region for the experiments examined here. There are other regions of predictable behavior of  $B_2$  that were discussed in section 5.3.

The normalized  $\overline{vq^2}$  parameter introduced in Chapter 4 maintains better correlation across the TBL and from experiment to experiment than the  $B_2$  parameter. It maintains a value of 0.3-0.4 for  $y/\delta > 0.4$  and tends to extend farther towards the wall for the upstream stations in a given experiment. Despite its desirable qualities, the normalized  $\overline{vq^2}$  parameter does not employ the triple products of interest for the modeling equations presented in Chapter 1. However if a model were to be formulated employing the transport equation for turbulent kinetic energy, this parameter would be useful. A similar parameter was devised based on the form of the  $\overline{vq^2}$  correlation which had similar behavior with less correlation. The degree of correlation was on the order of the  $B_2$  parameter presented earlier. It maintained values near 0.5 for  $y/\delta > 0.4$  with small variation from station to station and flow to flow.

The parameters presented above maintain most of the desirable traits for turbulence modeling parameters as mentioned above and should be beneficial to the future development of models for complex 3D TBLs. This study has illustrated a need for more experiments in TBLs with complex geometries and data closer to the wall. Also for turbulence modeling efforts, relationships for the pressure rate-of-strain correlations in equations 1.6-1.8 need to be empirically developed. This indicated a need for DNS experiments of high Re flows, which is yet not attainable, or experiments where these terms are investigated. It was seen that the  $\overline{uw}$  Reynolds stress may be significant for 3D TBLs and may need to be incorporated in future modeling efforts. The results presented here suggest that the fluctuating  $v$  velocity is a very important velocity scale. Finally for modeling complex 3D TBLs with an increased accuracy, the inherent anisotropy of the flow must be represented in the model.

## References

- Anderson, O.L. and Eaton, J.K., 1987 "An experimental investigation of pressure-driven three-dimensional turbulent boundary layers," Stanford Univ. Thermosciences. Div. Rept. MD-49.
- Barberis, D. and Molton, P., 1993 "Experimental study of 3-D separation on a large scale model," AIAA 24th Fluid Dynamics Conference, Orlando, FL USA, AIAA-93-3007.
- Barberis, D. and Chantez, B., 1986 "Decollement en écoulement incompressible tridimensionnel experiences de validation et modelisation," ONERA, T.P. n° 1986-180.
- Baskaran, V. and Bradshaw, P., 1987 "Experimental investigation of a three-dimensional turbulent boundary layer on an 'infinite' swept concave wing," *Imperial College of Sci. and Tech., Dept. of Aeronautics, Final Contract Rep.* MoD(PE) Agreement AT/2037/0243.
- Baskaran, V., Pontikis, Y. M., and Bradshaw, P., 1987 "Experimental investigation of a three-dimensional boundary layer over an 'infinite' swept convex wings," *Imperial College of Sci. and Tech., Dept. of Aeronautics, Final Contract Rep.*, MoD(PE) Agreement AT/2037/0243.
- Baskaran, V., Pontikis, Y. G., and Bradshaw, P., 1990 "An experimental investigation of a three-dimensional turbulent boundary layer on 'infinite' swept curved wings," *J. Fluid Mech.*, Vol. 211, p. 95-122.
- van den Berg, B., 1987 "Three-dimensional shear layer experiments and their use as test cases for calculation methods," In *Computation of 3D boundary layers including separation*, AGARD-R-741, p. 3-1.
- van den Berg, B., Elsenaar, A., Lindhout, J.P.F. & Wesseling, P., 1975 "Measurements in an incompressible three-dimensional turbulent boundary layer under infinite swept conditions, and comparison with theory," *J. Fluid Mech.*, Vol. 70, p. 127.
- Bradshaw, P., 1987a "Physics and modeling of three-dimensional boundary layers," In *Computation of 3D boundary layers including separation*, AGARD-R-741, p. 2-1.
- Bradshaw, P., 1987b "Turbulent secondary flows," *Annual Review of Fluid Mechanics*, Vol. 19, p. 53-71.
- Bradshaw, P. and Pontikos, N.S., 1985 "Measurements in the turbulent boundary layer on an 'infinite' swept wing," *J. Fluid Mech.*, Vol. 159, p. 105.
- Bradshaw, P., Ferris, D.H. and Atwell, N.P., 1967 "Calculation of boundary-layer development using the turbulent energy equation," *J. Fluid Mech.*, Vol. 28, p. 593-616.
- Chantez, B., 1988 "Contribution à l'Etude du Décollement Tridimensionnel en Ecoulement Turbulent Incompressible," Thèse de Doctorat, ONERA NT-1988-6.

Chesnাকas, C.J. and Simpson, R.L., 1994 "Three-dimensional turbulence structure in the vicinity of a 3-D separation," Forum on Turbulence in Complex Flows, ASME Winter Annual Meeting, Chicago, Illinois, November 6-11, 1994.

Chesnাকas, C.J., Simpson, R.L., and Madden, M.M., 1994 "Three-dimensional velocity measurements on a 6:1 prolate spheroid at 10° angle of attack," Department of Aerospace and Ocean Engineering, Virginia Polytechnic and State University, Report VPI-AOE-202.

Chesnাকas, C.J. and Simpson, R.L., 1992 "An investigation of the three-dimensional turbulent flow in the cross-flow separation region of a 6:1 prolate spheroid," Sixth International Symposium on Applications of Laser Techniques to Fluid Mechanics, Lisboa, Portugal, 20-23 July, 1992.

Cooke, J. C. and Hall, M. G., 1962 "Boundary layers in three-dimensions," *Prog. Aero. Sci.*, Vol. 2, p. 221.

Dechow, R., and Felsch, K.O., 1977 "Measurements of the mean velocity and of the Reynolds stress tensor in a three-dimensional turbulent boundary layer induced by a cylinder standing on a flat wall," in *Turbulent Shear Flows I* (eds. F. Durst et. al.), University Park, Pennsylvania.

Devenport, W.J., and Simpson, R.L., 1992 "Flow past a wing-body junction -- experimental evaluation of turbulence models," *AIAA Journal*, Vol. 30, No. 4, p. 873- 881.

Devenport, W.J., and Simpson, R.L., 1990 "Time-dependent and time-averaged turbulence structure near the nose of a wing-body junction," *J. Fluid Mech.*, Vol. 210, p. 23-55.

Devenport, W. J. and Simpson, R. L., 1990 "An experimental investigation of the flow past an idealized wing-body junction: final report," Department of Aerospace and Ocean Engineering, Virginia Polytechnic and State University, Report VPI-AOE-172.

Driver, D. M. and Johnston, J. P., 1990 "Experimental study of a three-dimensional shear-driven turbulent boundary layer with streamwise adverse pressure gradient," NASA TM 102211; Also Report MD-57, Thermosciences Division, Department of Mechanical Engineering, Stanford University.

Eaton, J. K., 1995 " Effects of mean flow three dimensionality on turbulent boundary-layer structure," *AIAA Journal*, Vol. 33, No. 11, p. 2020.

Elsenaar, A. and Bolsma, S.H., 1974 "Measurements of the Reynolds stress tensor in a three-dimensional turbulent boundary layer under infinite swept wing conditions," NLRTR 74095U.

Fernholz, H.H. and Vagt, J. D., 1981 "Turbulence measurements in an adverse-pressure-gradient three-dimensional boundary layer along a circular cylinder," *J. Fluid Mech.*, Vol. 111, p. 233-269.

Flack, K.A., and Johnston, J.P., 1995 "Near-wall structure of three-dimensional turbulent boundary layers," 10th Symposium in Turbulent Shear Flows, University Park, PA, 14-16 Aug. 1995.



Flack, K.A., and Johnston, J.P., 1994 "Near-wall flow in a three-dimensional turbulent boundary layer on the endwall of a rectangular bend," AIAA paper 94-0405, 32nd Aerospace Sciences Meeting, 10-13 January, Reno, Nevada.

Flack, K.A., and Johnston, J.P., 1993 "Near-wall investigation of three-dimensional turbulent boundary layers," Stanford University, Report MD-63.

Fleming, J. and Simpson, R.L. 1994 "Experimental investigation of the wall flow structure of a low Reynolds number 3-D turbulent boundary layer," AIAA paper no. 94-0649, 32nd Aerospace Sciences Meeting, Reno, NV, 10-13 Jan. 1994.

Ha, S. and Simpson, R.L., 1993 "An experimental investigation of a three-dimensional turbulent boundary layer using multiple-sensor probes," *9th Symposium on Turbulent Shear Flows*, Kyoto, Japan, 16-18 Aug. 1993, p.2-3-1.

Johnston, J.P., and Flack, K.A., 1996 "Review-advances in three-dimensional turbulent boundary layers with emphasis on the wall-layer regions," *Journal of Fluids Engineering*, Vol. 118, p. 219.

Johnston, J.P., 1976 "Experimental studies in three-dimensional turbulent boundary layers," Stanford Univ. Thermosciences Div. Rept., MD-34.

Klebanoff, P.S., 1955 "Characteristics of turbulence in a boundary layer with zero pressure gradient," NACA Report 1247, p. 1-19. (also [1954] NACA-TN-3178.)

Kreplin, H.P. and Stäger, R., 1993 "Measurements of the Reynolds stress tensor in the three dimensional boundary layer of an inclined body of revolution," Ninth Symposium on Turbulent Shear Flows, 2-4-1 -6.

Littell, H.S. and Eaton, J.K., 1991 "An experimental investigation on the three-dimensional boundary layer on a rotating disk," Thermosciences Division, Department of Mechanical Engineering, Stanford University, Report No. MD-60.

McMahon, H., Hubbart, J., and Kubendran, L., 1982 "Mean velocities and Reynolds stresses in a juncture flow," NASA Contractor Report 3605.

Nagano, Y and Tagawa, M., 1991 "Turbulence model for triple velocity and scalar correlations," International Symposium on Turbulent Shear Flows (7th : 1989: Stanford University) Turbulent shear flows 7 : selected papers from the Seventh International Symposium on Turbulent Shear Flows, Stanford University, USA, August 21-23, 1989 /editors: F. Durst [*et al.*]. Berlin ; New York : Springer-Verlag, c1991.

Nagano, Y and Tagawa, M., 1990 "A structural turbulence model for triple products of velocity and scalar," *J. Fluid Mech.*, Vol., 215, p.639-657.

- Ölçmen, S.M. and Simpson, R.L., 1995 "An experimental study of a three-dimensional pressure-driven turbulent boundary layer," *J. Fluid Mech.*, Vol. 290, p. 225-262.
- Ölçmen, S.M. and Simpson, R.L., 1992 "Perspective: On the near wall similarity of three-dimensional turbulent boundary layers," *J. Fluids Engineering*, Vol. 114, p.487-495.
- Pierce, F. J. and Zimmerman, B.B., 1973 "Wall shear stress inference from two-and three-dimensional boundary layer velocity profiles," *Trans. ASME I: J. Fluids Eng.* 95, 61.
- Pompeo, L.P., Bettelini, M.S.G., and Thomann, H., 1993 "Laterally strained turbulent boundary layers near a plane of symmetry," *J. Fluid Mech.*, Vol. 257, pp. 507-532.
- Pompeo, L.P., 1992 "An experimental study of three-dimensional turbulent boundary layers," Doctoral Dissertation-Swiss Fed. Inst. of Tech., Zurich., Diss. ETH No. 9780.
- Reynolds, W.C., 1989 "Fundamentals of turbulence for turbulence modeling and simulation," Lecture Notes for ME 261B, Stanford University (see Littell and Eaton, 1991).
- Robinson, S.K., 1992, NASA TM 103857.
- Robinson, S.K., 1991 "A perspective on coherent structures and conceptual models for turbulent boundary layer physics," NASA Langley Research Center.
- Rotta, J.C., 1962 "Turbulent boundary layers in incompressible flow", *Prog. Aero. Sci.*, Vol. 2, Pergamon Press Inc., New York, N.Y., Eds. Ferri, A., Kuchemann, D., Stern, L. H. G., 1962.
- Rotta, J.C., 1977 "A family of turbulence models for three-dimensional thin shear layers," *Symposium on Turbulent Shear Flows*, Pennsylvania State University., University Park, PA.
- Schetz, J.A., 1993 *Boundary Layer Analysis*, Prentice Hall, Englewood Cliffs, NJ.
- Schlichting, H., 1987 *Boundary-Layer Theory*, McGraw-Hill, New York, NY.
- Schumann, U. 1977 "Realizability of Reynolds-stress turbulence models," *Phys. of Fluids*, Vol. 20, No. 5, p.721-725.
- Schwarz, W.R. and Bradshaw, P., 1993 "Measurements in a pressure driven three-dimensional turbulent boundary layer during development and decay," *AIAA Journal*, Vol. 31, No. 7, p. 1207-1214.
- Schwarz, W.R. and Bradshaw, P. 1992, "Three-dimensional turbulent boundary layer in a 30 degree bend: experiment and modeling," Thermosciences Division Report No. MD-61, Stanford.
- Sendstad, O. and Moin, P., 1992 "The near-wall mechanics of three-dimensional turbulent boundary layers," Dept. of Mechanical Engineering, Stanford Univ., Rept. TF-57.

Simpson, R.L., 1995 "Three-dimensional turbulent boundary layers and separation" 33rd Aerospace Sciences Meeting & Exhibit, January 9-12, Reno, NV, AIAA 95-0226.

Taylor, J.R., 1982 *An Introduction to Error Analysis*, University Science Books, Oxford University Press, Mill Valley, CA, USA, p. 40-80.

Tennekes, H. and Lumley, J.L., 1992 *A First Course in Turbulence*, The MIT Press, Cambridge, MA.

Townsend, A.A., 1976 *The Structure of Turbulent Shear Flow*, Cambridge University Press, 2nd ed., New York, NY. (1st edition, 1956)

Van Dyke, M. (1982). *An Album of Fluid Motion*, Stanford CA, The Parabolic Press.

Wilmarth, W.W. and Lu, S.S., 1972 "Structure of the Reynolds stress near the wall," *J. Fluid Mechanics*, Vol. 55, 1972.

## APPENDIX A Uncertainty Analysis

The uncertainties in the parameters that were calculated were estimated based on techniques of the propagation of uncertainties as described by Taylor (1982). The most general rule for the uncertainty in a parameter,  $q$ , that is a function of several variables,  $q = q(x, \dots, z)$  is given by,

$$\delta q = \sqrt{\left(\frac{\partial q}{\partial x} \delta x\right)^2 + \dots + \left(\frac{\partial q}{\partial z} \delta z\right)^2} \quad (\text{B.1})$$

From this, rules governing the propagation of uncertainties in sums and differences, products and quotients, and functions of a single variable may be derived. For  $q = x + \dots + y - (u + \dots + w)$  we have,

$$\delta q = \sqrt{(\delta x)^2 + \dots + (\delta y)^2 + (\delta u)^2 + \dots + (\delta w)^2} \quad (\text{B.2})$$

And for  $q = (X * \dots * Y) / (U * \dots * W)$  we get the result,

$$\frac{\delta q}{|q|} = \sqrt{\left(\frac{\delta x}{|x|}\right)^2 + \dots + \left(\frac{\delta y}{|y|}\right)^2 + \left(\frac{\delta u}{|u|}\right)^2 + \dots + \left(\frac{\delta w}{|w|}\right)^2} \quad (\text{B.3})$$

The result for functions of a single variable is a simple reduction from the general case where only one term is needed and the derivative rather than the partial derivative is used. The special case of a variable raised to a power will be noted here due to its usefulness. For  $q = x^n$ , we get,

$$\frac{\delta q}{|q|} = |n| \frac{\delta x}{|x|} \quad (\text{B.4})$$

It should be noted that it was assumed that the uncertainties are better estimated by adding them in quadrature. This is usually reserved for uncertainties that are independent and random in the theory of uncertainty analysis. However, this is not entirely true for some techniques used to obtain the velocity components in the experiments that were examined. One example is for a LDV system where the measurement axes are not aligned with the direction in which the calculation was performed. In this case, the value of  $U$  that we use in the calculation may have been determined

from two orthogonal velocity signals measured at some angle to the calculation reference frame. The value of  $U$ , and its uncertainty, in the calculation reference frame is associated with  $U$ ,  $V$ , and possibly  $W$  in the measurement reference frame. Since the addition of uncertainties in quadrature produces an uncertainty less than the maximum, it should be noted that the uncertainties may be slightly larger than reported here. The addition of uncertainties in quadrature gives a more realistic estimate for the general case of independent and random uncertainties which covers a majority of the data represented. For uniformity, the uncertainties are added in quadrature. The use of equation B.1 rather than the individual formula's in B.2 - B.4 also tends to account for compensating errors. This formula was used to determine the uncertainty where the individual uncertainties were suspected to contribute to each other.

A summary of the uncertainties for each of the experiments is compiled in a table B.1. This allows for an easy comparison of the uncertainty between experiments. Blank spaces are left when the uncertainty in a velocity component was not reported. Baskaran and Bradshaw (1990) reported the uncertainty in the measured quantities, at the station with the maximum cross flow with respect to the probe. The uncertainties for Devenport and Simpson (1990) are given in table 2.3. The average values of the uncertainty in a velocity component were used for the uncertainty analysis for this flow. The reference velocity was 27 m/s. For Ölçmen and Simpson (1994) The uncertainty in the mean velocities normalized on  $U_{ref}$  were  $\pm 0.003$ ,  $\pm 0.001$ , and  $\pm 0.002$  for  $U/U_{ref}$ ,  $V/U_{ref}$ , and  $W/U_{ref}$  respectively. For the fluctuating velocity components,  $u'/U_{ref}$  had an uncertainty of  $\pm 0.001$ ,  $v'/U_{ref}$  had an uncertainty of  $\pm 0.0009$  except nearest the wall, and the  $w'/U_{ref}$  uncertainty was  $\pm 0.0008$ . For the Reynolds shear stresses,  $-\overline{uv}/U_{ref}^2$  had an uncertainty of  $\pm 0.00008$ ,  $-\overline{vw}/U_{ref}^2$  had an uncertainty of  $\pm 0.00002$ , and the uncertainty in the  $-\overline{uw}/U_{ref}^2$  stress was  $\pm 0.00004$ .

Pompeo, Littell, Schwarz, Baskaran, Chesnakas, Ölçmen, and Molton do not report uncertainties in the triple product measurements. For Driver and Johnston (1990), triple product quantities have an accuracy of  $\pm 4\%$  of  $u_i' u_j' u_k'$ .

The uncertainty in the  $1/S$  parameter was calculated by using equations B2, B3, and B4 above. The resulting uncertainties are given for each experiment in table B.2. Likewise the uncertainty is calculated for the  $B_1$  and  $B_2$  parameters and reported in table B.2. The  $\overline{v^3}/vTKE$  parameter also has an uncertainty estimate in table B.2 where  $vTKE = (\overline{u^2 v} + \overline{v^3} + \overline{vw^2})$ .

TABLE B.1 A Summary of the uncertainties in the experiments that were examined.

	U	V	W	$\overline{u^2}$	$\overline{v^2}$	$\overline{w^2}$	$\overline{uv}$	$\overline{vw}$	$\overline{uw}$
McMahon									
Baskaran				5%	5%	5%	15%	30%	30%
Devenport	3.3%			0.6 m/s	0.3 m/s	0.3 m/s	0.5 m/s	0.3 m/s	0.3 m/s
Driver	$\pm 0.3$ m/s			$\pm 10\%$ of local values			$\pm 5\%$ of rms values		
Littell	3%			5%	5%	5%	10%	15%	10%
Pompeo	< 2%			< 10%			< 10%		
Schwarz	3%			5%	5%	5%	10%	15%	10%
Molton									
Stäger									
Chesnakas				$\pm 2\%$ of $u_{ii}$			$\pm 3\%$ of $(u_i u_i^* + u_k u_k + 2[u_i u_k]^2)^{1/2}$		
Ölçmen $\pm(\ )/U_r^n$	0.003	0.001	0.002	0.002	0.0018	0.0016	0.00008	0.00002	0.00004

Table B.2 Uncertainties in Calculated Parameters

	1/S	$B_1$	$B_2$	$\overline{v^3}/vTKE$
Baskaran	45%			
Devenport	26%			
Driver	19%	$\pm 9\%$ of $u_i' u_j' u_k'$	$\pm 9\%$ of $u_i' u_j' u_k'$	$\pm 12\%$ of $u_i' u_j' u_k'$
Littell	25%			
Pompeo	22%			
Schwarz	25%			
Chesnakas	21%			
Ölçmen	18%	23%	23%	27%

## APPENDIX B Additional Figures for the Data of Pompeo

The experiment of Pompeo is described in detail in chapter 2. To summarize, there were three test geometries, a 2D nozzle, a diverging nozzle, and a converging nozzle. The data supplied for the 2D case were corrupted and hence no analysis was performed on that case. The converging / diverging nozzle was designed to have zero pressure gradient along the centerline with the only modification from 2D flow along the centerline as the addition of the  $dU/dz$  rate of strain. There were 2 stations of truly 3D data for each case both were located at  $x = 1000$  mm in the tunnel coordinate system as described in chapter 2, the  $z$  locations are designated in each figure. There were several  $x$  locations along the centerline and they are designated where applicable. This appendix contains data analysis not immediately required in the discussion of the thesis but of considerable value.

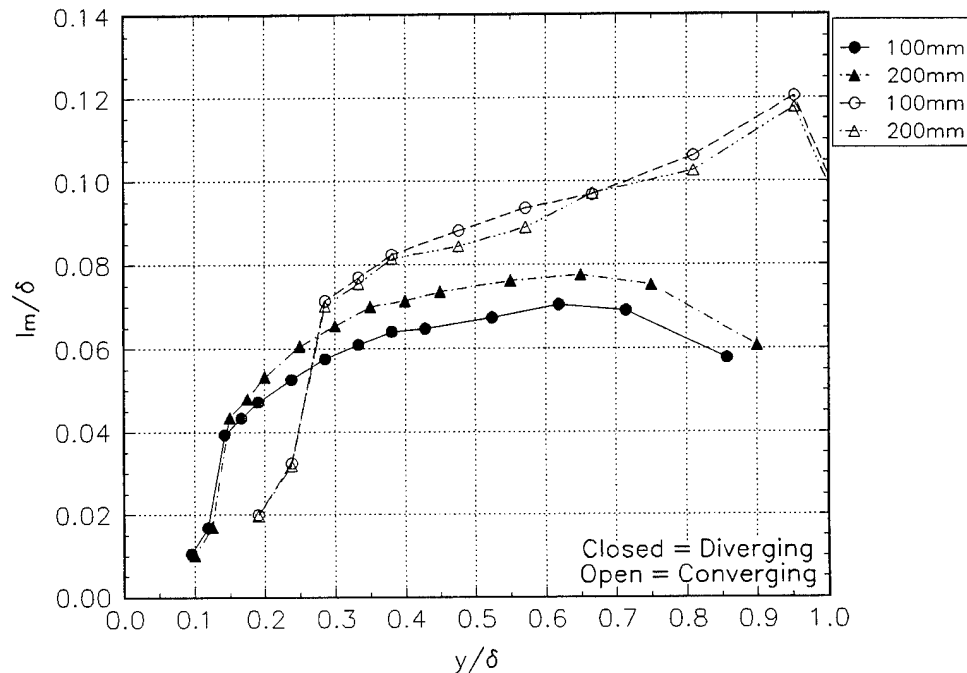


Figure B1 The mixing length, all data is at  $x = 1000$  mm with the  $z$  location is given in mm.

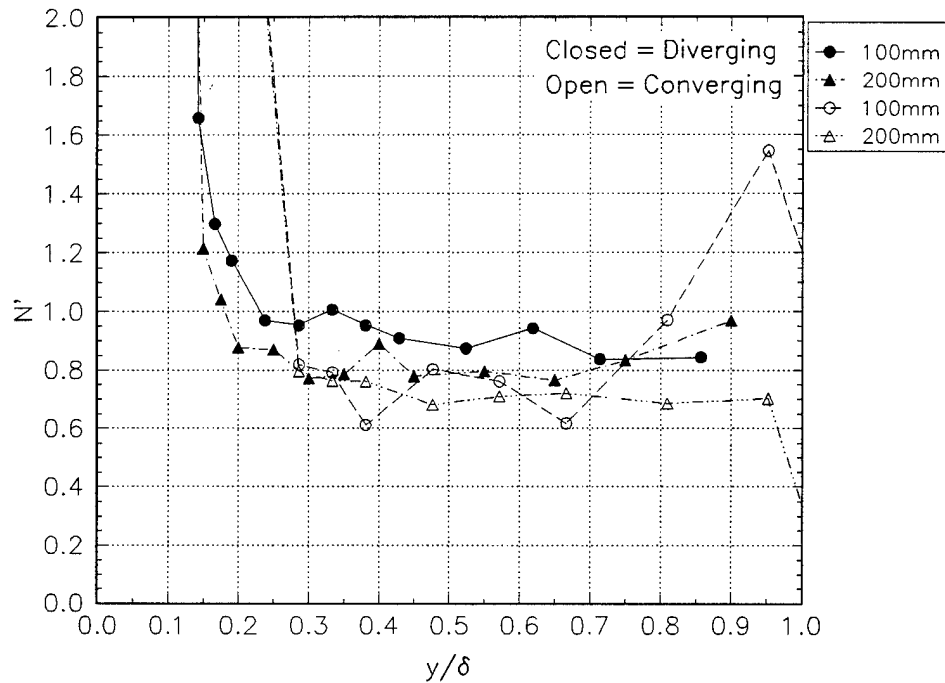


Figure B2 Rotta's T parameter, all data is at  $x = 1000$  mm with the  $z$  location is given in mm.

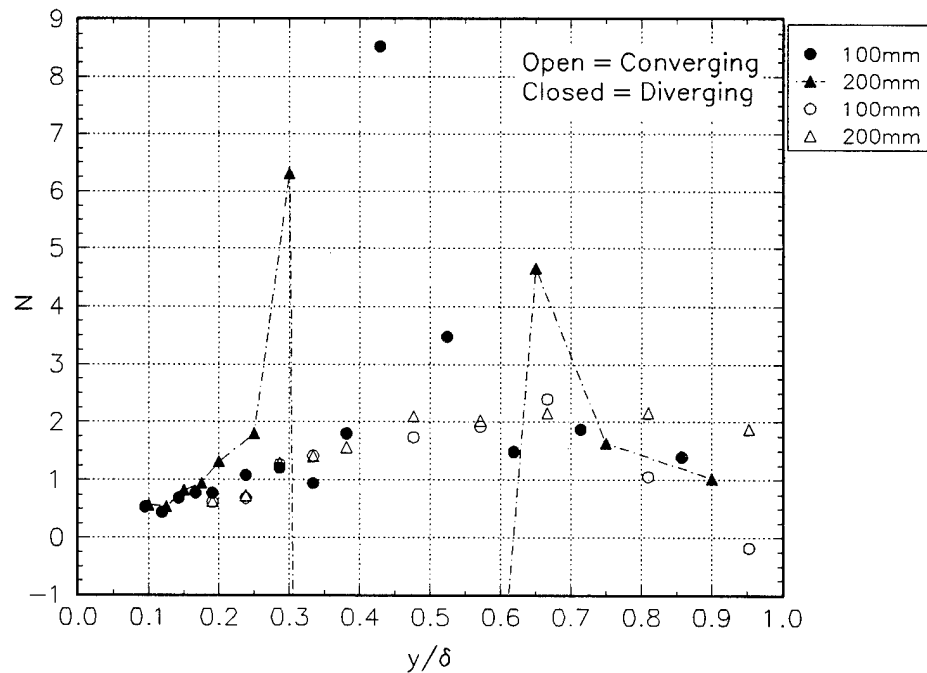


Figure B3 The N isotropy parameter in wall stress coordinates.  
All data is at  $x = 1000$  mm with the  $z$  location is given in mm.



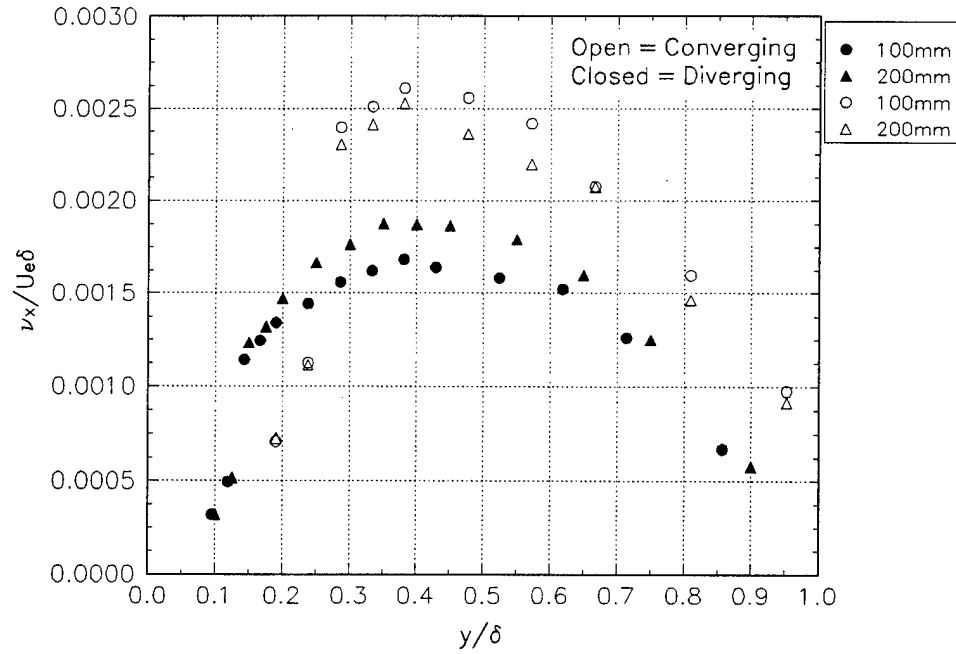


Figure B4.a The x-direction eddy viscosity in wall stress coordinates.  
All data is at  $x = 1000$  mm with the  $z$  location is given in mm.

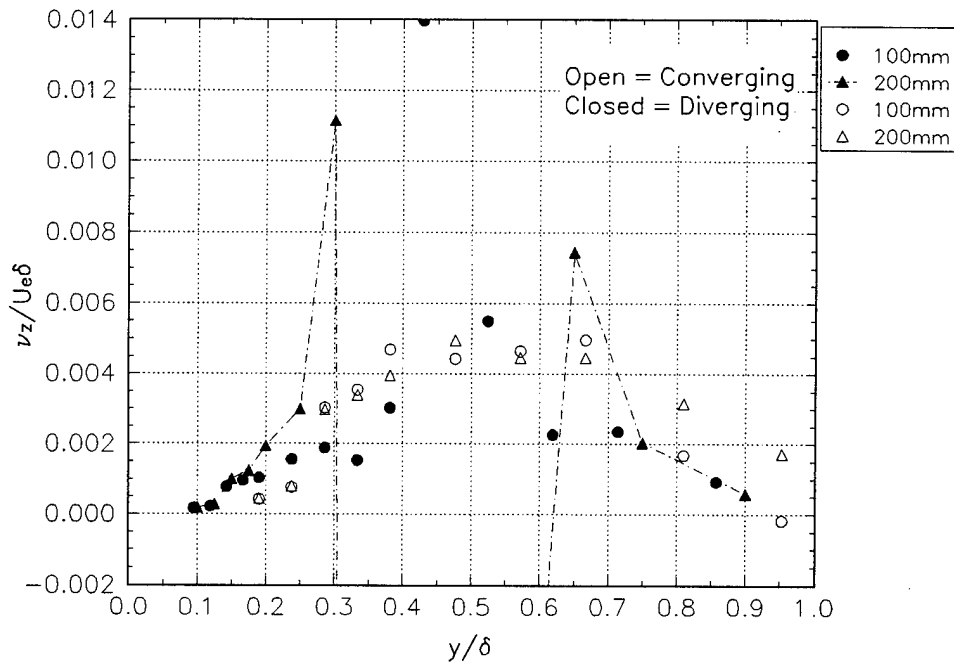


Figure B4.b The z-direction eddy viscosity in wall stress coordinates.  
All data is at  $x = 1000$  mm with the  $z$  location is given in mm.

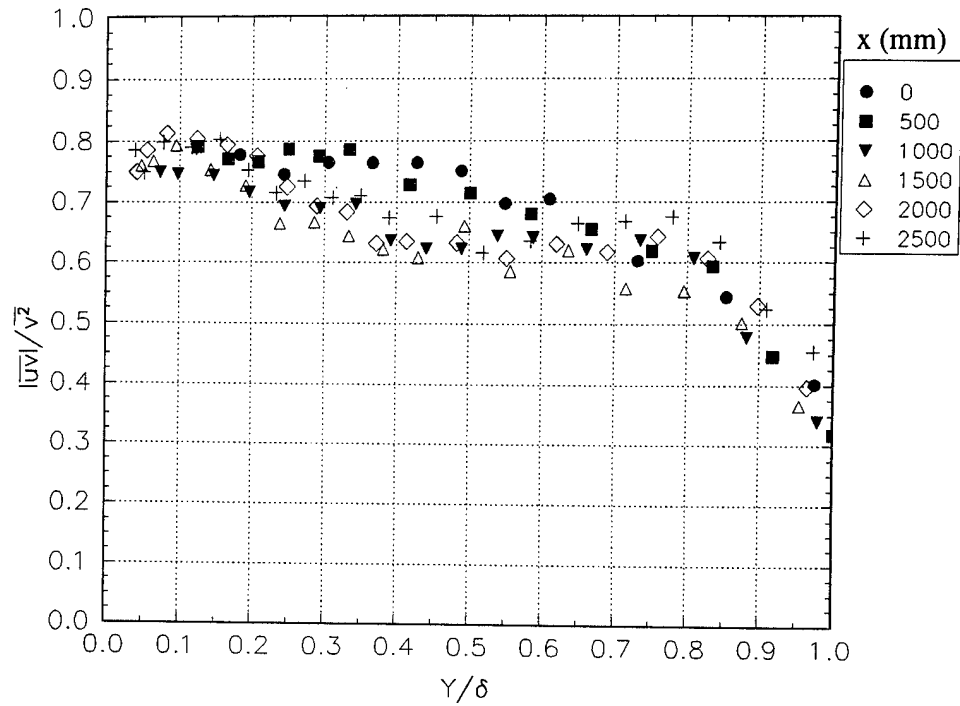


Figure B5.a Centerline stations for the converging test nozzle.

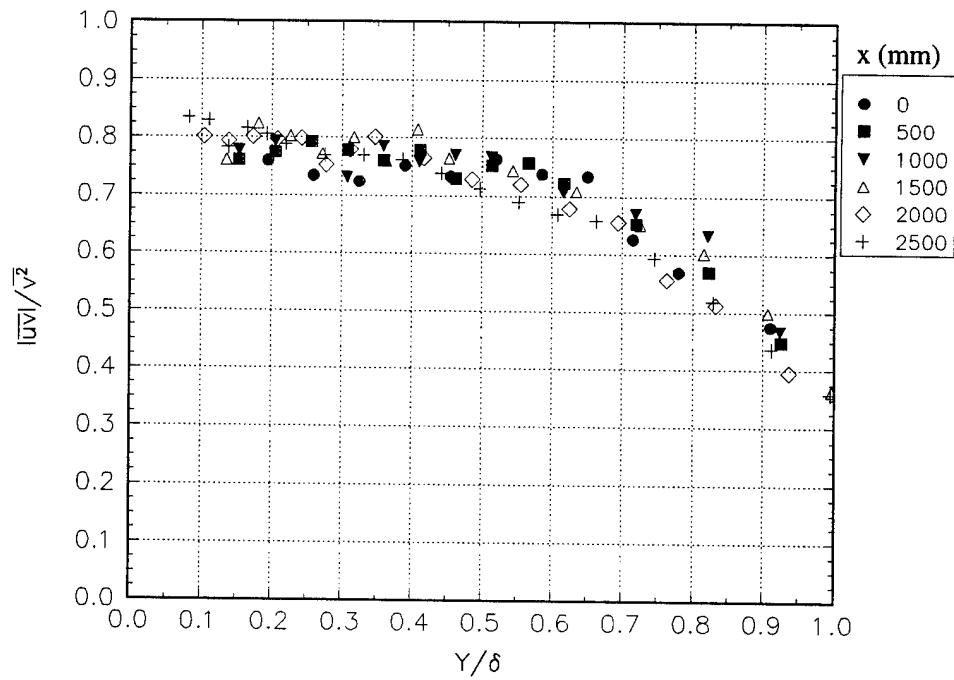


Figure B5.b Centerline stations for the diverging test nozzle.

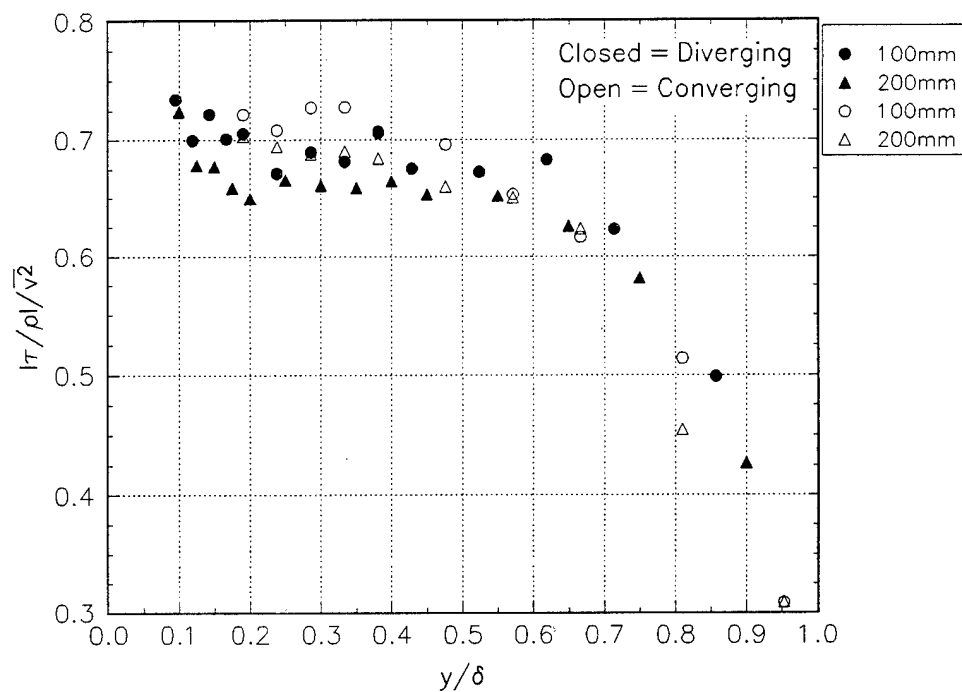


Figure B6 The 1/S parameter, all data is at  $x = 1000$  mm with the z location is given in mm.

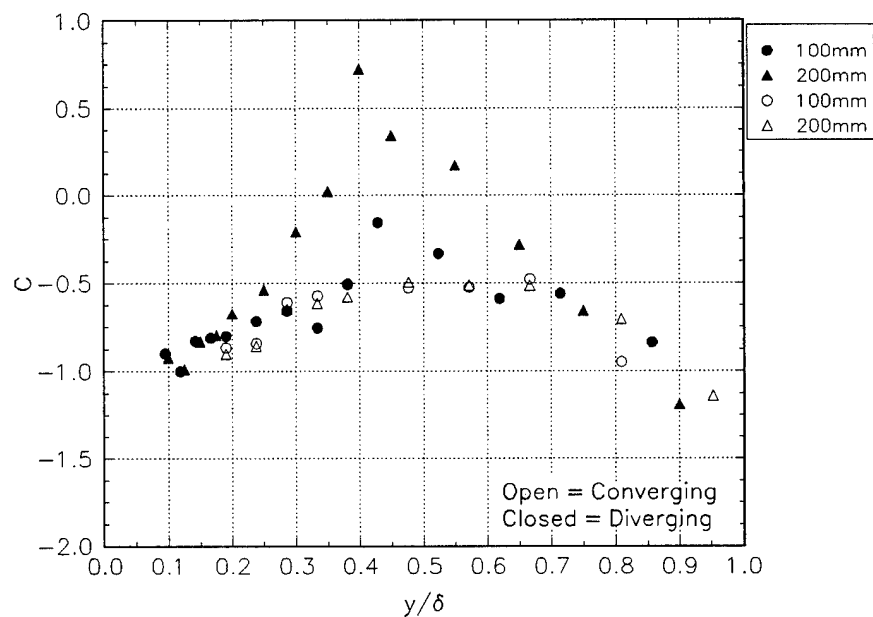


Figure B7 The C parameter in wall stress coordinates. All data is at  $x = 1000$  mm with the z location is given in mm.

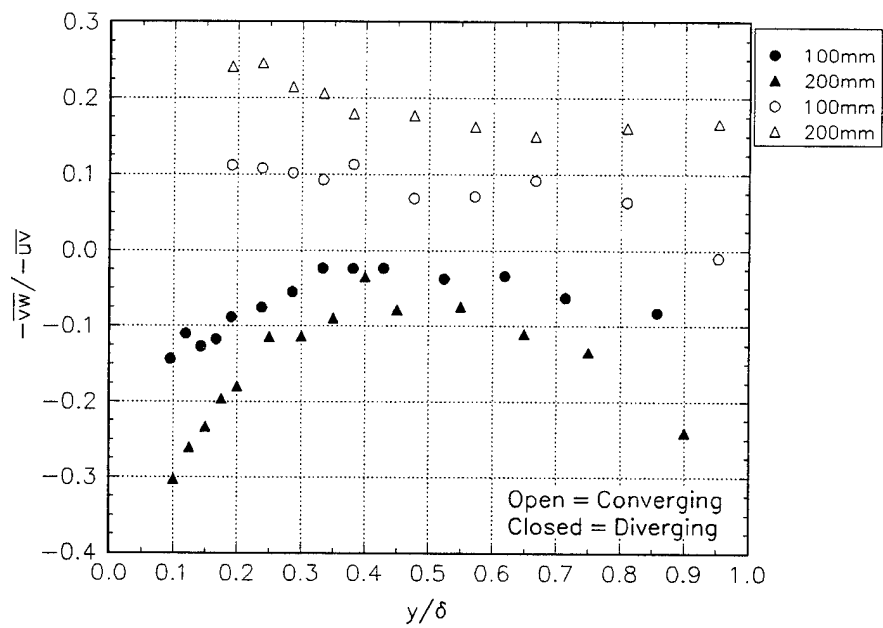


Figure B8 Shear stress ratio in wall stress coordinates.  
Data is at  $x = 1000$  mm with  $z$  locations given in mm.

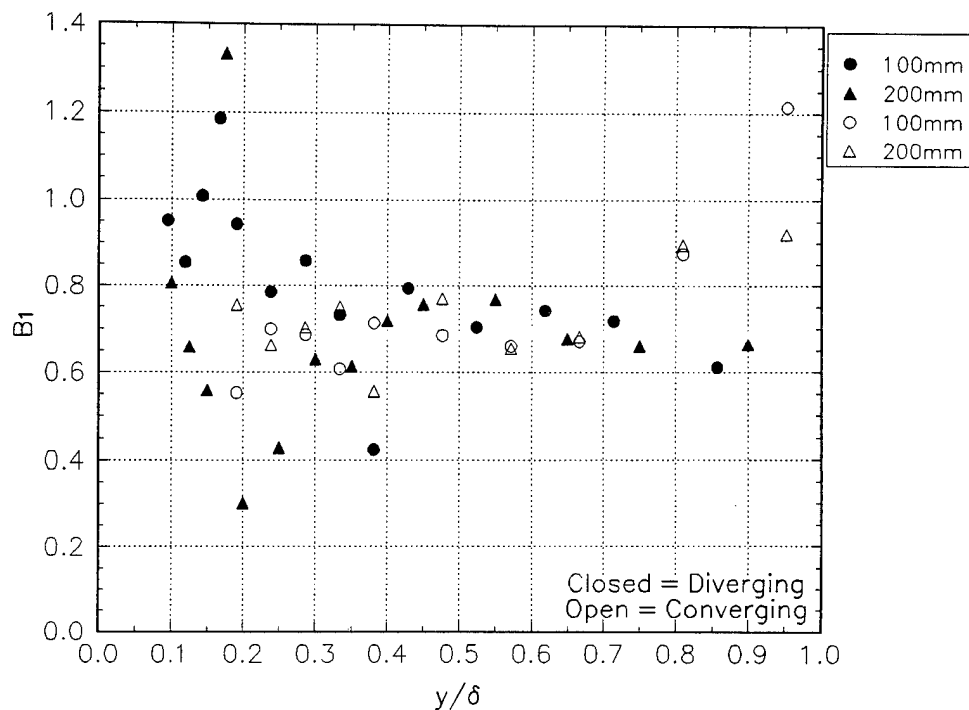


Figure B9 The  $B_1$  parameter in wall stress coordinates.  
Data at  $x = 1000$  mm with the  $z$  location is given in mm.

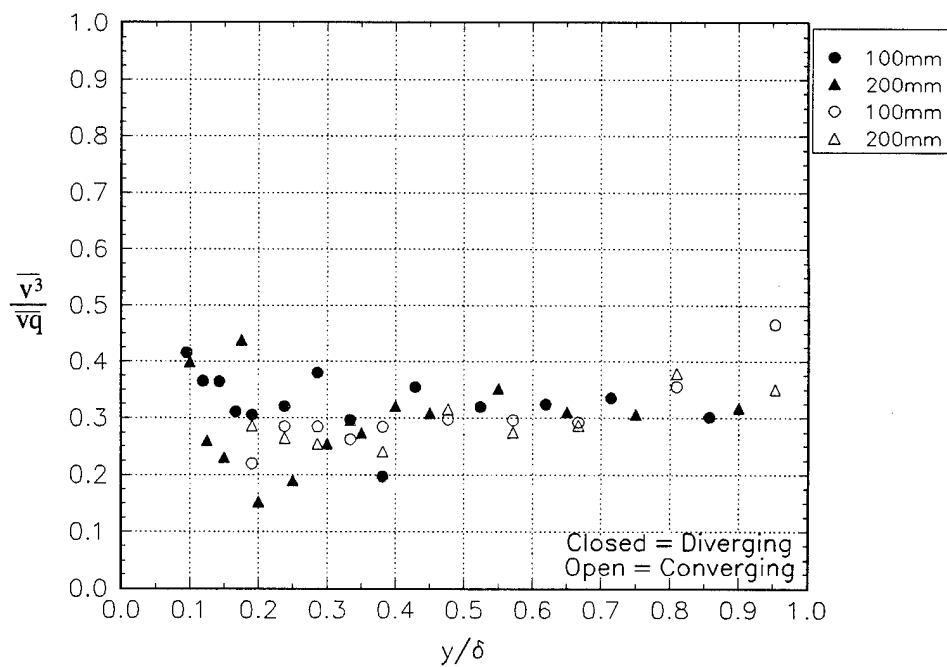


Figure B10 The  $\overline{vq}$  parameter, all data is at  $x = 1000$  mm with the  $z$  location is given in mm.

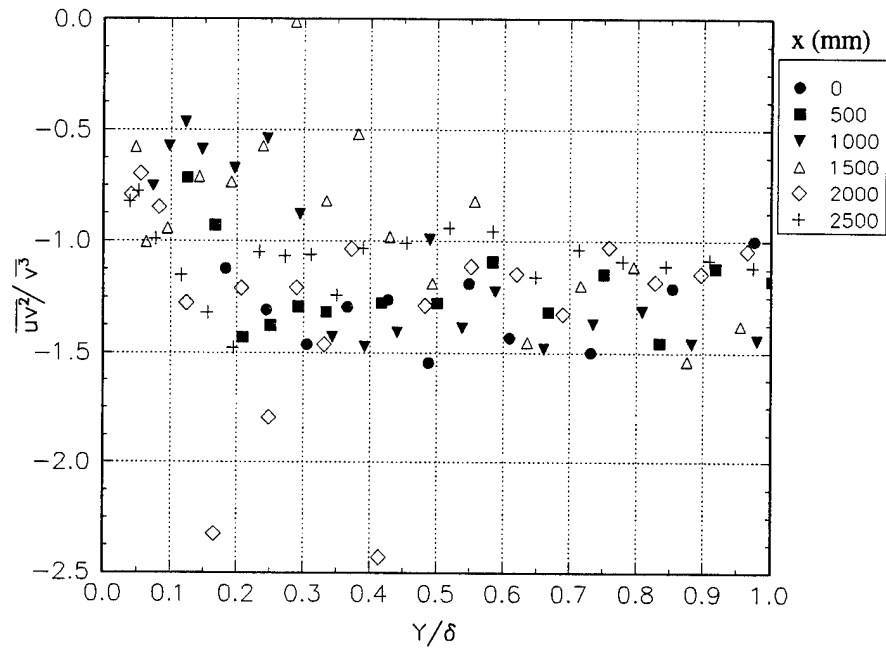


Figure B11.a Triple products in wall stress coordinates for the centerline stations of the converging test nozzle.

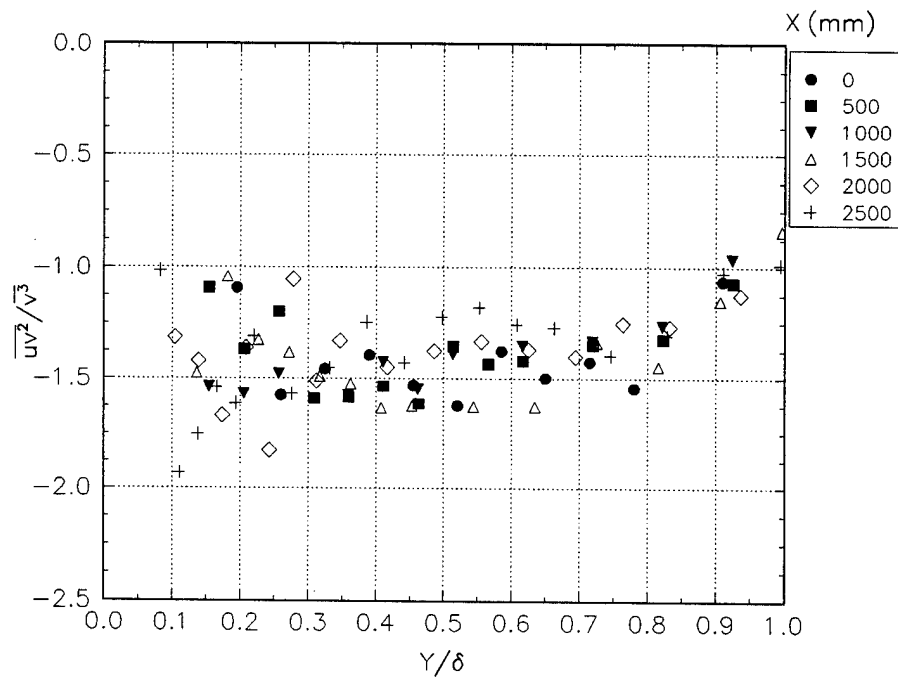


Figure B11.b Triple products in wall stress coordinates for the centerline stations for the diverging test nozzle.

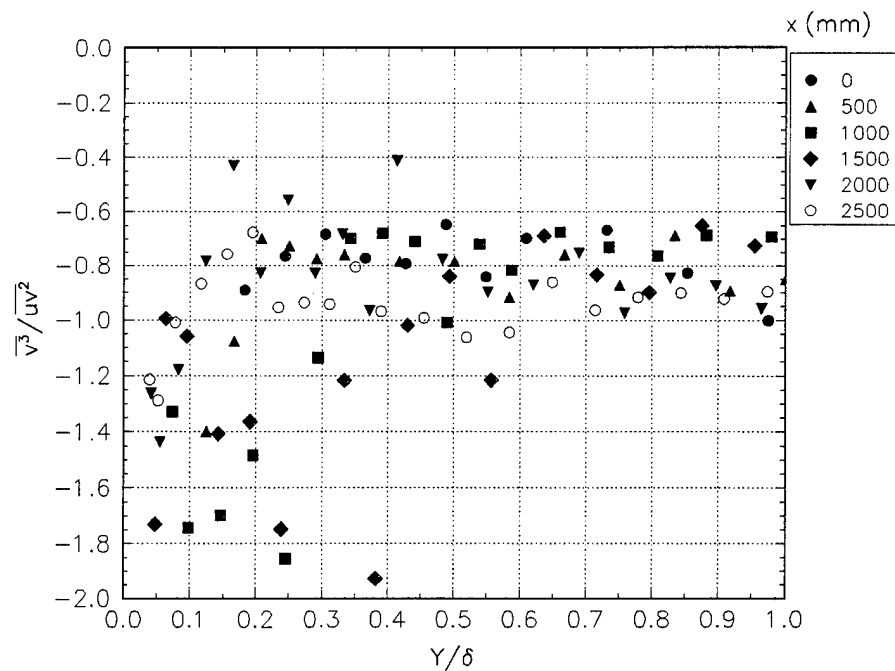


Figure B12.a Triple products in wall stress coordinates for the centerline stations for the converging test nozzle.

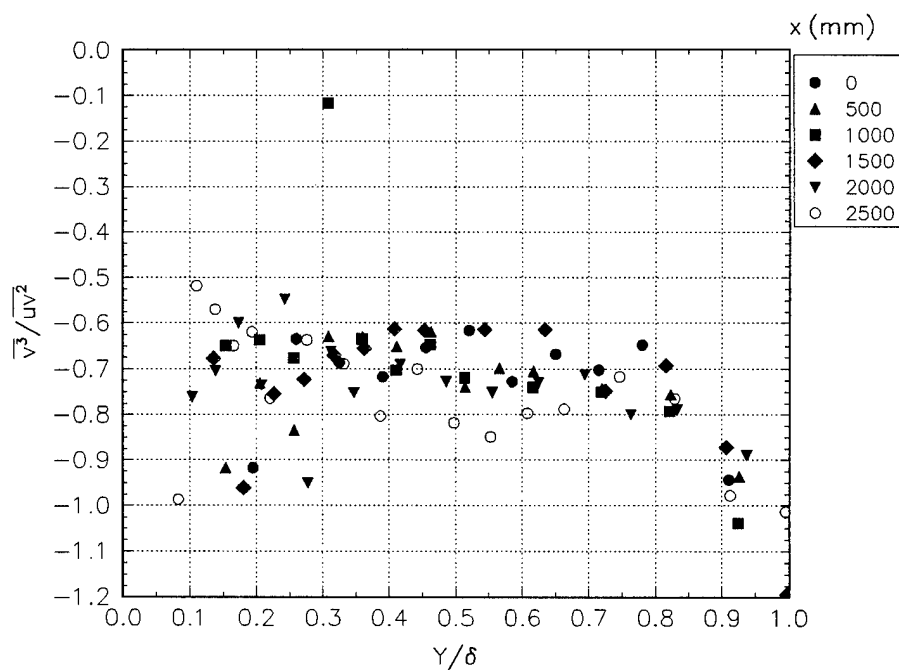


Figure B12.b Triple products in wall stress coordinates for the centerline stations for the diverging test nozzle.

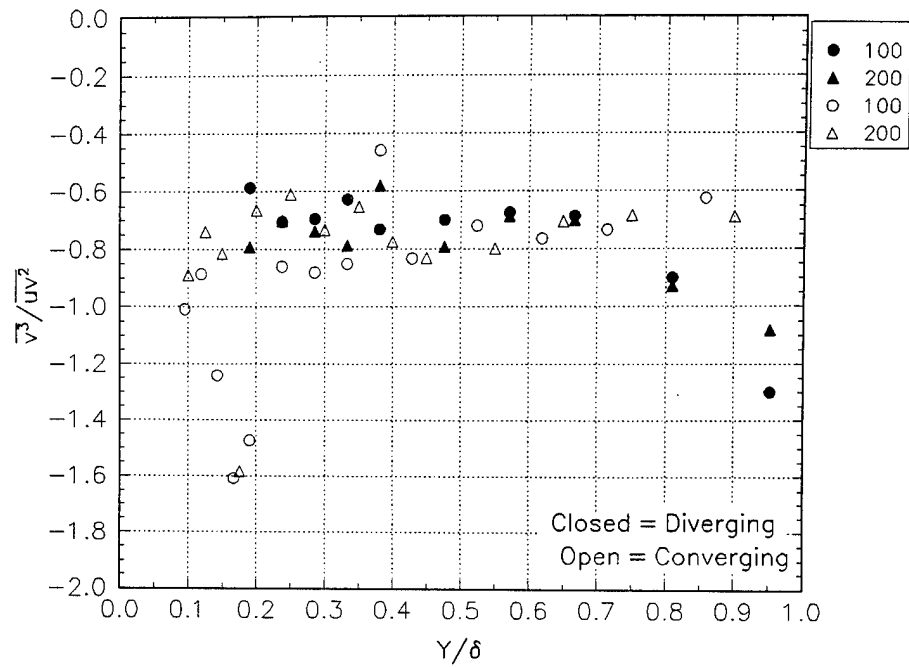


Figure B13 Triple products in wall stress coordinates  
at  $x = 1000$  mm with the  $z$  location is given in mm.

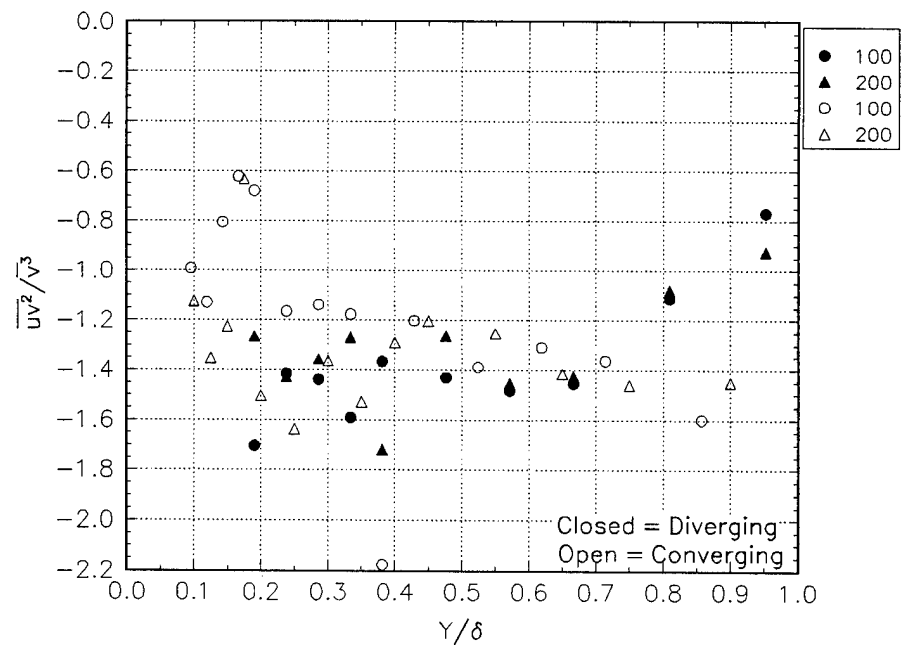


Figure B14 Triple products in wall stress coordinates  
at  $x = 1000$  mm with the  $z$  location is given in mm.



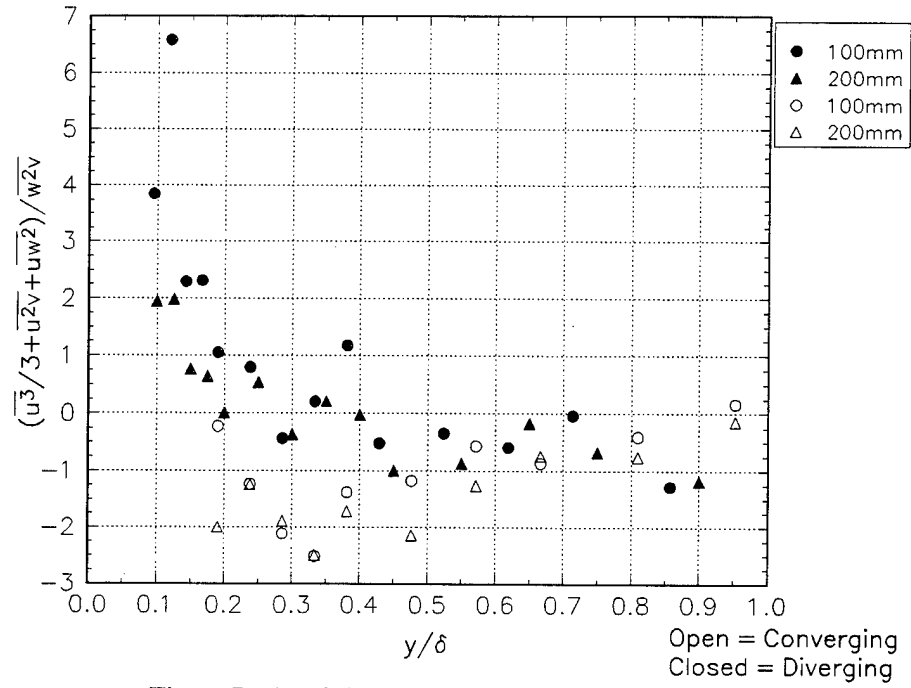


Figure B15 Triple products in wall stress coordinates at  $x = 1000$  mm with the  $z$  location is given in mm.

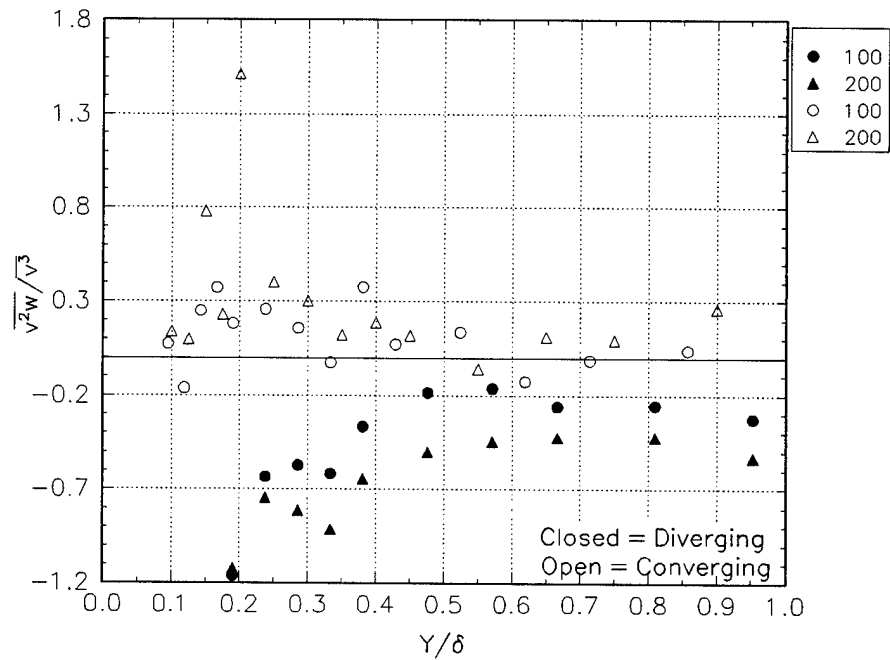


Figure B16 Triple products in wall stress coordinates at  $x = 1000$  mm with the  $z$  location is given in mm.

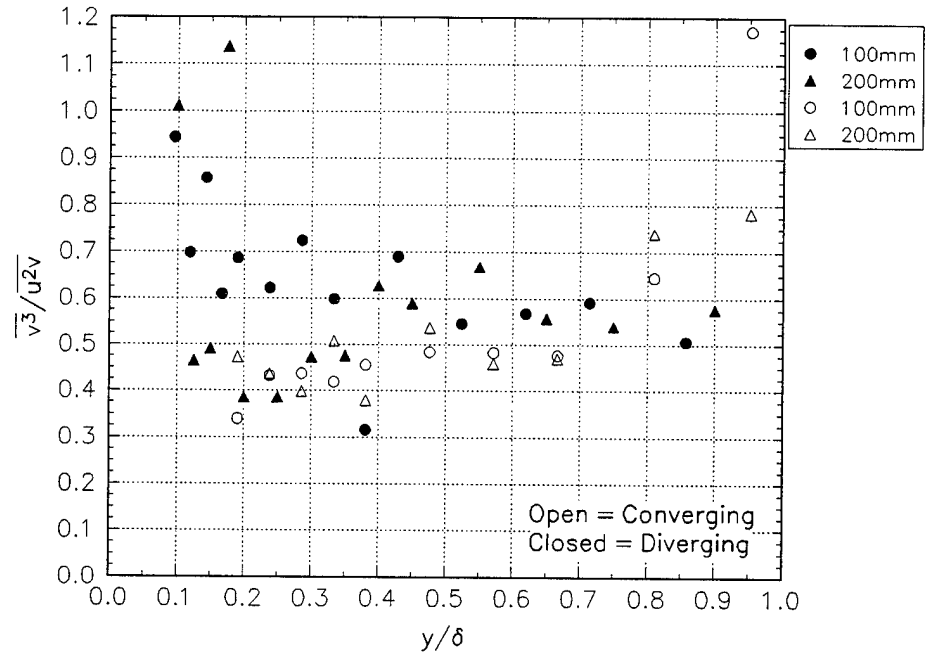


Figure B17 Triple products in wall stress coordinates at  $x = 1000$  mm with the  $z$  location is given in mm.

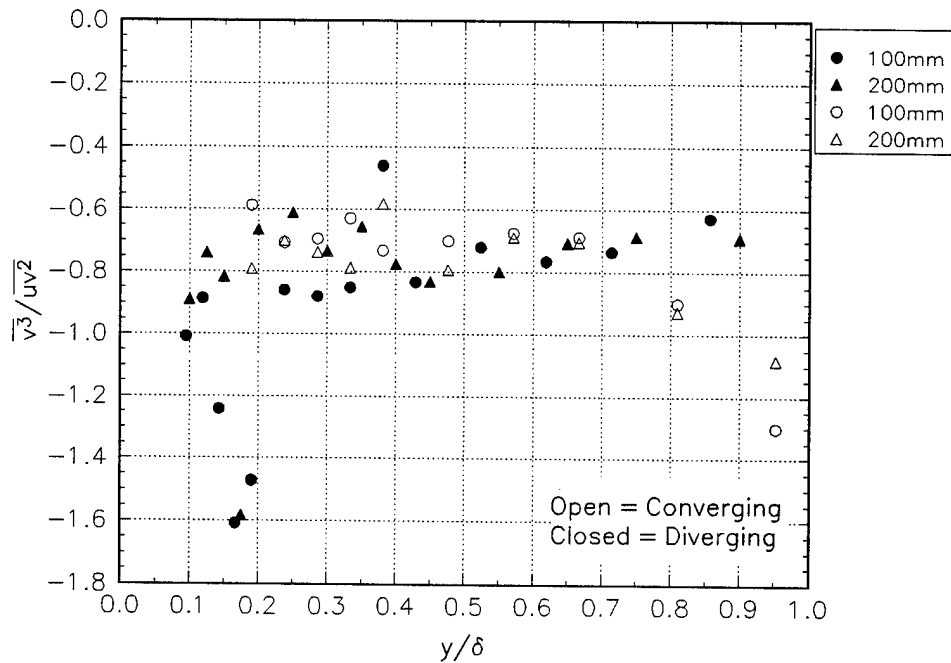


Figure B18 Triple products in wall stress coordinates at  $x = 1000$  mm with the  $z$  location is given in mm.

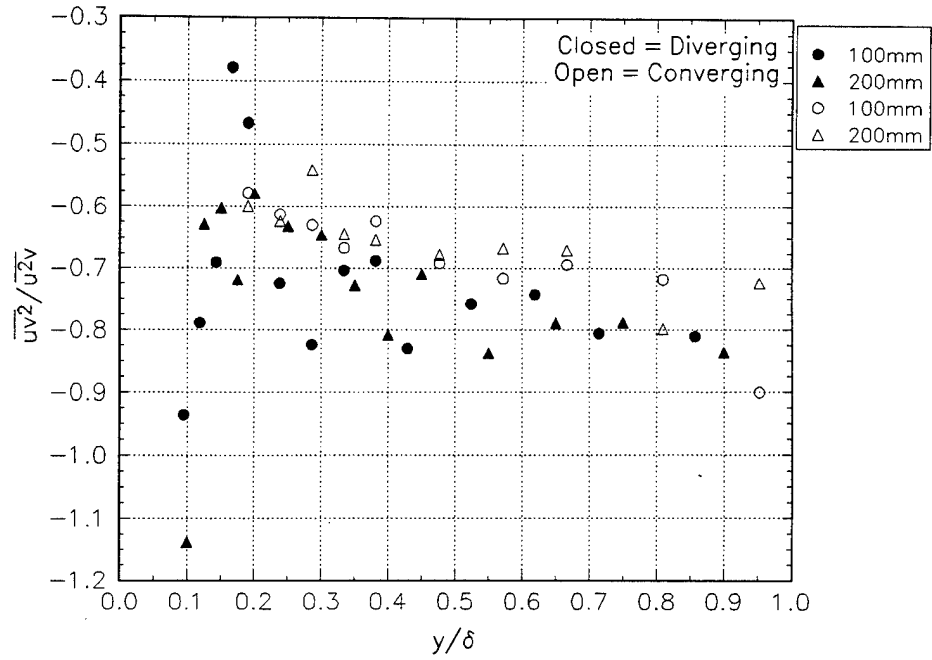


Figure B19 Triple products in wall stress coordinates at  $x = 1000$  mm with the  $z$  location is given in mm.

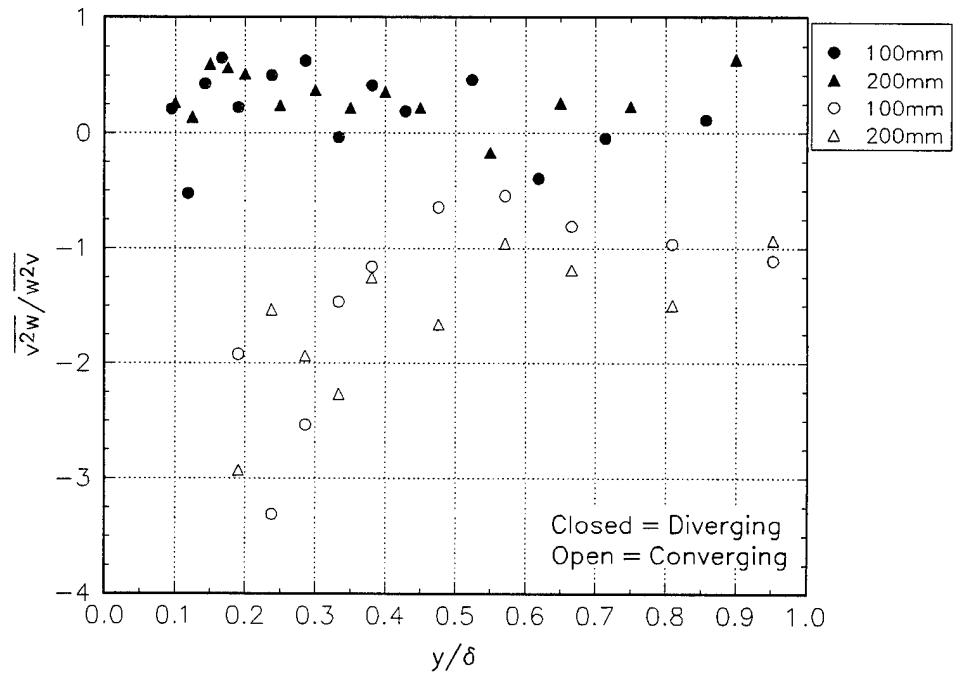


Figure B20 Triple products in wall stress coordinates at  $x = 1000$  mm with the  $z$  location is given in mm.

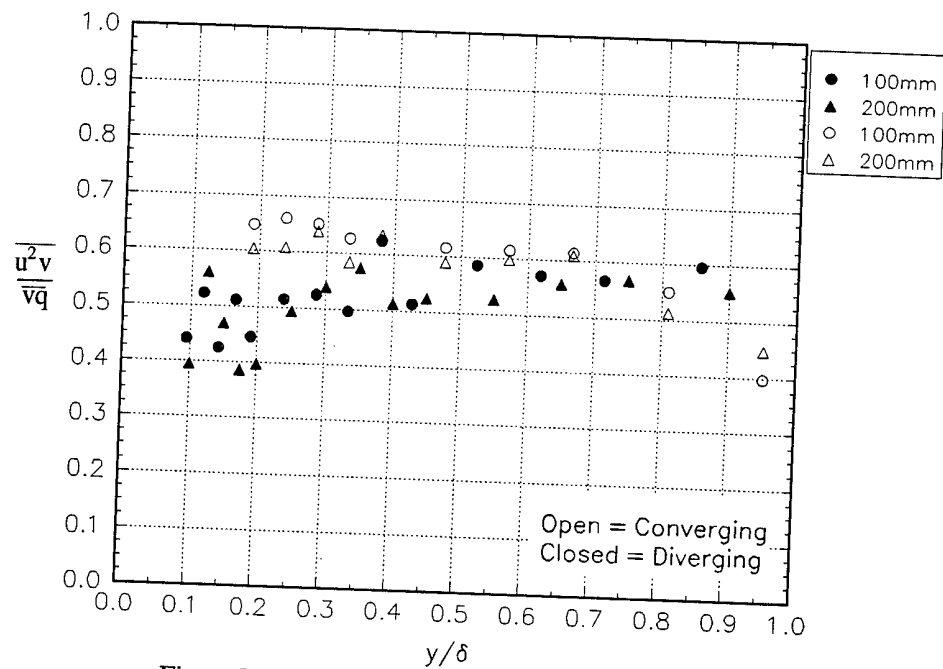


Figure B21 Triple products in wall stress coordinates at  $x = 1000$  mm with the  $z$  location is given in mm.

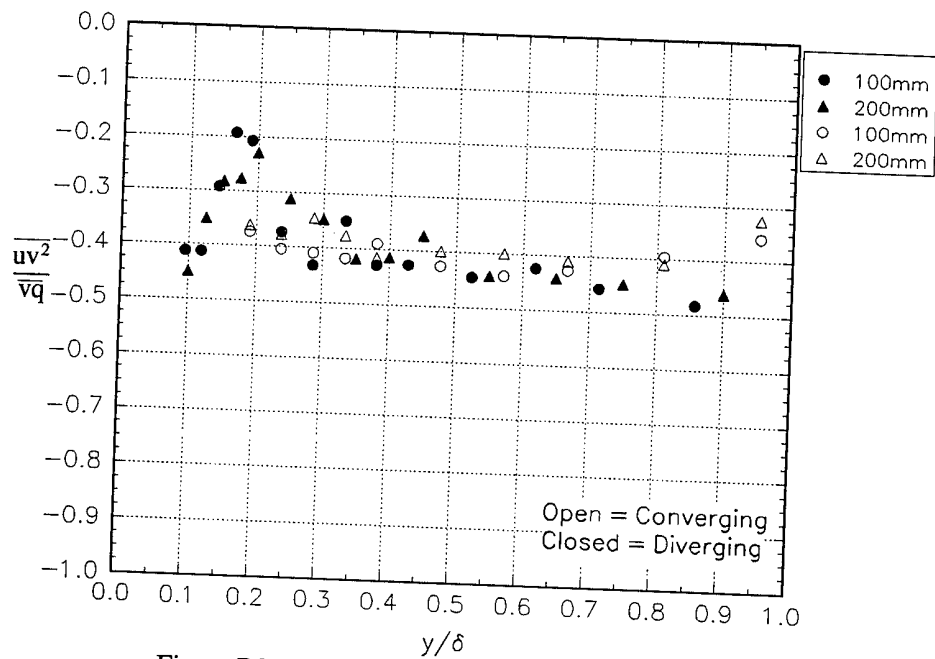


Figure B22 Triple products in wall stress coordinates at  $x = 1000$  mm with the  $z$  location is given in mm.

## APPENDIX C Additional Figures for the Data of Schwarz

This appendix covers extra figures generated from the data of Schwarz as described in chapter 2. The first set of figures will be those invariant to coordinate system choice.

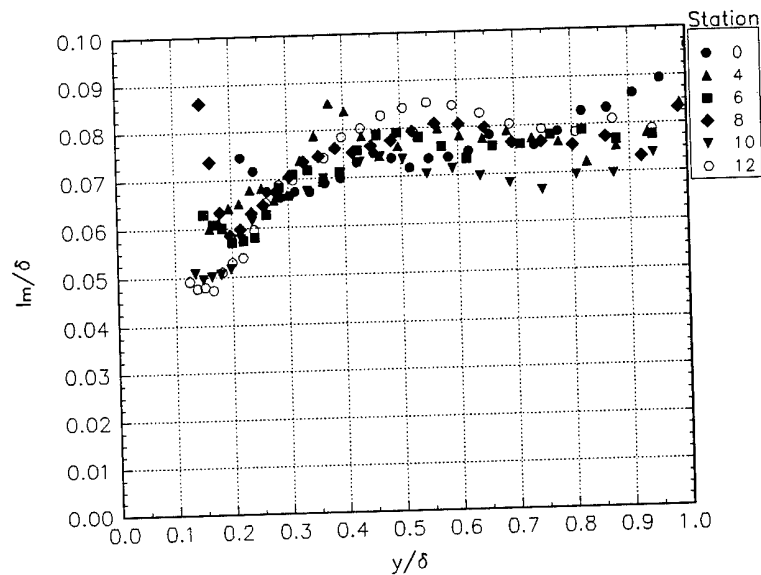


Figure C.1a The mixing length for the development region.

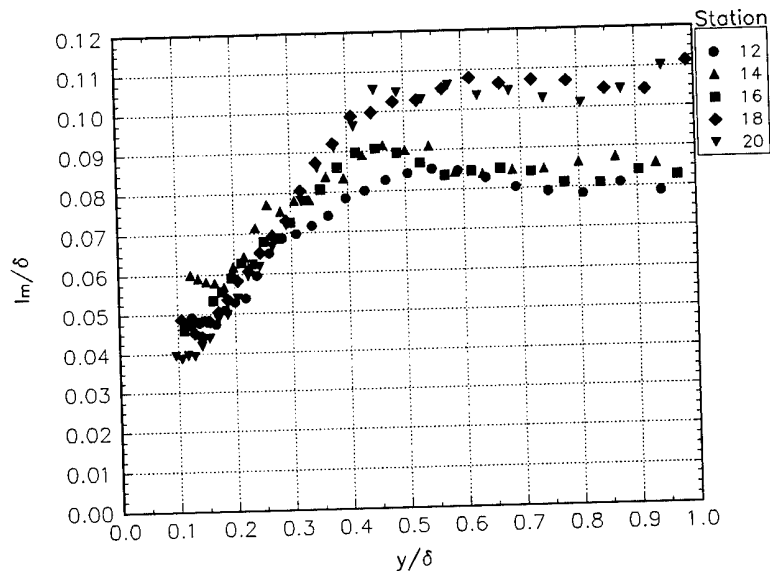


Figure C.1b The mixing length for the decay region.

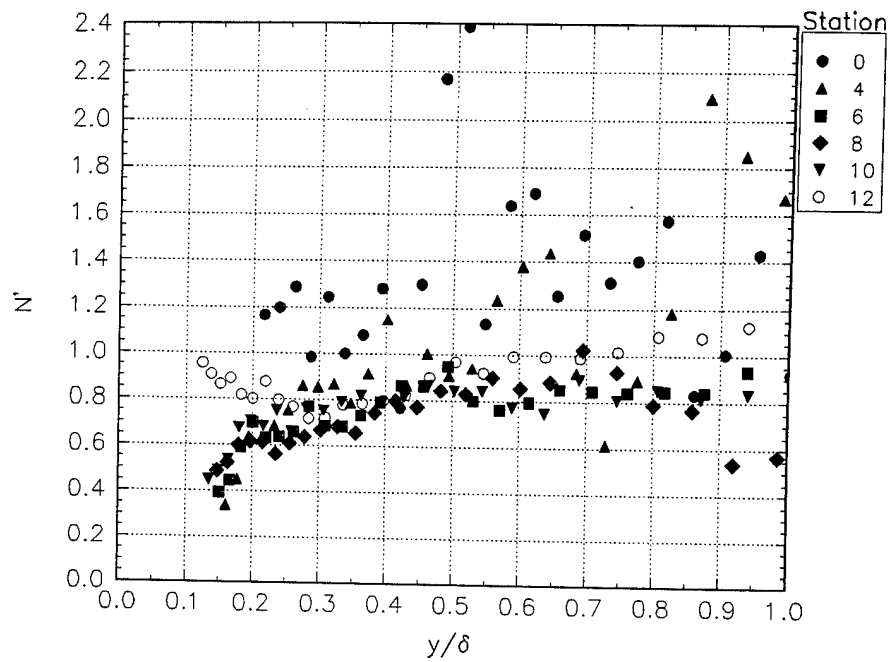


Figure C.2a Rotta's T parameter for the development region.

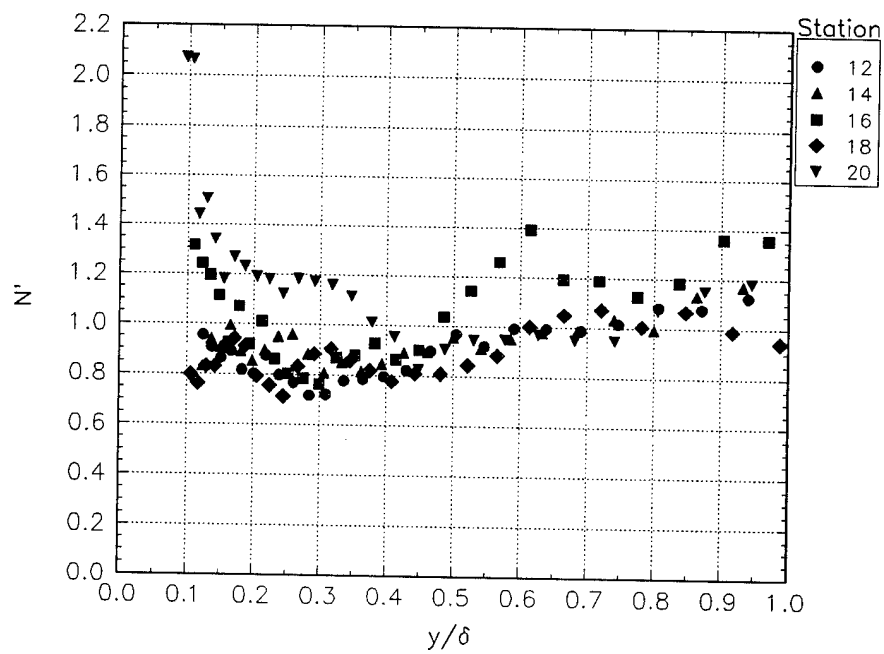


Figure C.2b Rotta's T parameter for the decay region.

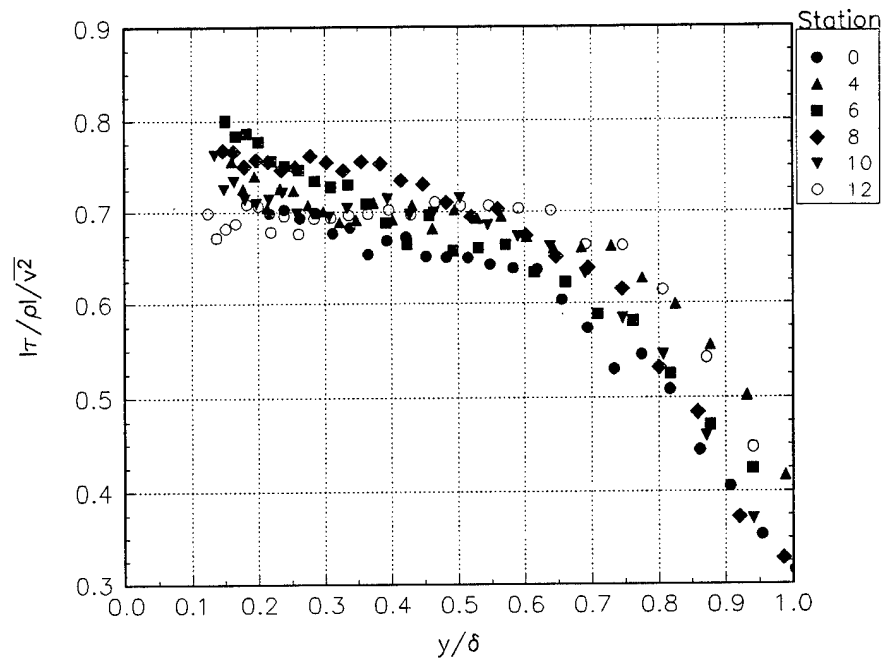


Figure C.3a The 1/S parameter for the development region.

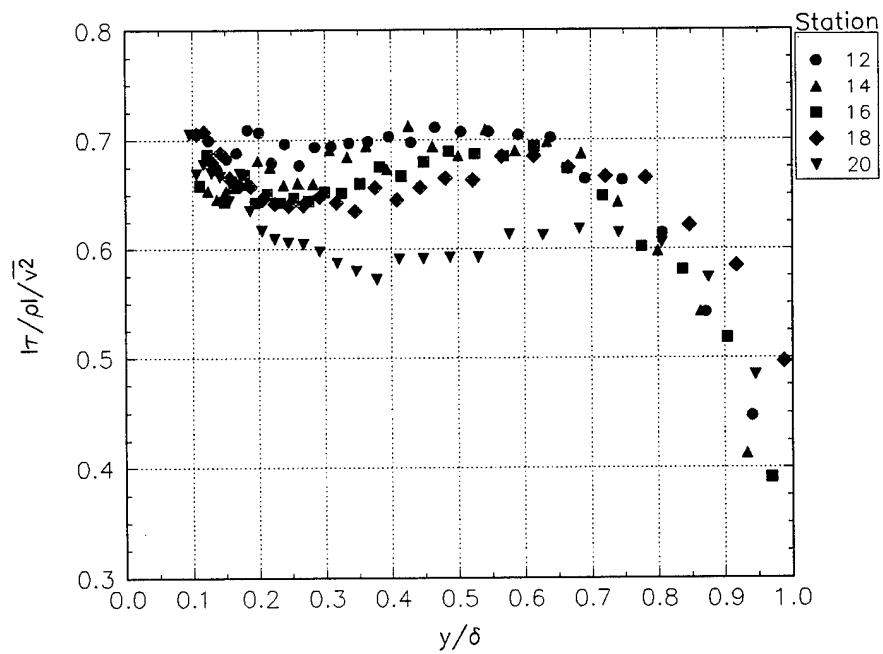


Figure C.3b The 1/S parameter for the decay region.

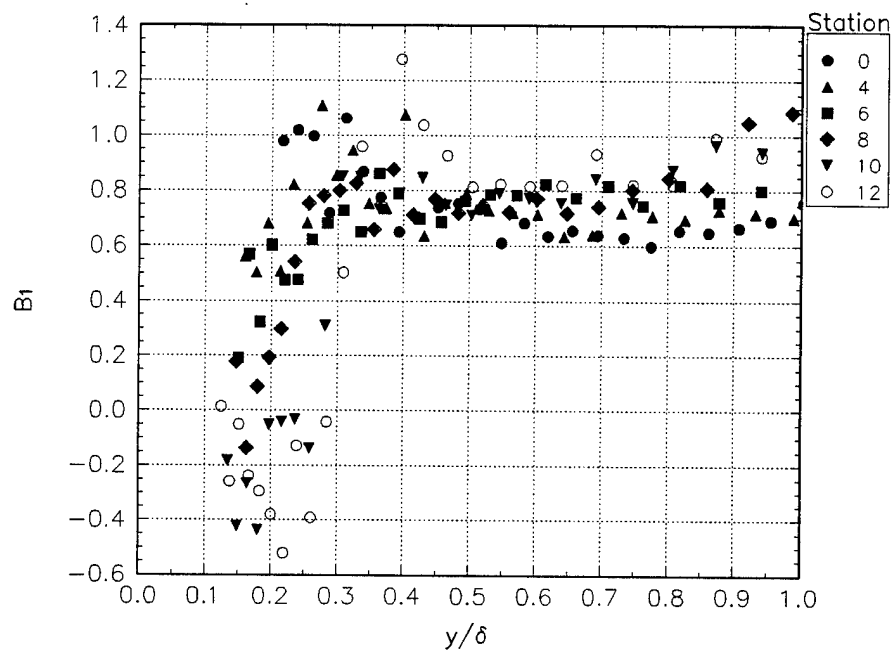


Figure C.4a The  $B_1$  parameter for the development region.

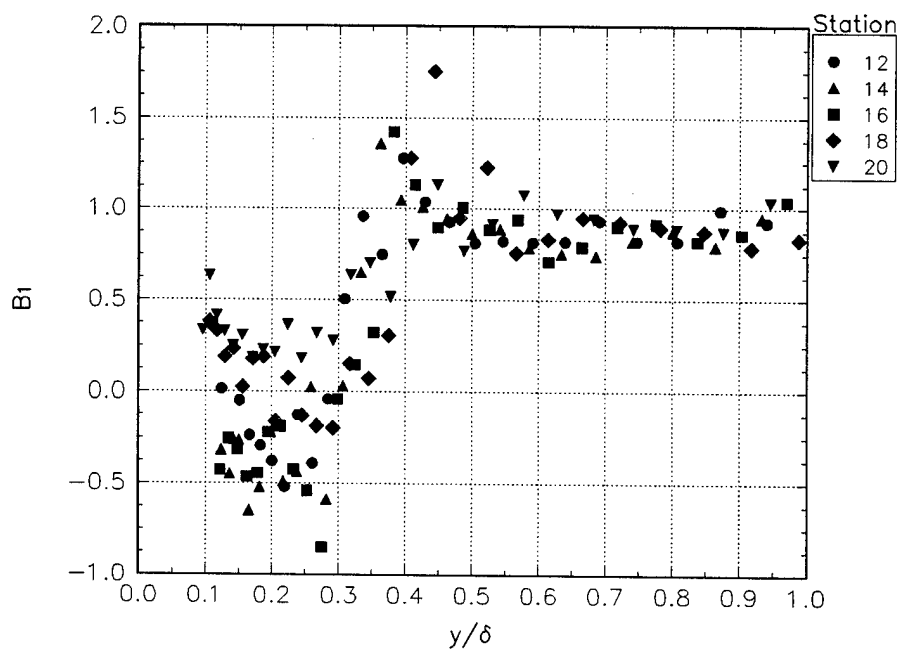


Figure C.4b The  $B_1$  parameter for the decay region.



The next set of plots are for data rotated to the free-stream coordinate system.

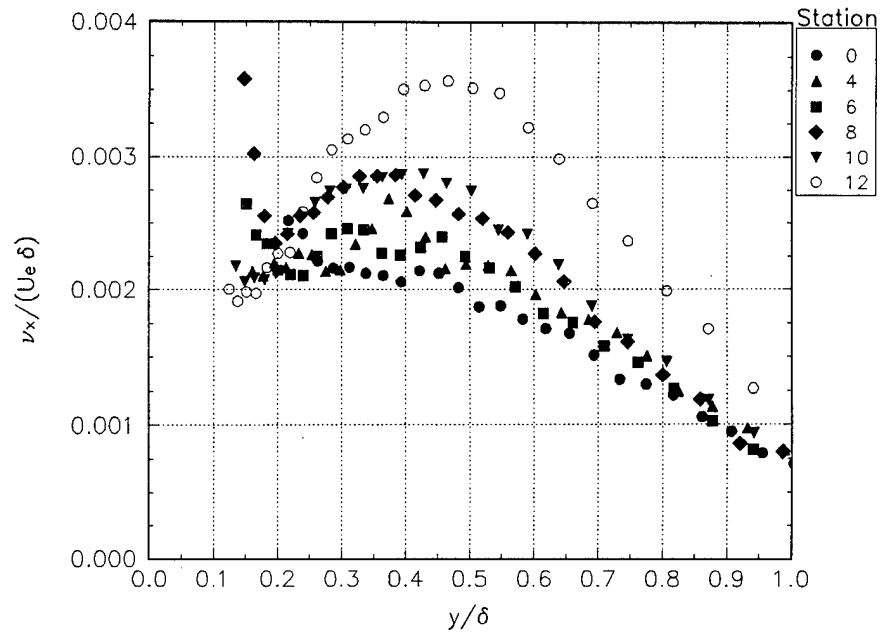


Figure C.5a The x-direction eddy viscosity for the development region.

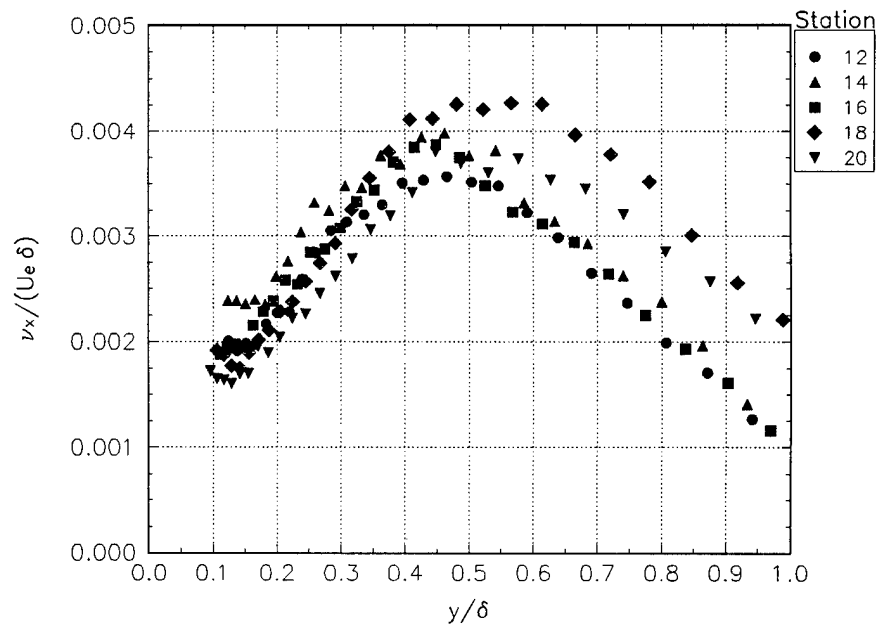


Figure C.5b The x-direction eddy viscosity for the decay region.

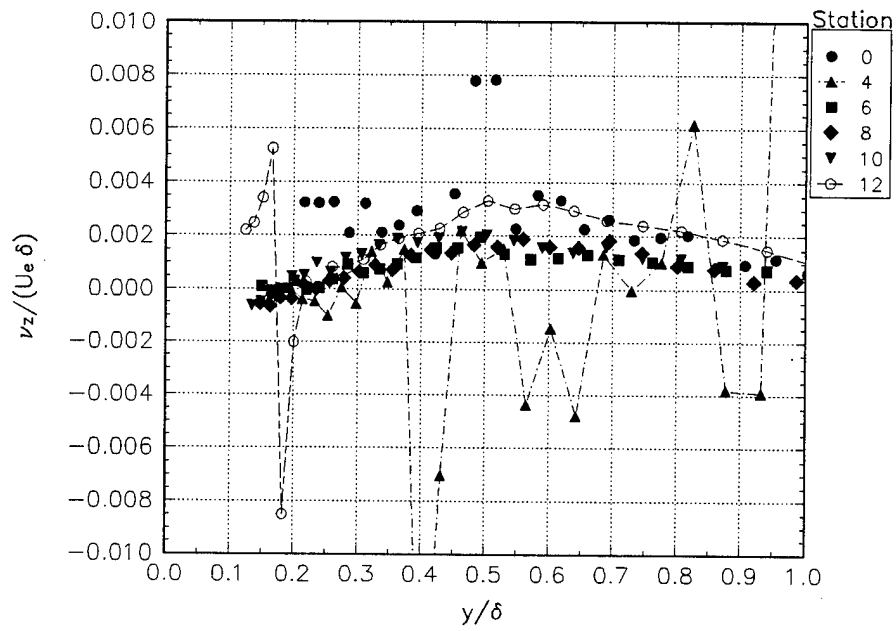


Figure C.6.a The z-direction eddy viscosity for the development region.

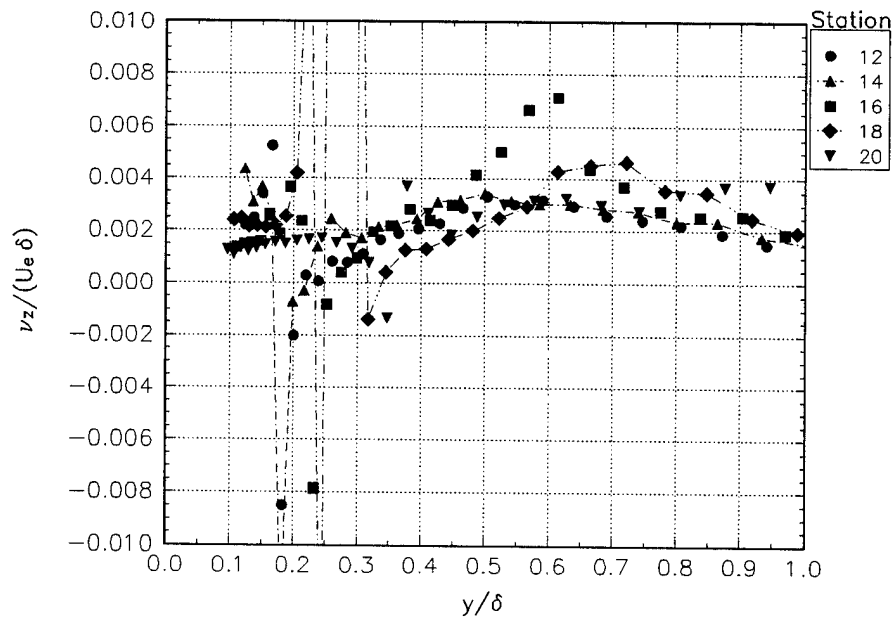


Figure C.6b The z-direction eddy viscosity for the decay region.

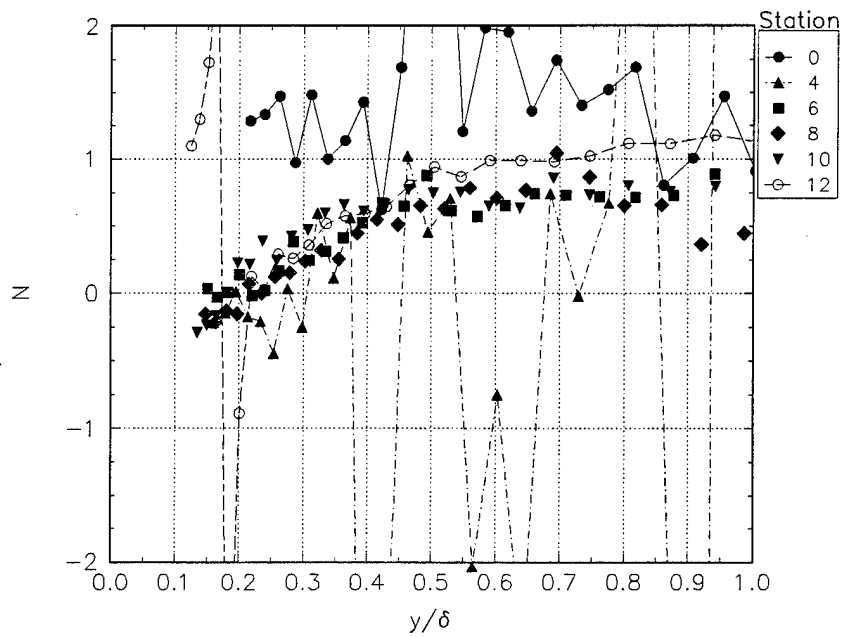


Figure C.7a The eddy viscosity ratio for the development region.

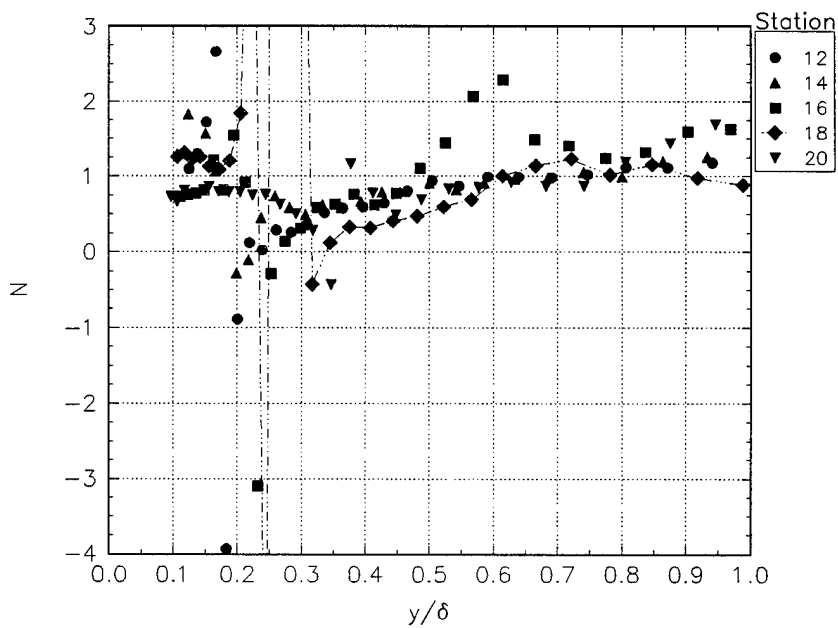


Figure C.7b The anisotropy parameter for the decay region.

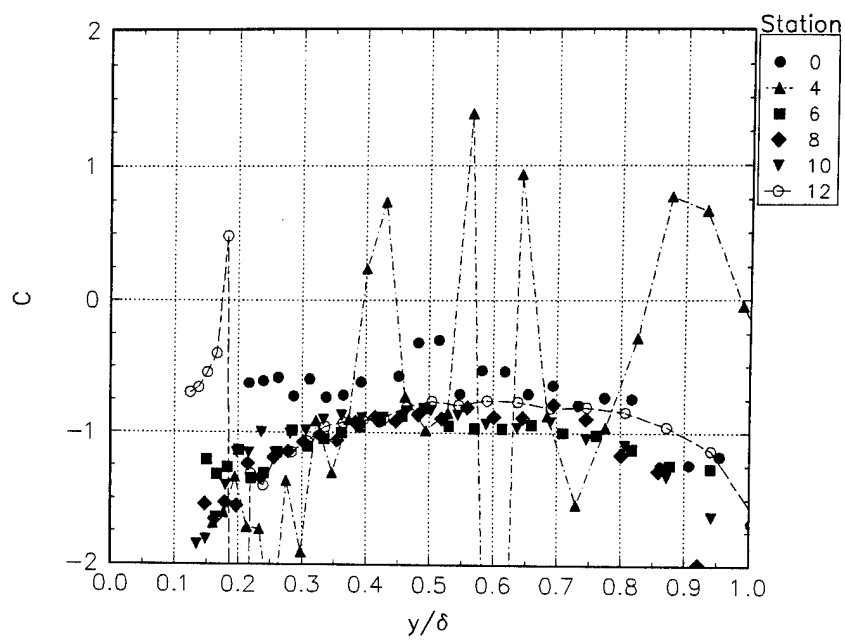


Figure C.8a The C parameter for the development region.

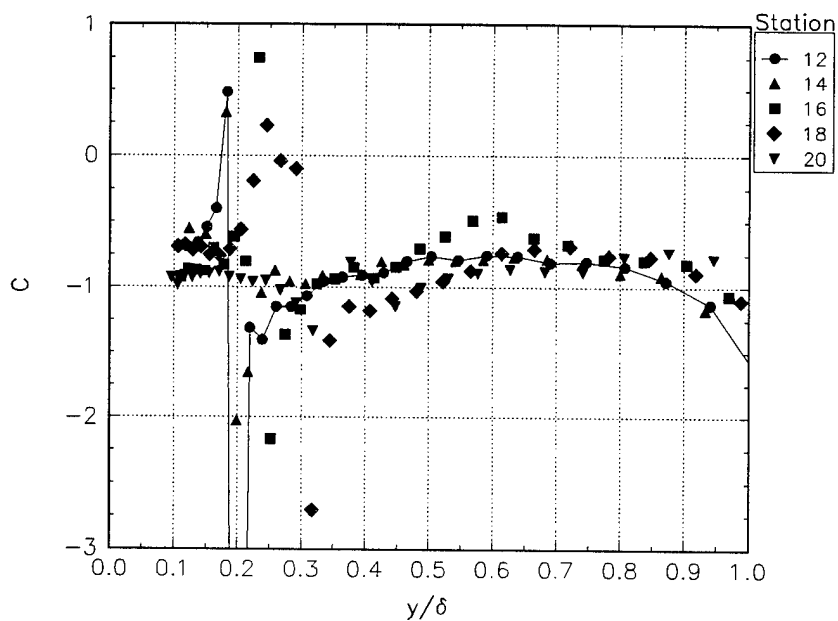


Figure C.8b The C parameter for the decay region.

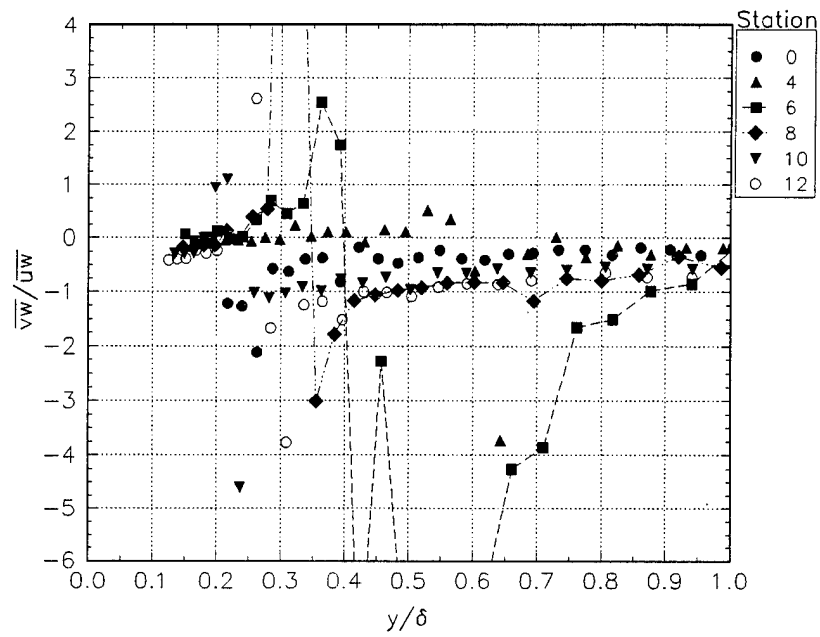


Figure C.9a Reynolds shear stress ratio for the development region.

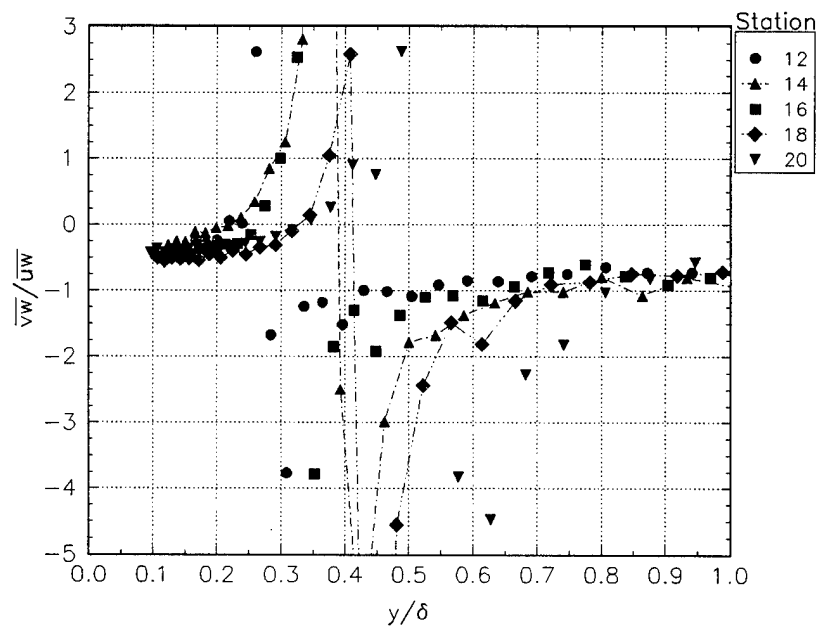


Figure C.9b Reynolds shear stress ratio for the decay region.

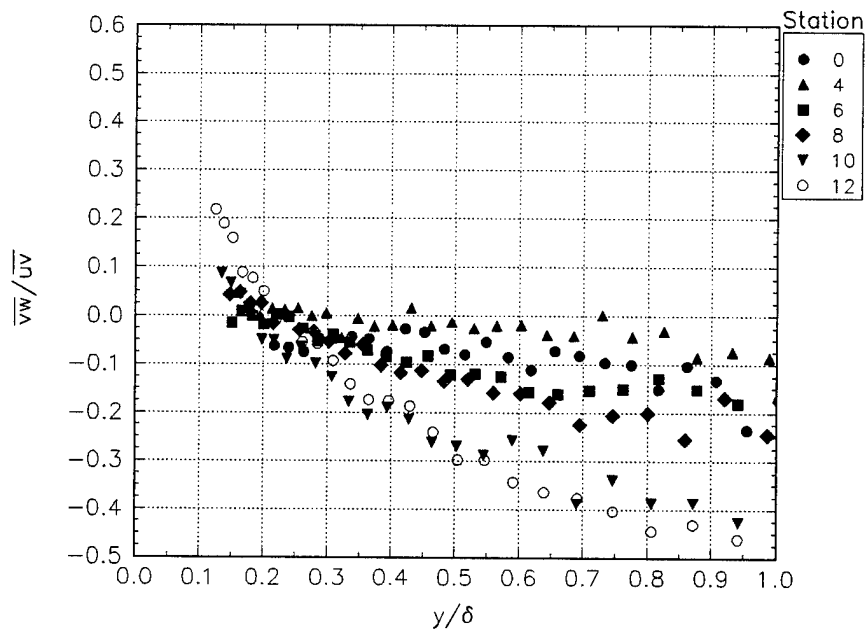


Figure C.10a Reynolds shear stress ratio for the development region.

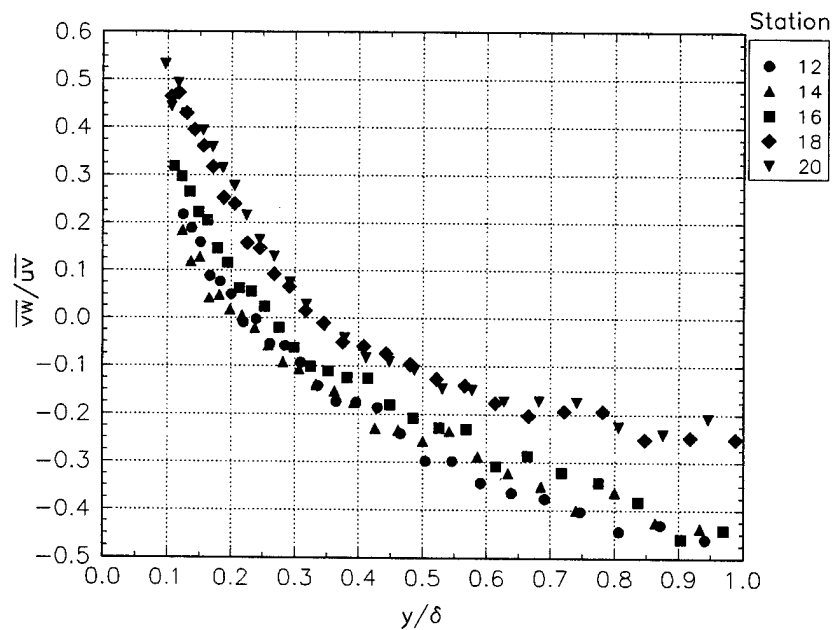


Figure C.10b Reynolds shear stress ratio for the decay region.

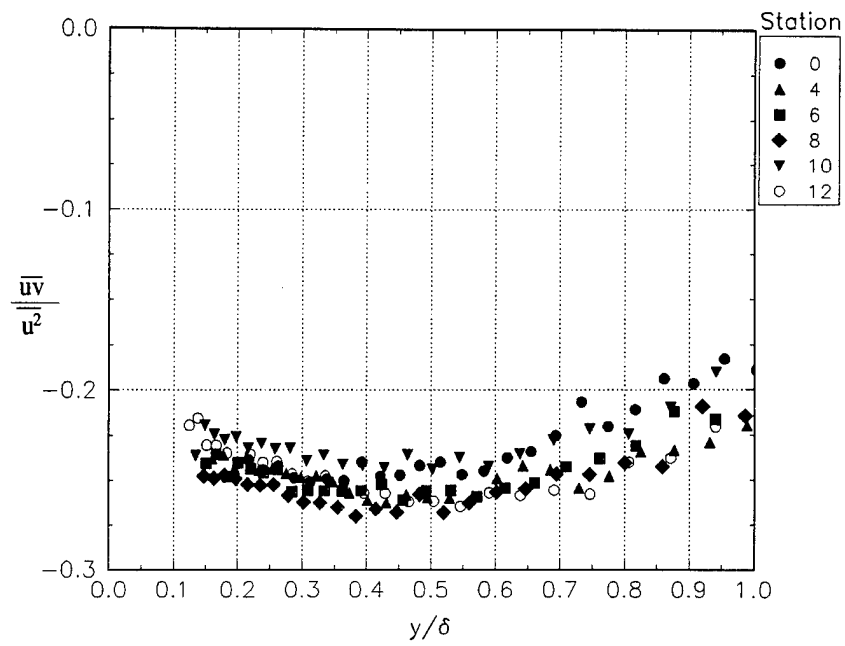


Figure C.11a Reynolds stress relationship for the development region.

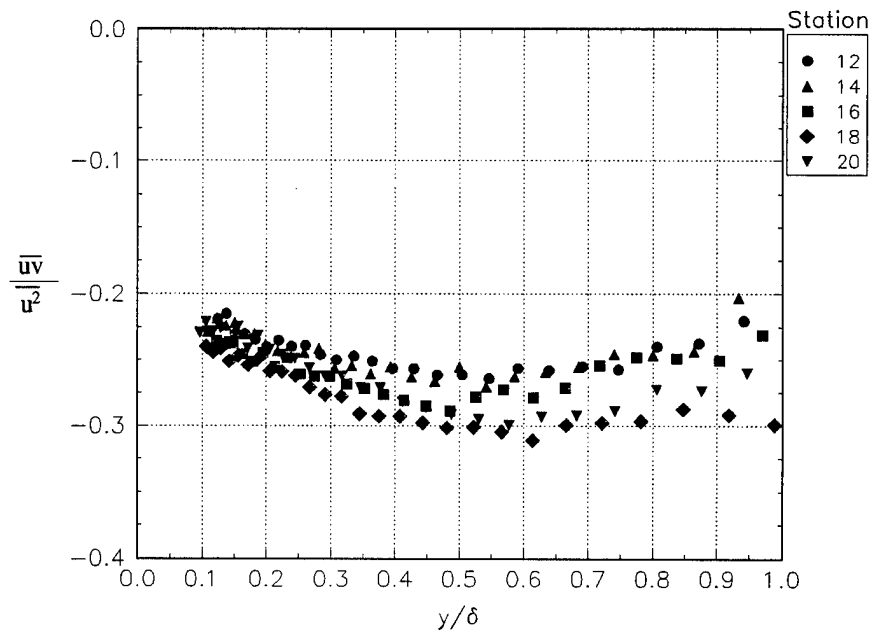


Figure C.11b Reynolds stress relationship for the decay region.

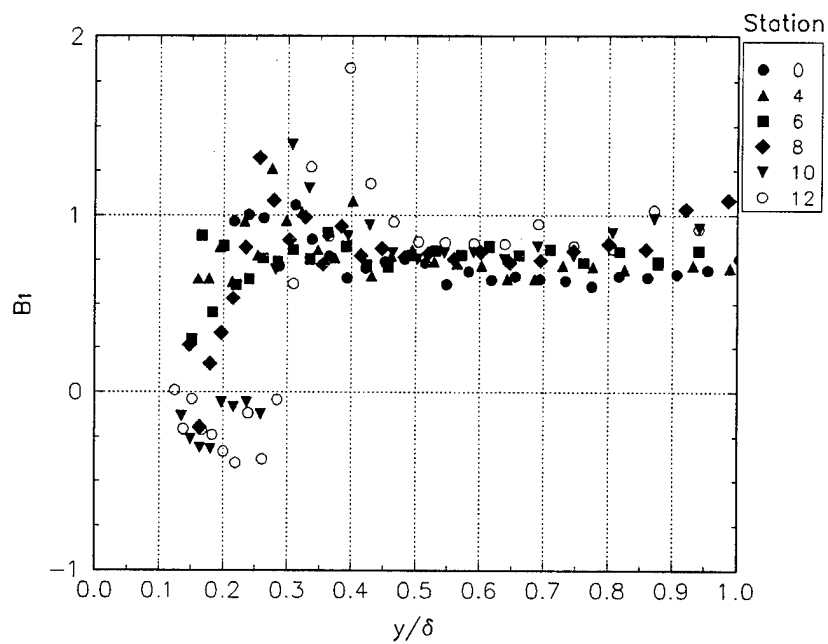


Figure C.12a The  $B_1$  parameter for the development region.

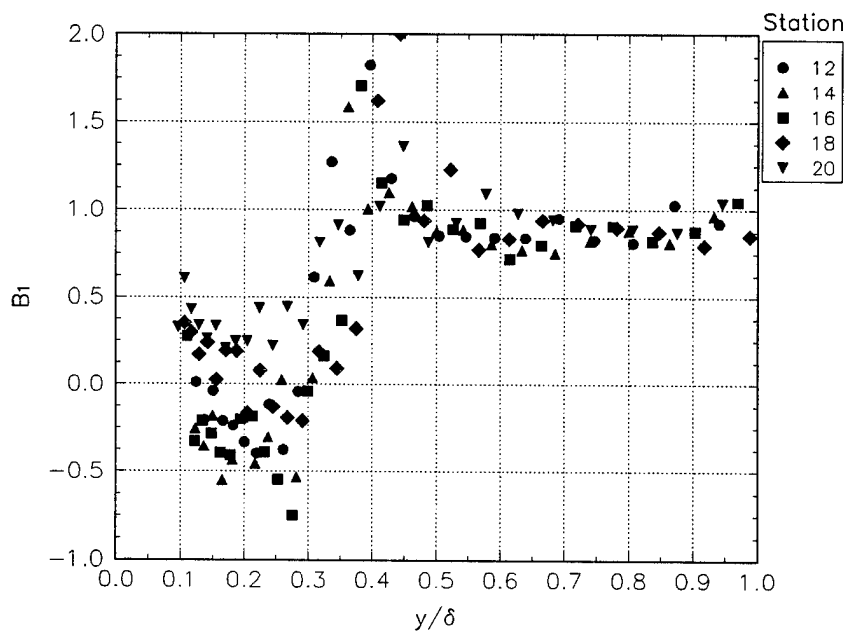


Figure C.12b The  $B_1$  parameter for the decay region.



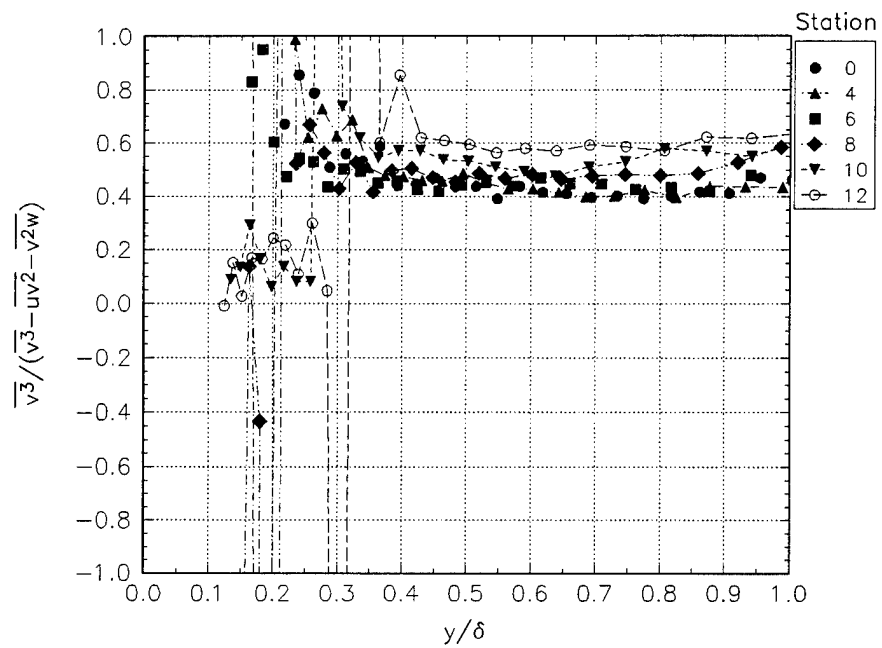


Figure C.13a Triple product relationships for the development region.

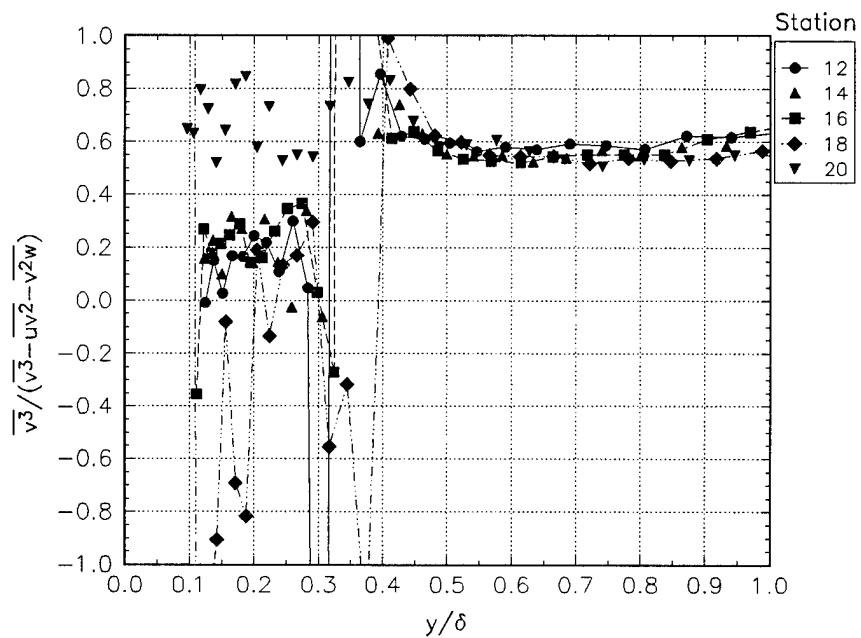


Figure C.13b Triple product relationships for the decay region.

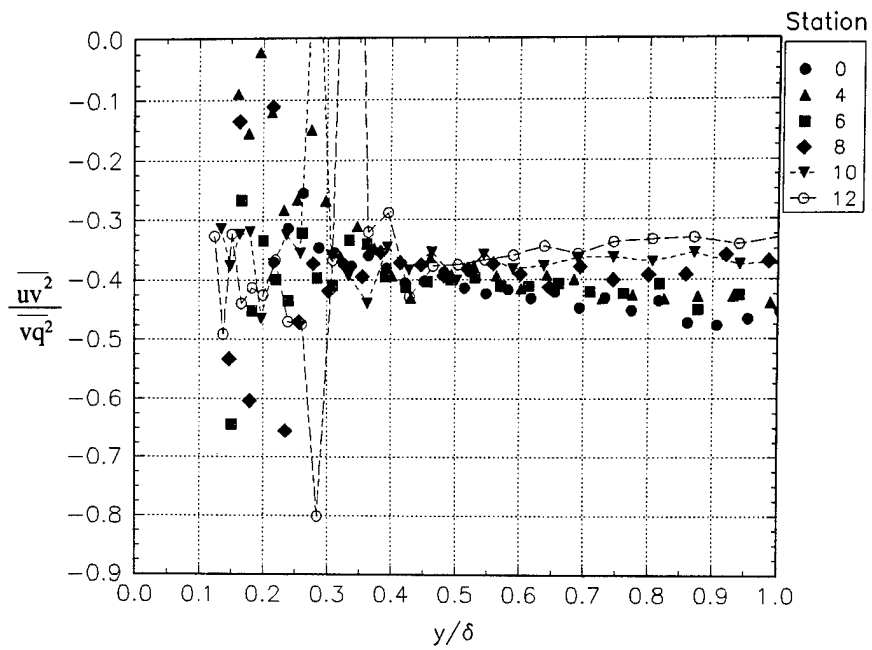


Figure C.14a Triple product relationships for the development region.

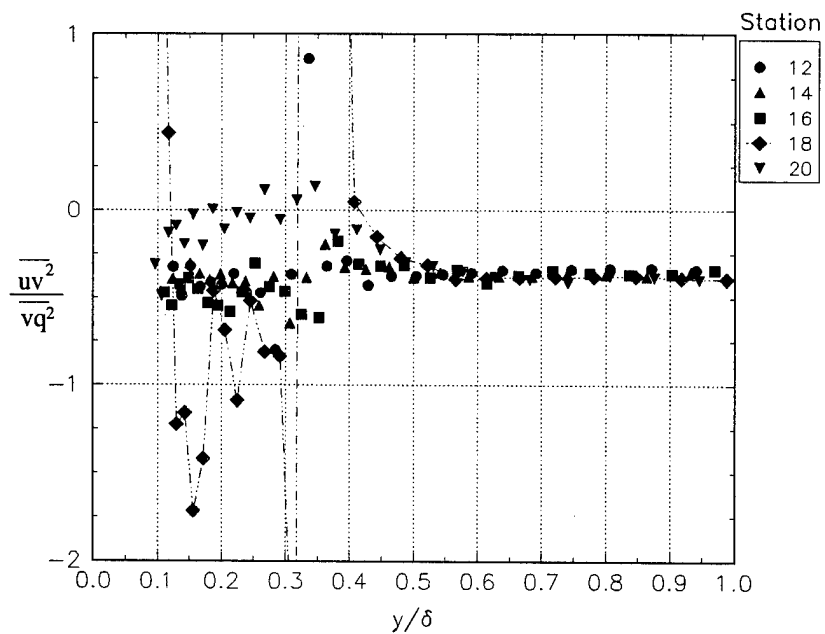


Figure C.14b Triple product relationships for the decay region.

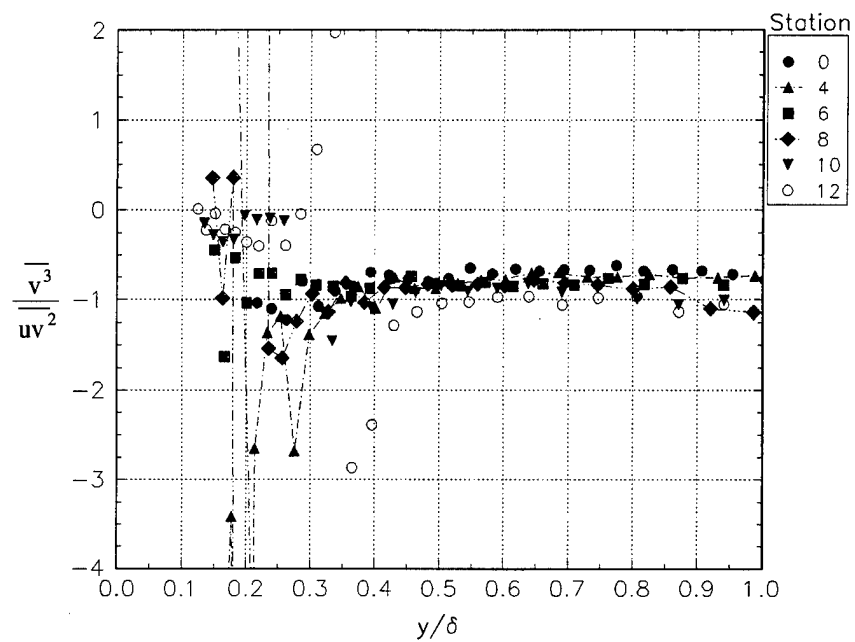


Figure C.15a Triple product relationships for the development region.

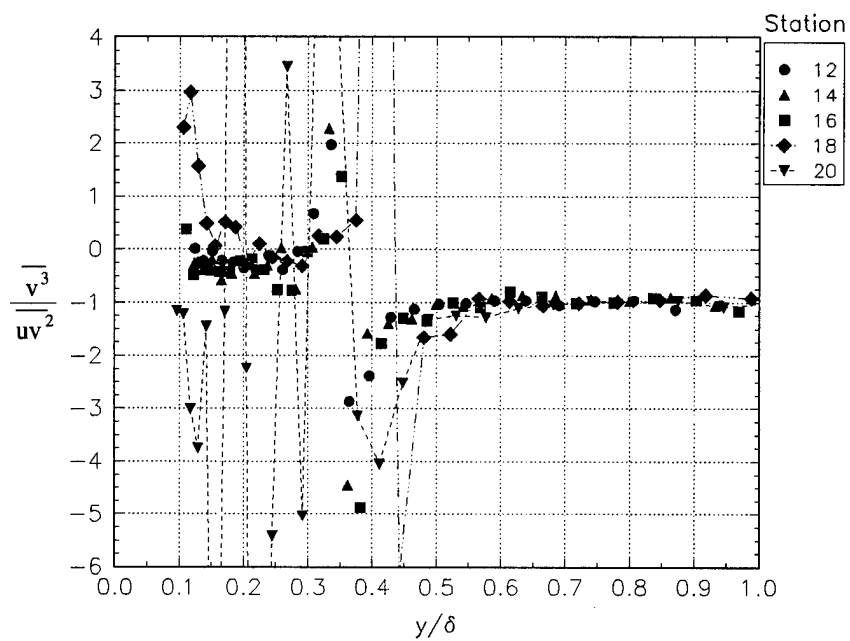


Figure C.15b Triple product relationships for the decay region.

The remainder of the figures in this appendix are in wall-stress coordinates.

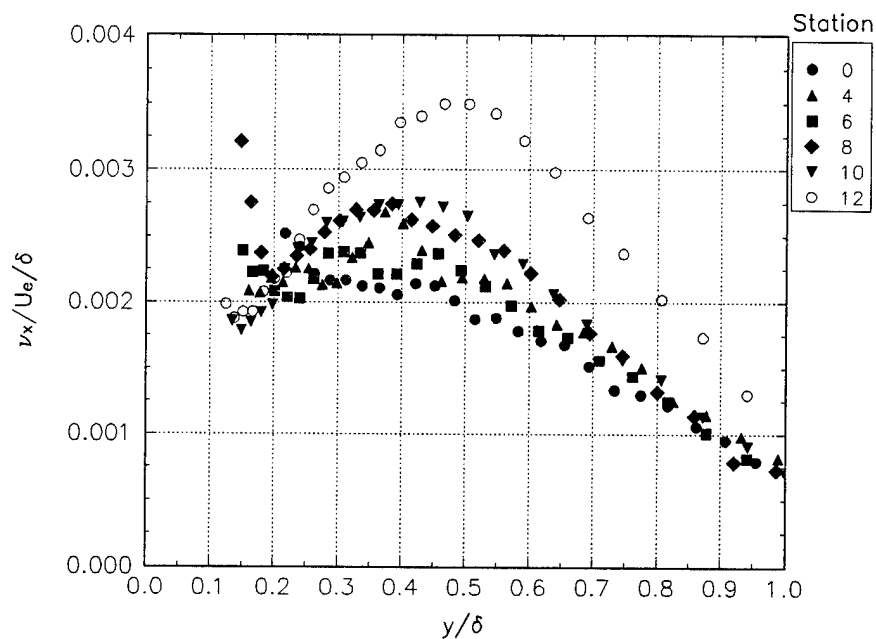


Figure C.16a X-direction eddy viscosity for the development region.

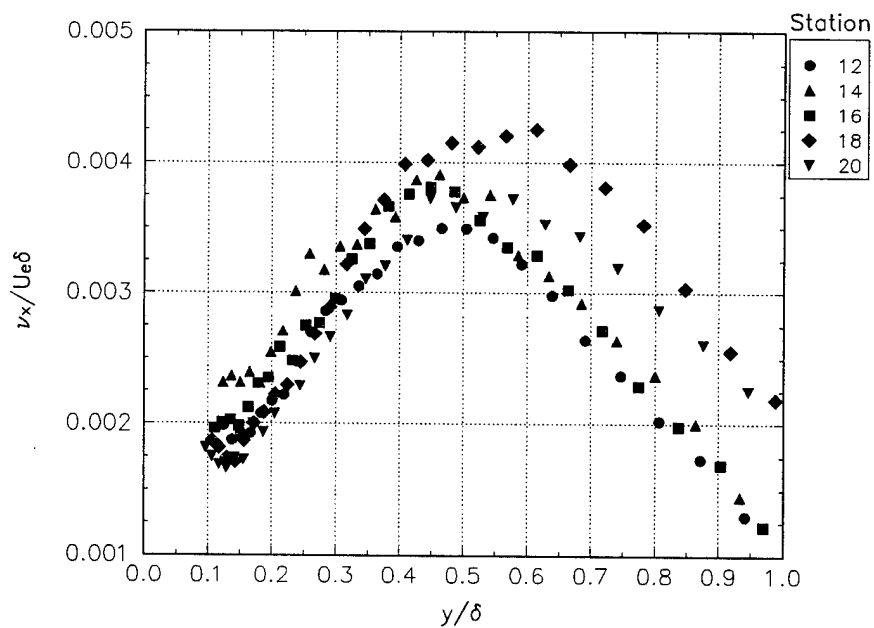


Figure C.16b X-direction eddy viscosity for the decay region.

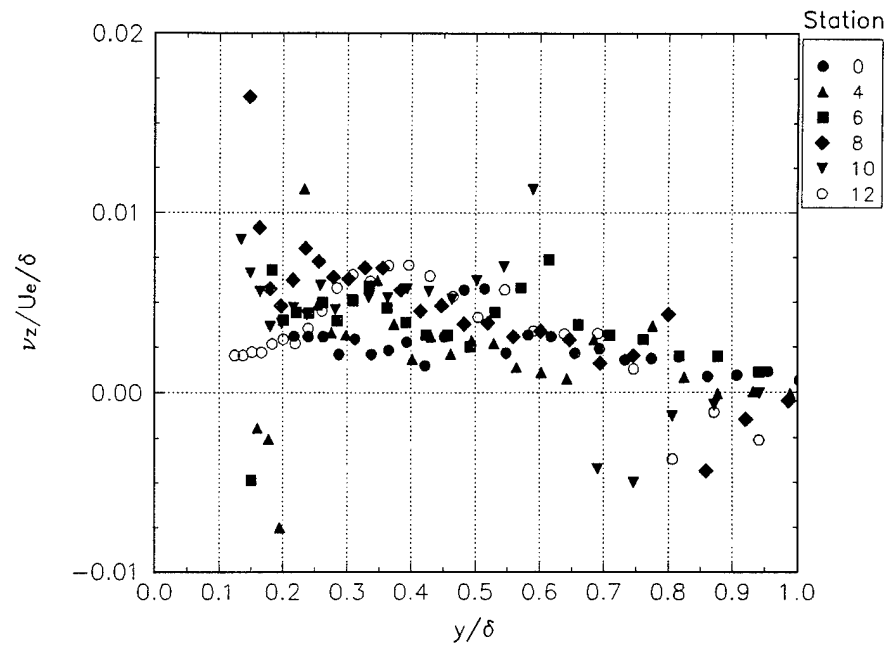


Figure C.17a The z-direction eddy viscosity for the development region.

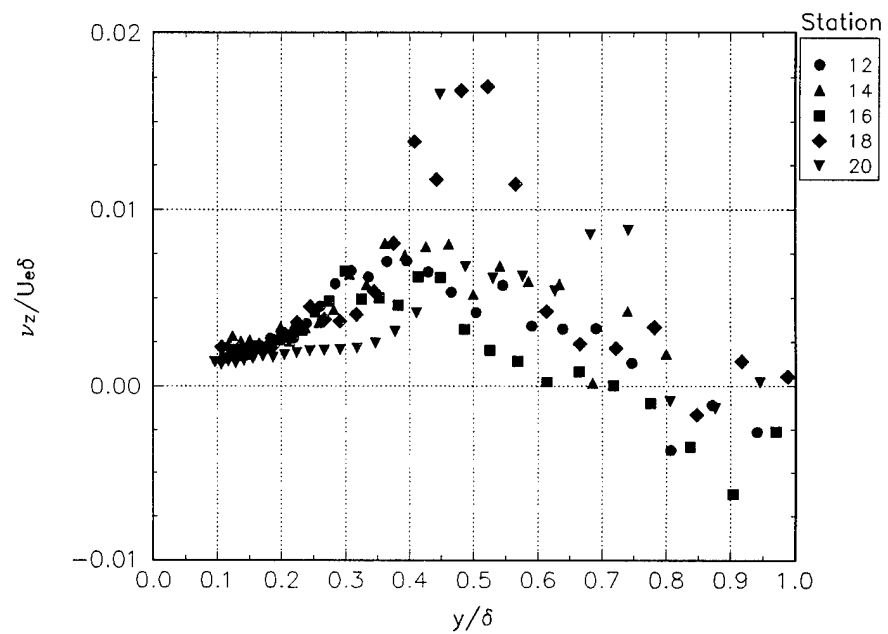


Figure C.17b The z-direction eddy viscosity for the decay region.

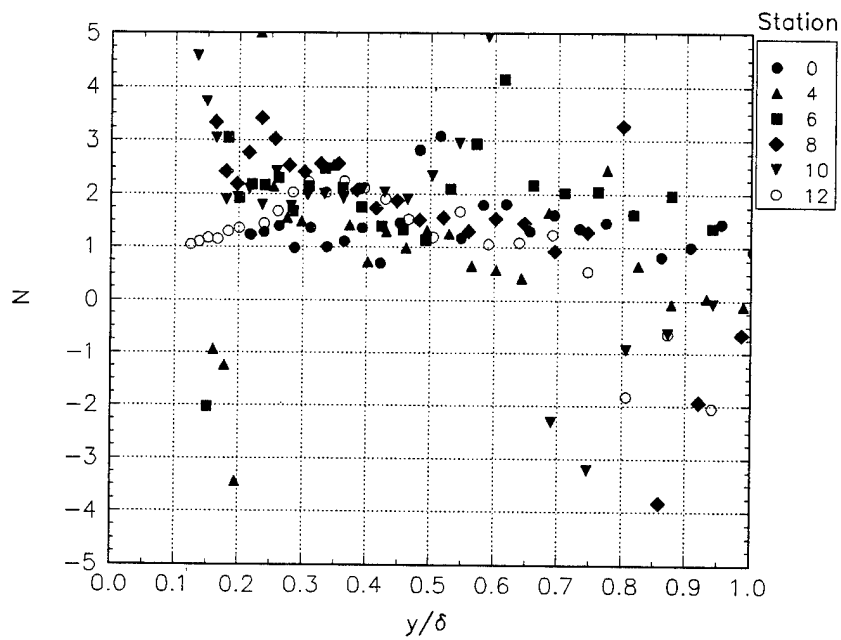


Figure C.18a The anisotropy parameter for the development region.

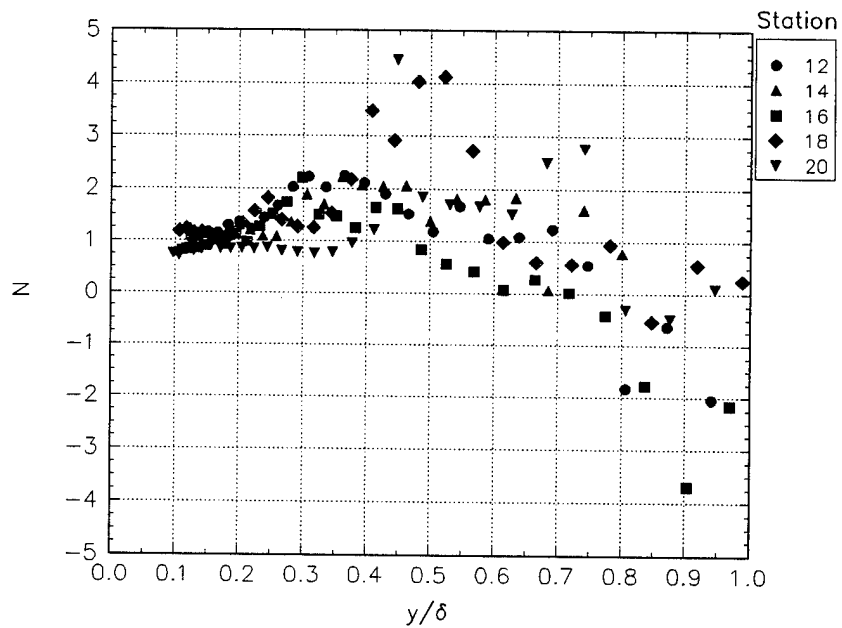


Figure C.18b The anisotropy parameter for the decay region.

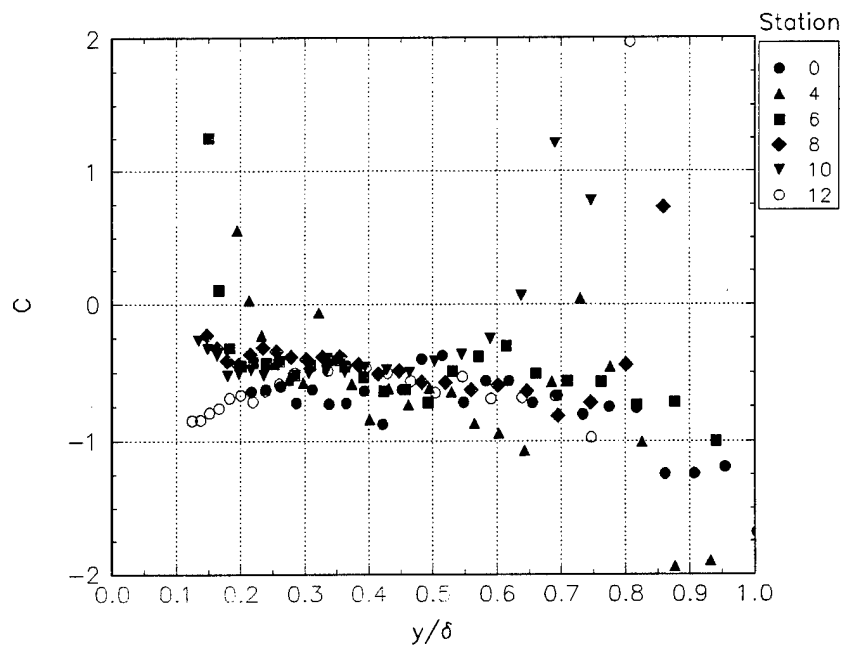


Figure C.19a The C parameter for the development region.

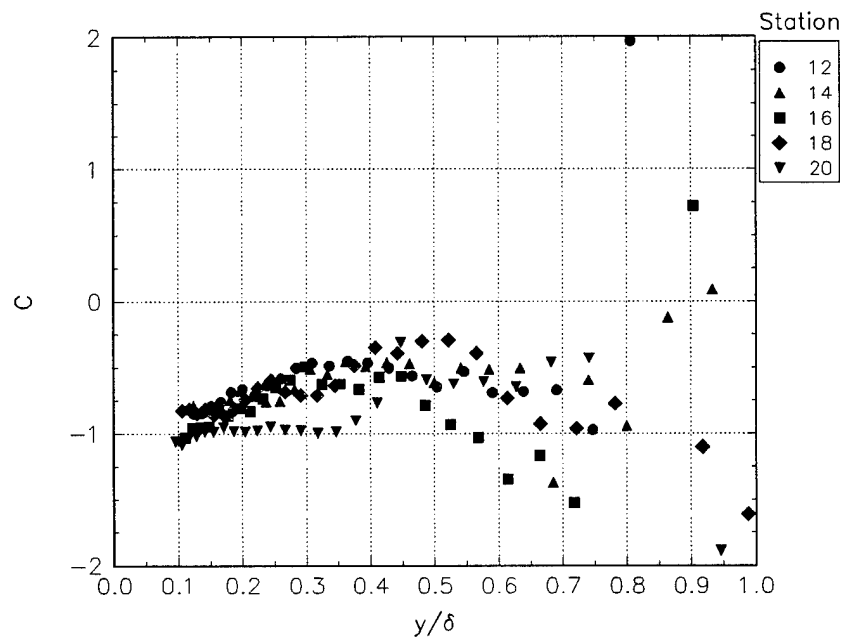


Figure C.19b The C parameter for the decay region.

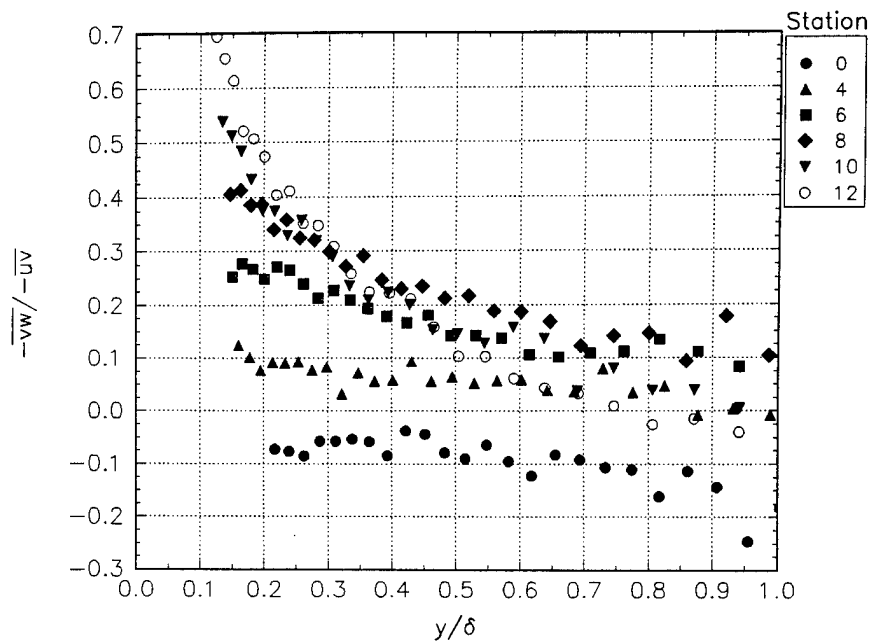


Figure C.20a Reynolds stress ratio for the development region.

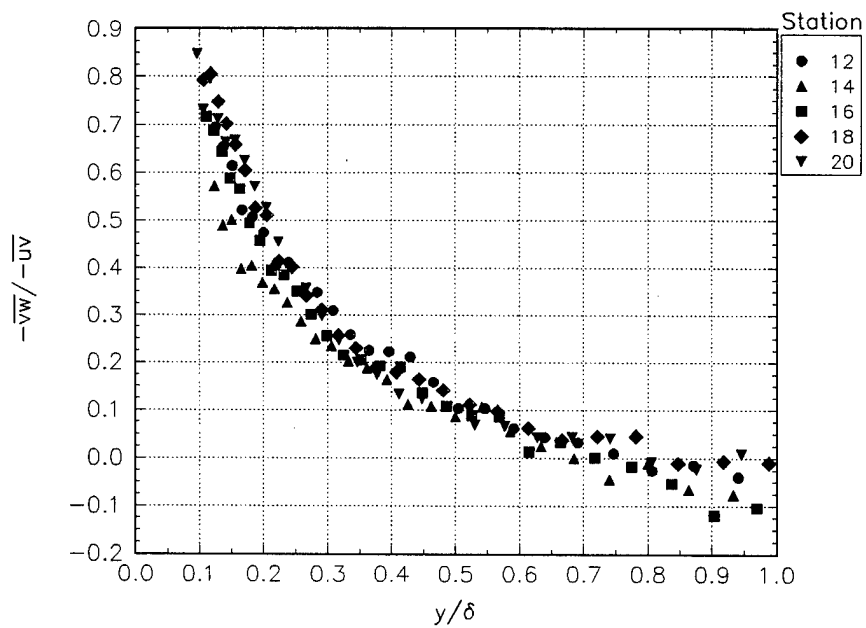


Figure C.20b Reynolds stress ratio for the decay region.



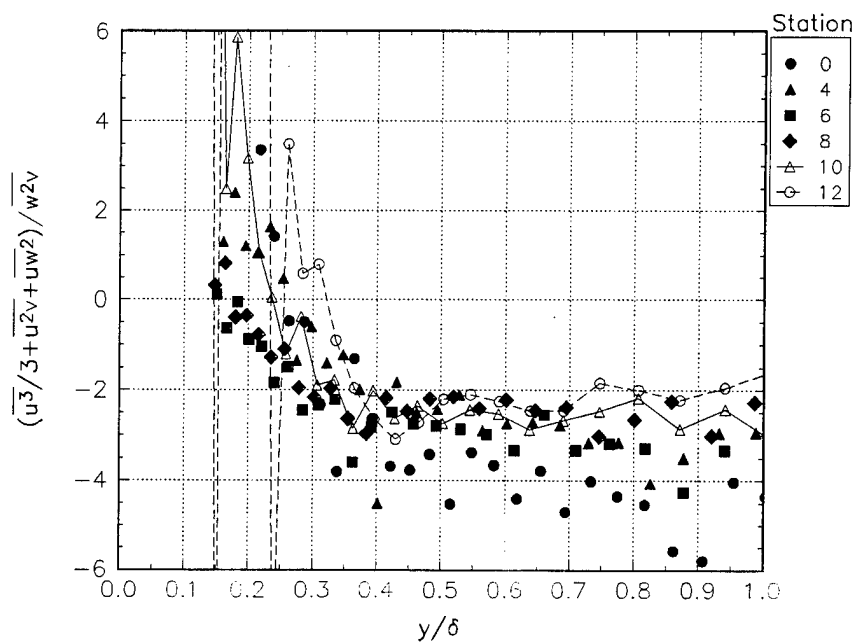


Figure C.21a Triple product relationship for the development region.

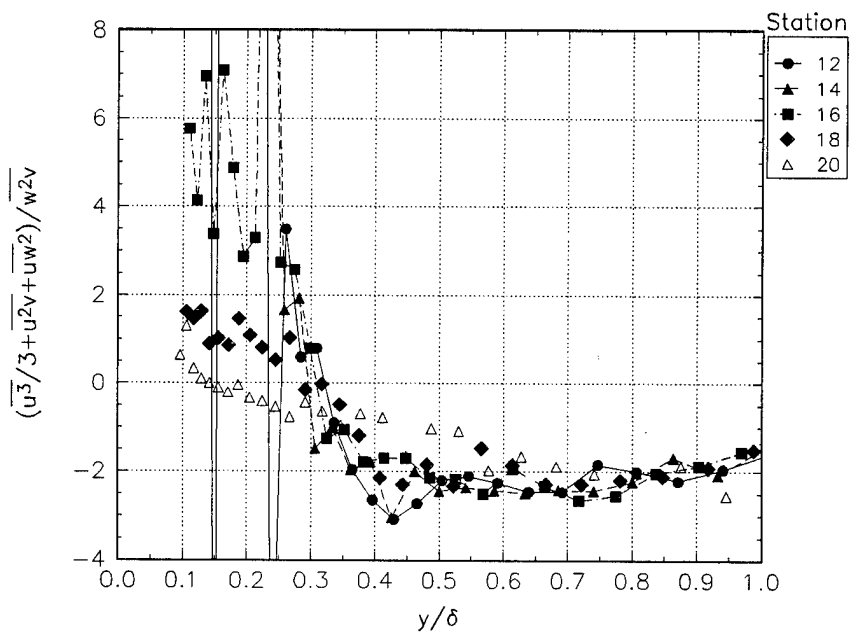


Figure C.21b Triple product relationship for the decay region.

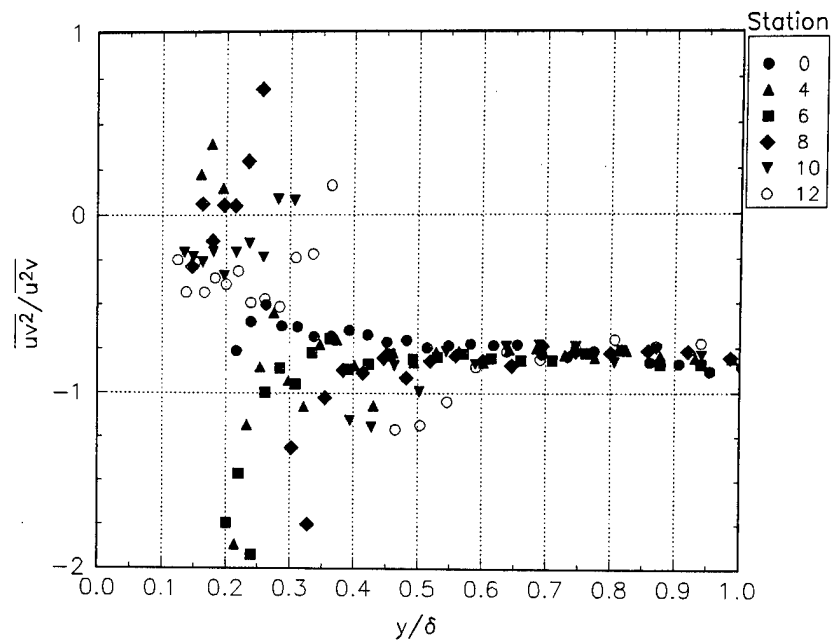


Figure C.22a Triple product ratio for the development region.

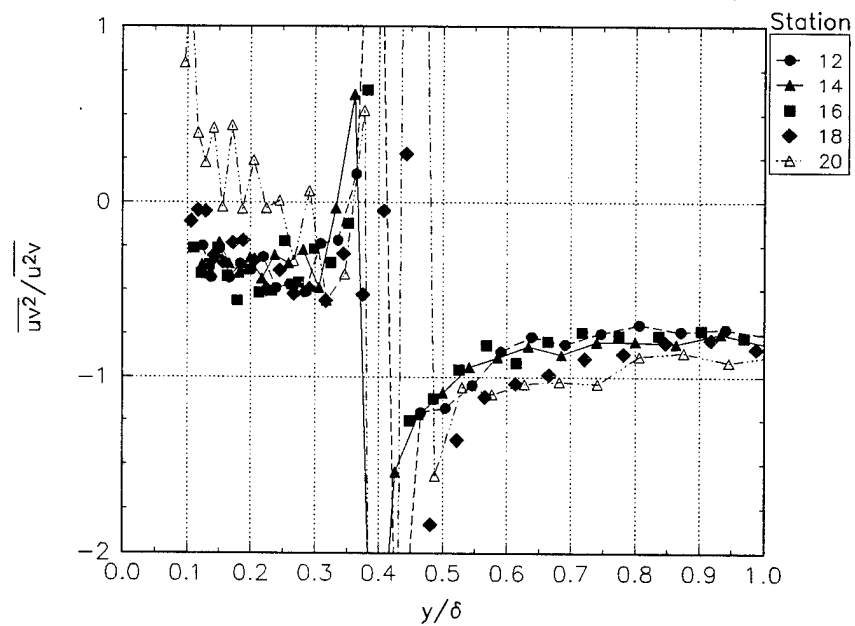


Figure C.22b Triple product ratio for the decay region.

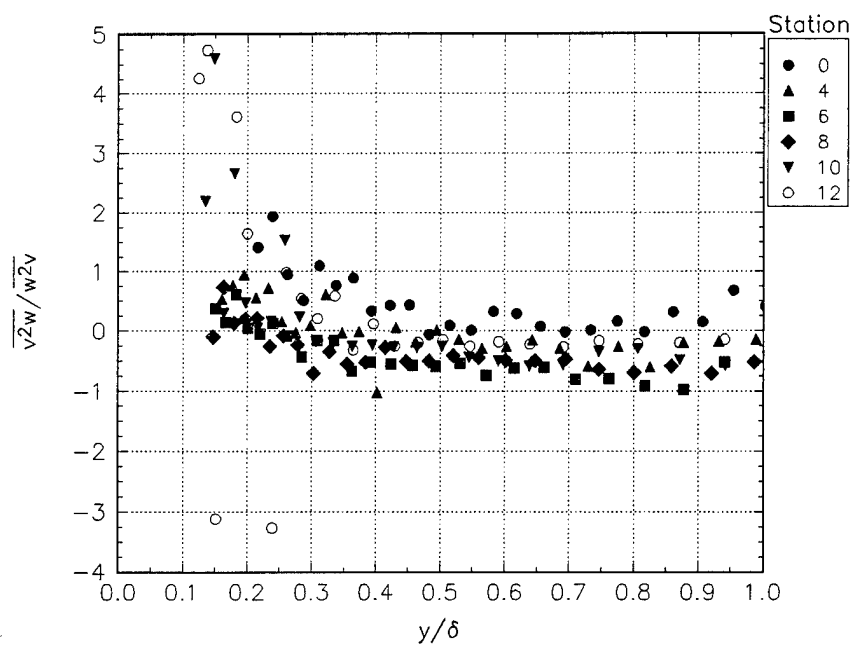


Figure C.23a Triple product ratio for the development region.

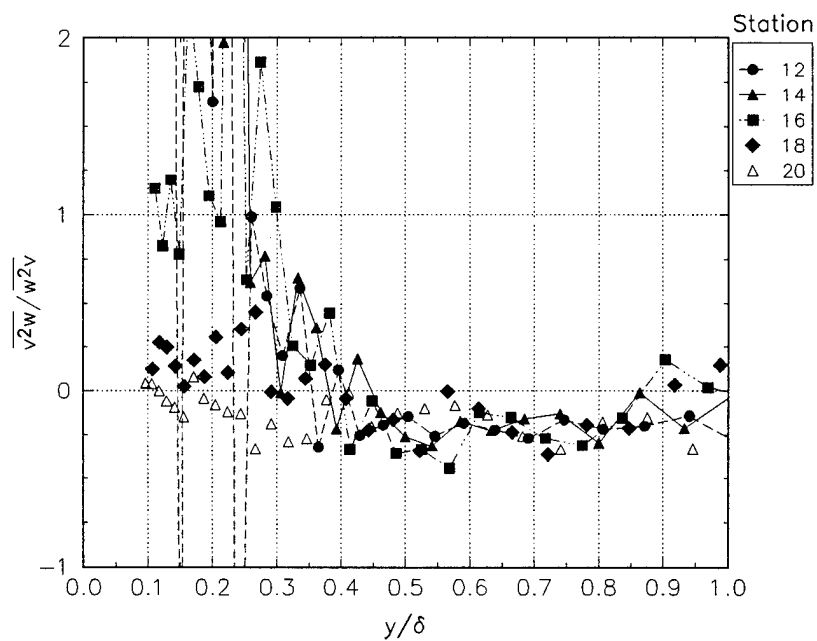


Figure C.23b Triple product ratio for the decay region.

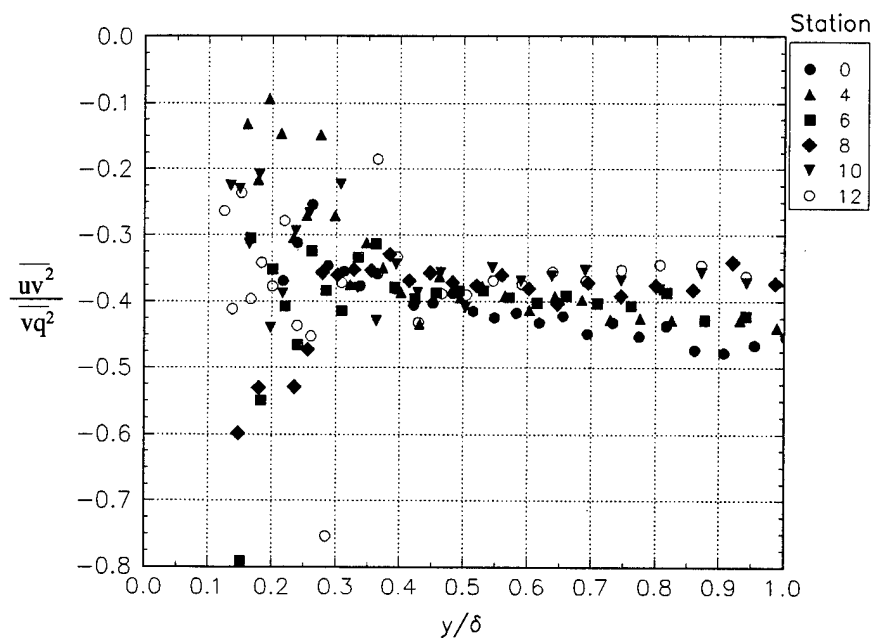


Figure C.24a Triple product relationship for the development region.

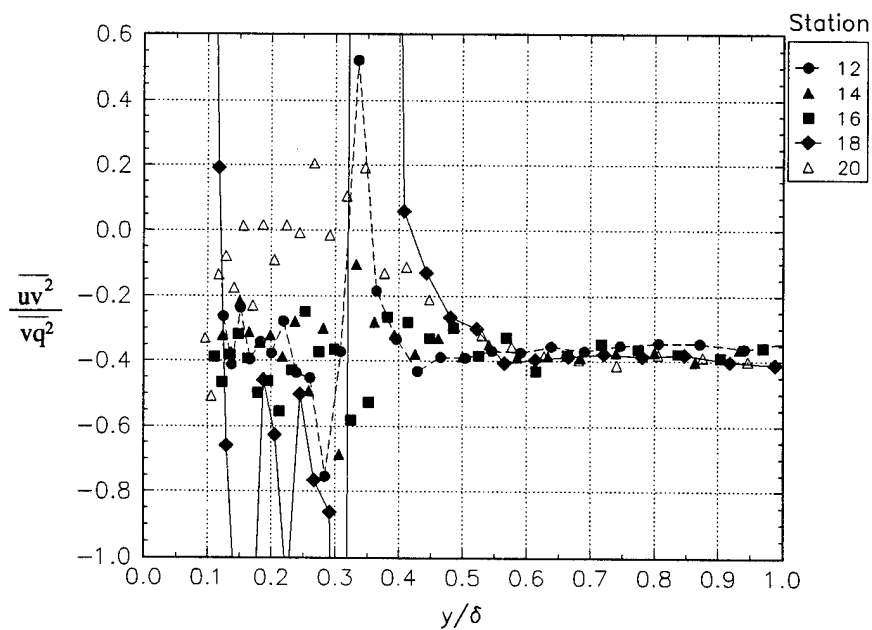


Figure C.24b Triple product relationship for the decay region.

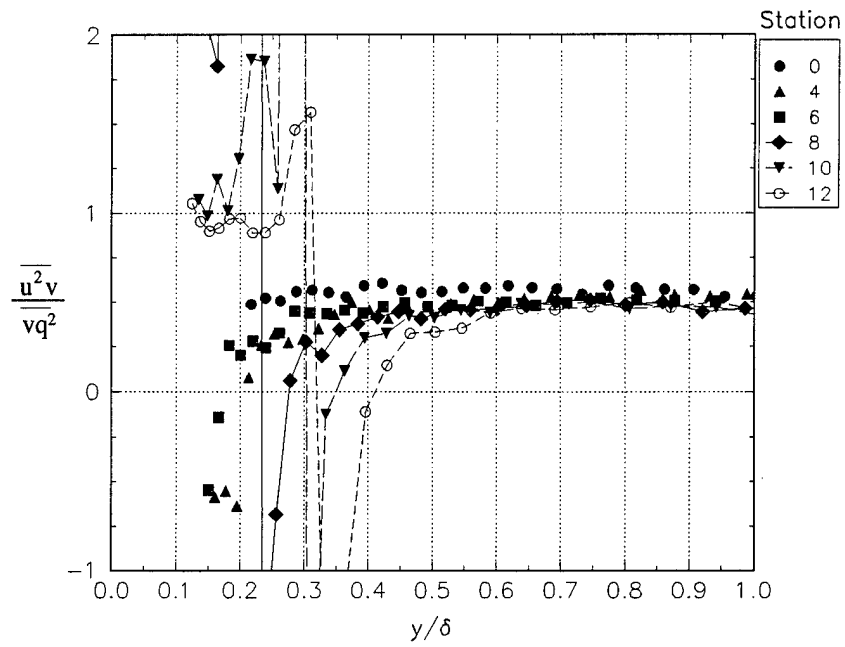


Figure C.25a Triple product relationship for the development region.

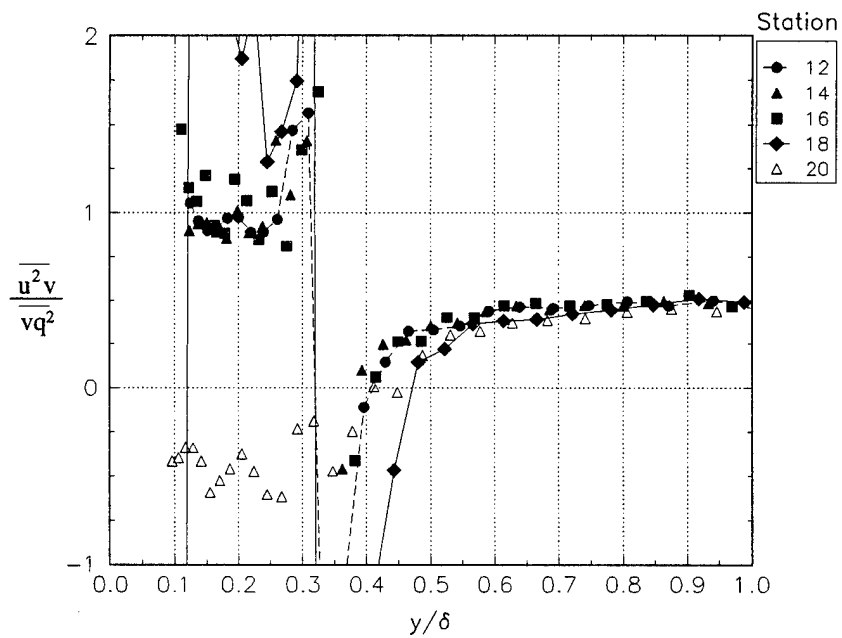


Figure C.25b Triple product relationship for the decay region.

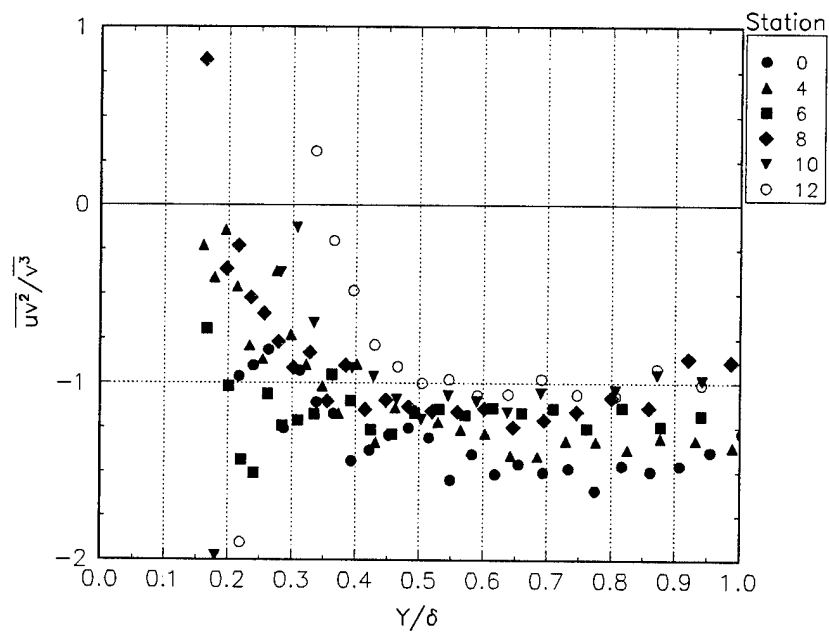


Figure C.26a Triple product ratio for the development region.

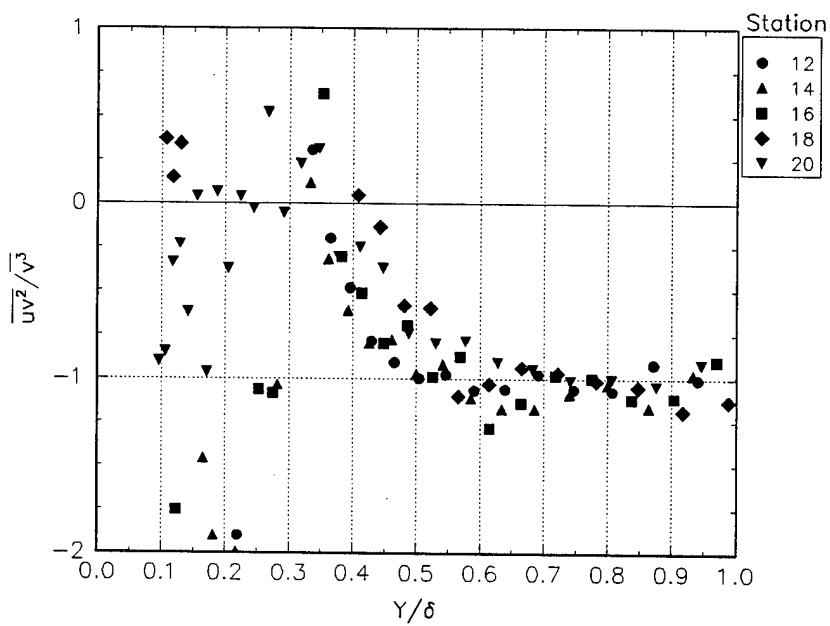


Figure C.26b Triple product ratio for the decay region.

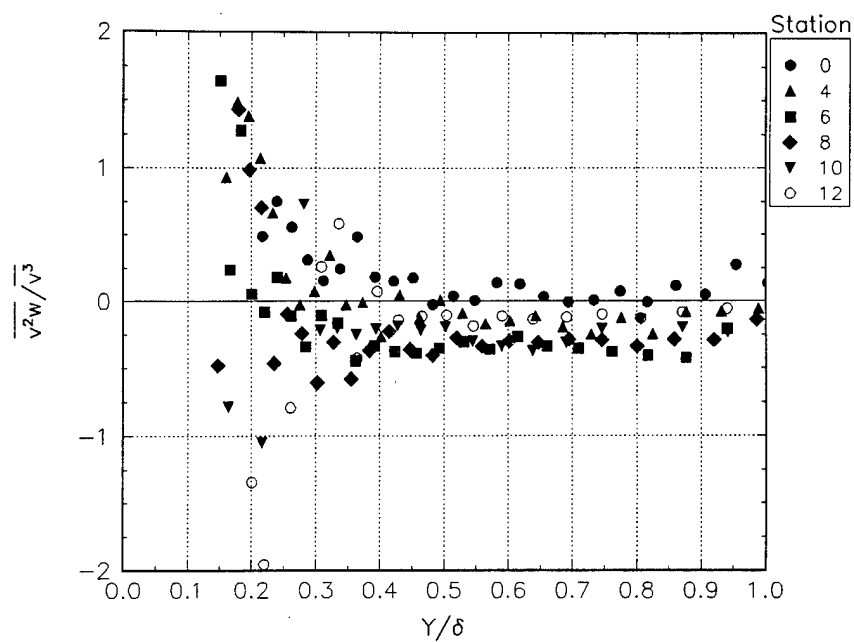


Figure C.27a Triple product ratio for the development region.

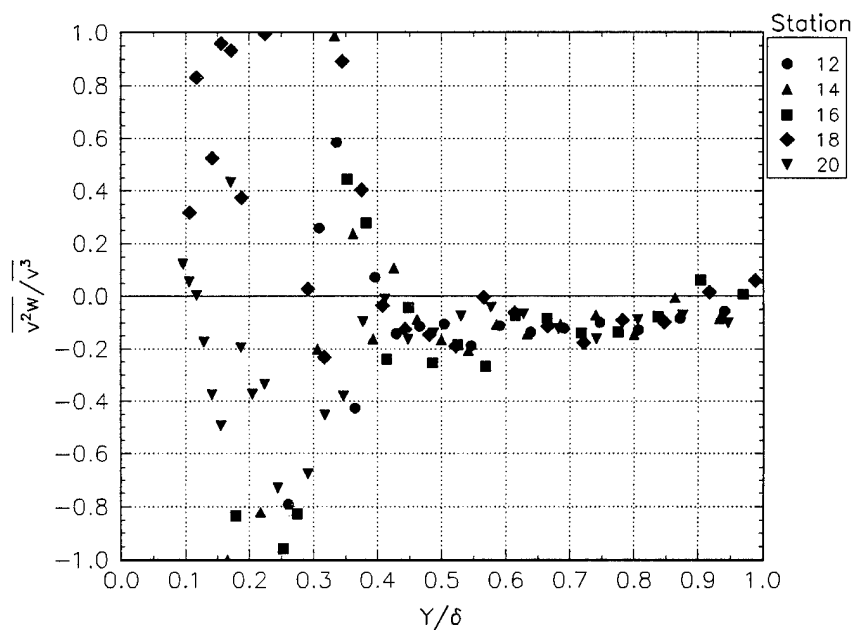


Figure C.27b Triple product ratio for the decay region.

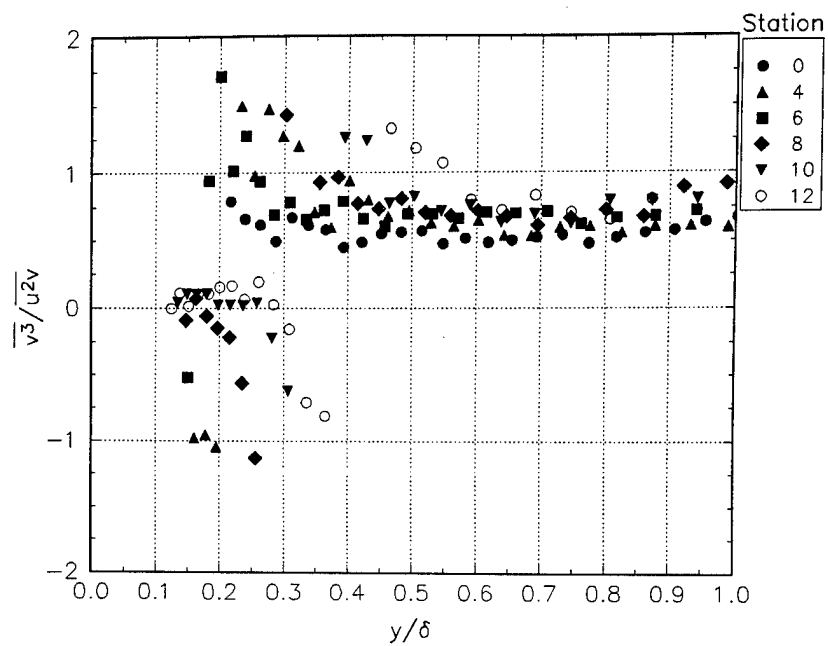


Figure C.28a Triple product ratio for the development region.

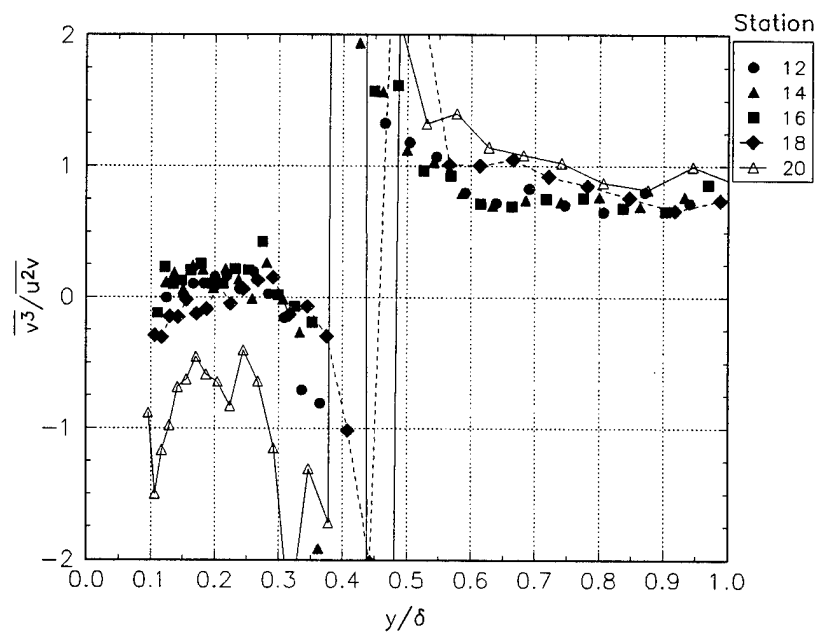


Figure C.28b Triple product ratio for the decay region.



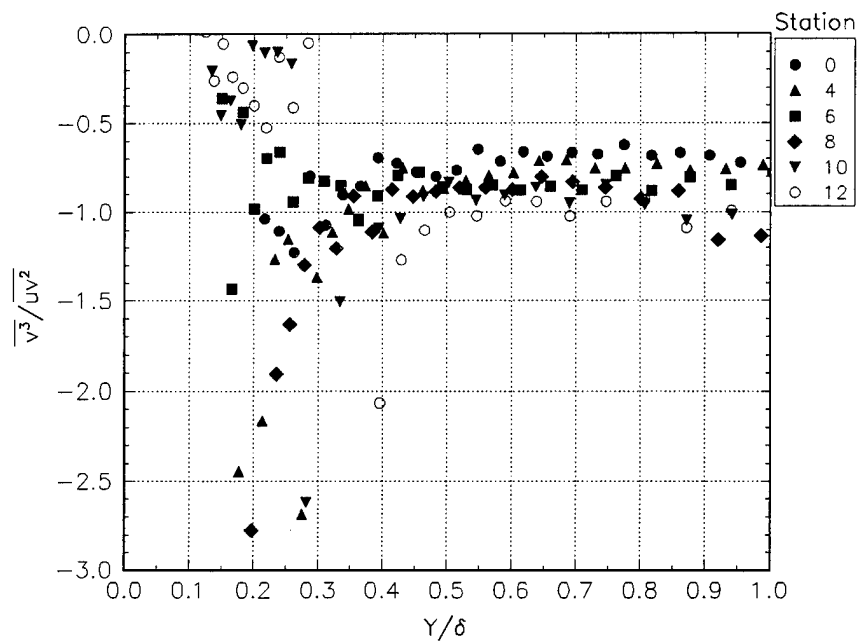


Figure C.29a Triple product ratio for the development region.

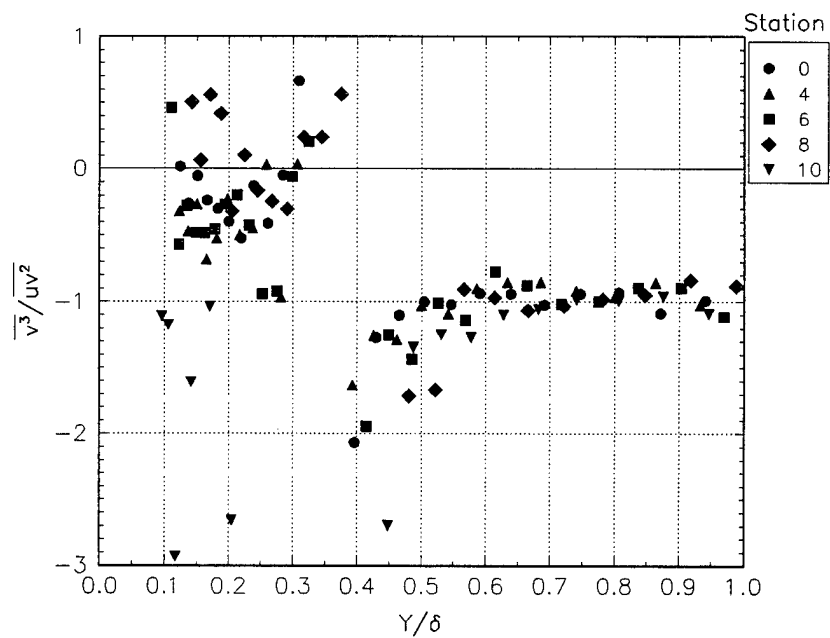


Figure C.29b Triple product ratio for the decay region.

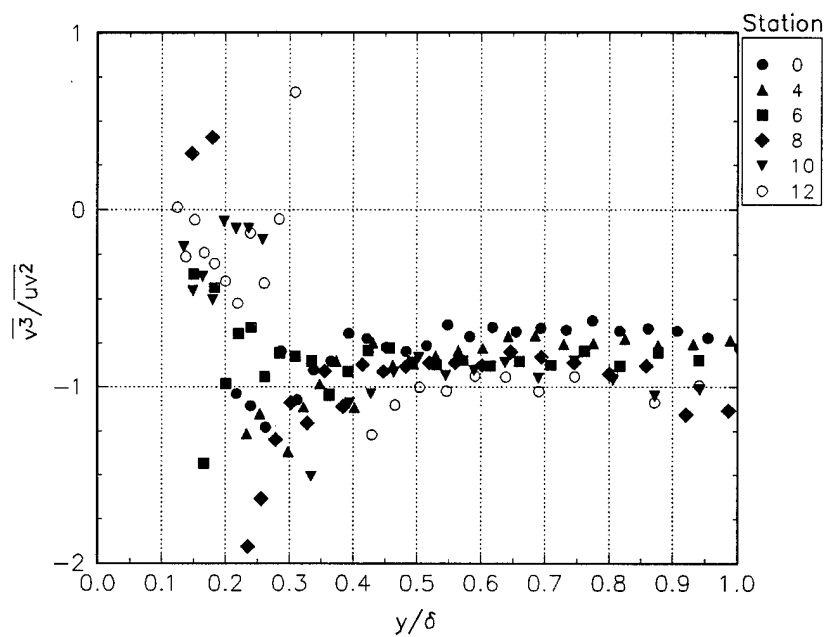


Figure C.30a Triple product ratio for the development region.

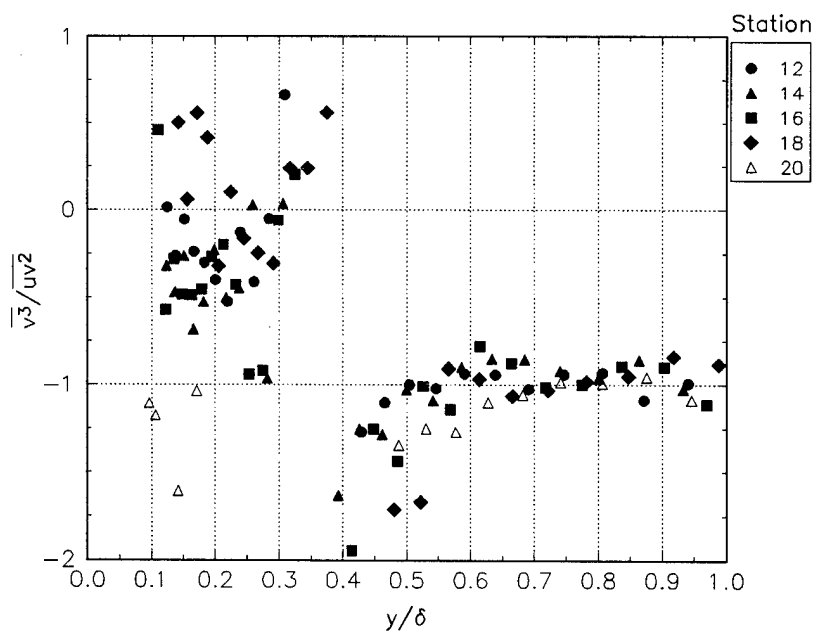


Figure C.30b Triple product ratio for the decay region.

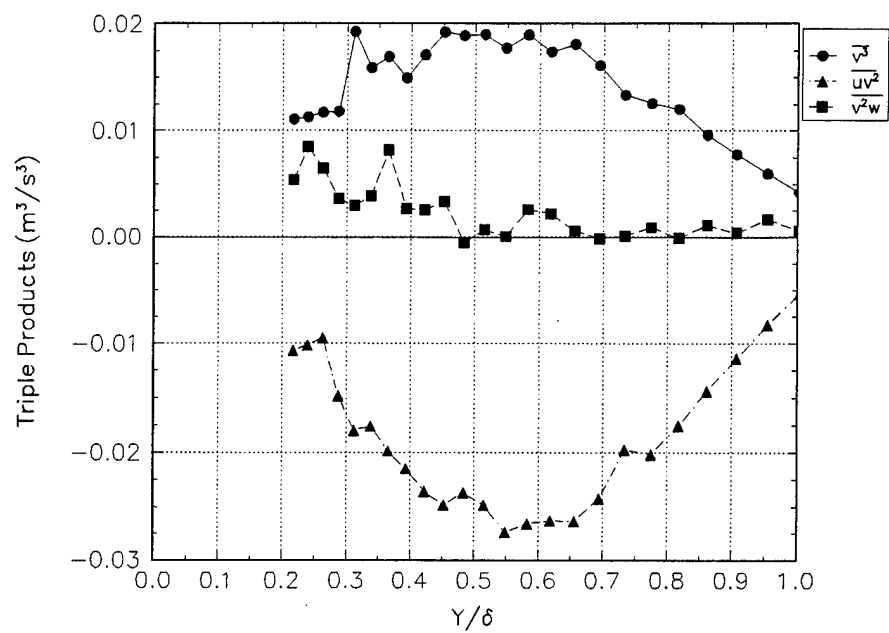


Figure C.31a Triple products for station 0.

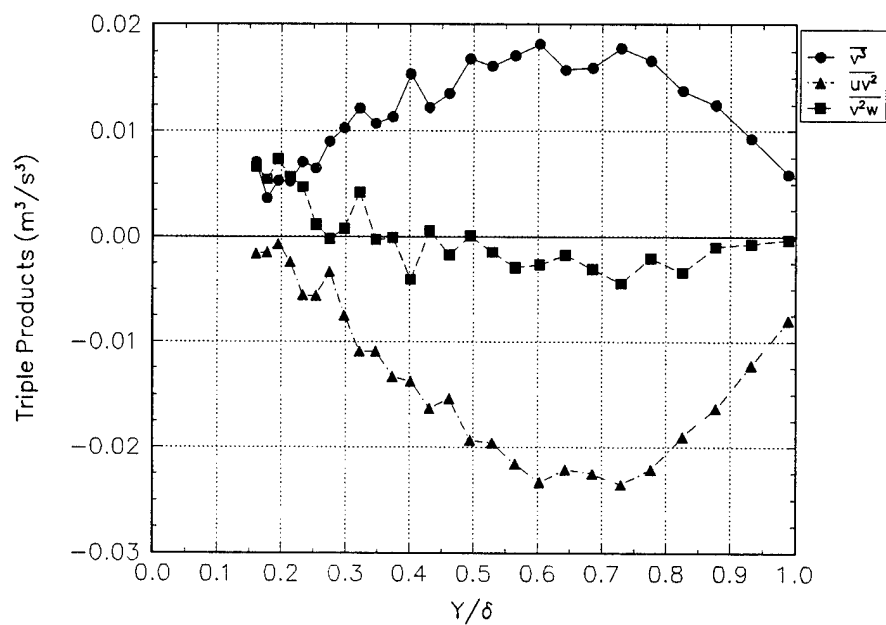


Figure C.31b Triple products for station 4.

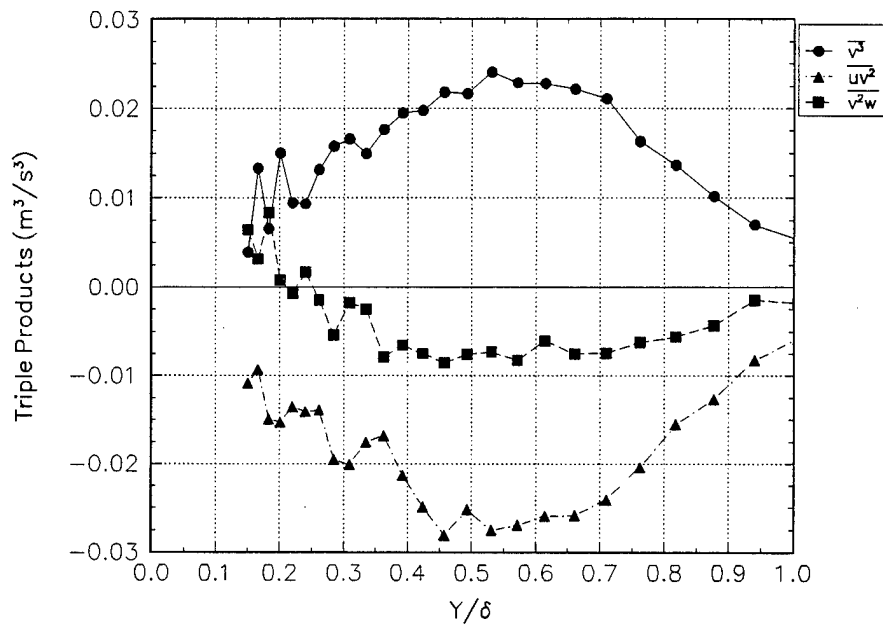


Figure C.31c Triple products for station 6.

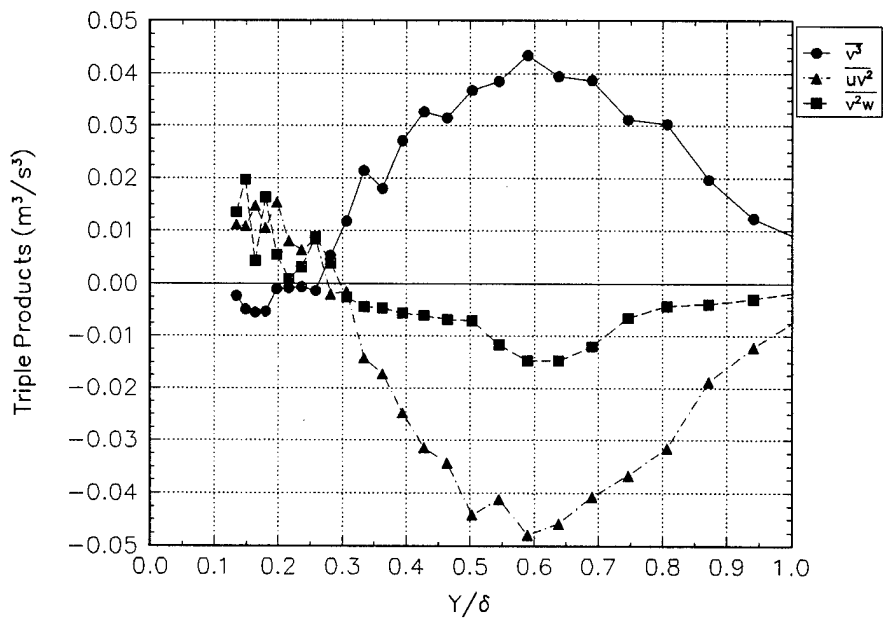


Figure C.31d Triple products for station 10.

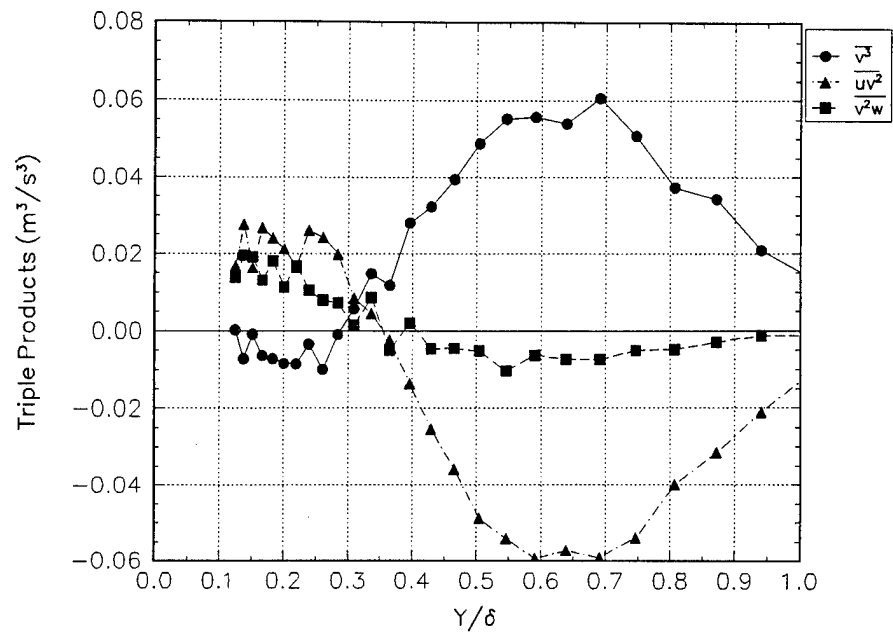


Figure C.31e Triple products for station 12.

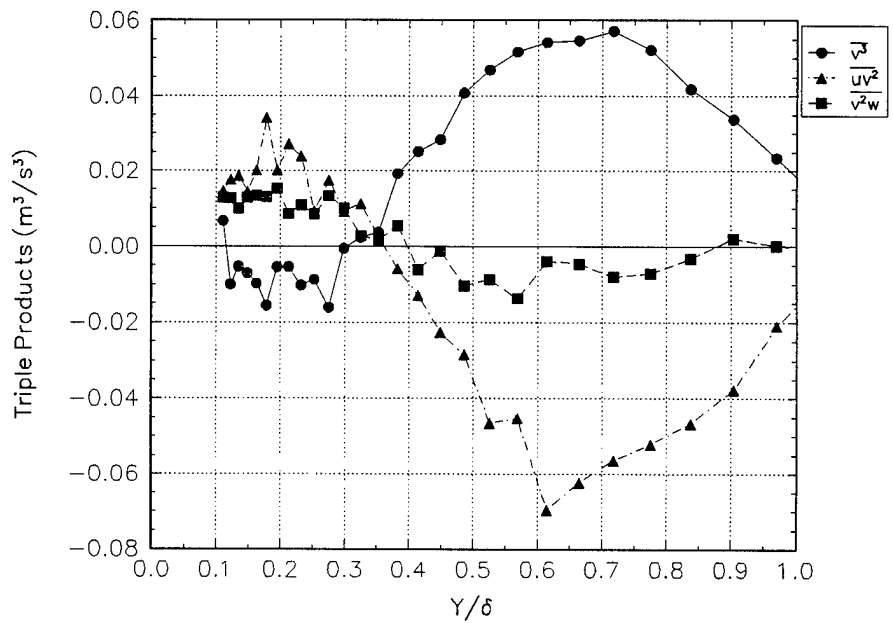


Figure C.31f Triple products for station 16.

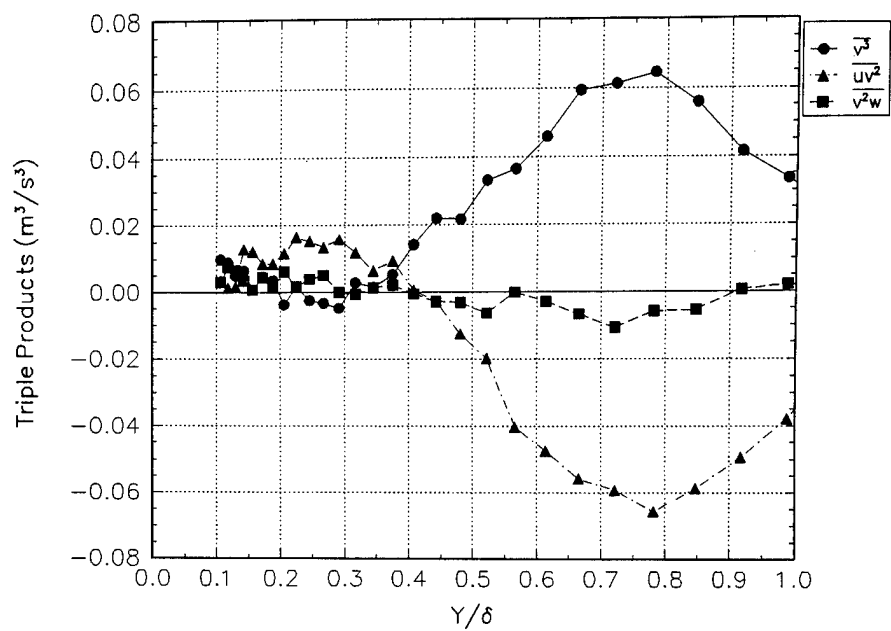


Figure C.31g Triple products for station 18.

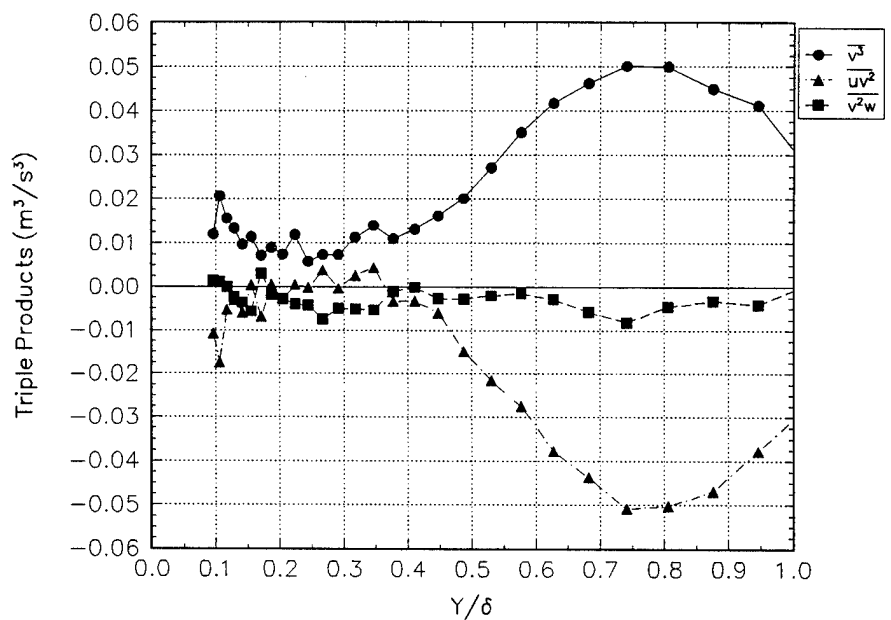


Figure C.31h Triple products for station 20.

## APPENDIX D Additional Figures for the Data of Ölcmen

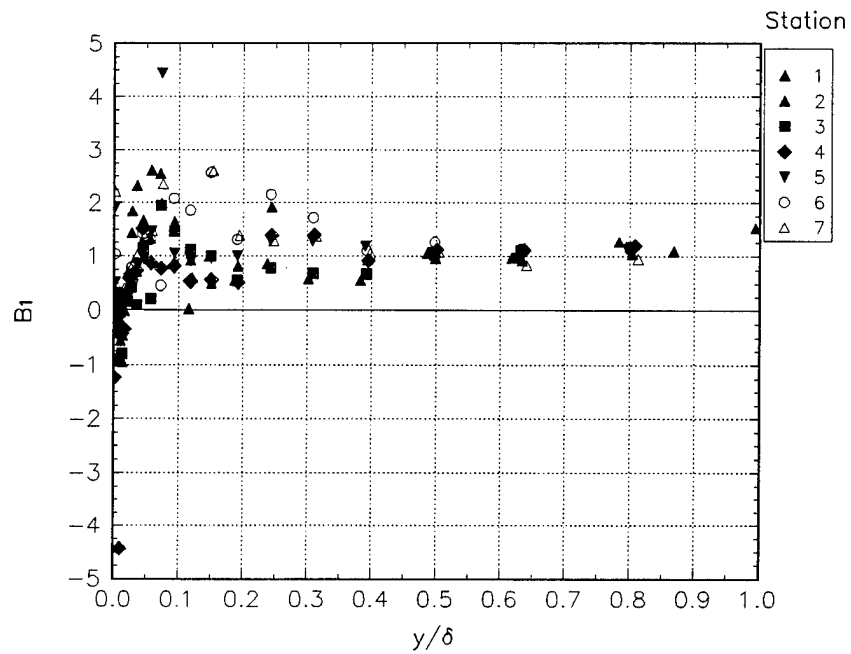


Figure D.1 The  $B_1$  parameter in local free- stream coordinates.

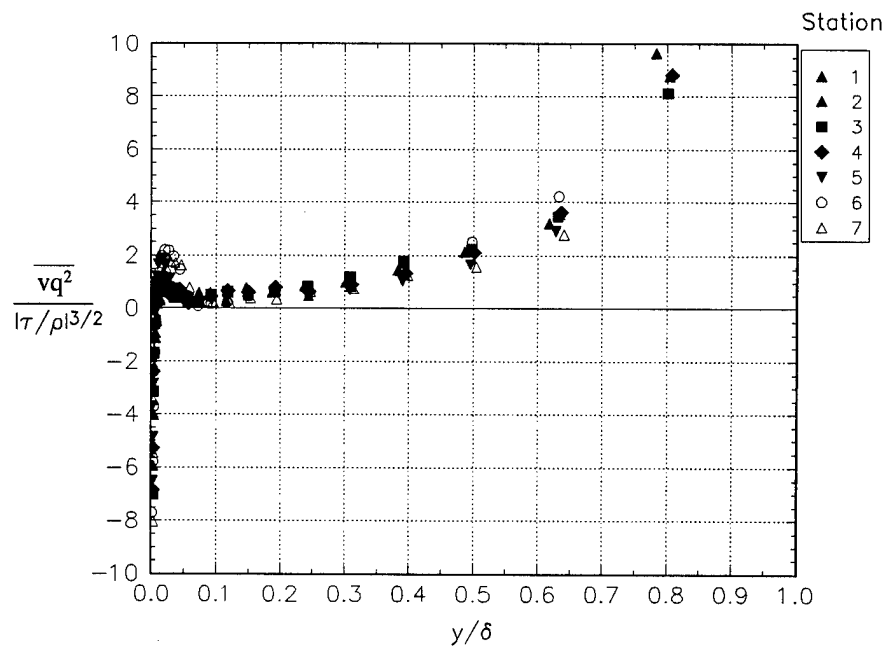


Figure D.2 Triple product relationship in local free-stream coordinates.

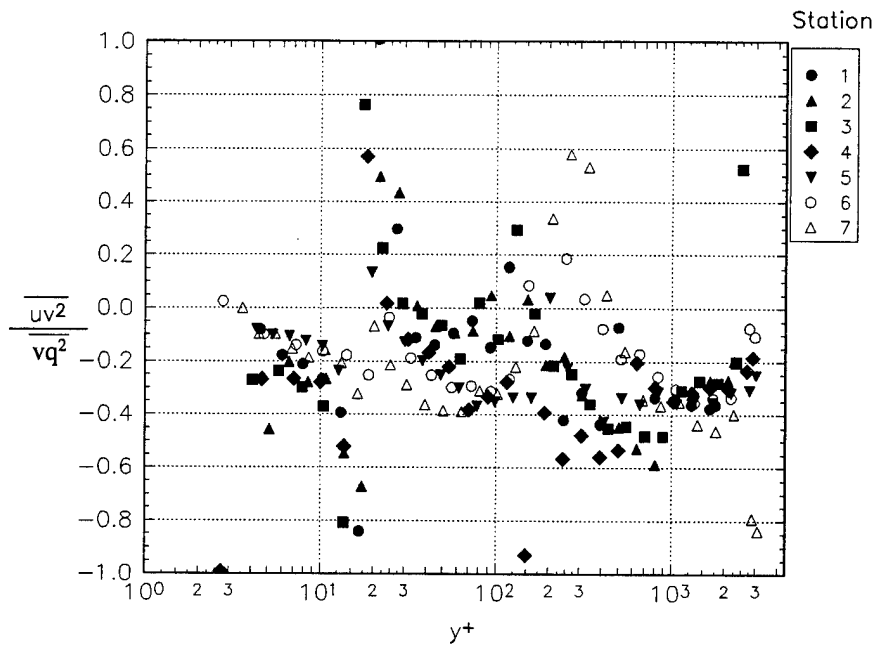


Figure D.3 Triple product relationship in local free-stream coordinates.

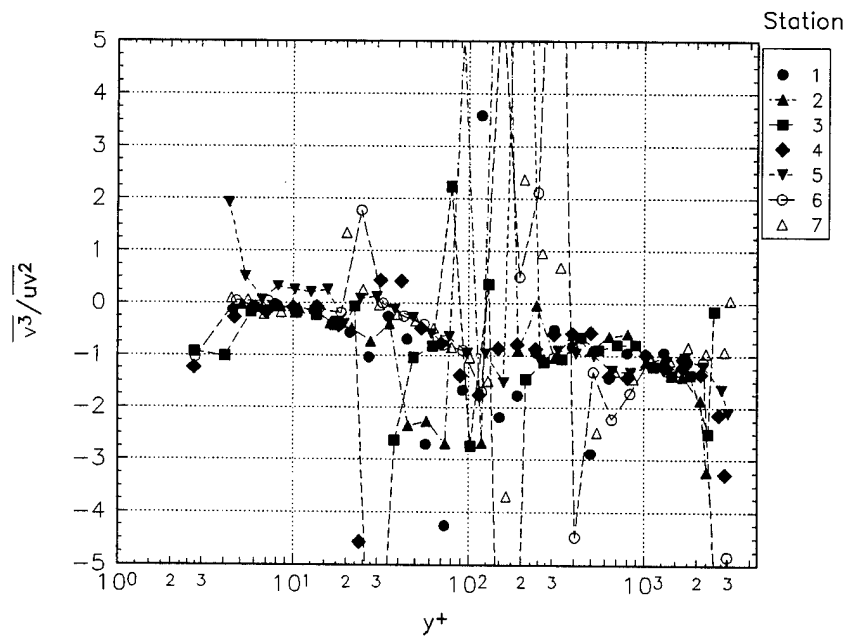


Figure D.4 Triple product relationship in local free-stream coordinates.



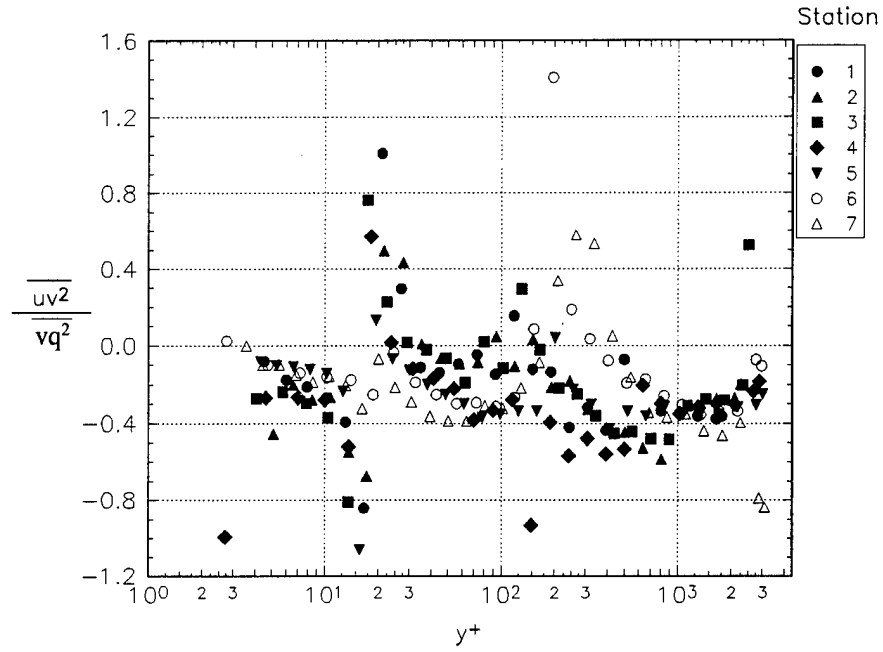


Figure D.5 Triple product relationship in wall-stress coordinates.

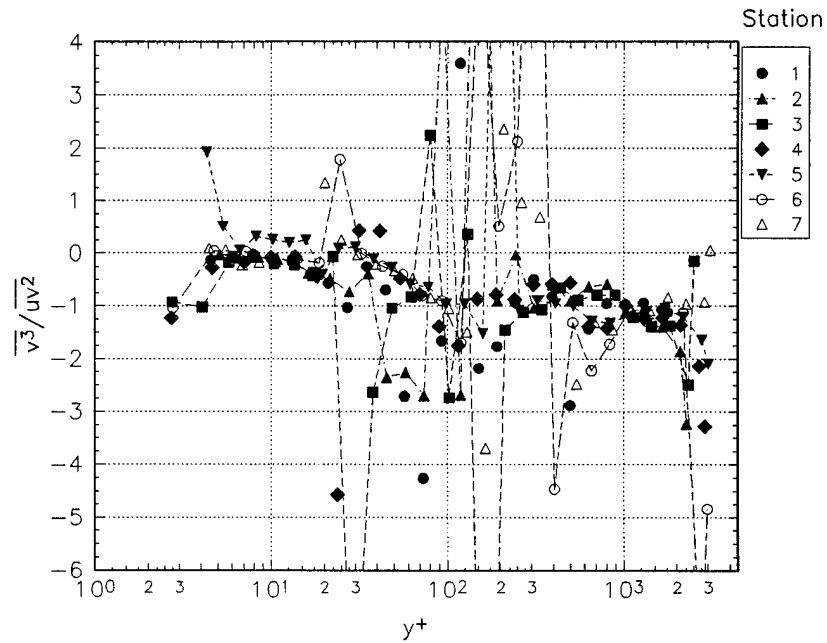


Figure D.6 Triple product relationship in wall-stress coordinates.

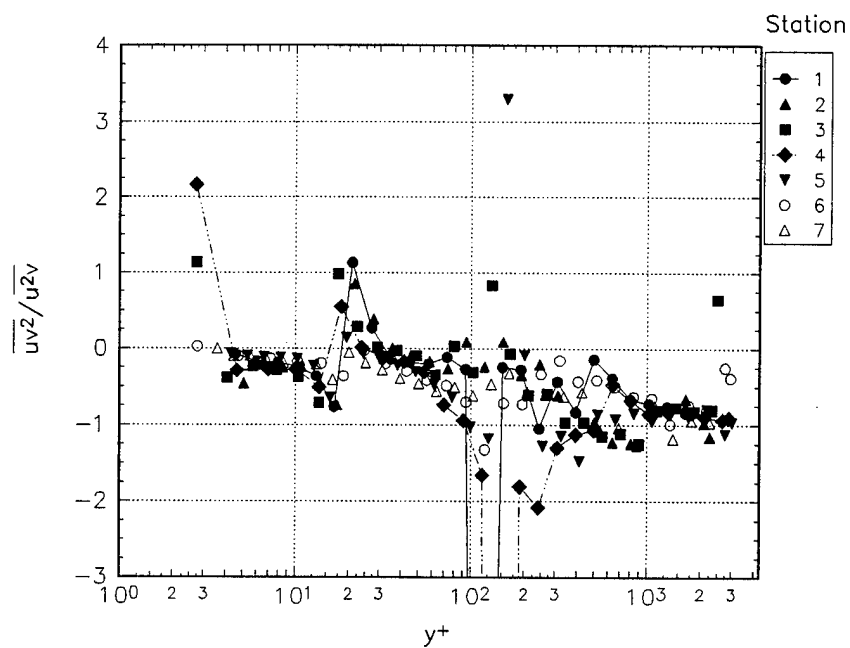


Figure D.7 Triple product relationship in wall-stress coordinates.

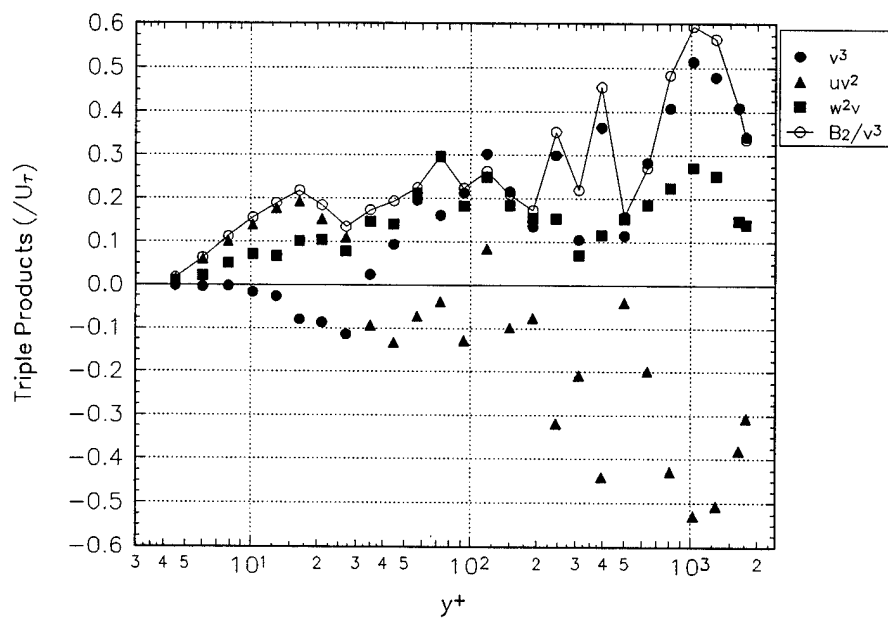


Figure D.8a Examination of the  $B_2$  parameter in wall-stress coordinates for station 1.

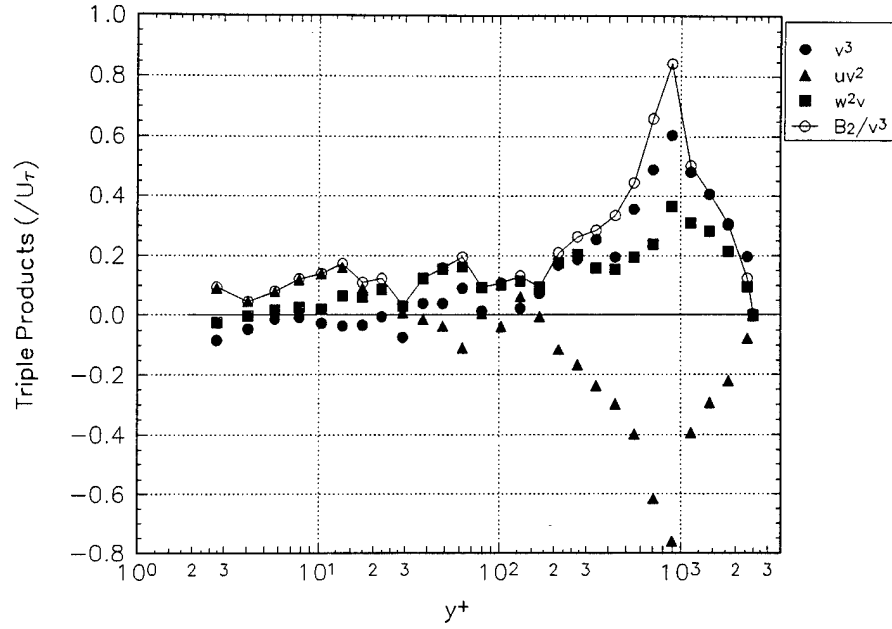


Figure D.8b Examination of the  $B_2$  parameter in wall-stress coordinates for station 3.

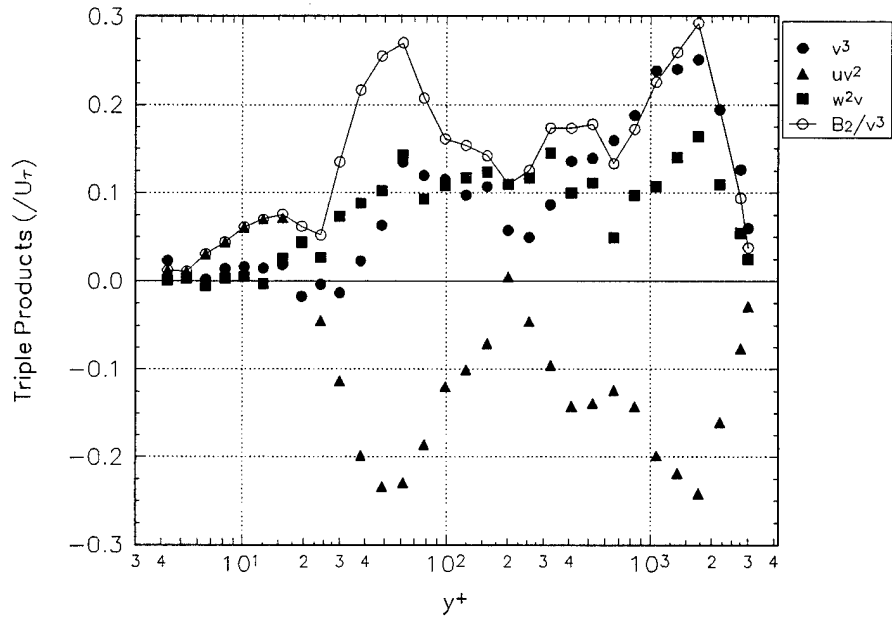


Figure D.8c Examination of the  $B_2$  parameter in wall-stress coordinates for station 5.

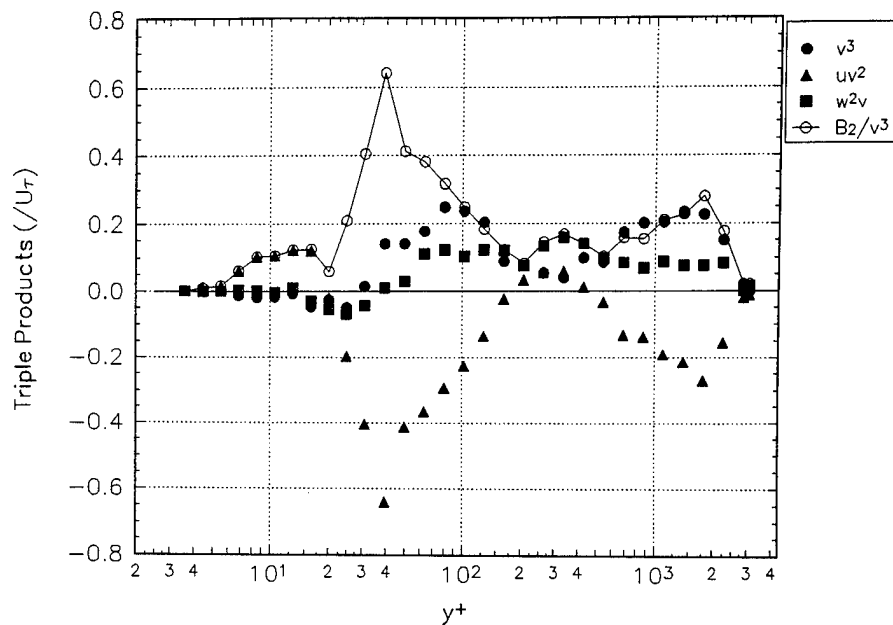


Figure D.8d Examination of the  $B_2$  parameter in wall-stress coordinates for station 7.

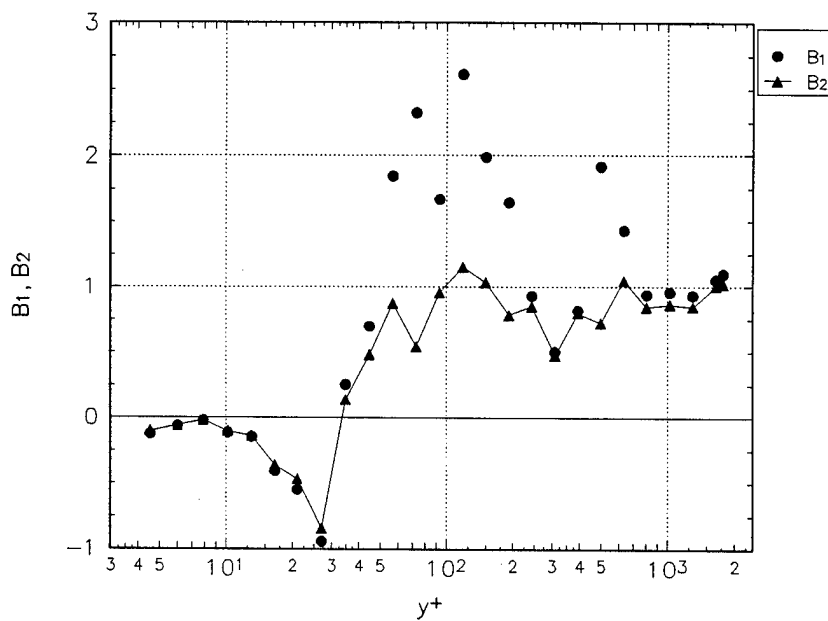


Figure D.9a B parameter examination in wall-stress coordinates for station 1.

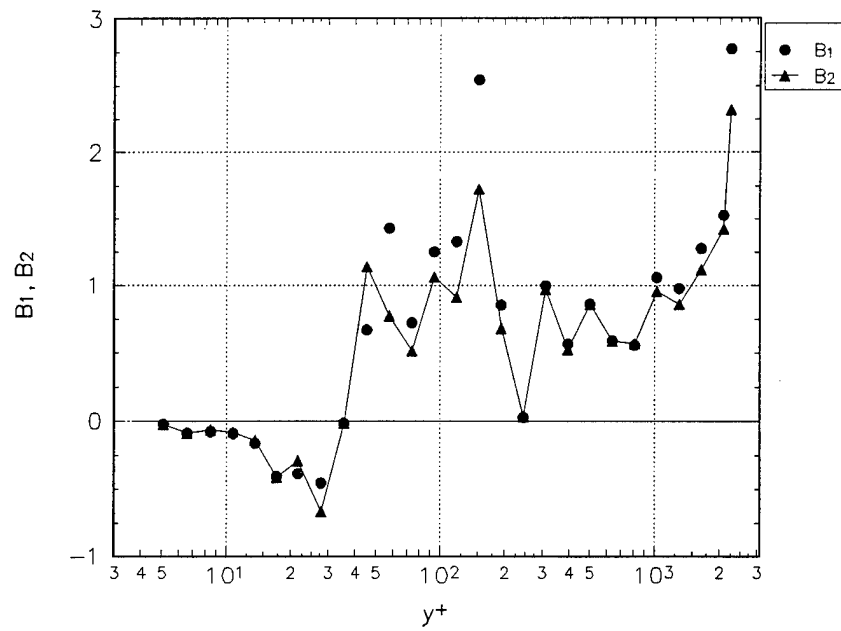


Figure D.9b B parameter examination in wall-stress coordinates for station 2.

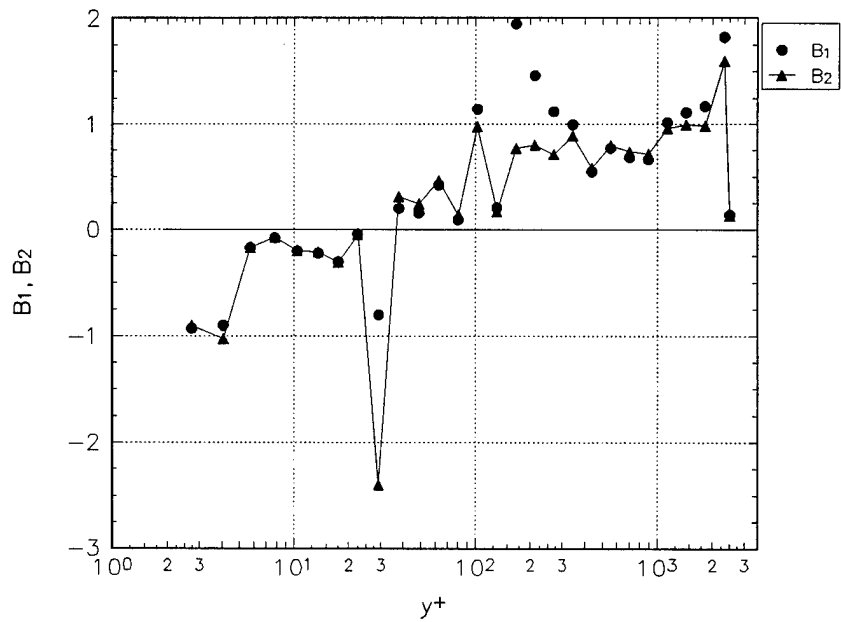


Figure D.9c B parameter examination in wall-stress coordinates for station 3.

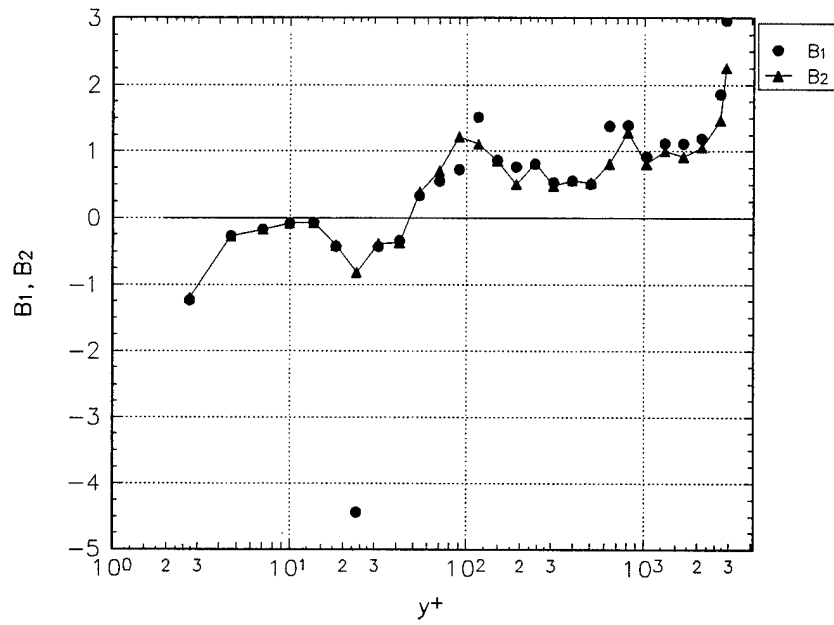


Figure D.9d B parameter examination in wall-stress coordinates for station 4.

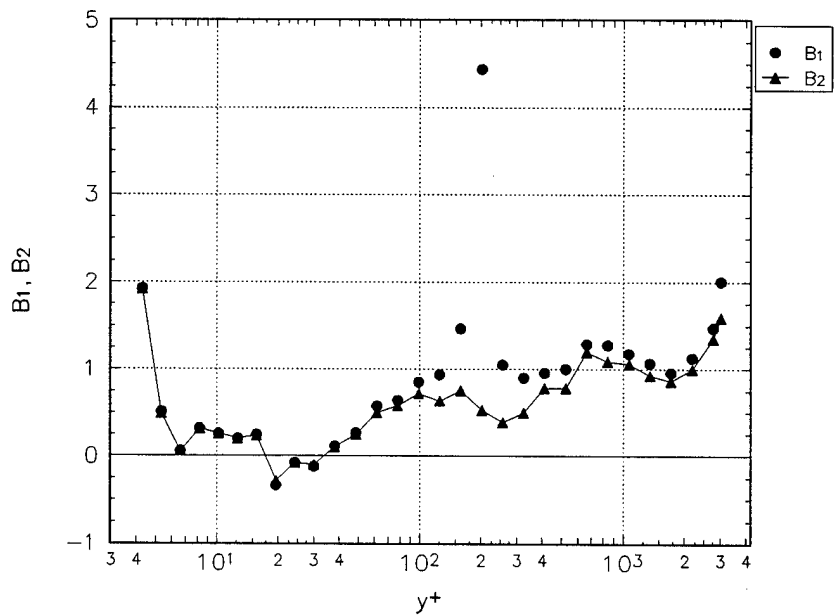


Figure D.9e B parameter examination in wall-stress coordinates for station 5.

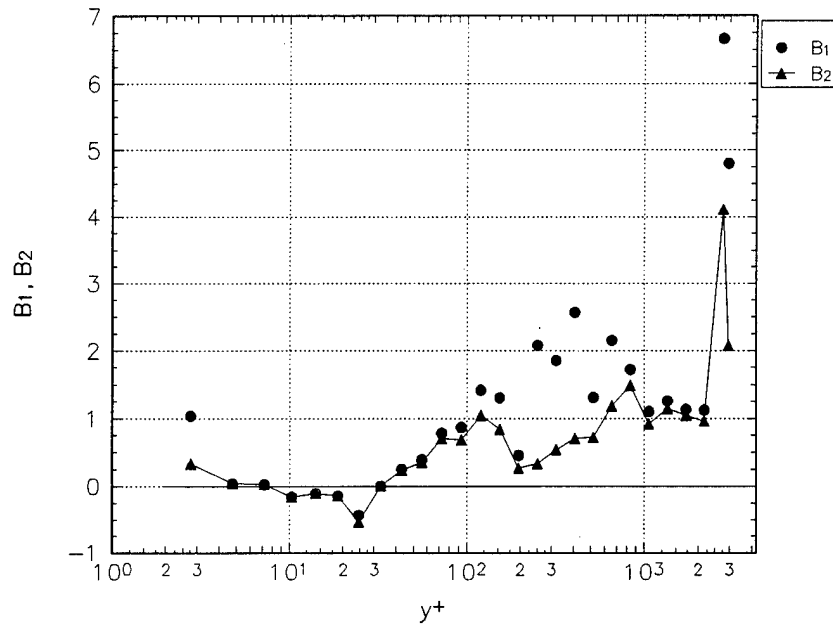


Figure D.9f B parameter examination in wall-stress coordinates for station 6.

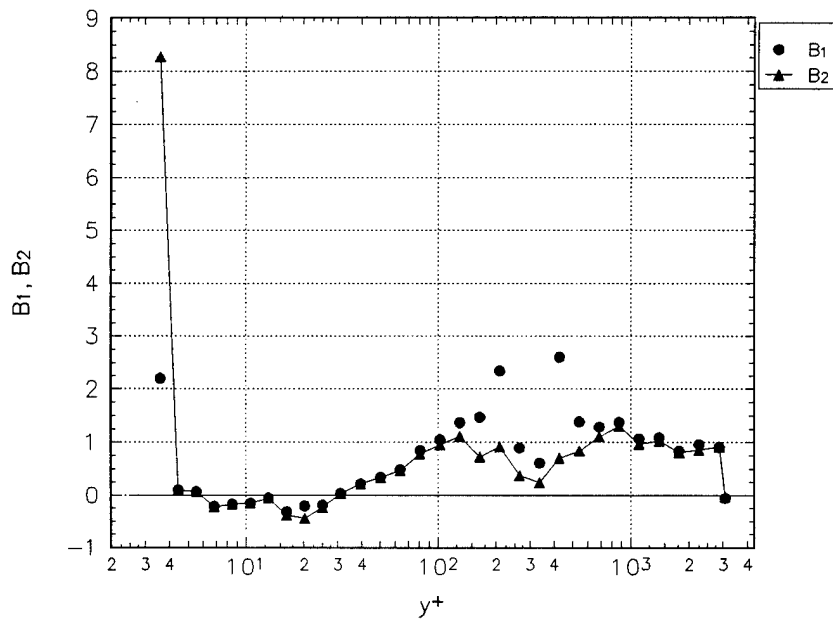


Figure D.9g B parameter examination in wall-stress coordinates for station 7.

## APPENDIX E Additional Figures for the Data of Baskaran

### Concave Flow Geometry

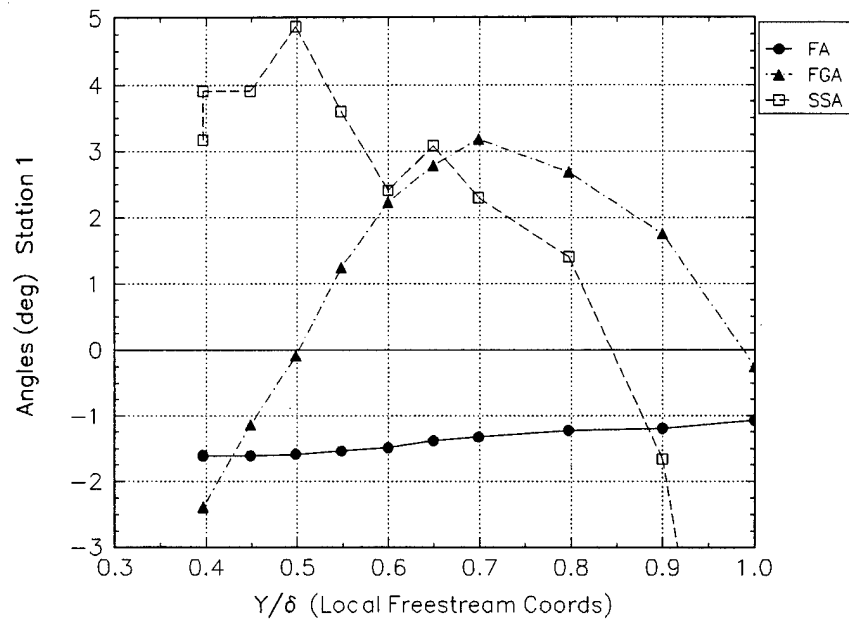


Figure E.1.a Comparison of characteristic angles in local freestream coordinates for station 1.

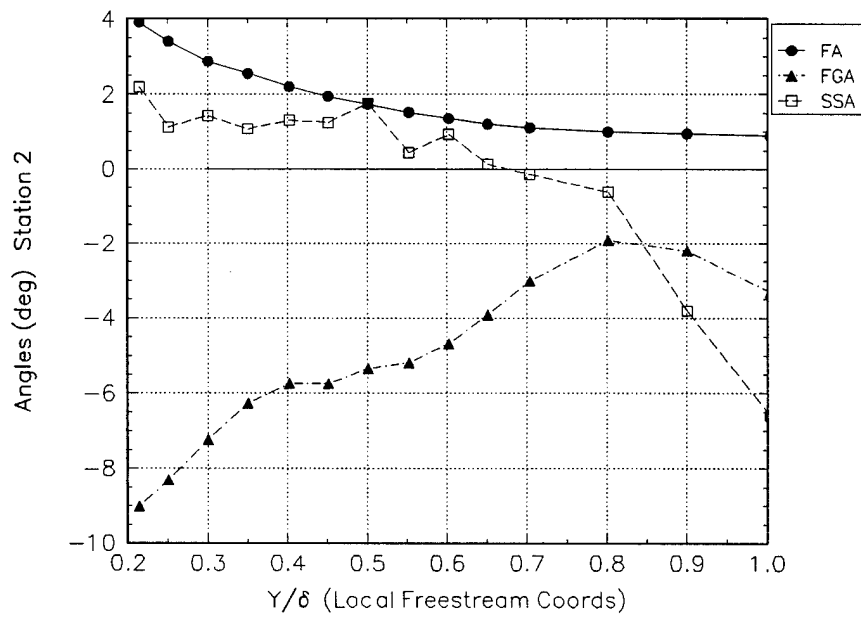


Figure E.1.b Comparison of characteristic angles in local freestream coordinates for station 2.



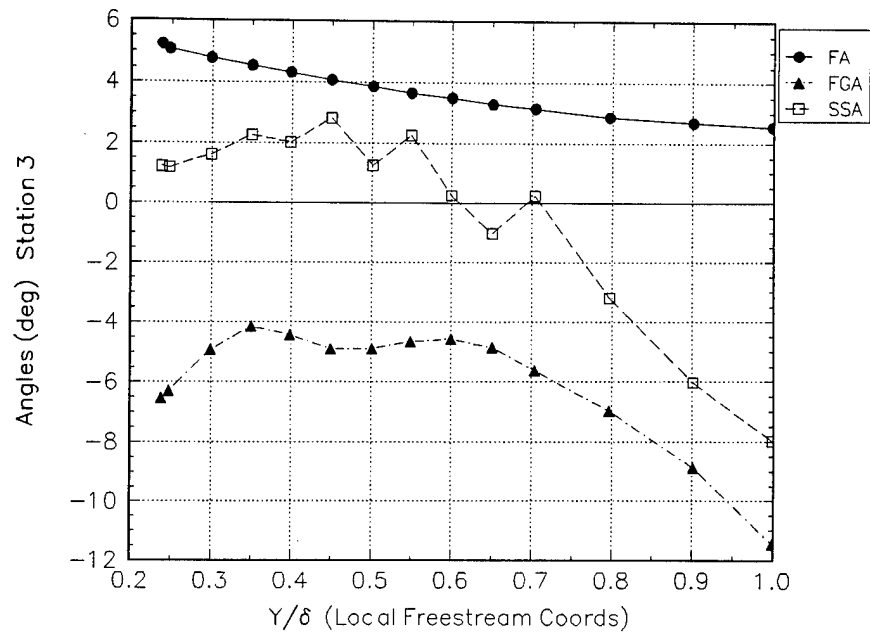


Figure E.1.c Comparison of characteristic angles in local freestream coordinates for station 3.

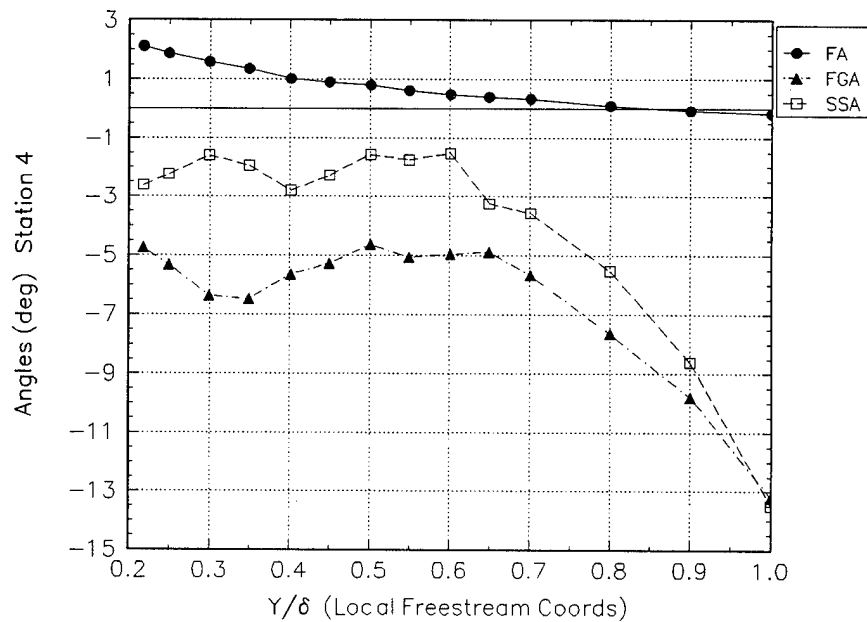


Figure E.1.d Comparison of characteristic angles in local freestream coordinates for station 4.

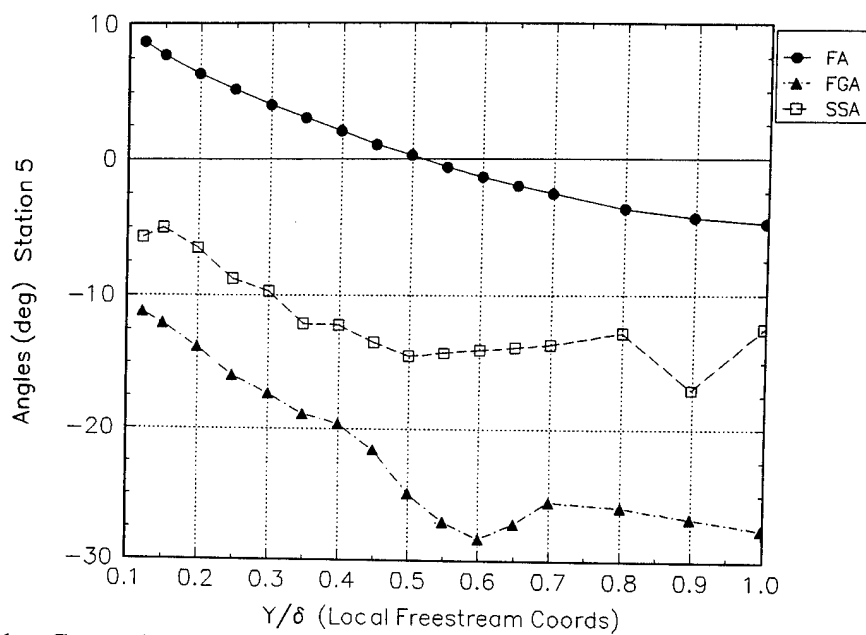


Figure E.1.e Comparison of characteristic angles in local freestream coordinates for station 5.

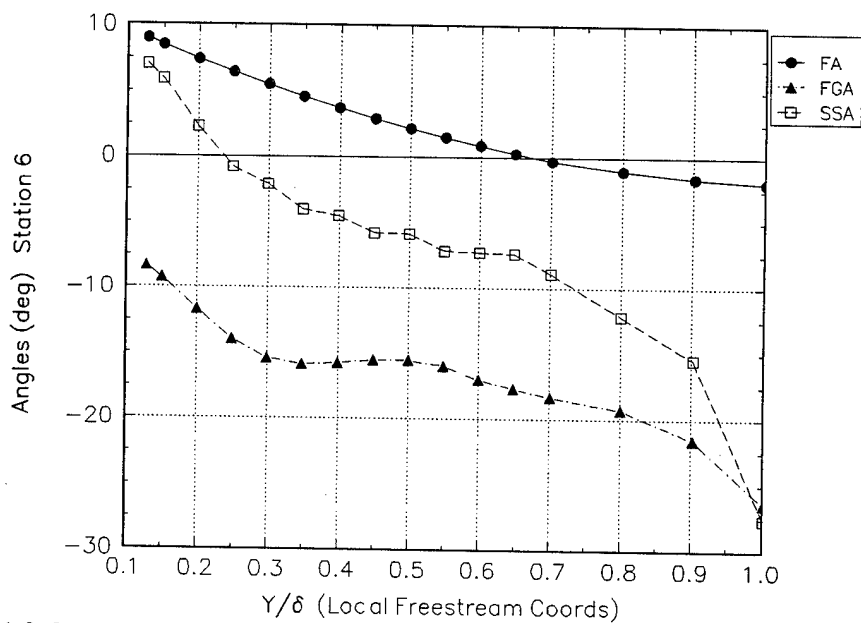


Figure E.1.f Comparison of characteristic angles in local freestream coordinates for station 6.

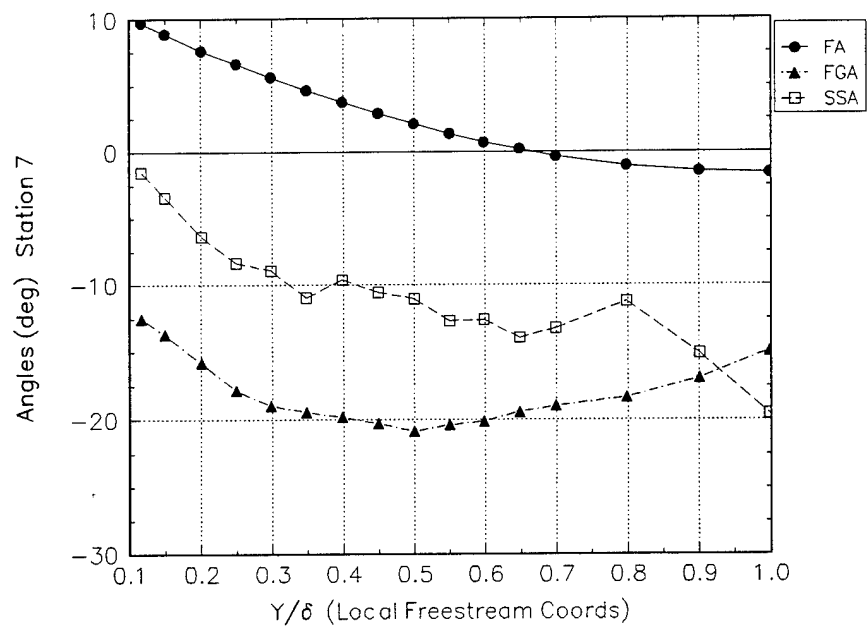


Figure E.1.g Comparison of characteristic angles in local freestream coordinates for station 7.

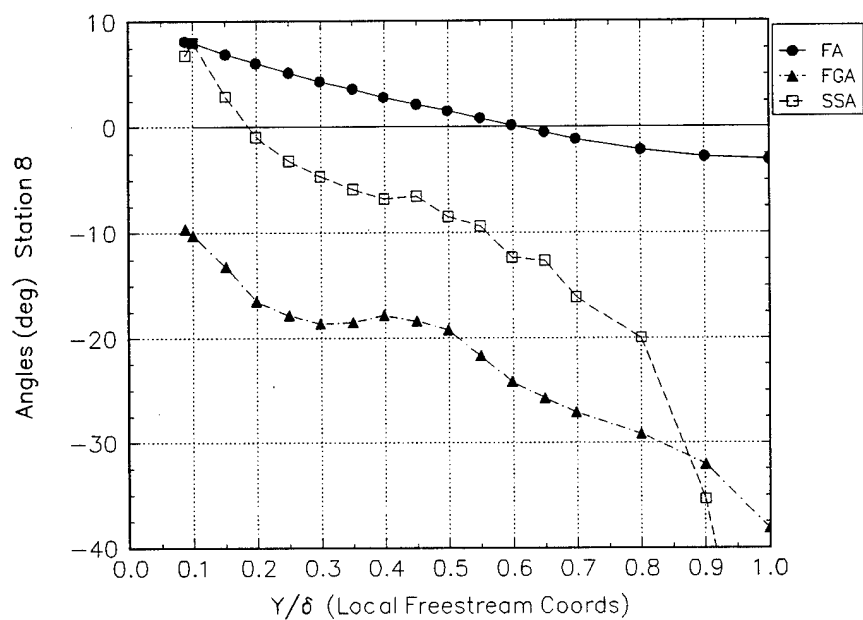


Figure E.1.h  
Comparison of characteristic angles in local freestream coordinates for station 8.

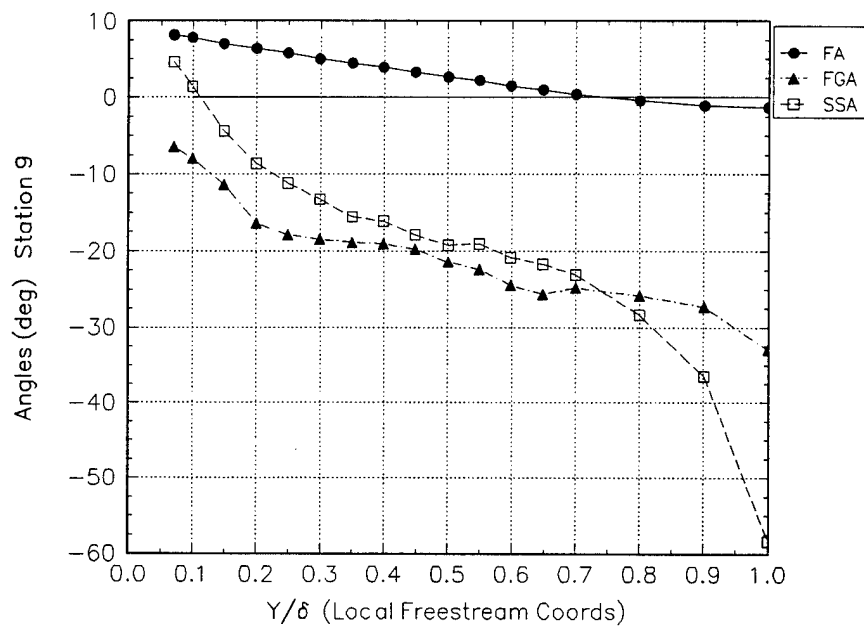


Figure E.1.i Comparison of characteristic angles in local freestream coordinates for station 9.

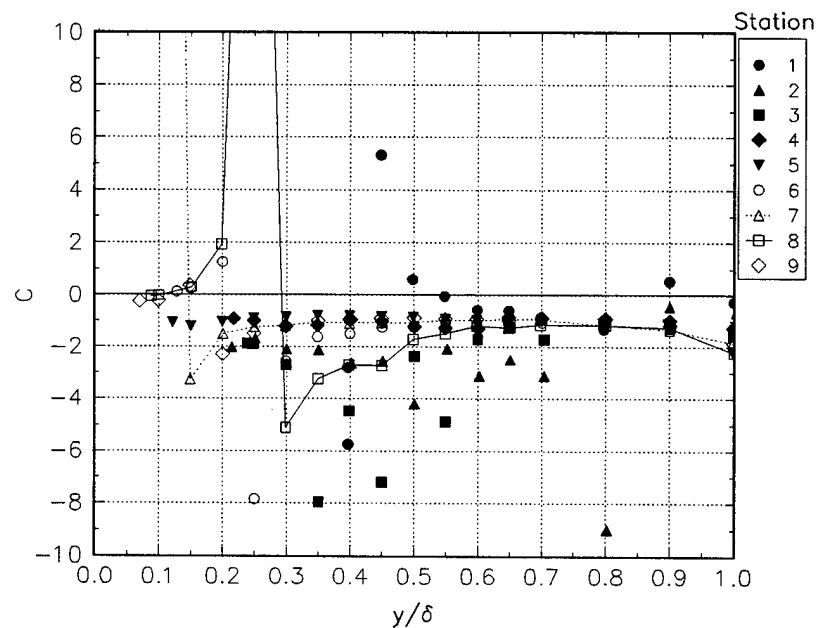


Figure E.2a The C parameter in tunnel coordinates.

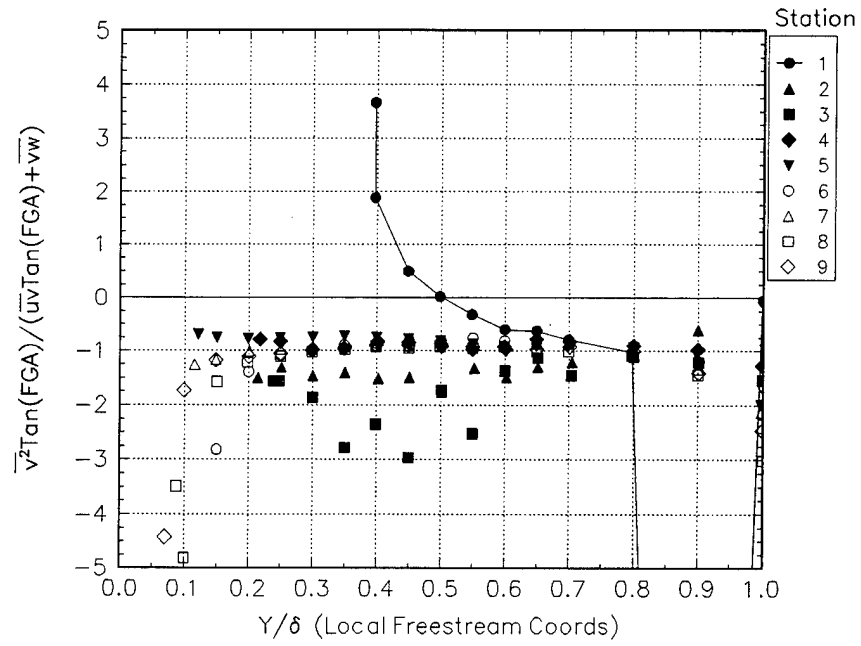


Figure E.2b The C parameter in local free-stream coordinates.

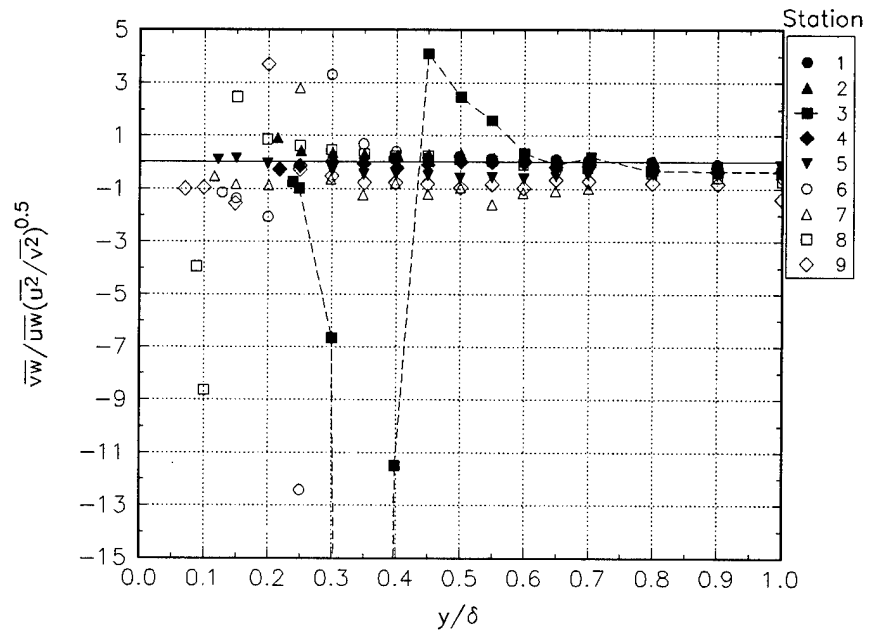


Figure E.3a Reynolds stress relationship in tunnel coordinates.

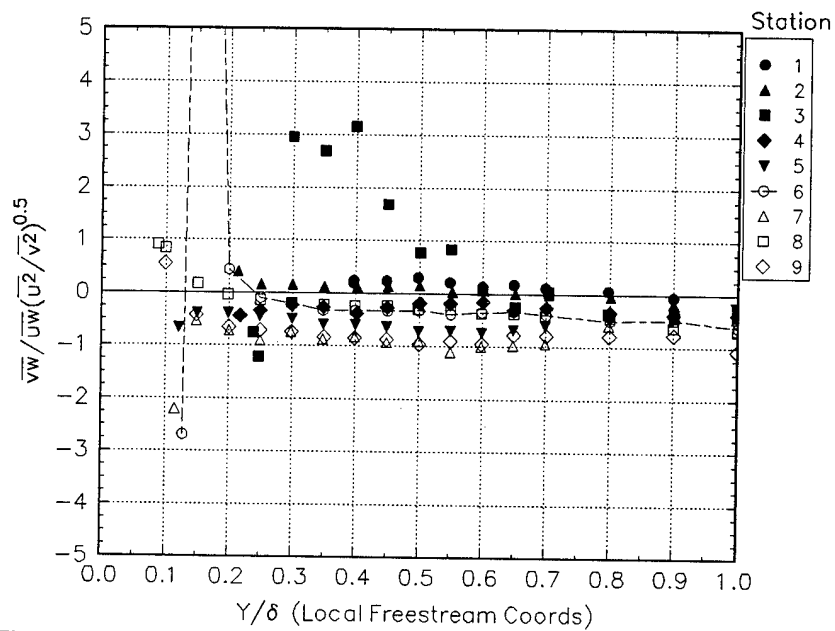


Figure E.3b Reynolds stress relationship in local free-stream coordinates.

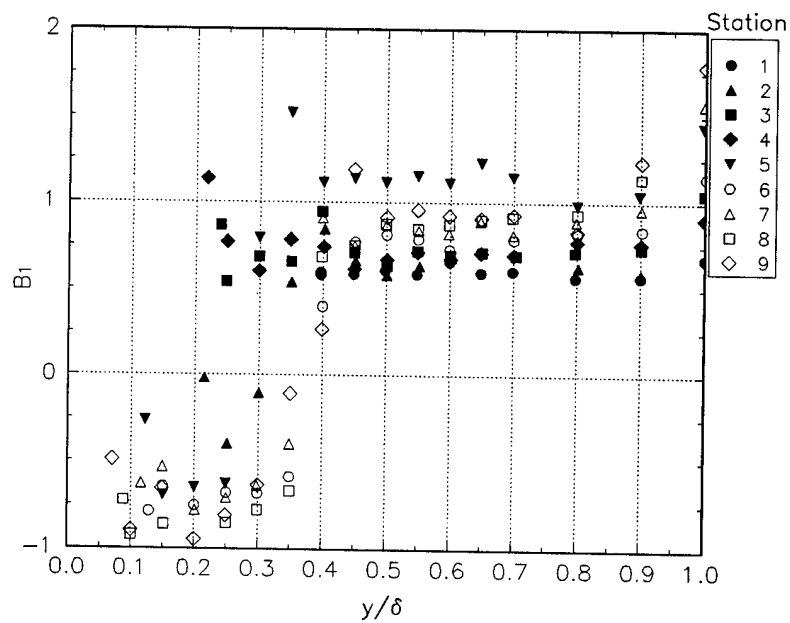


Figure E.4 The  $B_1$  parameter in tunnel coordinates.

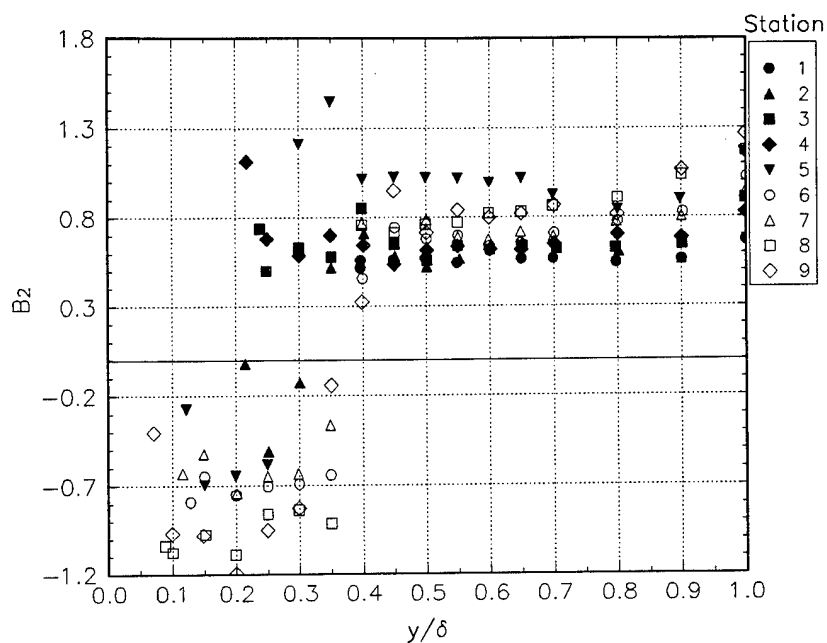


Figure E.5 The  $B_2$  parameter in tunnel coordinates.

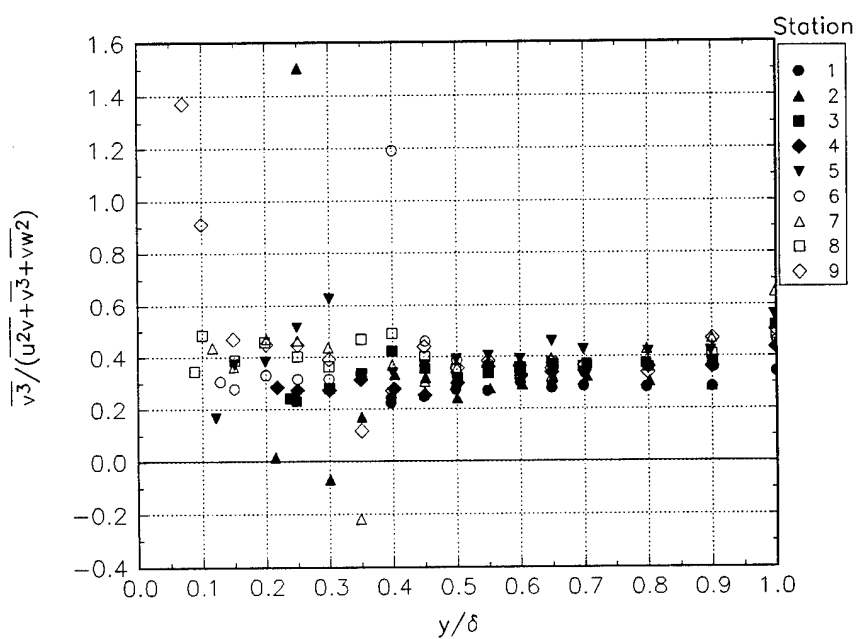


Figure E.6 Triple product relationship in tunnel coordinates.

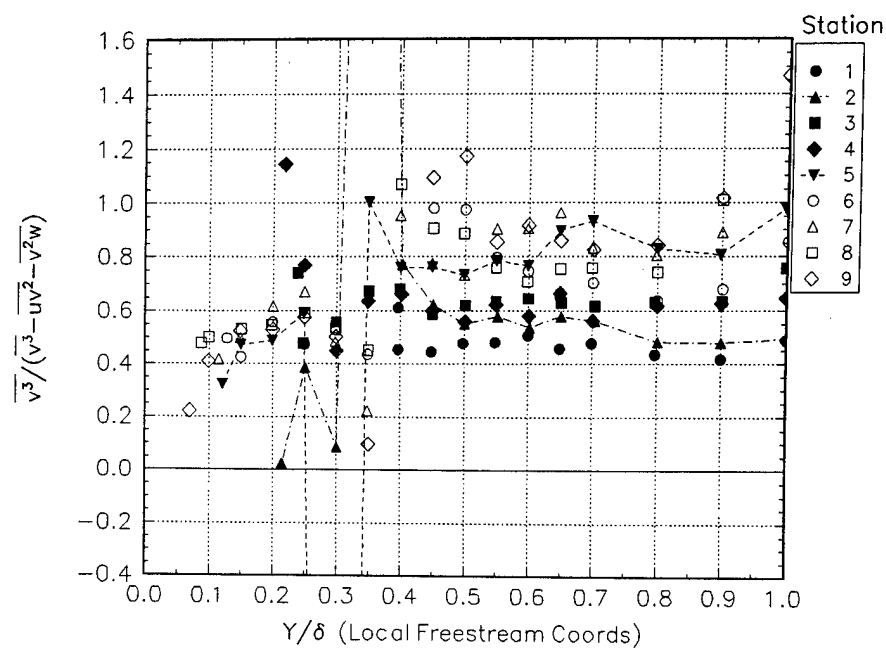


Figure E.7 Triple product relationship.

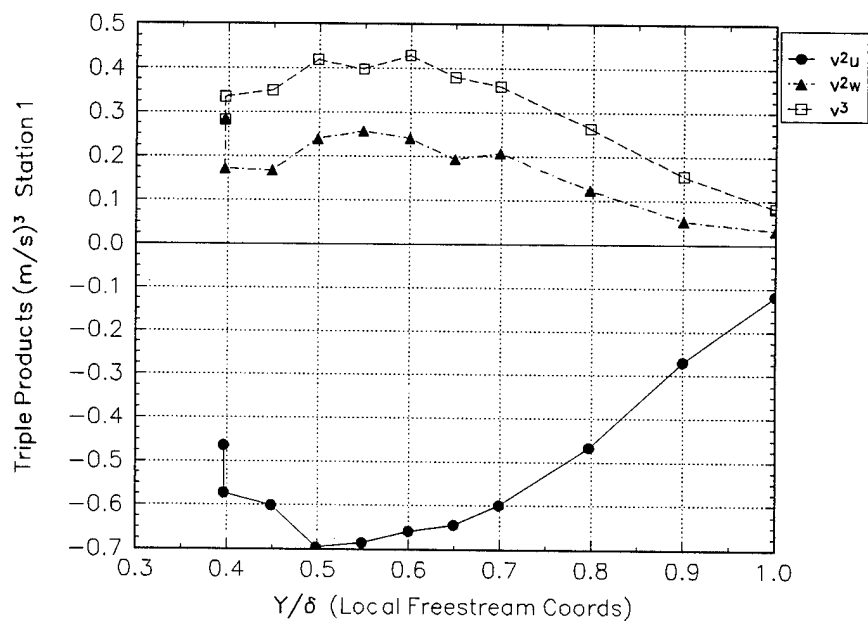


Figure E.8.a Triple products for station 1.



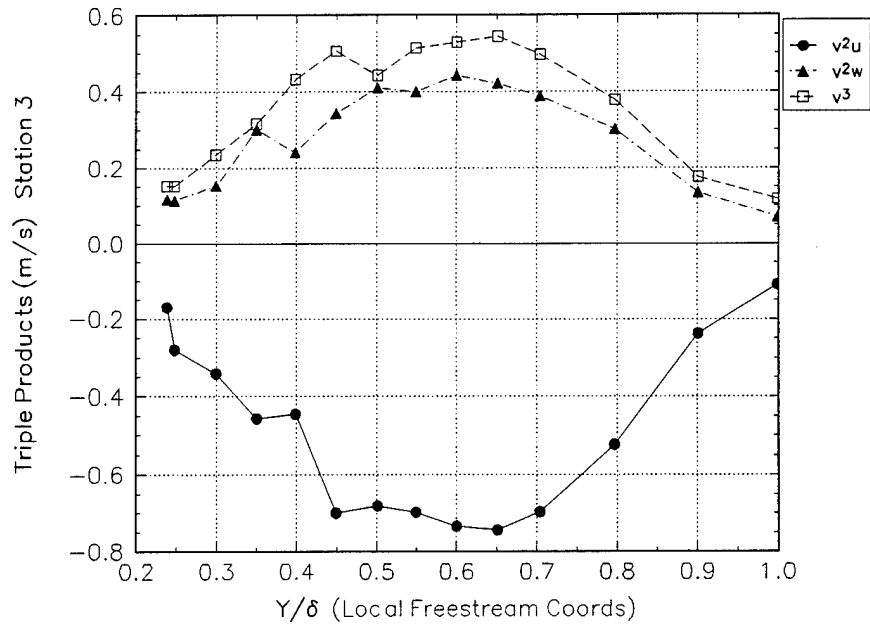


Figure E.8.b Triple products for station 3.

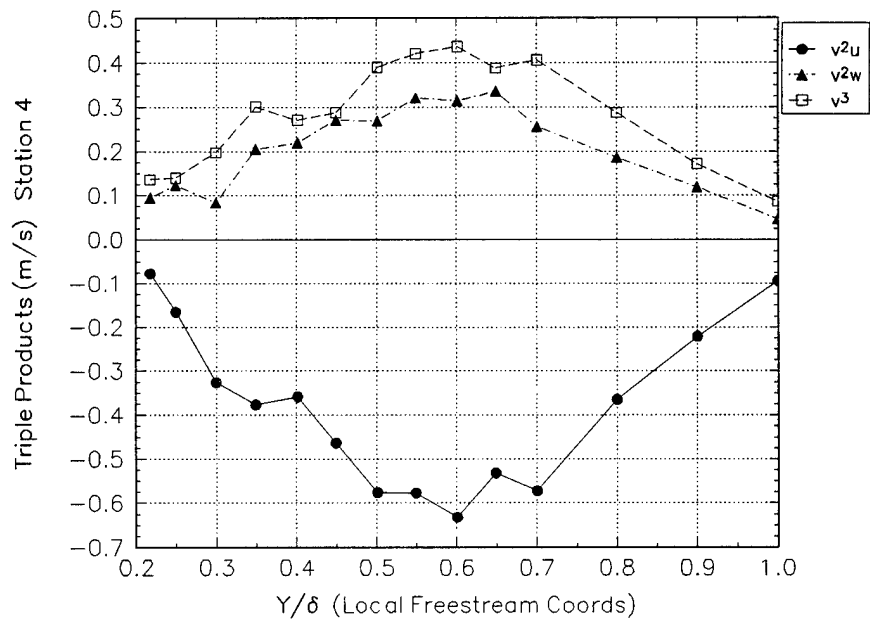


Figure E.8.c Triple products for station 4.

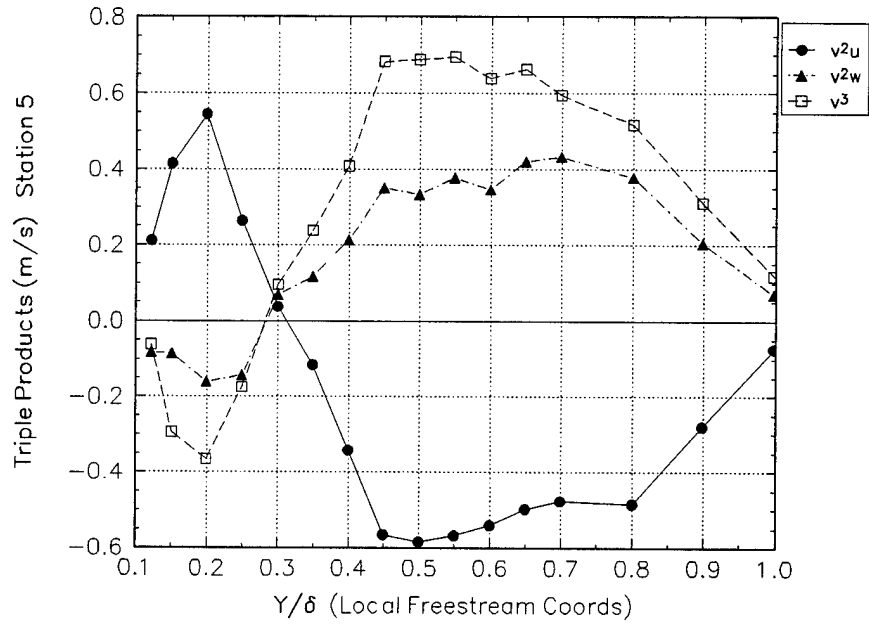


Figure E.8.d Triple products for station 5.

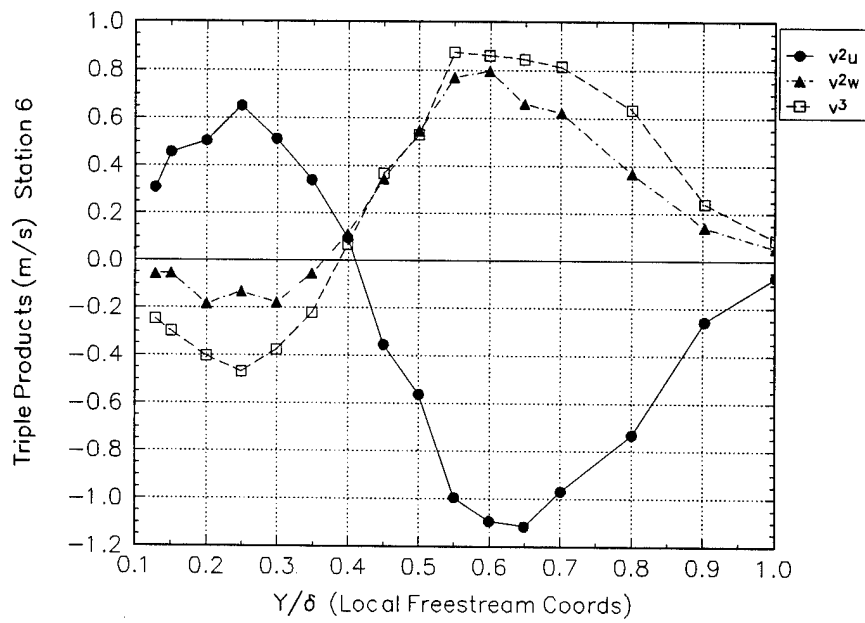


Figure E.8.e Triple products for station 6

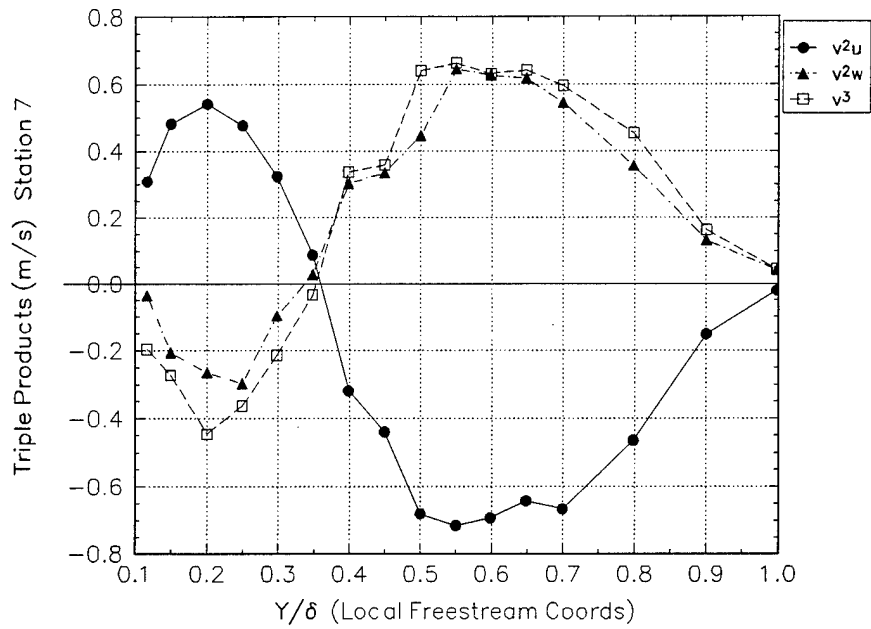


Figure E.8.f Triple products for station 7

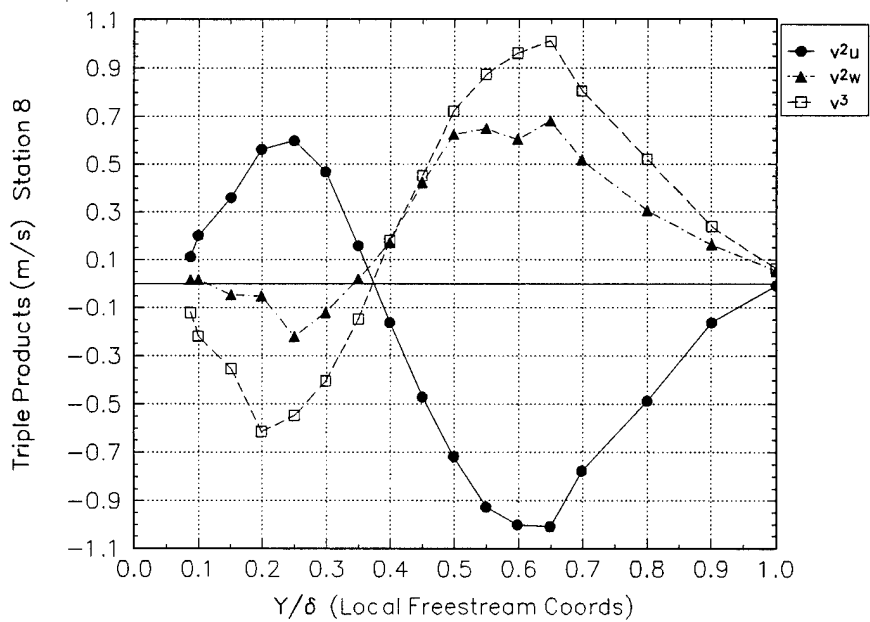


Figure E.8.g Triple products for station 8

**Convex geometry results** (from here till the end of this appendix)

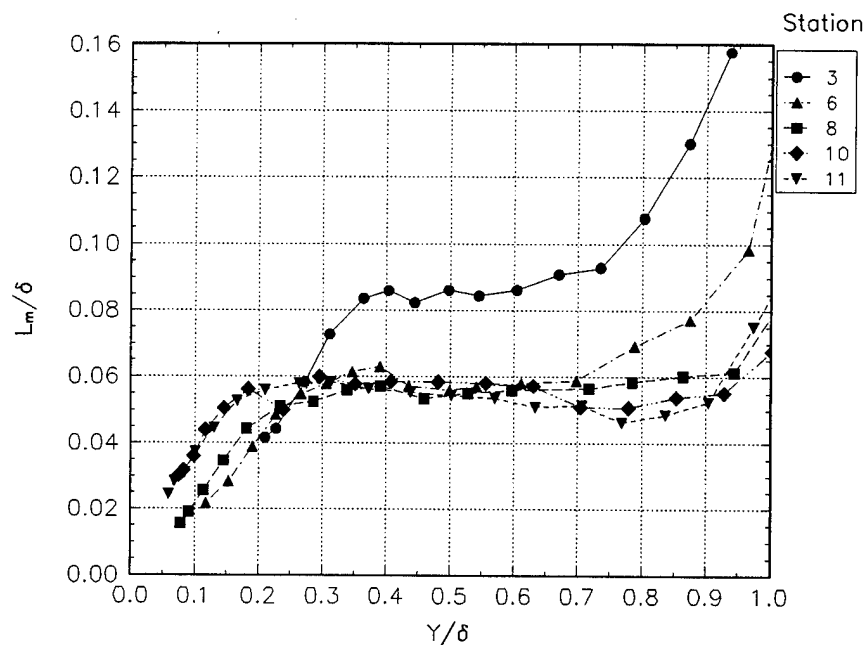


Figure E.9 The mixing length for the convex case.

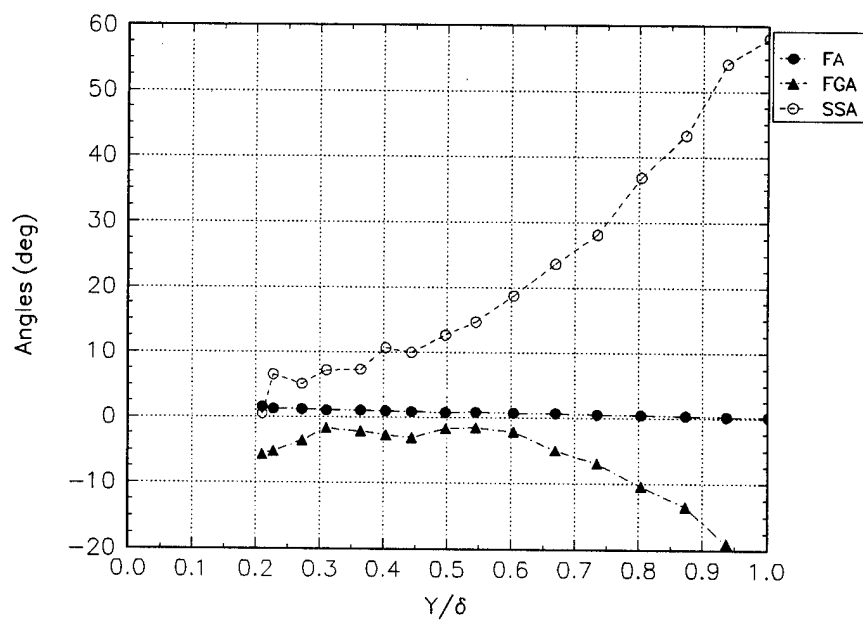


Figure E.10.a Significant flow angles for Station 3.

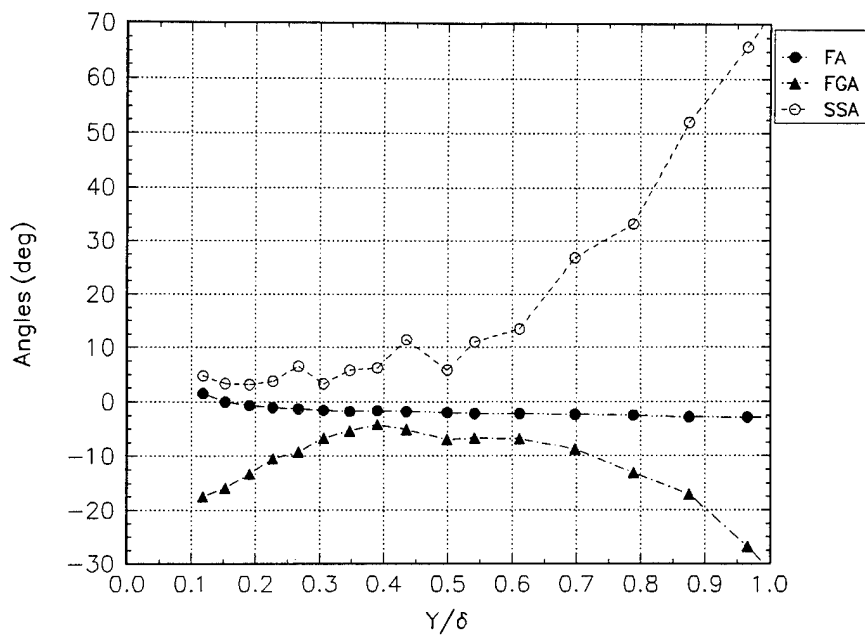


Figure E.10.b Significant flow angles for Station 6.

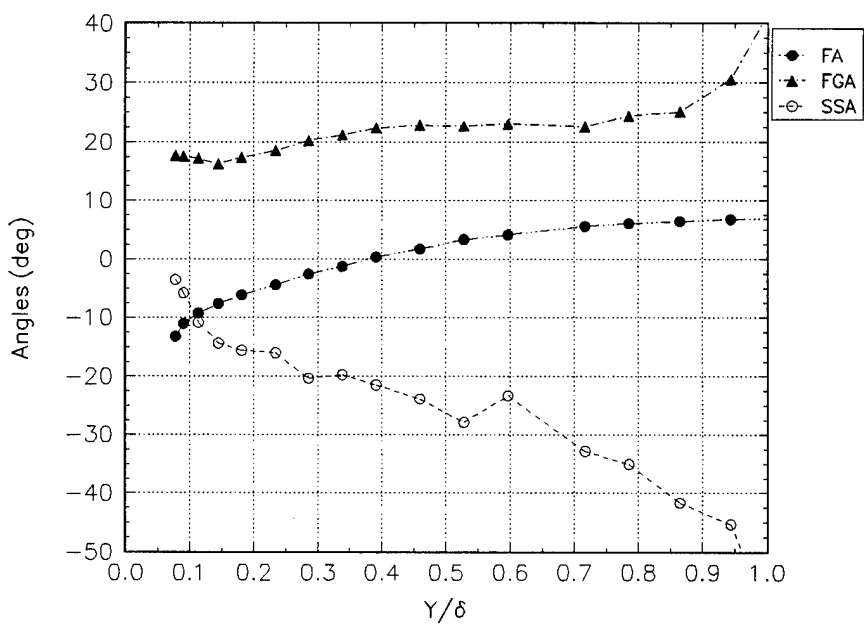


Figure E.10.c Significant flow angles for Station 8.

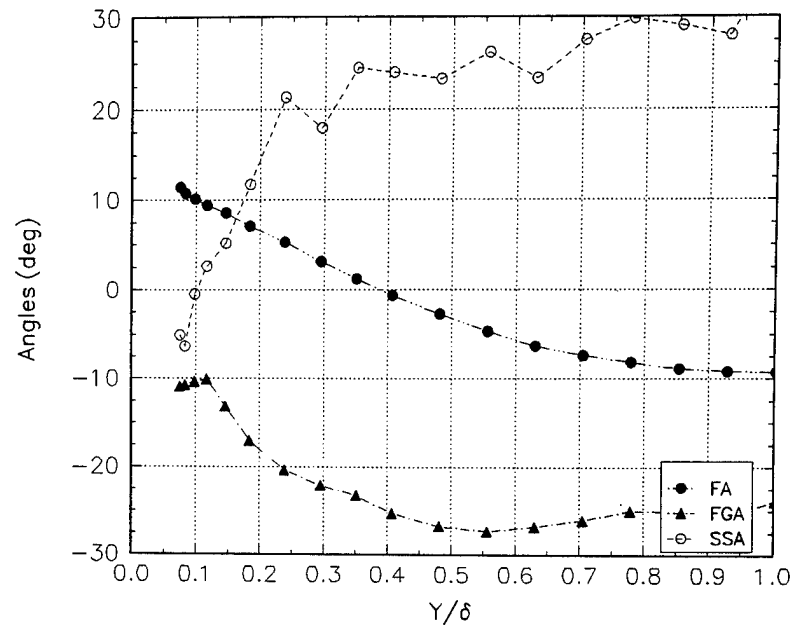


Figure E.10.d Significant flow angles for Station 10.

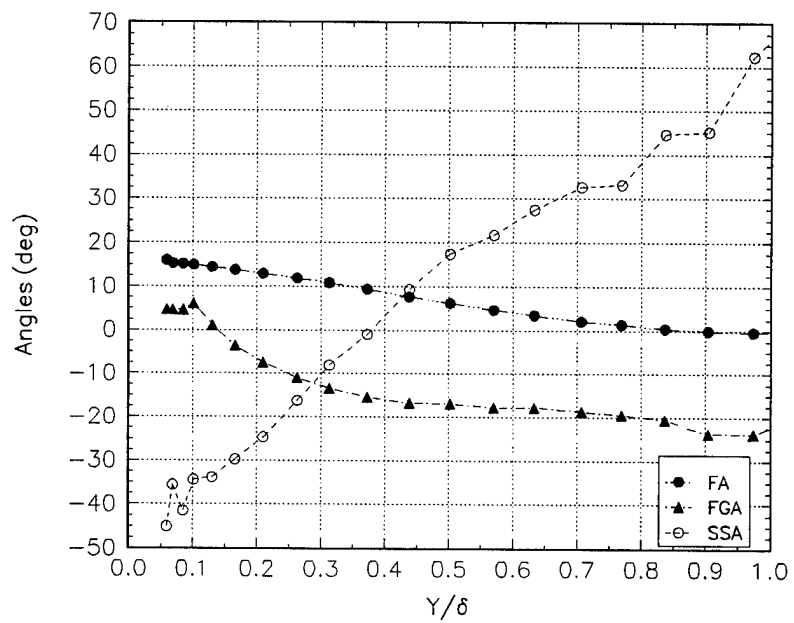


Figure E.10.e Significant flow angles for Station 11.

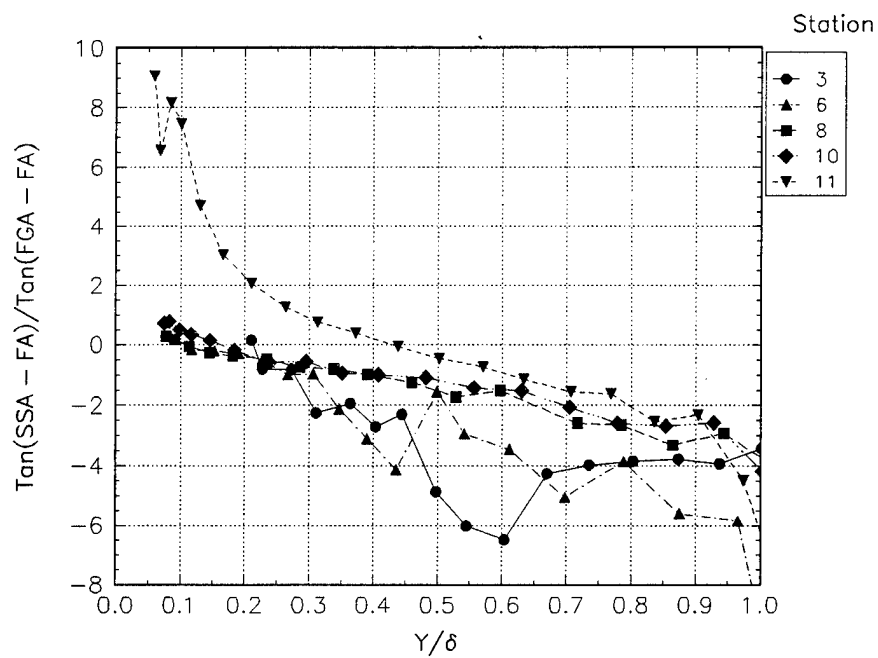


Figure E.11 Rotta's T parameter for the convex geometry.

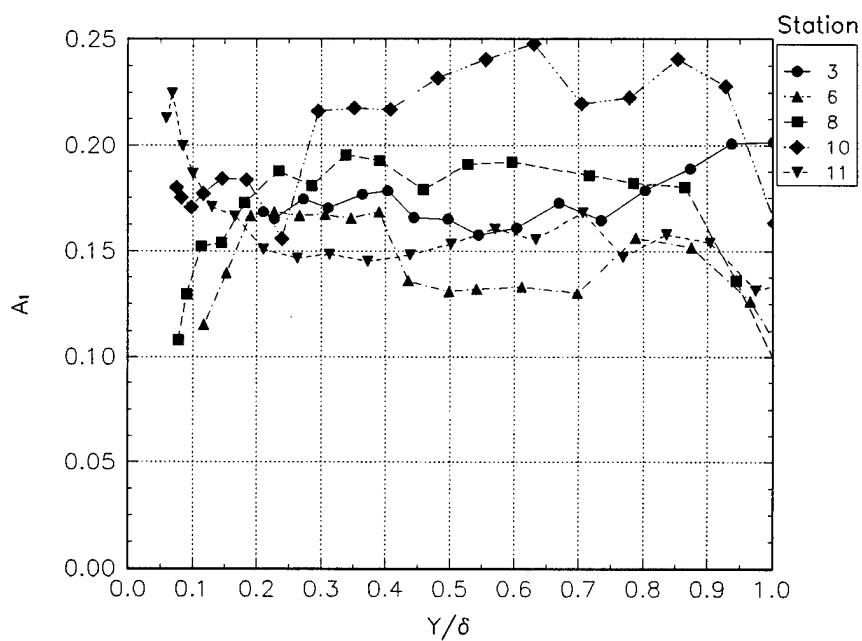


Figure E.12 The  $a_1$  parameter.

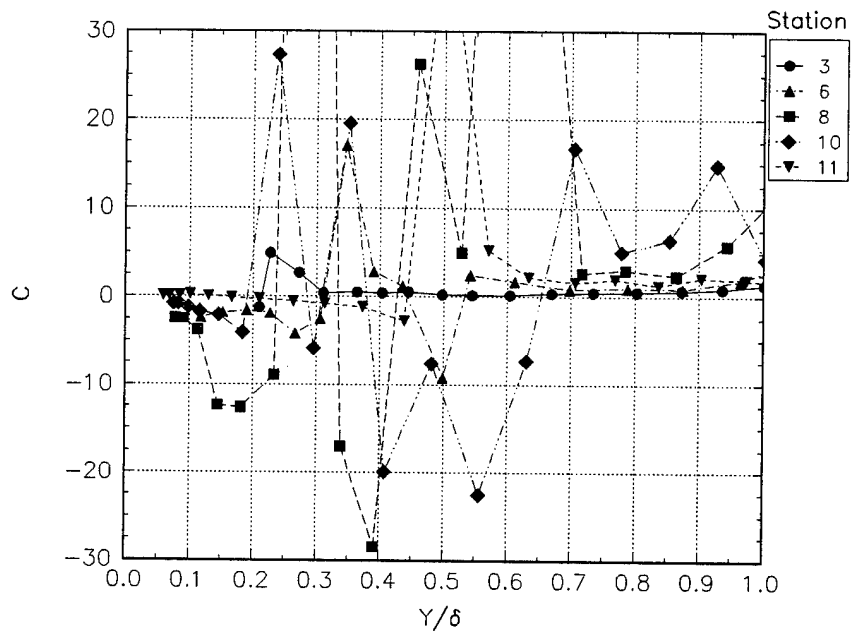


Figure E.13 The C parameter.

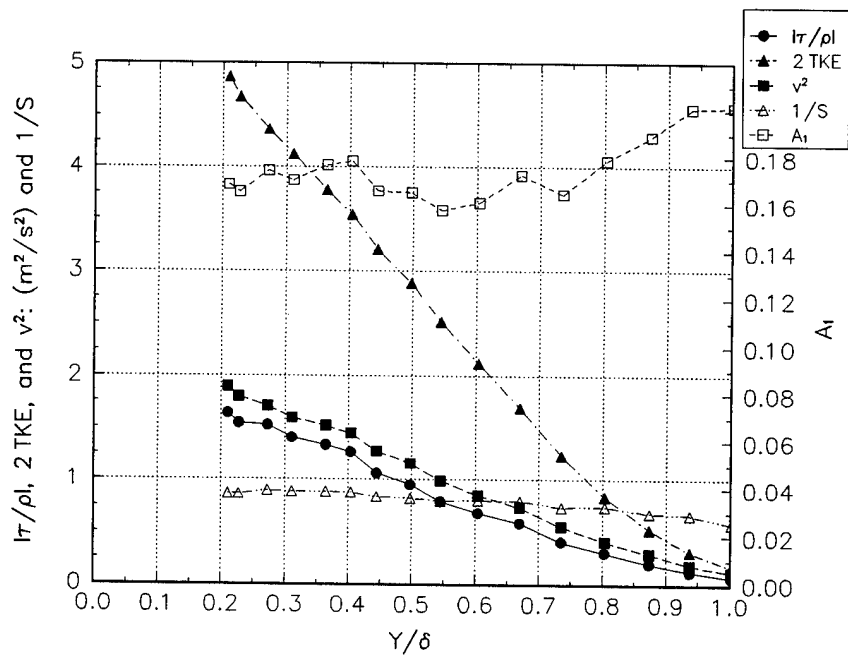


Figure E.14.a Analysis of the S parameter for station 3.



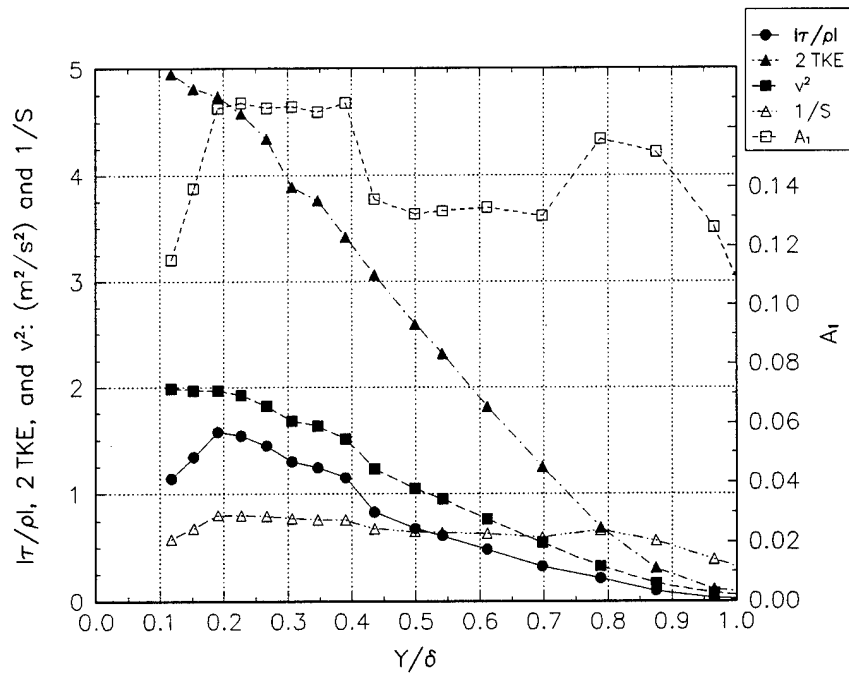


Figure E.14.b Analysis of the S parameter for station 6.

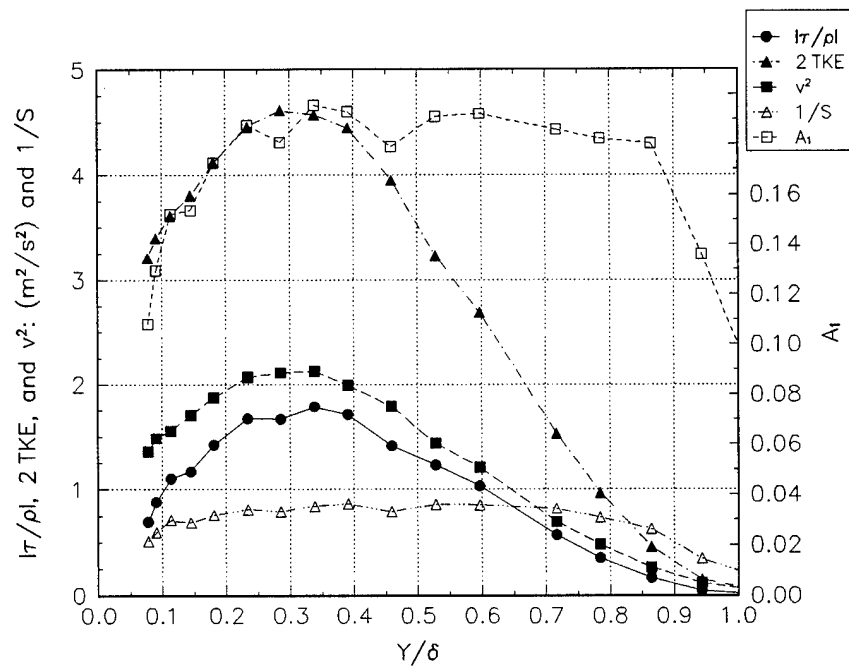


Figure E.14.c Analysis of the S parameter for station 8

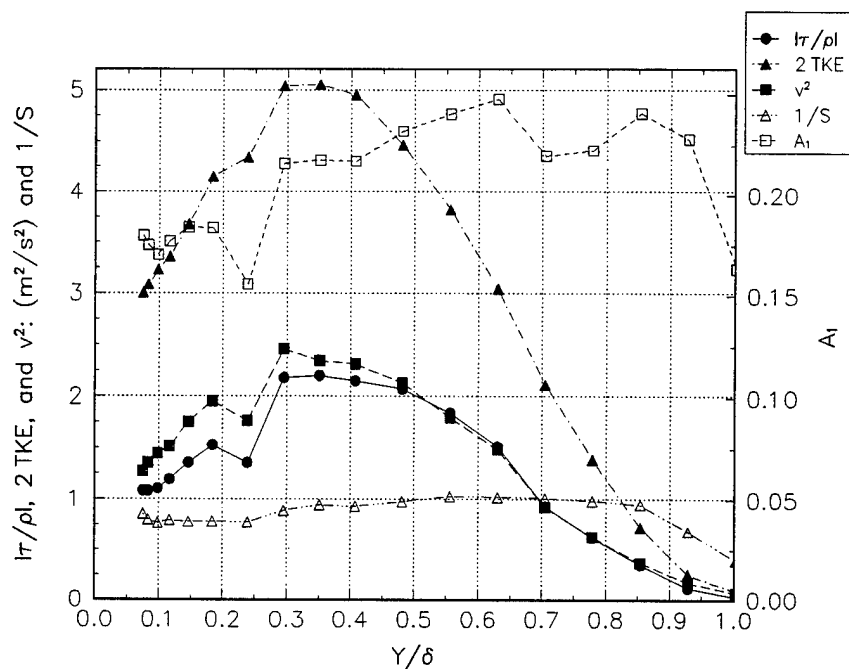


Figure E.14.d Analysis of the S parameter for station 10

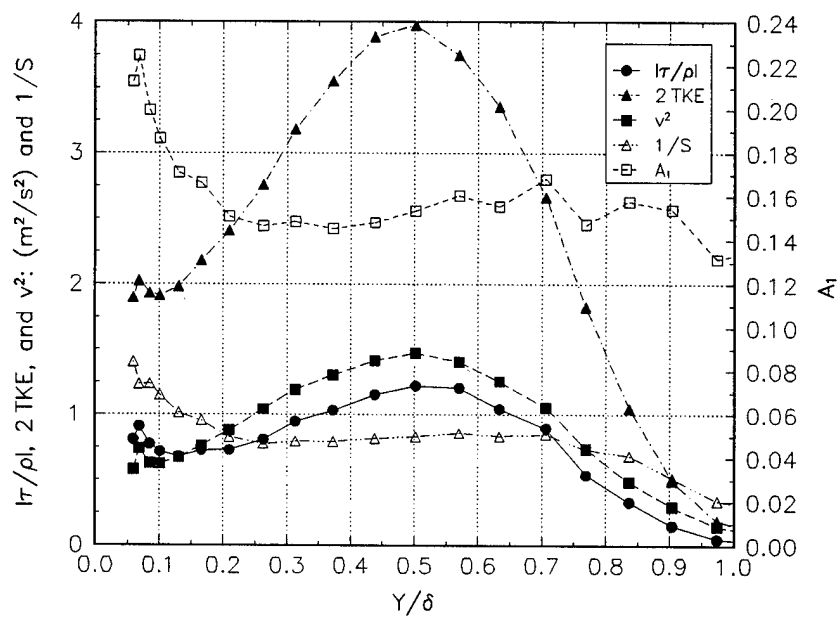


Figure E.14.e Analysis of the S parameter for station 11

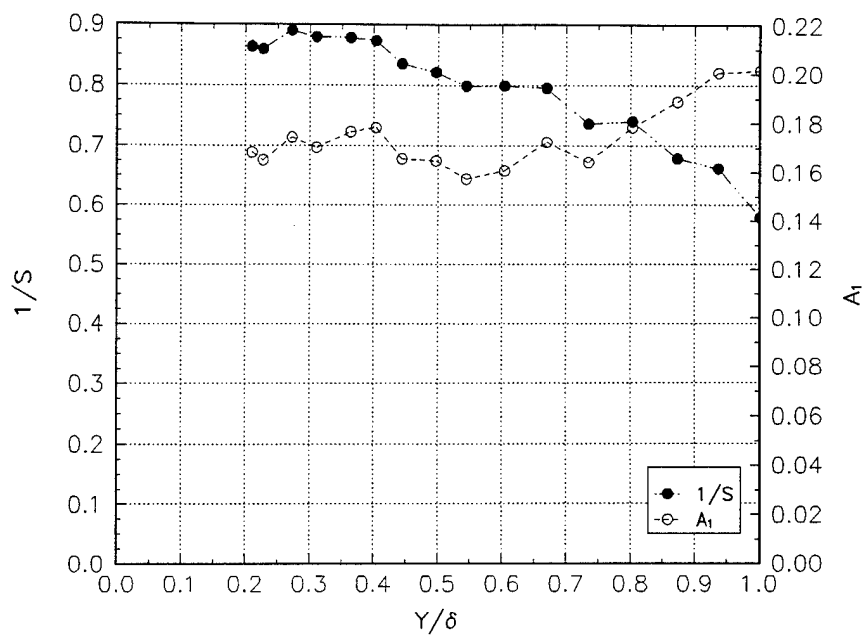


Figure E.15. Analysis of the S parameter for station 3.

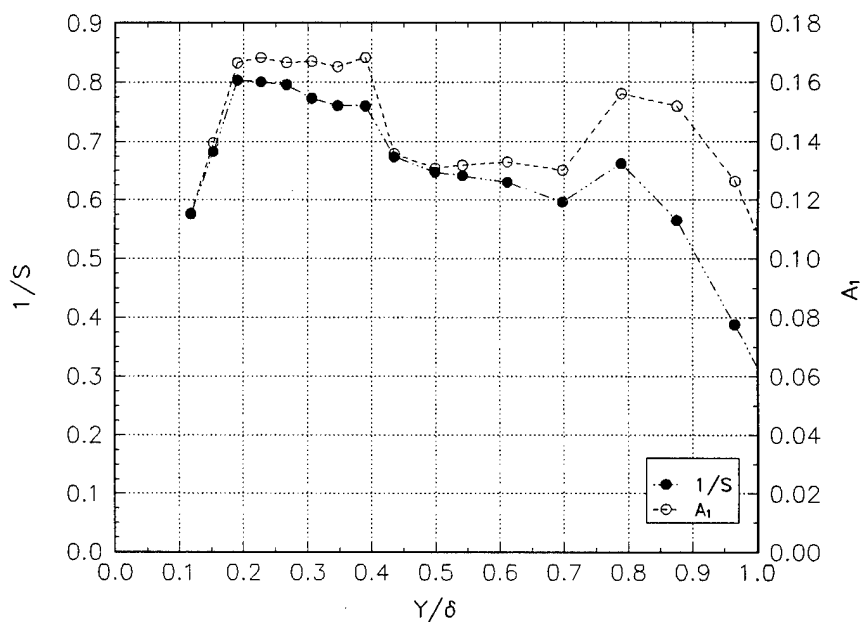


Figure E.15.b Analysis of the S parameter for station 6.

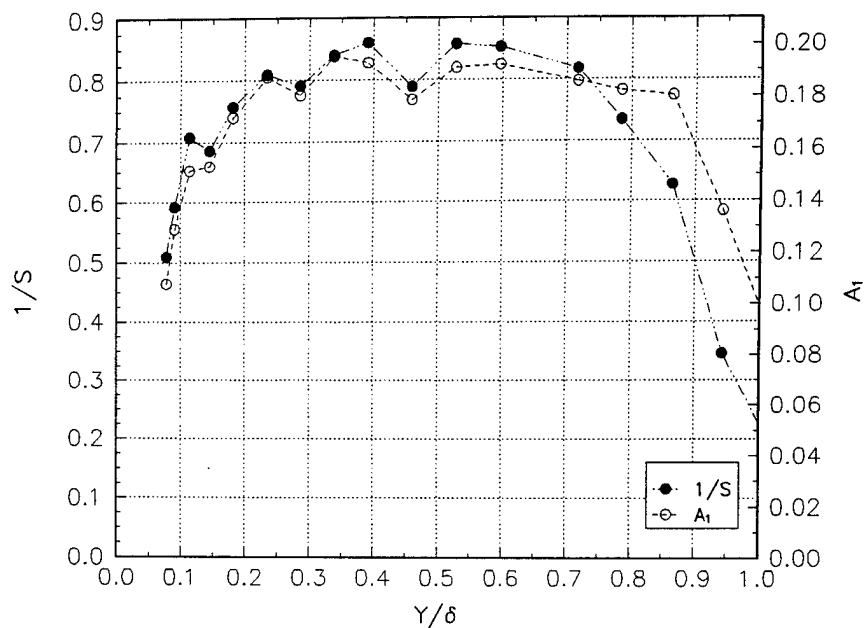


Figure E.15.c Analysis of the S parameter for station 8.

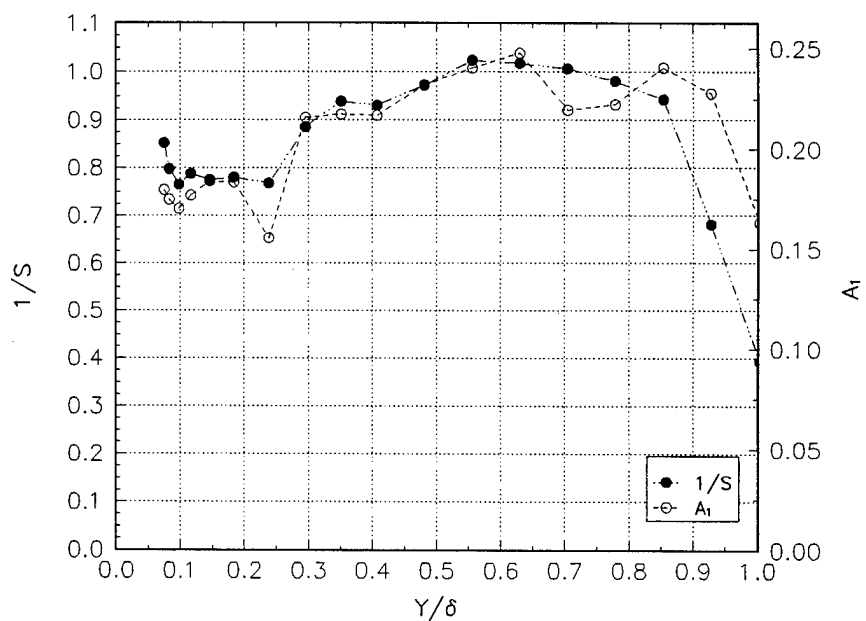


Figure E.15.d Analysis of the S parameter for station 10.

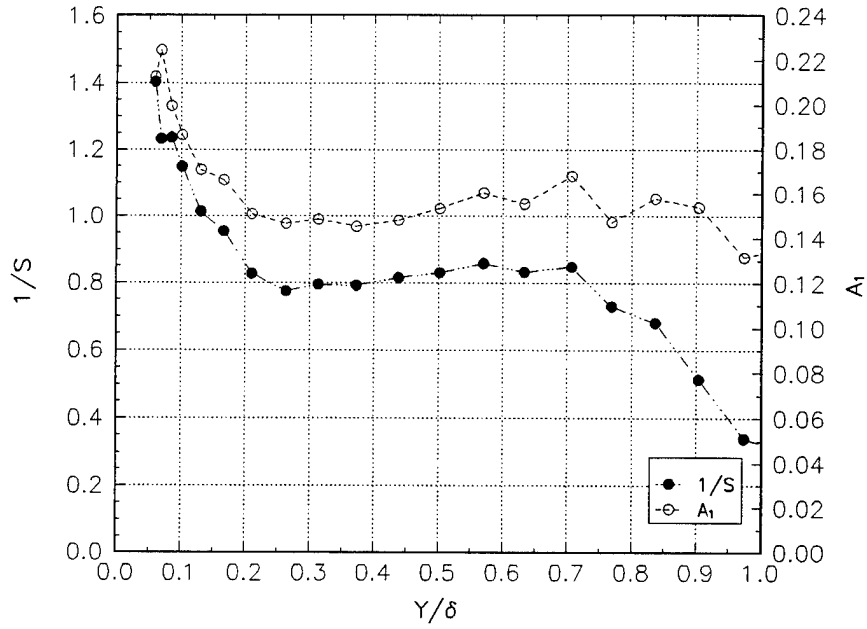


Figure E.15.e Analysis of the S parameter for station 11.

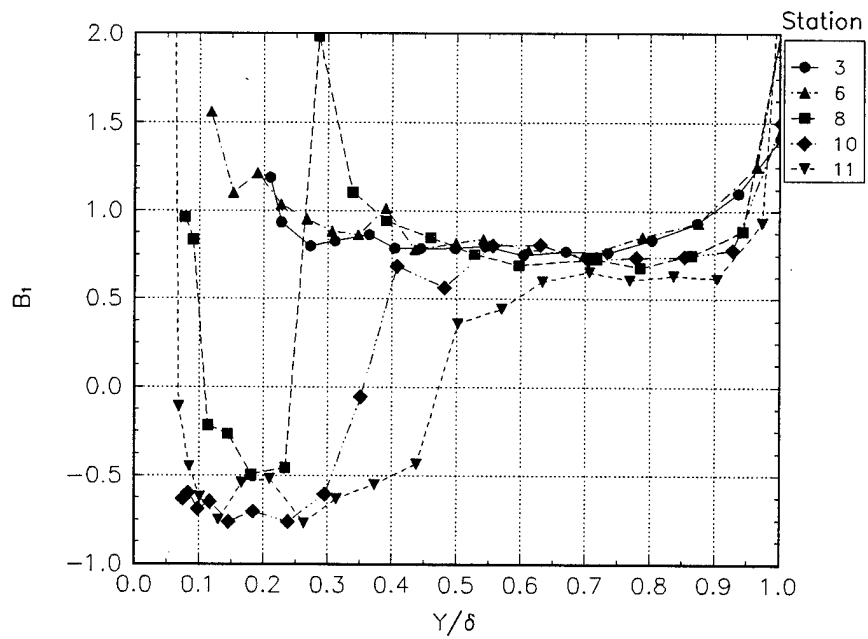


Figure E.16 The  $B_1$  parameter.

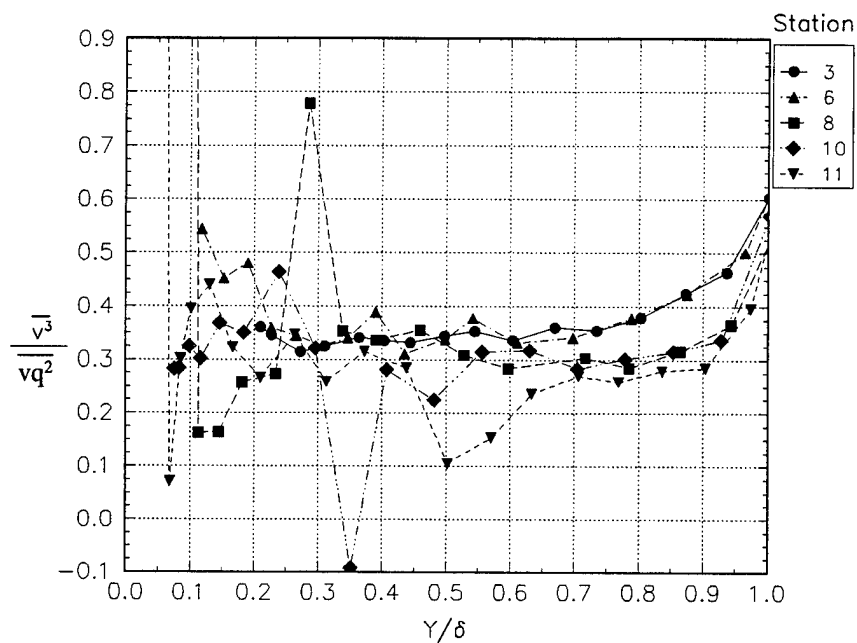


Figure E.17 Triple product relationship.

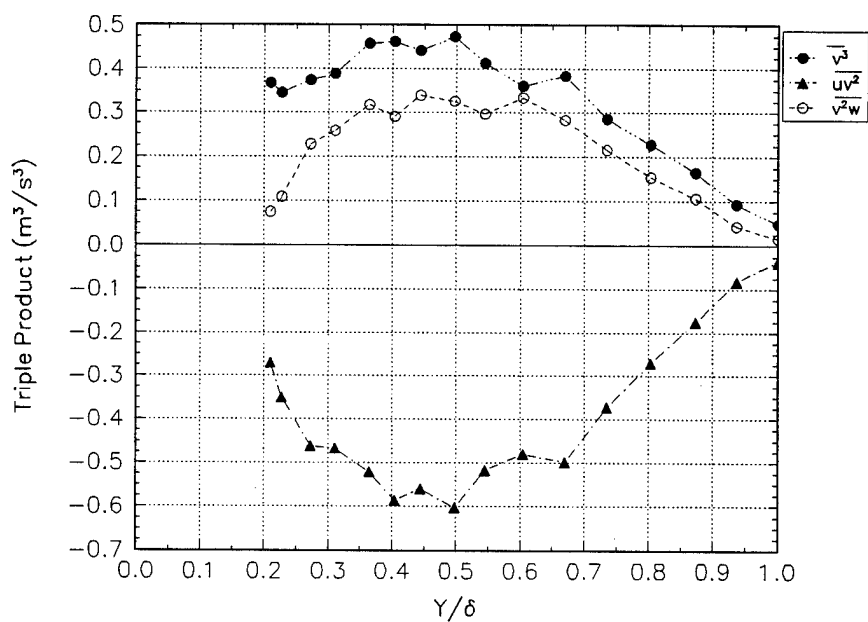


Figure E.18.a Significant triple products for station 3.

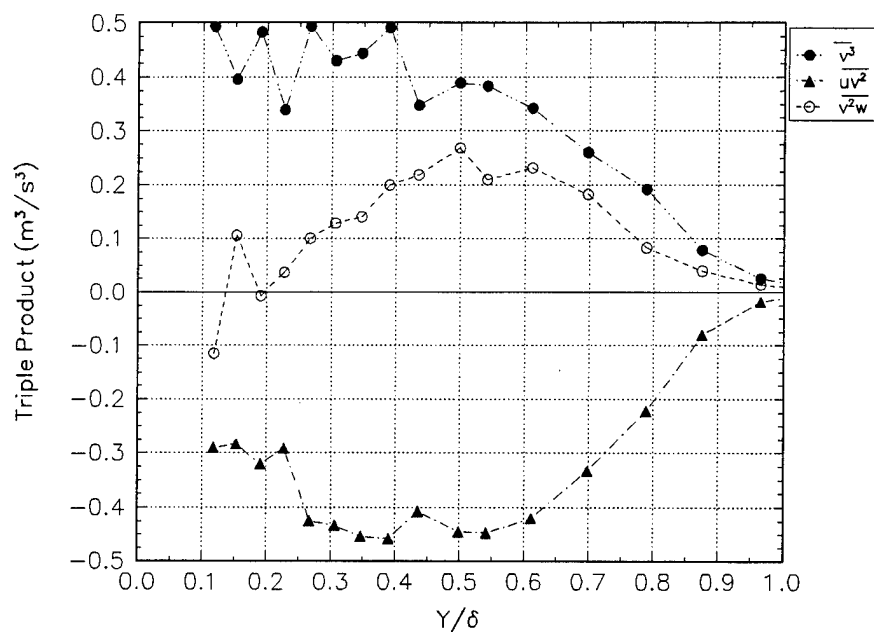


Figure E.18.b Significant triple products for station 6.

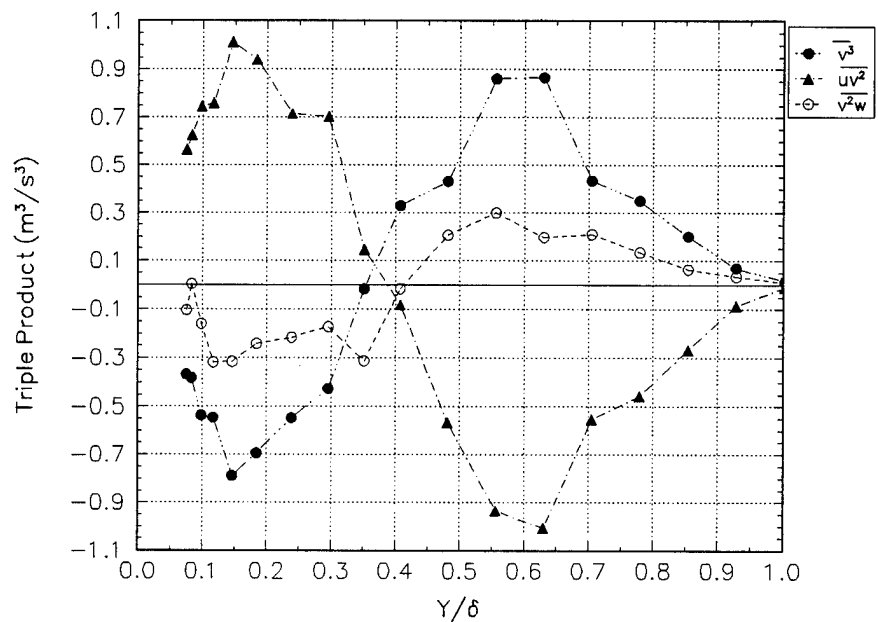


Figure E.18.c Significant triple products for station 10.

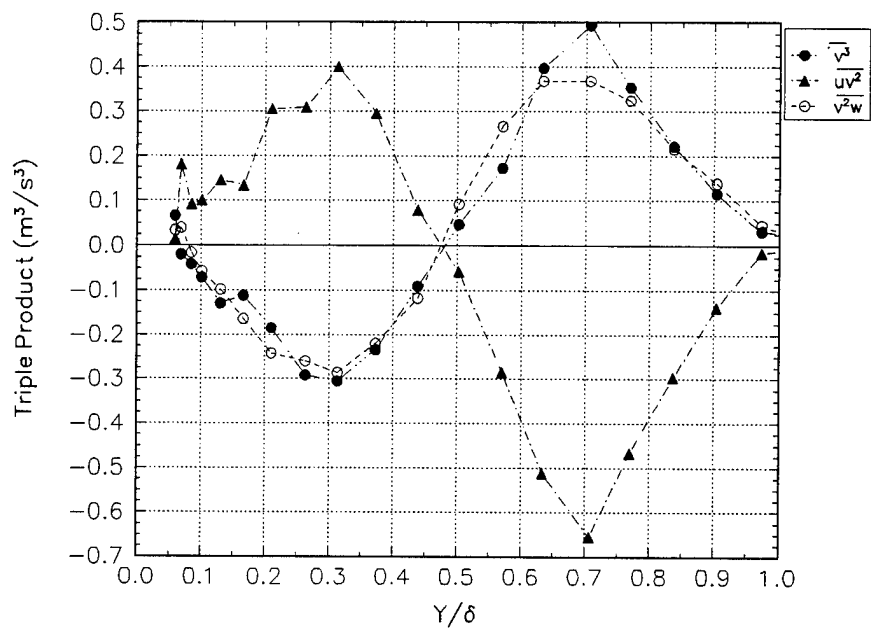


Figure E.18.d Significant triple products for station 11.

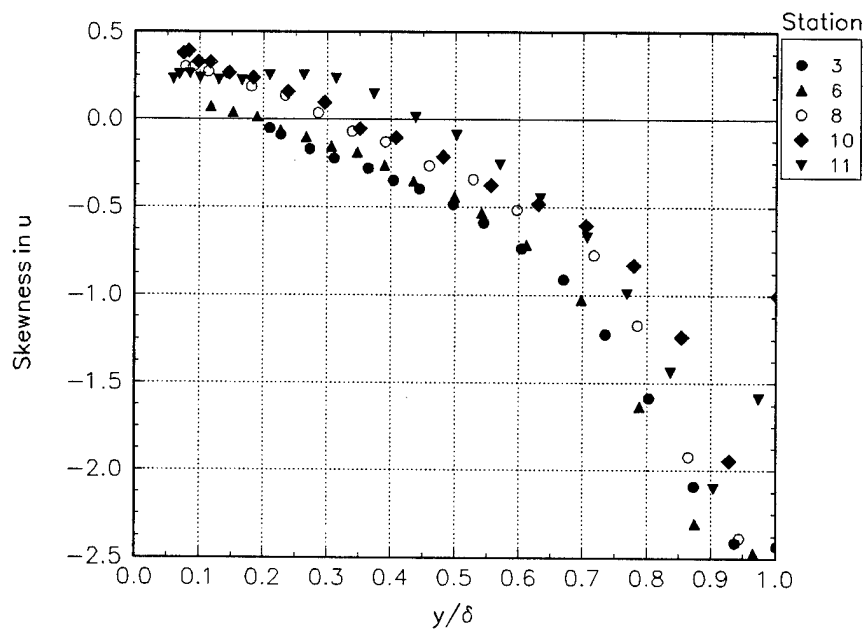


Figure E.19 Skewness in u.



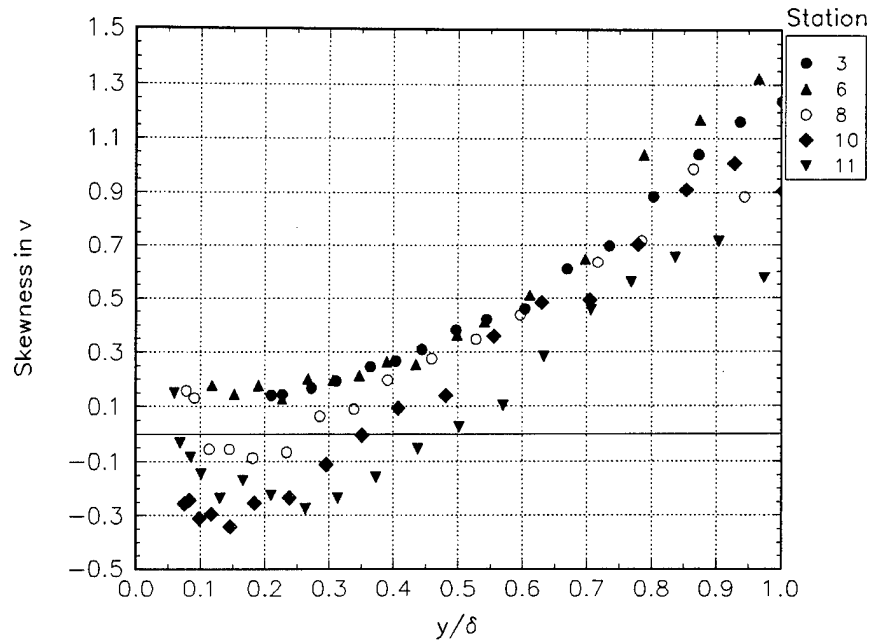


Figure E.20 Skewness in  $v$ .

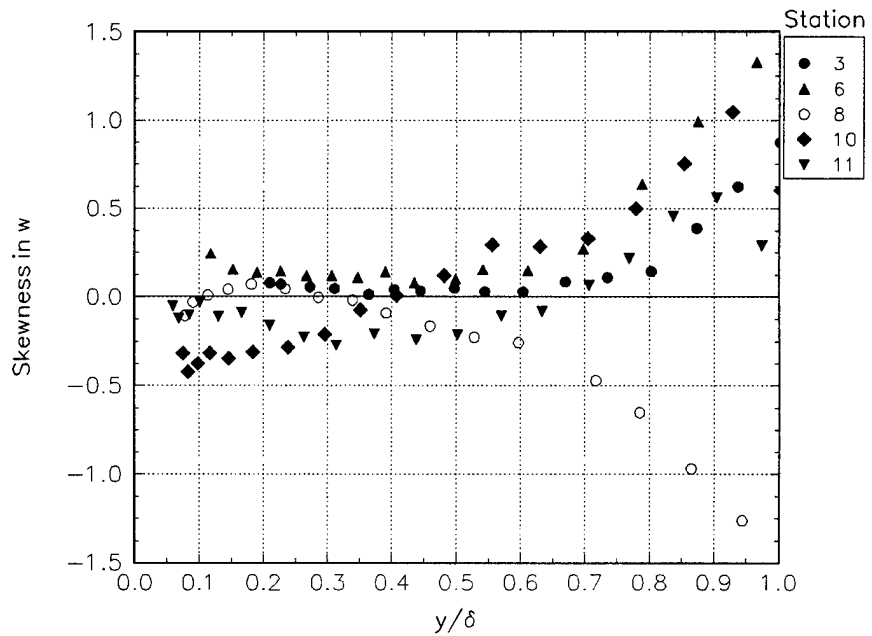


Figure E.21 Skewness in  $w$ .

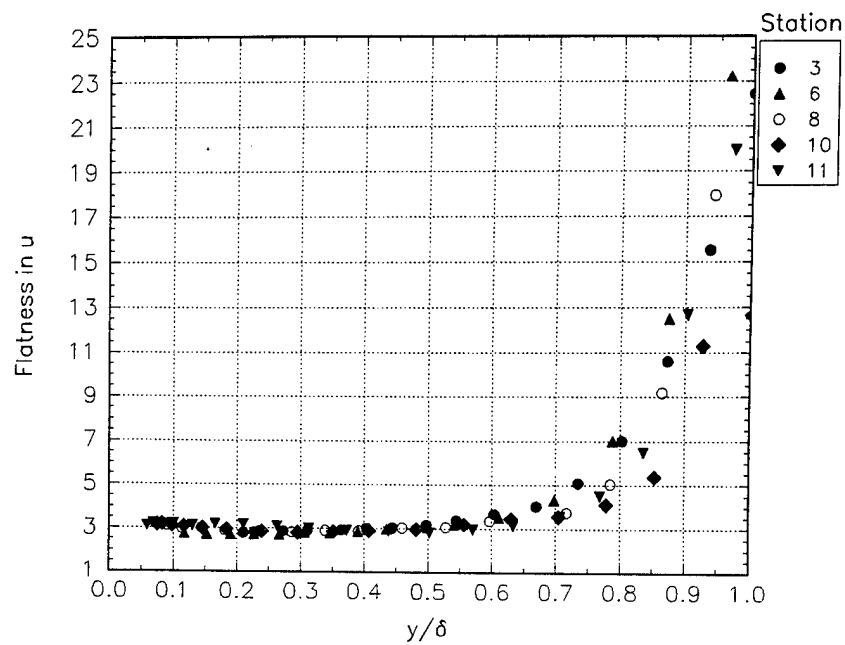


Figure E.22 Flatness in  $u$ .

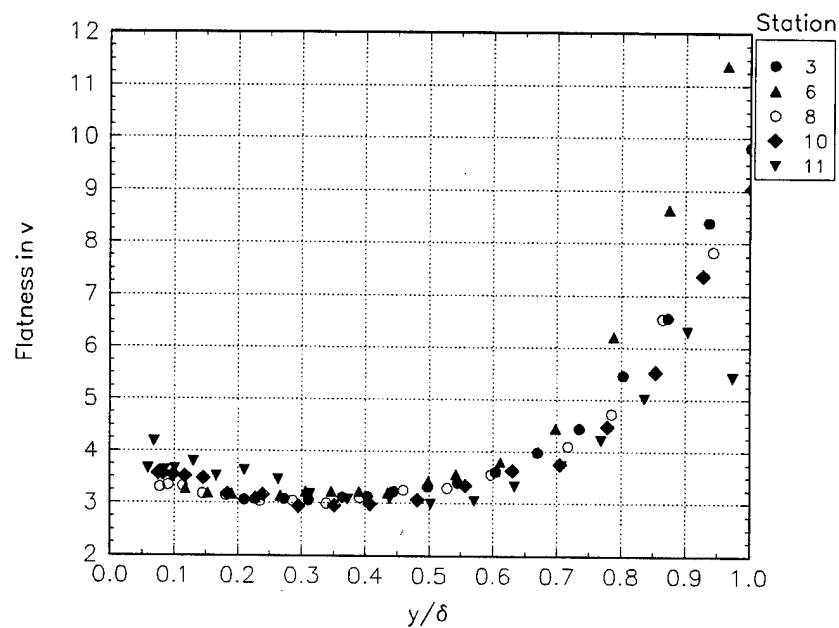


Figure E.23 Flatness in  $v$ .

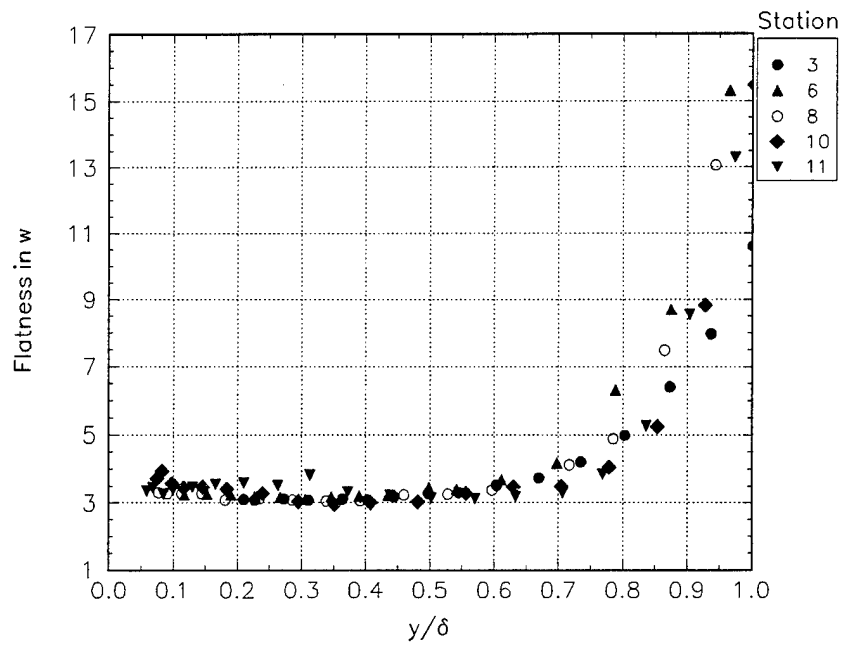


Figure E.24 Flatness in  $w$

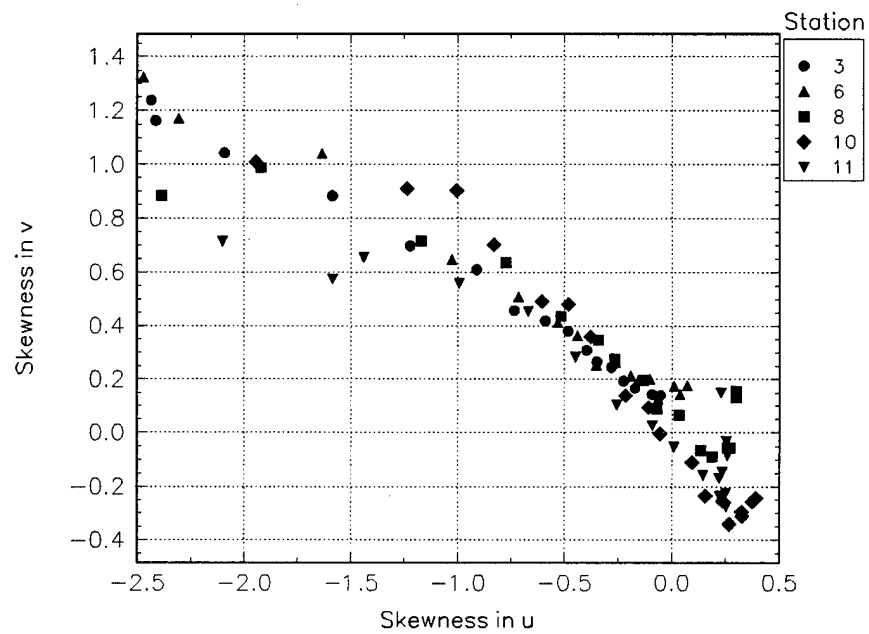


Figure E.25 Skewness relationship.

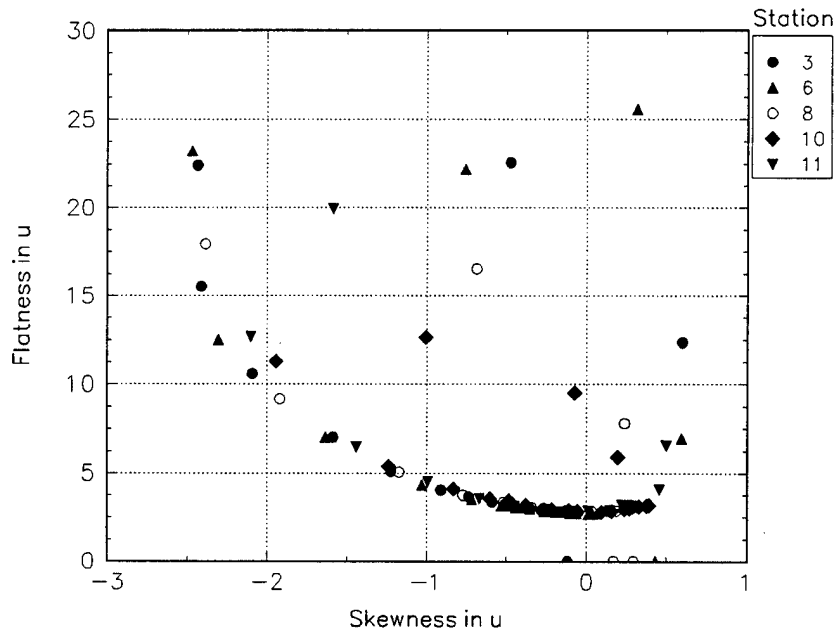


Figure E.26.a Skewness v. flatness in  $u$ .

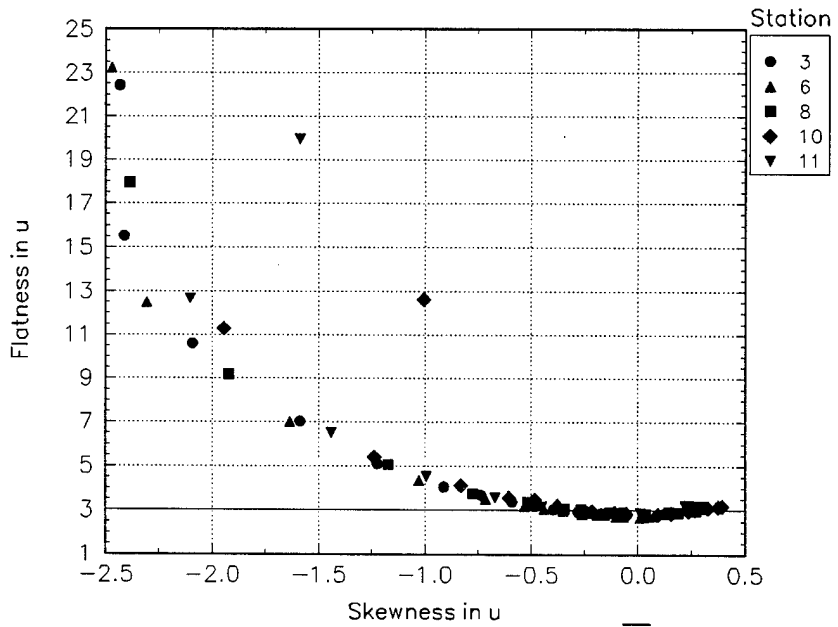


Figure E.26.b Skewness v. flatness in  $u^2$ .

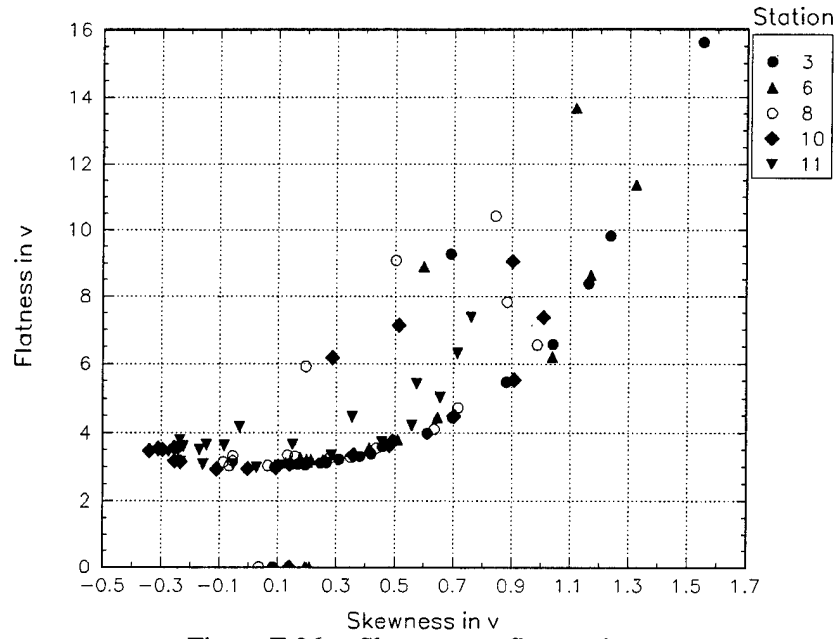


Figure E.26.c Skewness v. flatness in  $v$ .

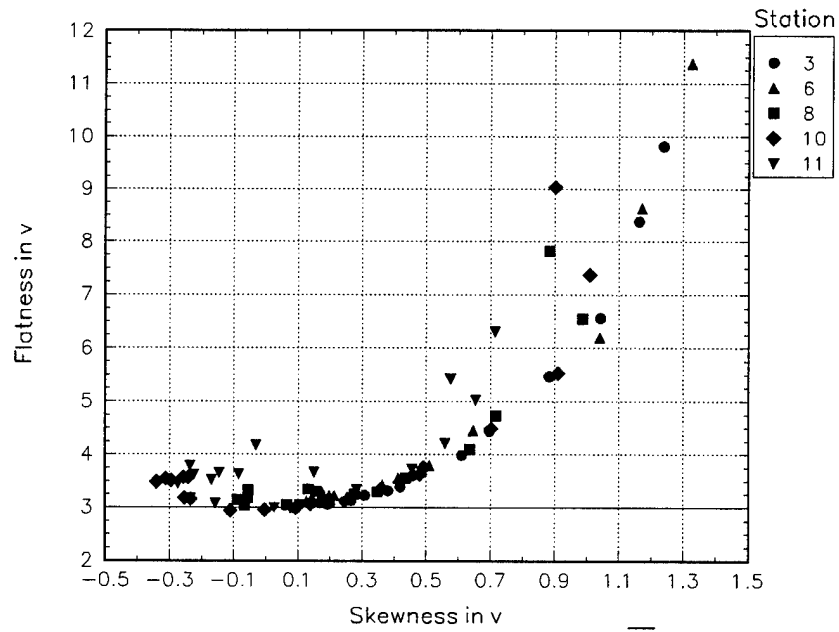


Figure E.26.d Skewness v. flatness in  $\overline{v^2}$ .

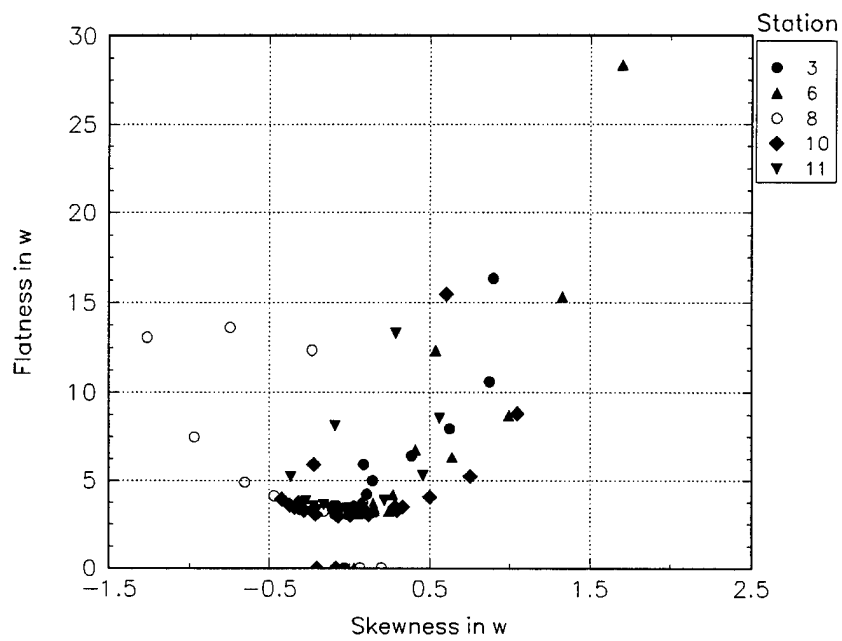


Figure E.26.e Skewness v. flatness in  $w$ .

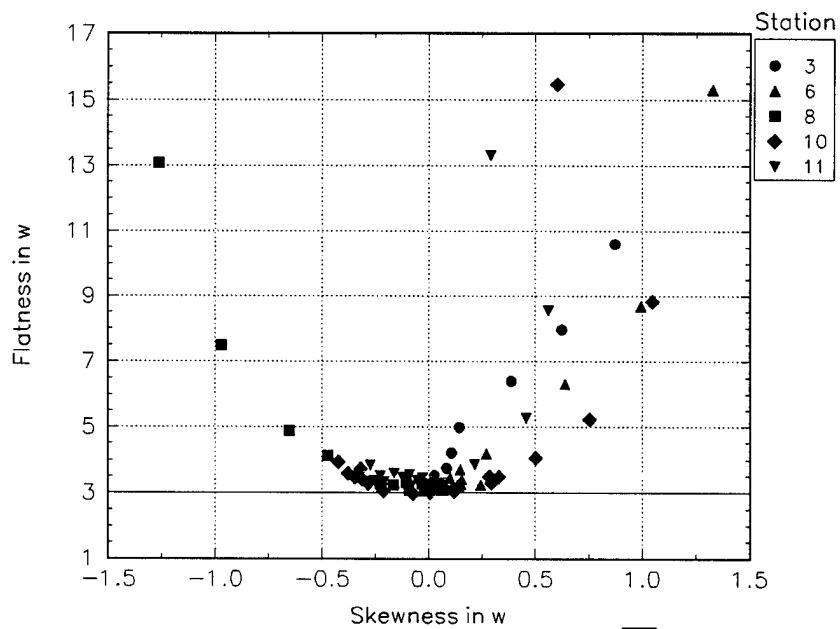


Figure E.26.f Skewness v. flatness in  $w^2$ .

## APPENDIX F Additional Figures for the Data of Chesnakas

(all data presented here is in local free-stream coordinates)

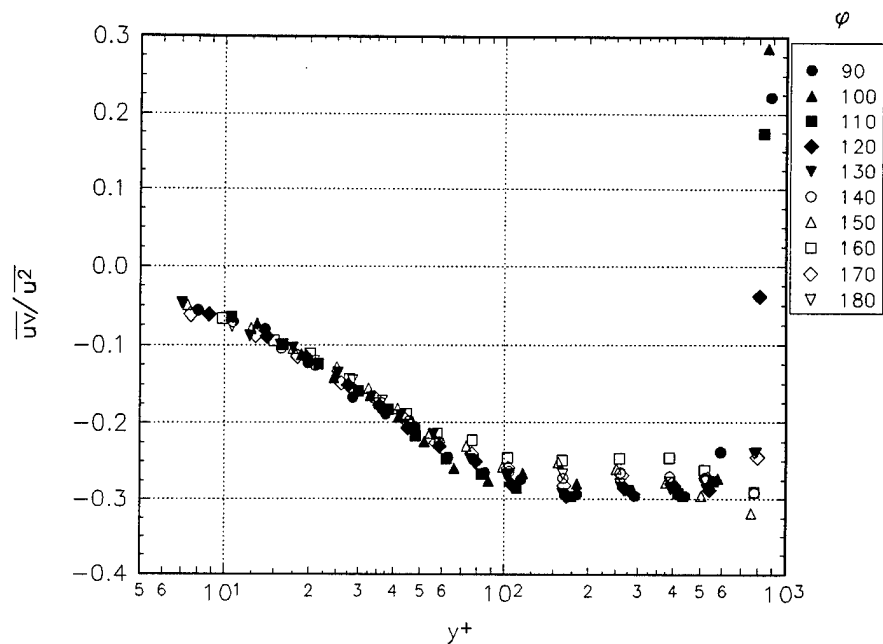


Figure F.1.a Reynolds stress ratio for  $x/L = 0.40$ .

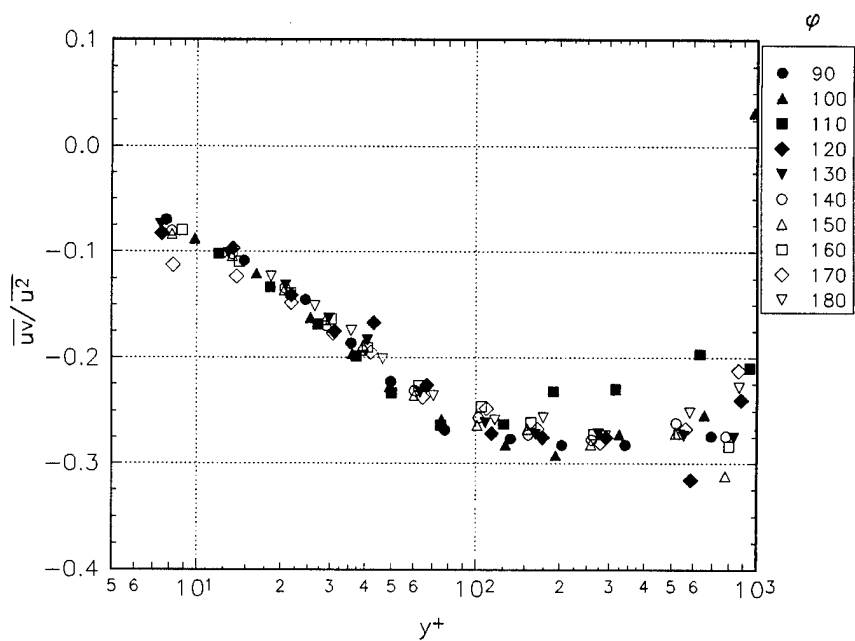


Figure F.1.b Reynolds stress ratio for  $x/L = 0.60$ .

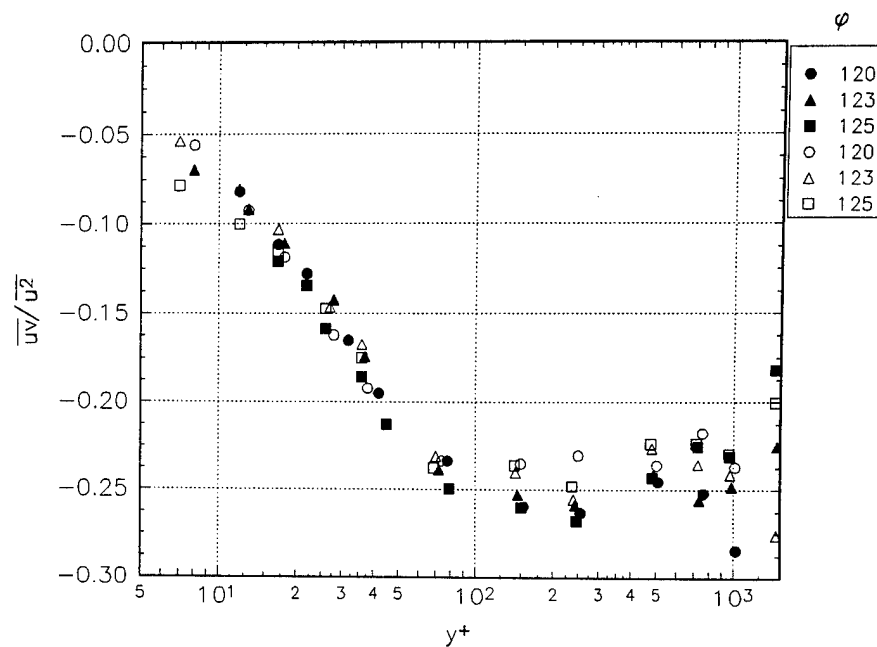


Figure F.1.c Reynolds stress ratio, closed symbols for  $x/L = 0.75$  and open for  $x/L = 0.76$ .

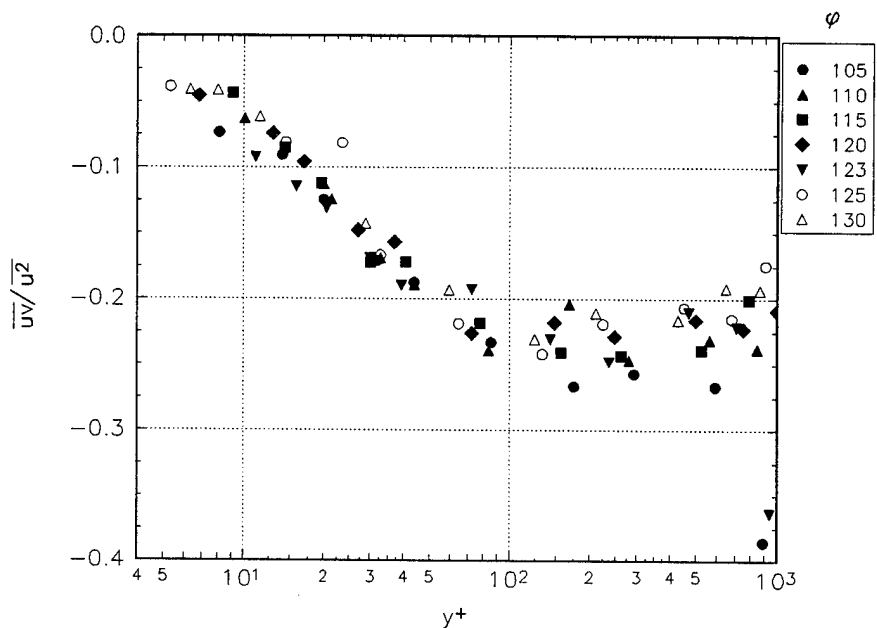


Figure F.1.d Reynolds stress ratio for  $x/L = 0.77$ .



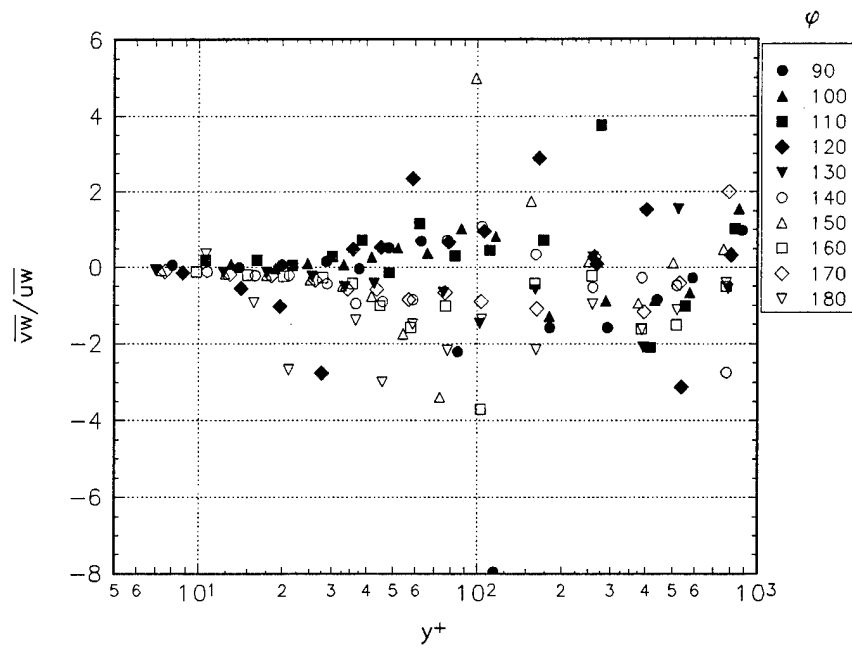


Figure F.2.a Reynolds stress ratio for  $x/L = 0.40$ .

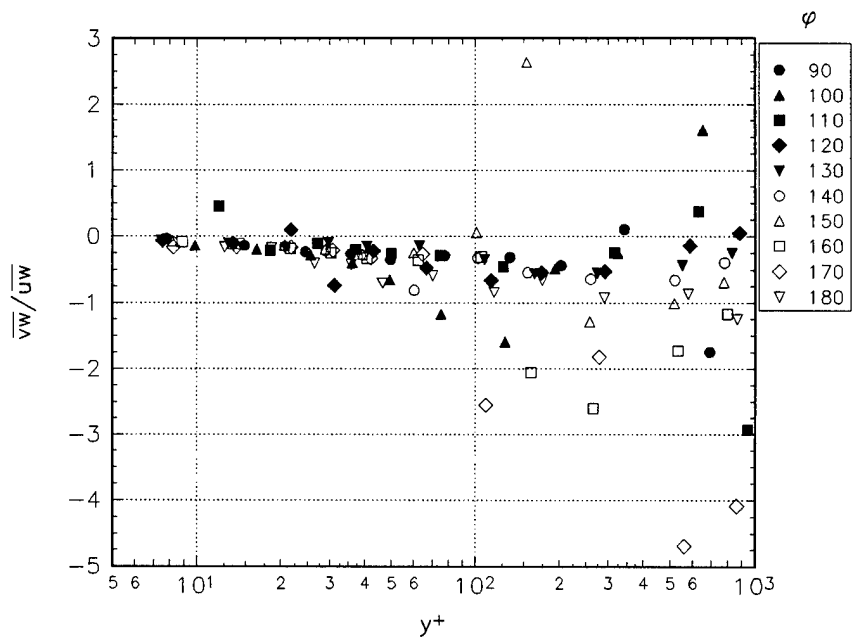


Figure F.2.b Reynolds stress ratio for  $x/L = 0.60$ .

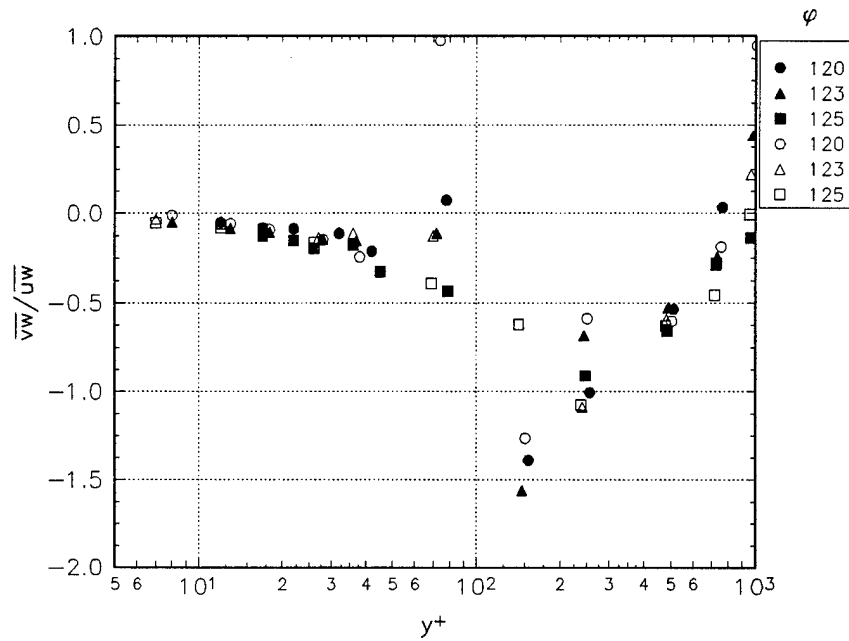


Figure F.2.c Reynolds stress ratio, closed symbols for  $x/L = 0.75$  and open for  $x/L = 0.76$ .

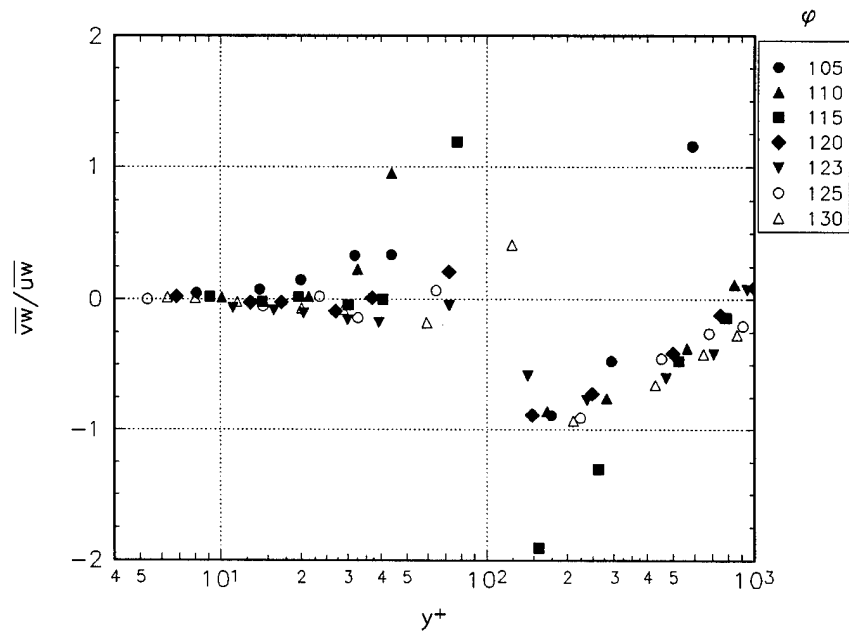


Figure F.2.d Reynolds stress ratio for  $x/L = 0.77$ .

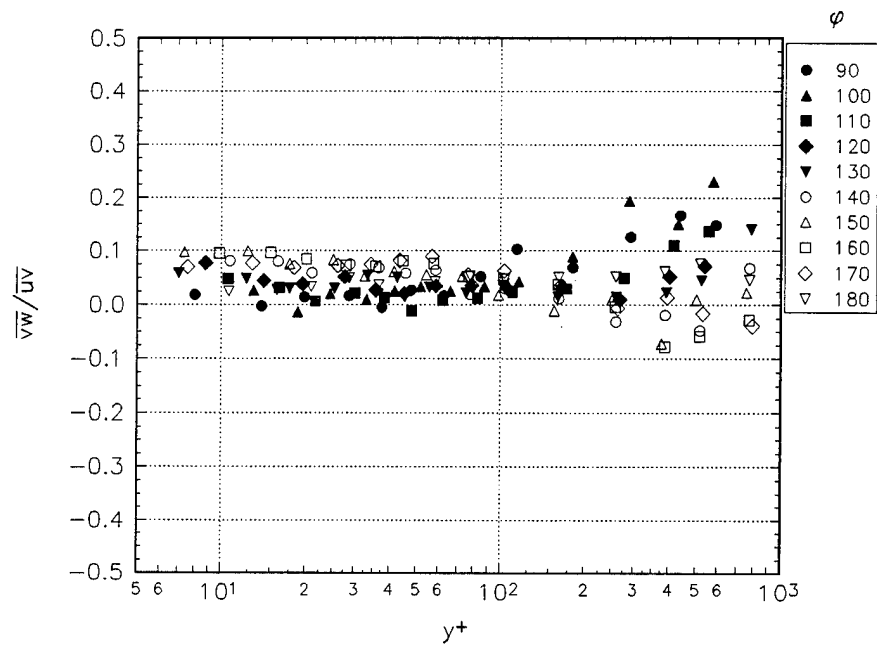


Figure F.3.a Reynolds stress ratio for  $x/L = 0.40$ .

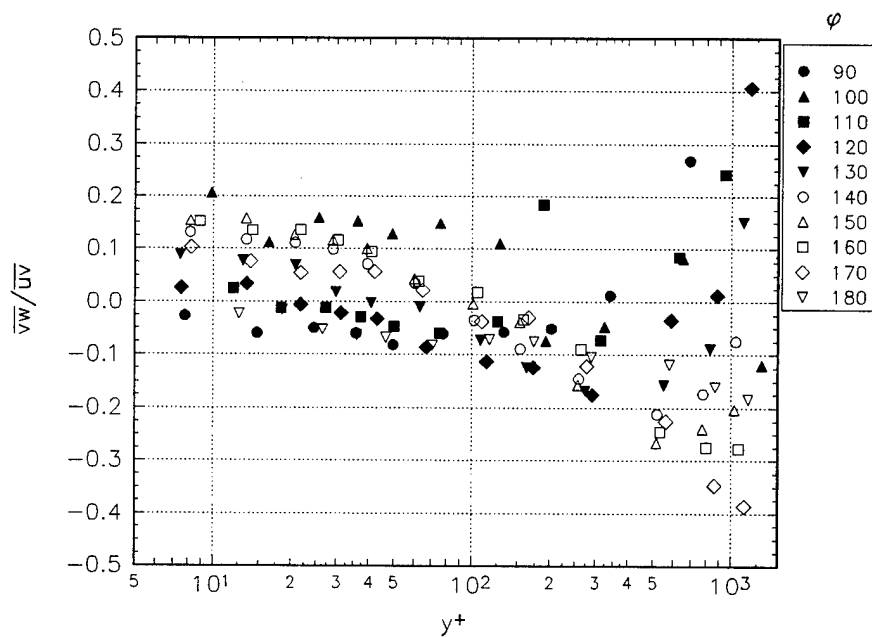


Figure F.3.b Reynolds stress ratio for  $x/L = 0.60$ .

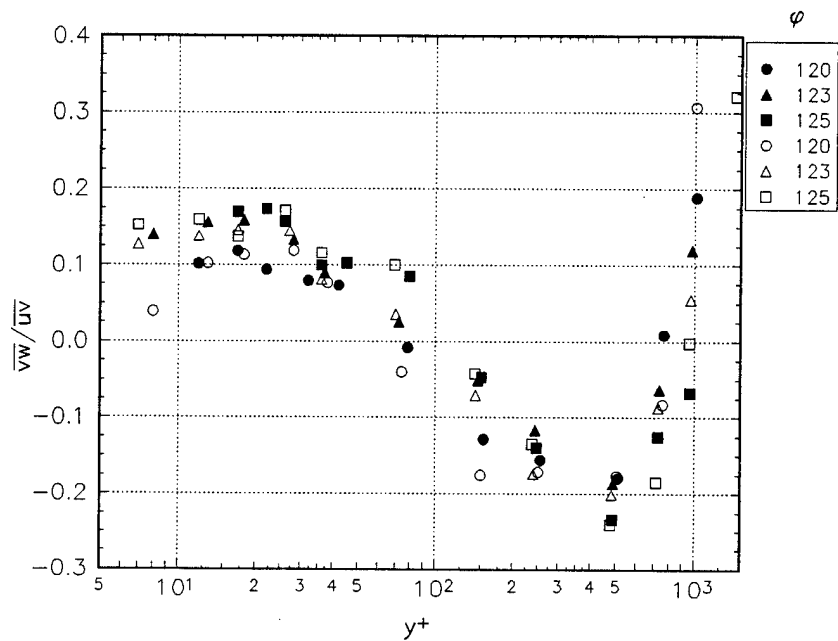


Figure F.3.c Reynolds stress ratio, closed symbols for  $x/L = 0.75$  and open for  $x/L = 0.76$ .

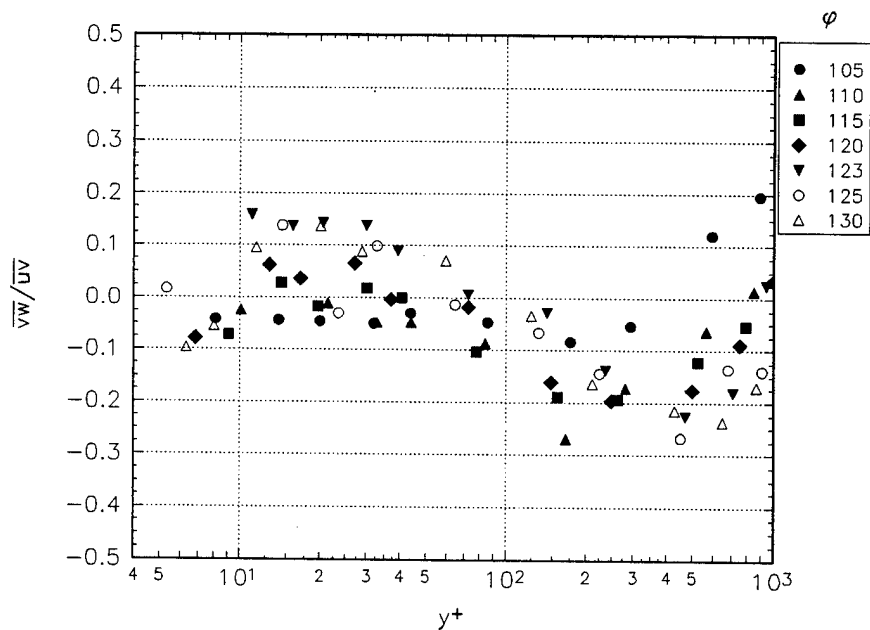


Figure F.3.d Reynolds stress ratio for  $x/L = 0.77$ .

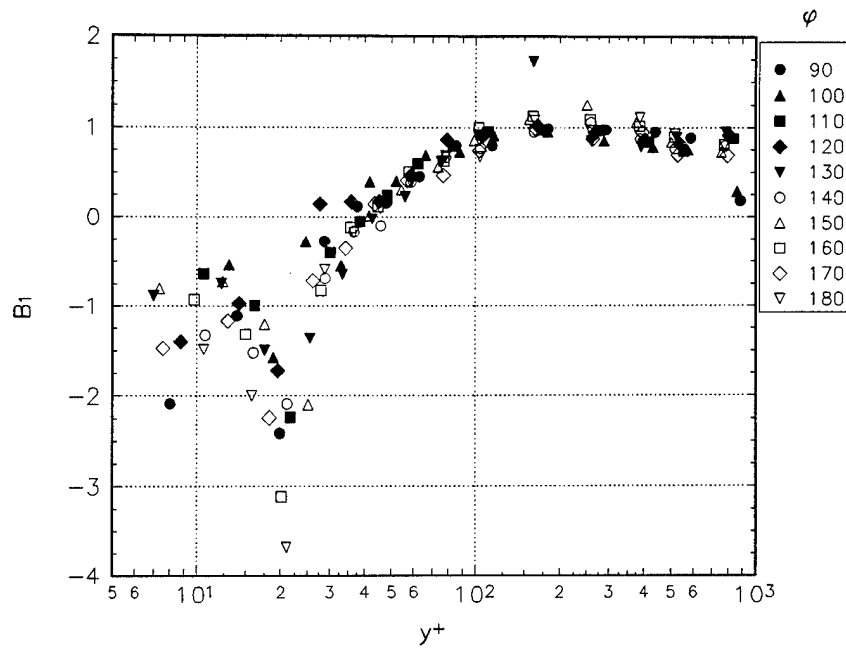


Figure F.4.a The  $B_1$  parameter for  $x/L = 0.40$ .

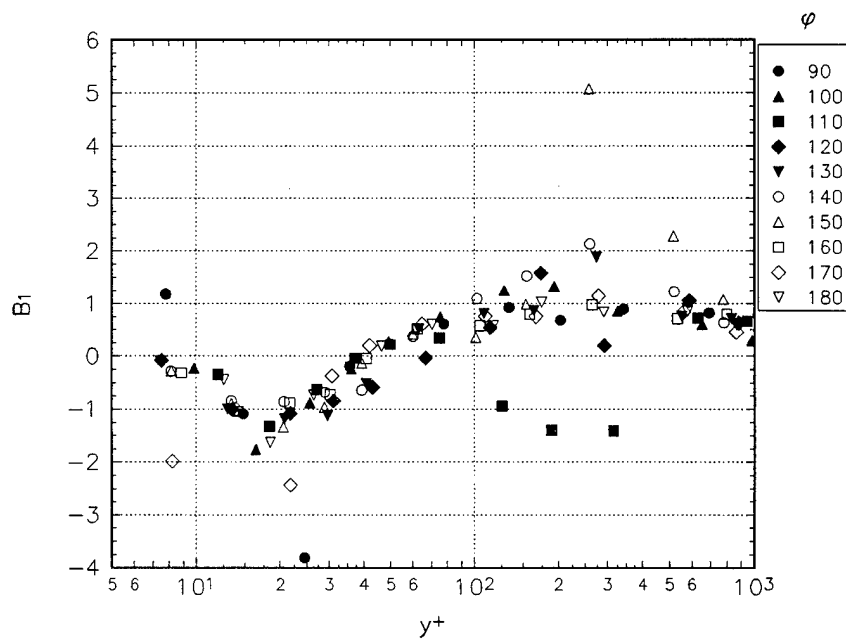


Figure F.4.b The  $B_1$  parameter for  $x/L = 0.60$ .

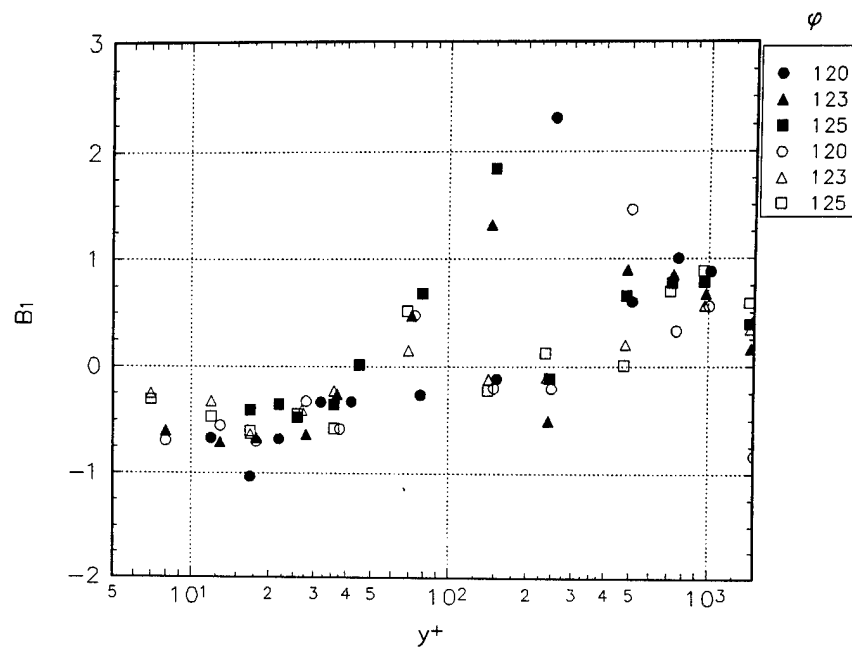


Figure F.4.c The  $B_1$  parameter, closed symbols for  $x/L = 0.75$  and open for  $x/L = 0.76$ .

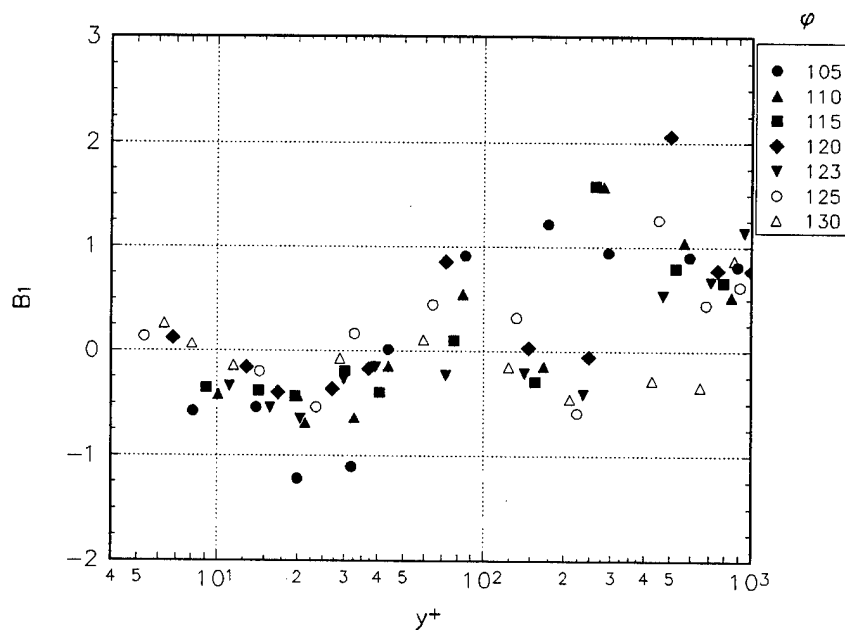


Figure F.4.d The  $B_1$  parameter for  $x/L = 0.77$ .

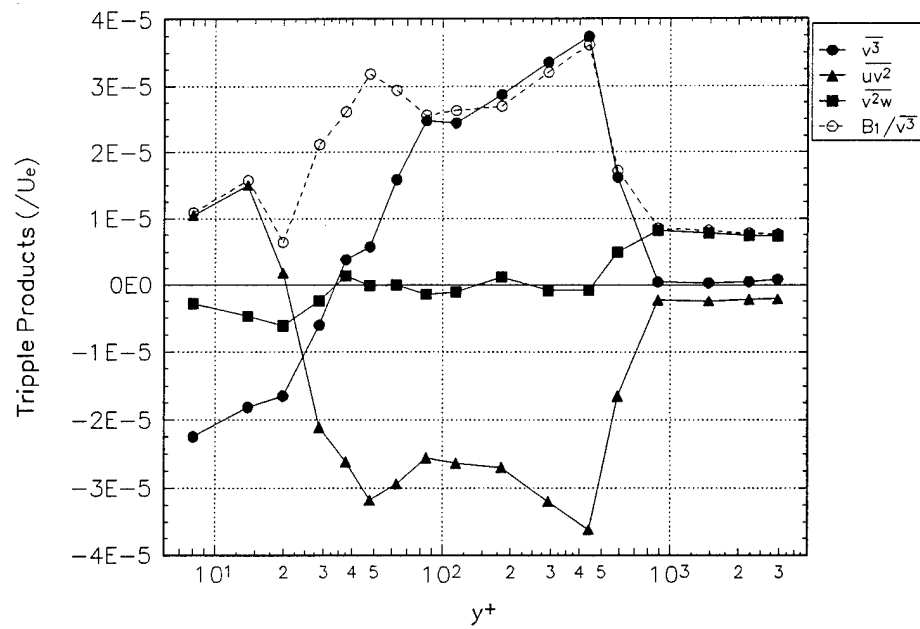


Figure F.5.a Analysis of  $B_1$  for  $x/L = 0.40$ ,  $\phi = 90^\circ$ .

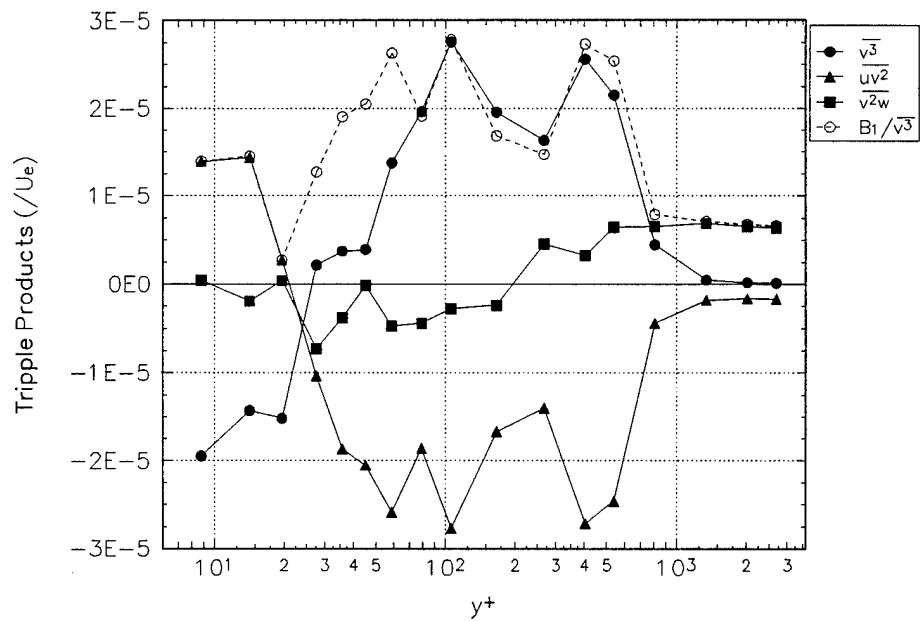


Figure F.5.b Analysis of  $B_1$  for  $x/L = 0.40$ ,  $\phi = 120^\circ$ .

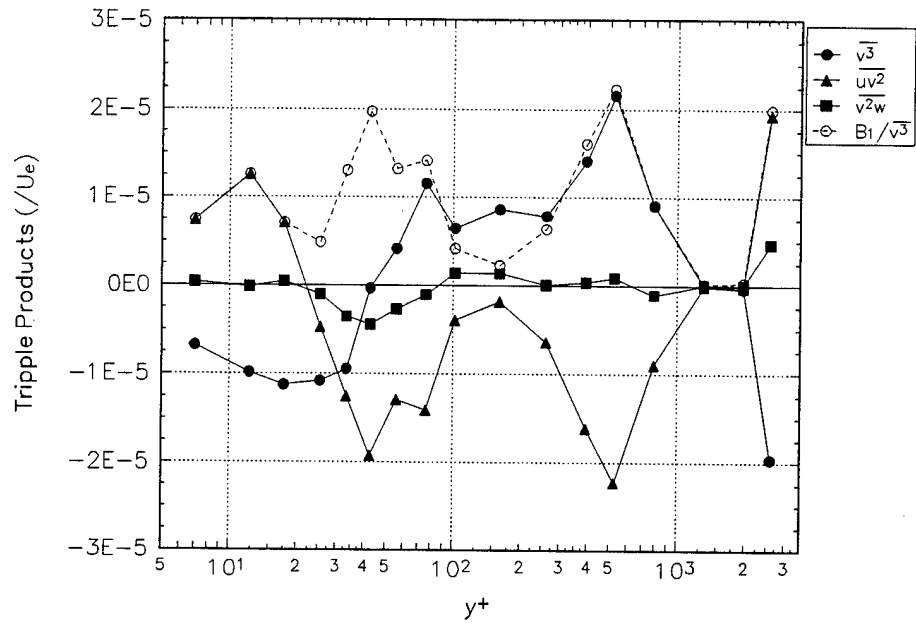


Figure F.5.c Analysis of  $B_1$  for  $x/L = 0.40$ ,  $\phi = 130^\circ$ .

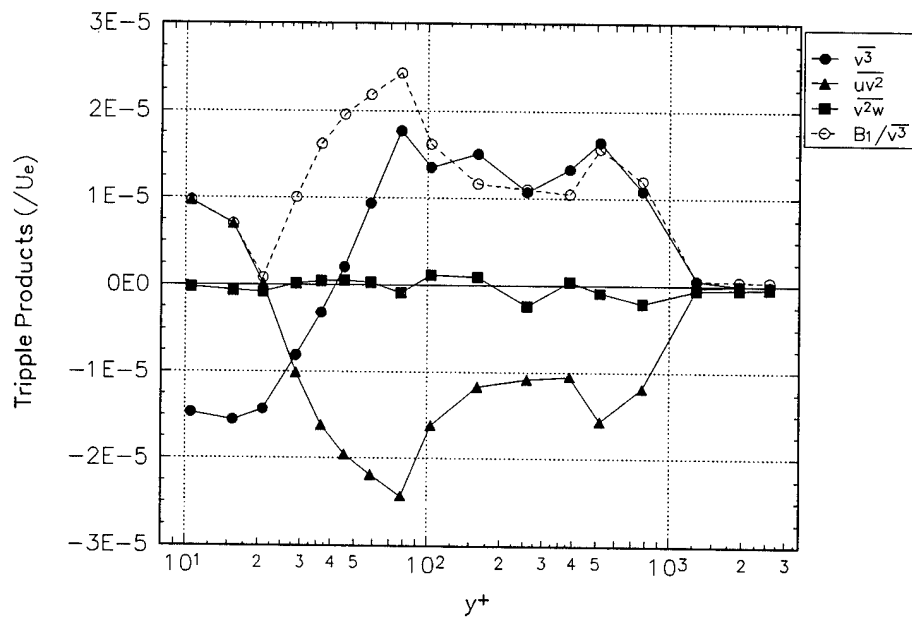


Figure F.5.d Analysis of  $B_1$  for  $x/L = 0.40$ ,  $\phi = 180^\circ$ .



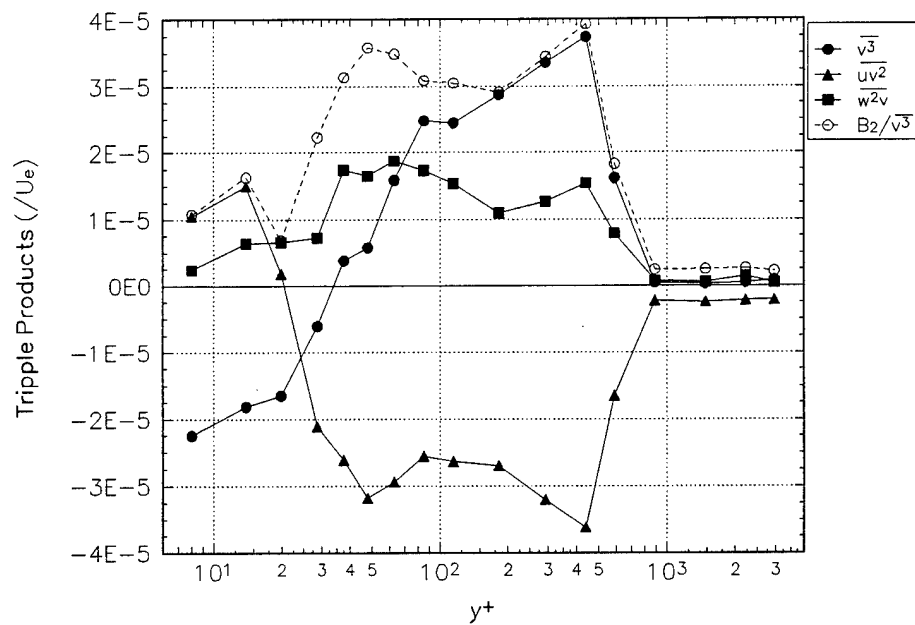


Figure F.6.a Analysis of  $B_2$  for  $x/L = 0.40$ ,  $\phi = 90^\circ$ .

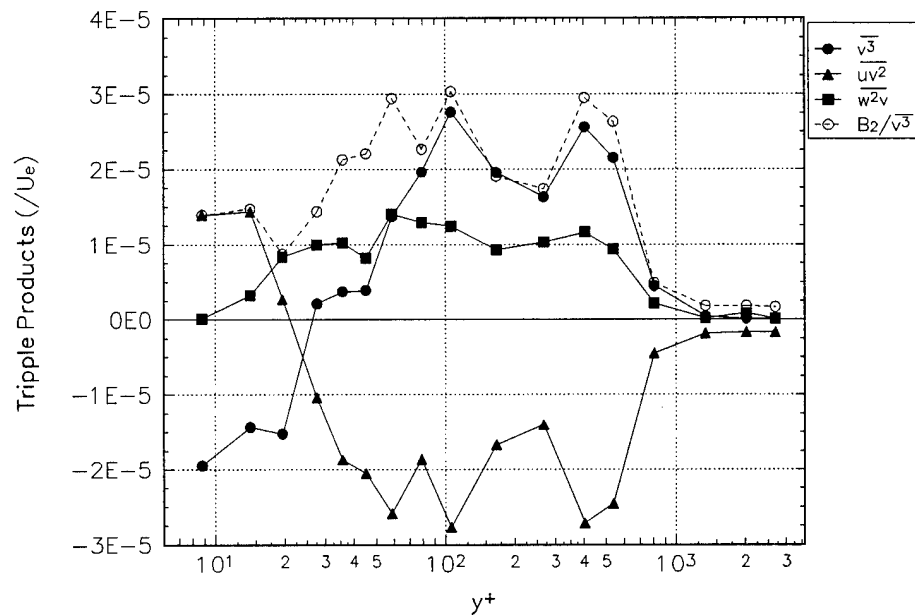
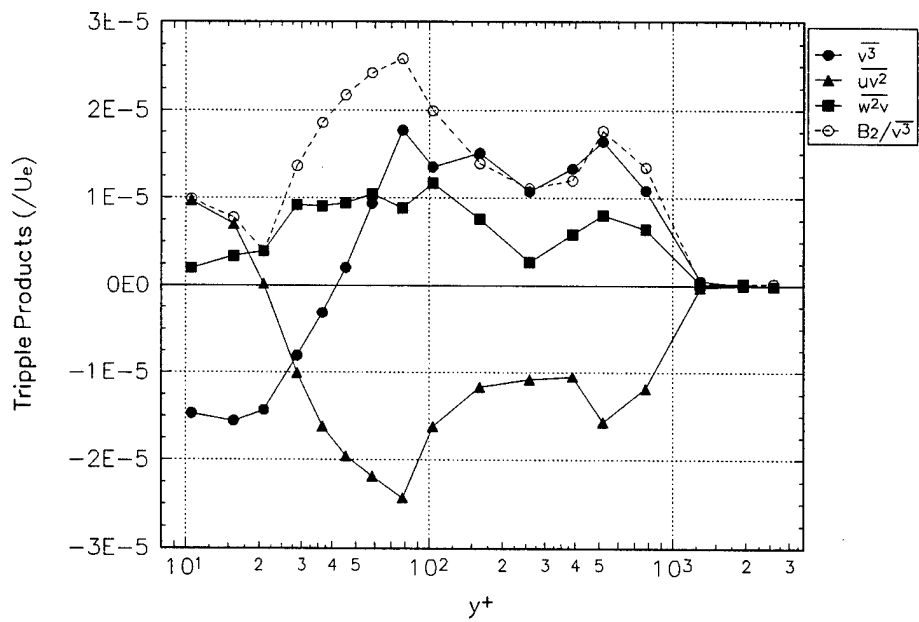
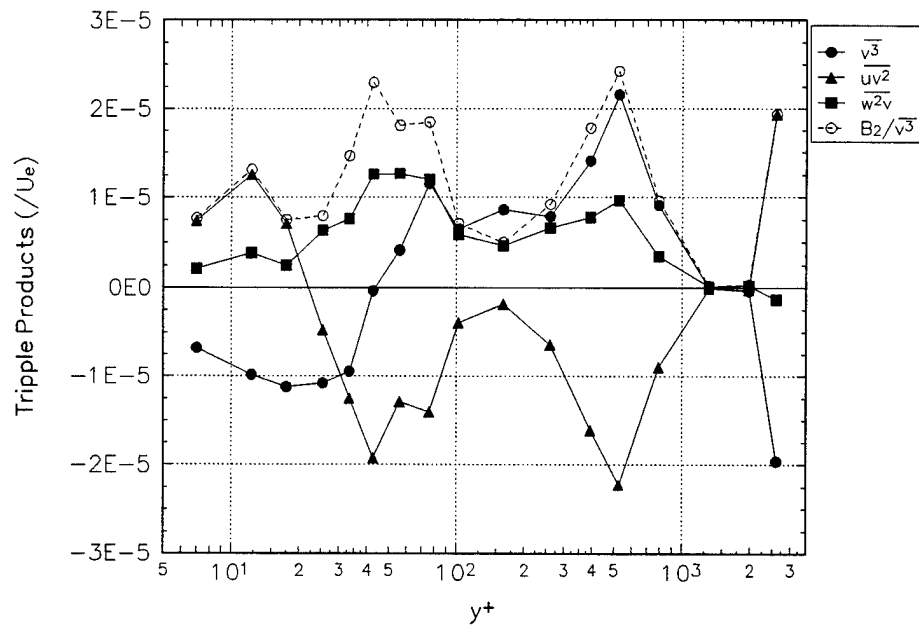


Figure F.6.b Analysis of  $B_2$  for  $x/L = 0.40$ ,  $\phi = 120^\circ$ .



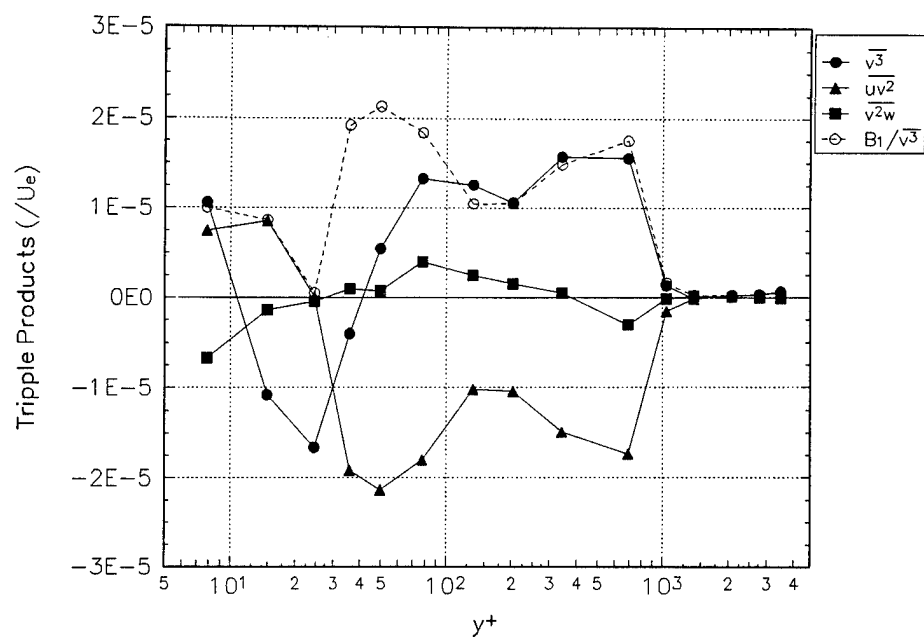


Figure F.7.a Analysis of  $B_1$  for  $x/L = 0.60$ ,  $\phi = 90^\circ$ .

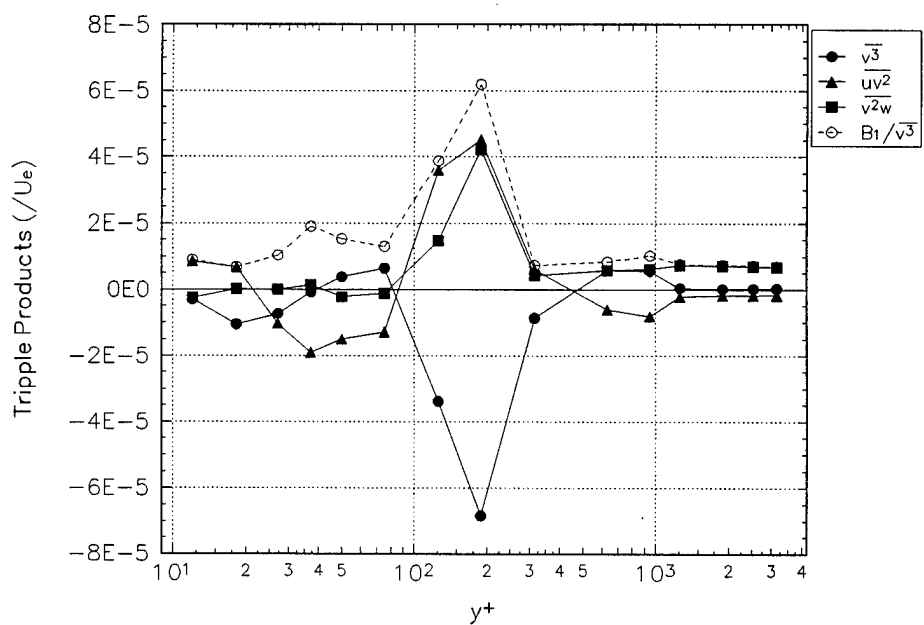


Figure F.7.b Analysis of  $B_1$  for  $x/L = 0.60$ ,  $\phi = 110^\circ$ .

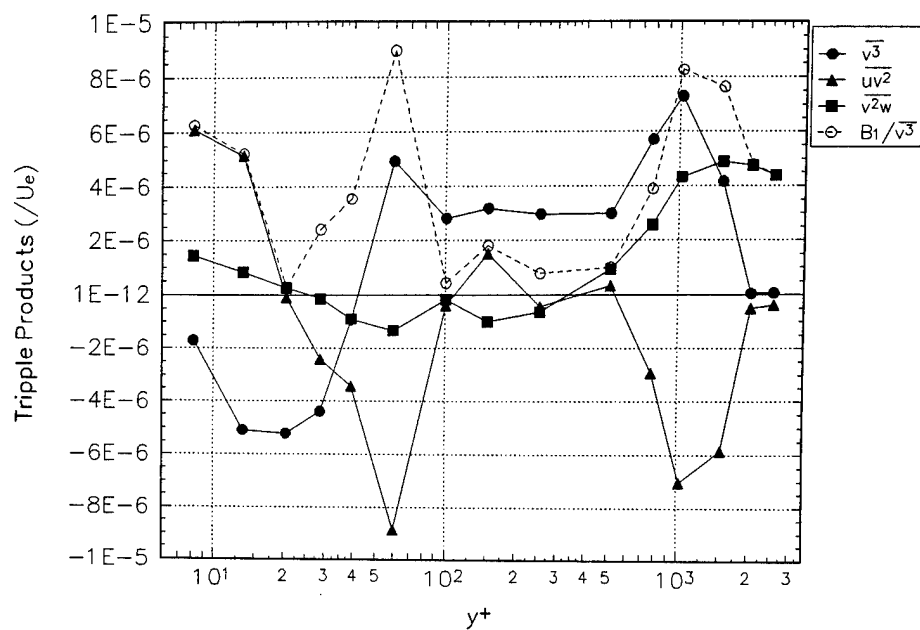


Figure F.7.c Analysis of  $B_1$  for  $x/L = 0.60$ ,  $\phi = 150^\circ$ .

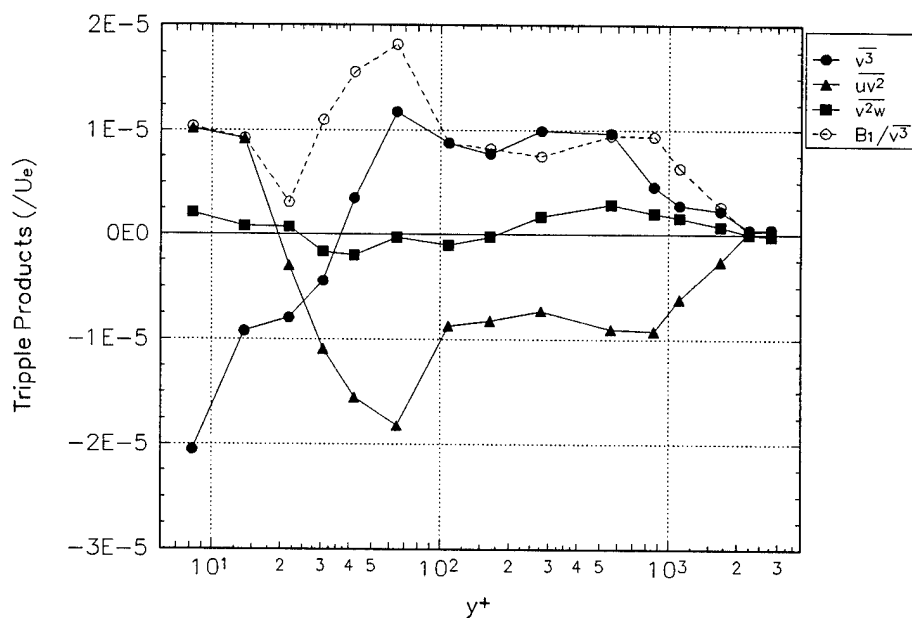


Figure F.7.d Analysis of  $B_1$  for  $x/L = 0.60$ ,  $\phi = 170^\circ$ .

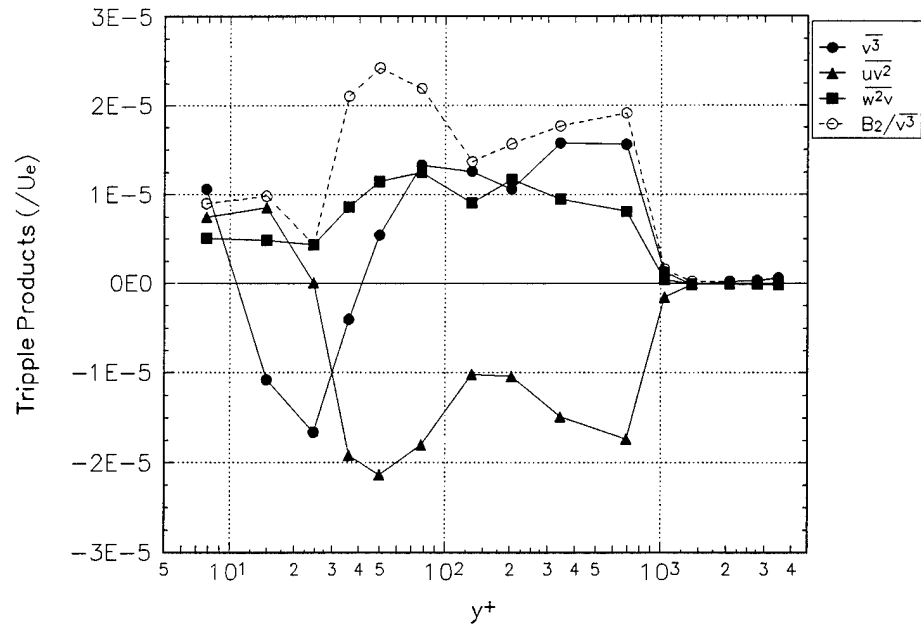


Figure F.8.a Analysis of  $B_2$  for  $x/L = 0.60$ ,  $\phi = 90^\circ$ .

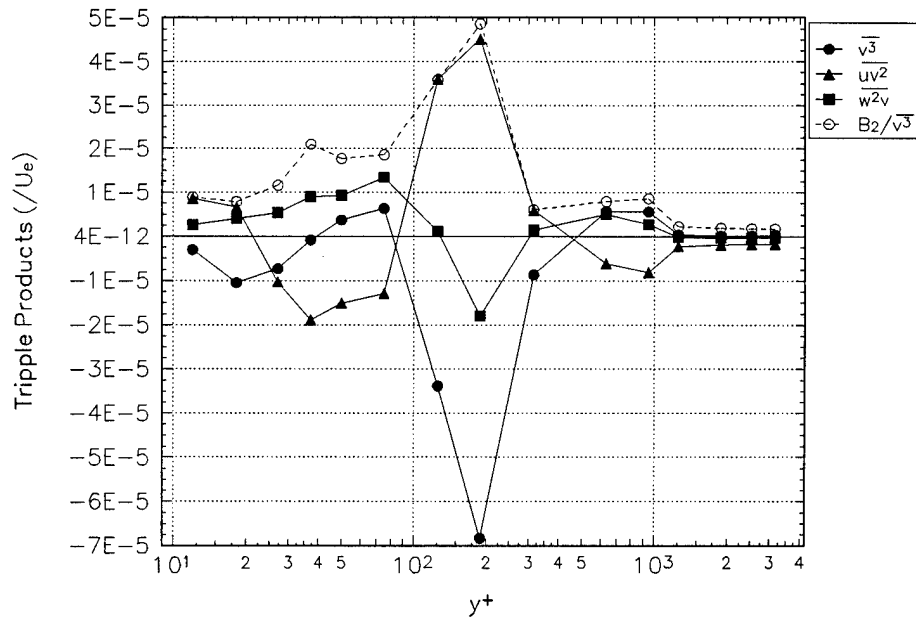


Figure F.8.b Analysis of  $B_2$  for  $x/L = 0.60$ ,  $\phi = 110^\circ$ .

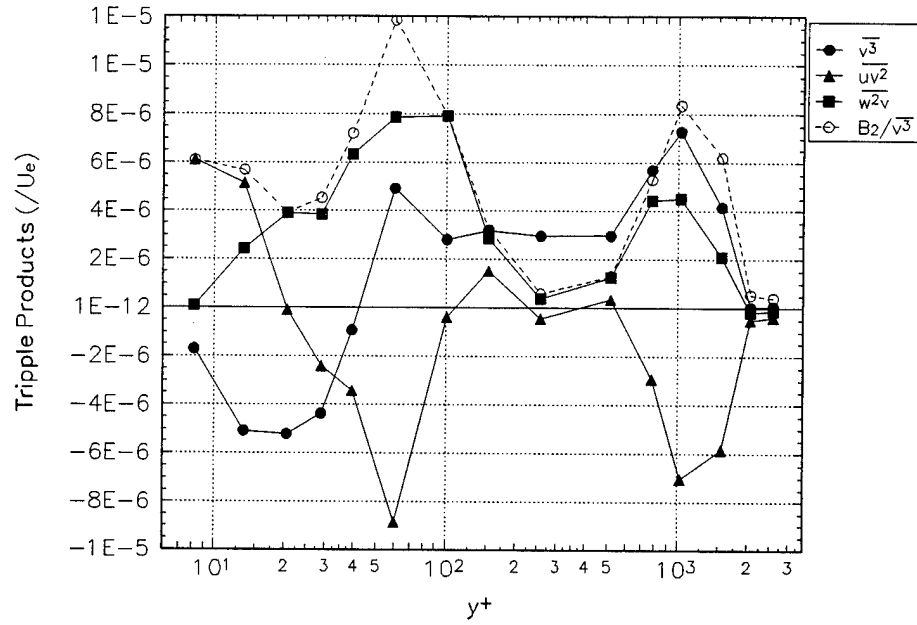


Figure F.8.c Analysis of  $B_2$  for  $x/L = 0.60$ ,  $\phi = 150^\circ$ .

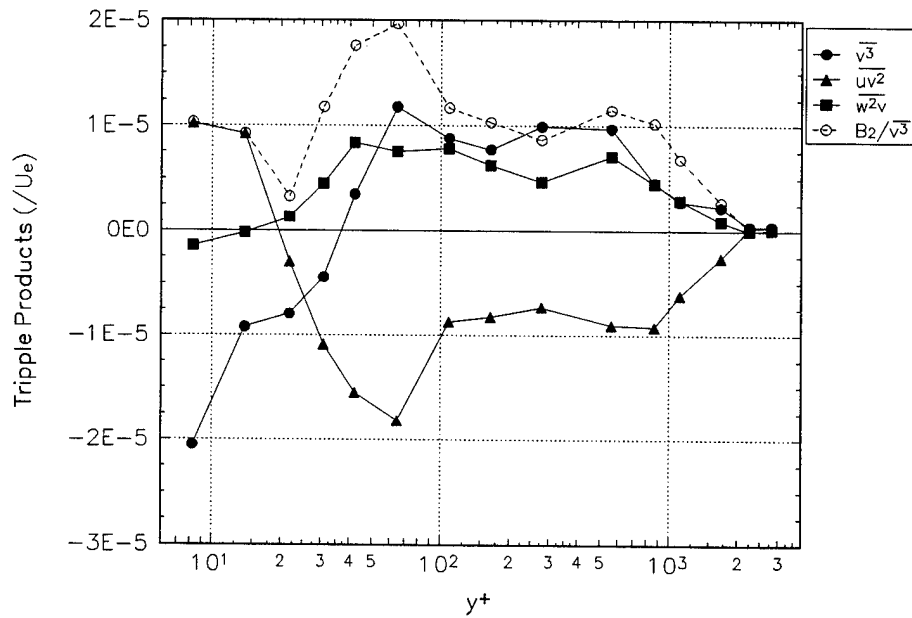


Figure F.8.d Analysis of  $B_2$  for  $x/L = 0.60$ ,  $\phi = 170^\circ$ .

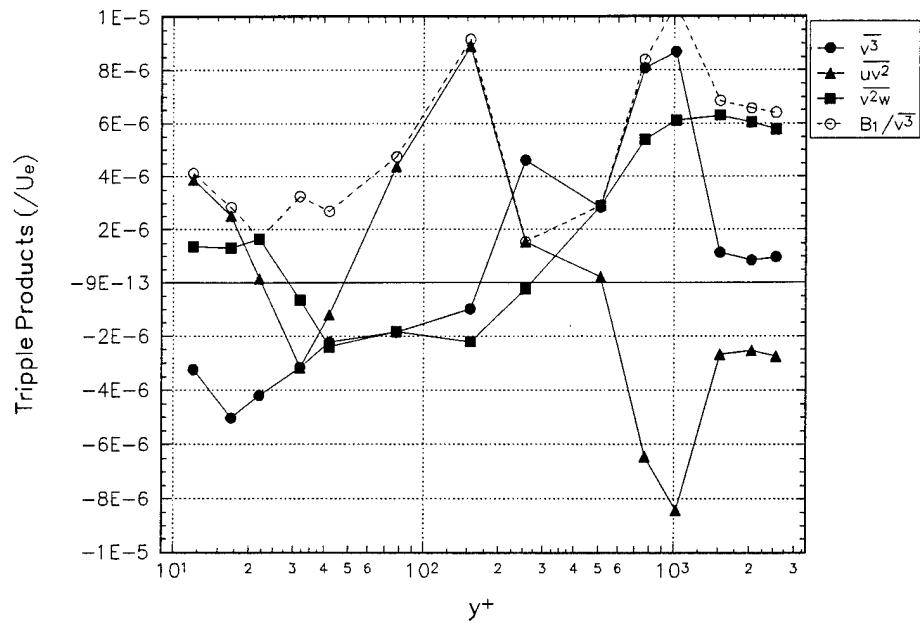


Figure F.9.a Analysis of  $B_1$  for  $x/L = 0.75$ ,  $\phi = 120^\circ$ .

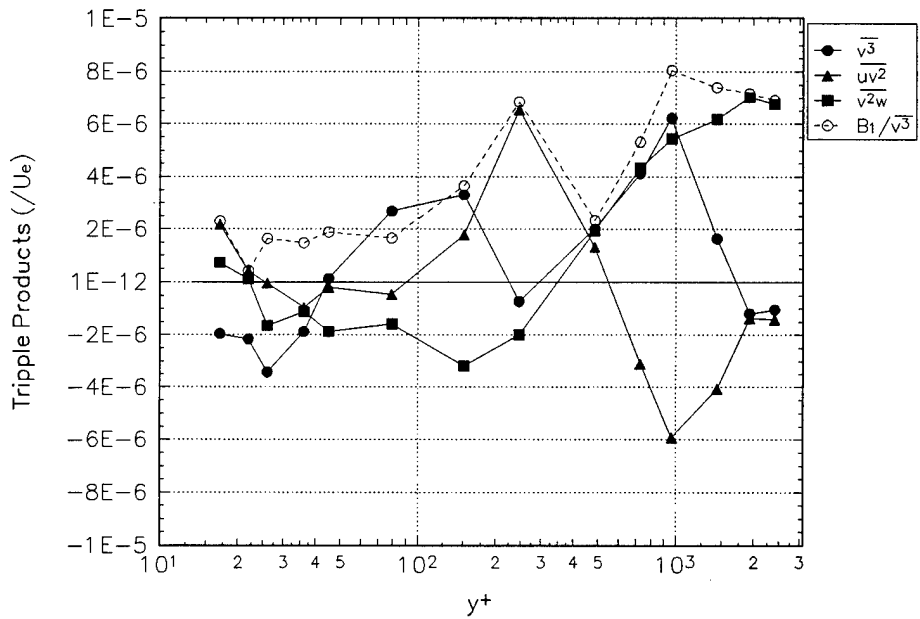
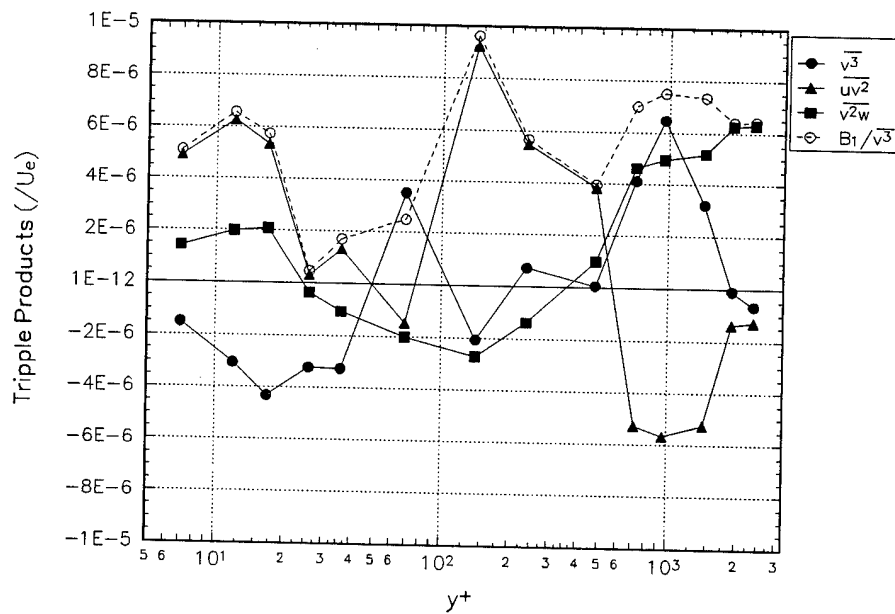
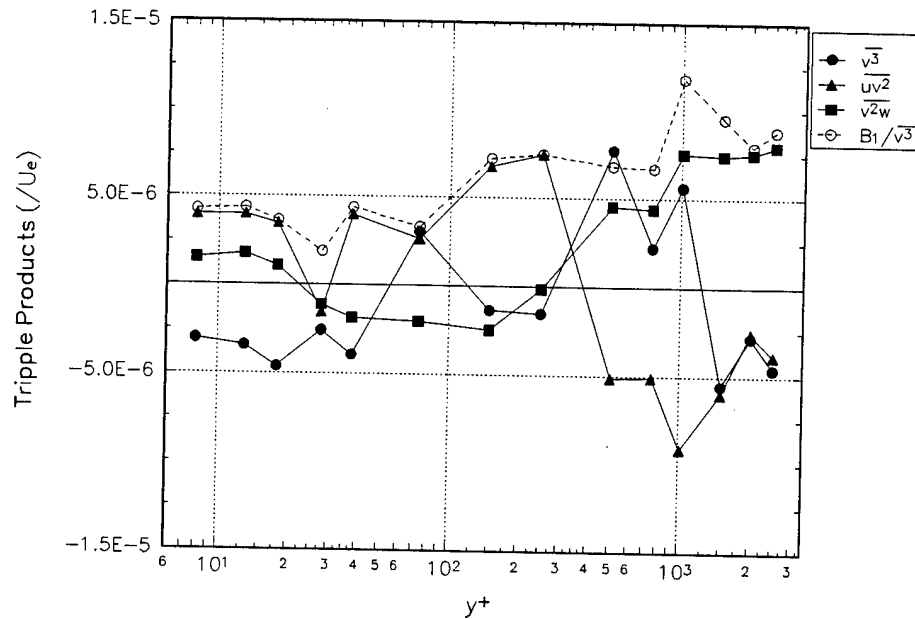


Figure F.9.b Analysis of  $B_1$  for  $x/L = 0.75$ ,  $\phi = 125^\circ$ .





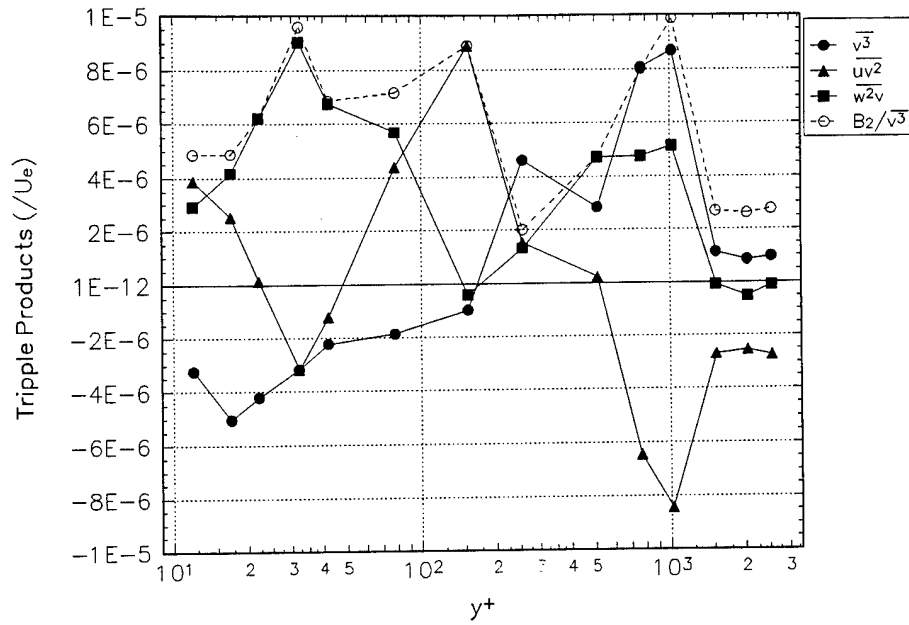


Figure F.10.a Analysis of  $B_2$  for  $x/L = 0.75$ ,  $\phi = 120^\circ$ .

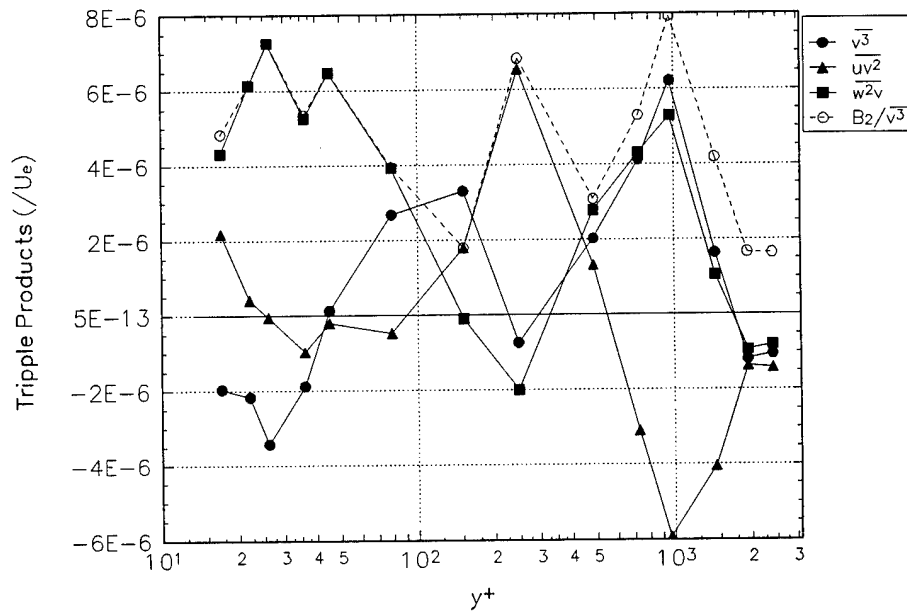


Figure F.10.b Analysis of  $B_2$  for  $x/L = 0.75$ ,  $\phi = 125^\circ$ .

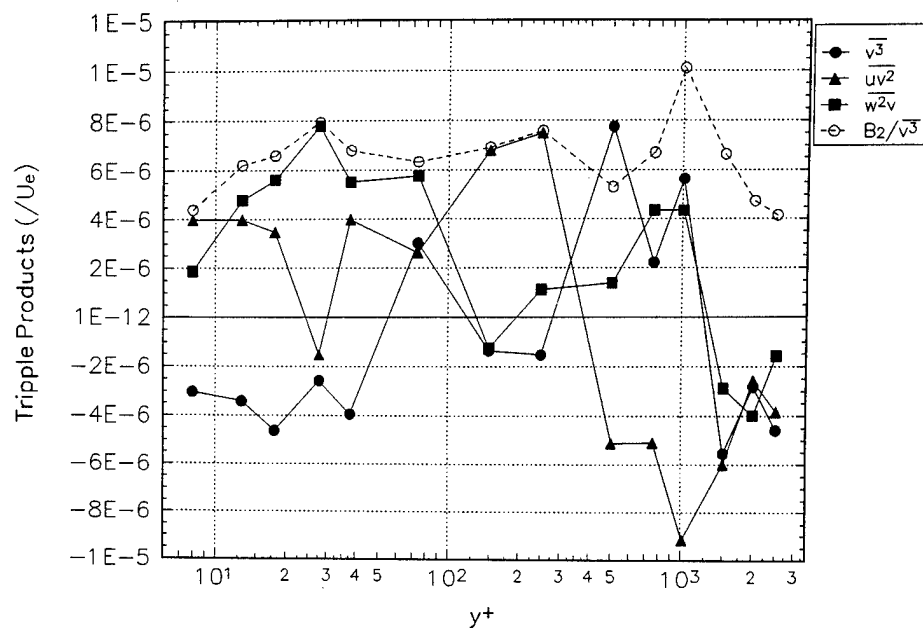


Figure F.10.c Analysis of  $B_2$  for  $x/L = 0.76$ ,  $\phi = 120^\circ$ .

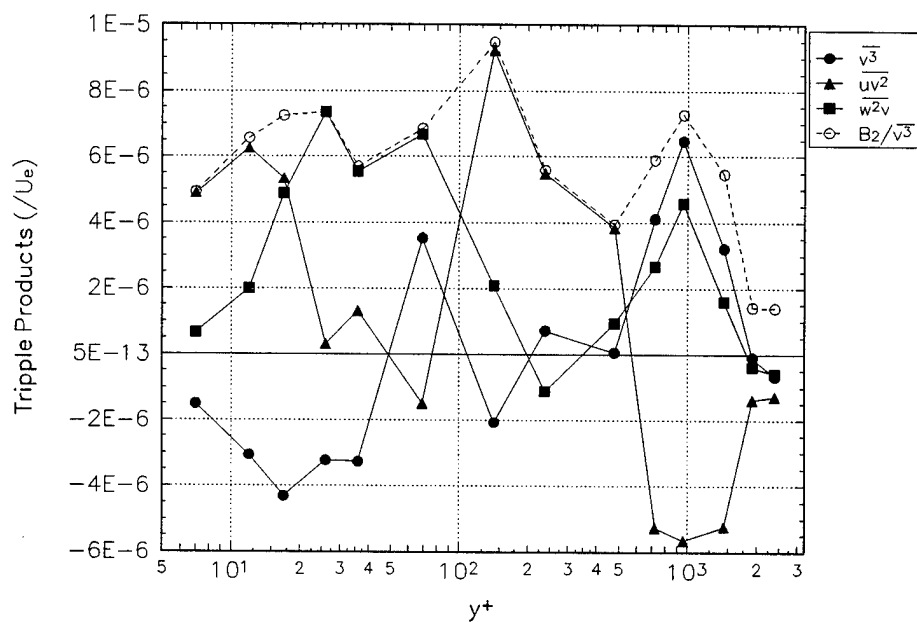


Figure F.10.d Analysis of  $B_2$  for  $x/L = 0.76$ ,  $\phi = 125^\circ$ .

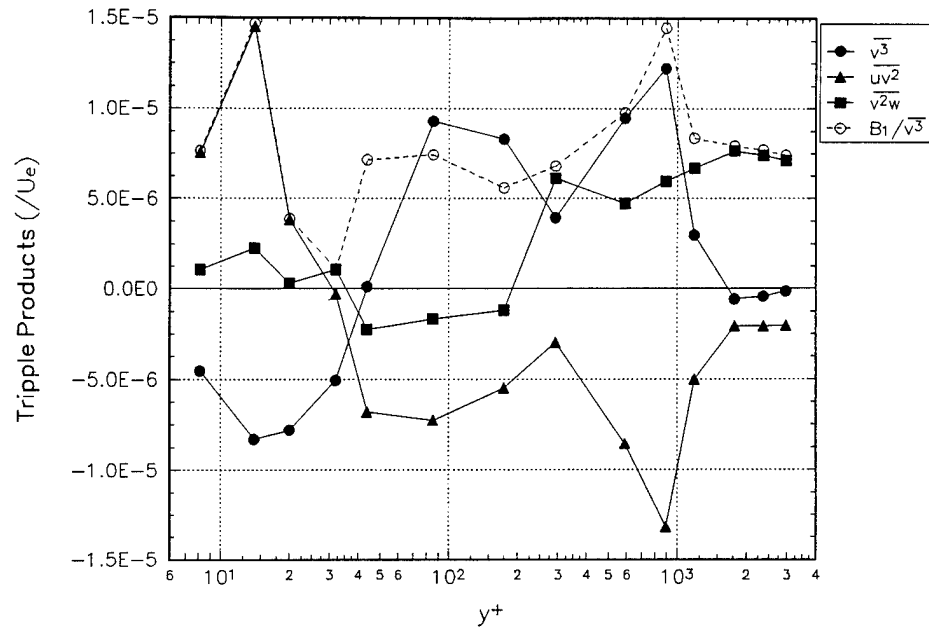


Figure F.11.a Analysis of  $B_1$  for  $x/L = 0.77$ ,  $\phi = 105^\circ$ .

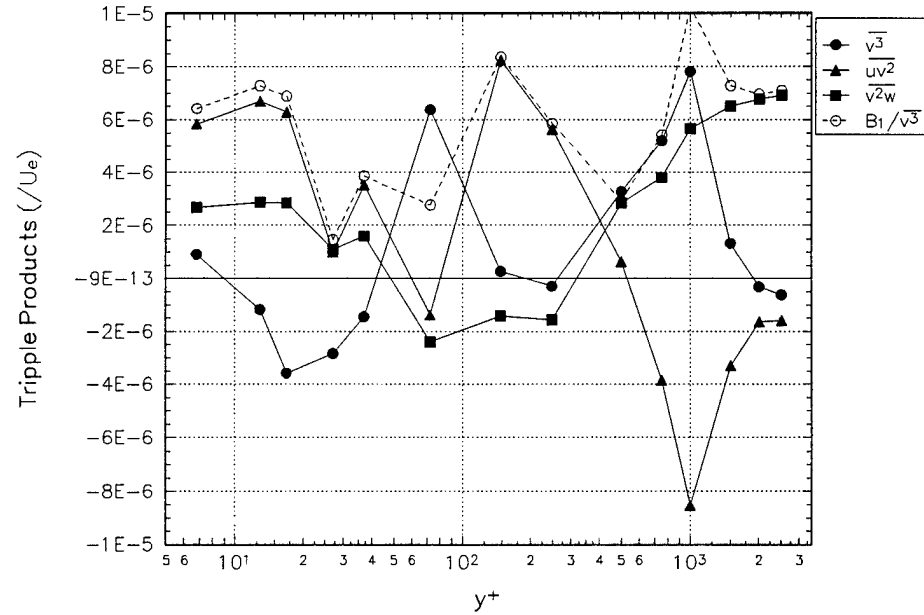


Figure F.11.b Analysis of  $B_1$  for  $x/L = 0.77$ ,  $\phi = 120^\circ$ .

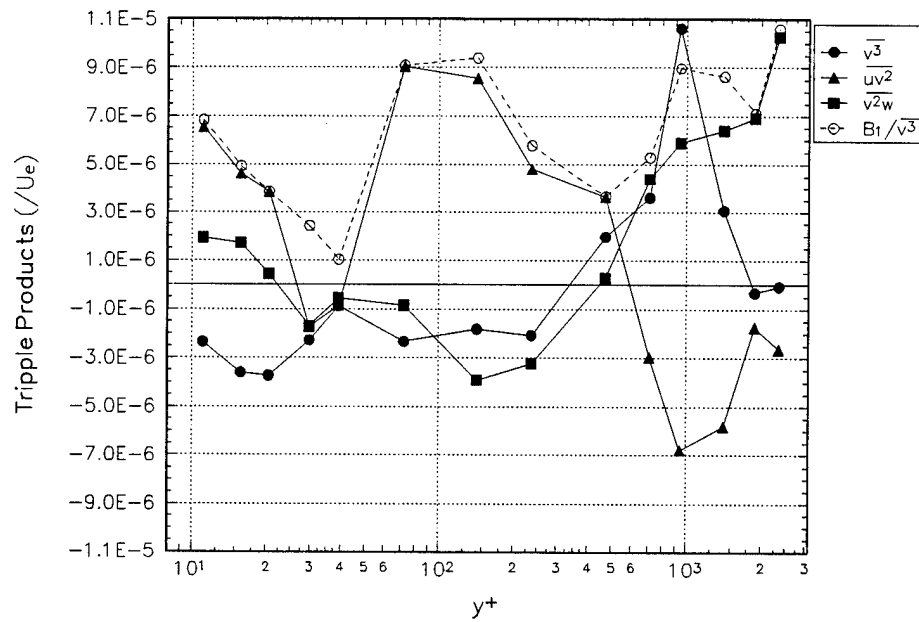


Figure F.11.c Analysis of  $B_1$  for  $x/L = 0.77$ ,  $\phi = 123^\circ$ .

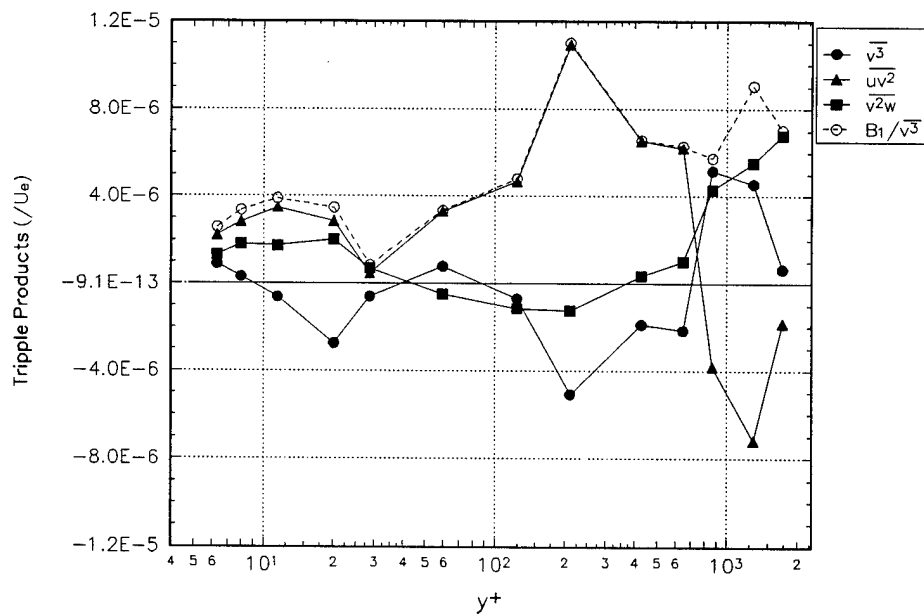


Figure F.11.d Analysis of  $B_1$  for  $x/L = 0.77$ ,  $\phi = 130^\circ$ .

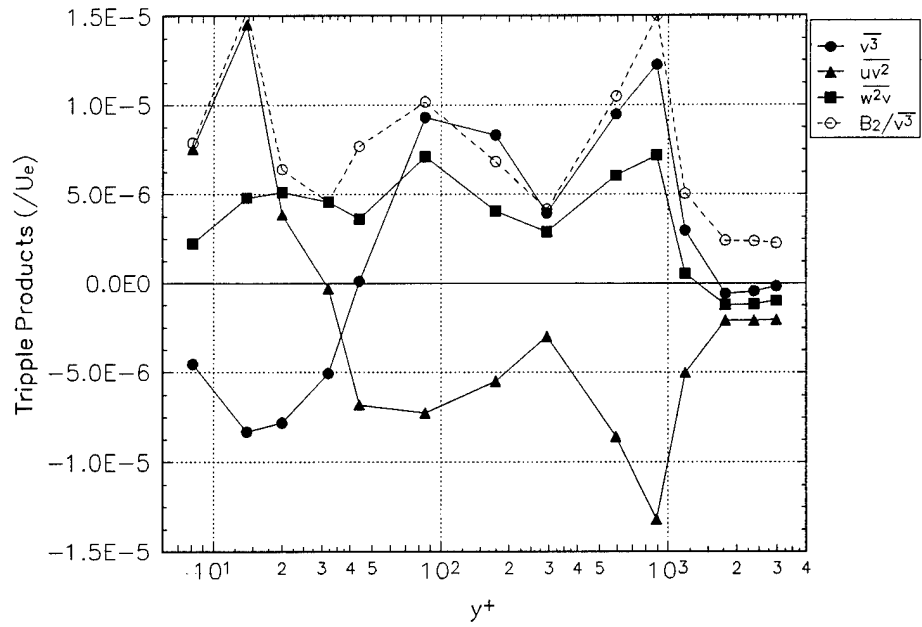


Figure F.12.a Analysis of  $B_2$  for  $x/L = 0.77$ ,  $\phi = 105^\circ$ .

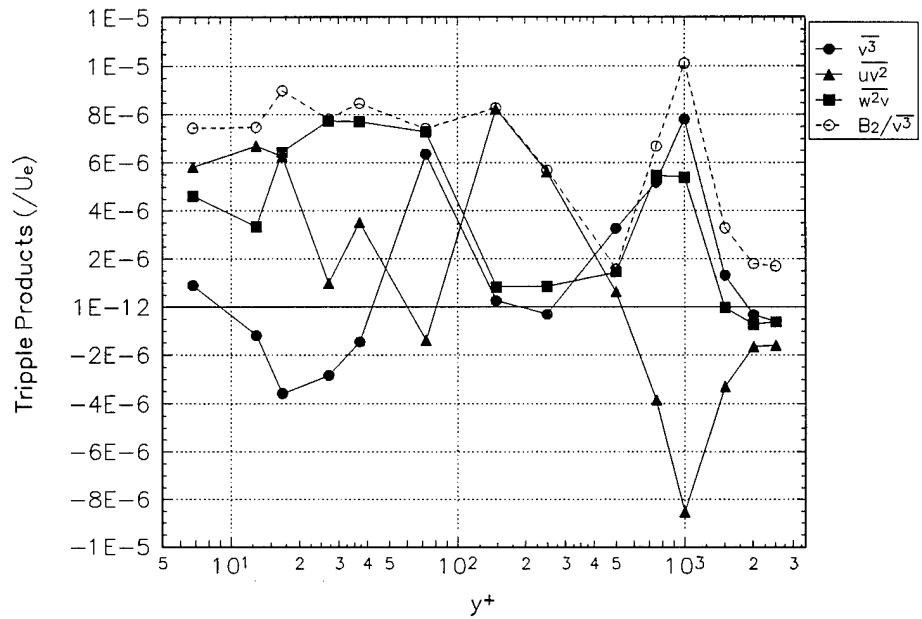


Figure F.12.b Analysis of  $B_2$  for  $x/L = 0.77$ ,  $\phi = 120^\circ$ .

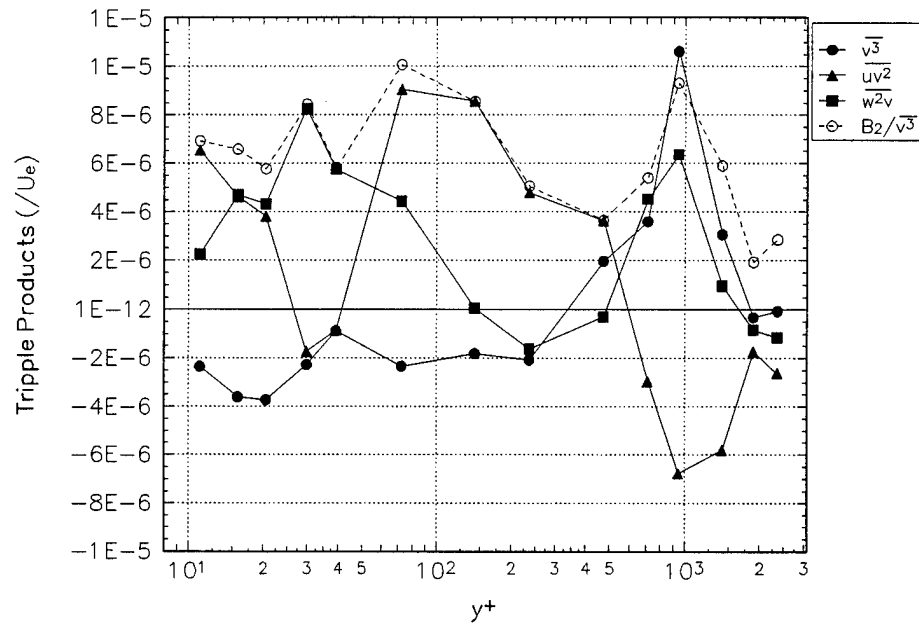


Figure F.12.c Analysis of  $B_2$  for  $x/L = 0.77$ ,  $\phi = 123^\circ$ .

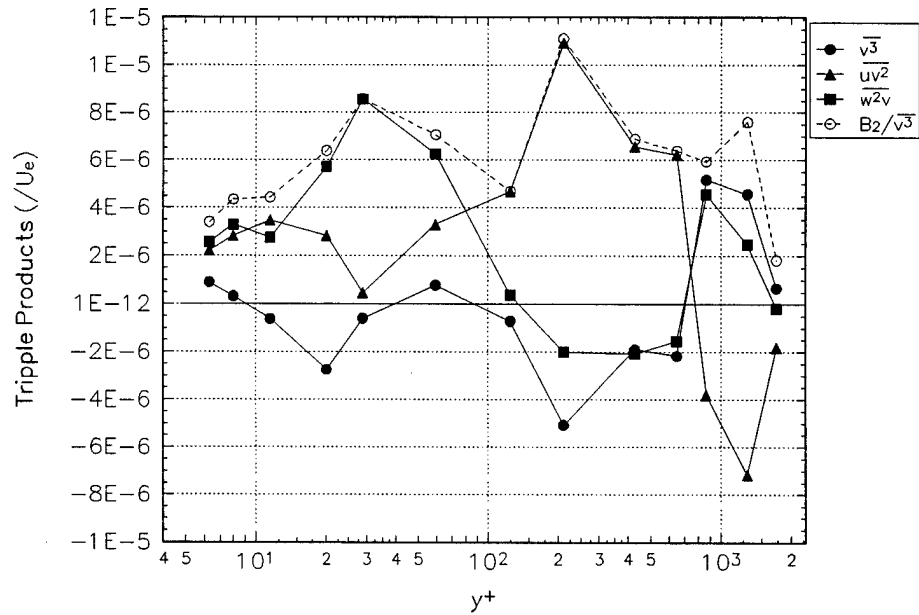


Figure F.12.d Analysis of  $B_2$  for  $x/L = 0.77$ ,  $\phi = 130^\circ$ .

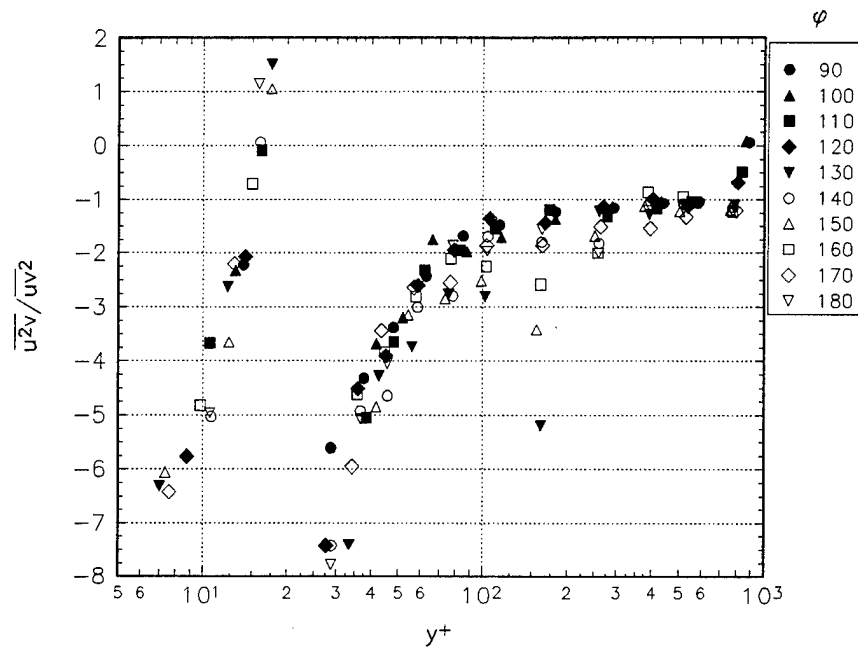


Figure F.13.a Triple product ratio for  $x/L = 0.40$ .

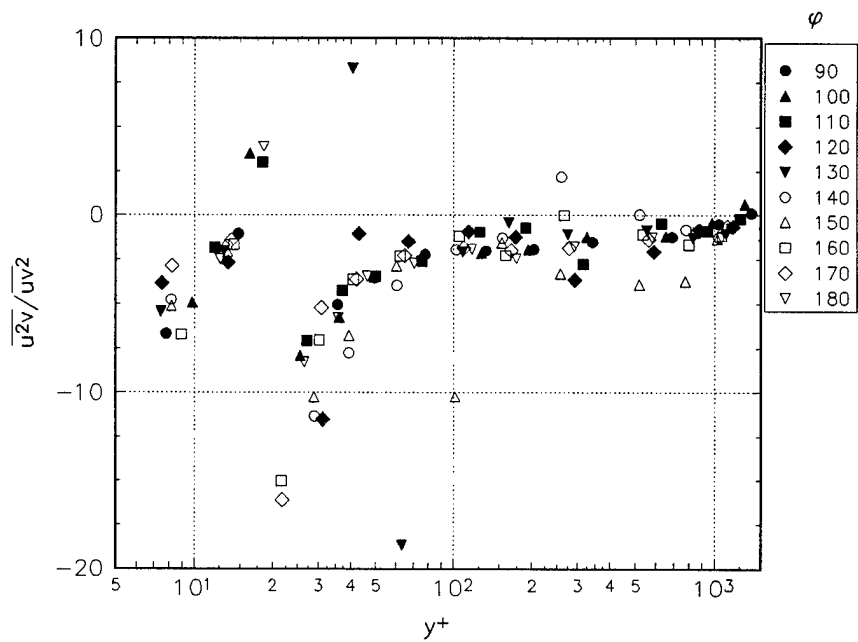


Figure F.13.b Triple product ratio for  $x/L = 0.60$ .

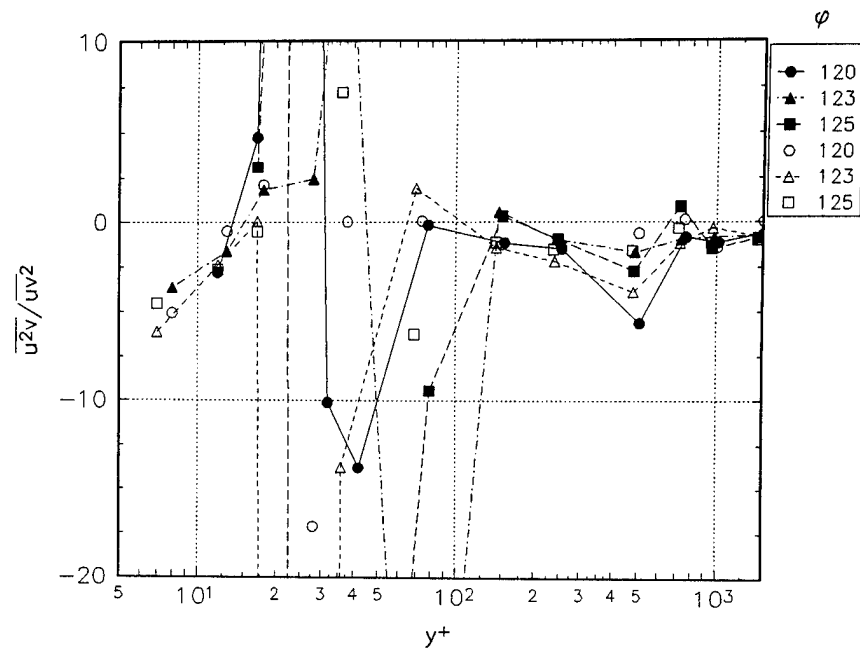


Figure F.13.c Triple product ratio, closed symbols for  $x/L = 0.75$  and open for  $x/L = 0.76$ .

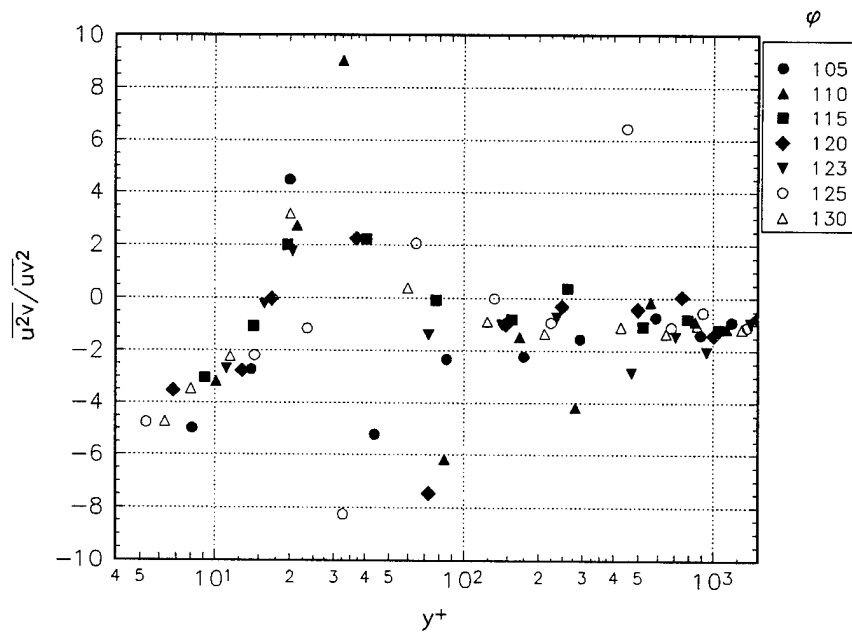


Figure F.13.d Triple product ratio for  $x/L = 0.77$ .



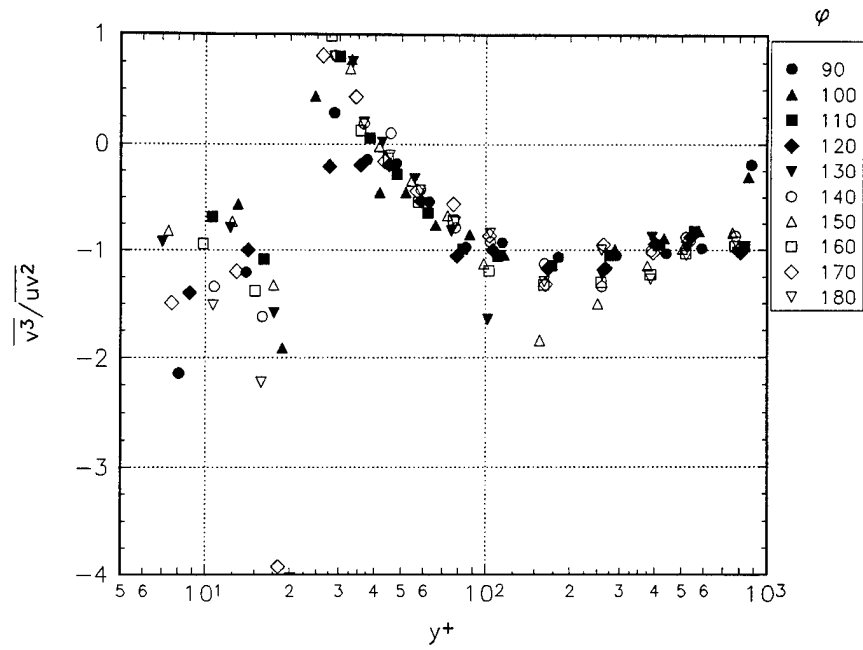


Figure F.14.a Triple product ratio for  $x/L = 0.40$ .

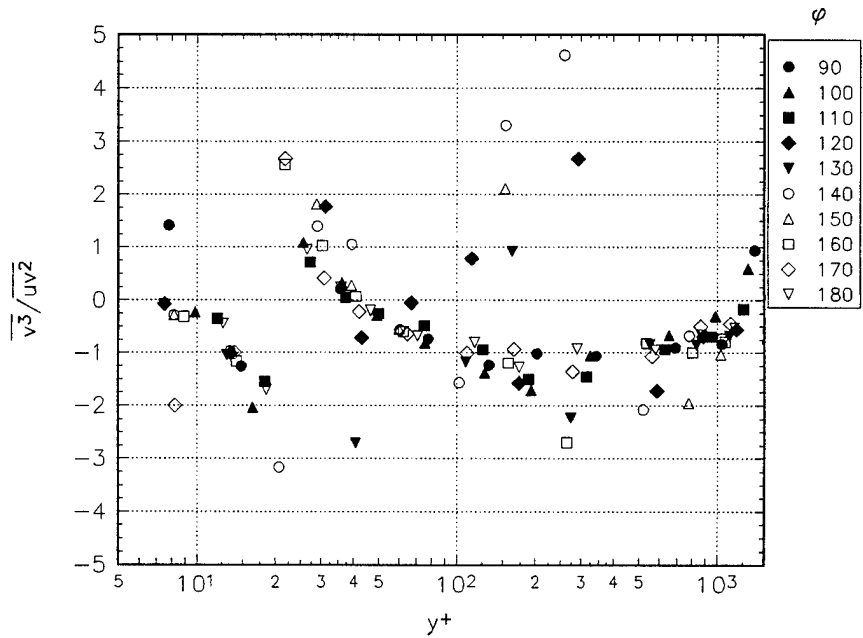


Figure F.14.b Triple product ratio for  $x/L = 0.60$ .

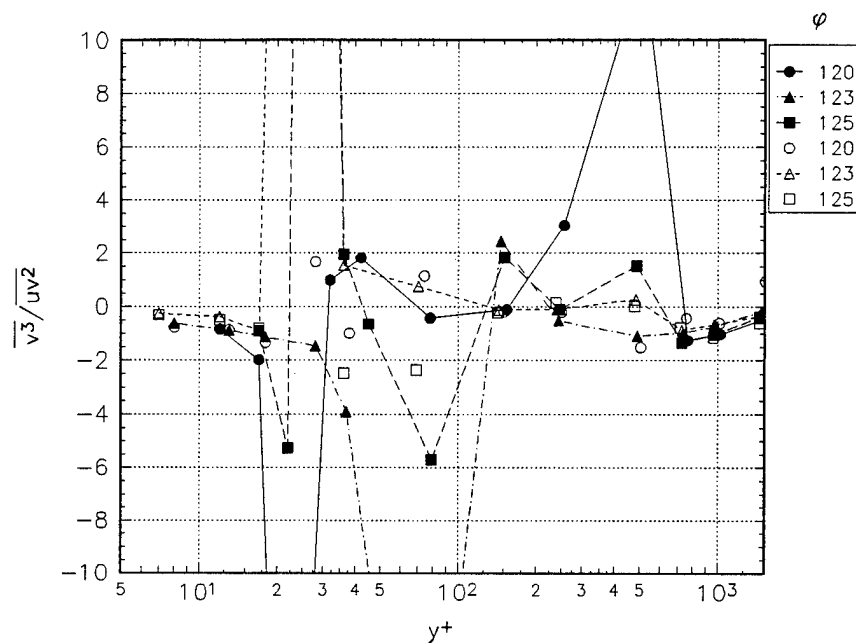


Figure F.14.c Triple product ratio, closed symbols for  $x/L = 0.75$  and open for  $x/L = 0.76$ .

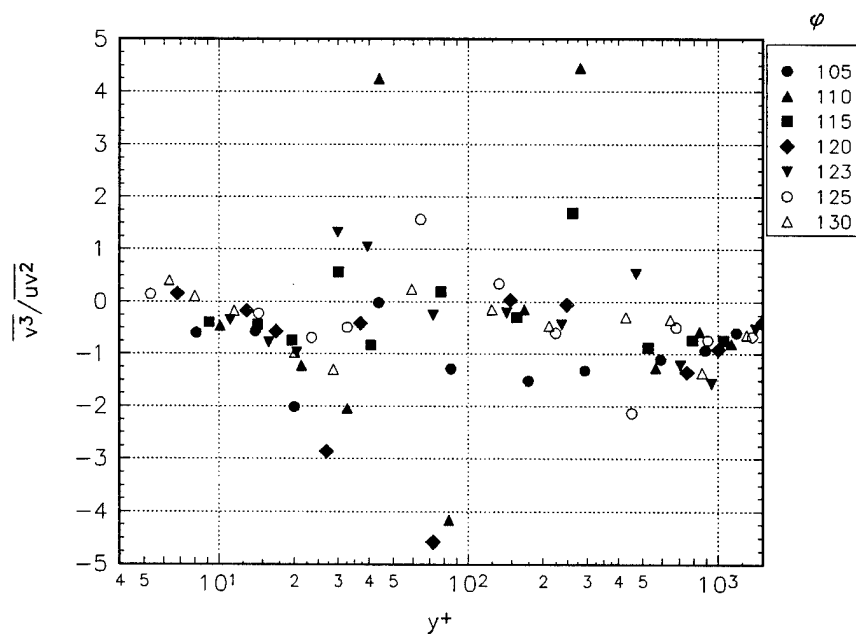


Figure F.14.d Triple product ratio for  $x/L = 0.77$ .

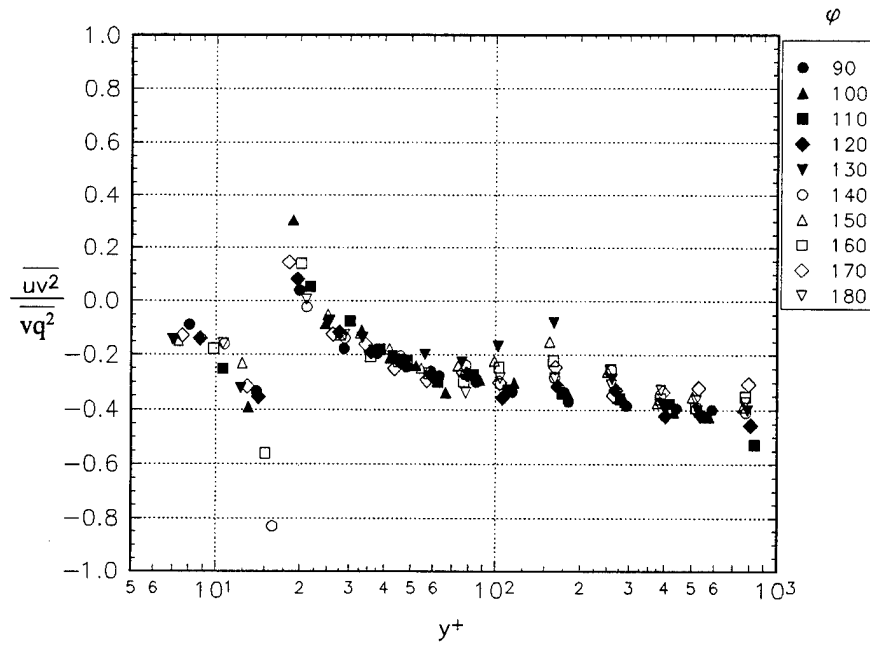


Figure F.15.a Triple product relationship for  $x/L = 0.40$ .

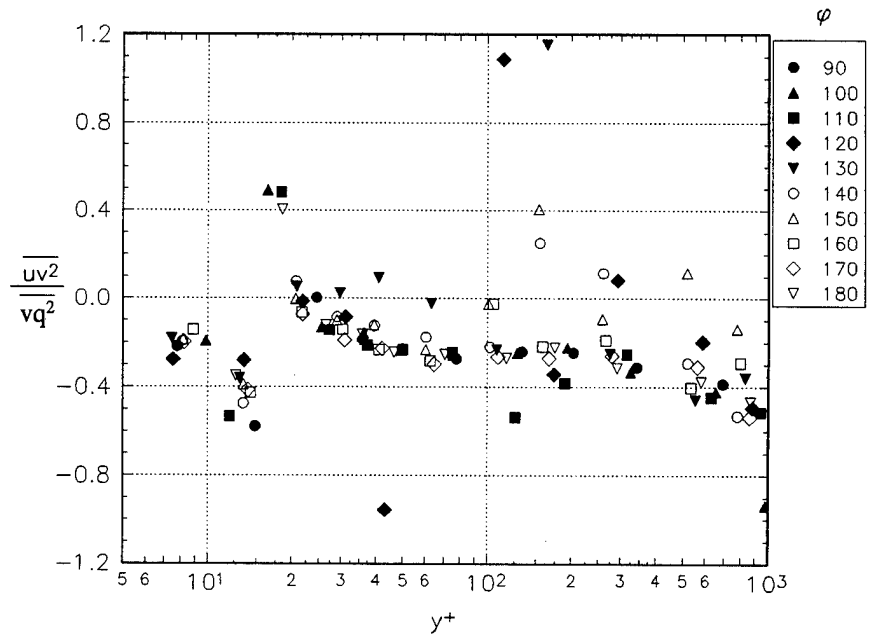


Figure F.15.b Triple product relationship for  $x/L = 0.60$ .

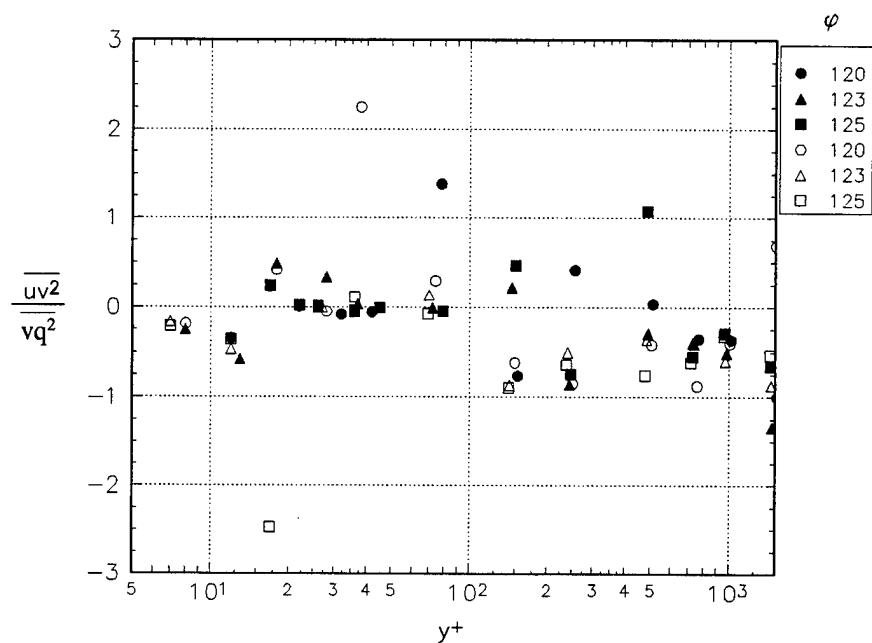


Figure F.15.c Triple product relationship, closed symbols for  $x/L = 0.75$  and open  $x/L = 0.76$ .

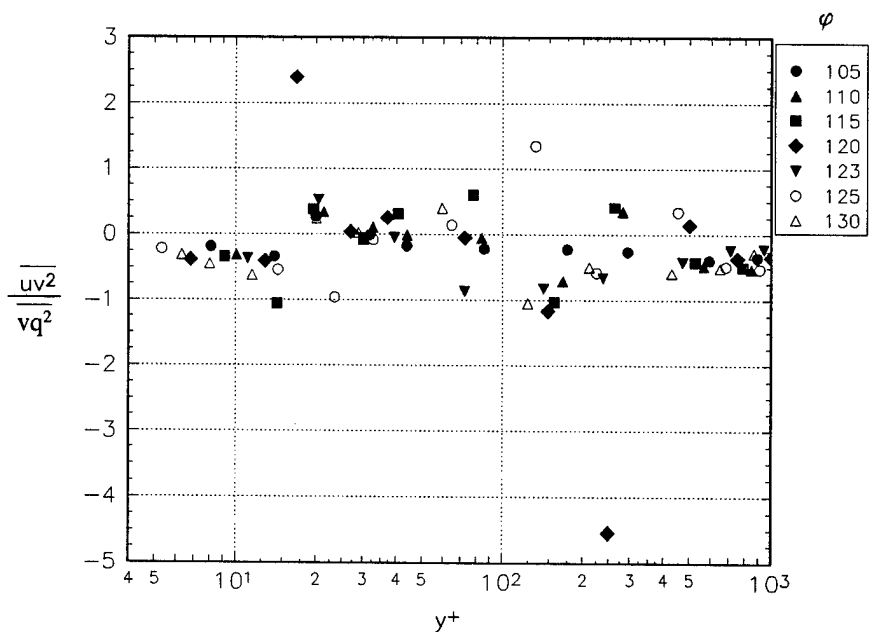


Figure F.15.d Triple product relationship for  $x/L = 0.77$ .

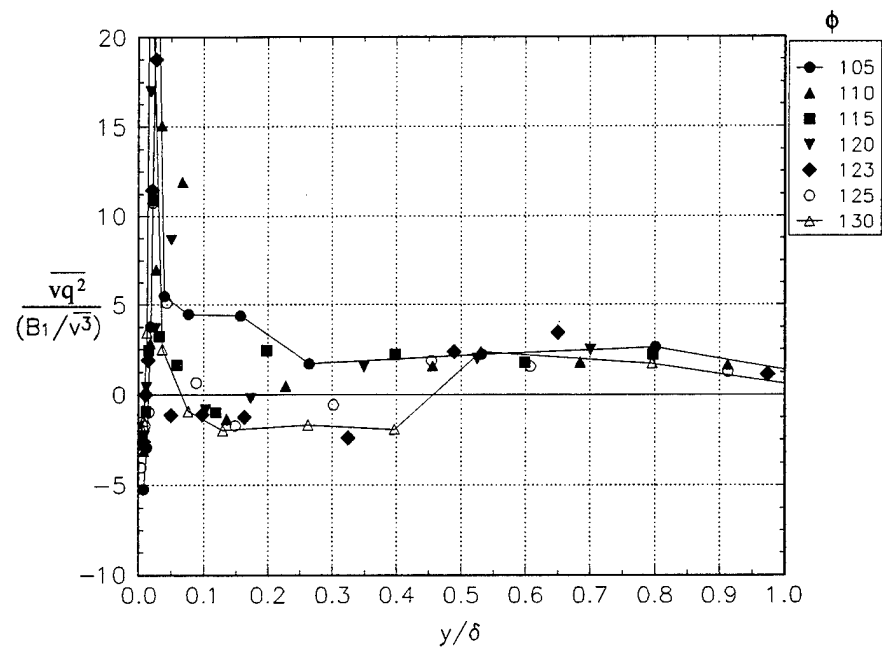


Figure F.16.a Triple product relationship for  $x/L = 0.77$ .

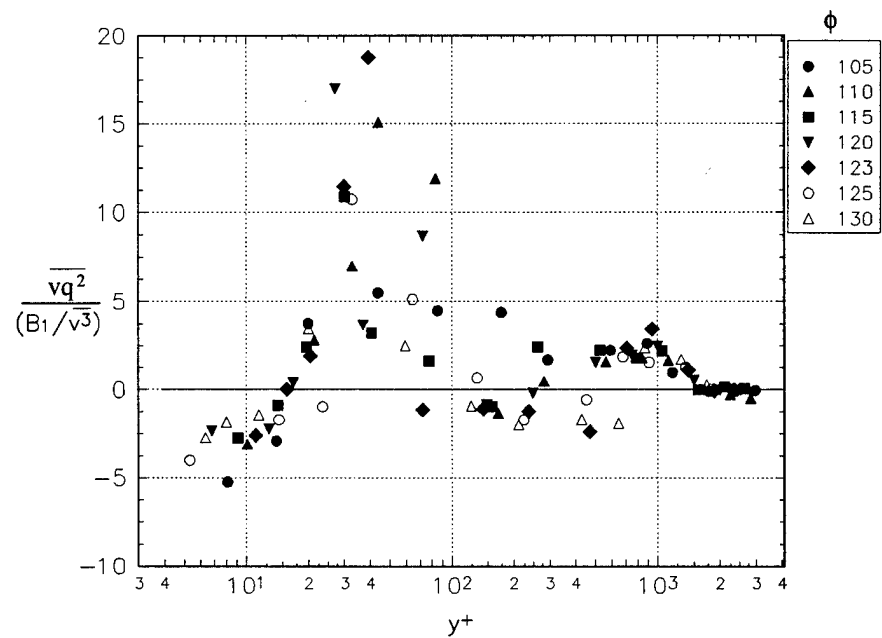


Figure F.16.b Triple product relationship for  $x/L = 0.77$ .

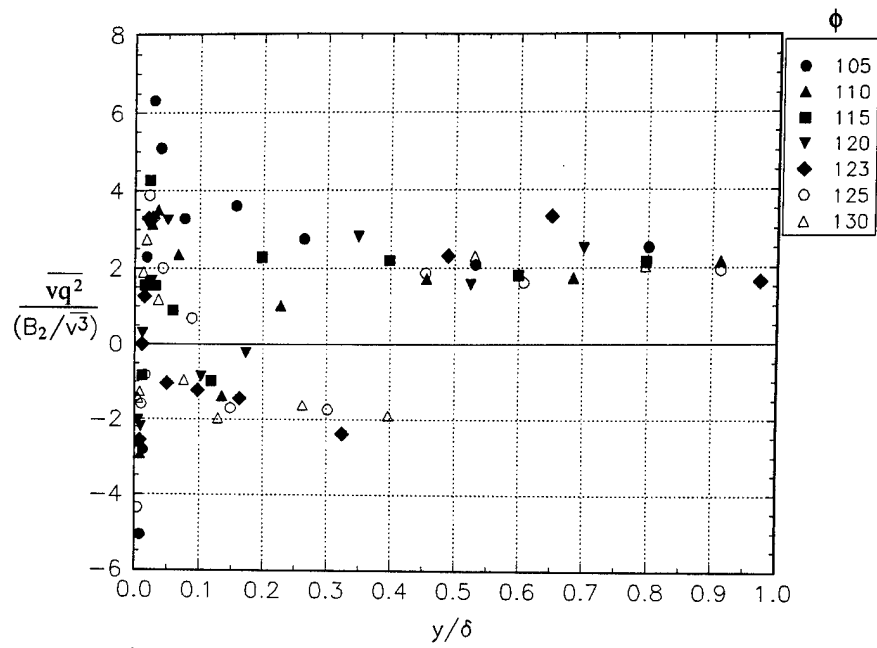


Figure F.16.c Triple product relationship for  $x/L = 0.77$ .

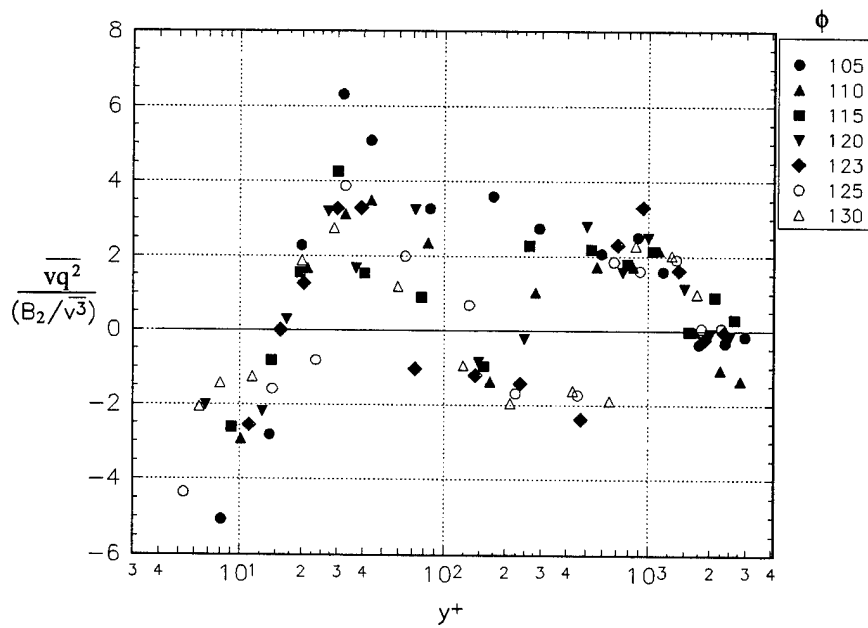


Figure F.16.d Triple product relationship for  $x/L = 0.77$ .

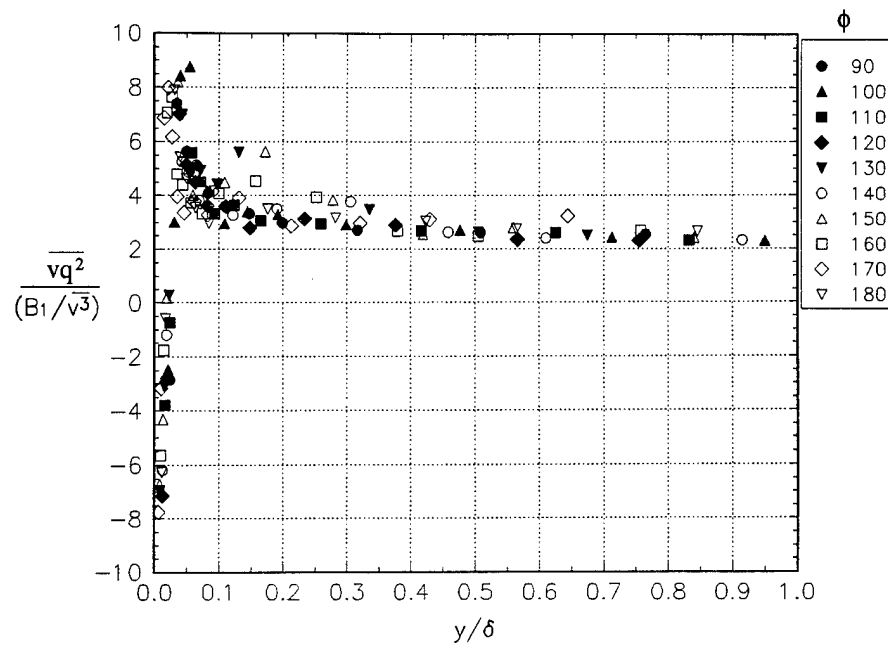


Figure F.17.a Triple product relationship for  $x/L = 0.40$ .

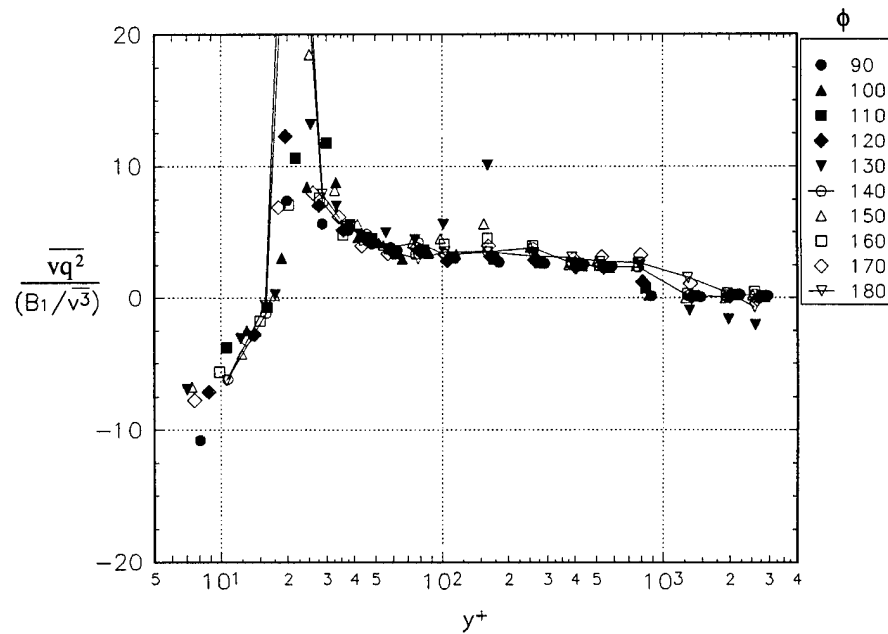
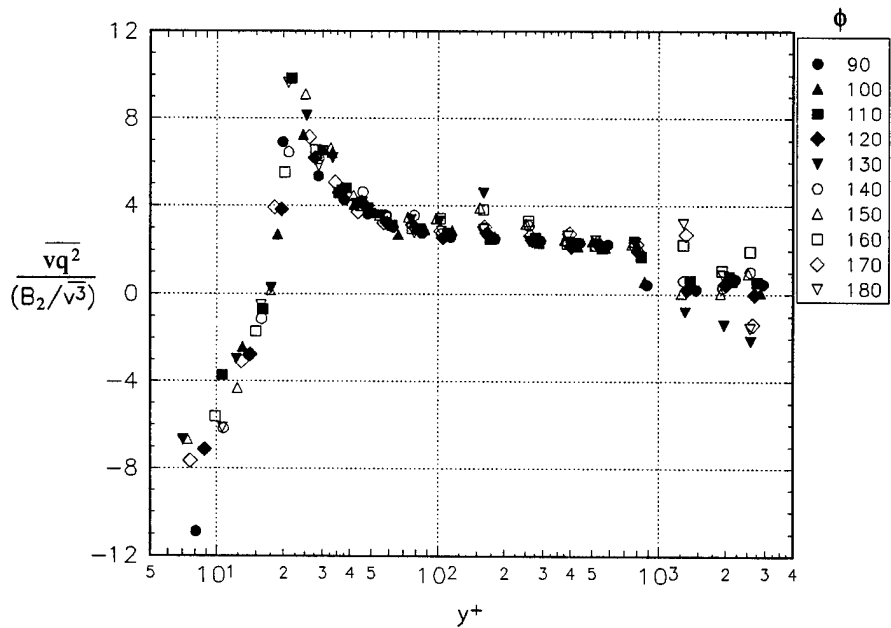
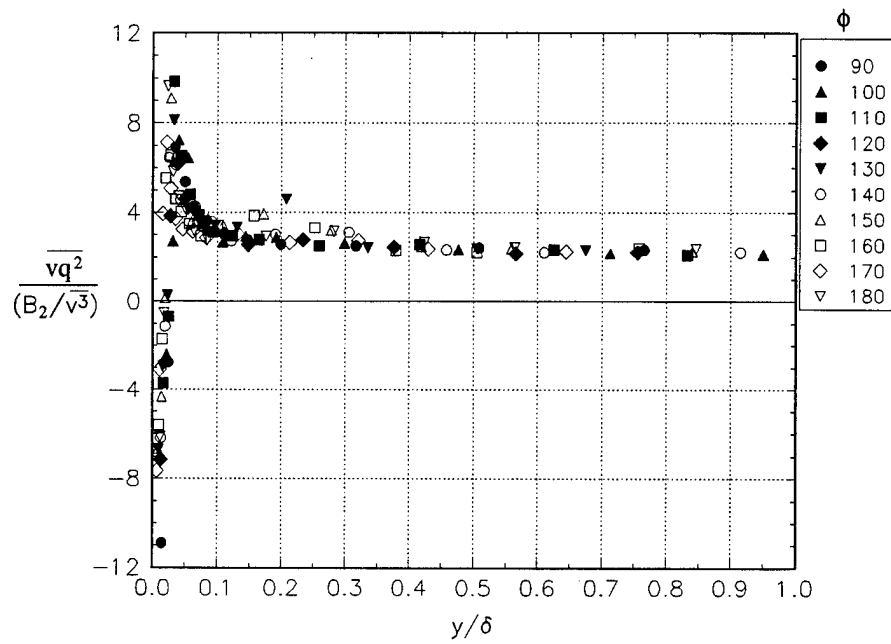


Figure F.17.b Triple product relationship for  $x/L = 0.40$ .





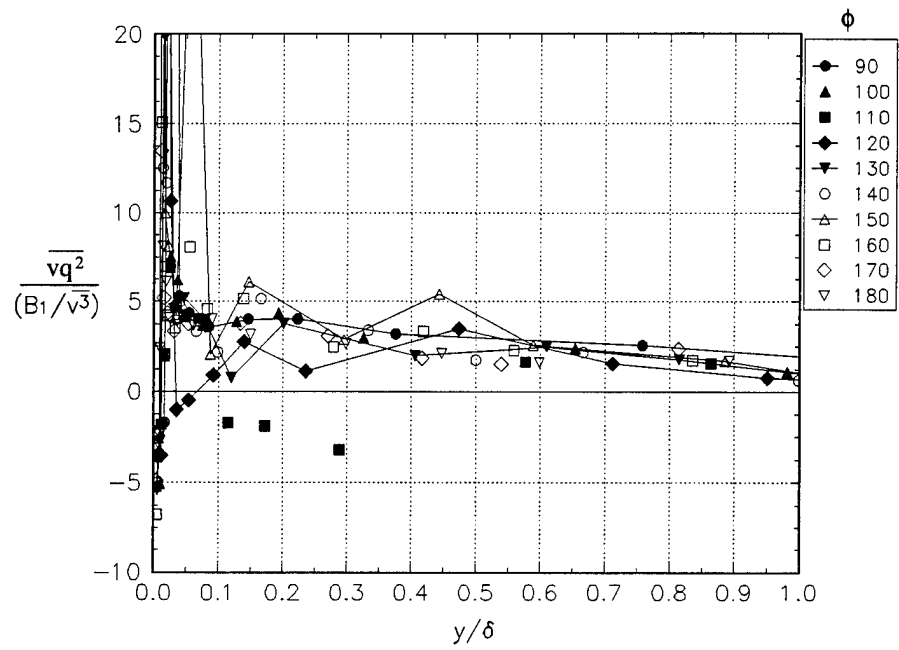


Figure F.18.a Triple product relationship for  $x/L = 0.60$ .

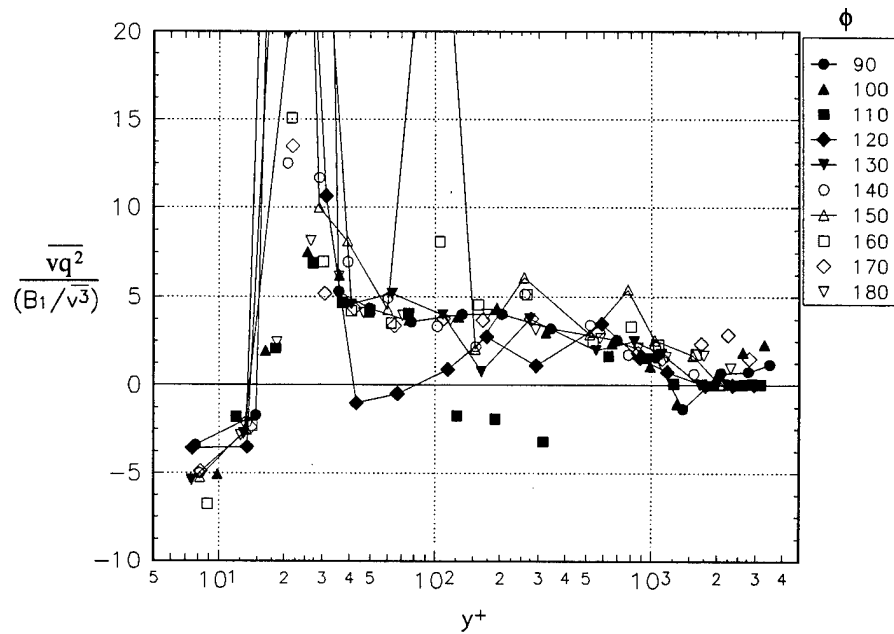


Figure F.18.b Triple product relationship for  $x/L = 0.60$ .

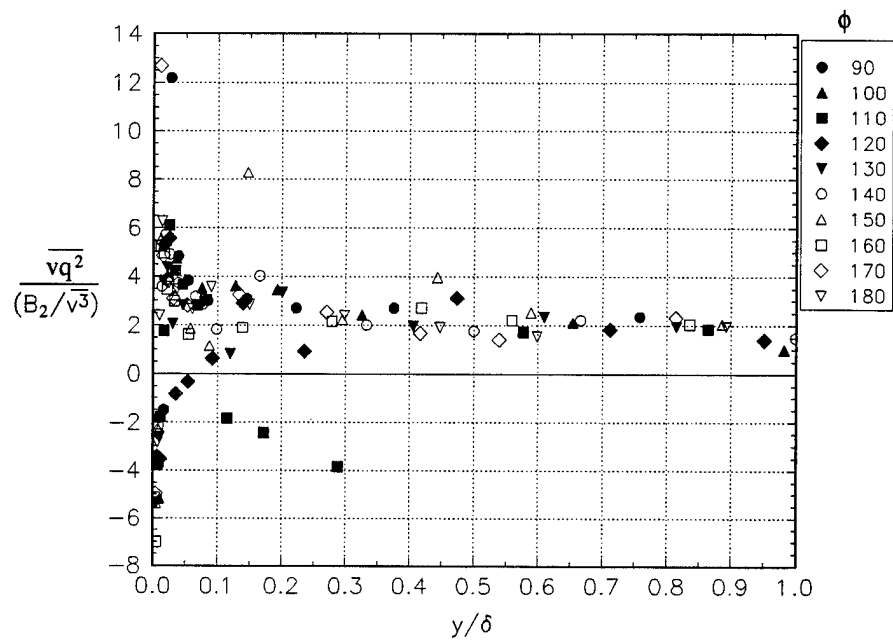


Figure F.18.c Triple product relationship for  $x/L = 0.60$ .

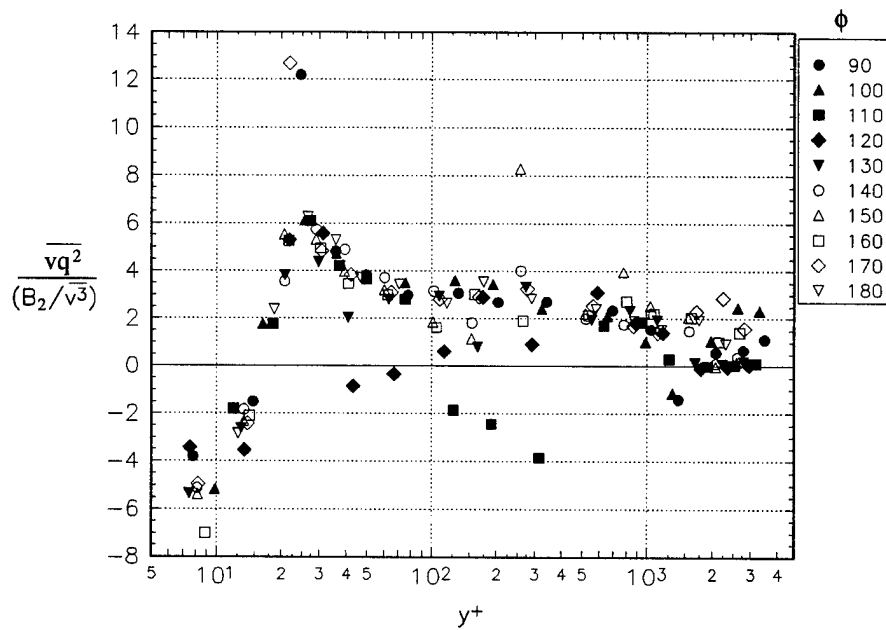


Figure F.18.d Triple product relationship for  $x/L = 0.60$ .

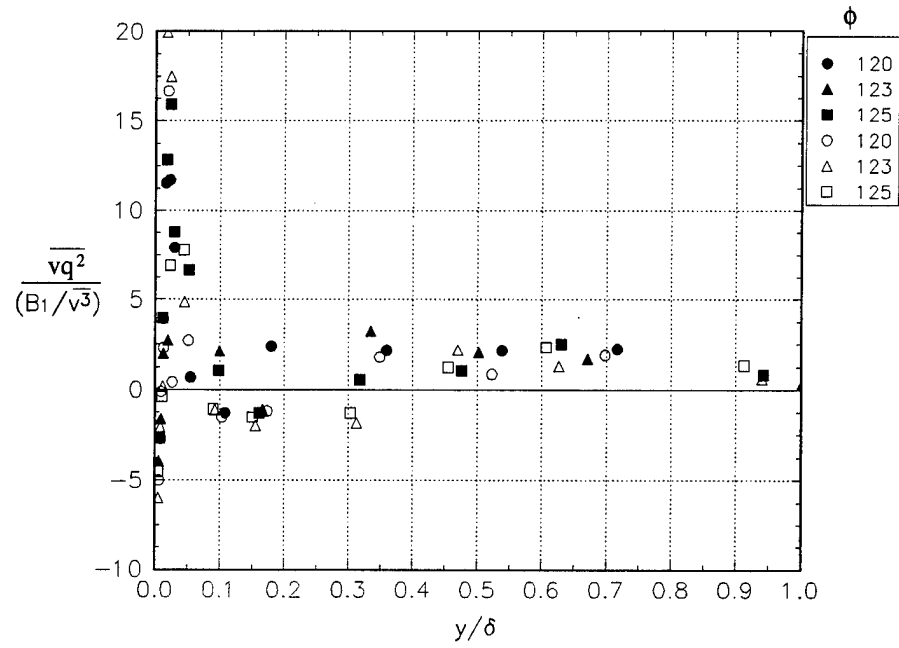


Figure F.19.a Triple product relationship, closed symbols for  $x/L = 0.75$  and open  $x/L = 0.76$ .

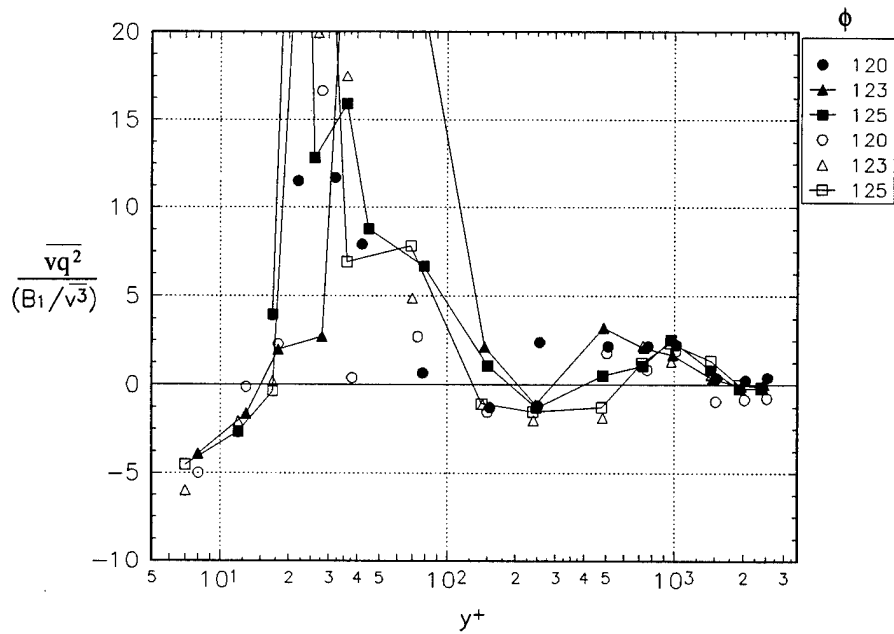


Figure F.19.b Triple product relationship, closed symbols for  $x/L = 0.75$  and open  $x/L = 0.76$ .

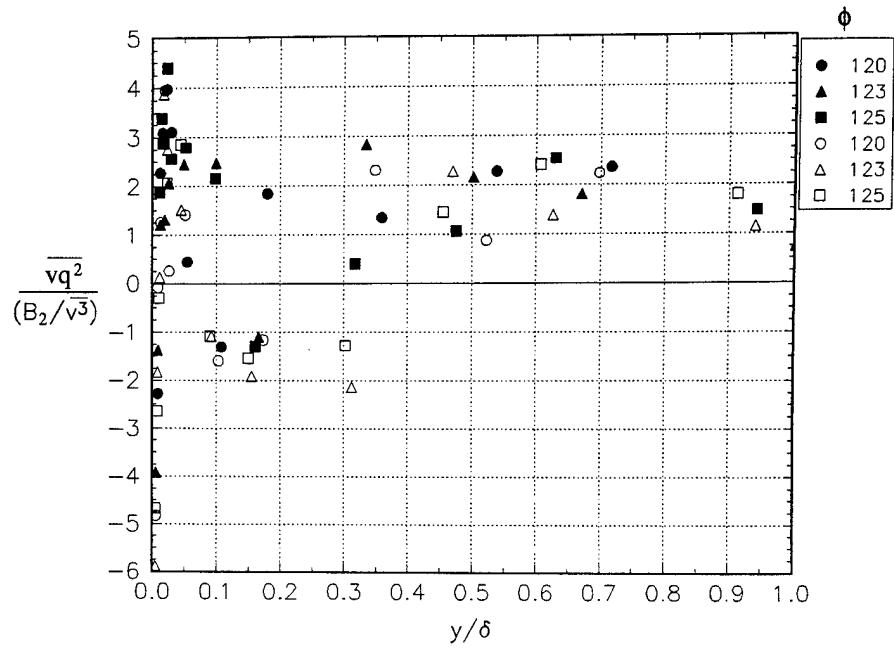


Figure F.19.c Triple product relationship, closed symbols for  $x/L = 0.75$  and open  $x/L = 0.76$ .

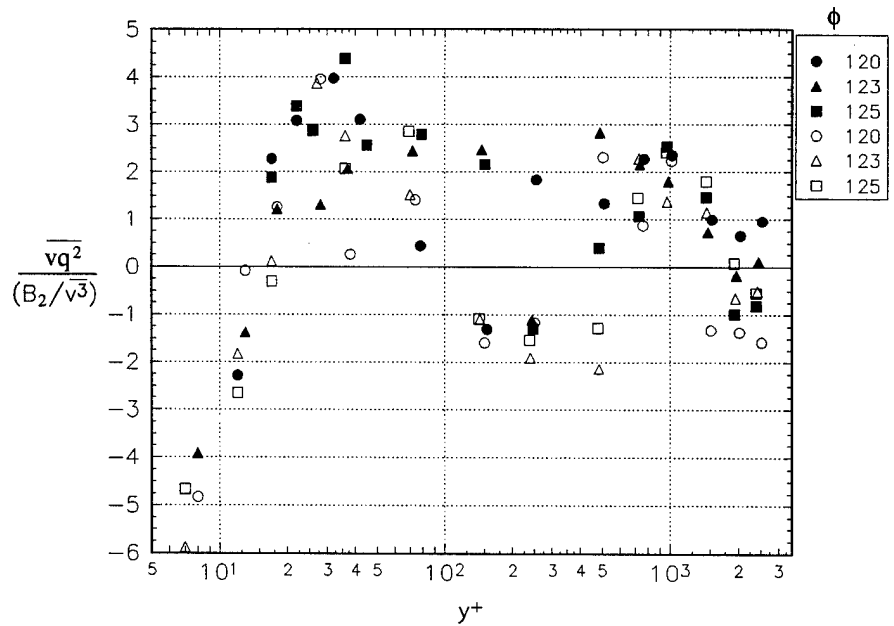
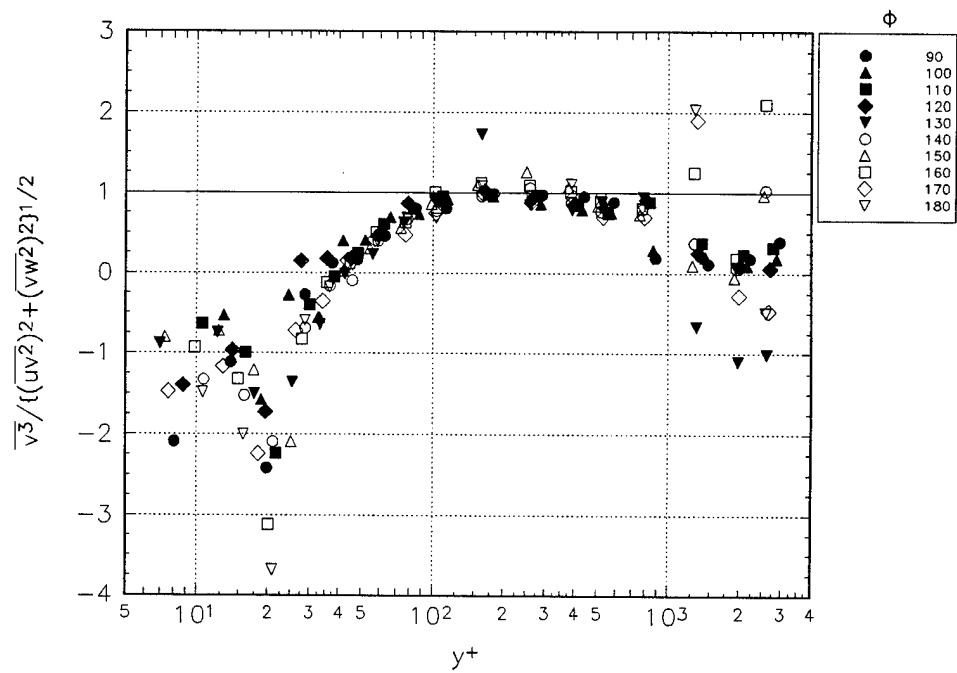
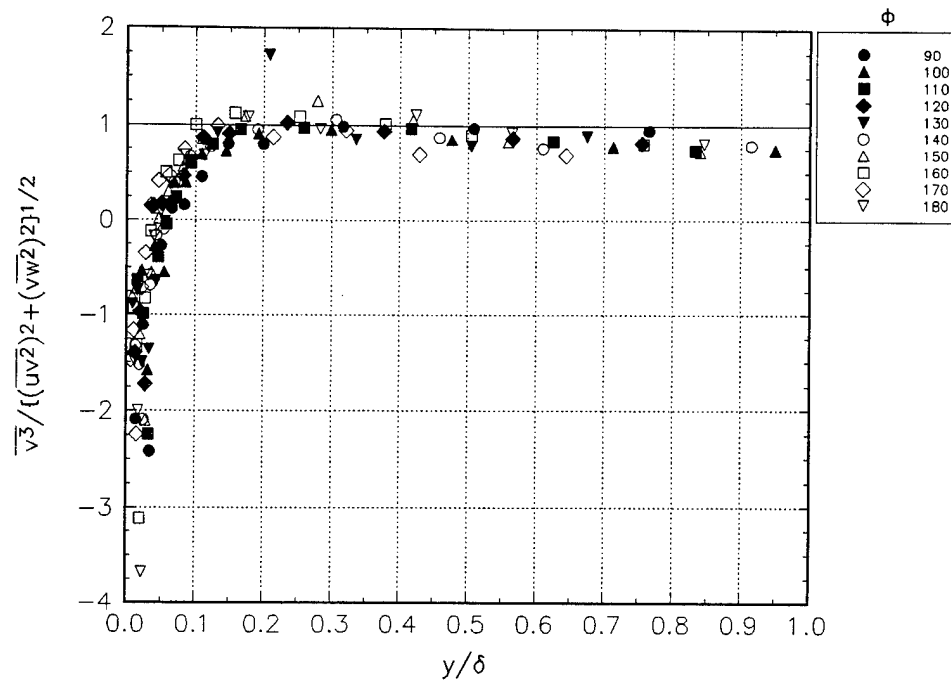


Figure F.19.d Triple product relationship, closed symbols for  $x/L = 0.75$  and open  $x/L = 0.76$ .



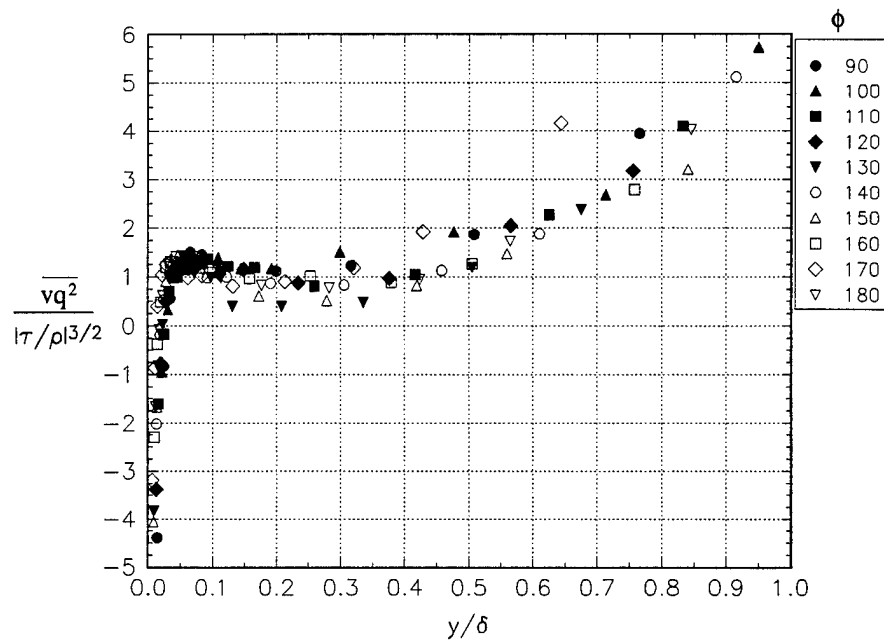


Figure F.21.a Triple product relationship for  $x/L = 0.40$ .

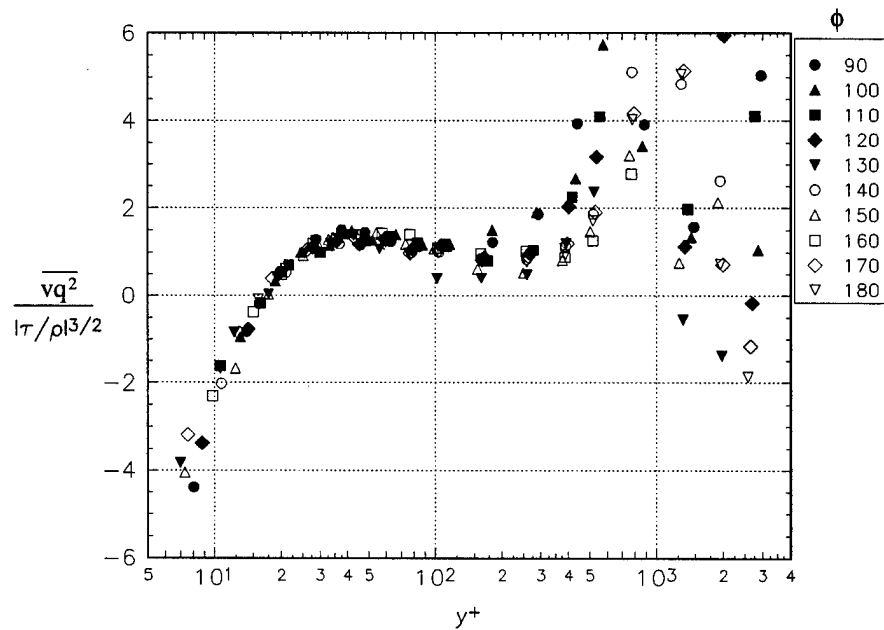


Figure F.21.b Triple product relationship for  $x/L = 0.40$ .

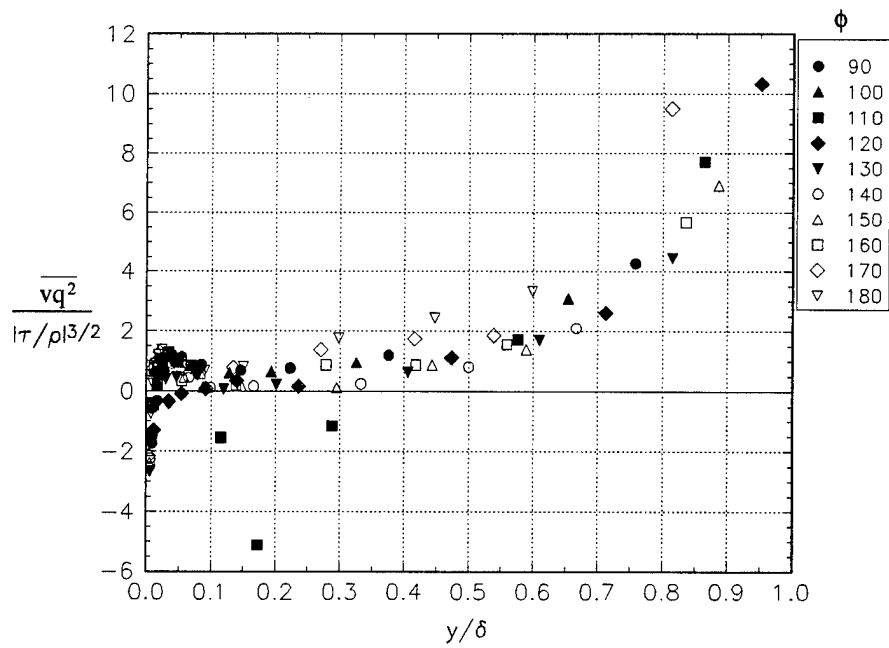


Figure F.22.a Triple product relationship for  $x/L = 0.60$ .

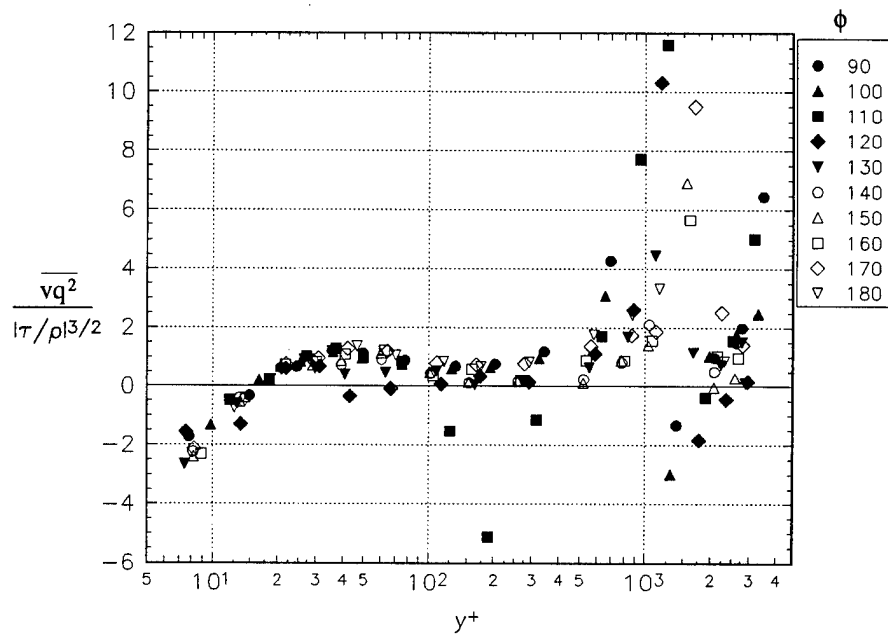


Figure F.22.b Triple product relationship for  $x/L = 0.60$ .

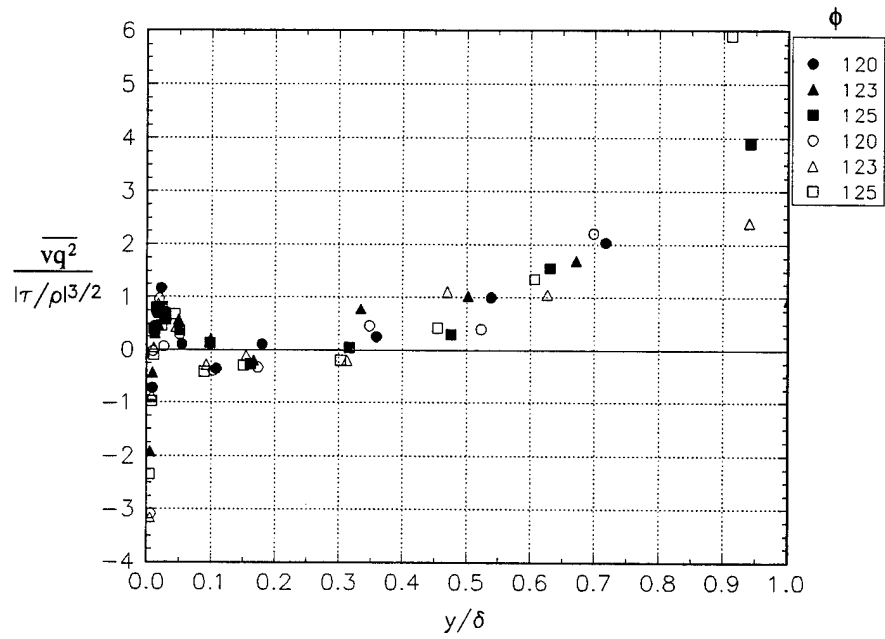


Figure F.23.a Triple product relationship, closed symbols for  $x/L = 0.75$  and open for 0.76.

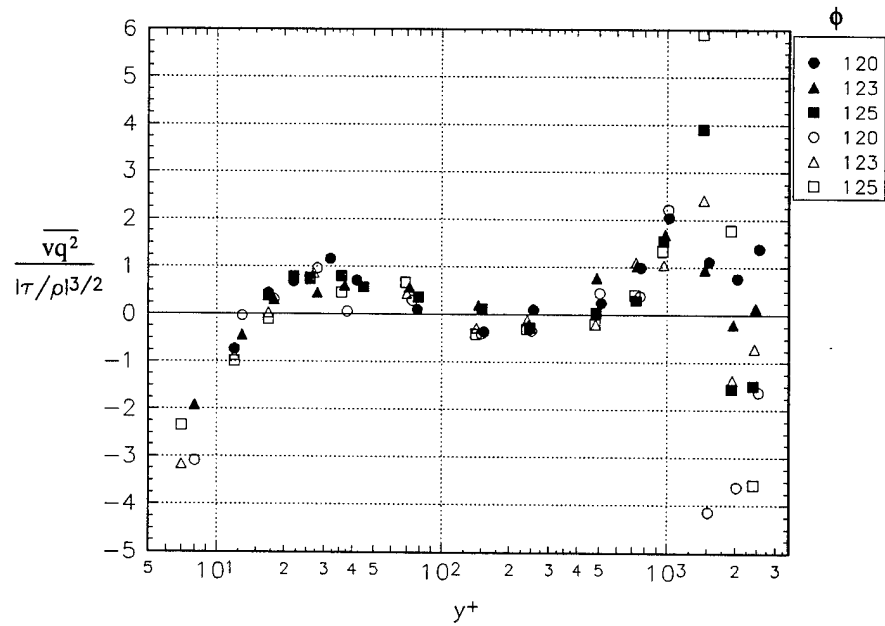
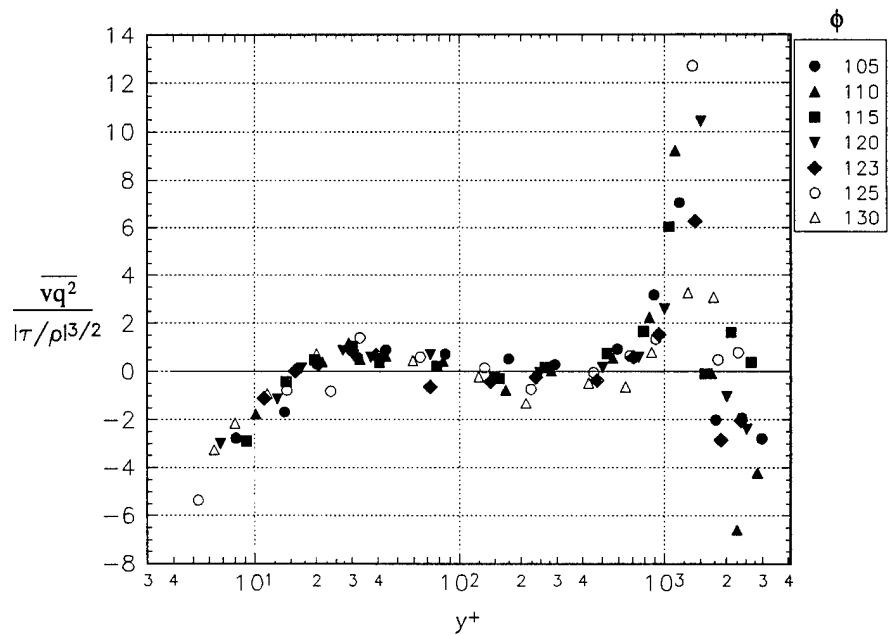
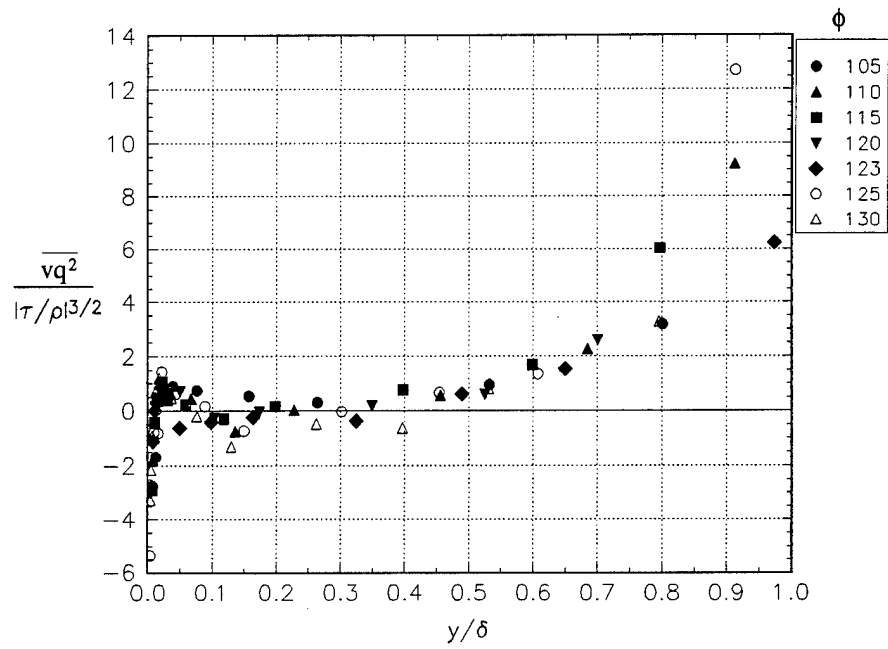


Figure F.23.b Triple product relationship, closed symbols for  $x/L = 0.75$  and open for 0.76.





# APPENDIX G Additional Figures for the Data of Stäger

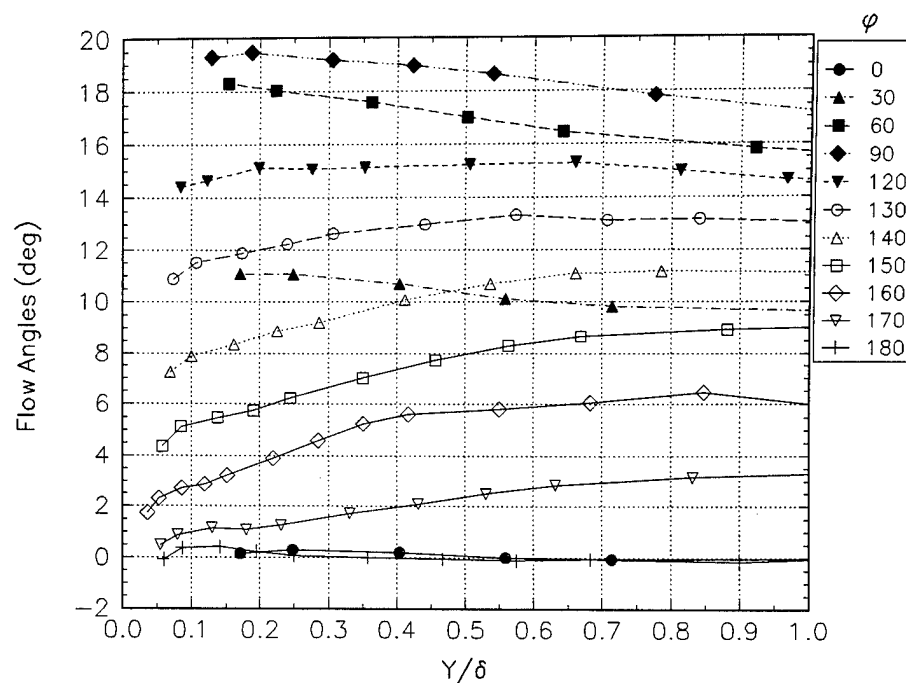


Figure G.1.a Flow angles for  $x/L = 0.48$ .

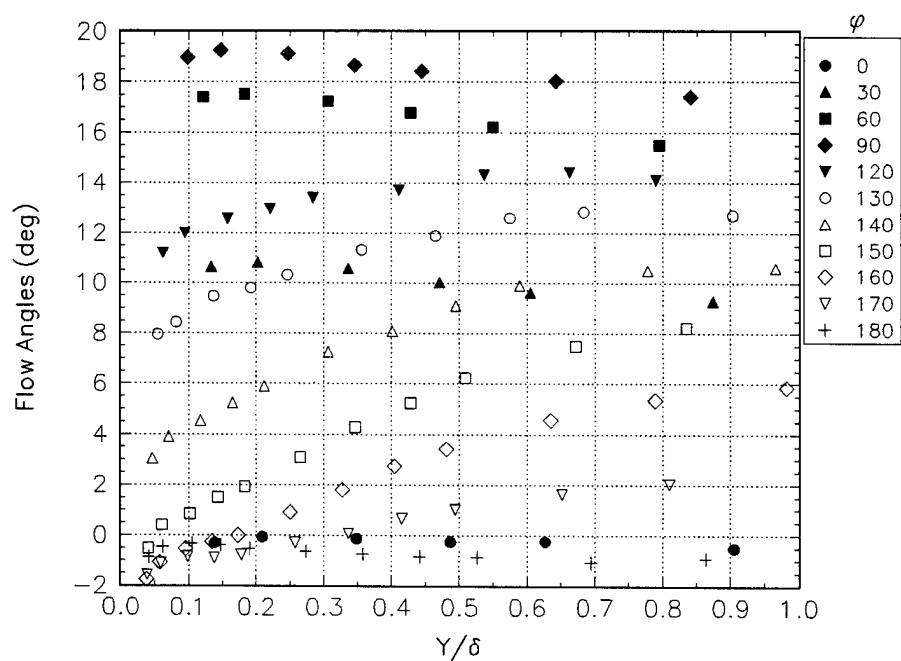


Figure G.1.b Flow angles for  $x/L = 0.56$ .

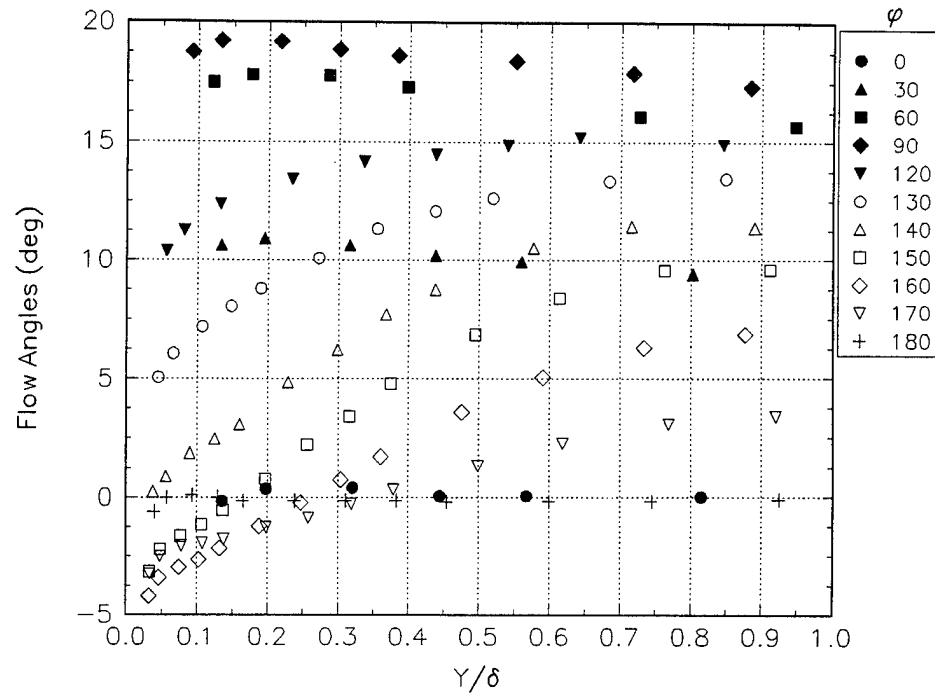


Figure G.1.c Flow angles for  $x/L = 0.64$ .

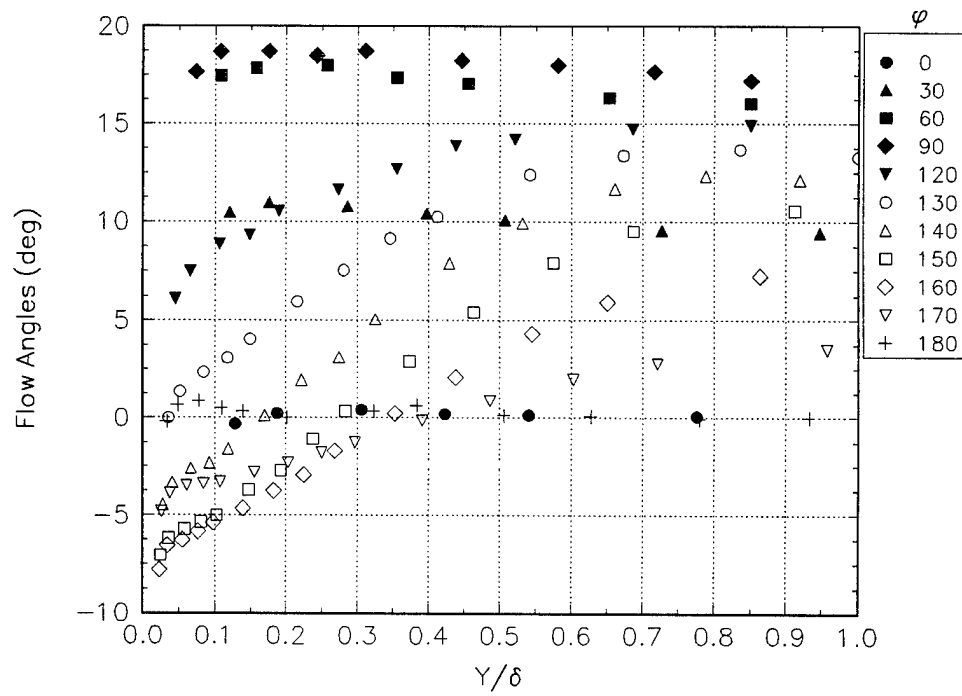


Figure G.1.d Flow angles for  $x/L = 0.73$ .

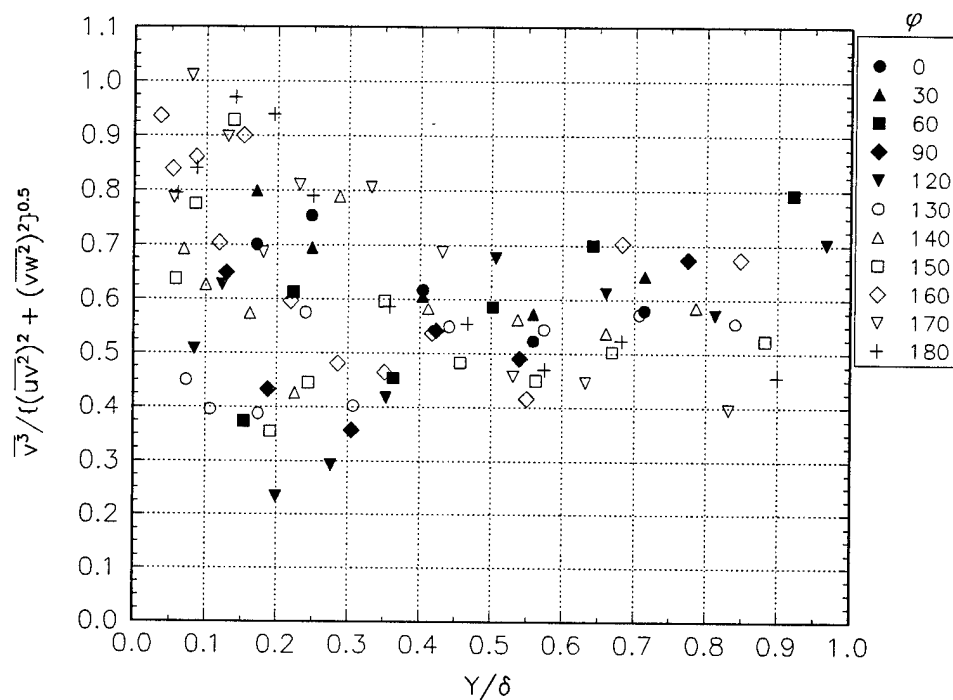


Figure G.2.a  $B_1$  for  $x/L = 0.48$  in free-stream coordinates.

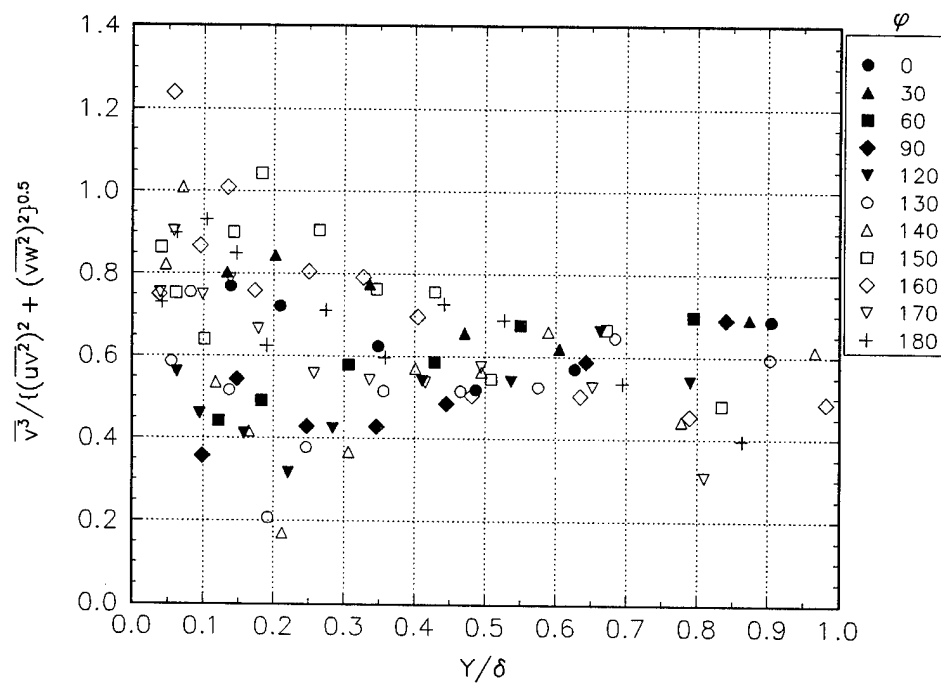


Figure G.2.b  $B_1$  for  $x/L = 0.56$  in free-stream coordinates.

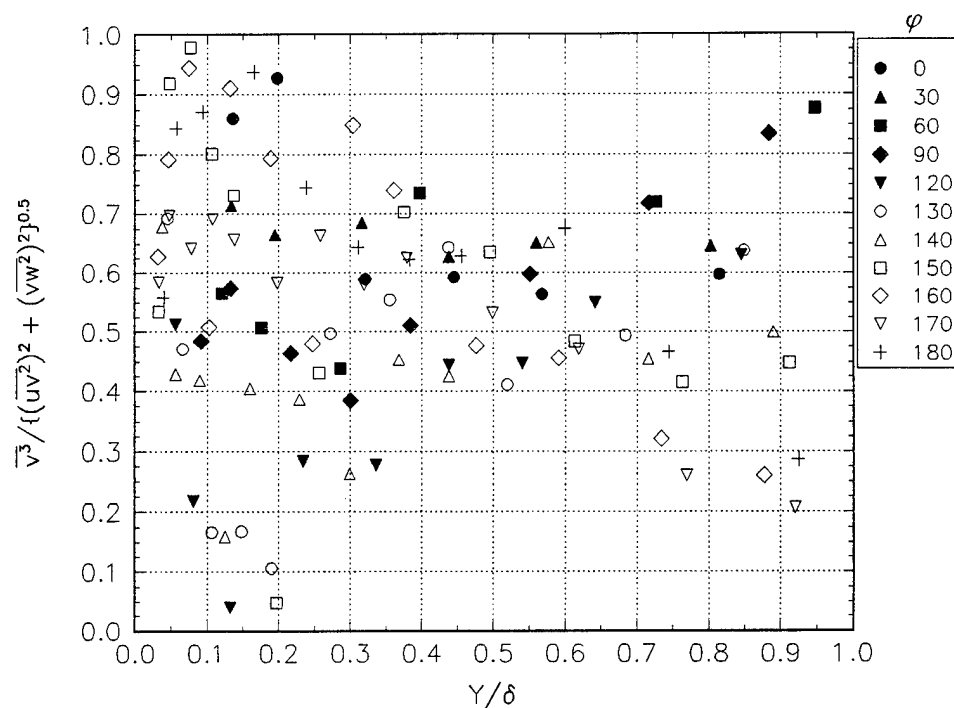


Figure G.2.c  $B_1$  for  $x/L = 0.64$  in free-stream coordinates.

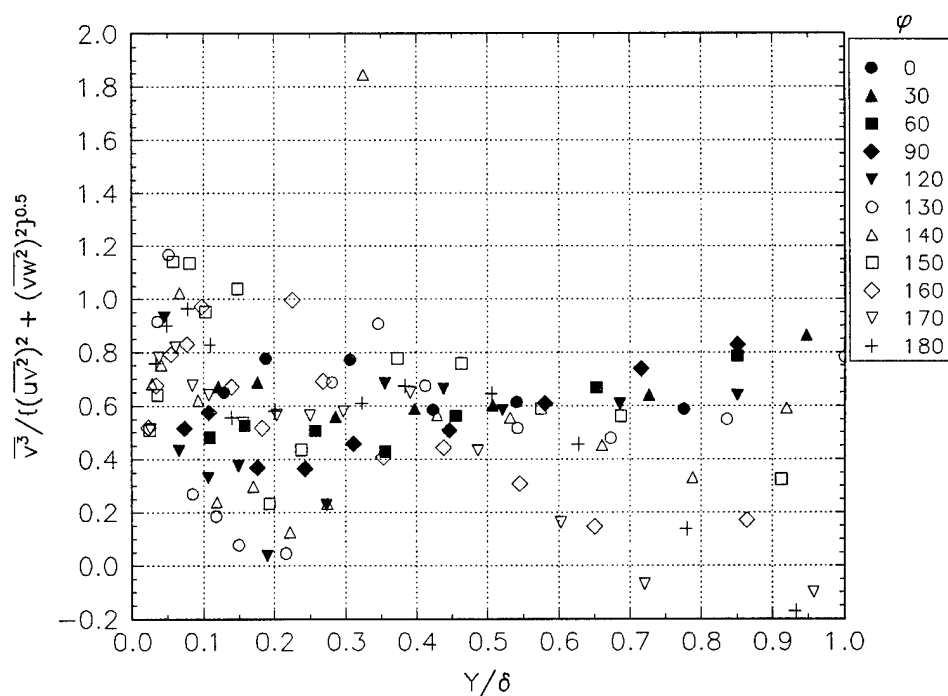


Figure G.2.d  $B_1$  for  $x/L = 0.73$  in free-stream coordinates.

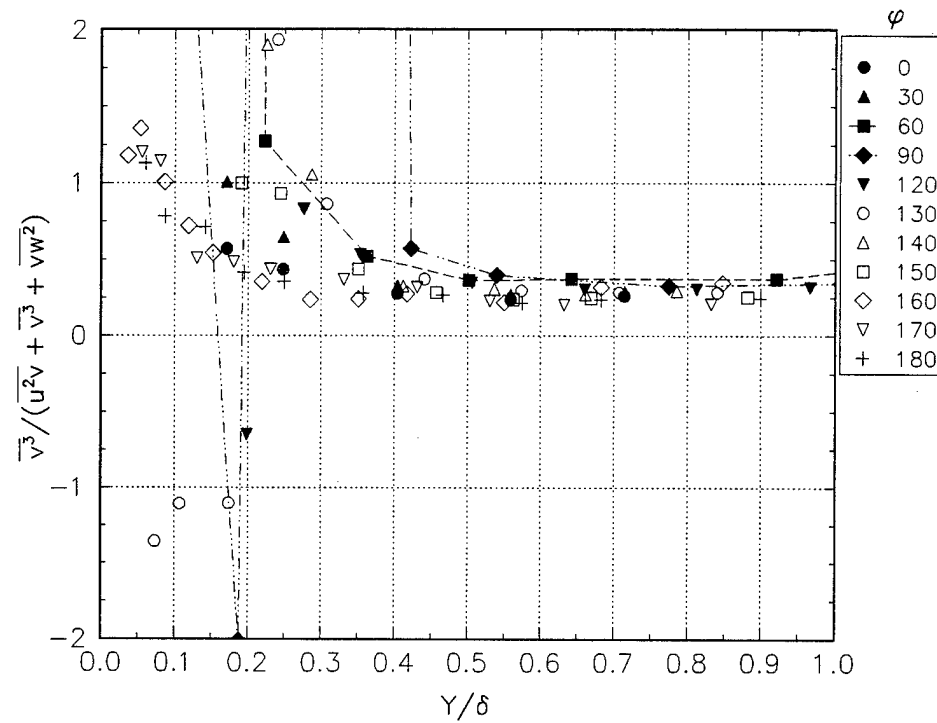


Figure G.3 The  $vq$  parameter for  $x/L = 0.48$ .

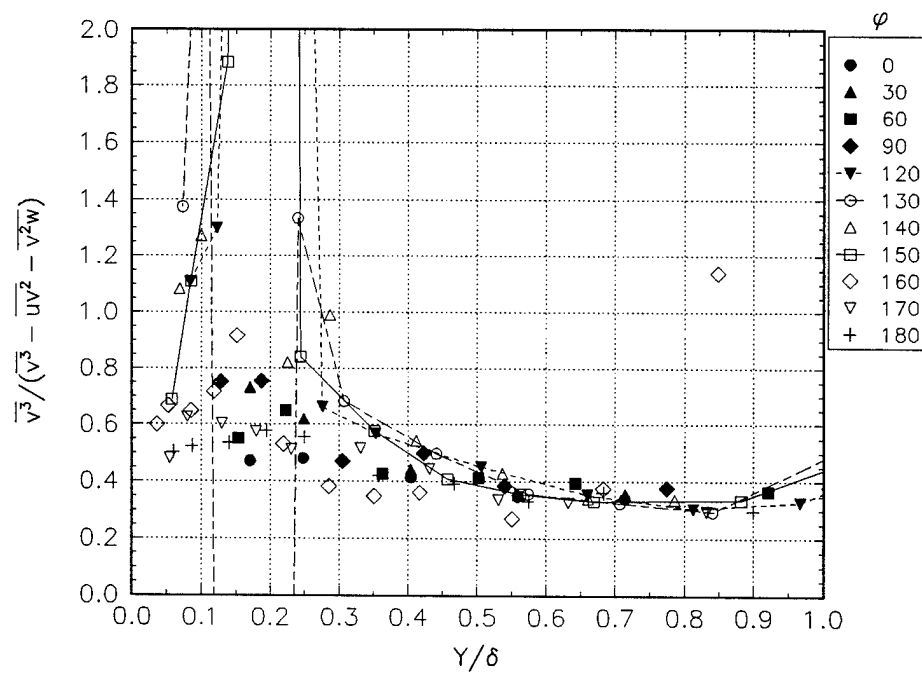


Figure G.3 A Triple product parameter for  $x/L = 0.48$  in free-stream coordinates.

## APPENDIX H Additional Figures for the Data of Molton

The data of Molton was taken in two regions with two different light collection angles. The first region is the forward scatter region where the data was taken along a line coincident with the longitudinal axis of the body. The origin of the XG1 (longitudinal direction) coordinate axis was at the nose of the body. The origin of the angle  $\phi$  is located at the windward plane of symmetry. The second region was farther back in the region of separation and the light was collected in back scatter mode. The data presented in this appendix is in local freestream coordinates. See chapter 2 for specifics on the conditions.

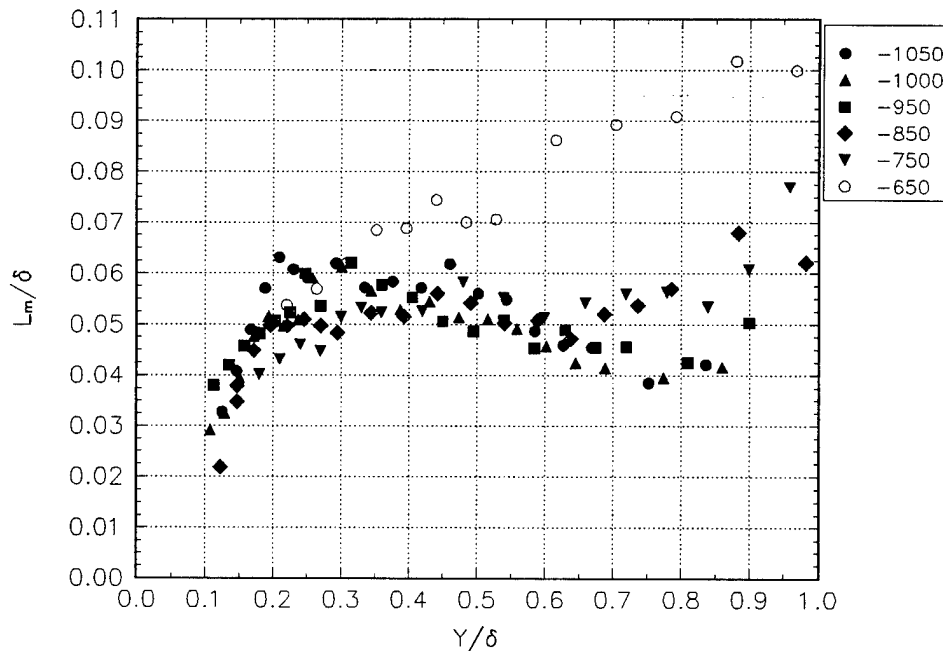


Figure H1.1 Mixing length for the forward scatter case at  $\phi = 165^\circ$ .  
The XG1 location in mm is indicated in the legend.

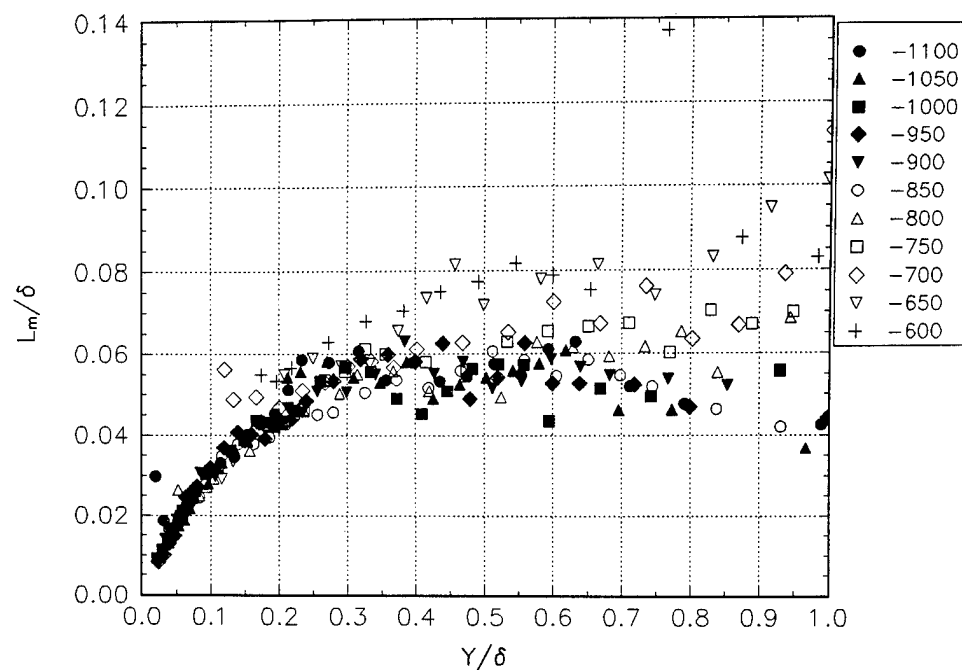


Figure H1.2 Mixing length for the forward scatter case at  $\phi = 170^\circ$ .  
The XG1 location in mm is indicated in the legend.

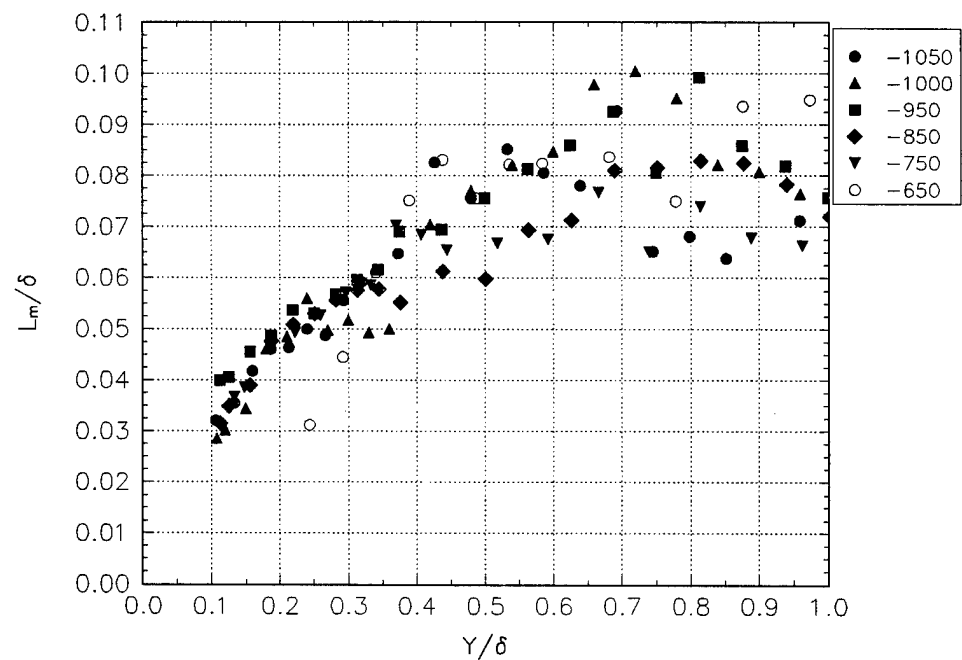


Figure H1.3 Mixing length for the forward scatter case at  $\phi = 175^\circ$ .  
The XG1 location in mm is indicated in the legend.



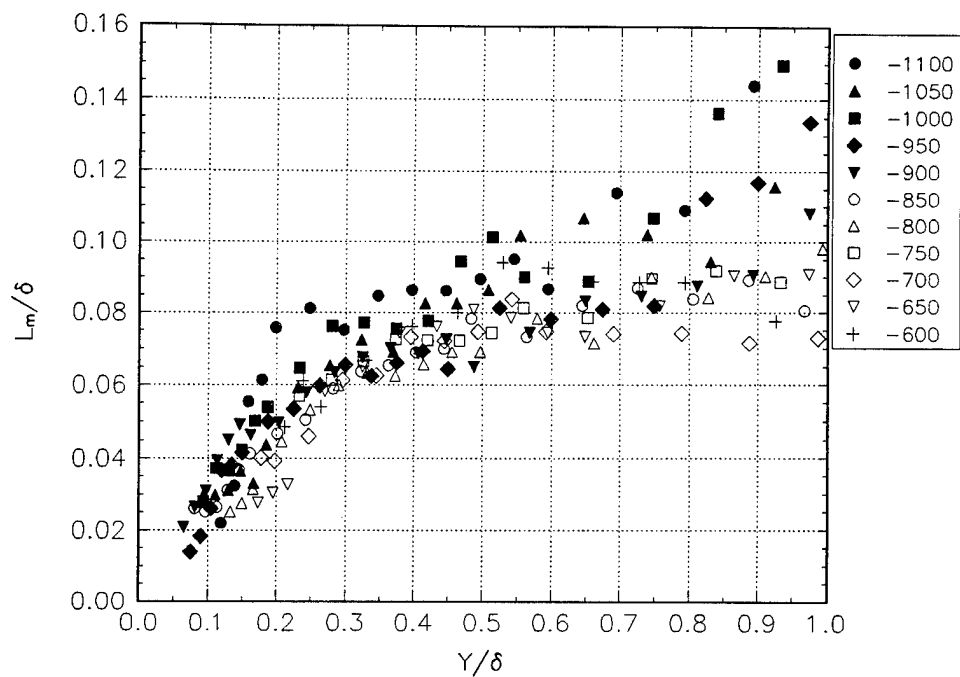


Figure H1.4 Mixing length for the forward scatter case at  $\phi = 180^\circ$ .  
The XG1 location in mm is indicated in the legend.

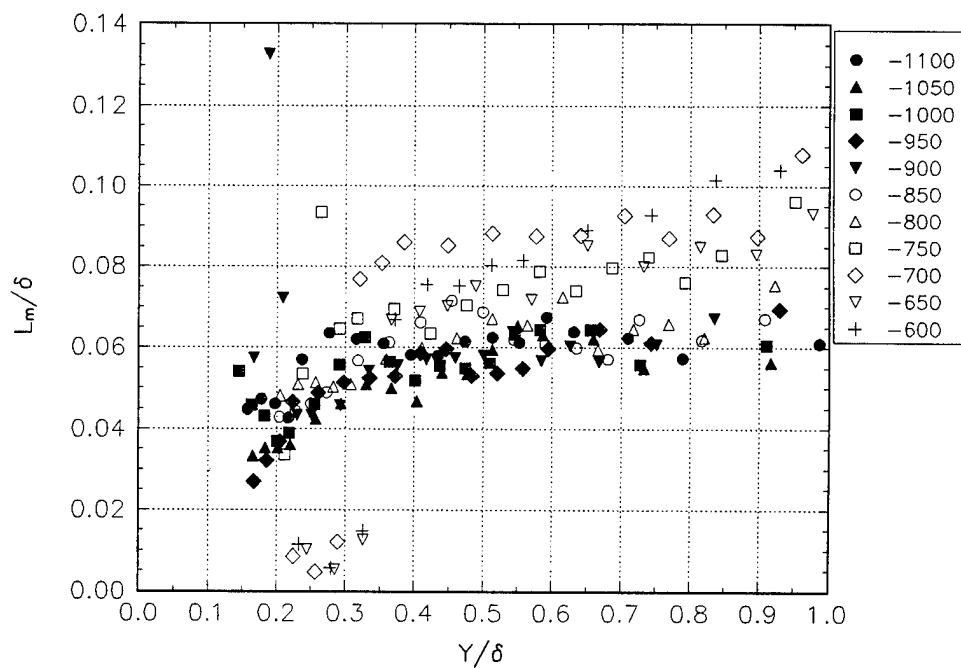


Figure H1.5 Mixing length for the forward scatter case at  $\phi = 190^\circ$ .  
The XG1 location in mm is indicated in the legend.

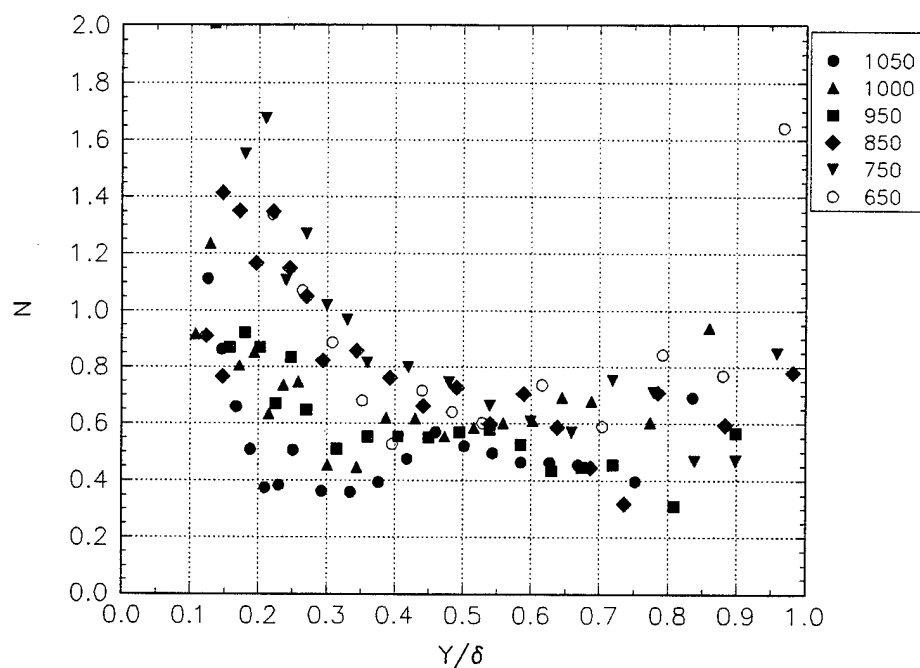


Figure H2.1 The Anisotropy parameter for  $\phi = 165^\circ$  for the forward scatter data. The legend gives the x-location in mm.

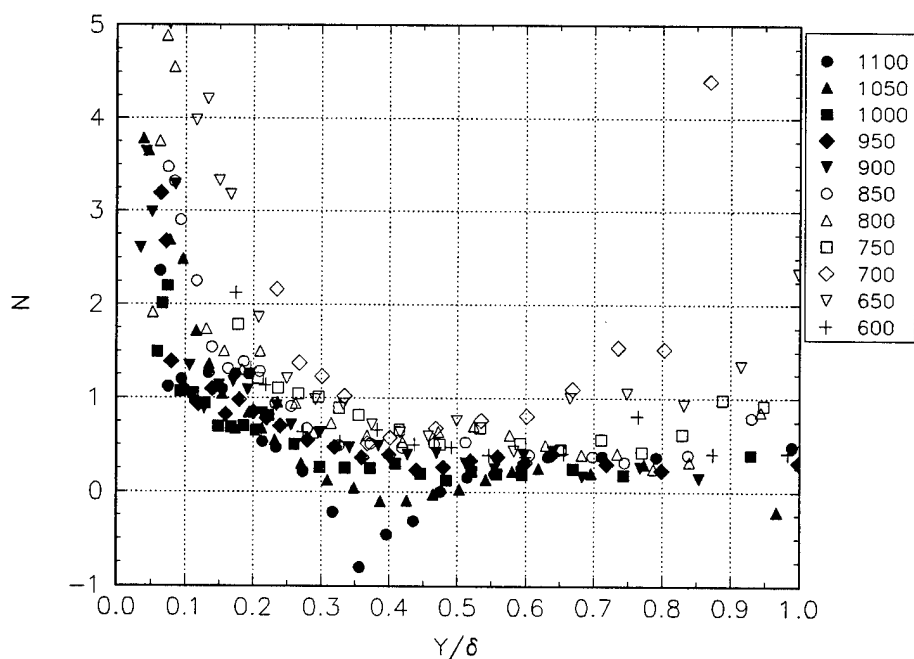


Figure H2.2 The Anisotropy parameter for  $\phi = 170^\circ$  for the forward scatter data. The legend gives the x-location in mm.

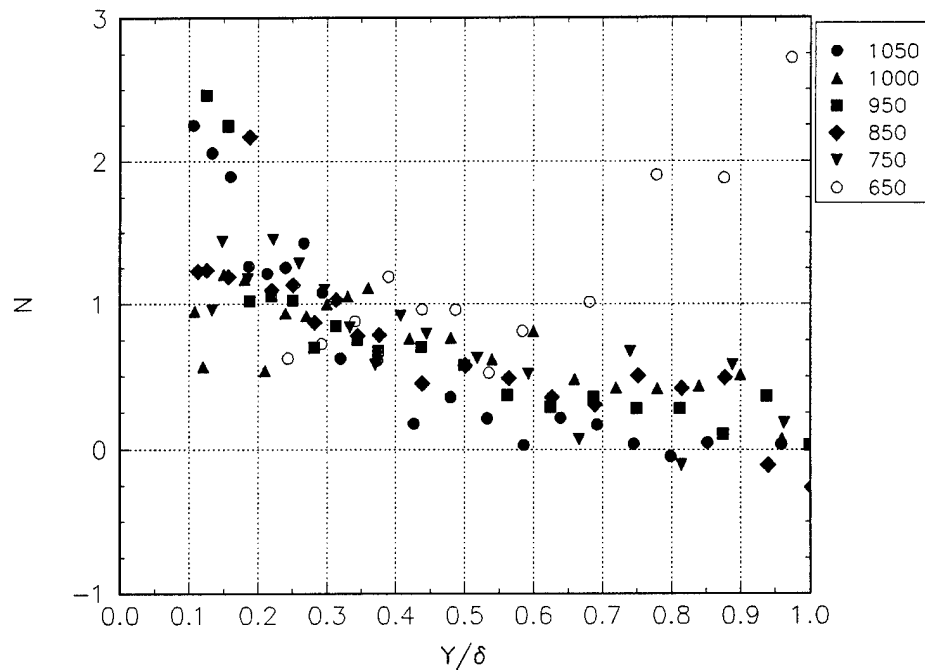


Figure H2.3 The Anisotropy parameter for  $\phi = 175^\circ$  for the forward scatter data. The legend gives the x-location in mm.

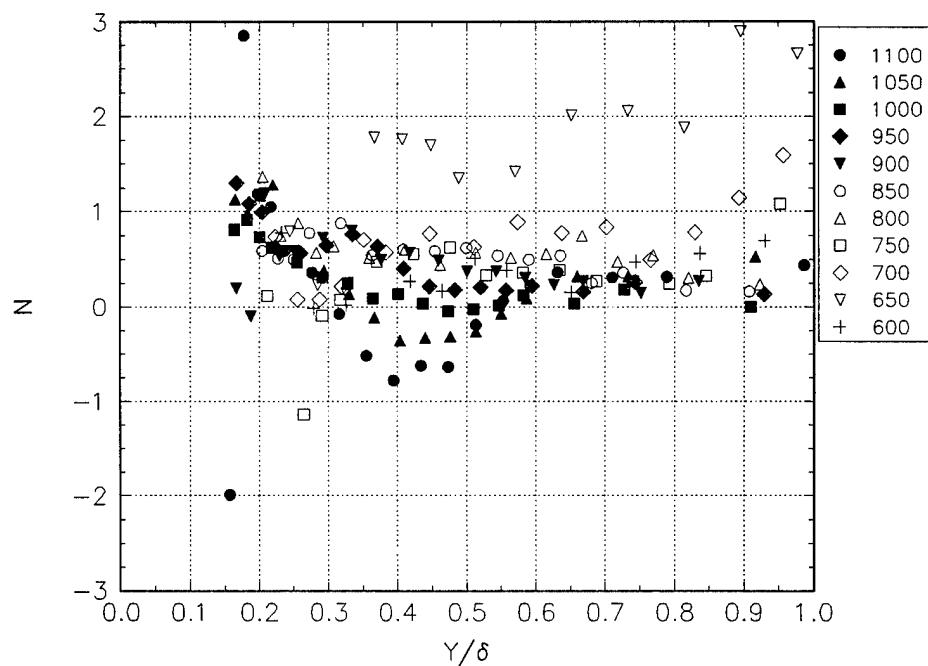


Figure H2.4 The Anisotropy parameter for  $\phi = 190^\circ$  for the forward scatter data. The legend gives the x-location in mm.

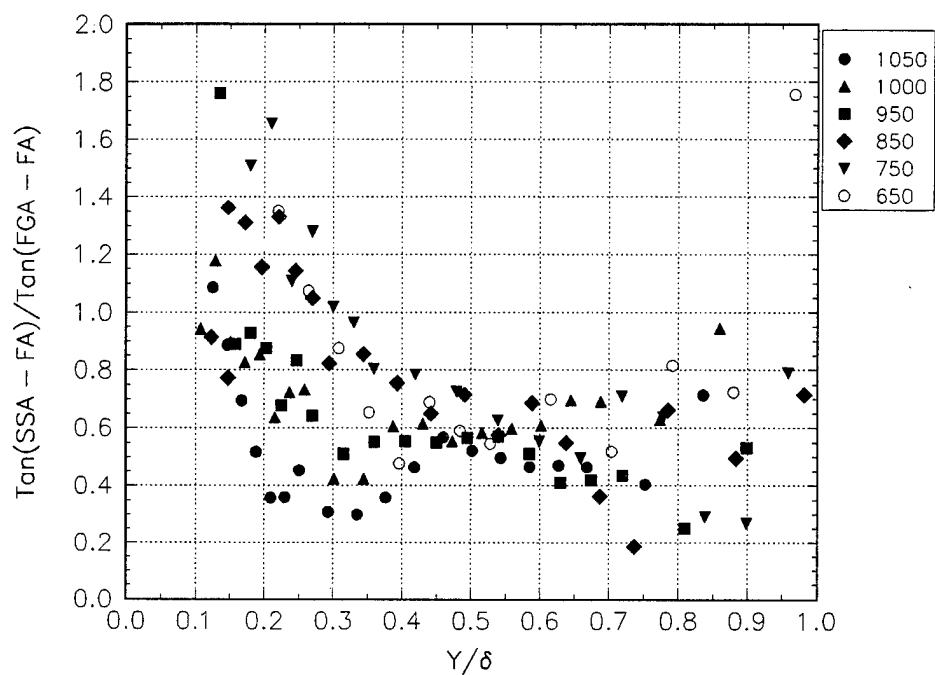


Figure H3.1 Rotta's T parameter for  $\phi = 165^\circ$  for the forward scatter data. The legend gives the x-location in mm.

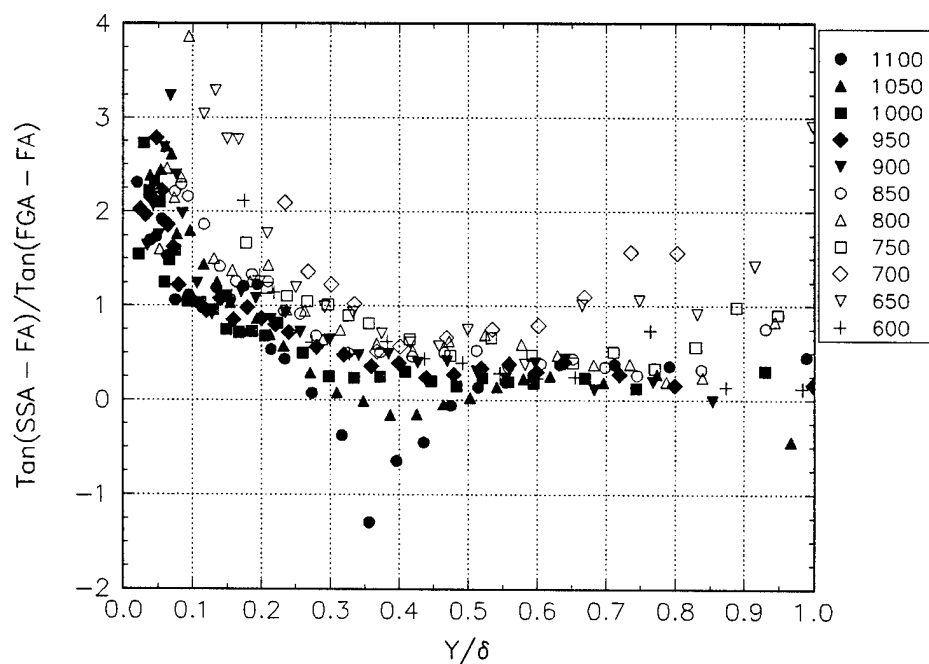


Figure H3.2 Rotta's T parameter for  $\phi = 170^\circ$  for the forward scatter data. The legend gives the x-location in mm.

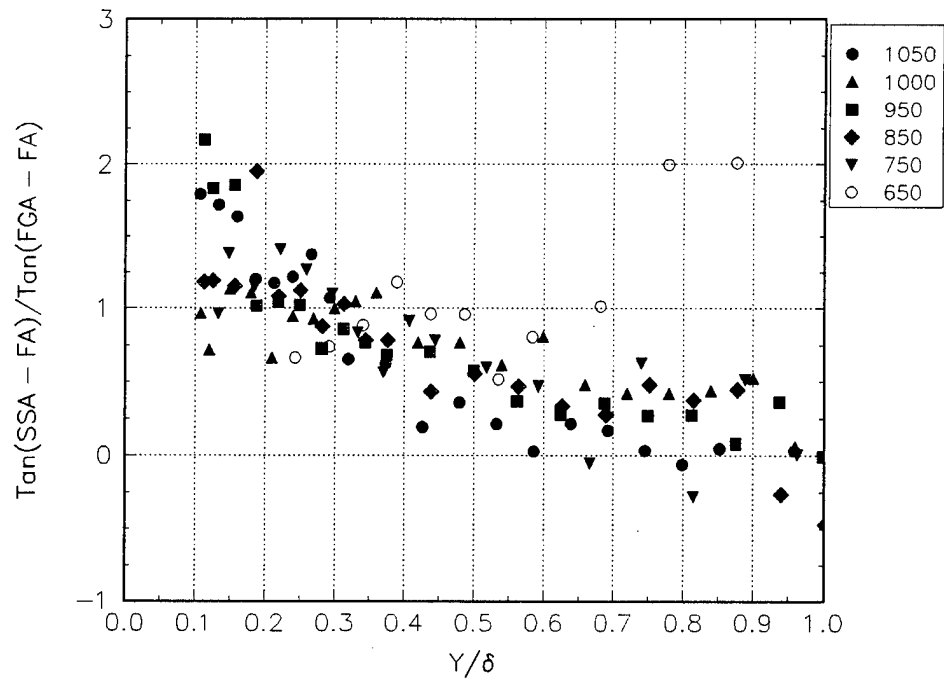


Figure H3.3 Rotta's T parameter for  $\phi = 175^\circ$  for the forward scatter data. The legend gives the x-location in mm.

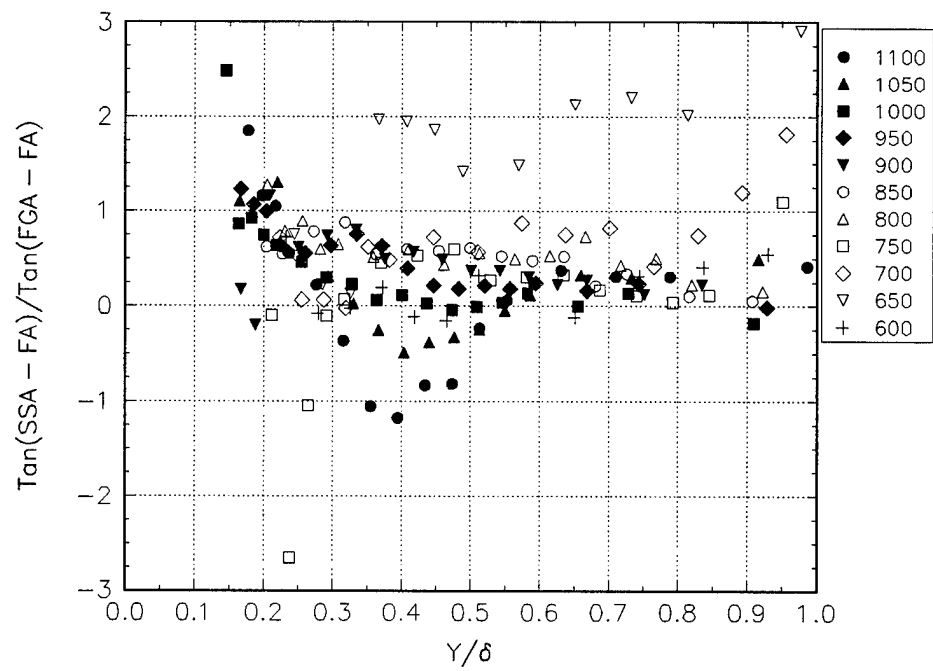


Figure H3.4 Rotta's T parameter for  $\phi = 190^\circ$  for the forward scatter data. The legend gives the x-location in mm.

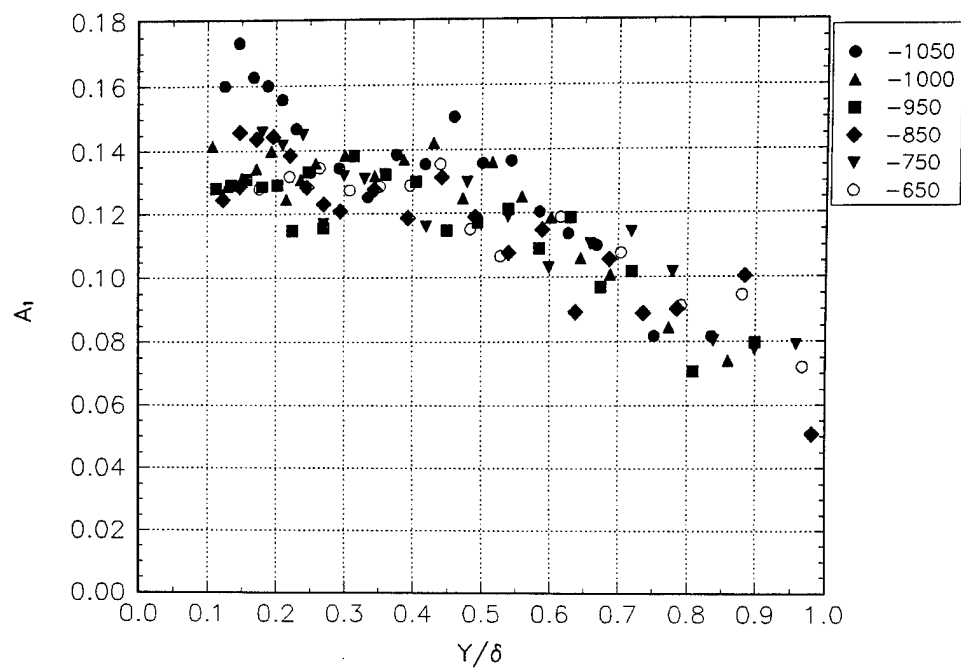


Figure H4.1 The  $a_1$  structural parameter for  $\phi = 165^\circ$  for the forward scatter data. The legend gives the XG1 location in mm.

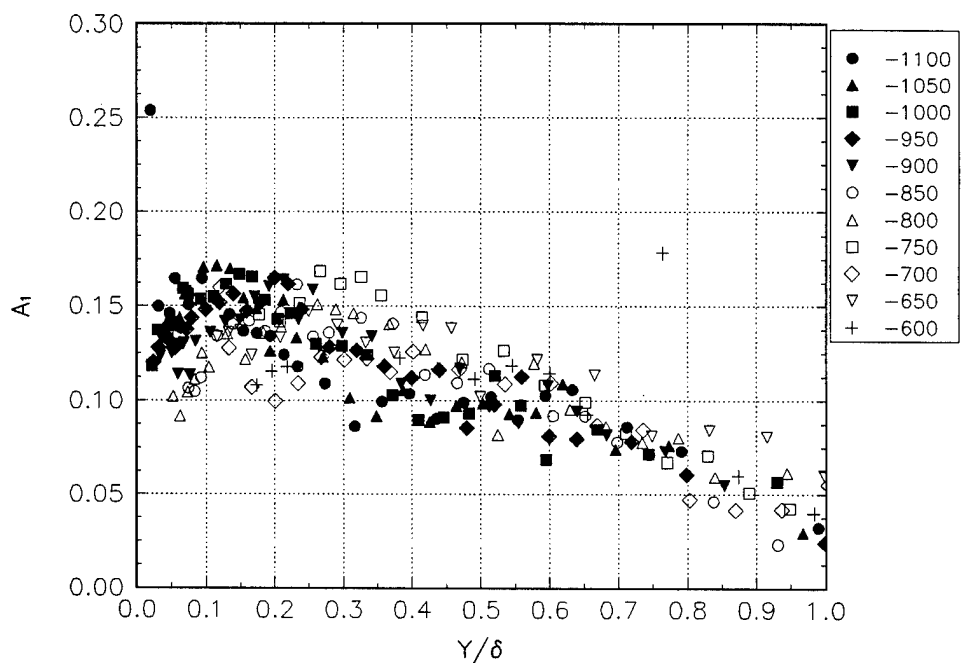


Figure H4.2 The  $a_1$  structural parameter for  $\phi = 170^\circ$  for the forward scatter data. The legend gives the XG1 location in mm.

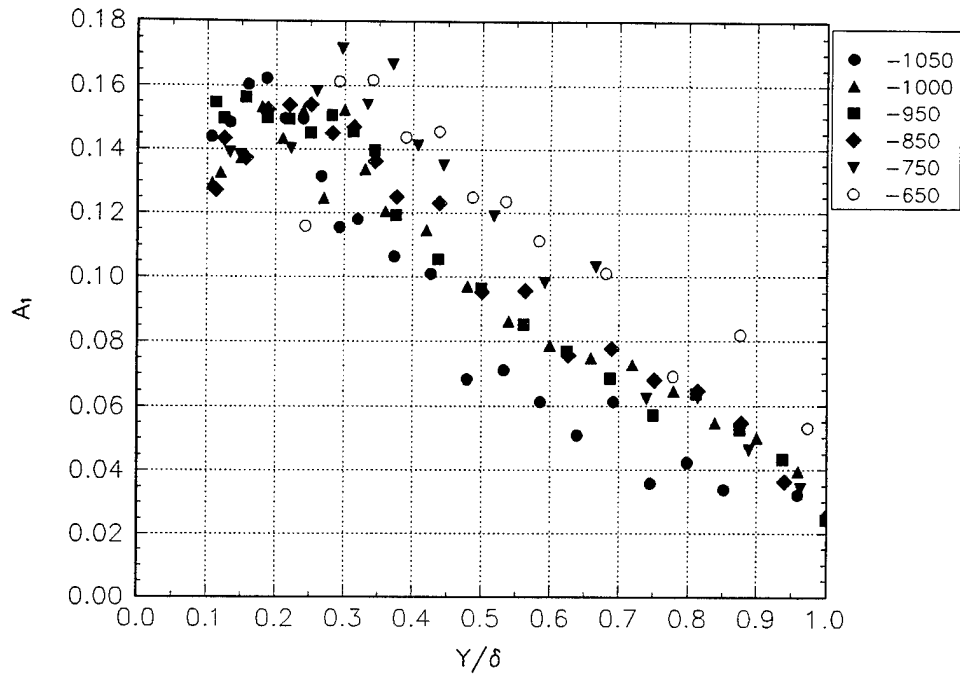


Figure H4.3 The  $a_1$  structural parameter for  $\phi = 175^\circ$  for the forward scatter data. The legend gives the XG1 location in mm.

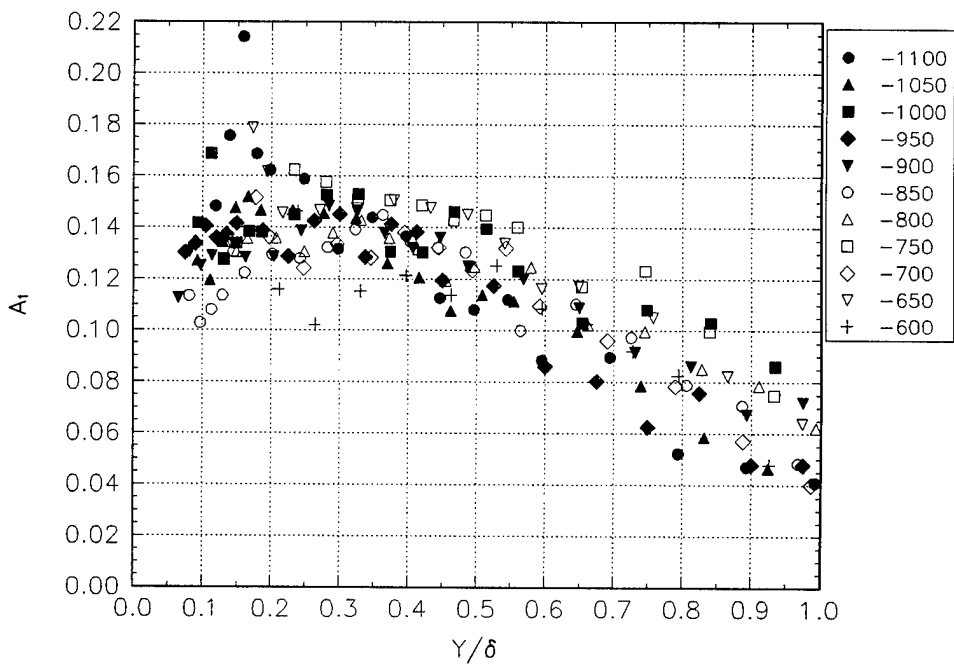


Figure H4.4 The  $a_1$  structural parameter for  $\phi = 180^\circ$  for the forward scatter data. The legend gives the XG1 location in mm.

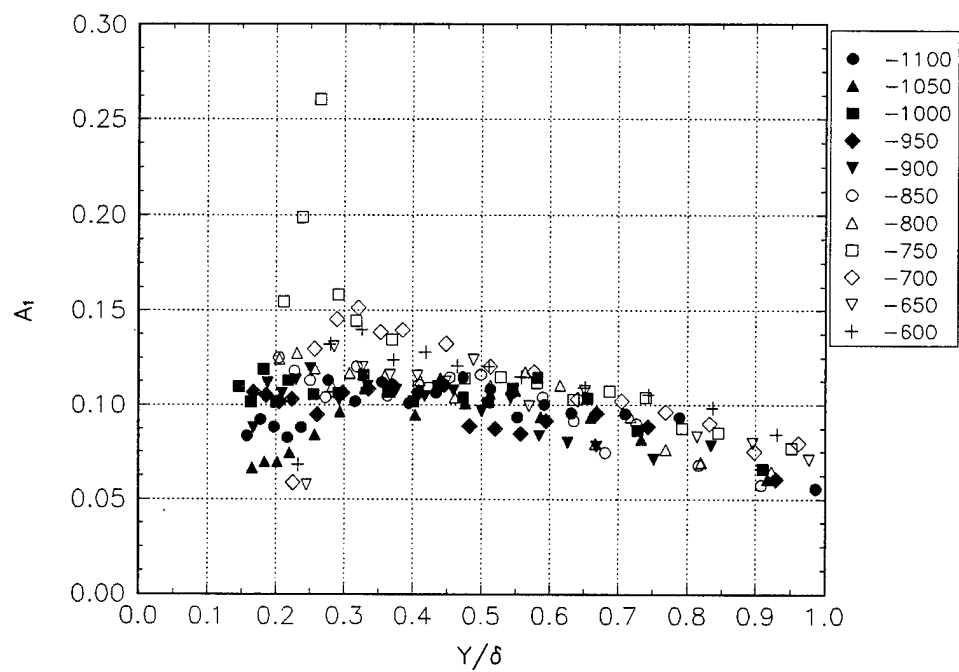


Figure H4.5 The  $a_1$  structural parameter for  $\phi = 190^\circ$  for the forward scatter data. The legend gives the XG1 location in mm.



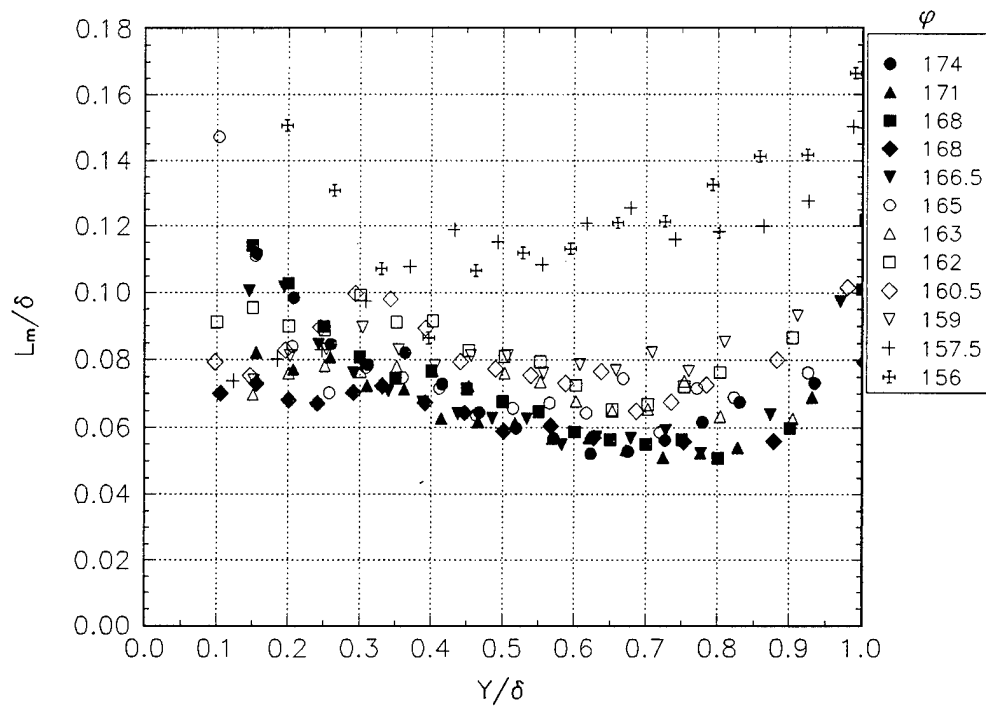


Figure H5.1 Mixing length for the backward scatter case at  $x = 900\text{mm}$ .

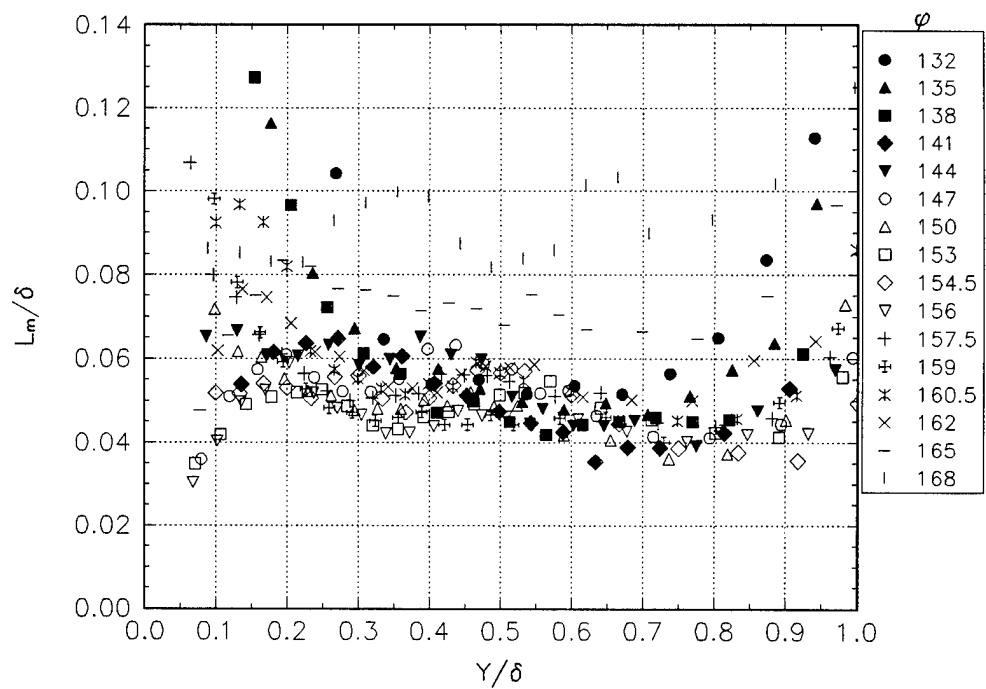


Figure H5.2 Mixing length for the backward scatter case at  $x = 1100\text{mm}$ .

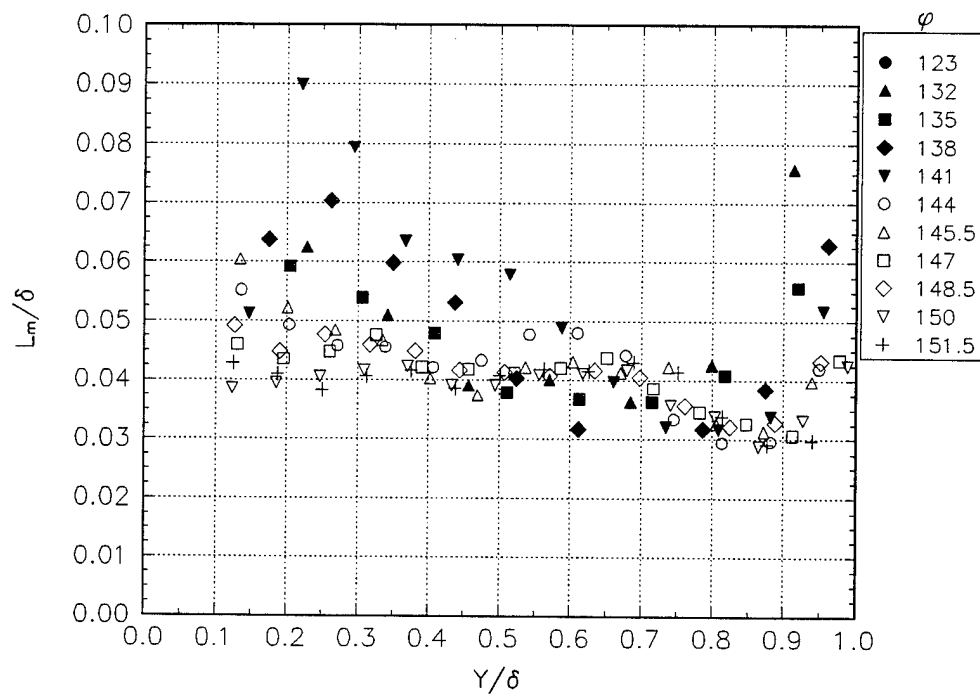


Figure H5.3 Mixing length for the backward scatter case at  $x = 1300\text{mm}$ .

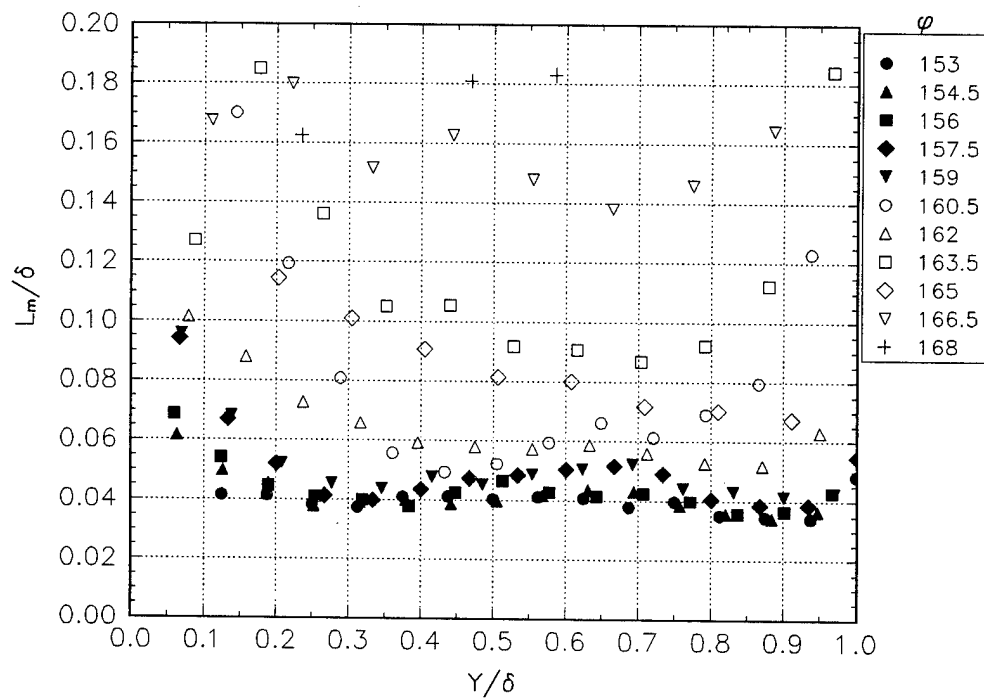


Figure H5.4 Mixing length for the backward scatter case at  $x = 1300\text{mm}$ .

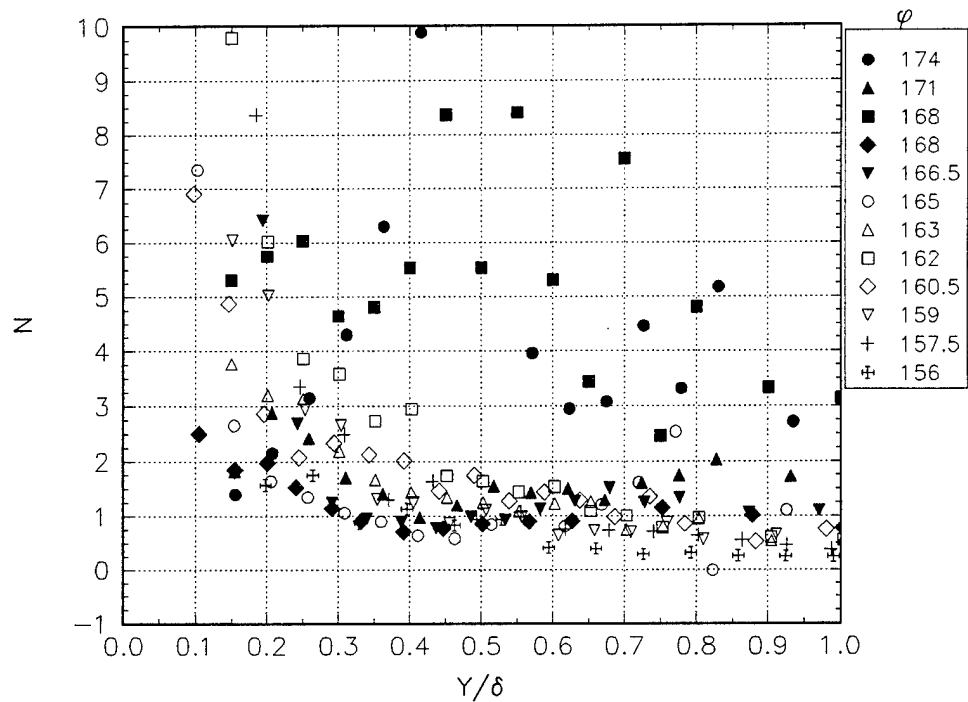


Figure H6.1 Anisotropy parameter for the backward scatter case at  $x = 900\text{mm}$ .

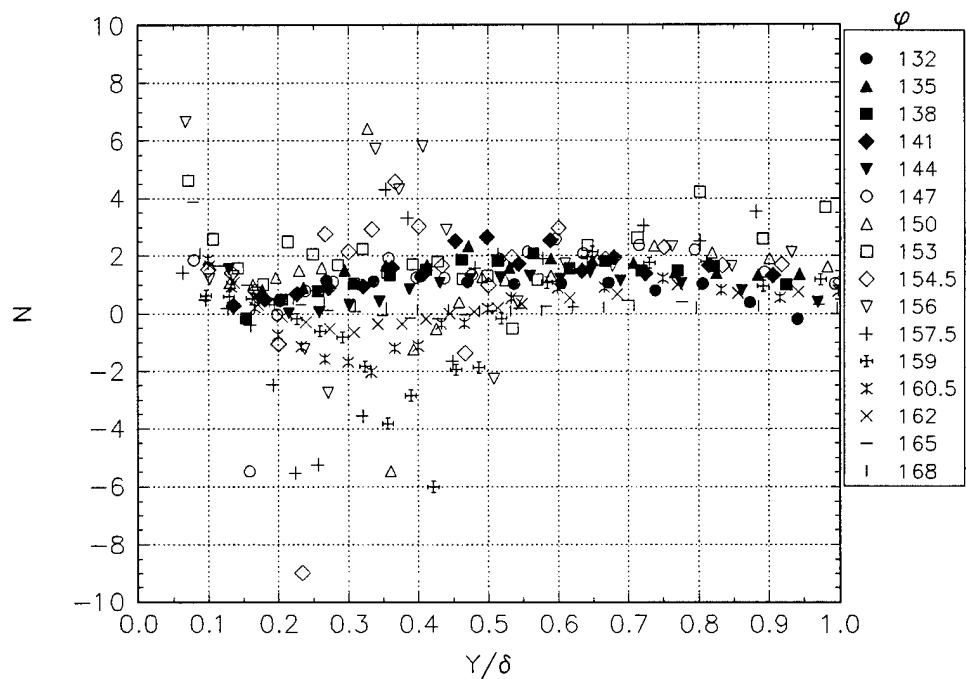


Figure H6.2 Anisotropy parameter for the backward scatter case at  $x = 1100\text{mm}$ .

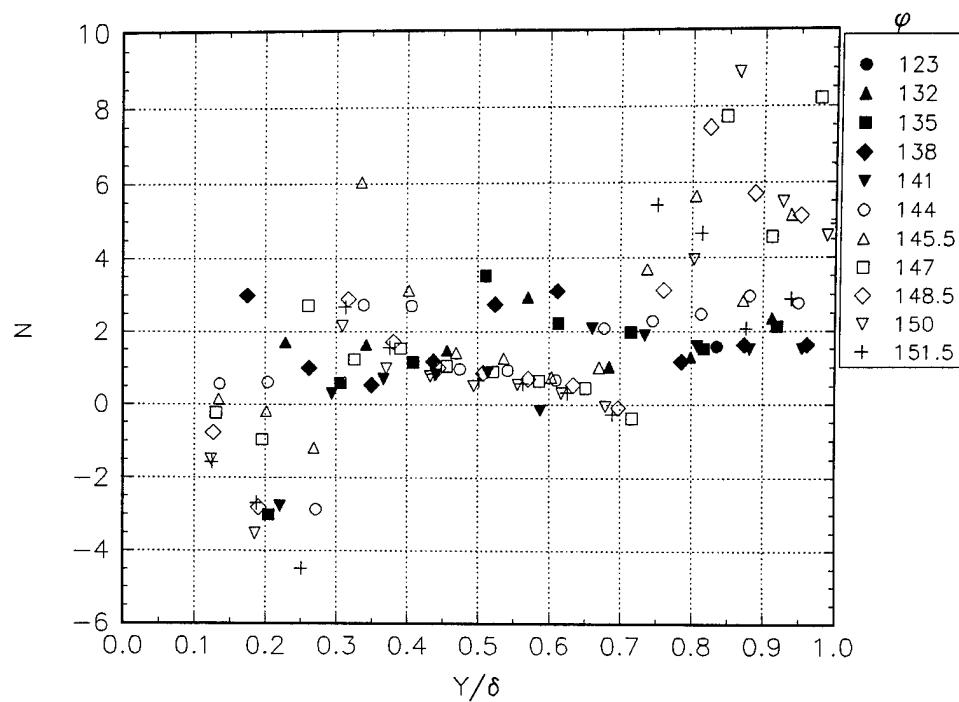


Figure H6.3 Anisotropy parameter for the backward scatter case at  $x = 1300\text{mm}$ .

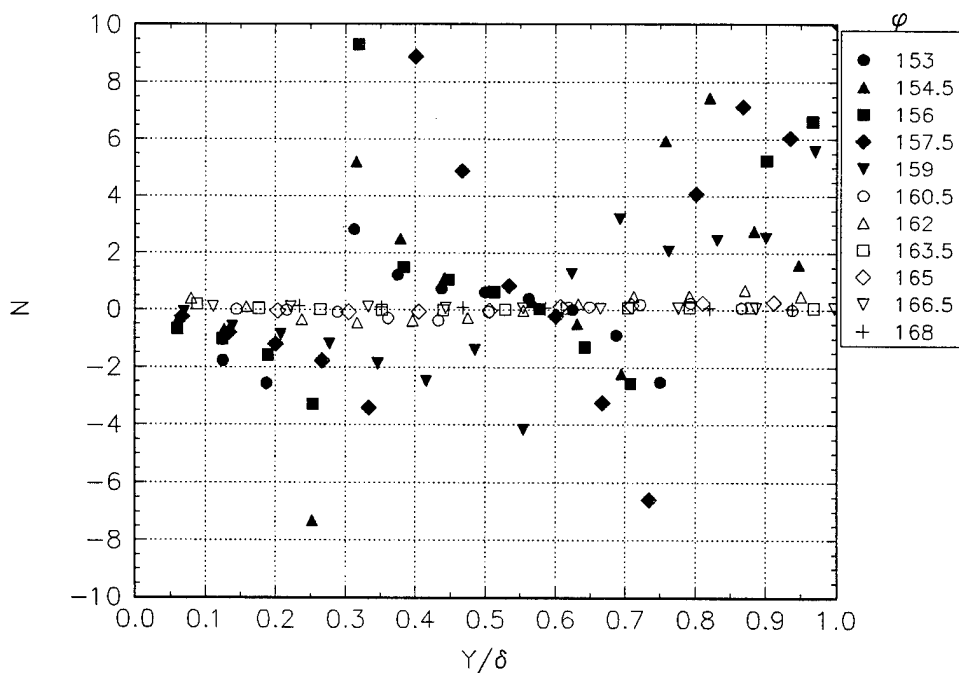


Figure H6.4 Anisotropy parameter for the backward scatter case at  $x = 1300\text{mm}$ .

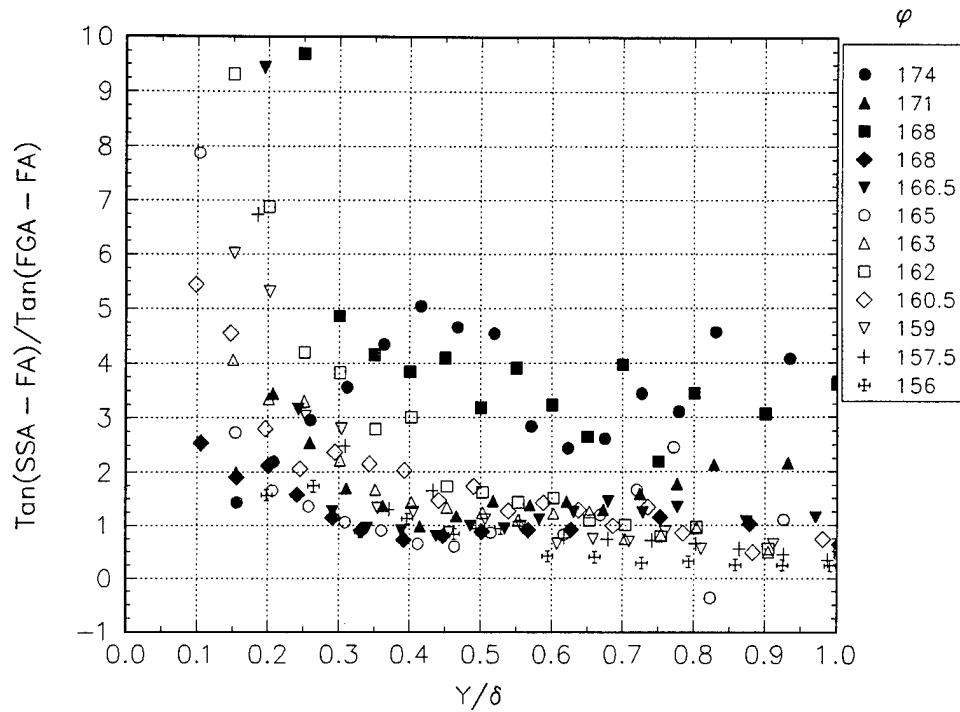


Figure H7.1 Rotta's T parameter for the backward scatter case at  $x = 900\text{mm}$ .

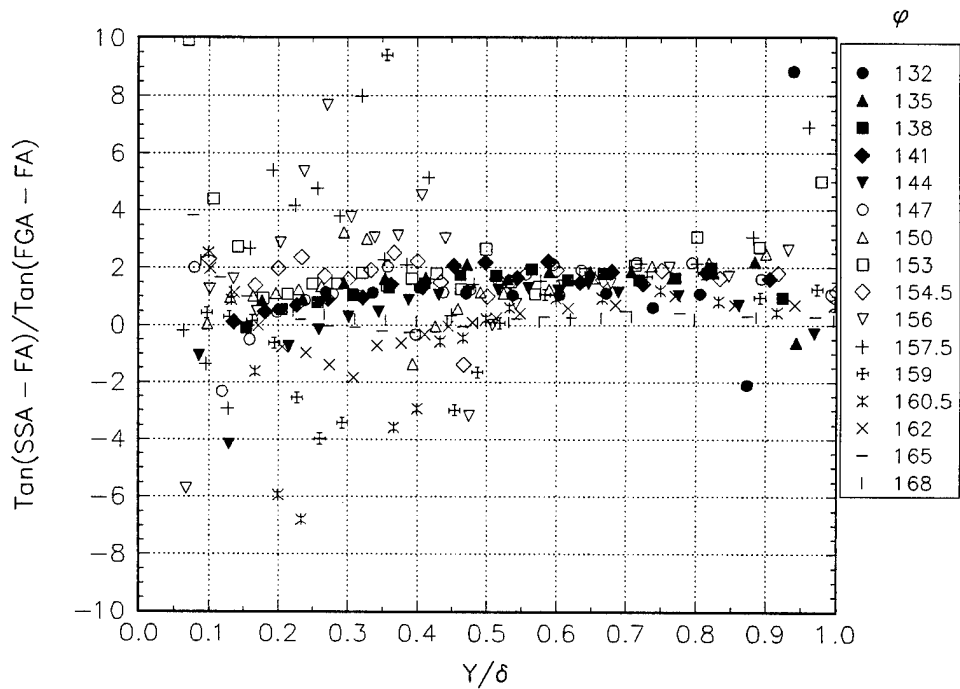


Figure H7.2 Rotta's T parameter for the backward scatter case at  $x = 1100\text{mm}$ .

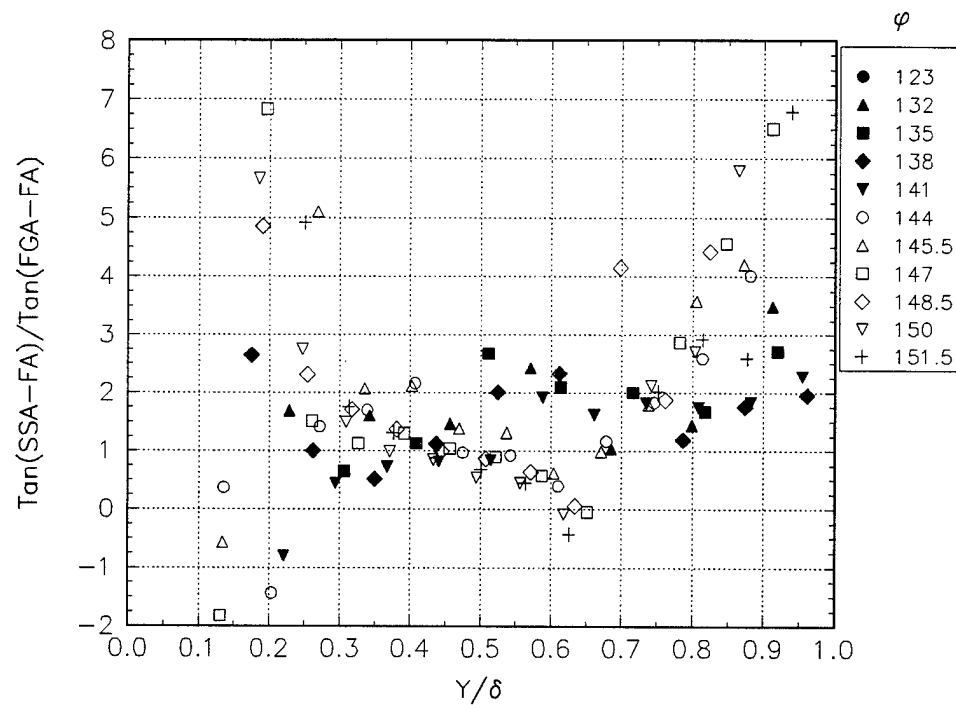


Figure H7.3 Rotta's T parameter for the backward scatter case at  $x = 1300\text{mm}$ .

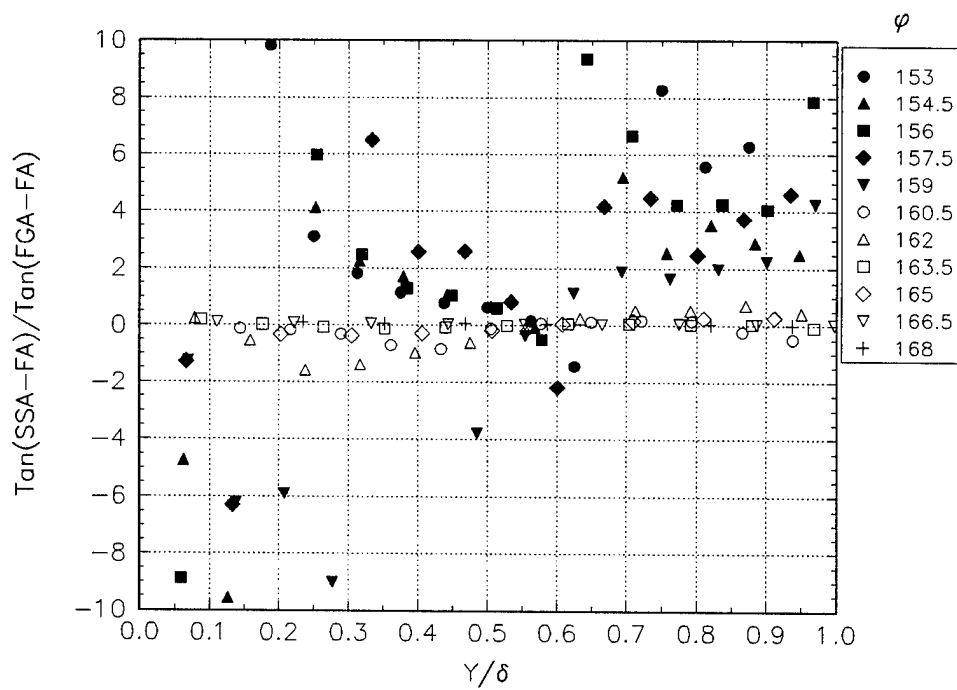


Figure H7.4 Rotta's T parameter for the backward scatter case at  $x = 1300\text{mm}$ .

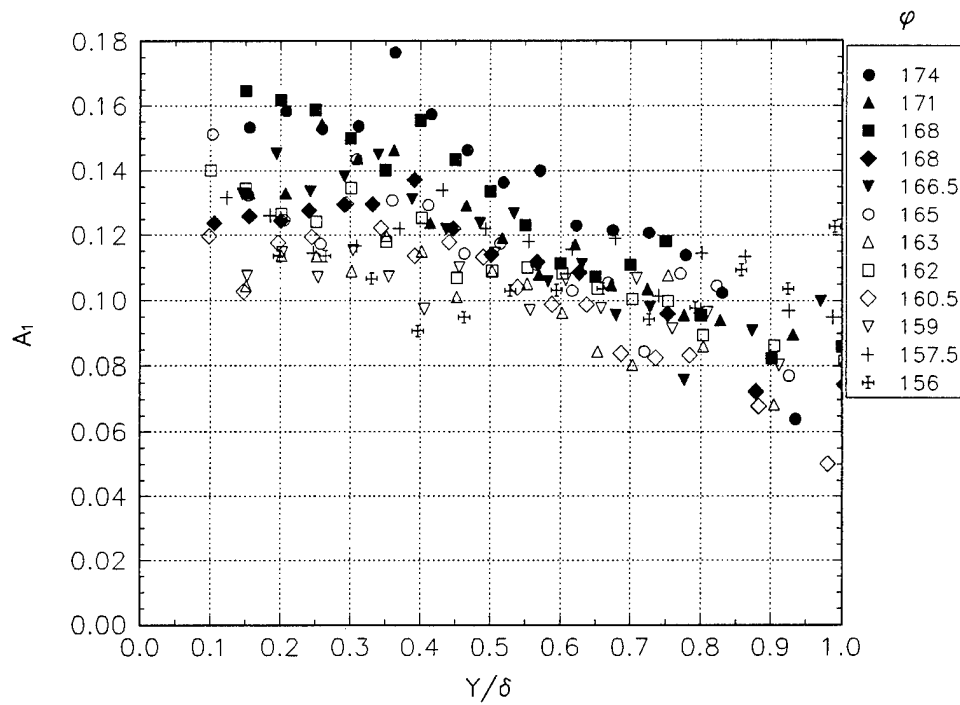


Figure H8.1 The  $a_1$  structural parameter for the backward scatter case at  $x = 900\text{mm}$ .

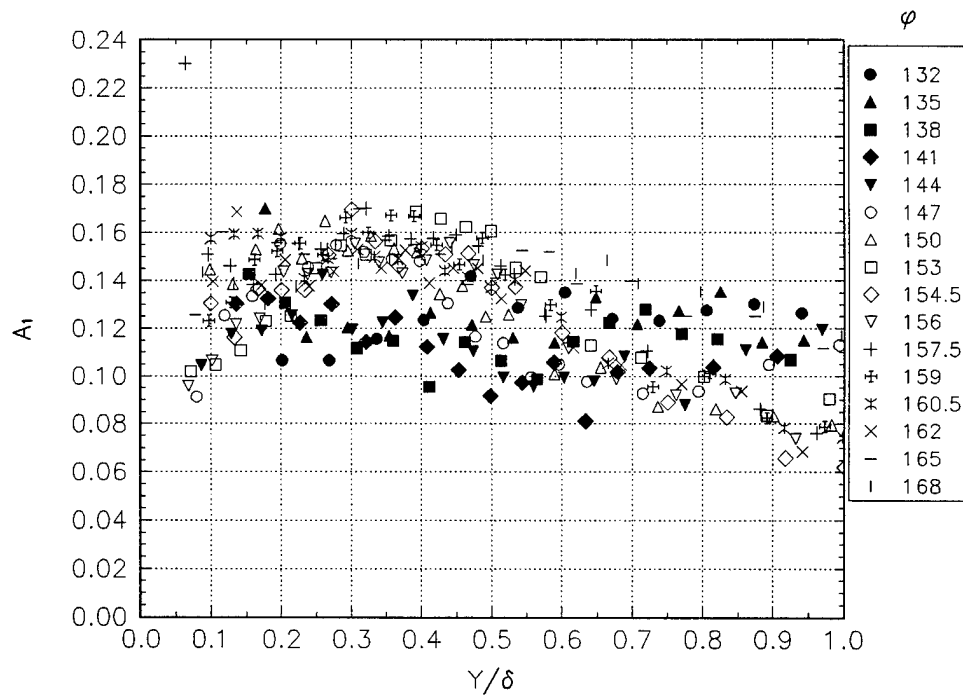


Figure H8.2 The  $a_1$  structural parameter for the backward scatter case at  $x = 1100\text{mm}$ .

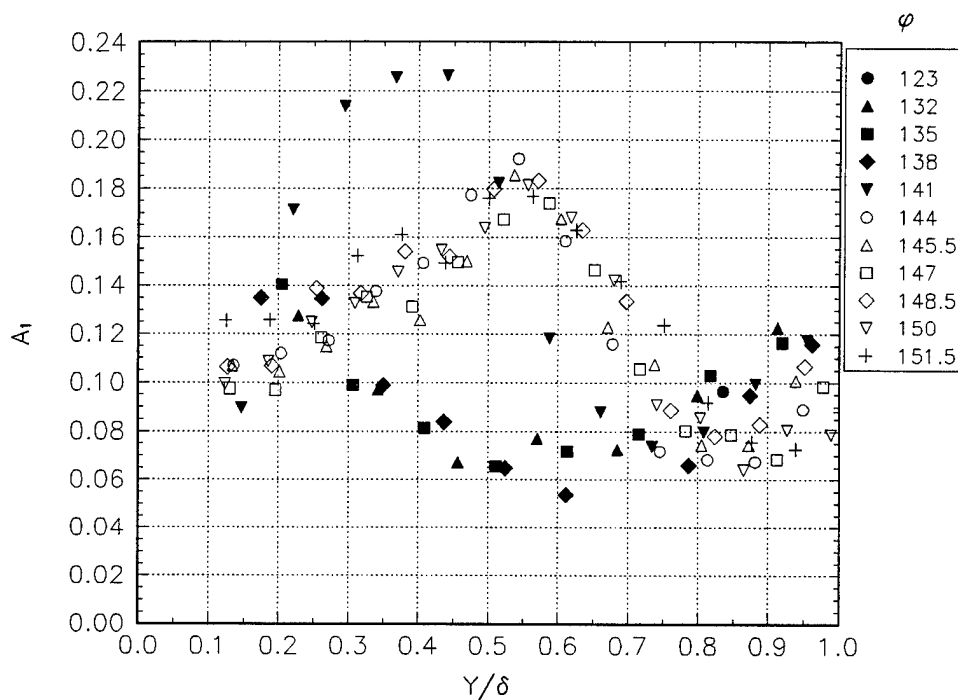


Figure H8.3 The  $a_1$  structural parameter for the backward scatter case at  $x = 1300\text{mm}$ .

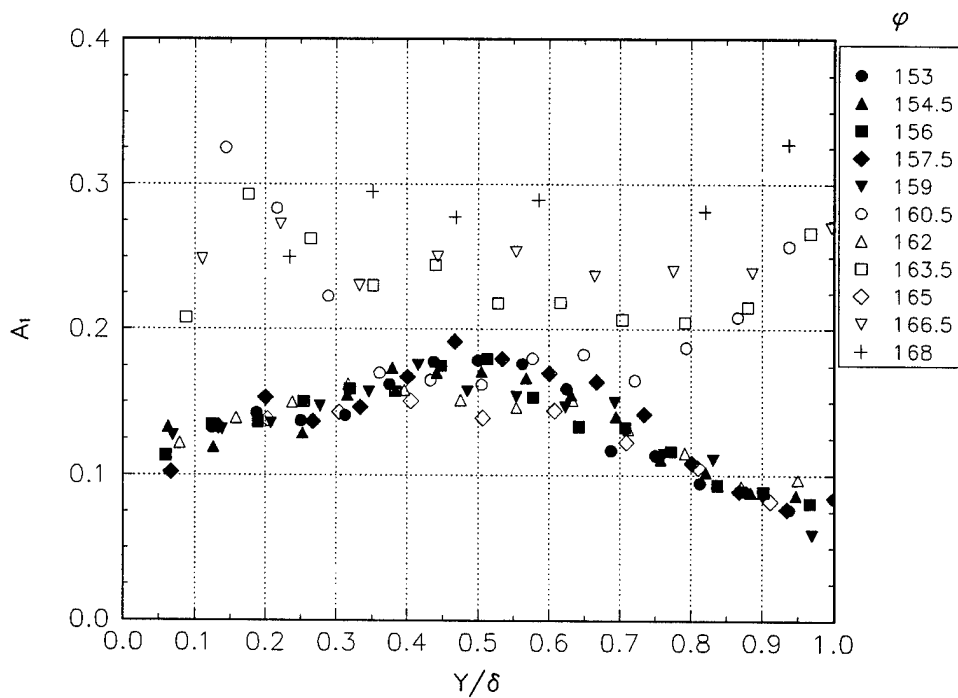


Figure H8.4 The  $a_1$  structural parameter for the backward scatter case at  $x = 1300\text{mm}$ .



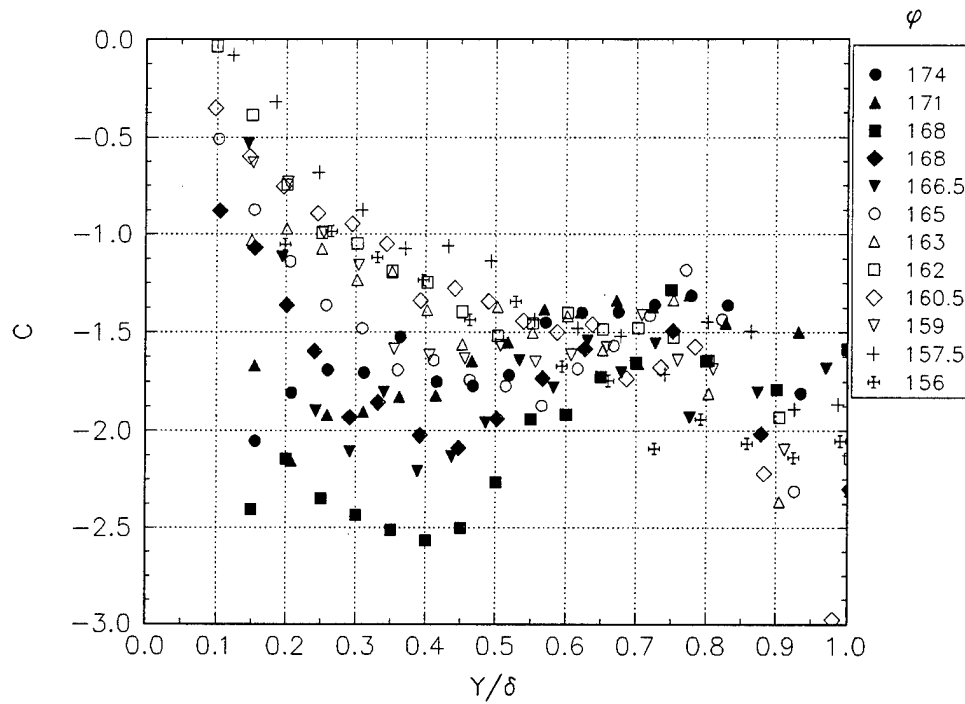


Figure H9.1 The C parameter for the backward scatter case at  $x = 900\text{mm}$ .

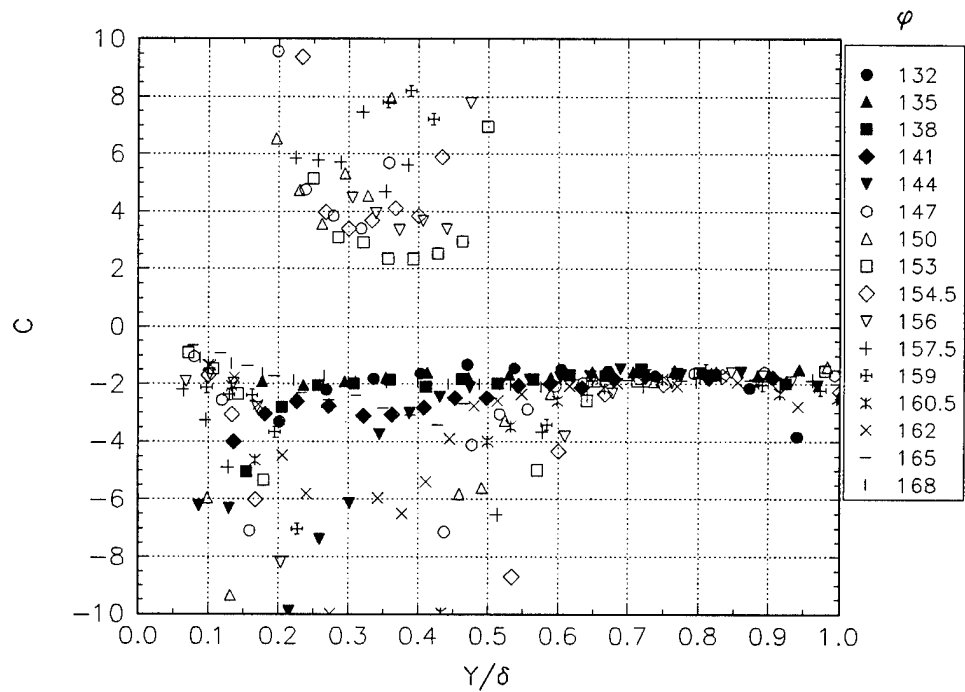


Figure H9.2 The C parameter for the backward scatter case at  $x = 1100\text{mm}$ .

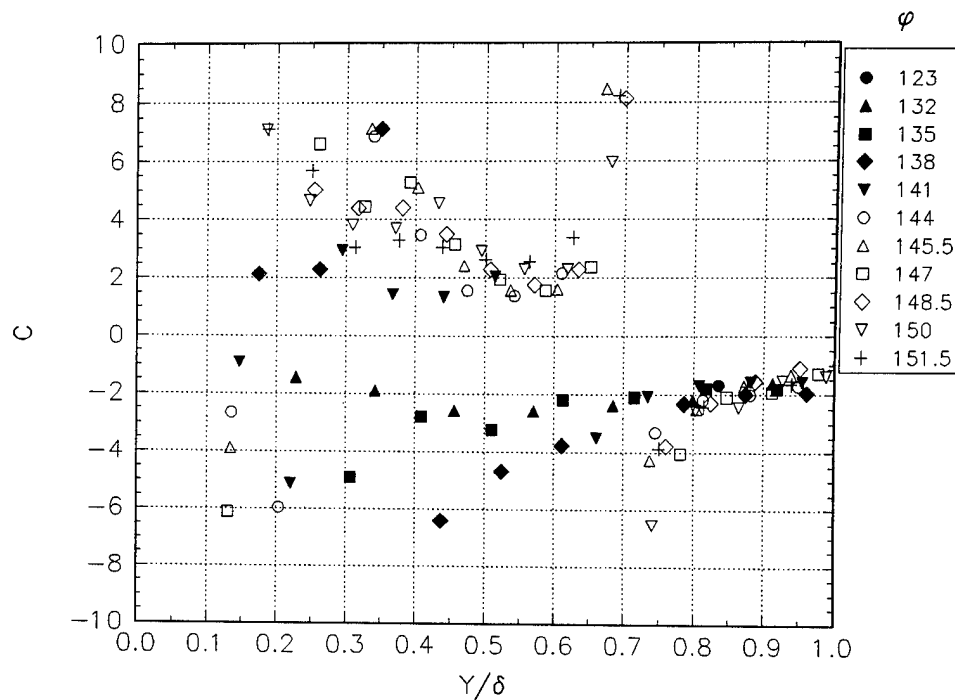


Figure H9.3 The C parameter for the backward scatter case at  $x = 1300\text{mm}$ .

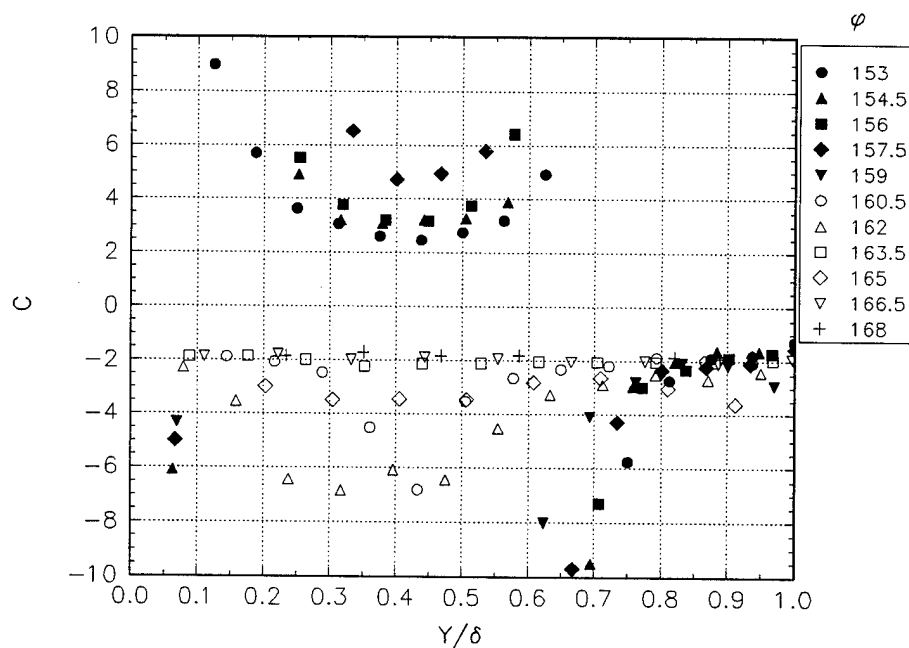


Figure H9.4 The C parameter for the backward scatter case at  $x = 1300\text{mm}$ .

## APPENDIX I Additional Figures for the Data of Devenport

This appendix presents some additional figures for the dataset of Devenport as discussed in chapter 2. There were 5 planes of data that traversed normally outward from the surface of the airfoil. All of the data was obtained in the horse-shoe vortex region of the flow. All of the data is presented in the laboratory coordinate system as shown in figure 2.3a. The maximum thickness (T) was 71.7 mm and the chord length (L) was 305 mm. S is the distance from the wing to the measurement station along the direction of the data plane (normal to the wing surface).

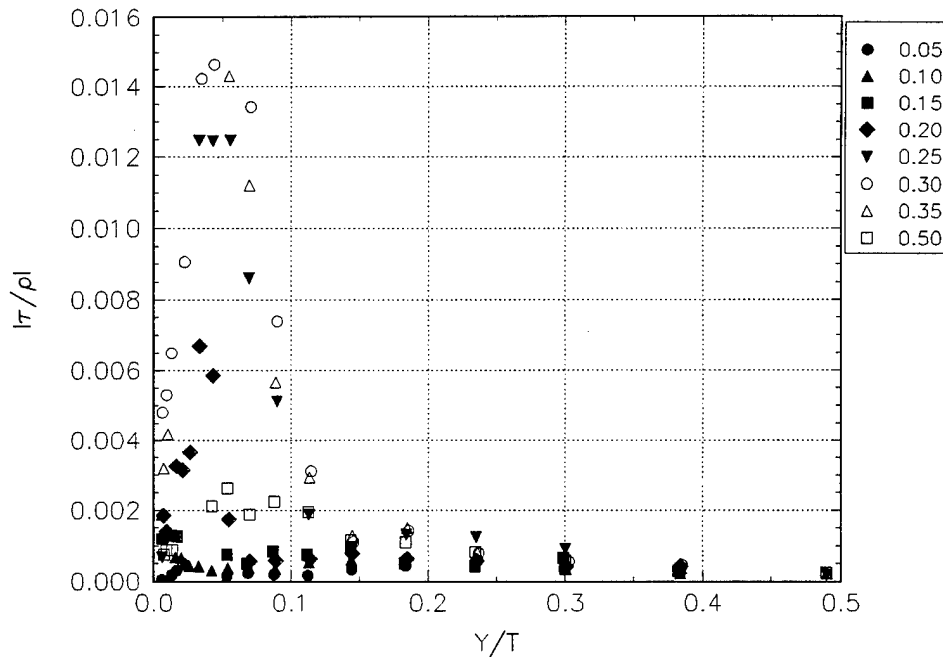


Figure I.1a The shear stress magnitude normalized by  $U_{ref}^2$ .  
Data is at plane 3, the S/T location is given in the legend.

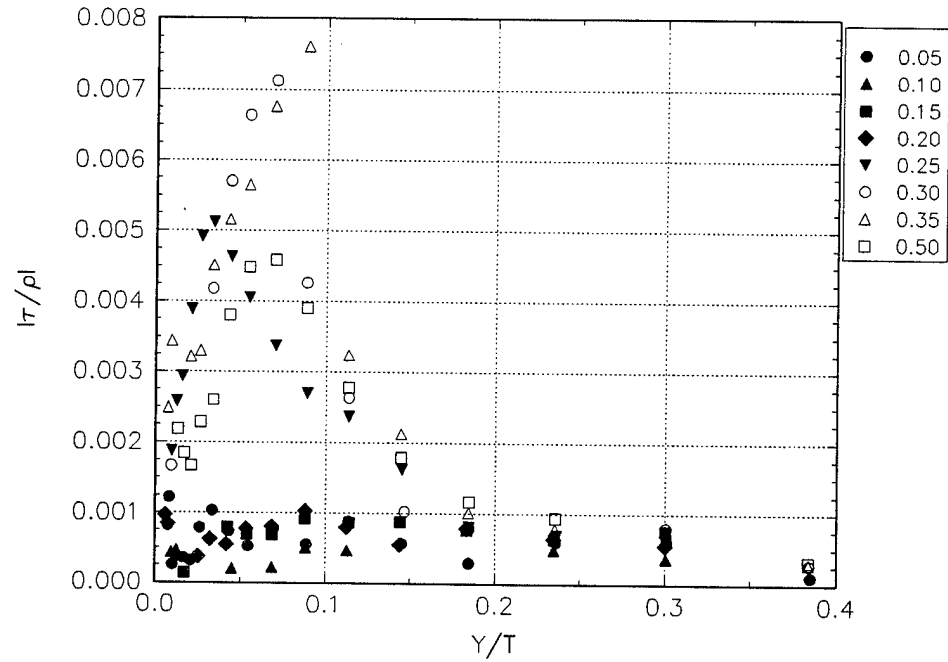


Figure I.1b The shear stress magnitude normalized by  $U_{ref}^2$ .  
Data is at plane 4, the S/T location is given in the legend.

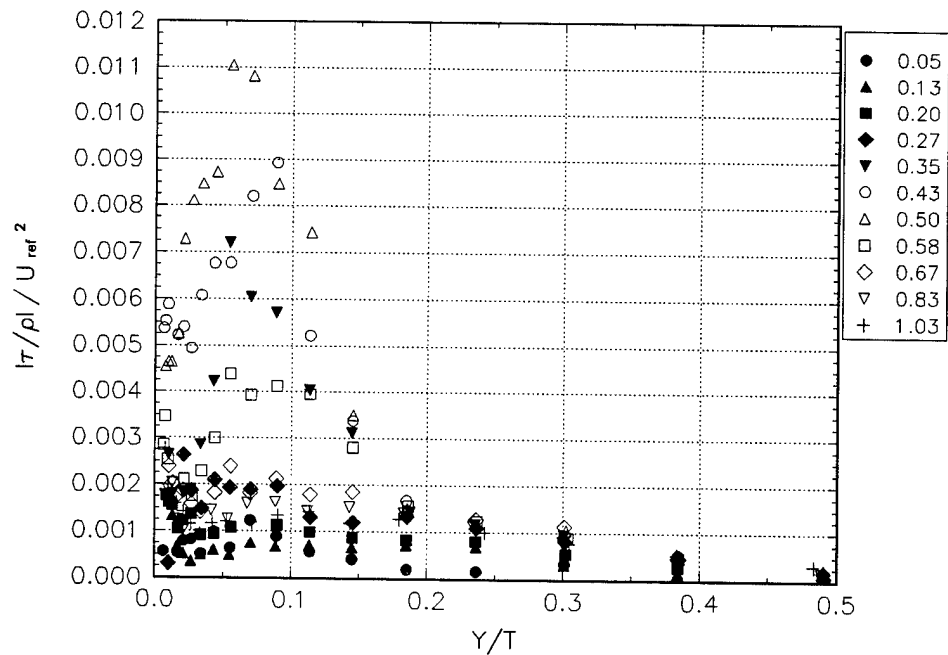


Figure I.1c The shear stress magnitude normalized by  $U_{ref}^2$ .  
Data is at plane 5, the S/T location is given in the legend.

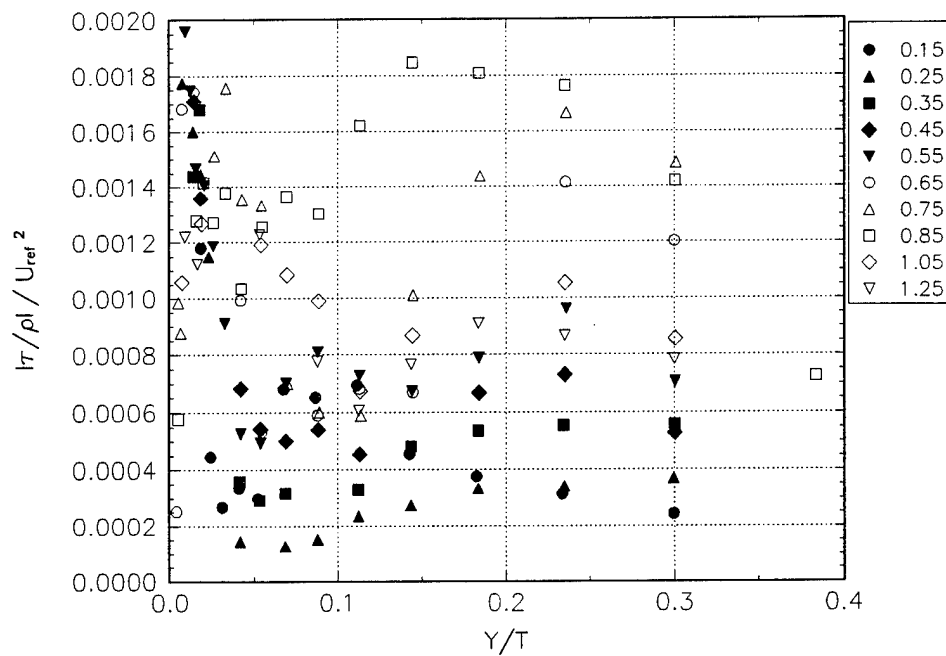


Figure I.1d The shear stress magnitude normalized by  $U_{ref}^2$ .  
Data is at plane 8, the S/T location is given in the legend.

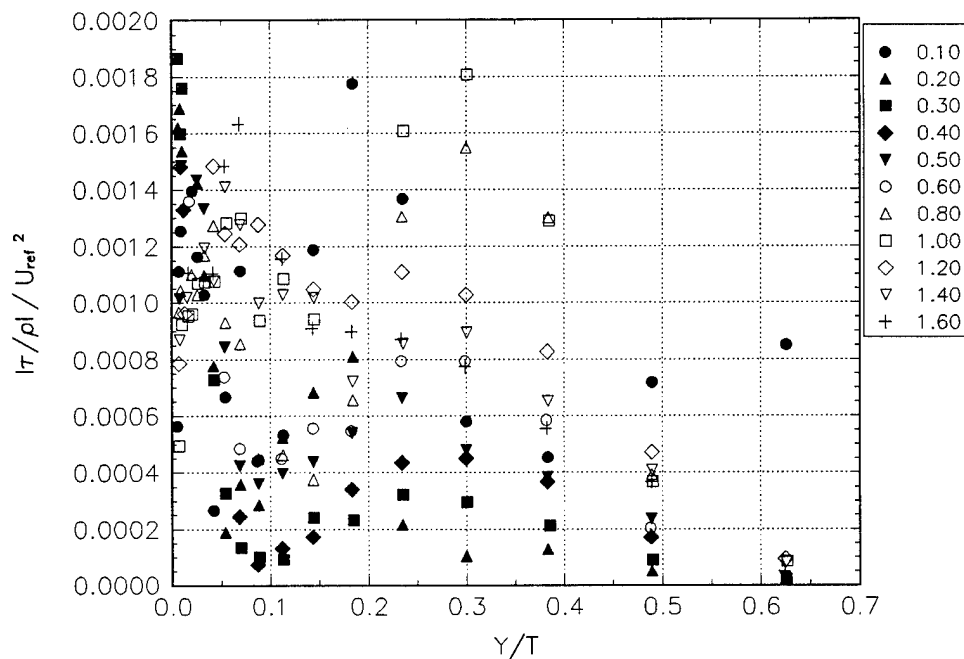


Figure I.1e The shear stress magnitude normalized by  $U_{ref}^2$ .  
Data is at plane 10, the S/T location is given in the legend.

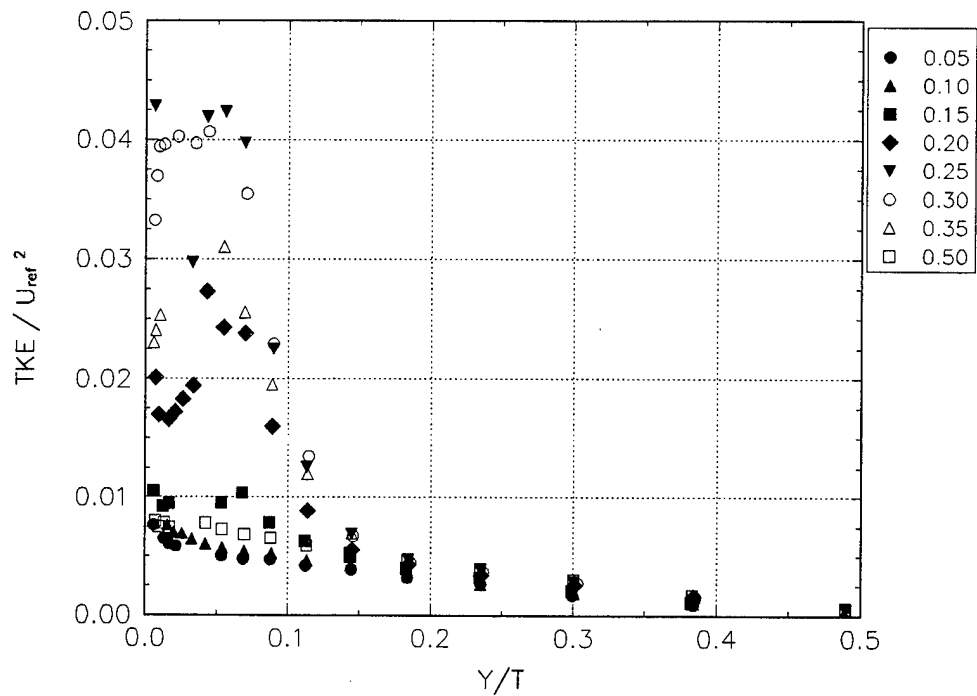


Figure I.2a The TKE normalized by  $U_{ref}^2$  for plane 3, the S/T location is given in the legend.

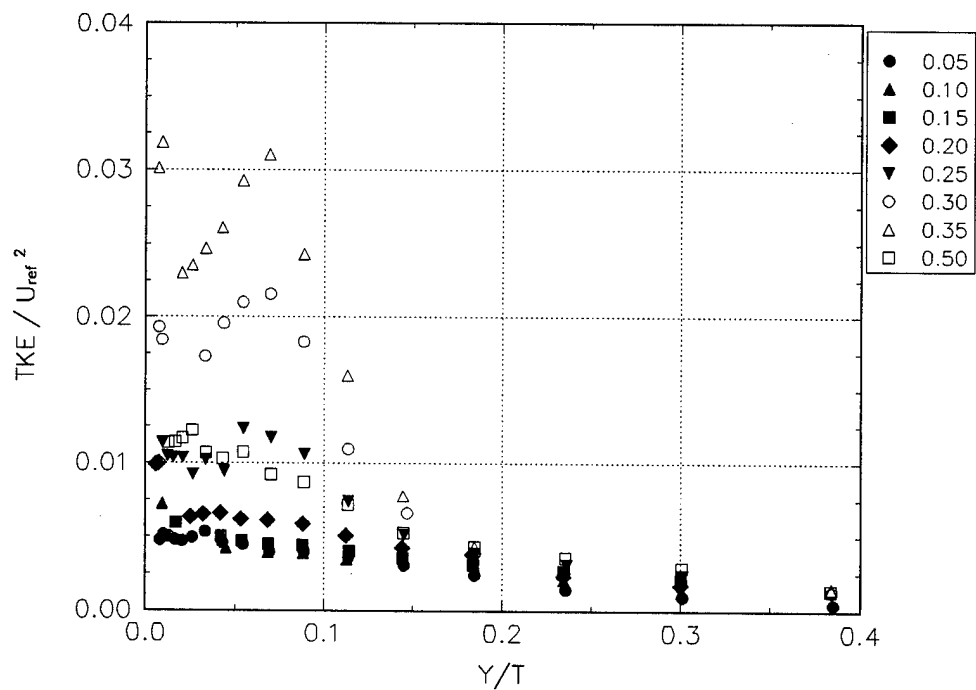


Figure I.2b The TKE normalized by  $U_{ref}^2$  for plane 4, the S/T location is given in the legend.

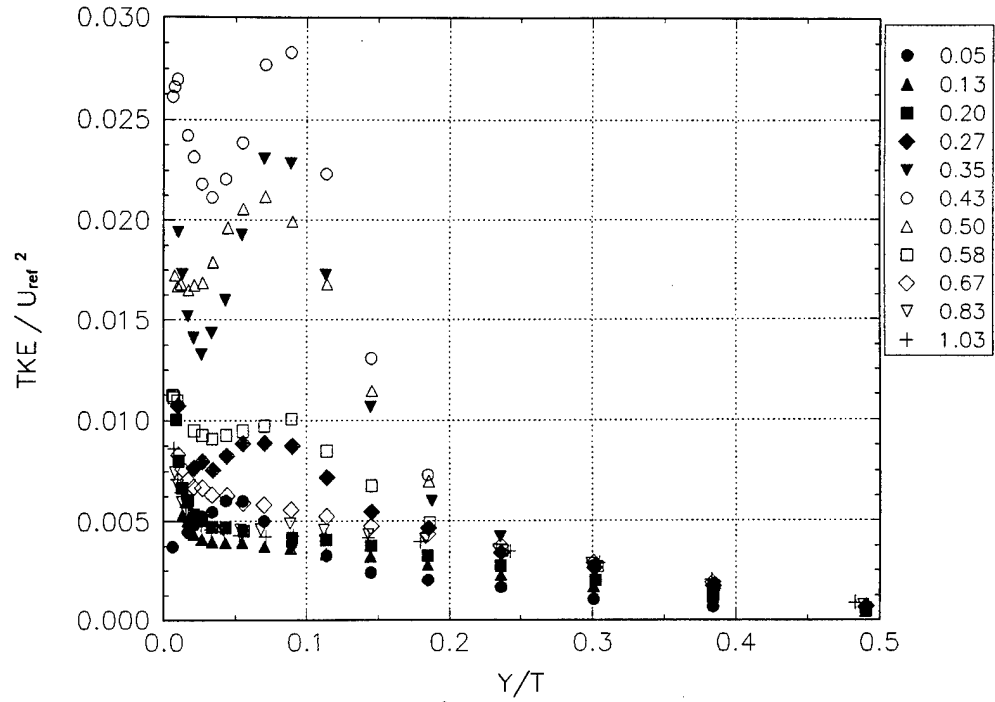


Figure I.2c The TKE normalized by  $U_{ref}^2$  for plane 5, the S/T location is given in the legend.

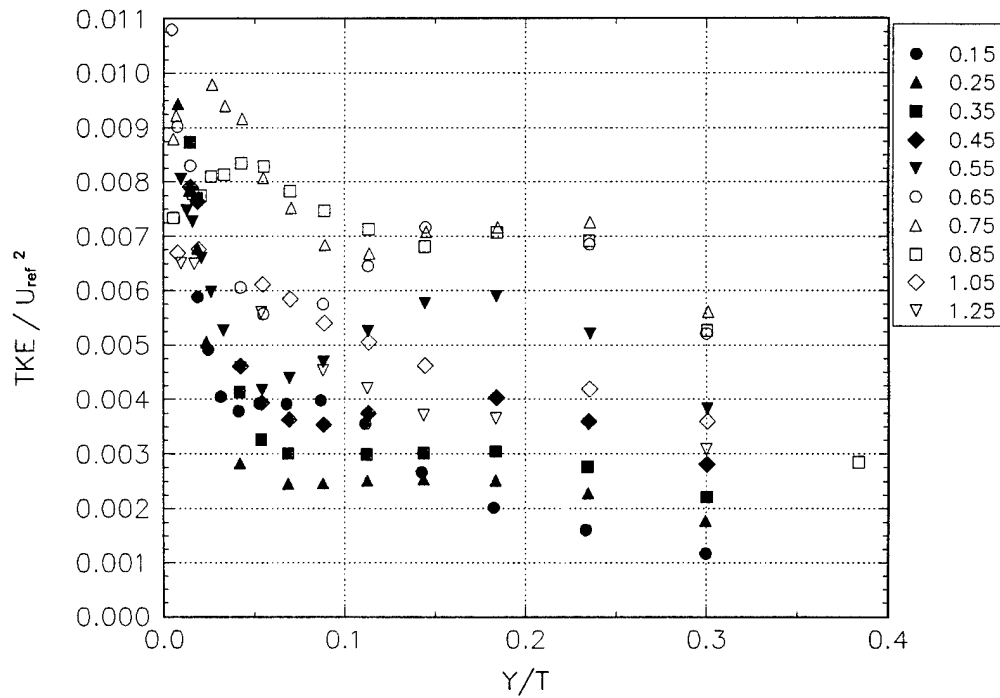


Figure I.2d The TKE normalized by  $U_{ref}^2$  for plane 8, the S/T location is given in the legend.

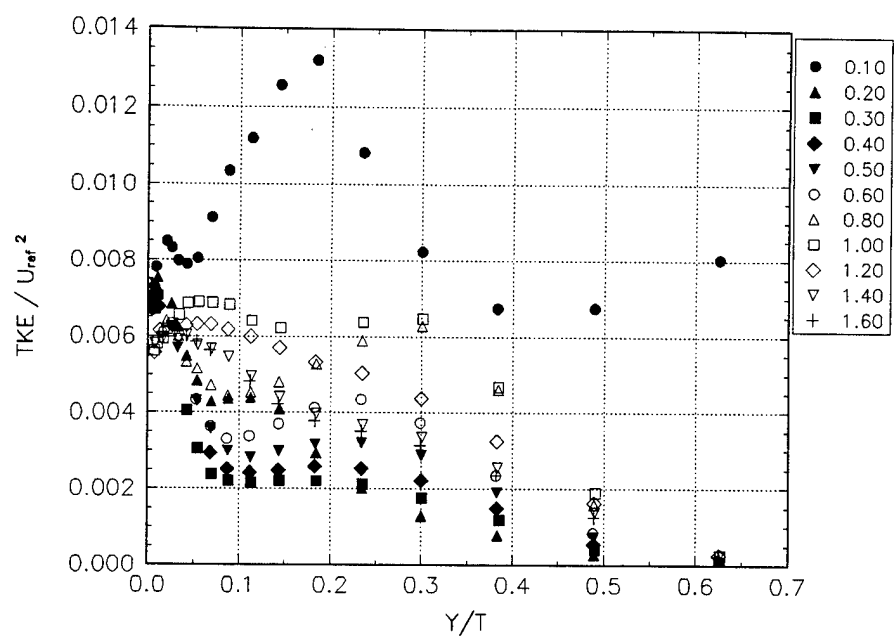


Figure I.2e The TKE normalized by  $U_{ref}^2$  for plane 10, the S/T location is given in the legend.



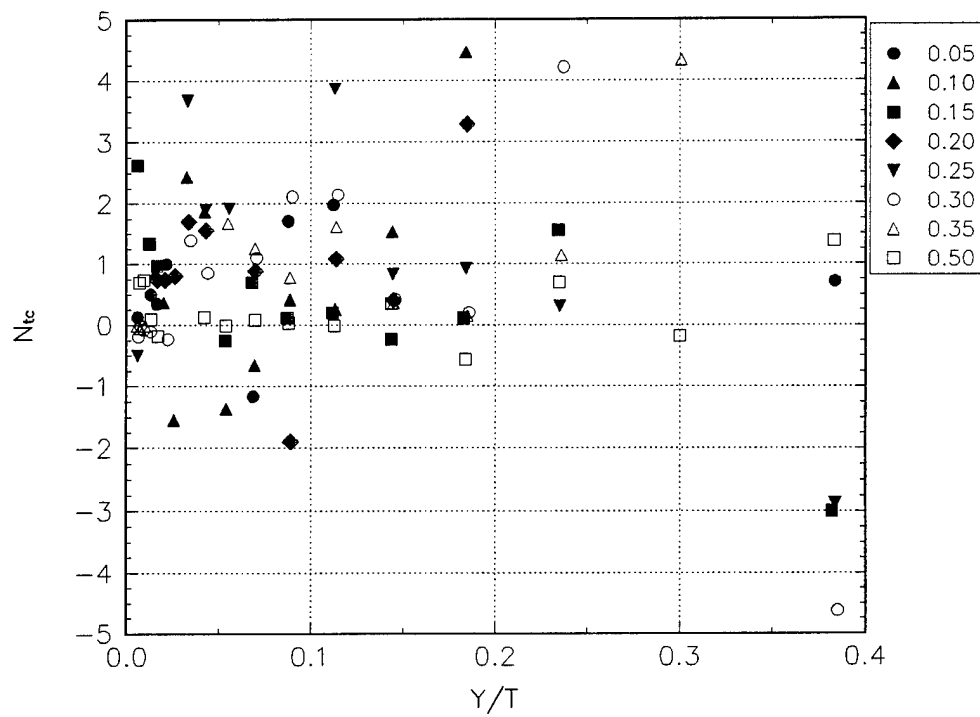


Figure I.3a The N isotropy parameter for plane 3, the S/T location is given in the legend.

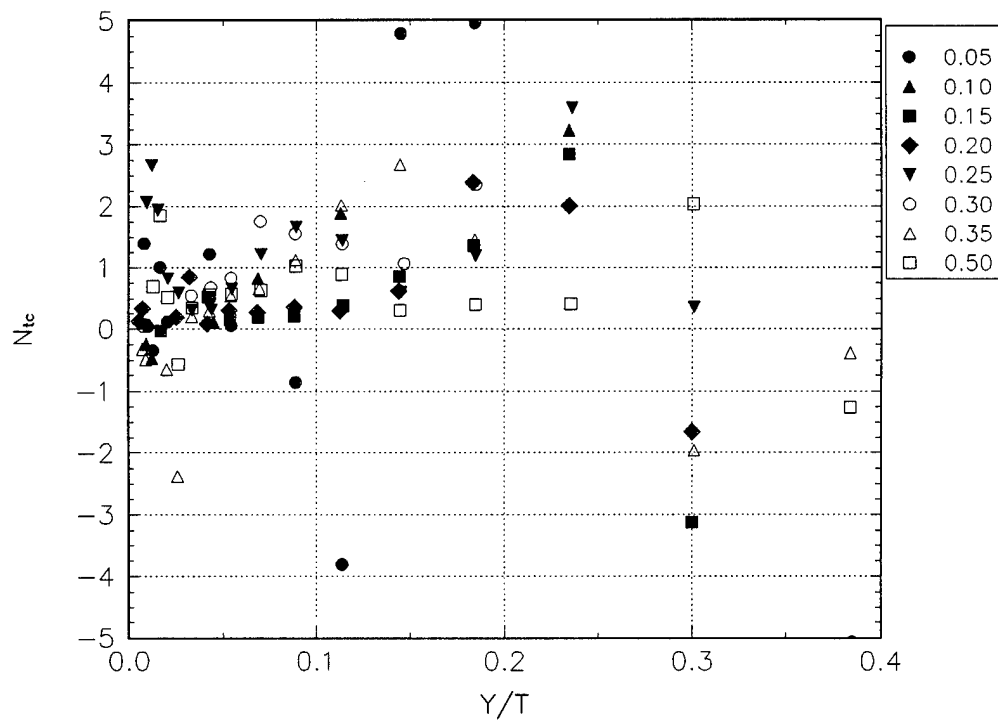


Figure I.3b The N isotropy parameter for plane 4, the S/T location is given in the legend.

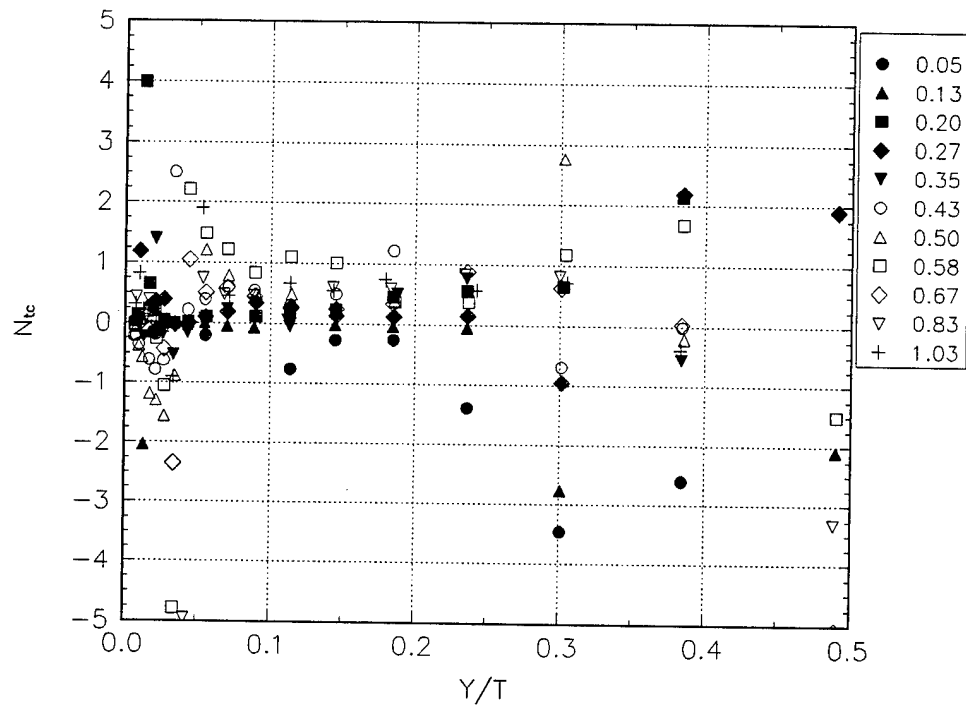


Figure I.3c The N isotropy parameter for plane 5, the S/T location is given in the legend.

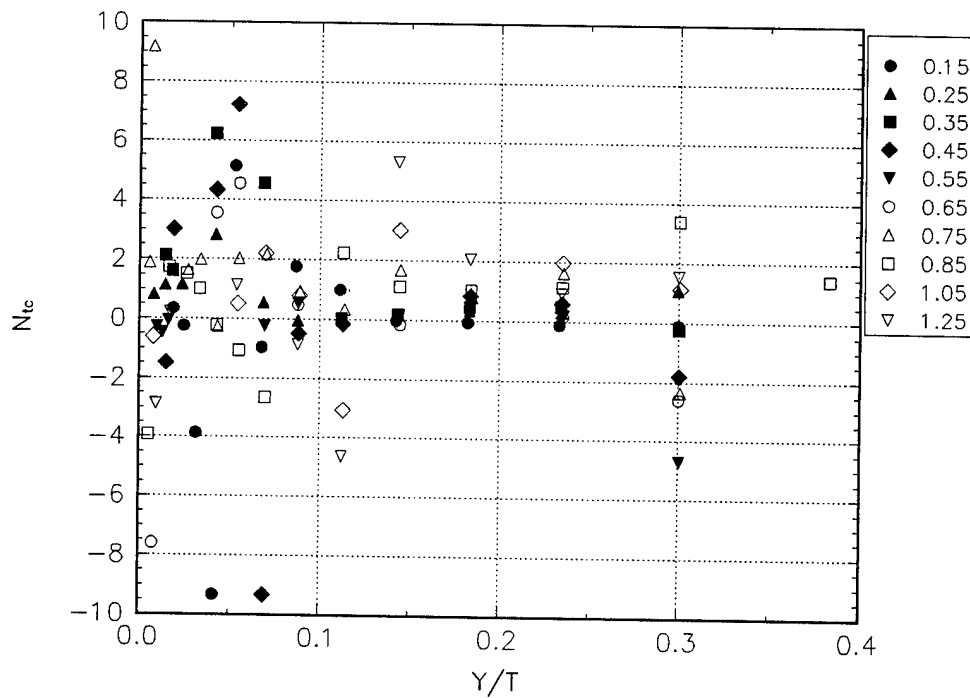


Figure I.3d The N isotropy parameter for plane 8, the S/T location is given in the legend.

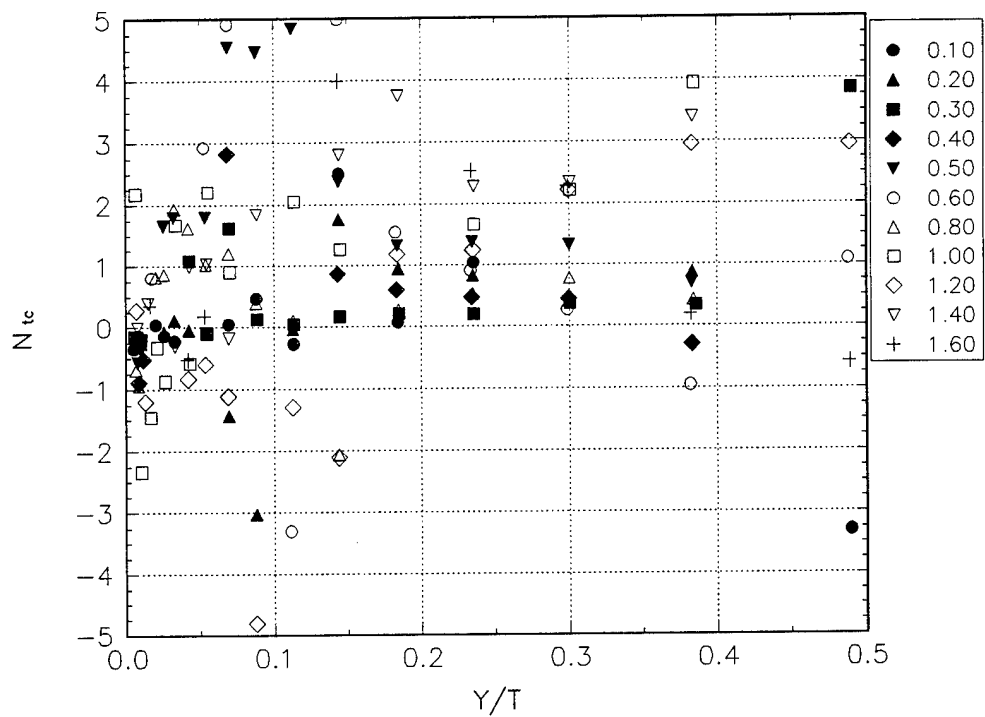


Figure I.3e The N isotropy parameter for plane 10, the S/T location is given in the legend.

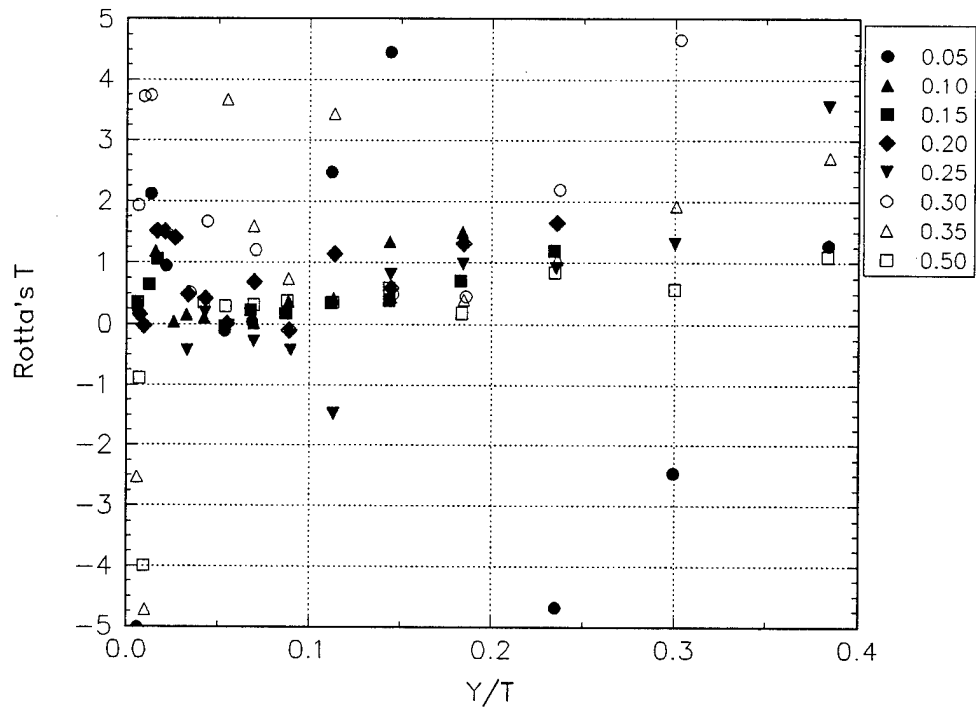


Figure I.4a Rotta's T parameter for plane 3, the S/T location is given in the legend.

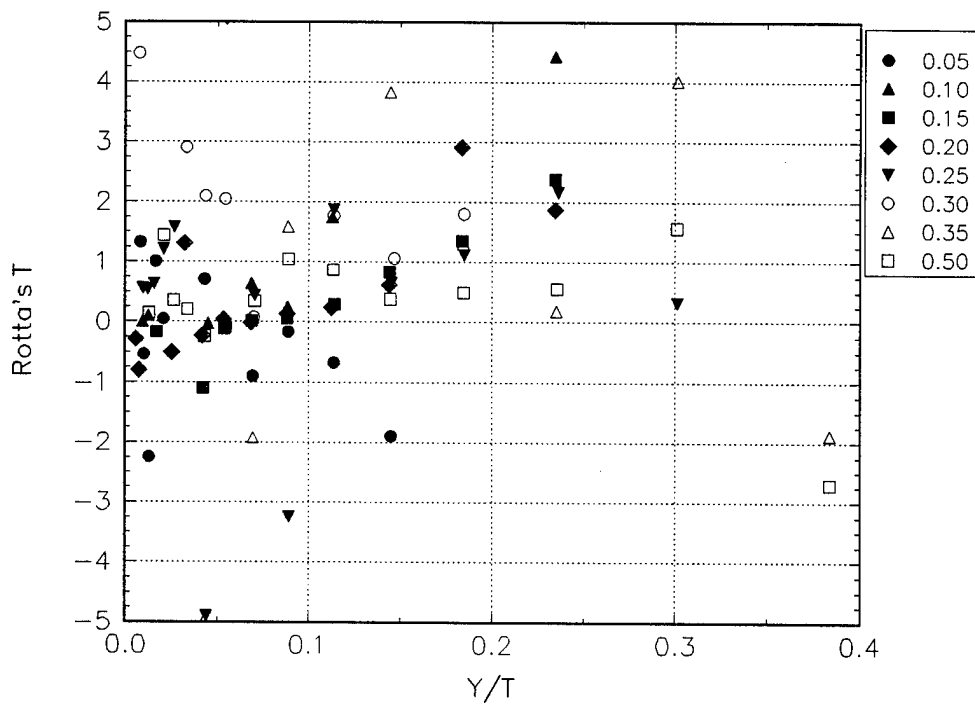


Figure I.4b Rotta's T parameter for plane 4, the S/T location is given in the legend.

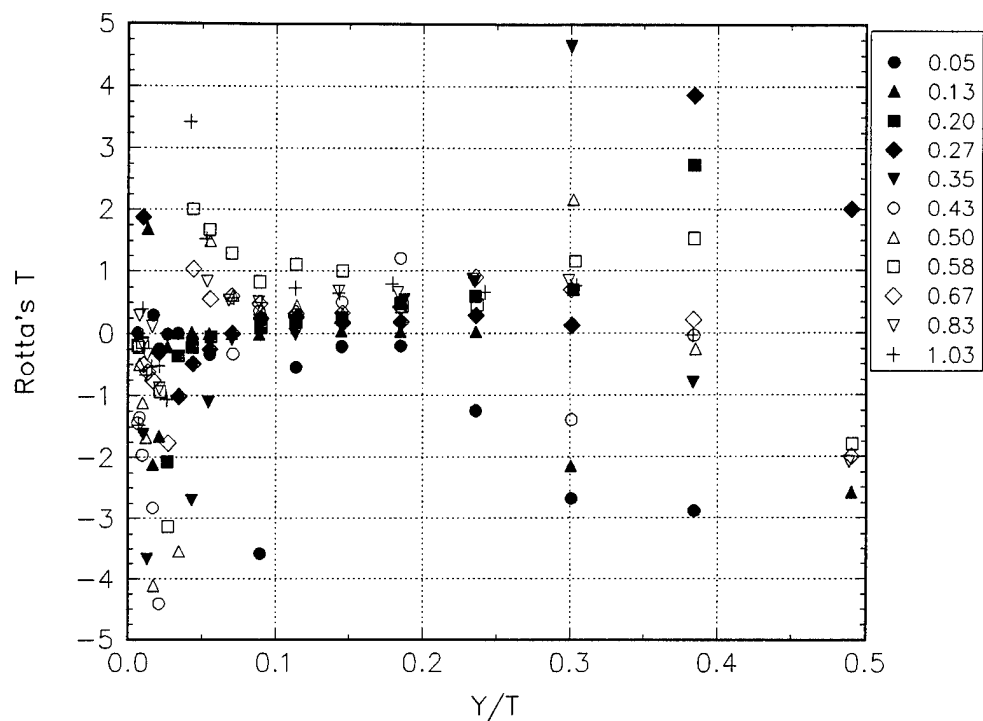


Figure I.4c Rotta's T parameter for plane 5, the S/T location is given in the legend.

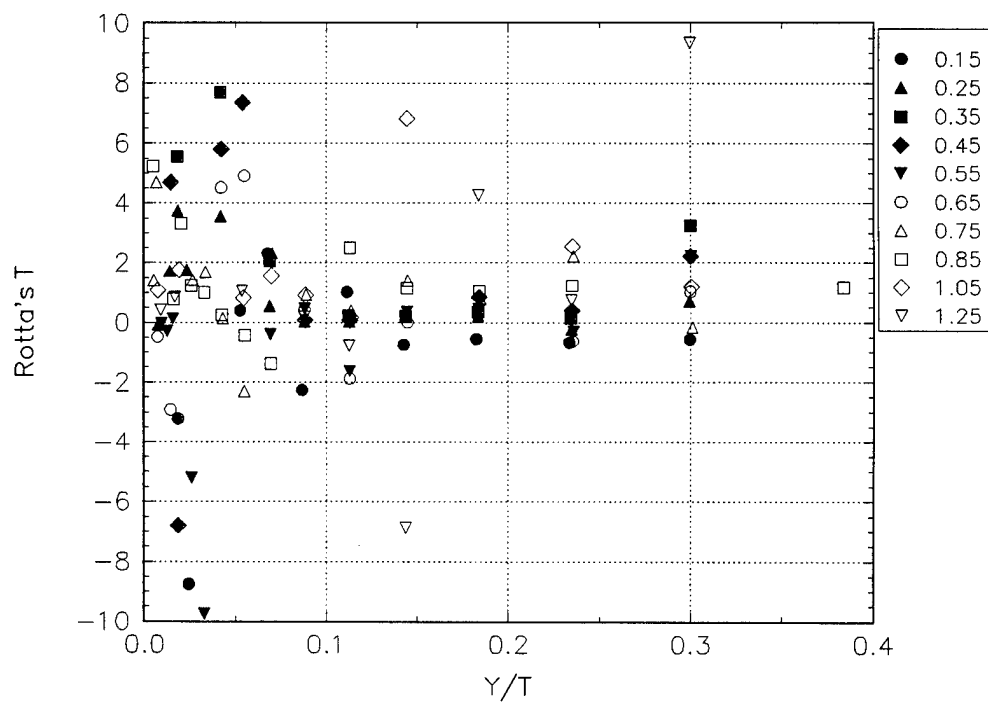


Figure I.4d Rotta's T parameter for plane 8, the S/T location is given in the legend.

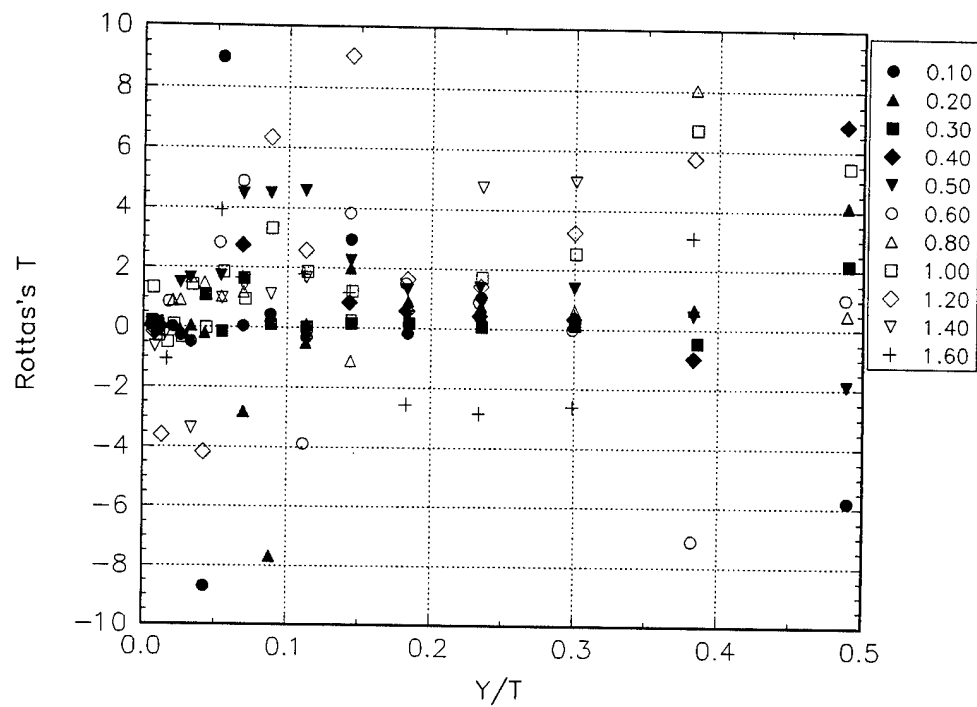


Figure I.4e Rotta's T parameter for plane 10, the S/T location is given in the legend.

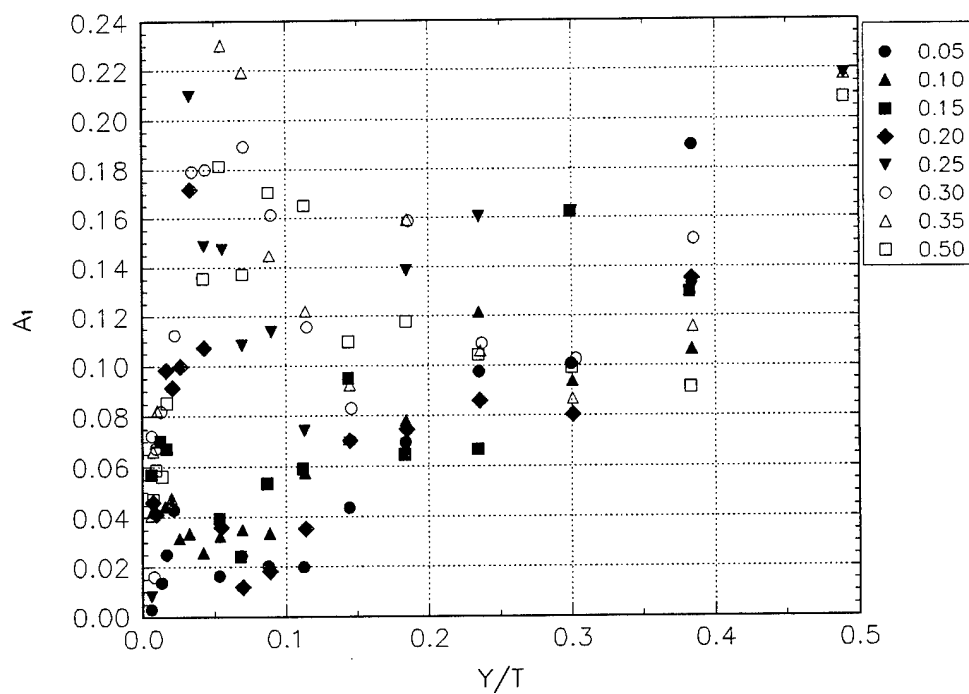


Figure I.5a The  $a_1$  parameter for plane 3, the  $S/T$  location is given in the legend.

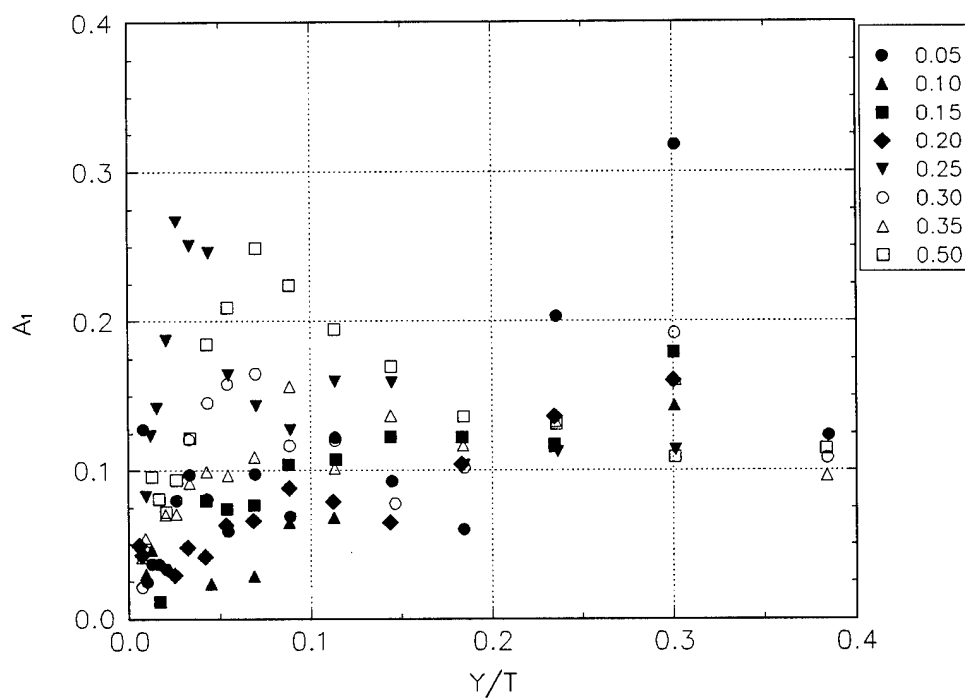


Figure I.5b The  $a_1$  parameter for plane 4, the  $S/T$  location is given in the legend.

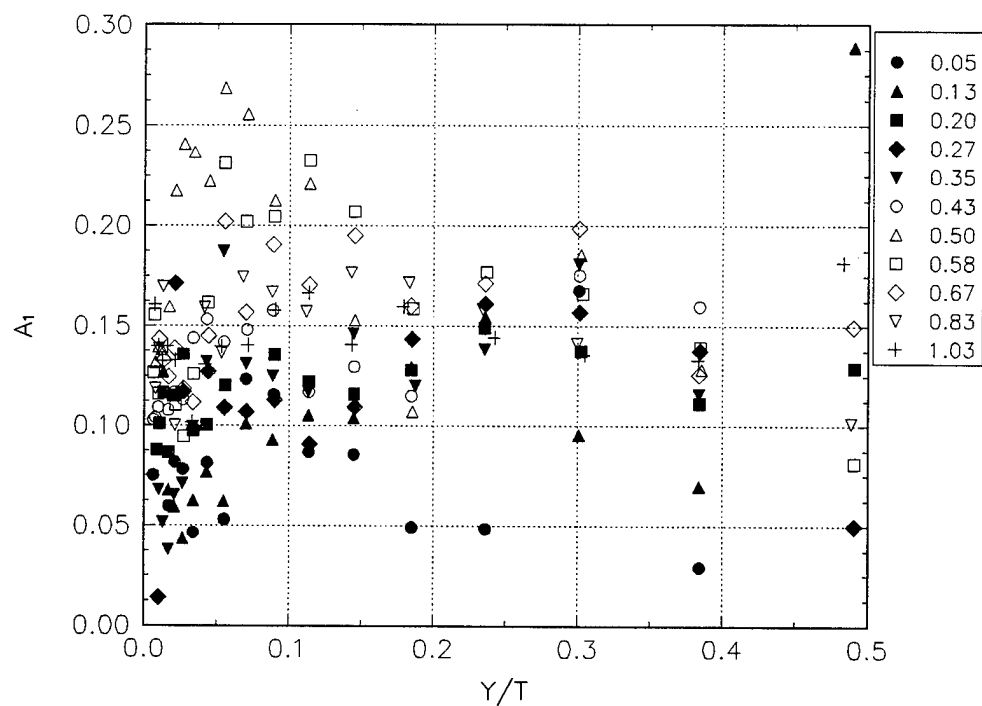


Figure I.5c The  $a_1$  parameter for plane 5, the  $S/T$  location is given in the legend.

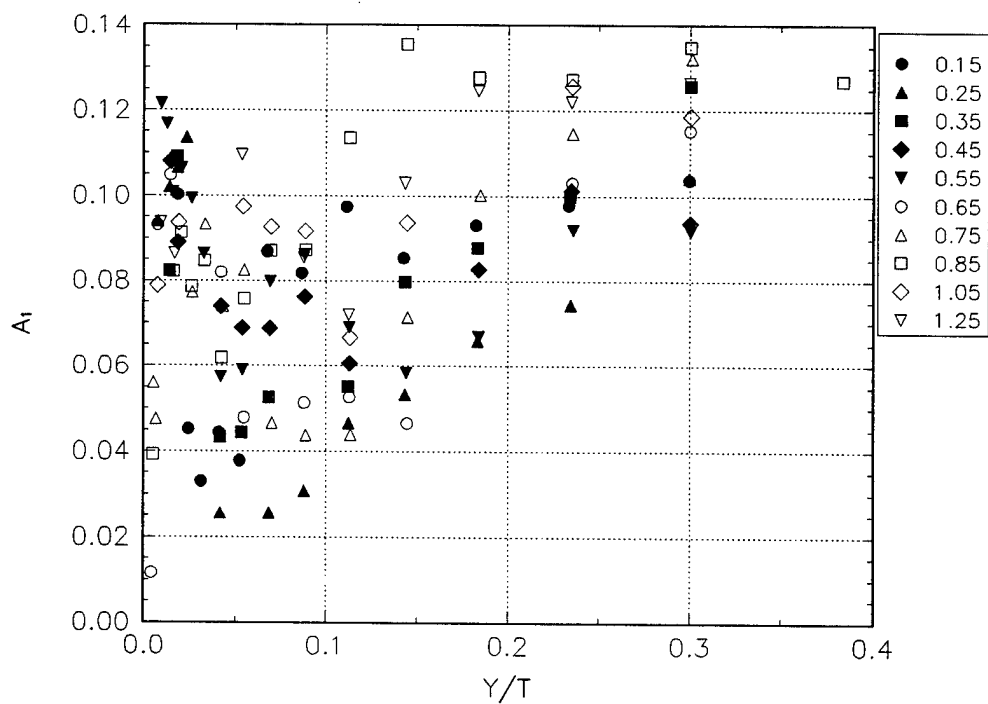


Figure I.5d The  $a_1$  parameter for plane 8, the  $S/T$  location is given in the legend.



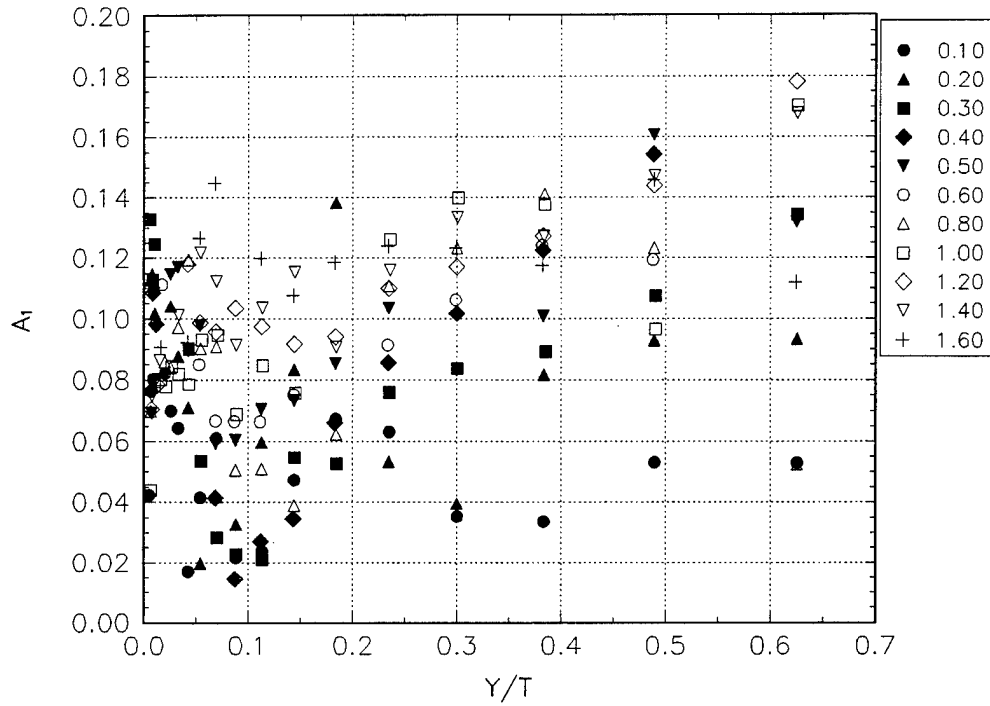


Figure I.5e The  $a_1$  parameter for plane 10, the S/T location is given in the legend.

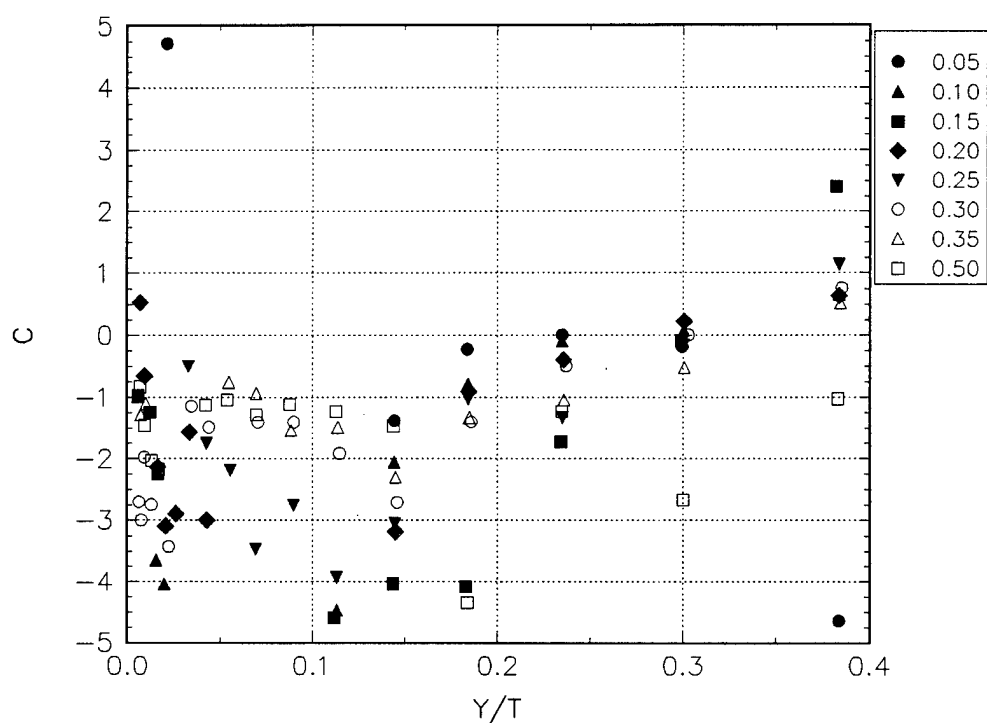


Figure I.6a The C parameter for plane 3, the S/T location is given in the legend.

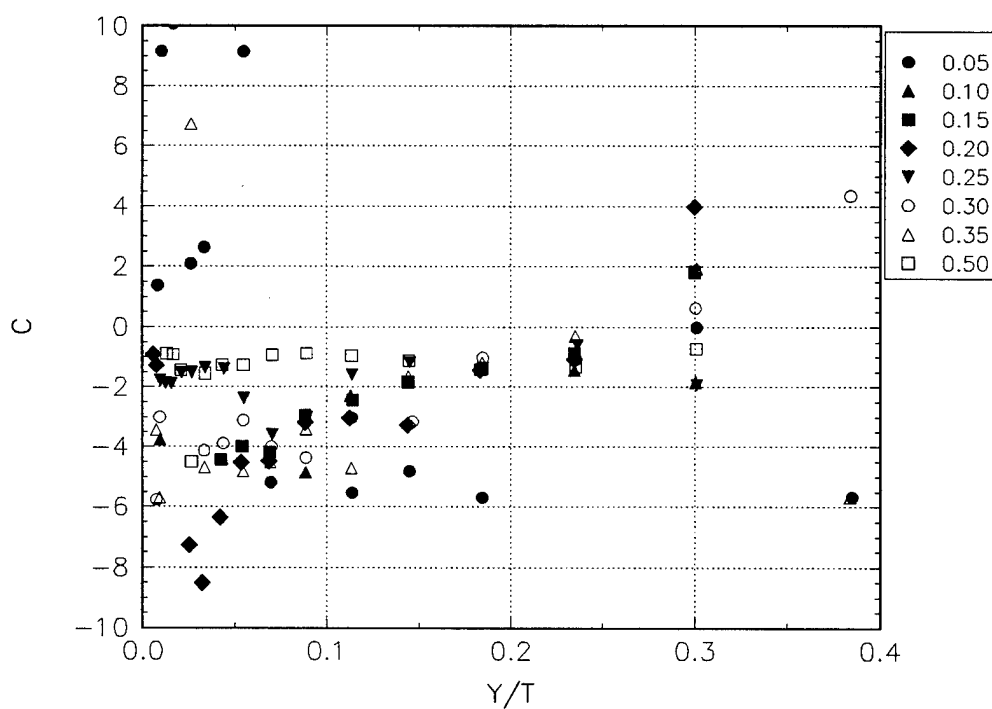


Figure I.6b The C parameter for plane 4, the S/T location is given in the legend.

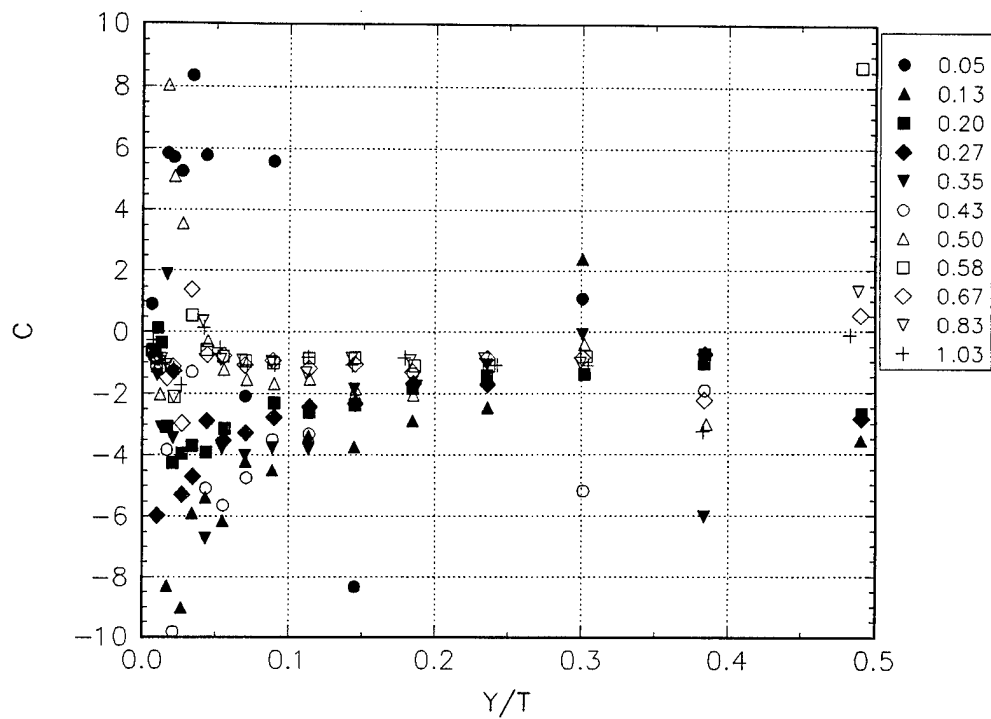


Figure I.6c The C parameter for plane 5, the S/T location is given in the legend.

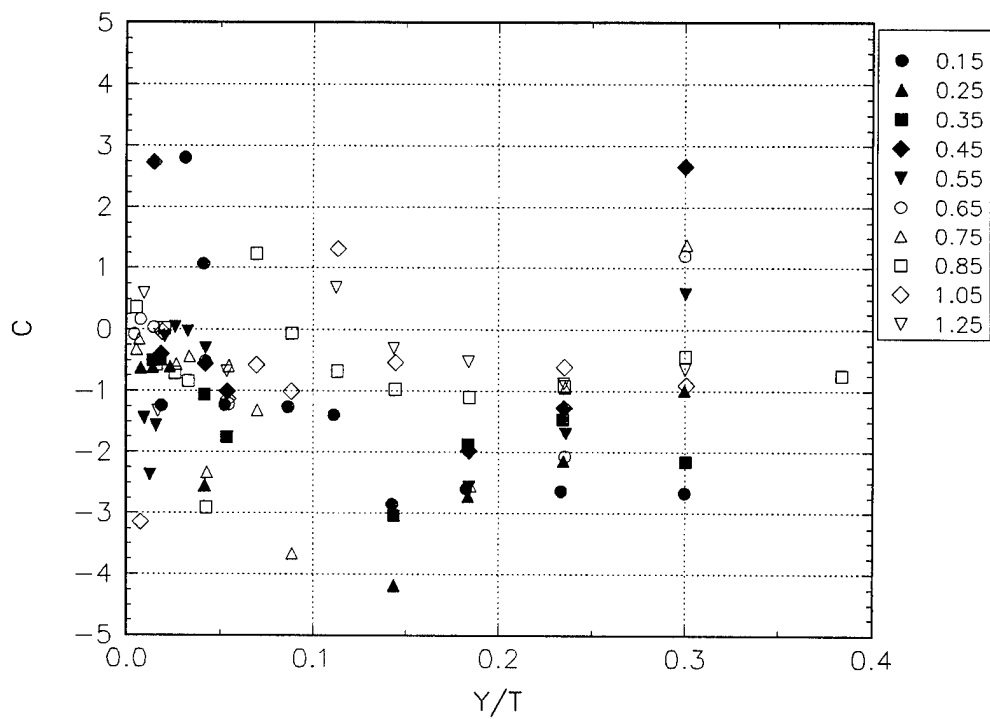


Figure I.6d The C parameter for plane 8, the S/T location is given in the legend.

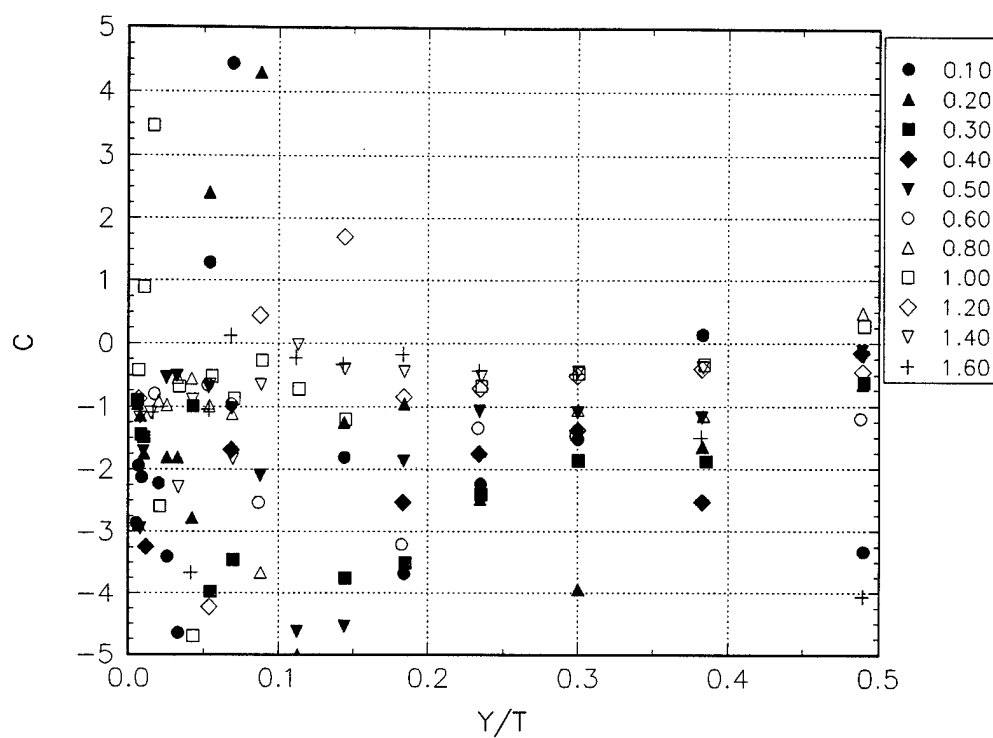


Figure I.6e The C parameter for plane 10, the S/T location is given in the legend.

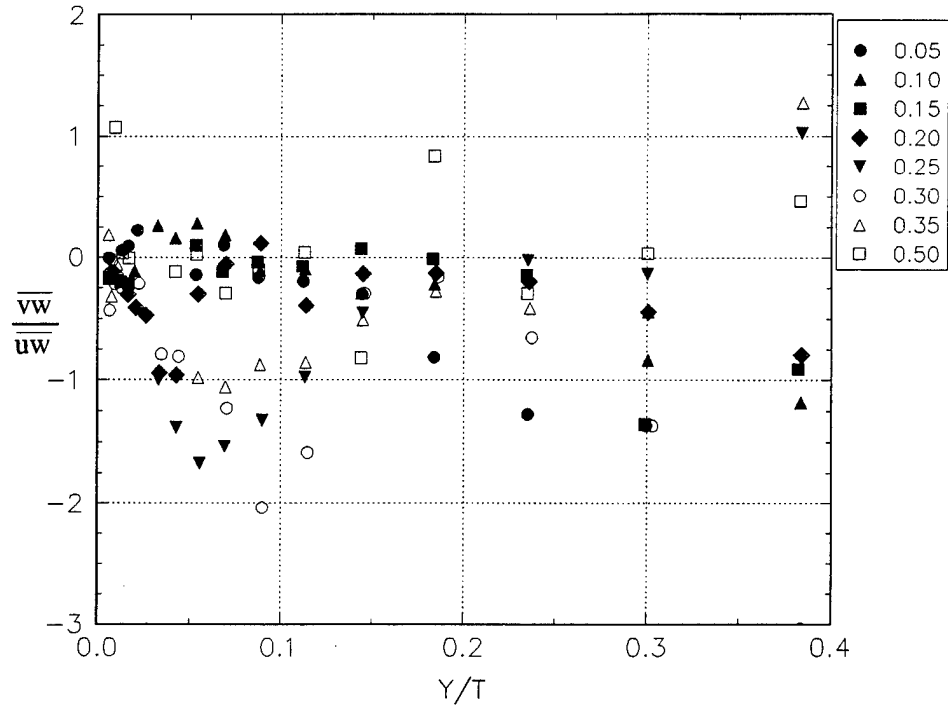


Figure I.7a The shear stress ratio for plane 3, the S/T location is given in the legend.

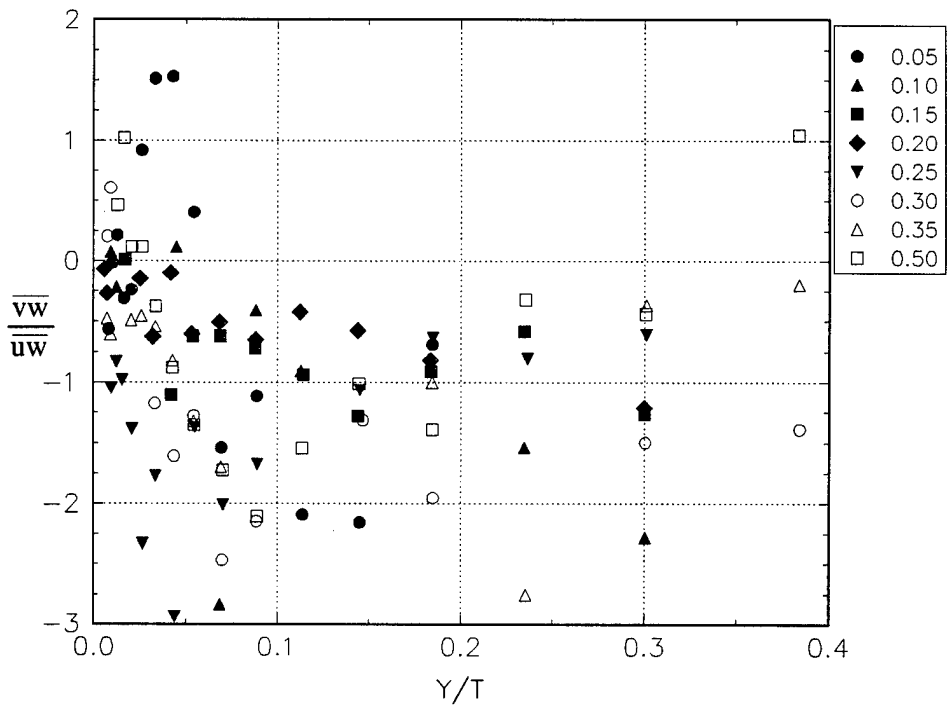


Figure I.7b The shear stress ratio for plane 4, the S/T location is given in the legend.

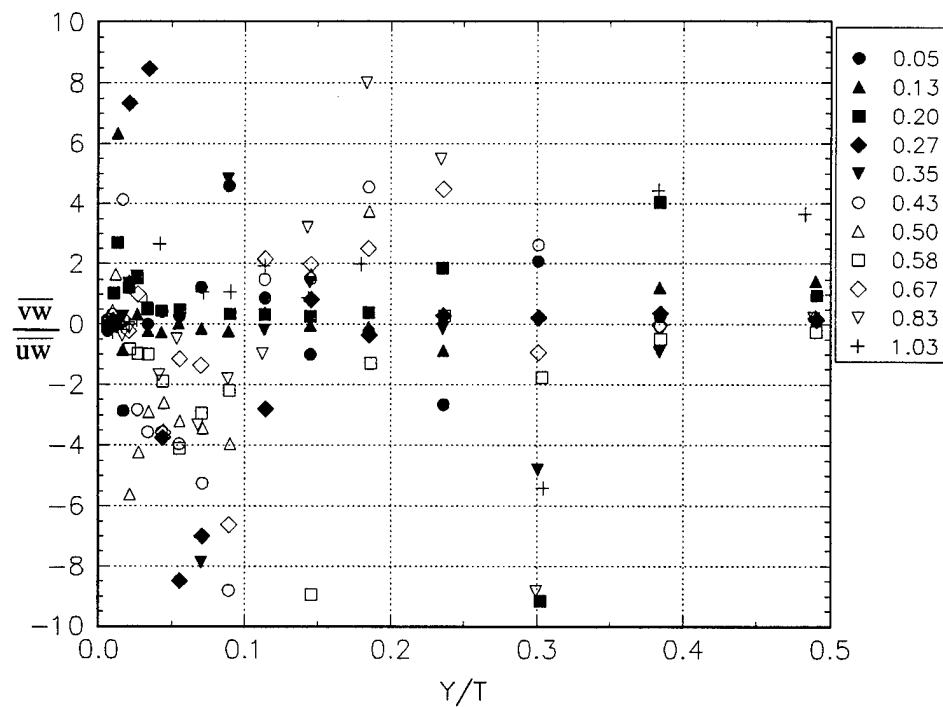


Figure I.7c The shear stress ratio for plane 5, the S/T location is given in the legend.

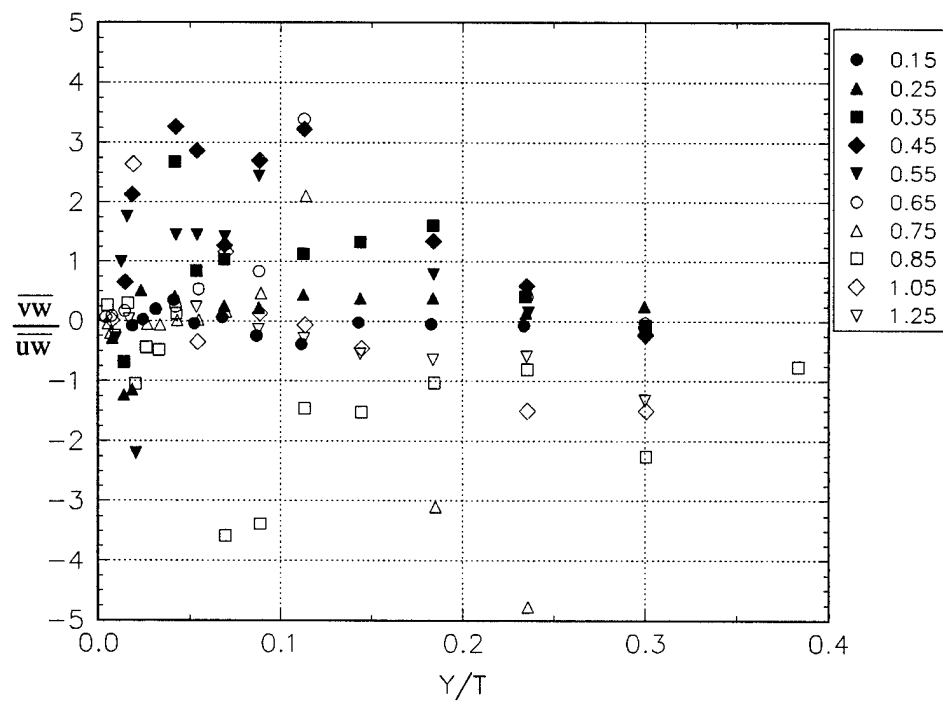


Figure I.7d The shear stress ratio for plane 8, the S/T location is given in the legend.

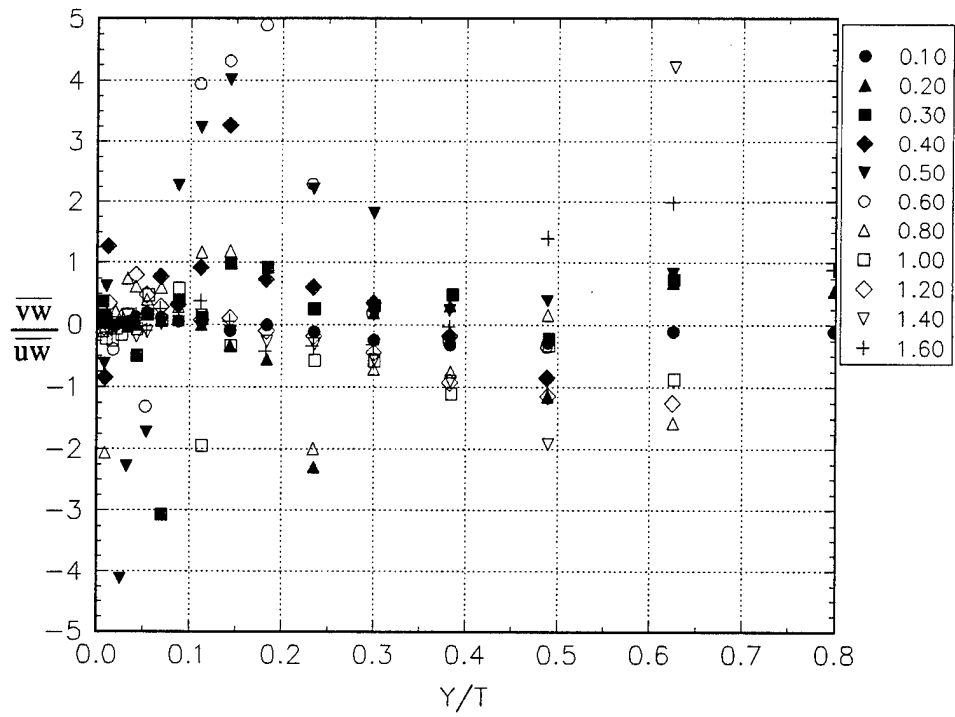


Figure I.7e The shear stress ratio for plane 10, the  $S/T$  location is given in the legend.

## APPENDIX J Additional Figures for the Data of McMahon

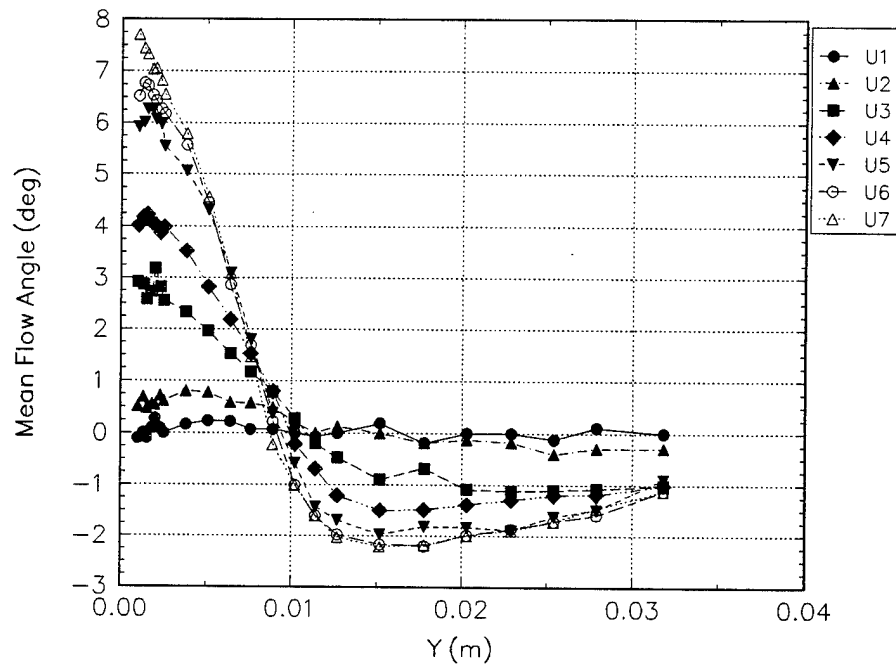


Figure J.1.a Flow angles, stations are given in the legend.

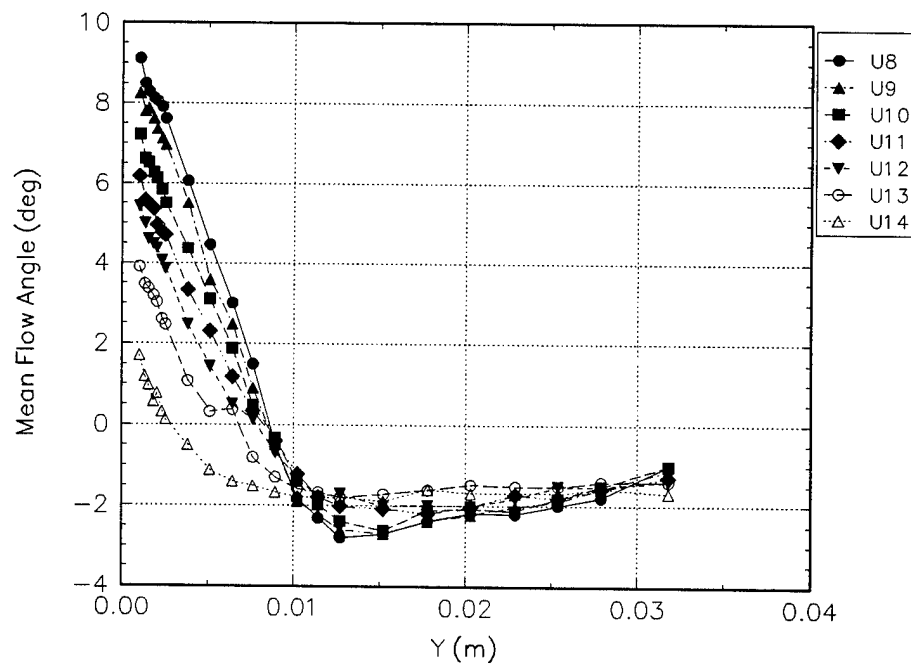


Figure J.1.b Flow angles, stations are given in the legend.



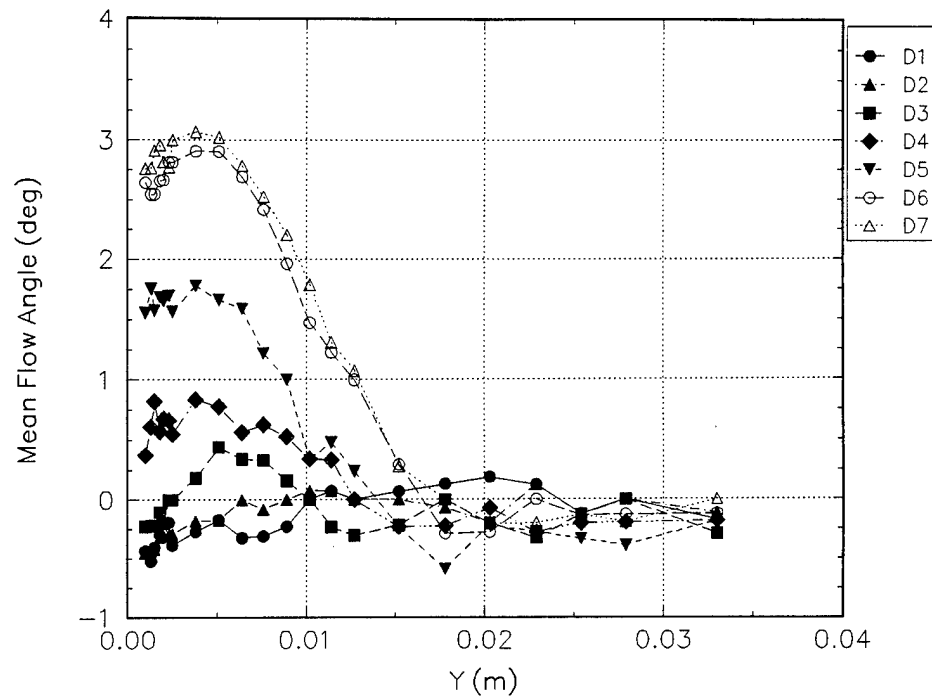


Figure J.1.c Flow angles, stations are given in the legend.

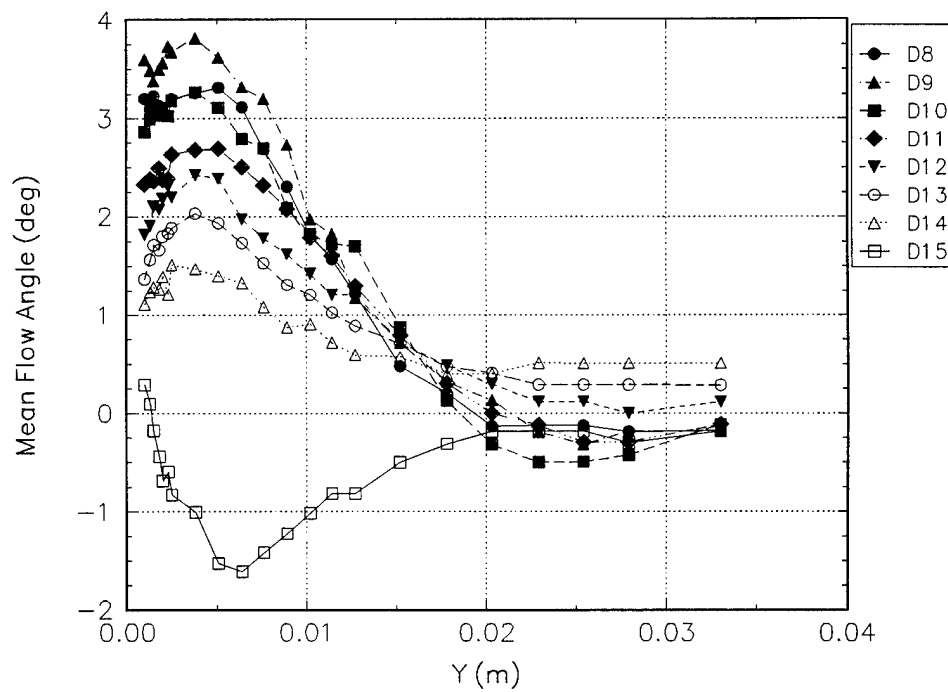


Figure J.1.d Flow angles, stations are given in the legend.

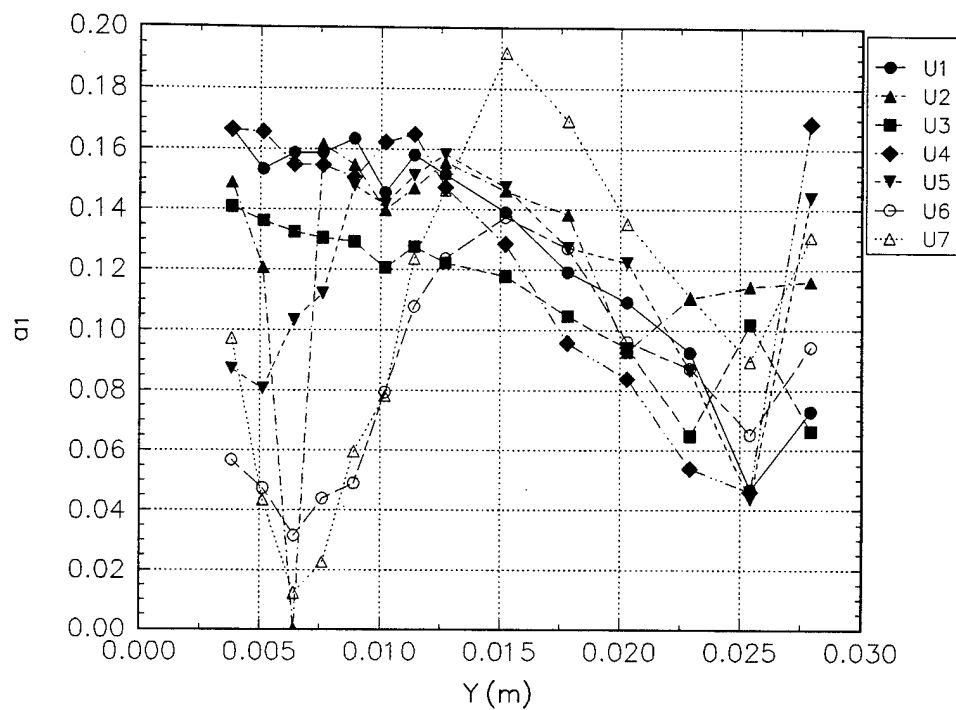


Figure J.2.a The  $a_1$  parameter, stations are given in the legend.

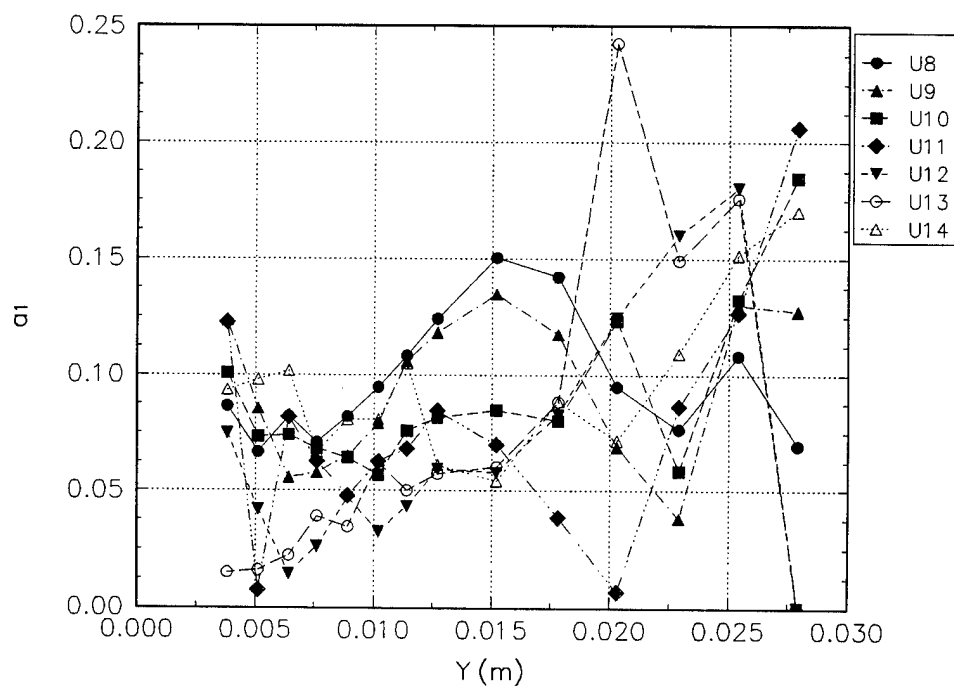


Figure J.2.b The  $a_1$  parameter, stations are given in the legend.

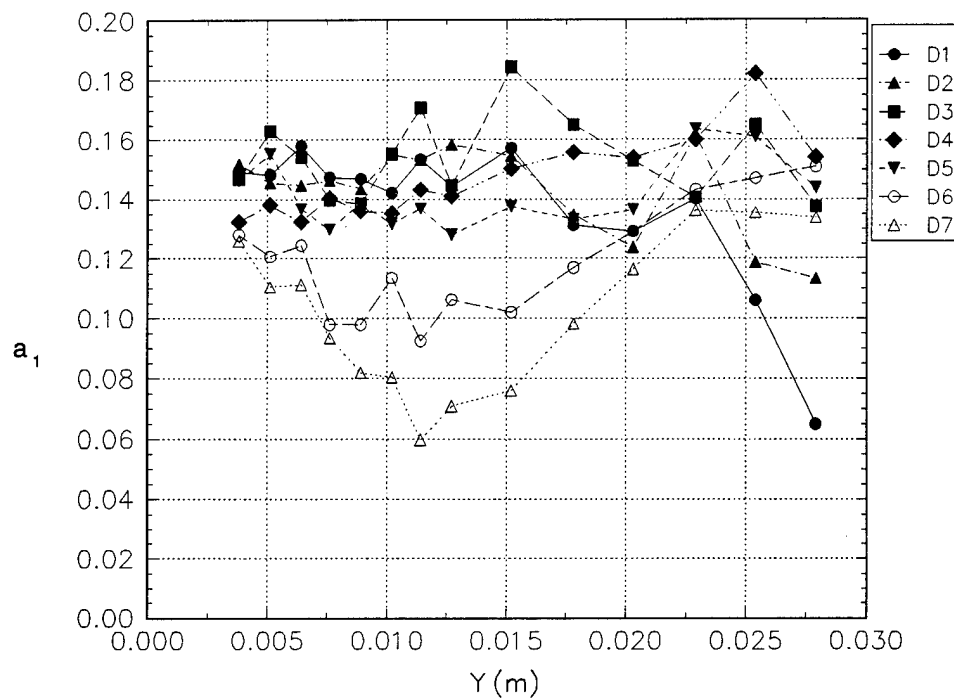


Figure J.2.c The  $a_1$  parameter, stations are given in the legend.

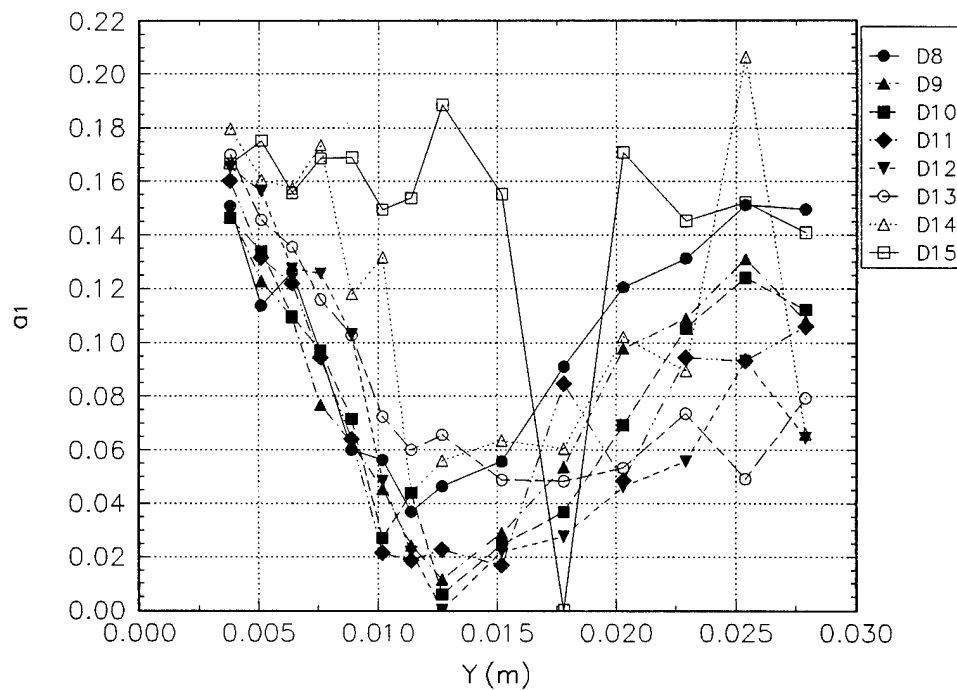


Figure J.2.d The  $a_1$  parameter, stations are given in the legend.

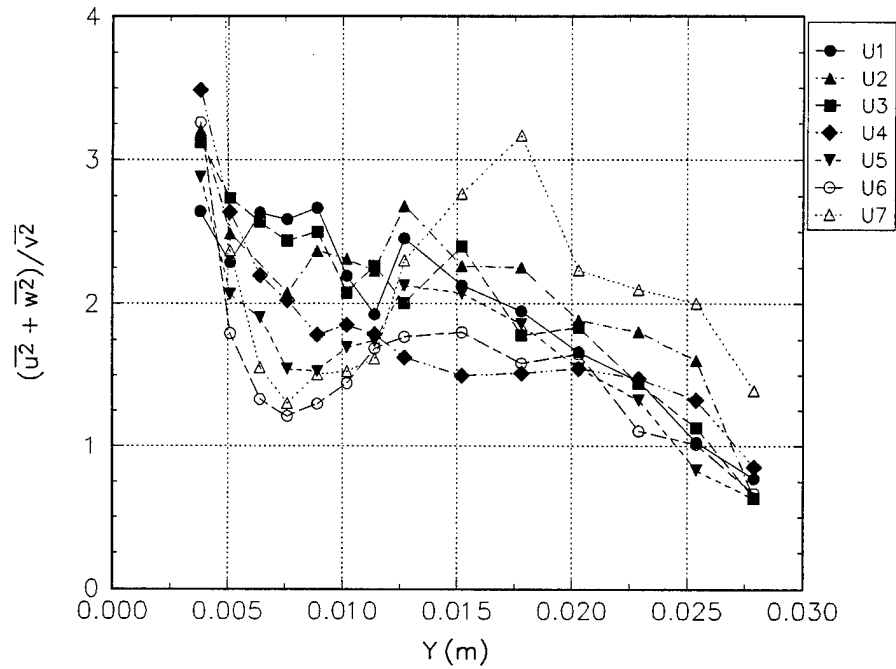


Figure J.3.a Ratio of normal Reynolds stresses in tunnel coordinates, stations are given in the legend.

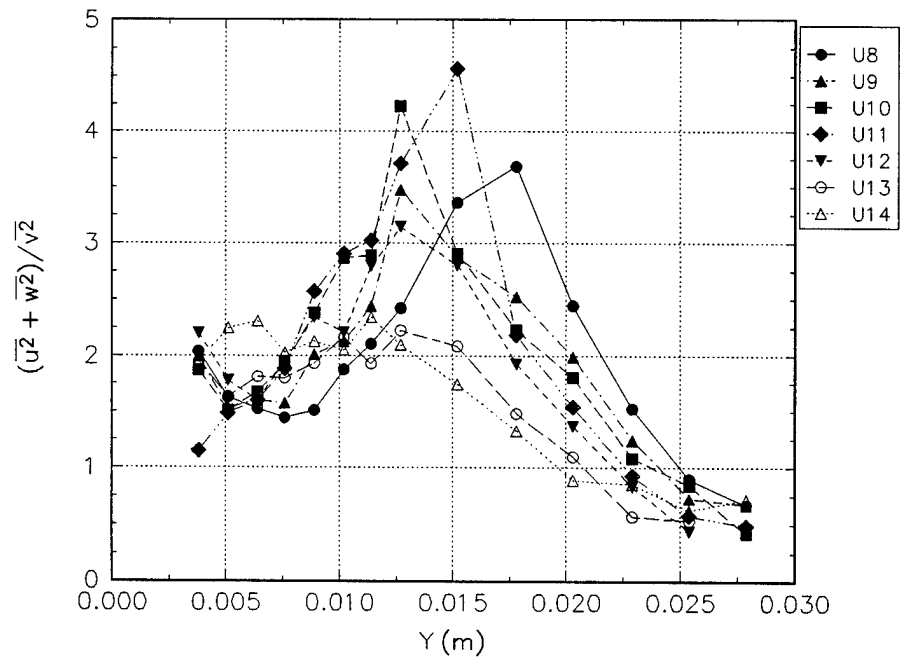


Figure J.3.b Ratio of normal Reynolds stresses in tunnel coordinates, stations are given in the legend.

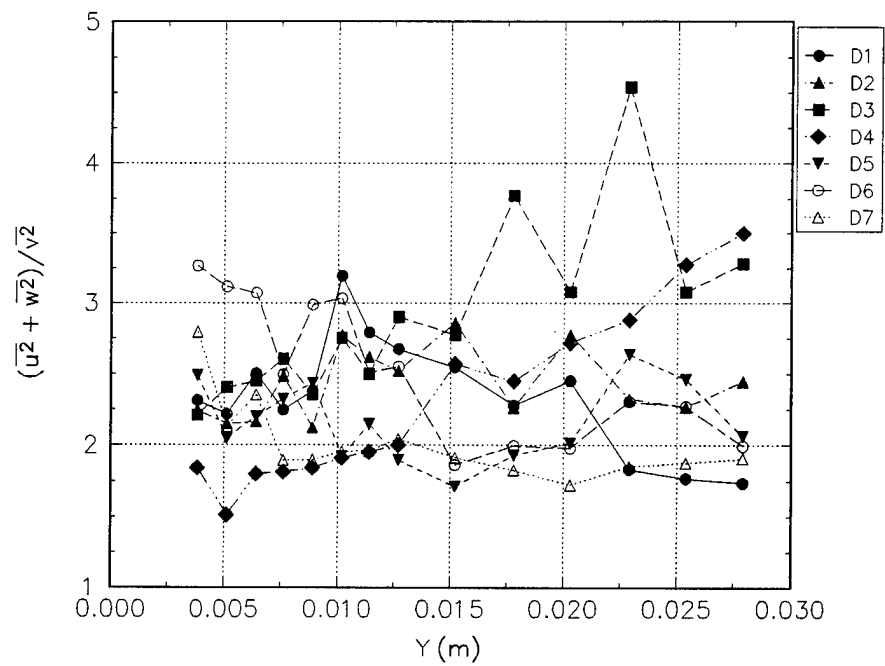


Figure J.3.c Ratio of normal Reynolds stresses in tunnel coordinates, stations are given in the legend.

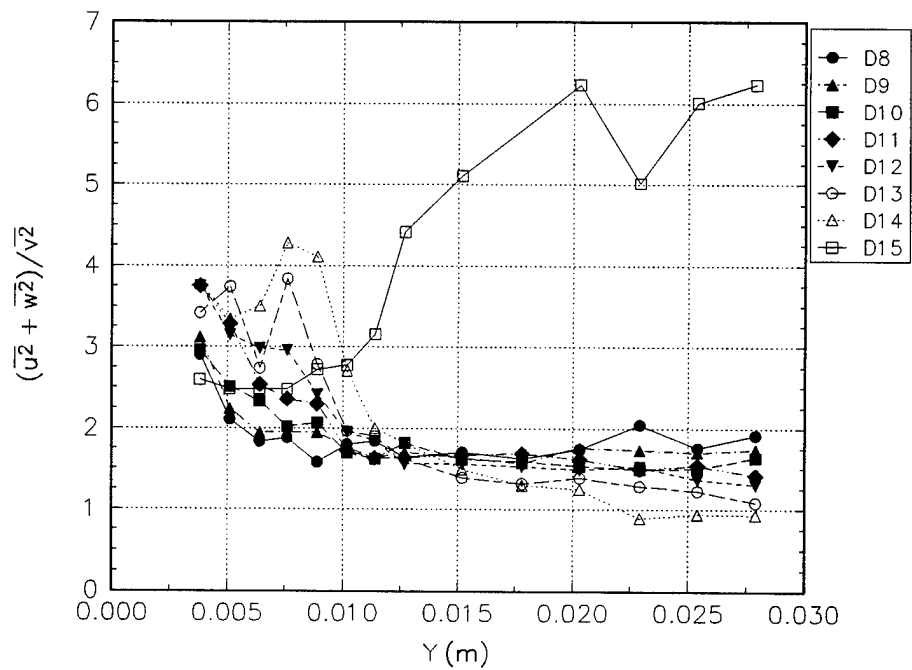


Figure J.3.d Ratio of normal Reynolds stresses in tunnel coordinates, stations are given in the legend.

## APPENDIX K Additional Figures for the Data of Driver

This appendix contains additional figures for the data of Driver. For a description of the experiment see Chapter 2. Case A had no adverse pressure gradient and the adverse pressure gradient increases as the test cases progress through the letters. S0 indicates that the shear was not present while S1 indicates that the cylinder was spinning with a wall velocity equal to the freestream velocity.

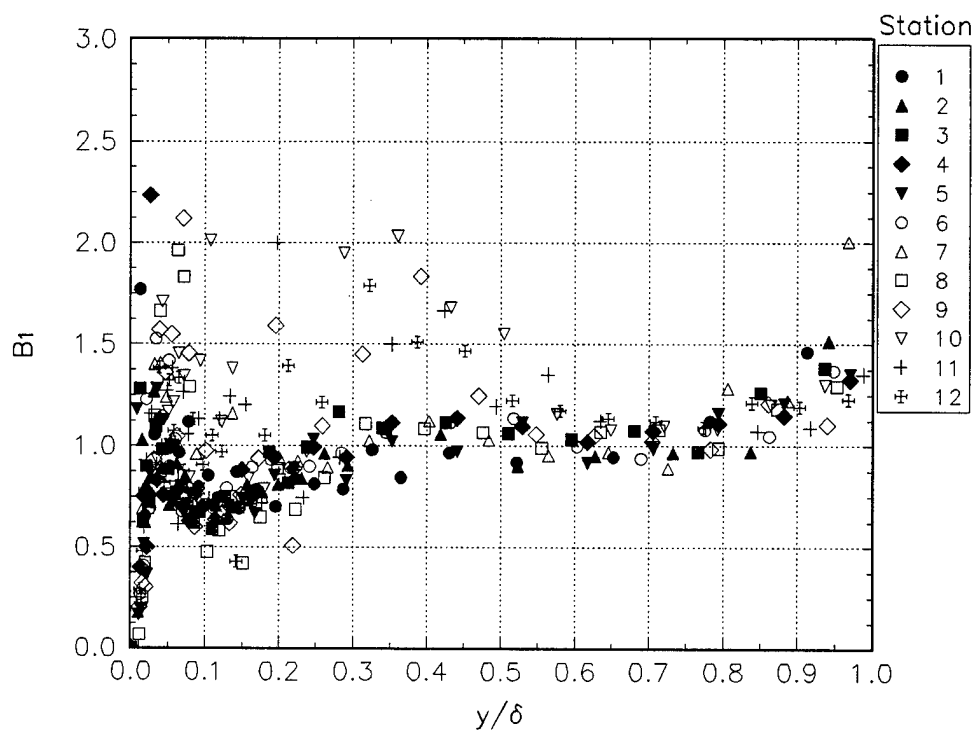


Figure K.1a The  $B_1$  parameter for test case AS1.

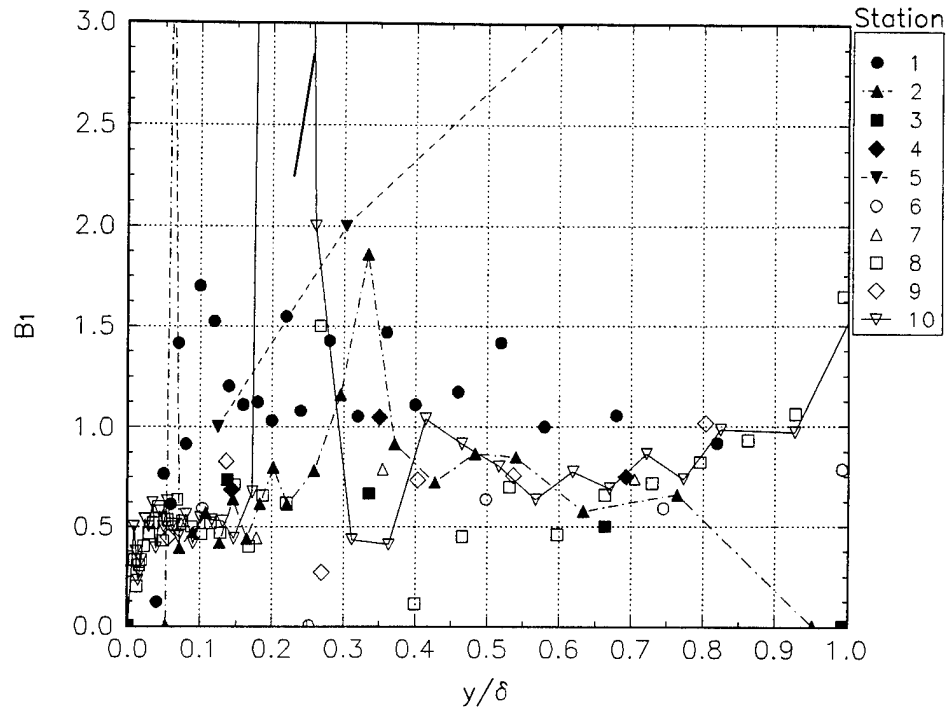


Figure K.1b The  $B_1$  parameter for test case BS0.

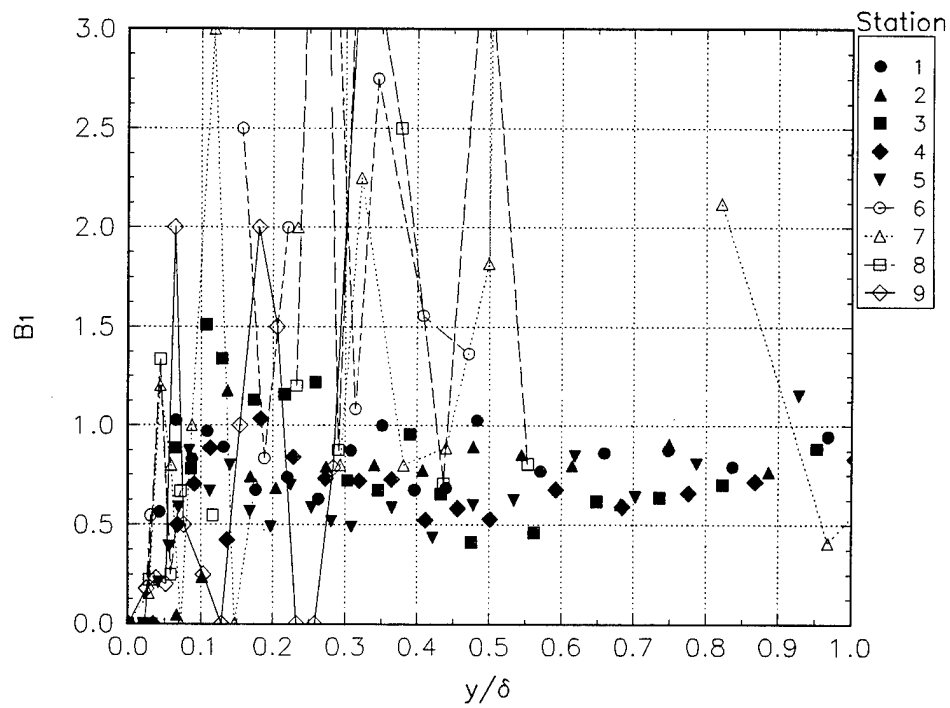


Figure K.1c The  $B_1$  parameter for test case BS1.

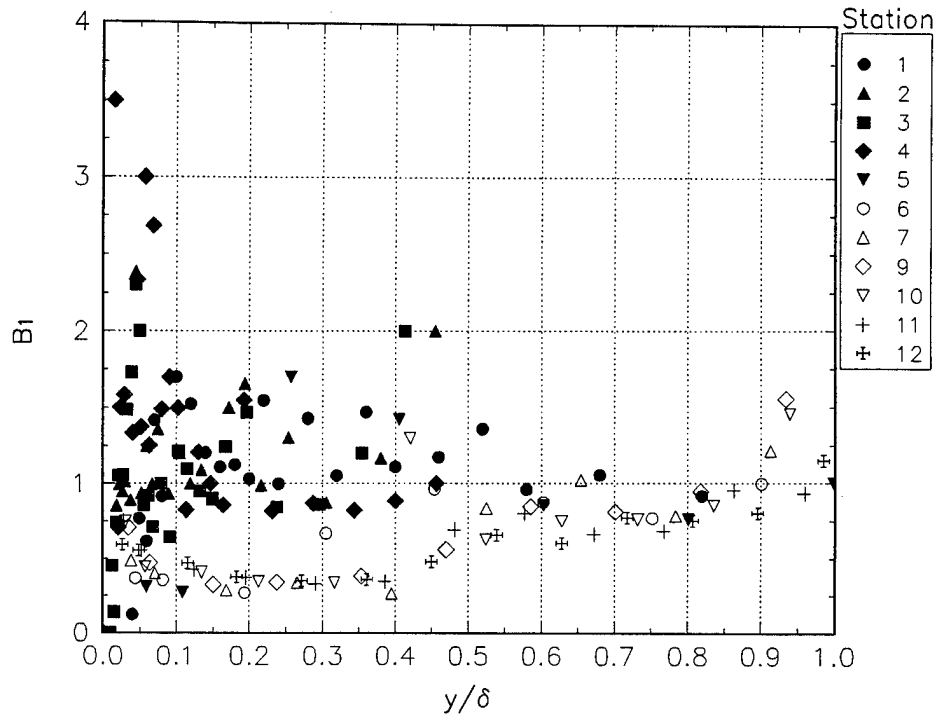


Figure K.1d The  $B_1$  parameter for test case CS0.

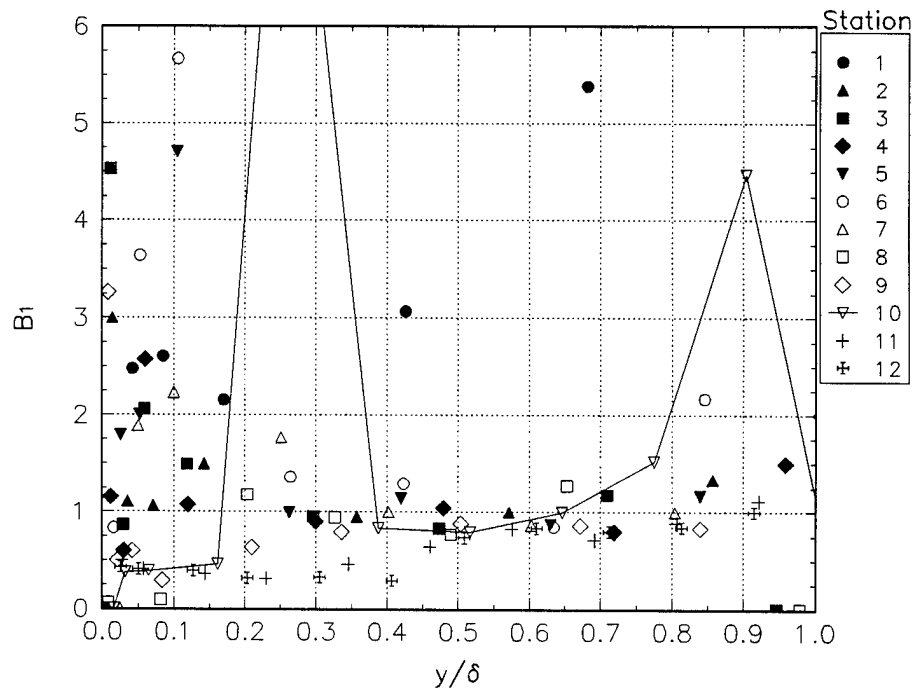


Figure K.1e The  $B_1$  parameter for test case DS0.



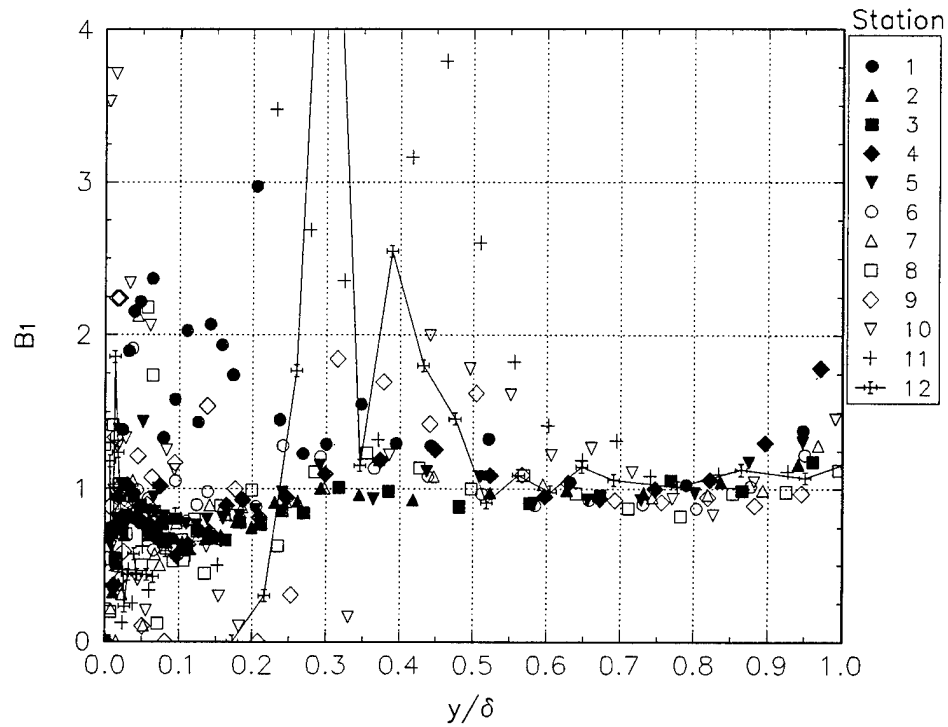


Figure K.1f The  $B_1$  parameter for test case D1.

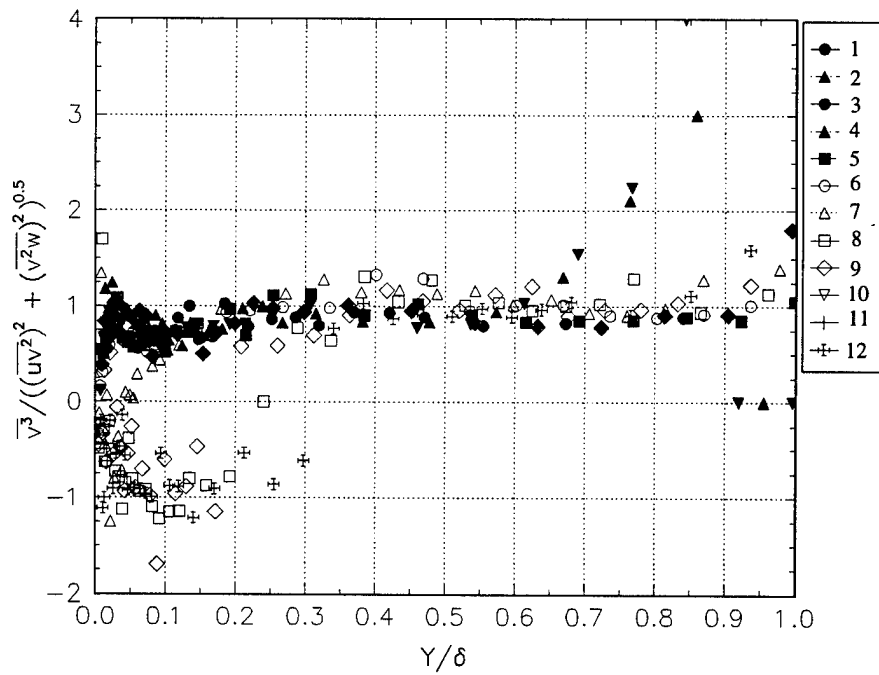


Figure K.2 The  $B_2$  parameter for case CS1.

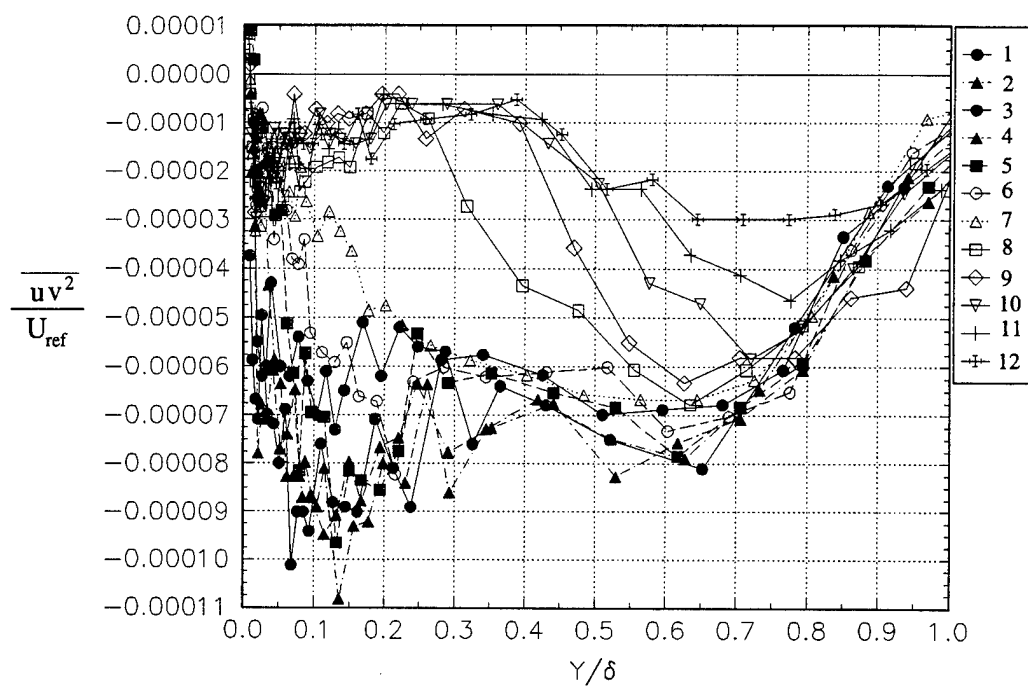


Figure K.3a The  $\overline{uv^2}$  triple product for case AS1.

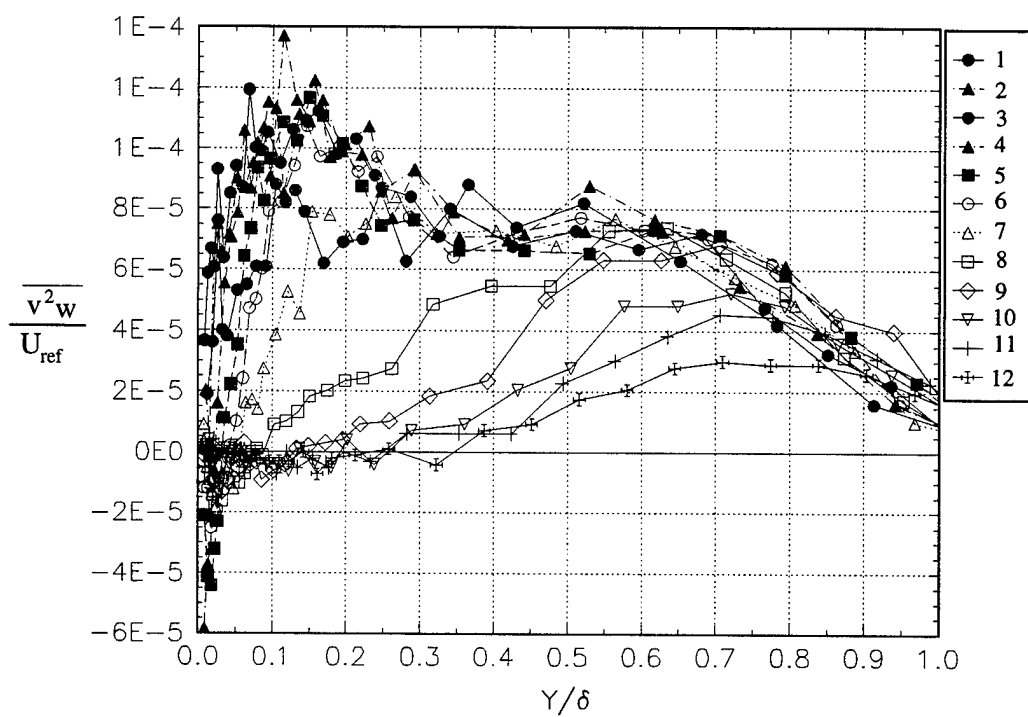


Figure K.3b The  $\overline{v^2 w}$  triple product for case AS1.

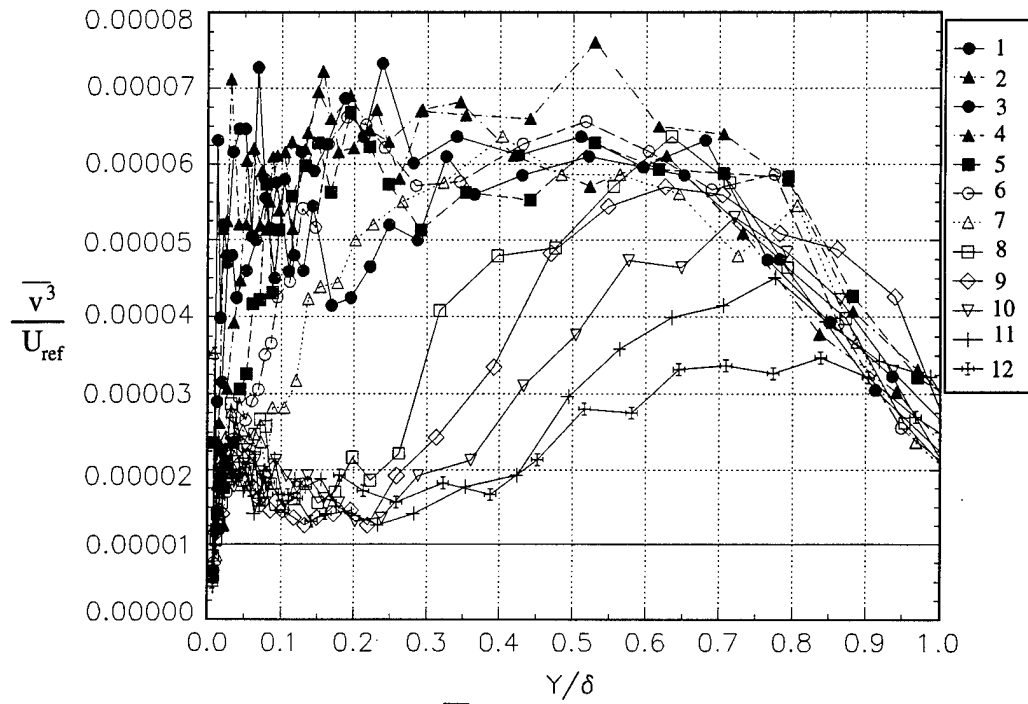


Figure K.3c The  $\overline{v^3}$  triple product for case AS1.

## APPENDIX L Additional Figures for the Data of Littell

This appendix contains some additional figures that were generated from the data of Littell. For specific information on the experiment, refer to chapter 2. Seven different experiments are represented in each plot. The location of radius and rotational rate varies between cases. Three radii are used; 0.235 m, 0.356 m and 0.421 m. They are designated as 2\_, 3\_, or 4\_ respectively. The Reynolds numbers used were; 400,000,  $65 \times 10^4$ ,  $94 \times 10^4$ ,  $100 \times 10^4$ ,  $130 \times 10^4$ , and  $160 \times 10^4$ . They were designated by the Reynolds number /  $1 \times 10^4$  for this study. For example, at  $r = 0.235$  m and  $Re = 400000$ , the station is designated 2\_40. The others are similarly designated. All data is presented in laboratory coordinates.

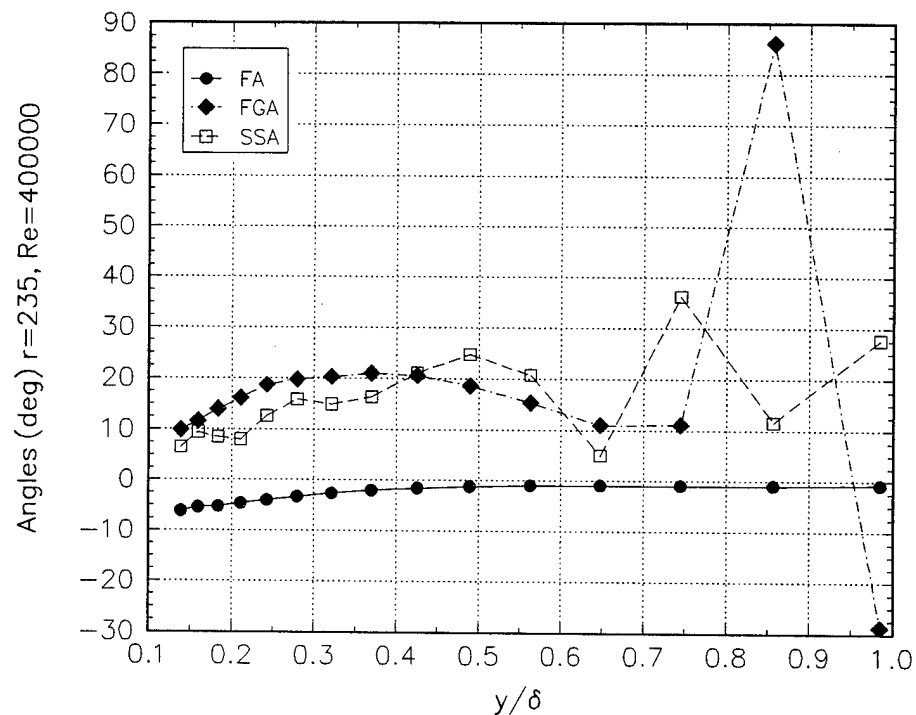


Figure L.1a Characteristic angles.

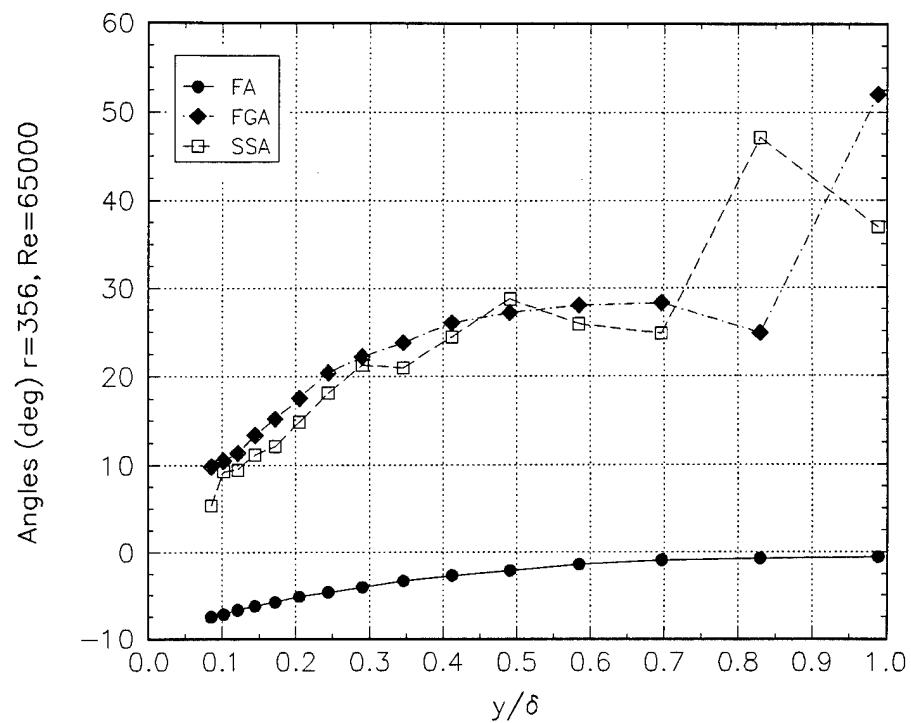


Figure L.1b Characteristic angles.

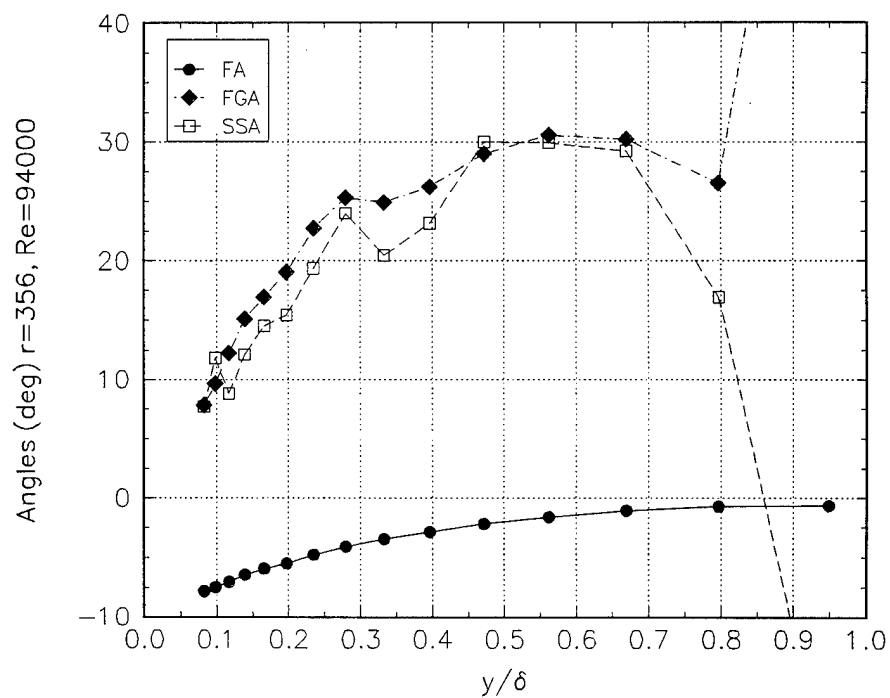


Figure L.1c Characteristic angles.

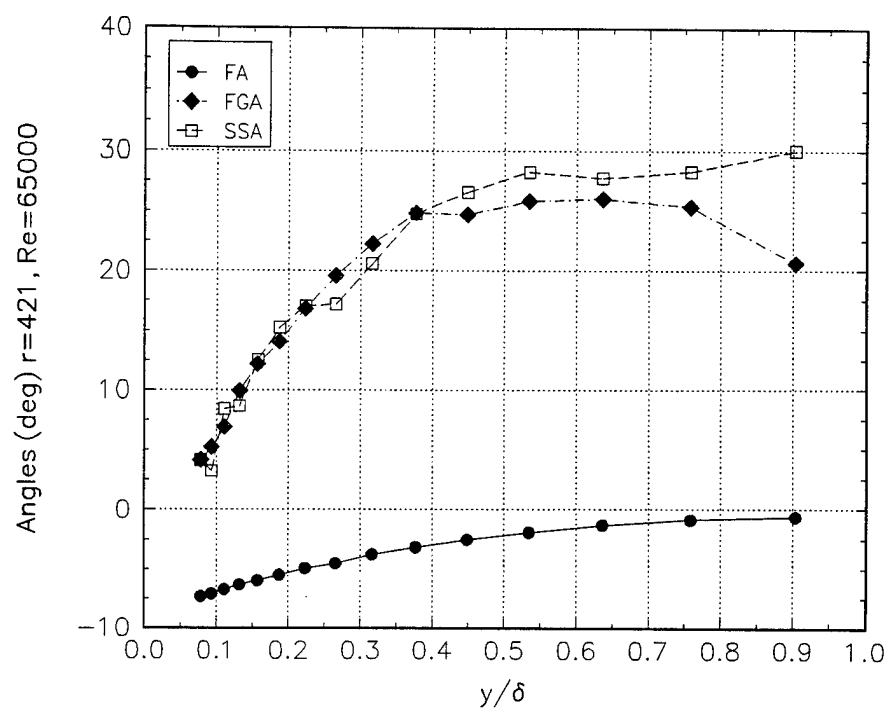


Figure L.1d Characteristic angles.

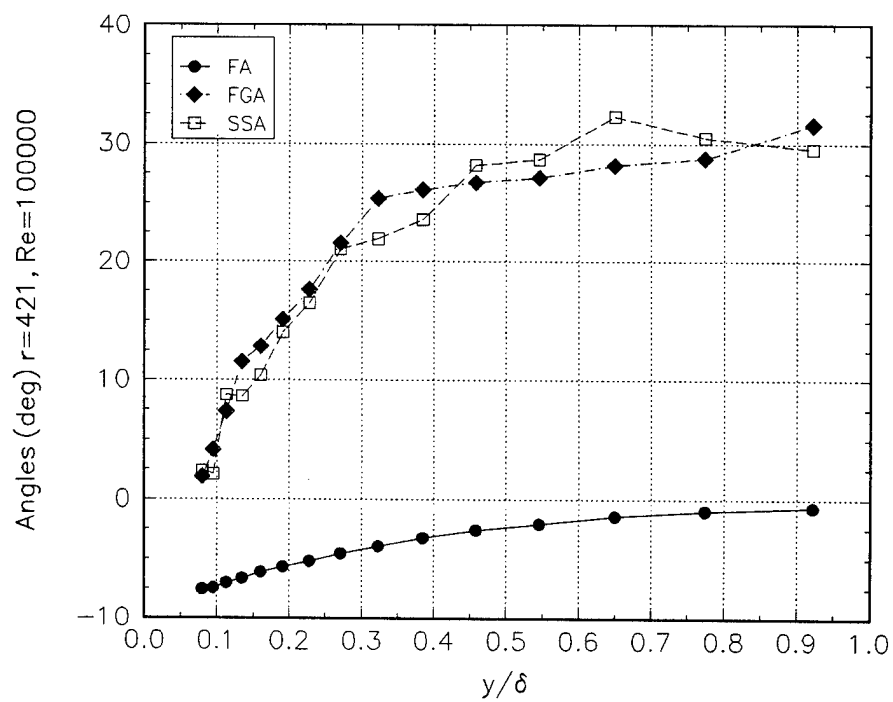


Figure L.1e Characteristic angles.

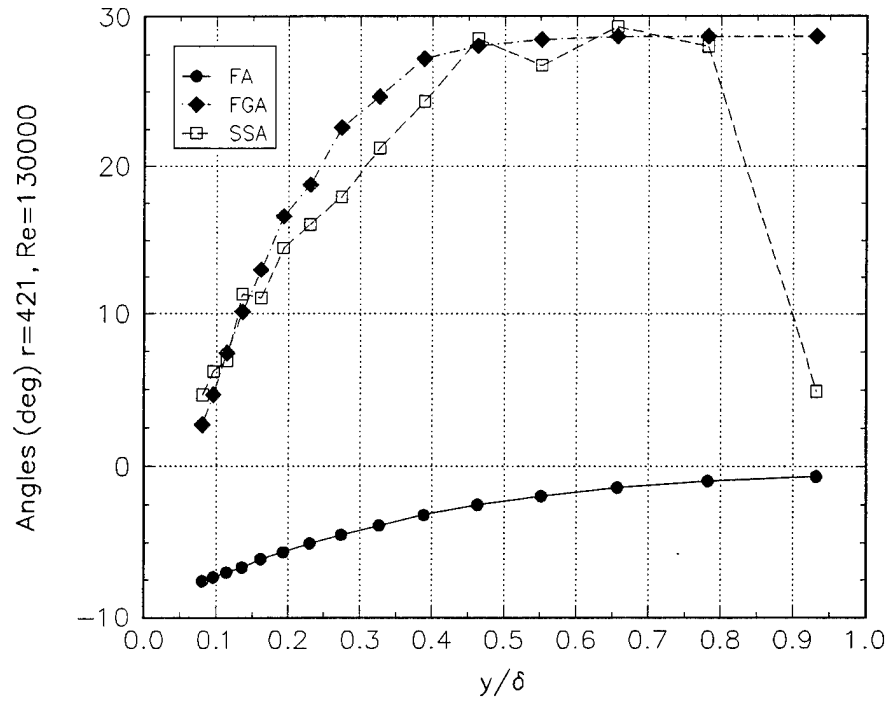


Figure L.1f Characteristic angles.

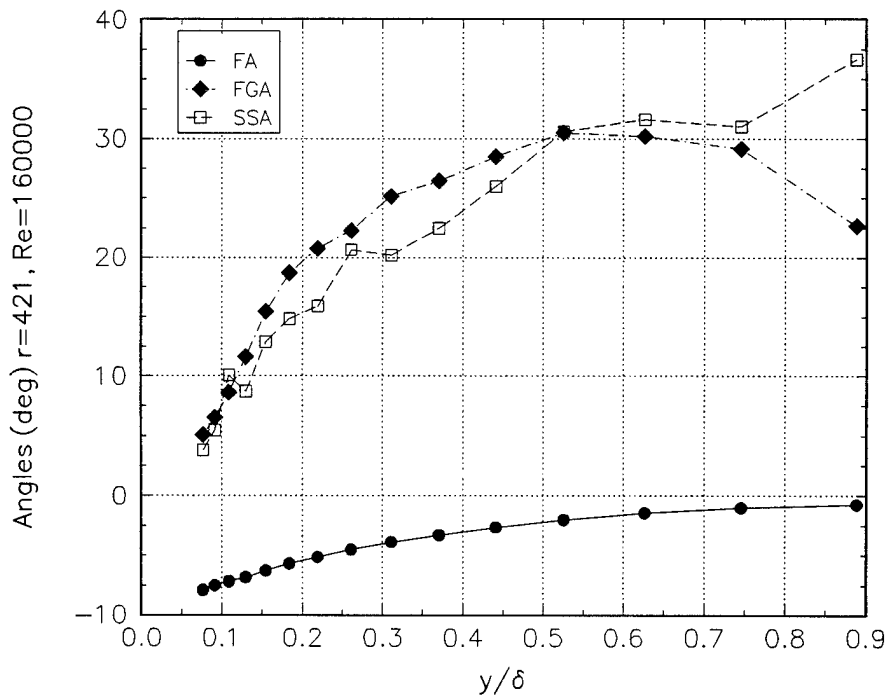


Figure L.1g Characteristic angles.

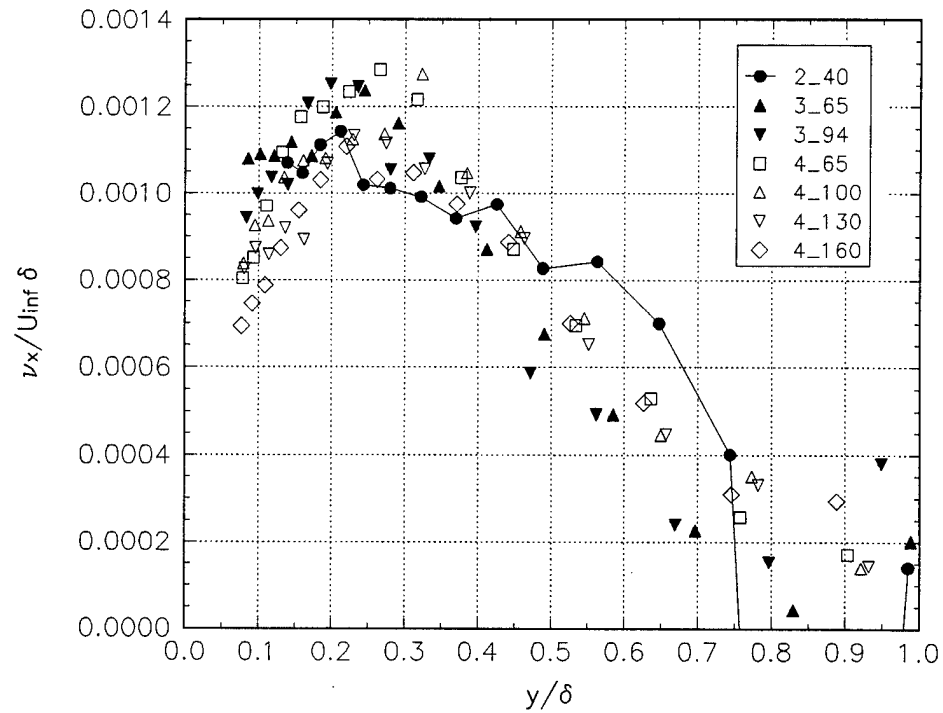


Figure L.2a Eddy viscosity in the x-direction.

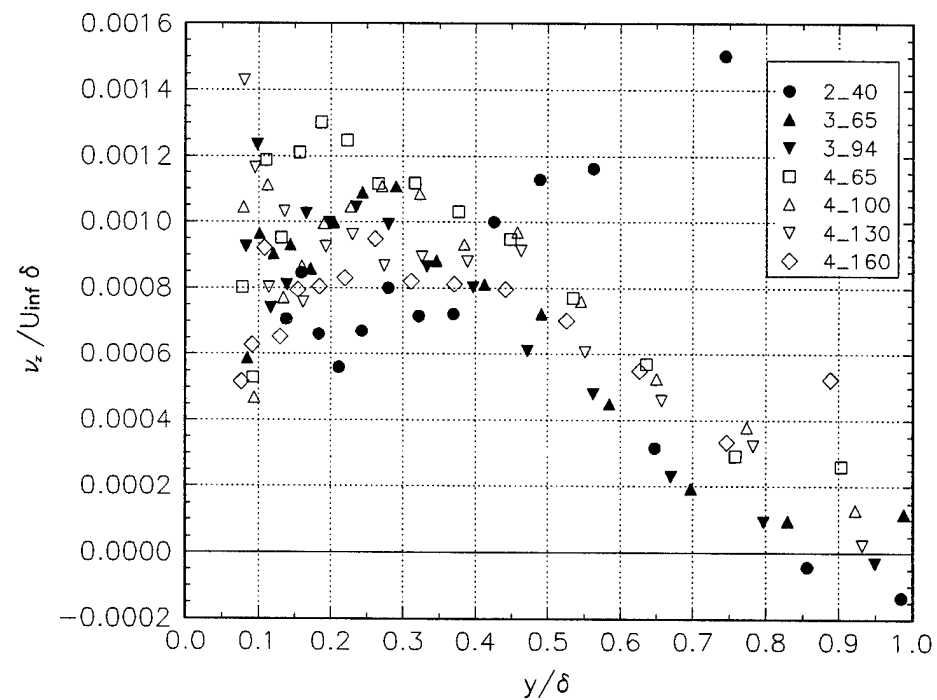


Figure L.2b Eddy viscosity in the z-direction.



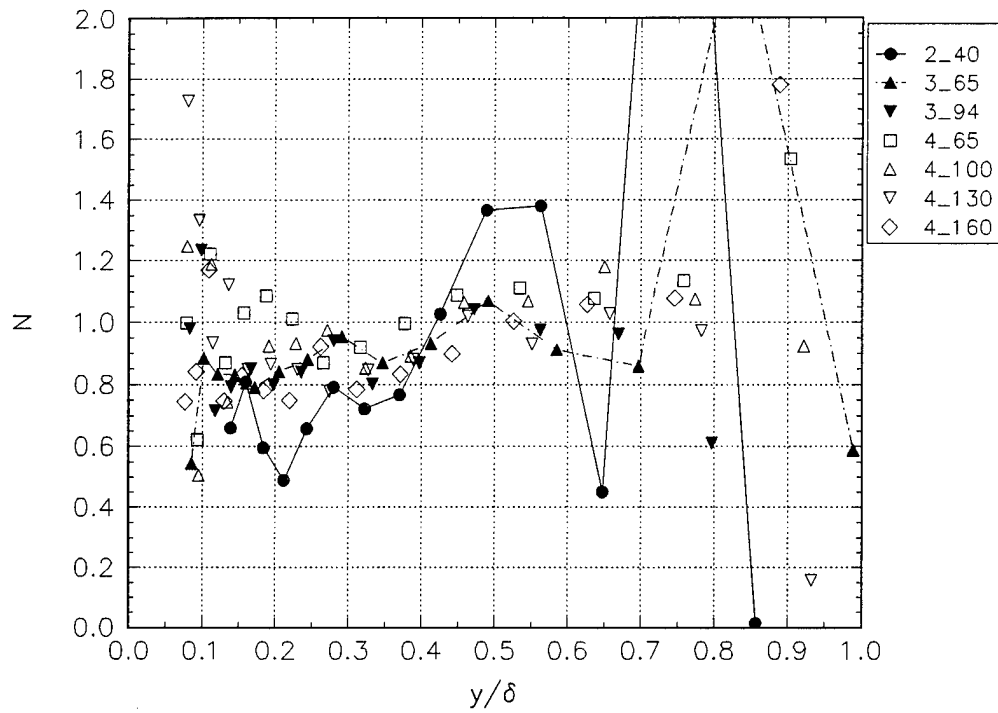


Figure L.3a The anisotropy parameter.

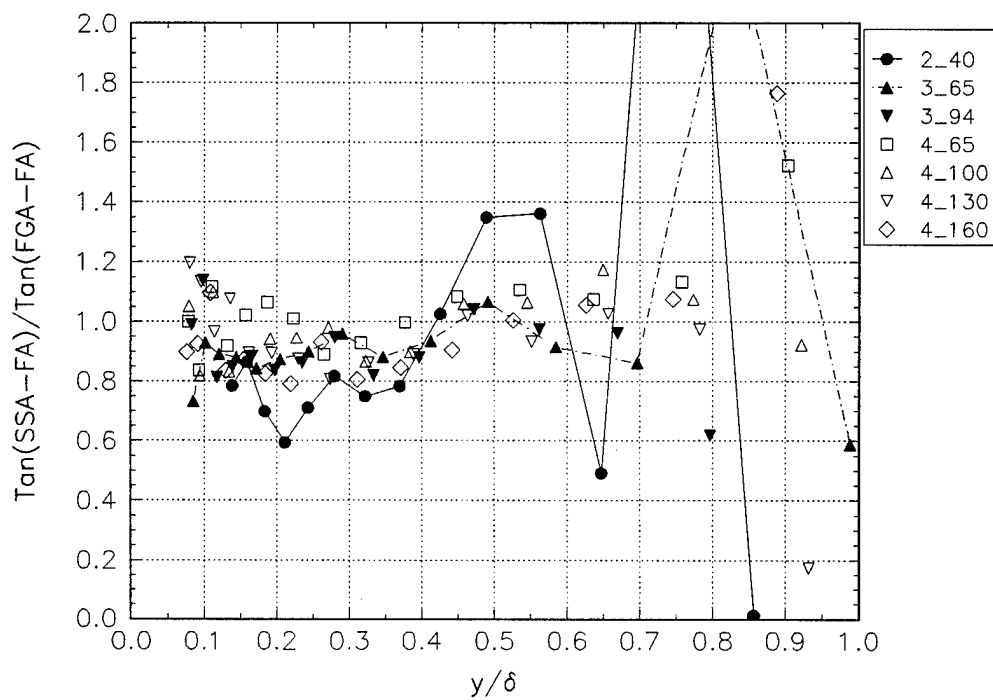


Figure L.3b Rotta's T parameter.

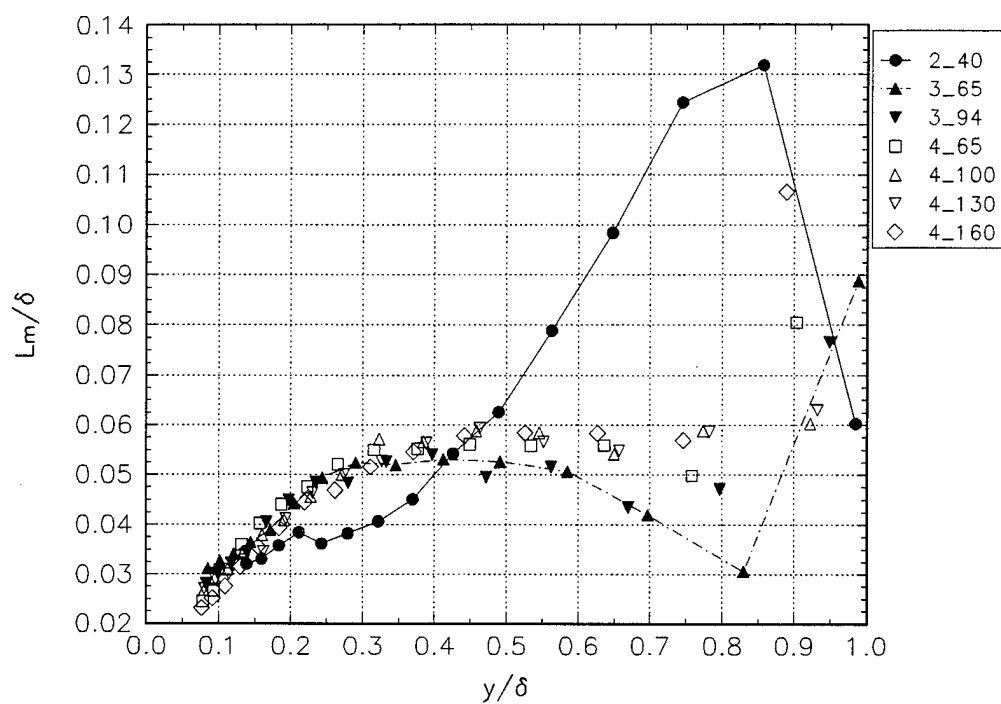


Figure L.4 The mixing length.

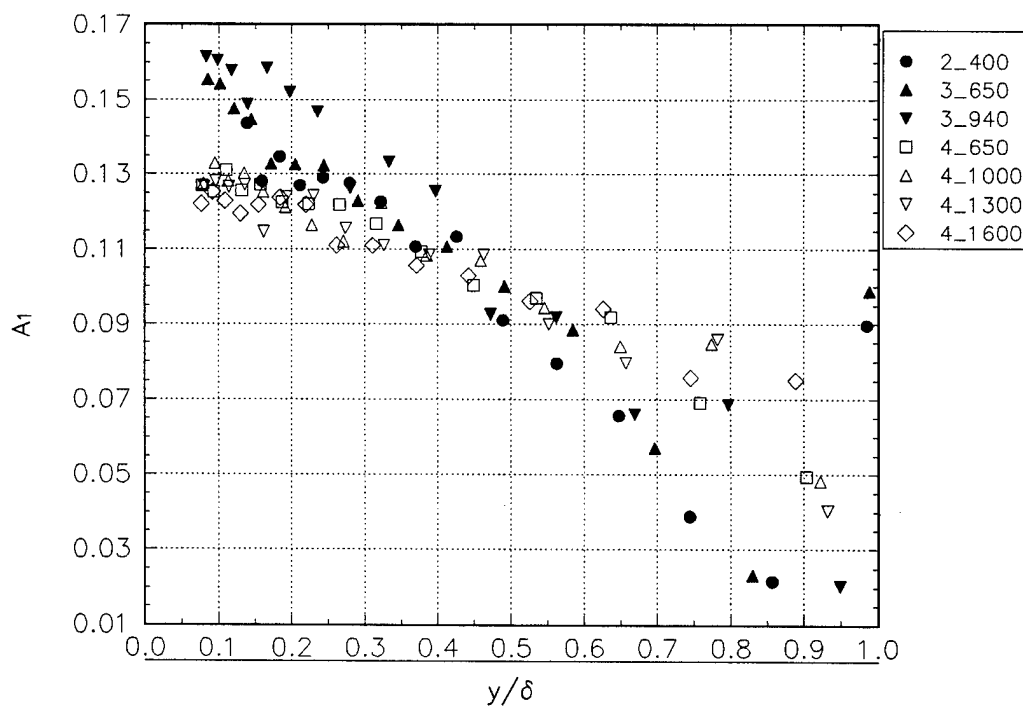


Figure L.5 The  $a_1$  structural parameter.

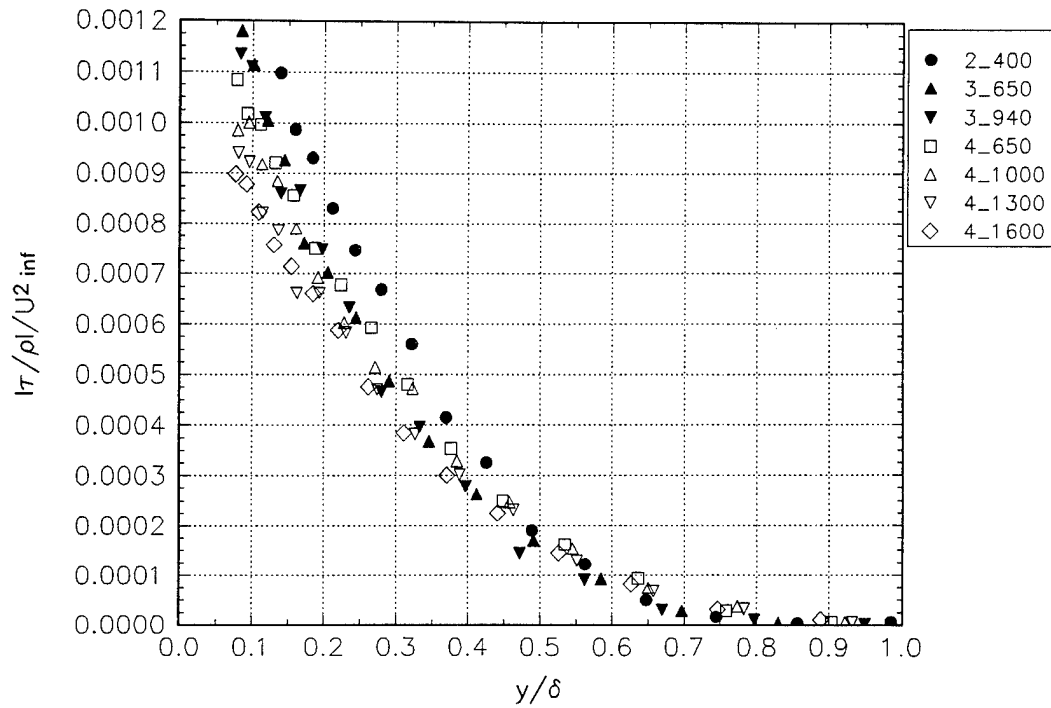


Figure L.6 The magnitude of the Reynolds shear stresses.

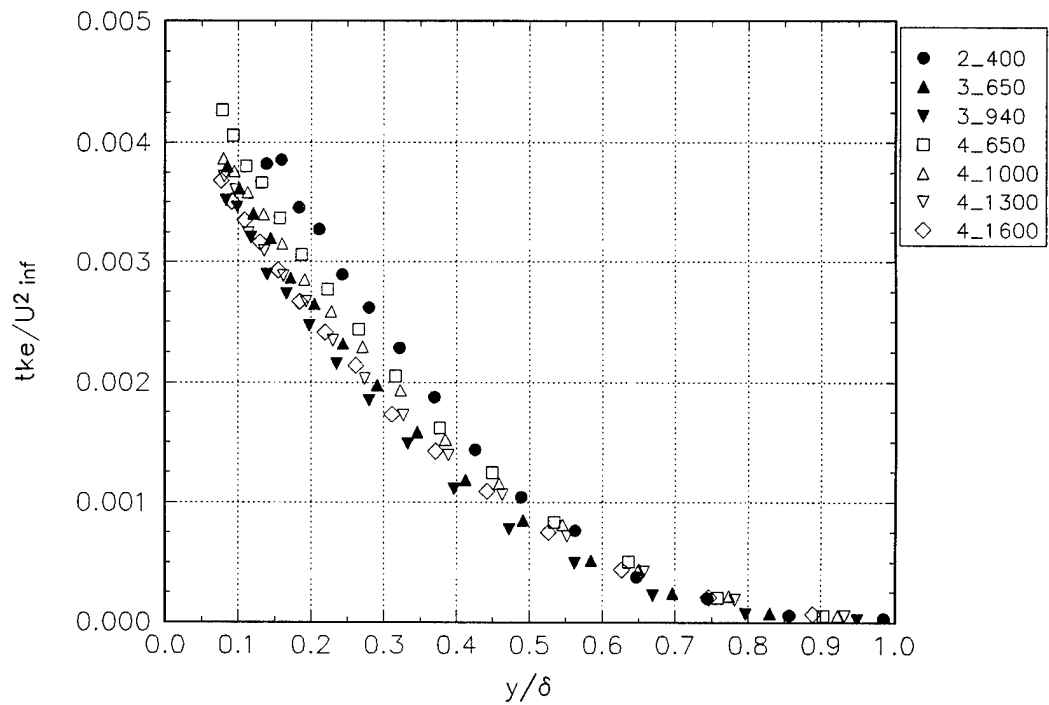


Figure L.7 The TKE.

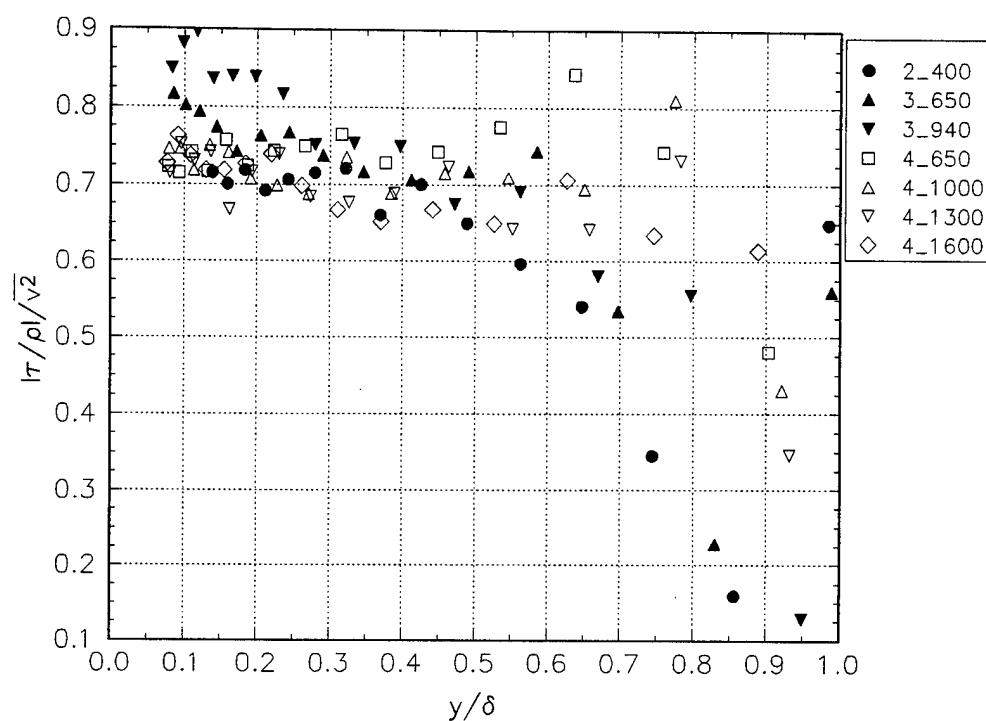


Figure L.8 The 1/S parameter.

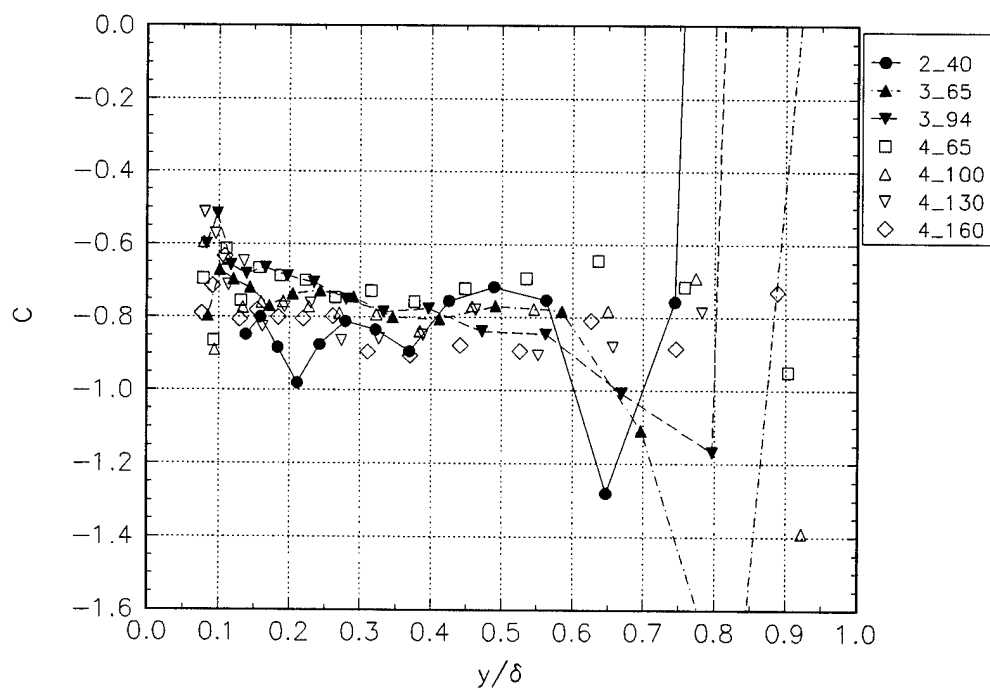


Figure L.9 The C parameter.

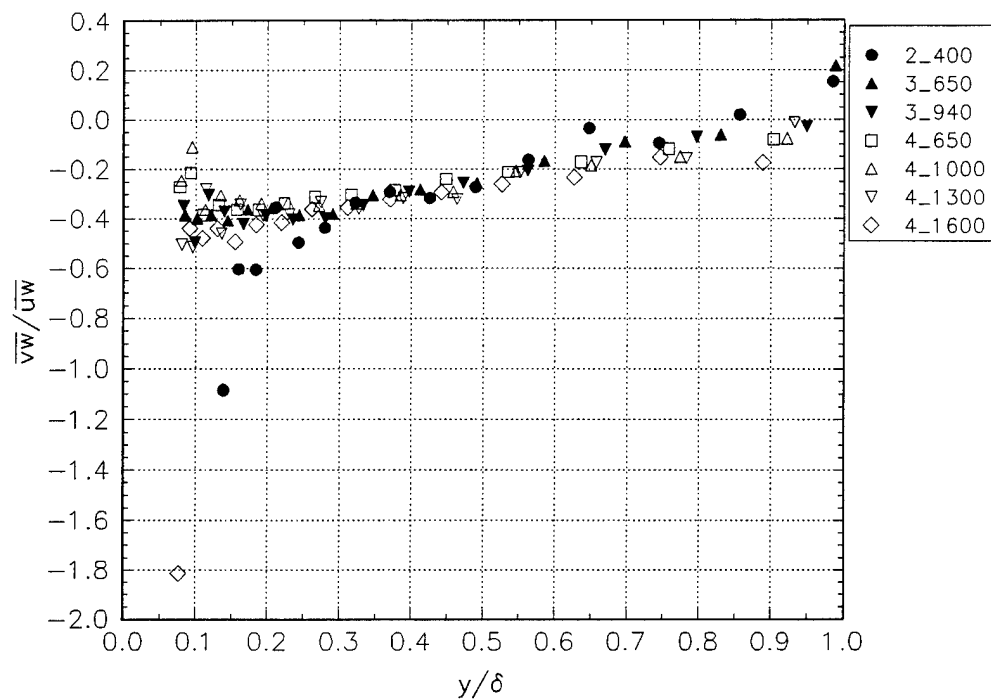


Figure L.10 Reynolds stress ratio.

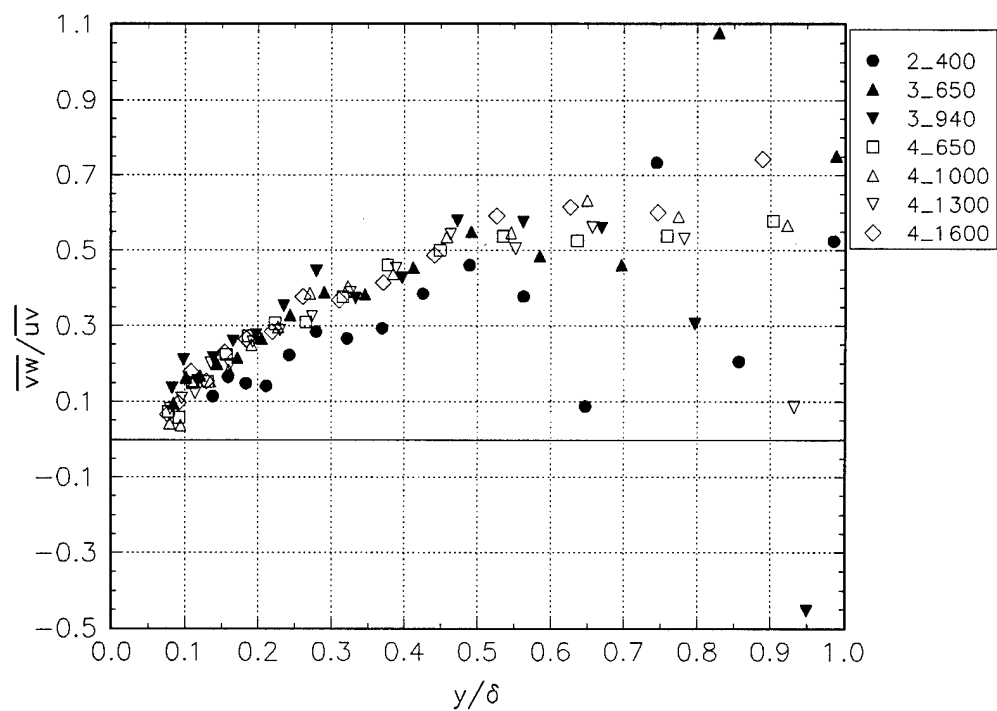


Figure L.11 Reynolds stress ratio.

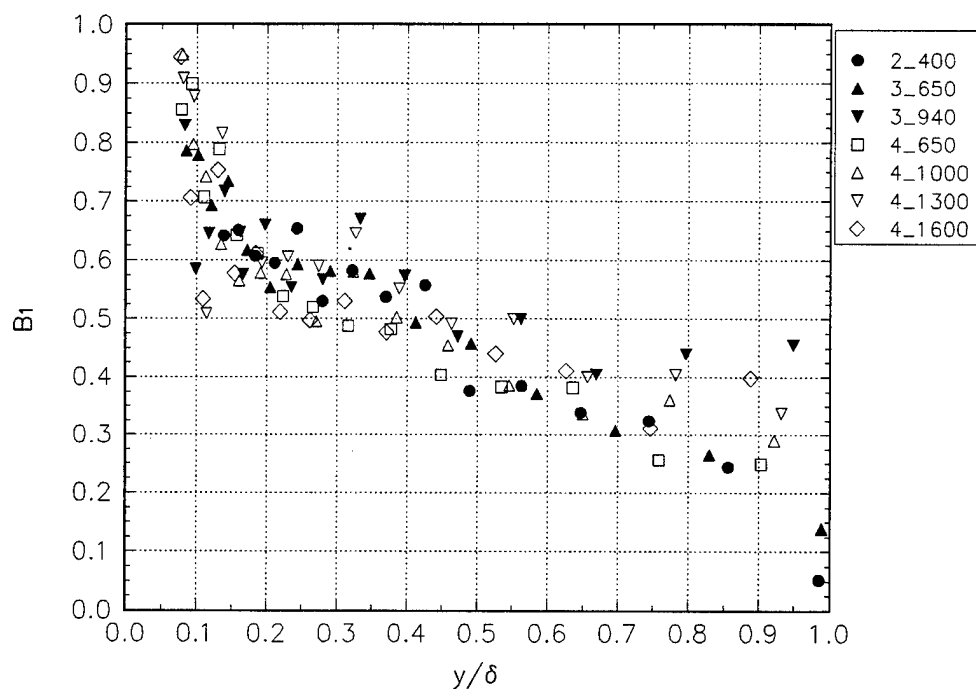


Figure L.12 The  $B_1$  parameter.

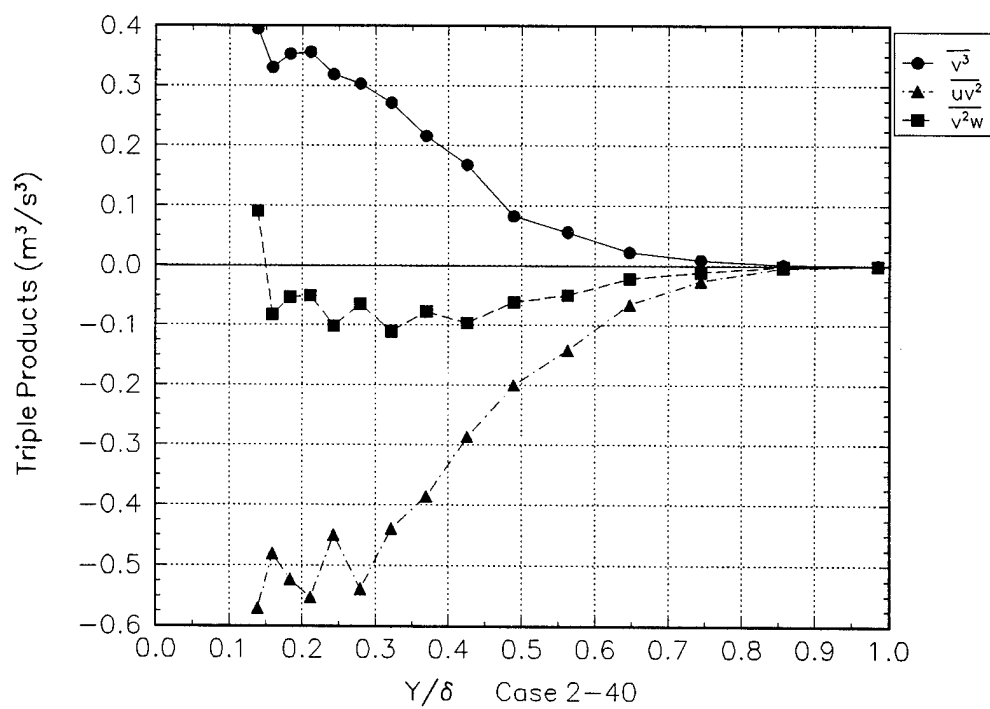


Figure L.13a Triple products.

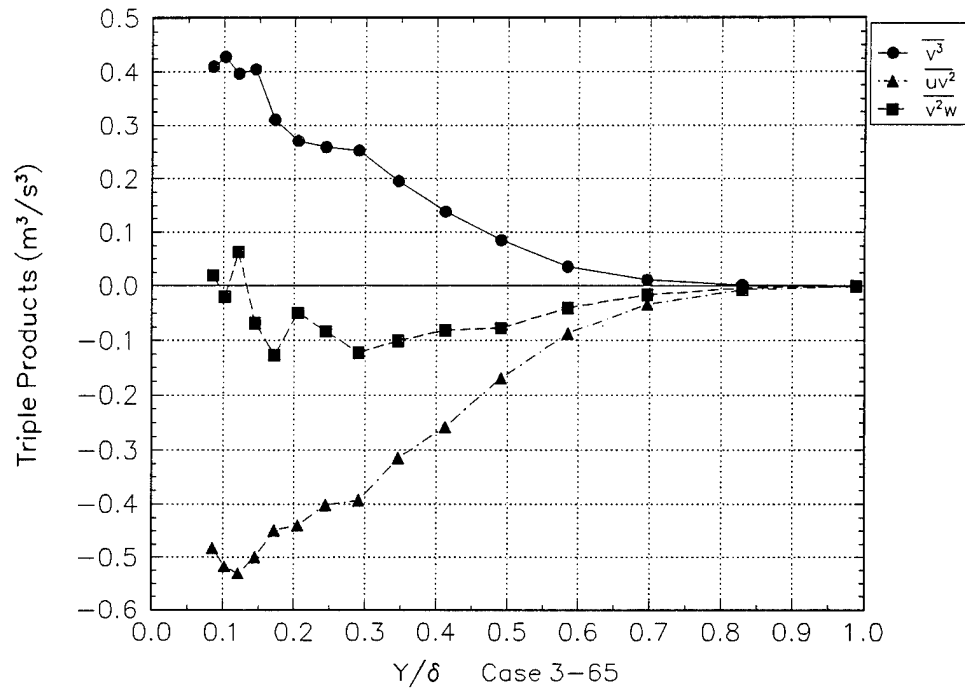


Figure L.13b Triple products.

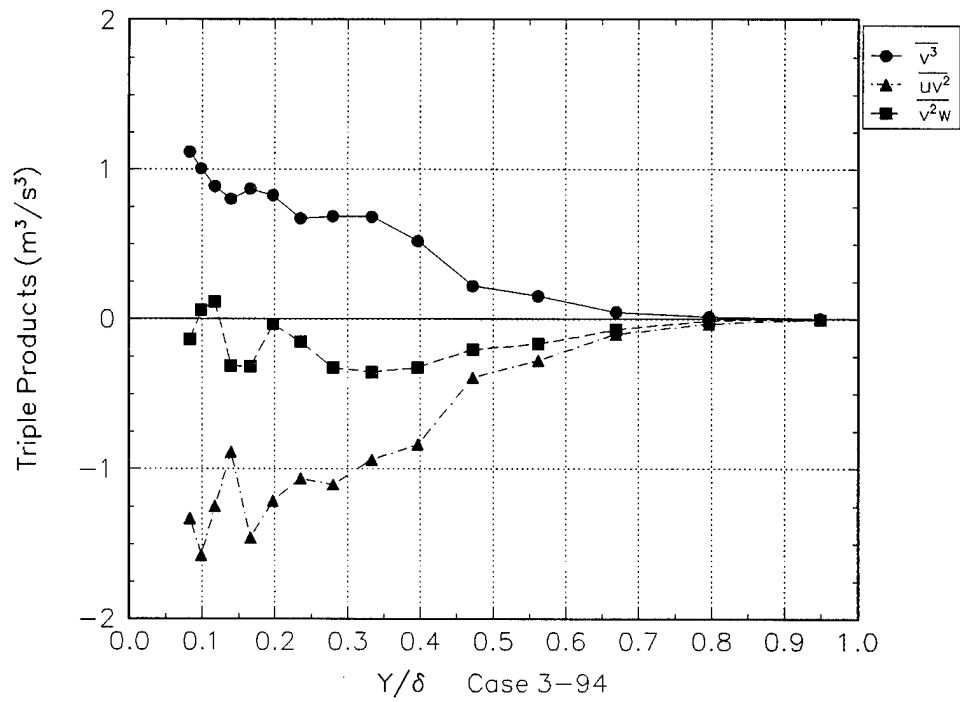


Figure L.13c Triple products.

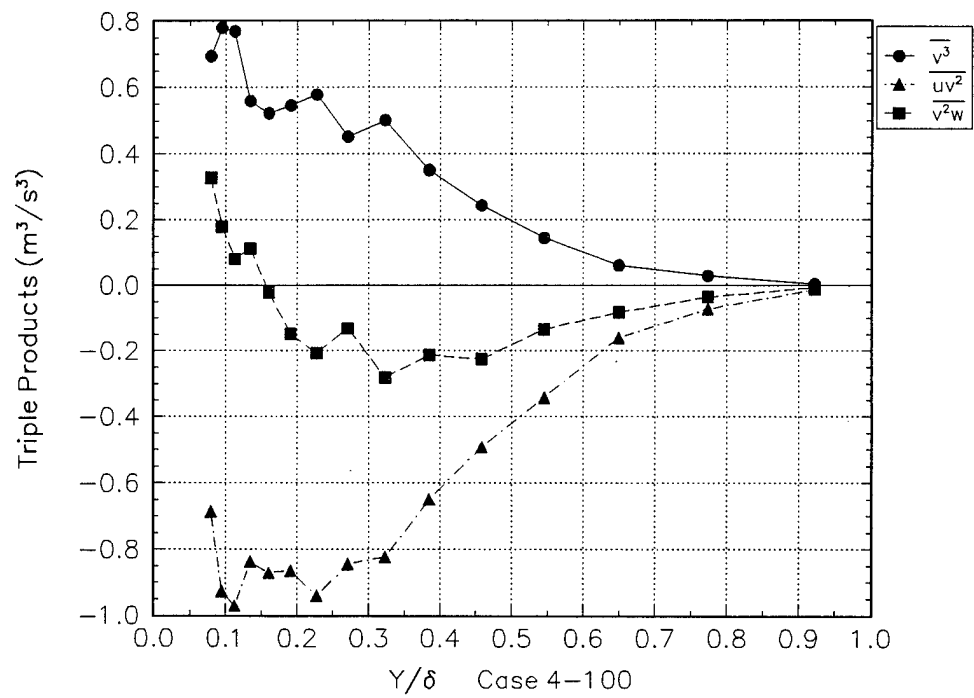


Figure L.13d Triple products.

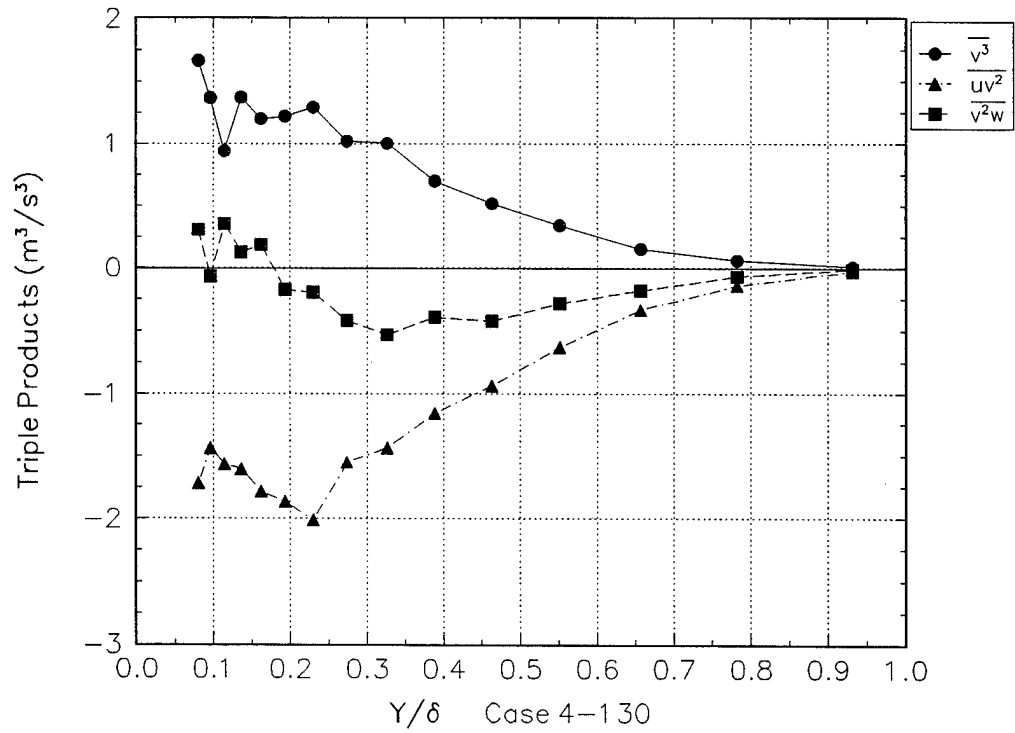
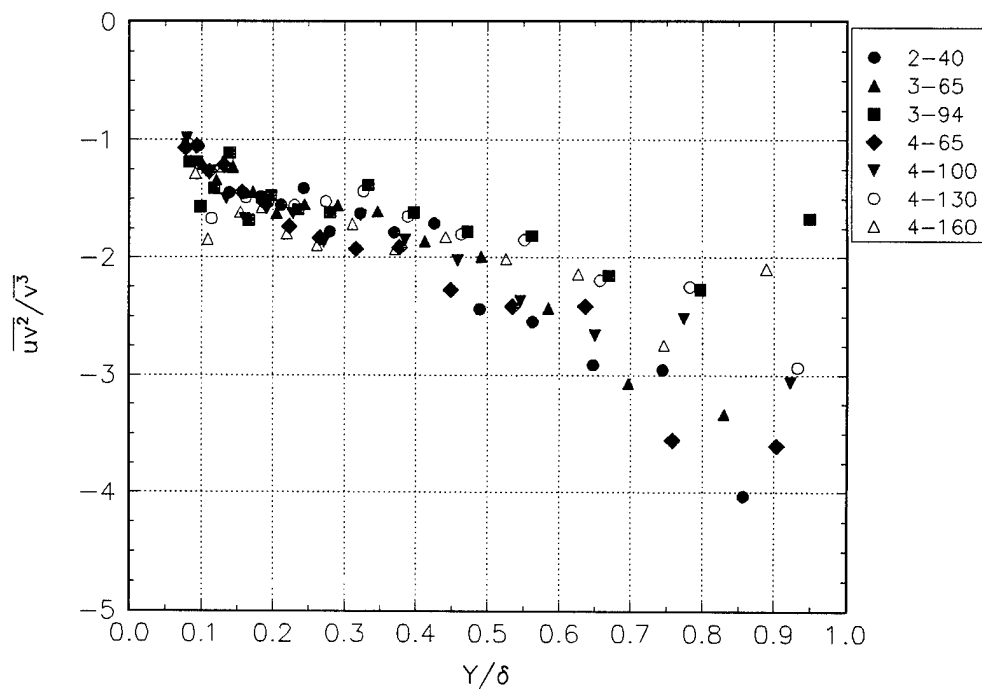
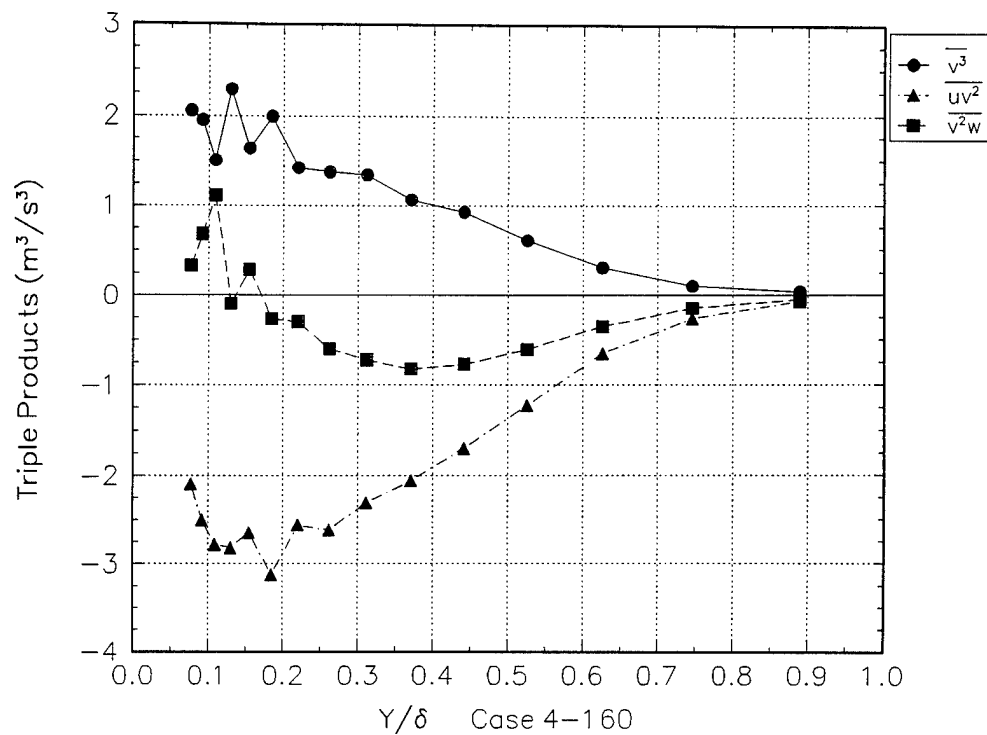
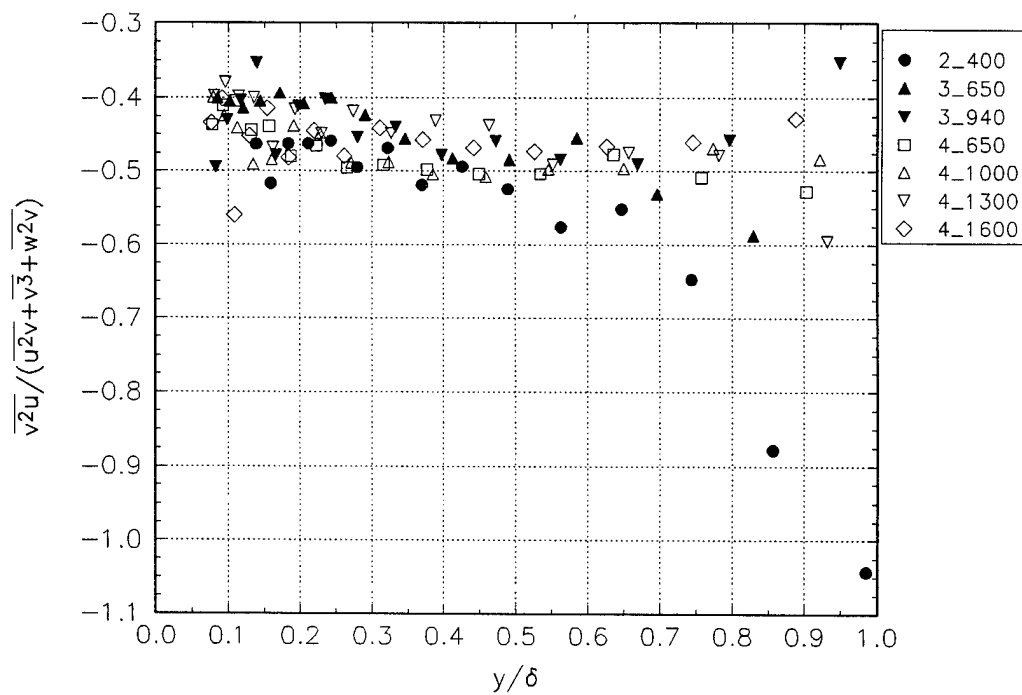
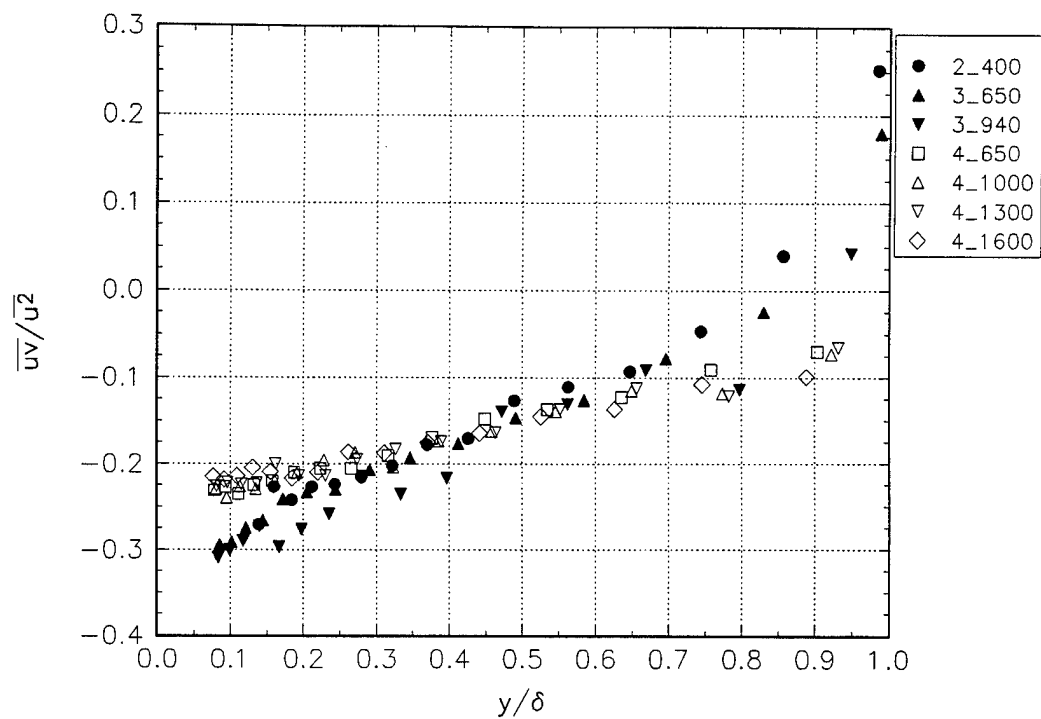
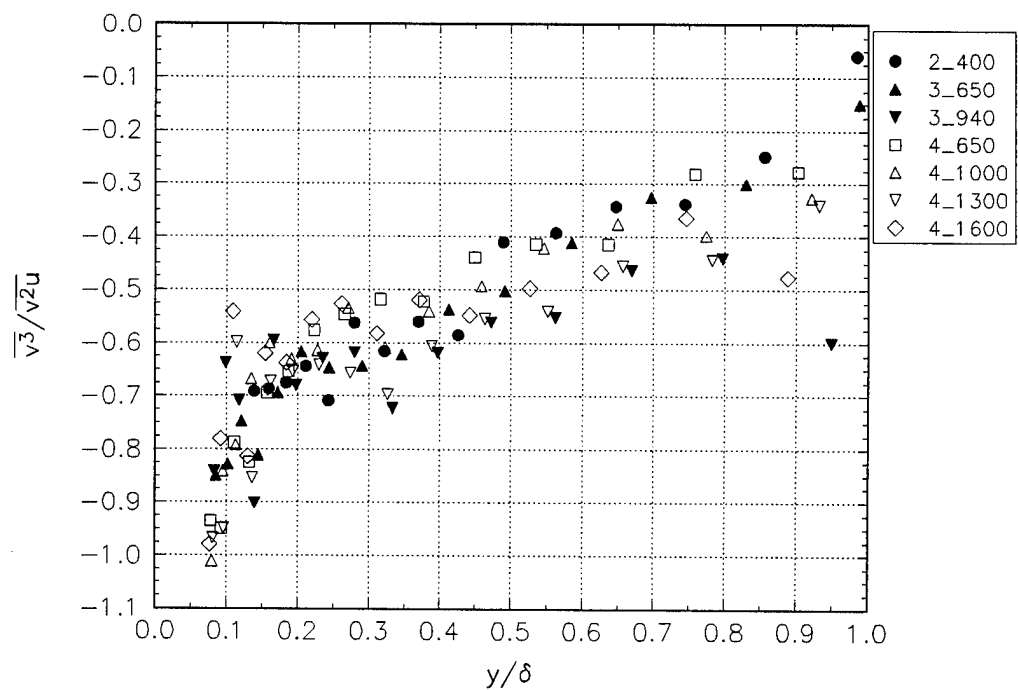
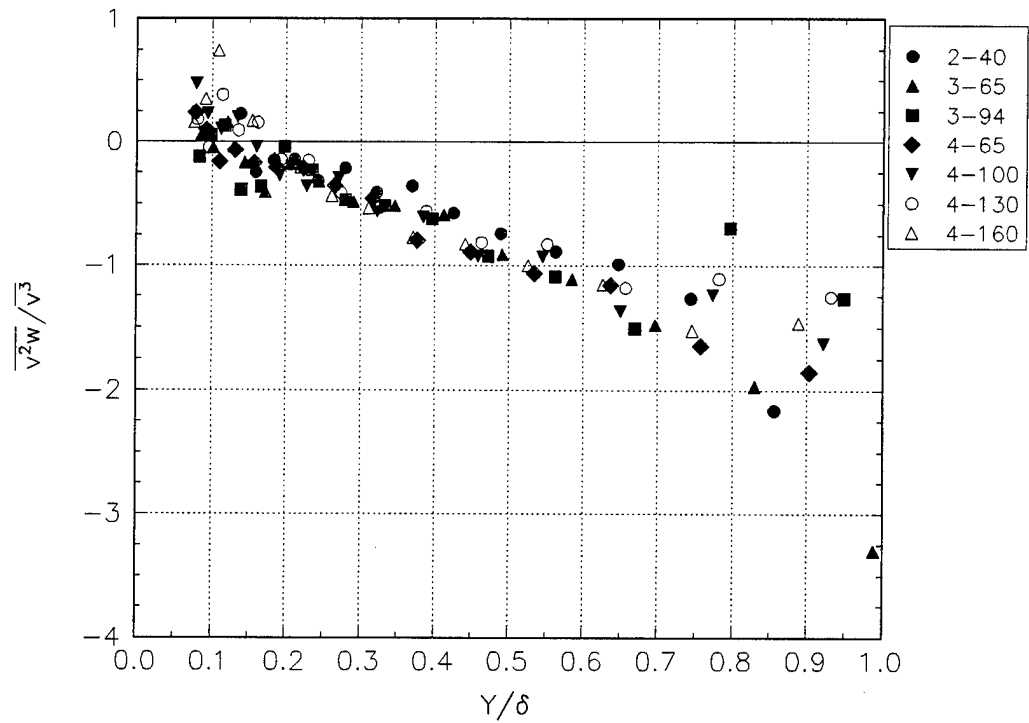


Figure L.13e Triple products.









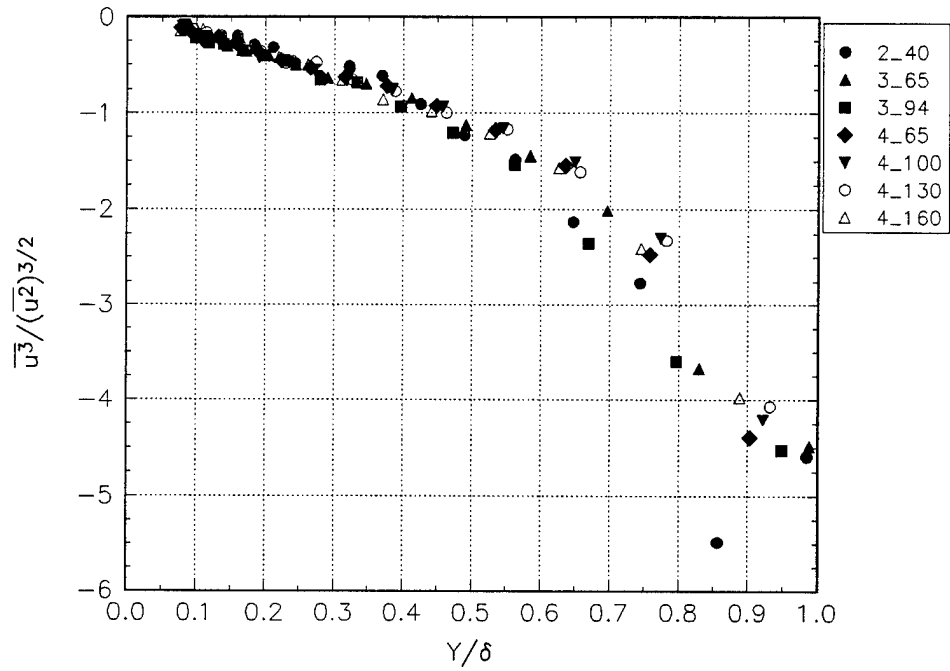


Figure L.19a Skewness in the u velocity.

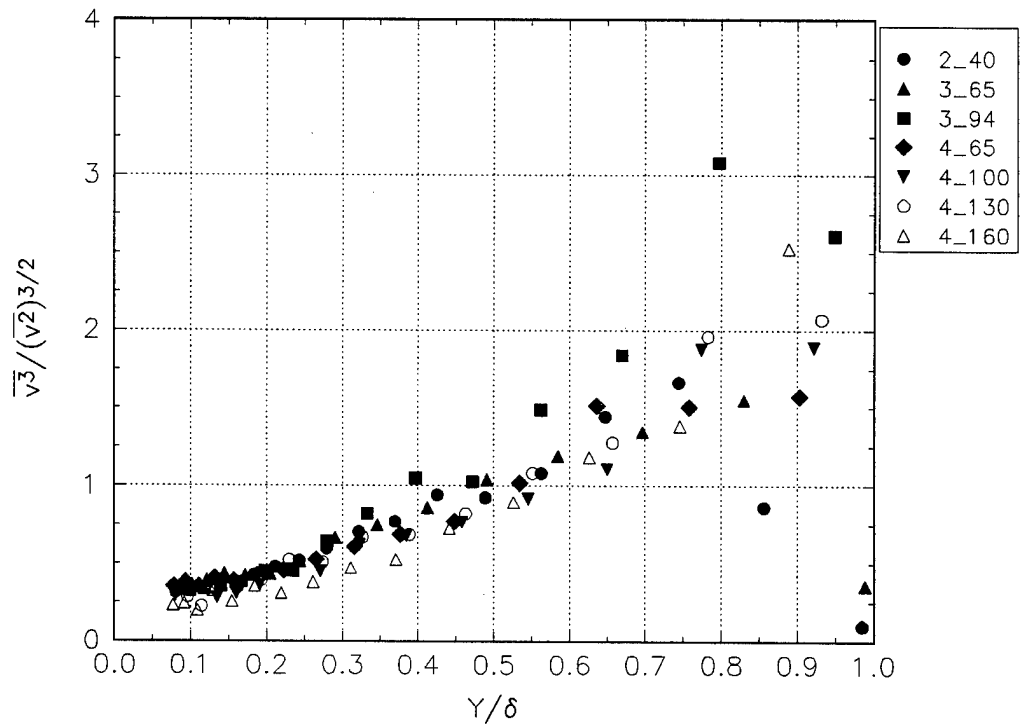


Figure L.19b Skewness in the v velocity.

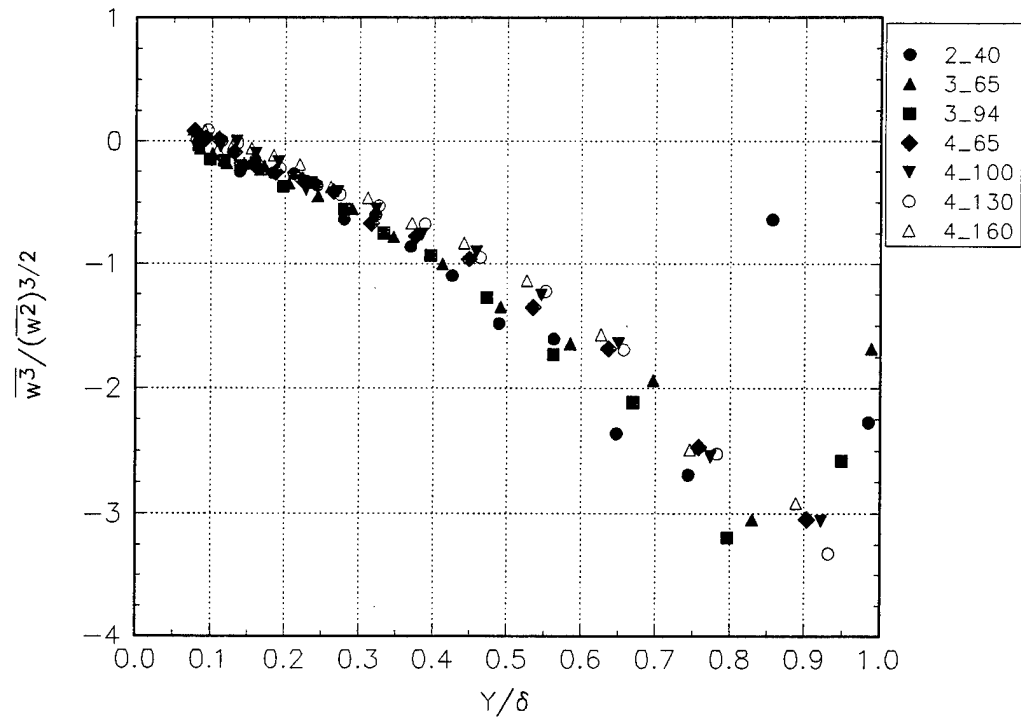


Figure L.19c Skewness in the  $w$  velocity.

## APPENDIX M Nagano and Tagawa Parameters

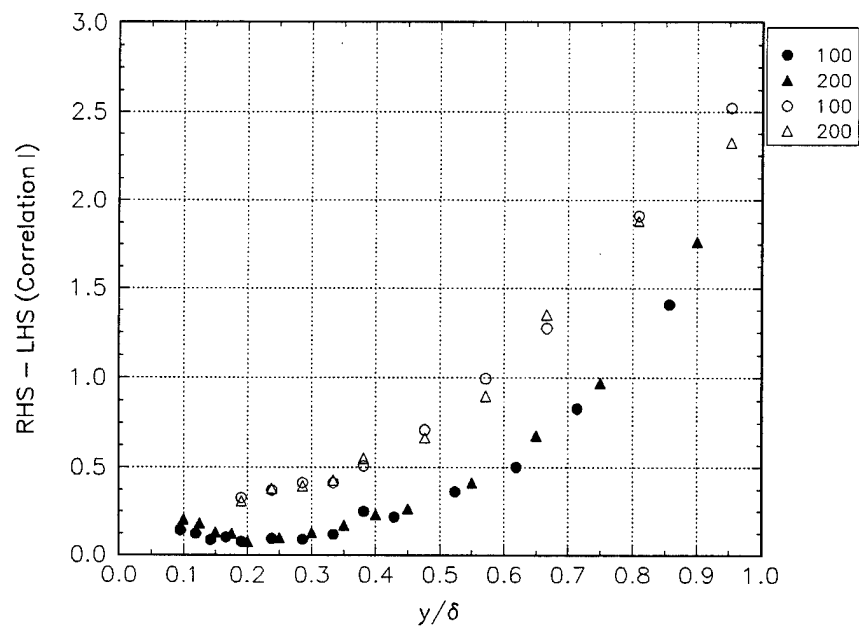


Figure M.1.a Correlation I for Pompeo in wall-stress coordinates. Open symbols represent the diverging test case and the closed symbols the converging case. Z-locations are given in mm.

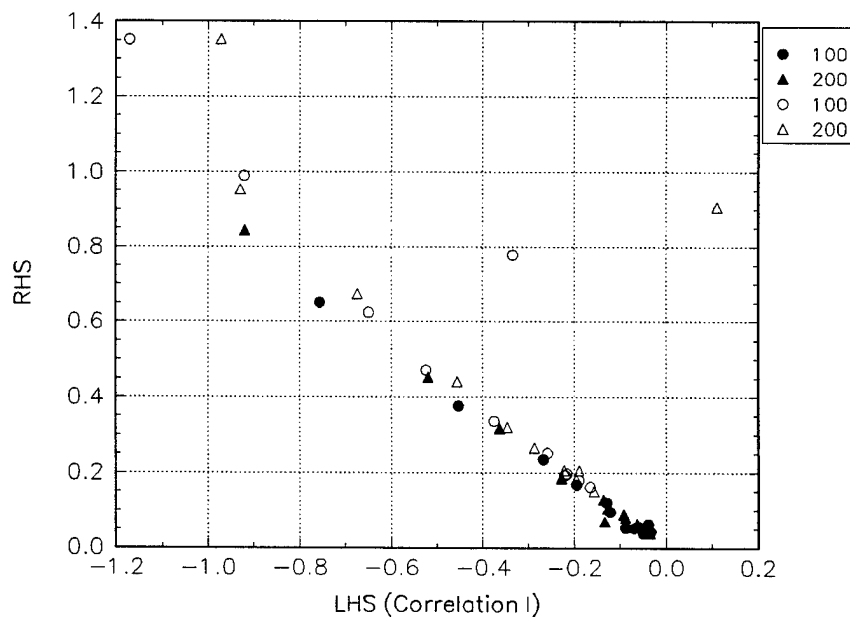


Figure M.1.b Correlation I for Pompeo in wall-stress coordinates. Open symbols represent the diverging test case and the closed symbols the converging case. Z-locations are given in mm.

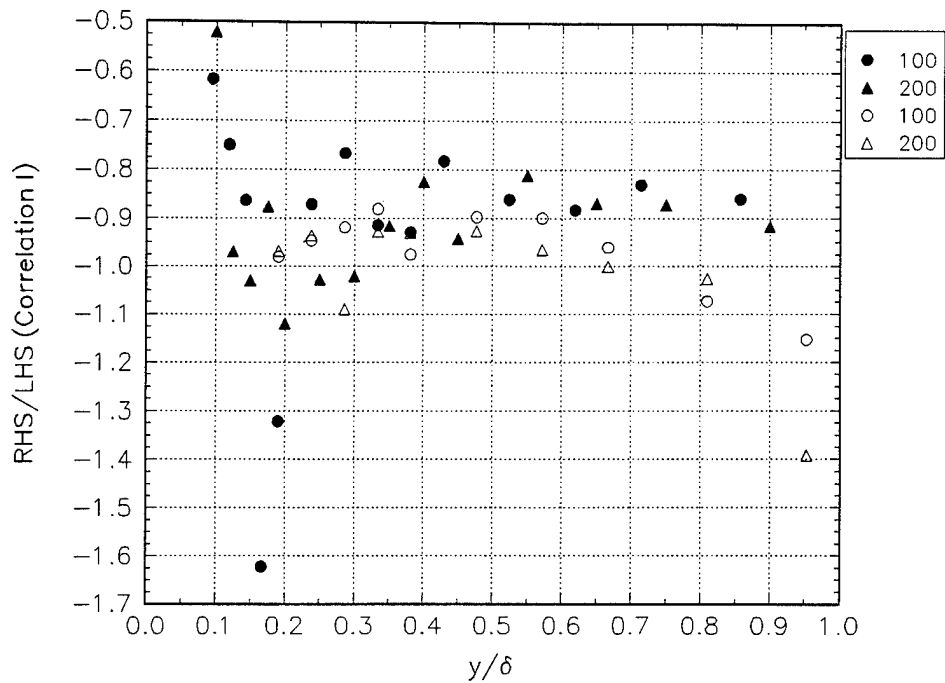


Figure M.1.c Correlation I for Pompeo in wall-stress coordinates. Open symbols represent the diverging test case and the closed symbols the converging case. Z-locations are given in mm.

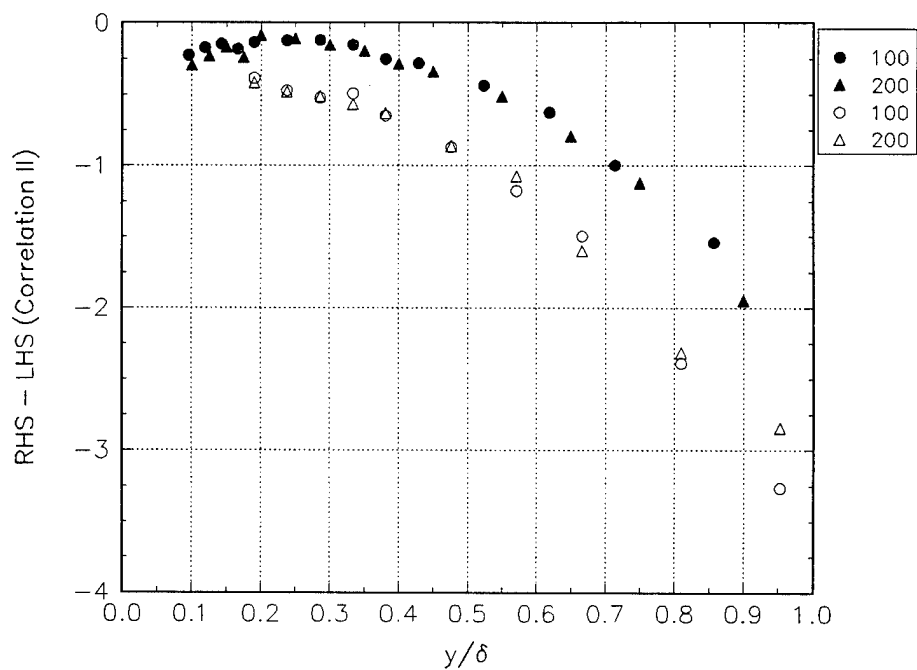


Figure M.2.a Correlation II for Pompeo in wall-stress coordinates. Open symbols represent the diverging test case and the closed symbols the converging case. Z-locations are given in mm.

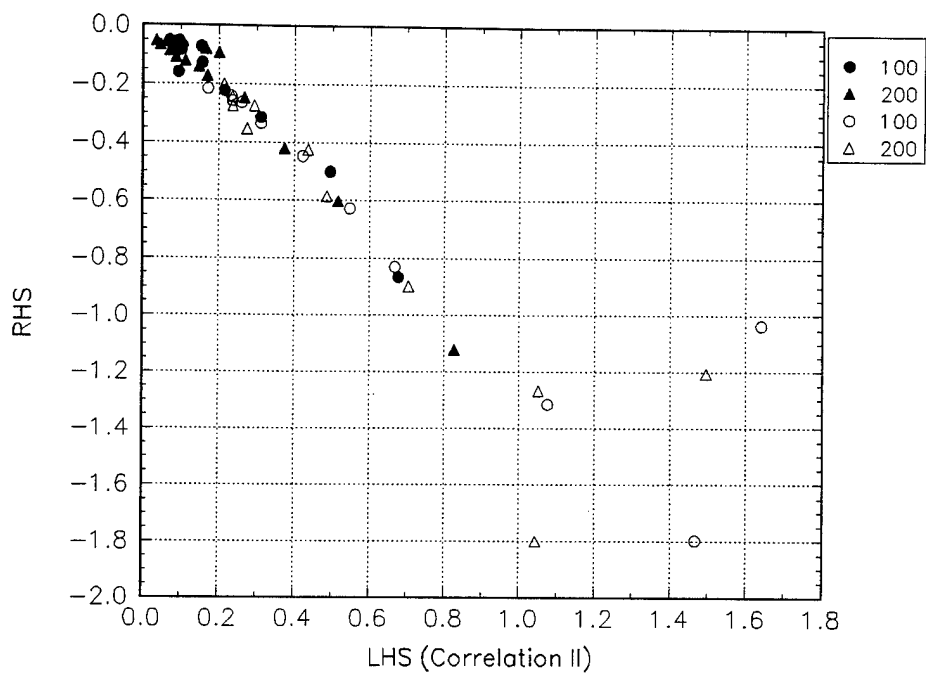


Figure M.2.b Correlation II for Pompeo in wall-stress coordinates. Open symbols represent the diverging test case and the closed symbols the converging case. Z-locations are given in mm.

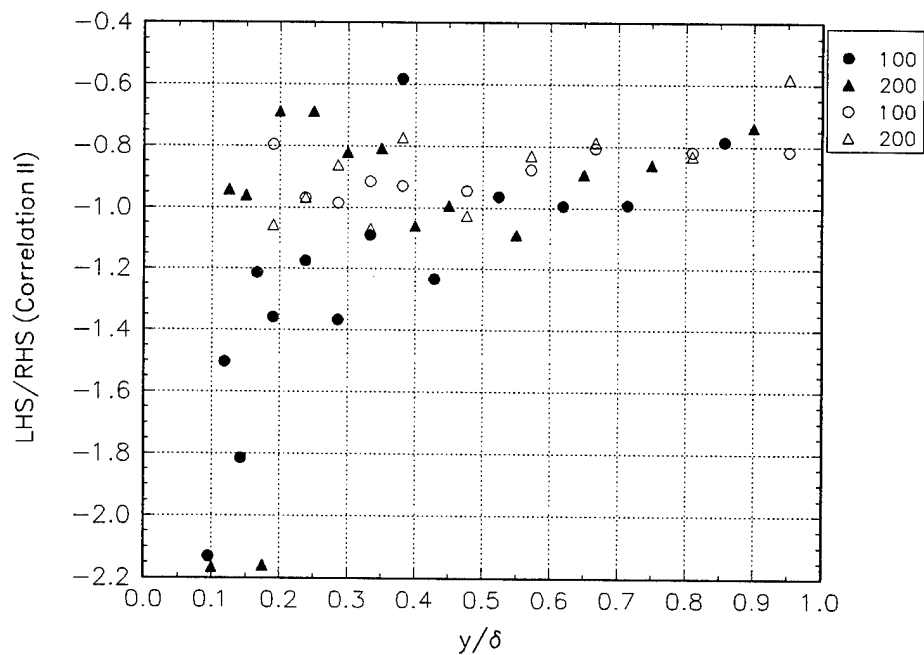


Figure M.2.c Correlation II for Pompeo in wall-stress coordinates. Open symbols represent the diverging test case and the closed symbols the converging case. Z-locations are given in mm.



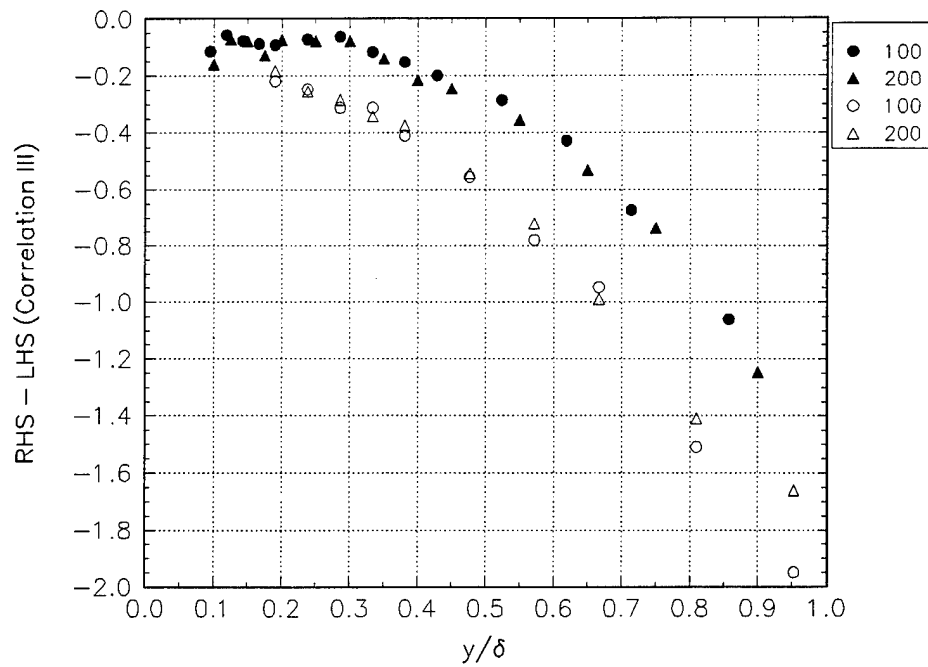


Figure M.3.a Correlation III for Pompeo in wall-stress coordinates. Open symbols represent the diverging test case and the closed symbols the converging case. Z-locations are given in mm.

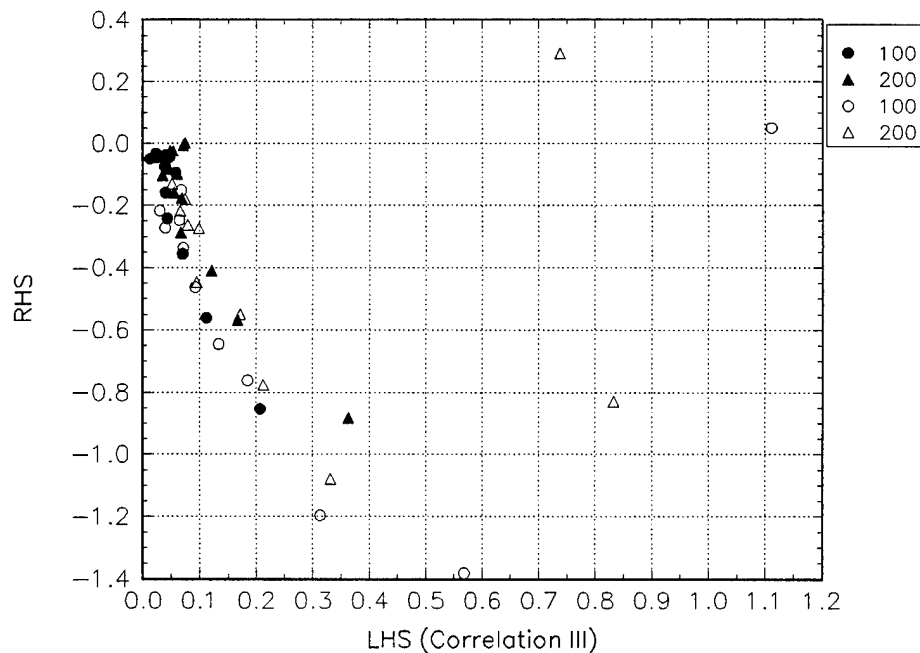


Figure M.3.b Correlation III for Pompeo in wall-stress coordinates. Open symbols represent the diverging test case and the closed symbols the converging case. Z-locations are given in mm.

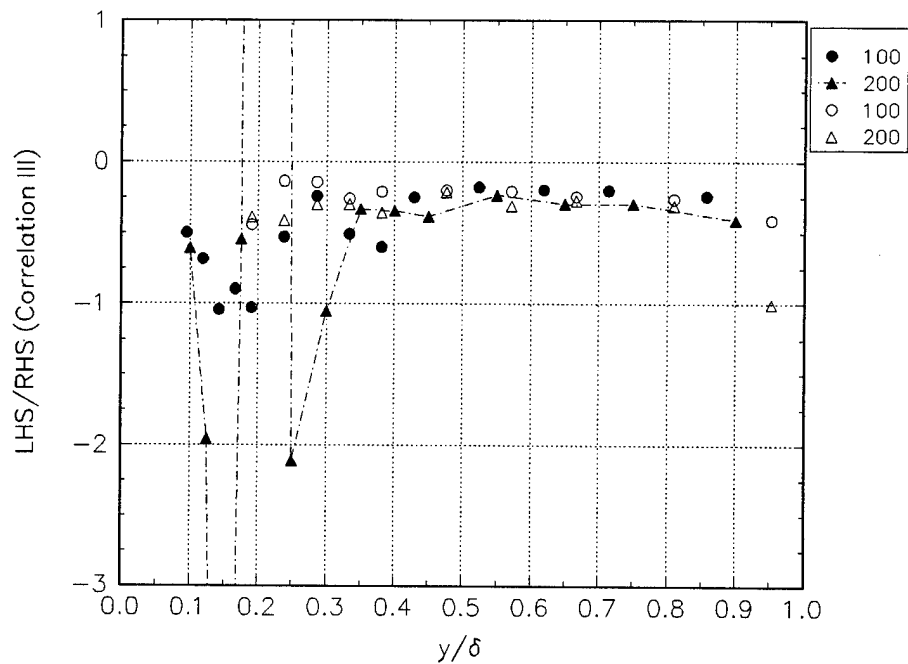


Figure M.3.c Correlation III for Pompeo in wall-stress coordinates. Open symbols represent the diverging test case and the closed symbols the converging case. Z-locations are given in mm.

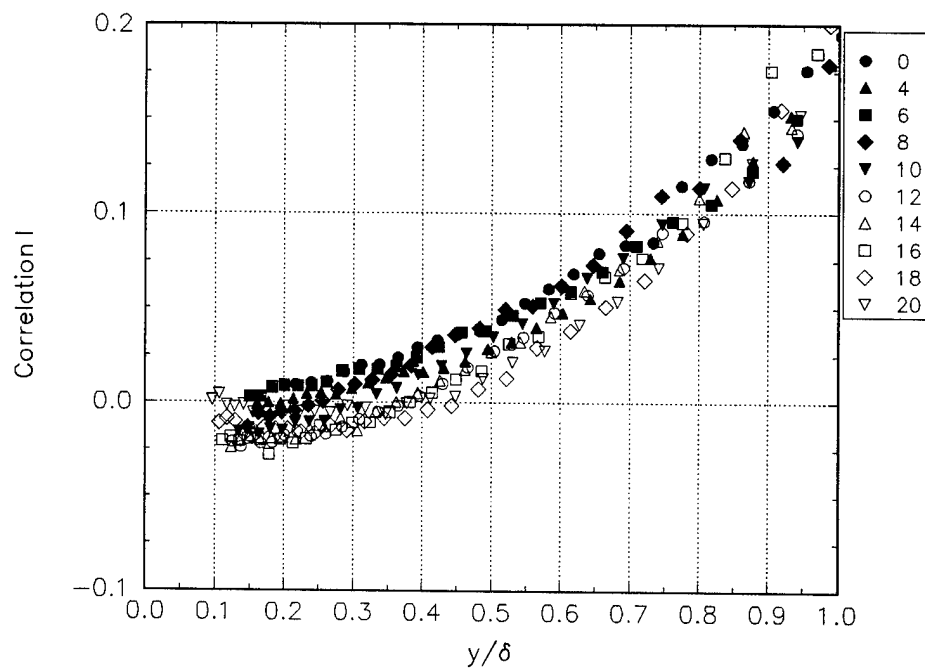


Figure M.4.a Correlation I for Schwarz in wall-stress coordinates. Closed symbols represent the development region and the open symbols the decay region. Station numbers are shown.

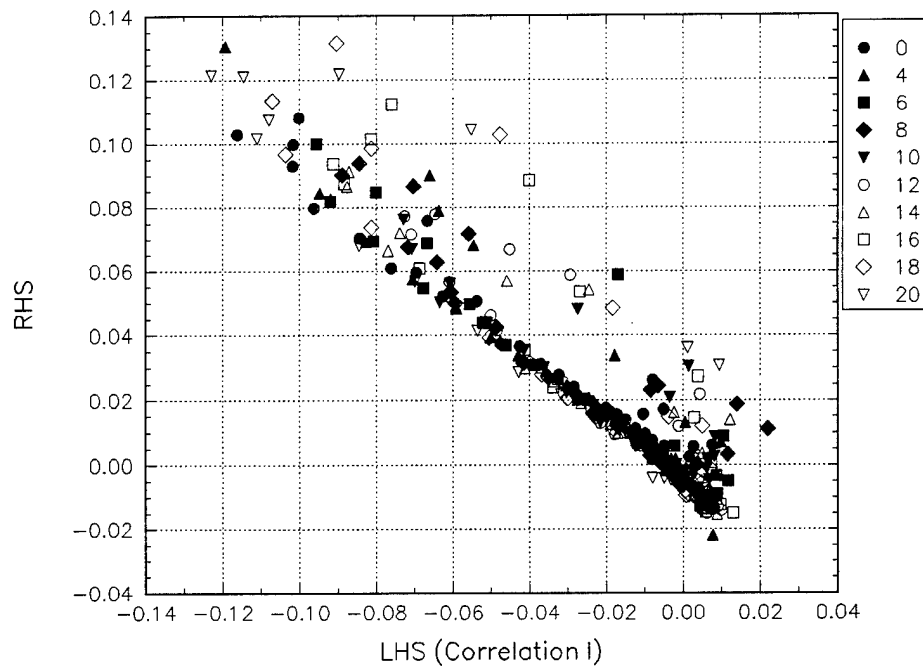


Figure M.4.b Correlation I for Schwarz in wall-stress coordinates. Closed symbols represent the development region and the open symbols the decay region. Station numbers are shown.

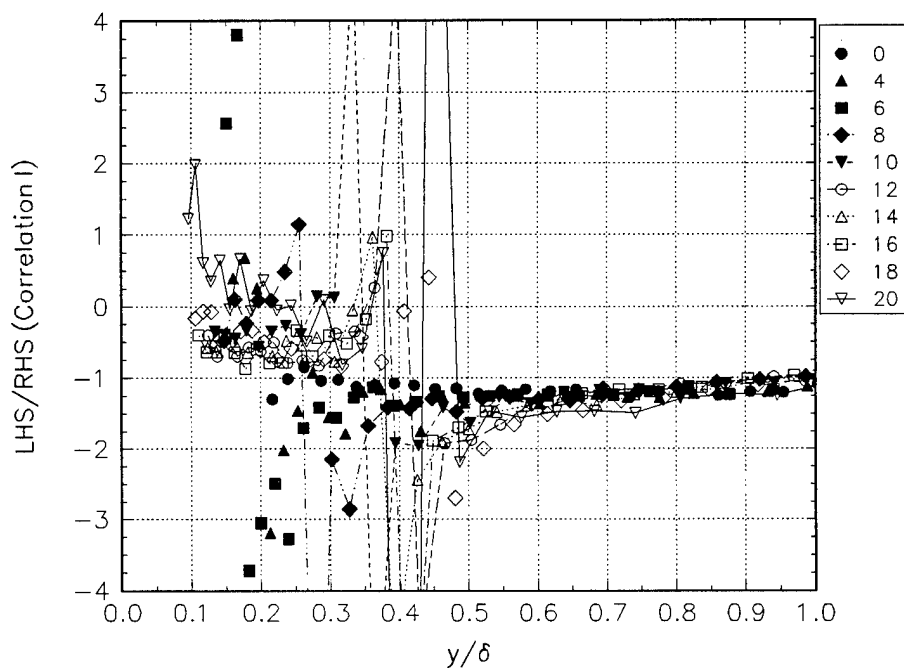


Figure M.4.c Correlation I for Schwarz in wall-stress coordinates. Closed symbols represent the development region and the open symbols the decay region. Station numbers are shown.

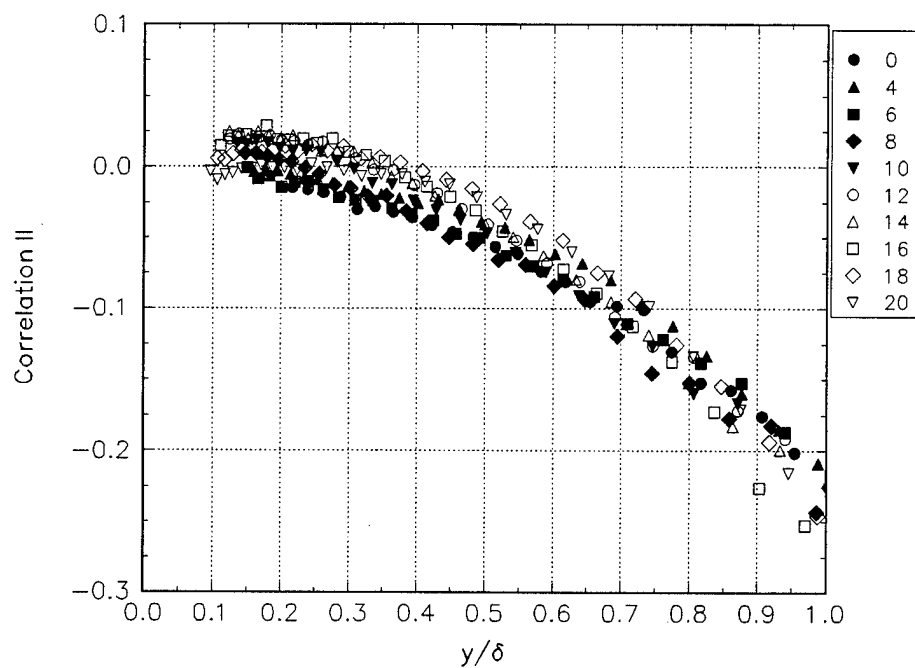


Figure M.5.a Correlation II for Schwarz in wall-stress coordinates. Closed symbols represent the development region and the open symbols the decay region. Station numbers are shown.

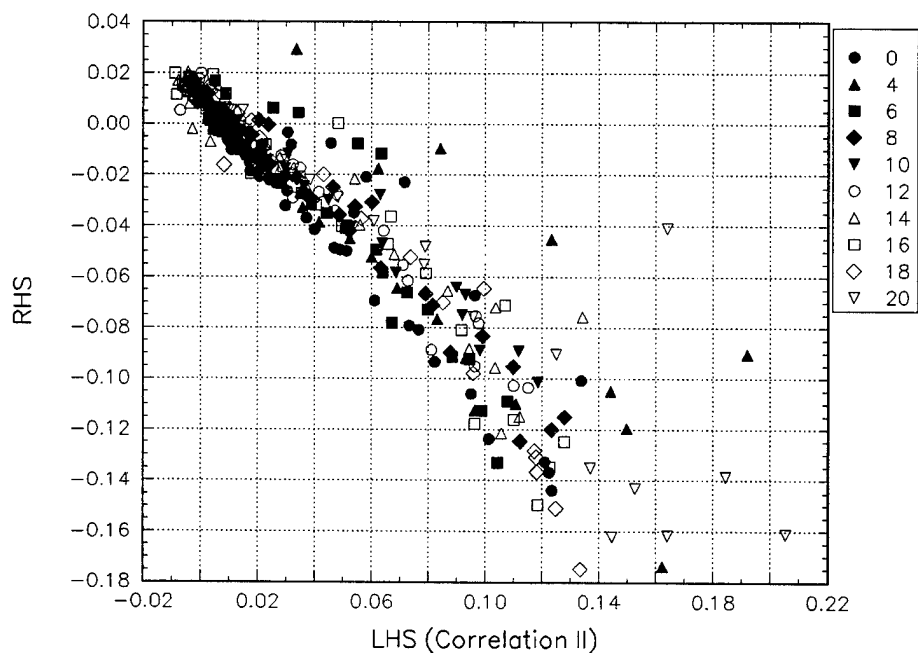


Figure M.5.b Correlation II for Schwarz in wall-stress coordinates. Closed symbols represent the development region and the open symbols the decay region. Station numbers are shown.

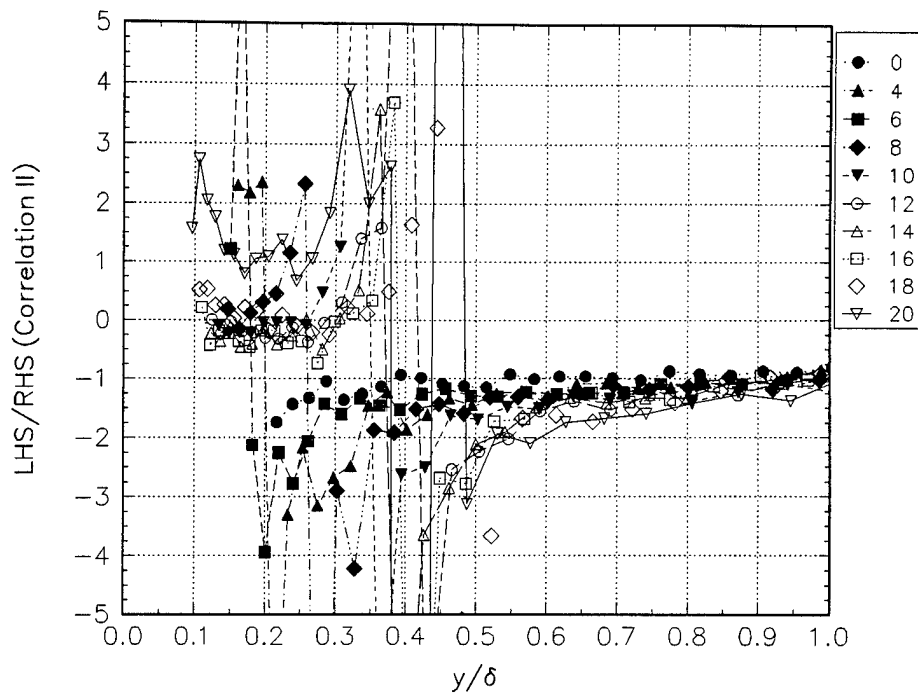


Figure M.5.c Correlation II for Schwarz in wall-stress coordinates. Closed symbols represent the development region and the open symbols the decay region. Station numbers are shown.

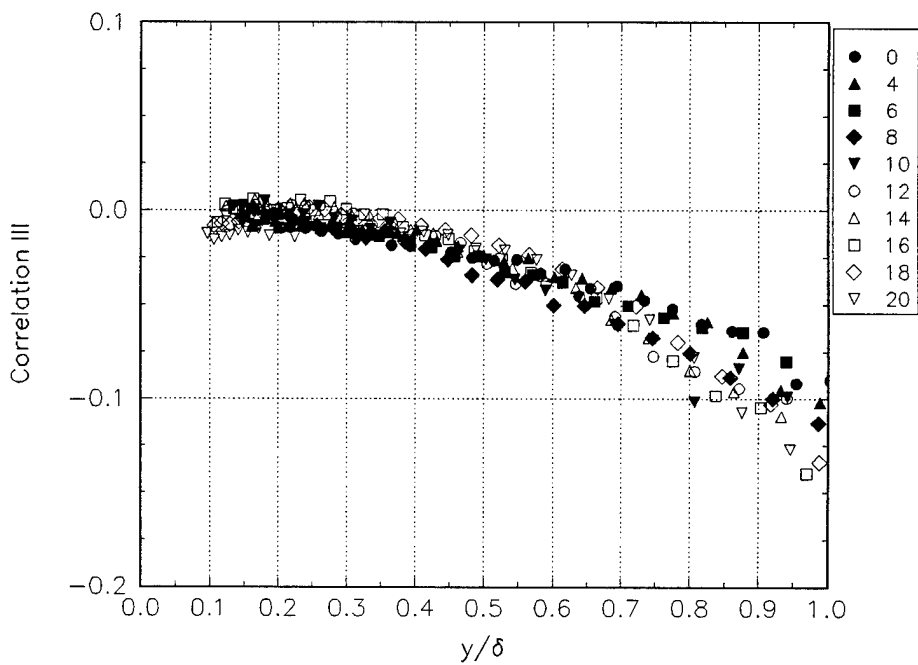


Figure M.6.a Correlation III for Schwarz in wall-stress coordinates. Closed symbols represent the development region and the open symbols the decay region. Station numbers are shown.

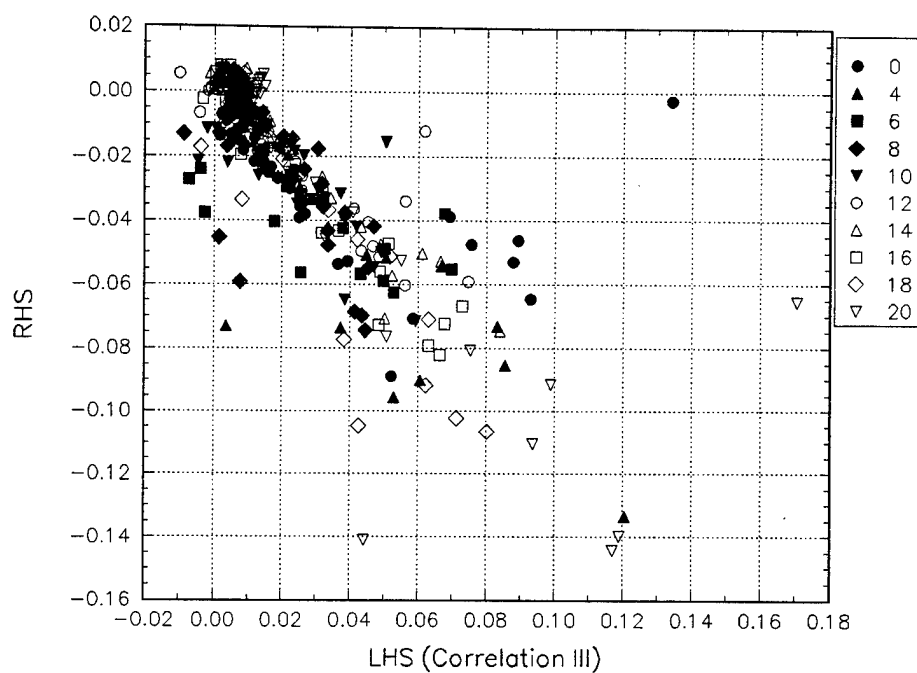


Figure M.6.b Correlation III for Schwarz in wall-stress coordinates. Closed symbols represent the development region and the open symbols the decay region. Station numbers are shown.

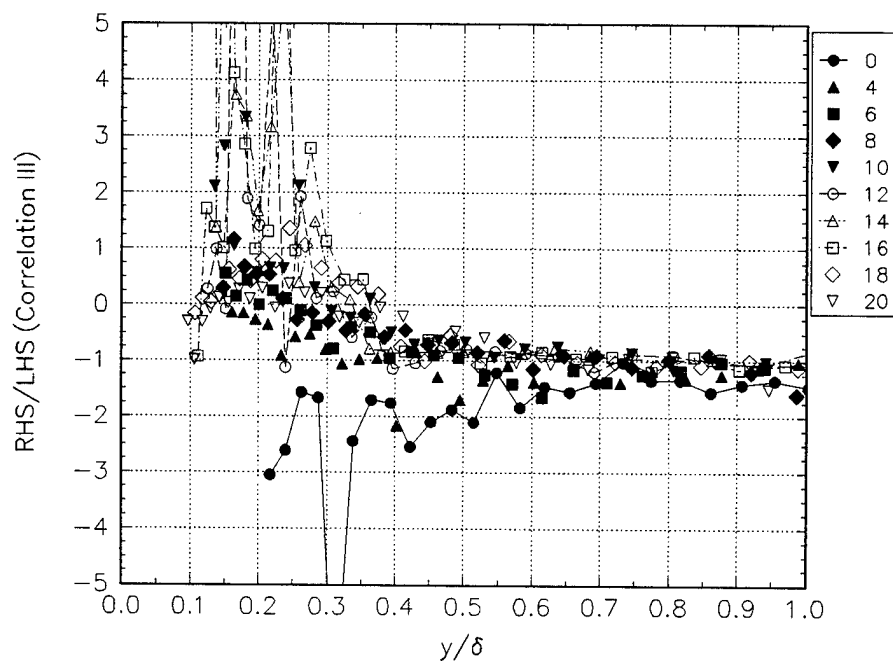


Figure M.6.c Correlation III for Schwarz in wall-stress coordinates. Closed symbols represent the development region and the open symbols the decay region. Station numbers are shown.

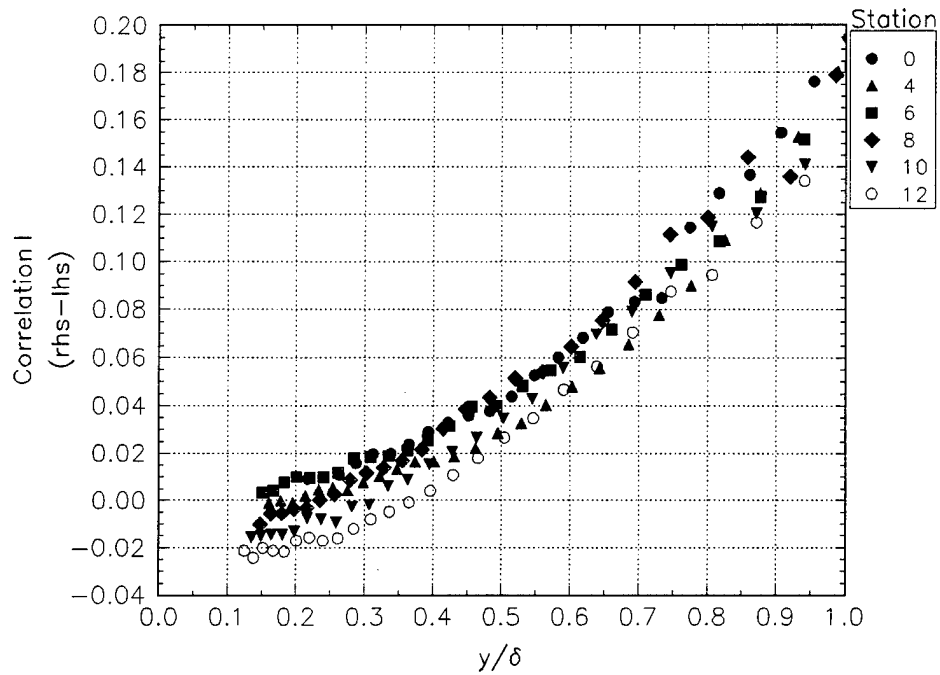


Figure M.7.a Correlation I for Schwarz in free-stream coordinates for crossflow development.

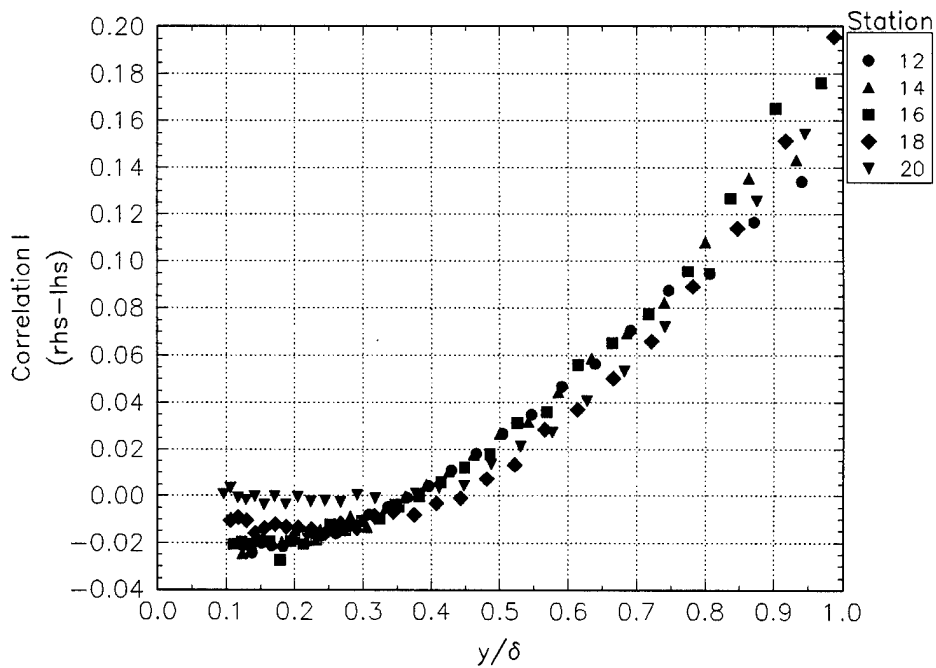


Figure M.7.b Correlation I for Schwarz in free-stream coordinates for crossflow decay.

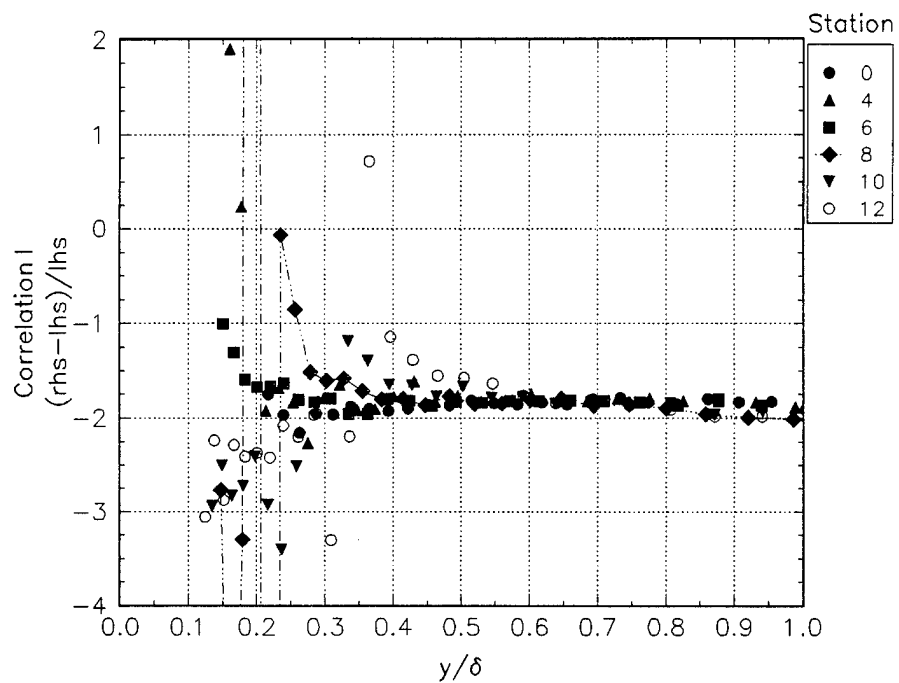


Figure M.8.a Correlation I for Schwarz in free-stream coordinates for crossflow development.

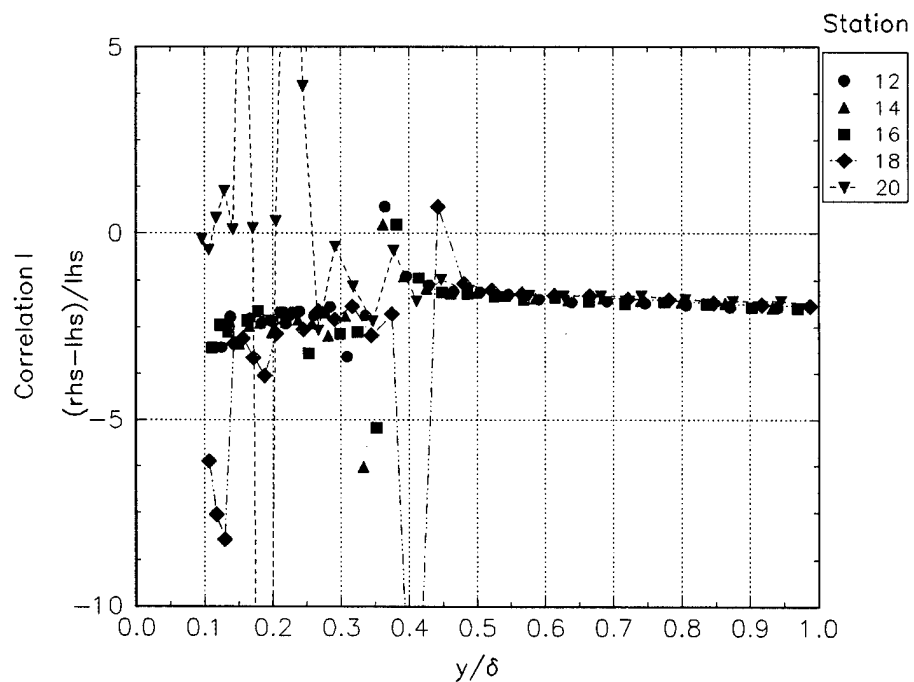


Figure M.8.b Correlation I for Schwarz in free-stream coordinates for crossflow decay.



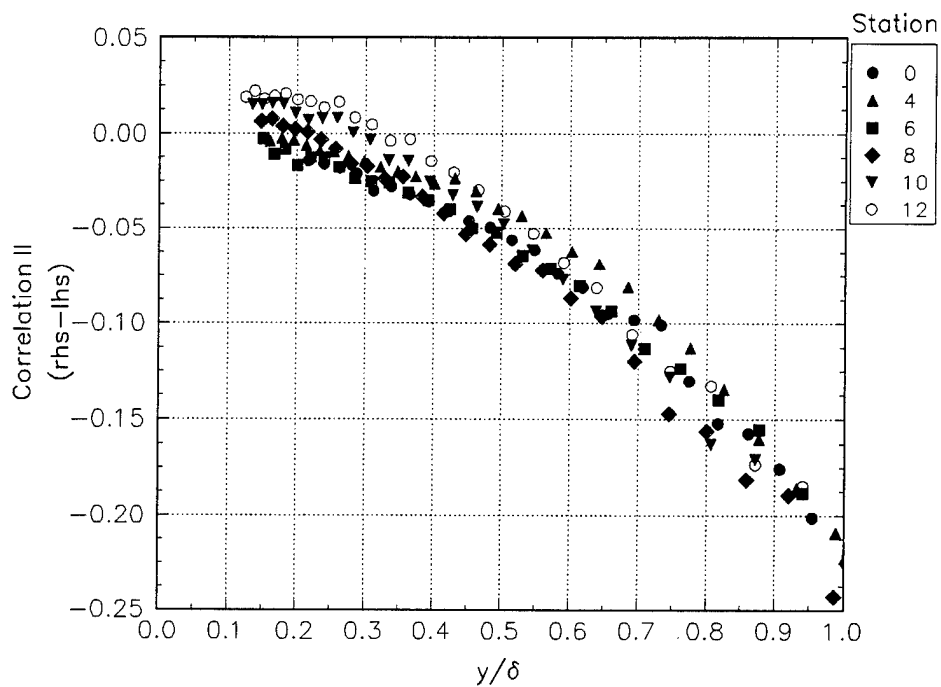


Figure M.9.a Correlation II for Schwarz in free-stream coordinates for crossflow development.

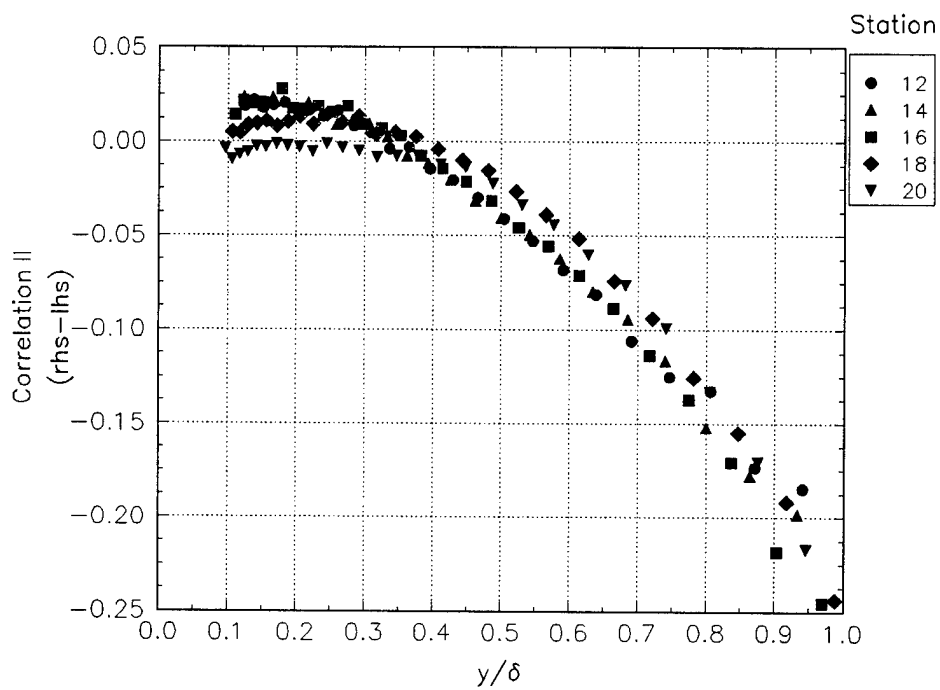


Figure M.9.b Correlation II for Schwarz in free-stream coordinates for crossflow decay.

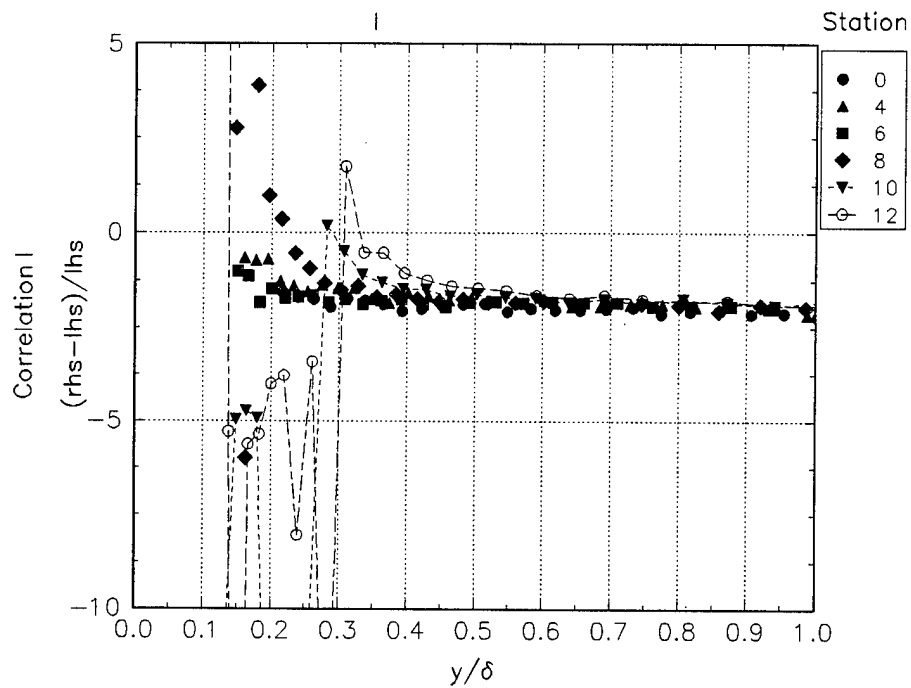


Figure M.10.a Correlation II for Schwarz in free-stream coordinates for crossflow development.

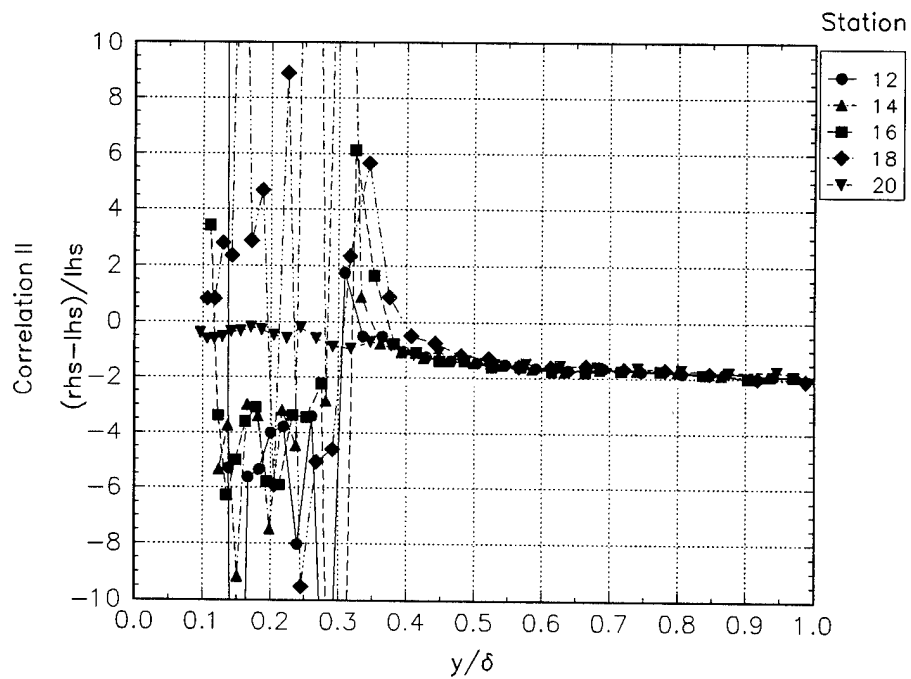


Figure M.10.b Correlation II for Schwarz in free-stream coordinates for crossflow decay.

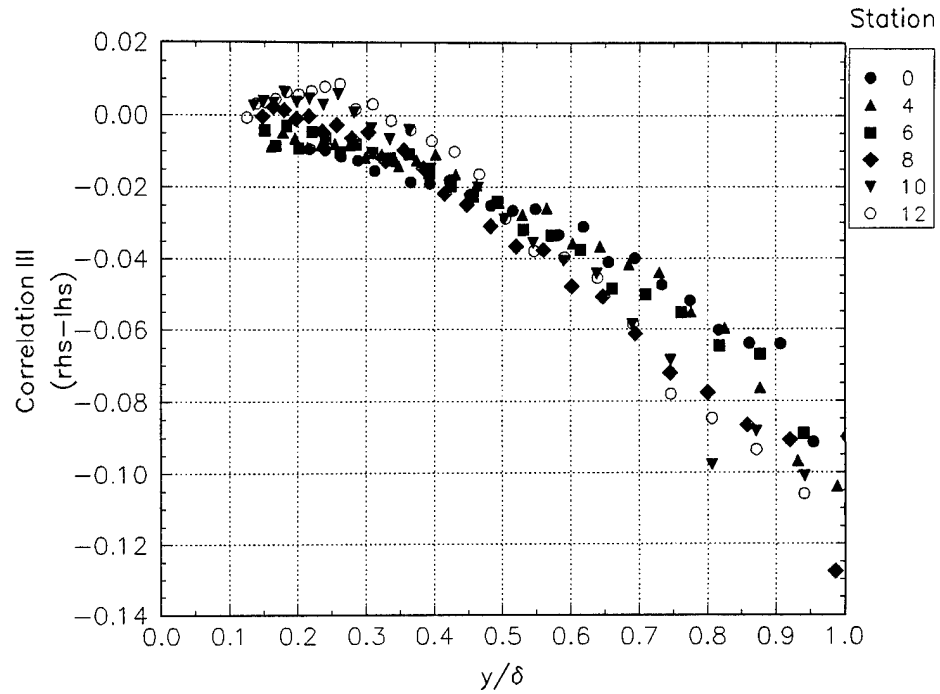


Figure M.11.a Correlation III for Schwarz in free-stream coordinates for crossflow development.

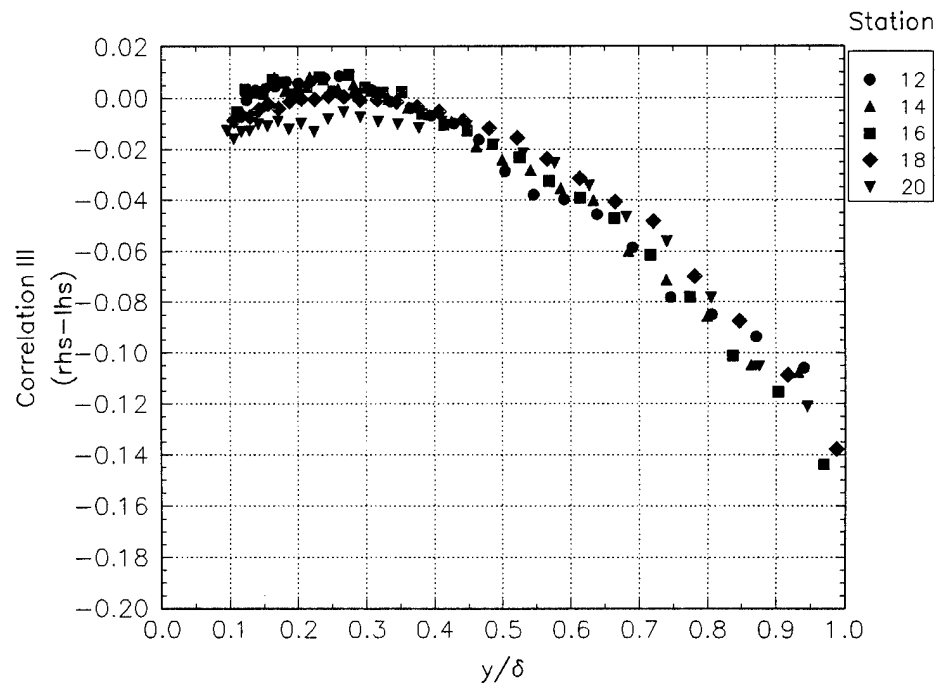


Figure M.11.b Correlation III for Schwarz in free-stream coordinates for crossflow decay.

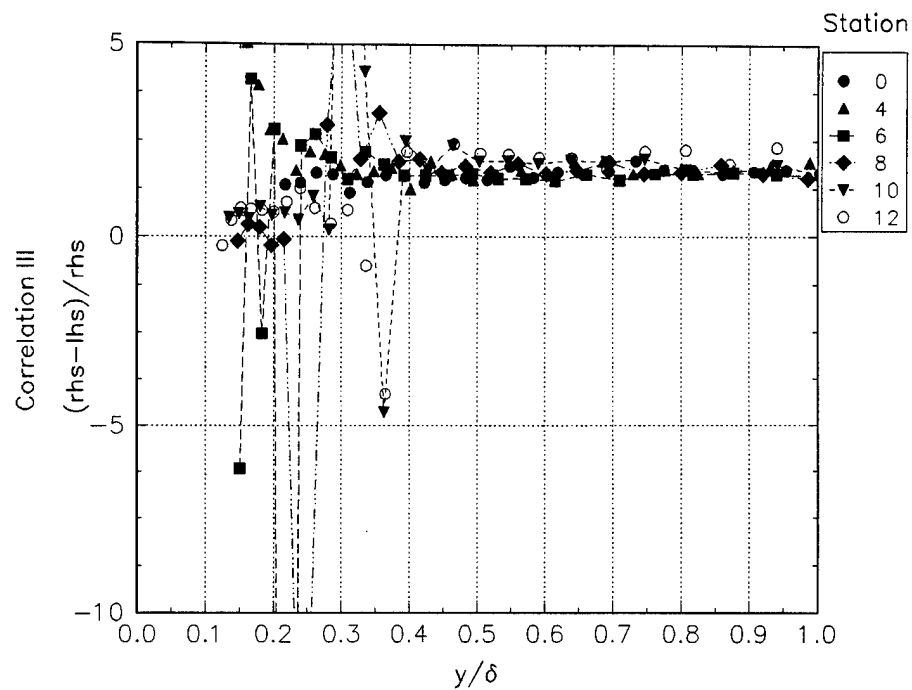


Figure M.12.a Correlation III for Schwarz in free-stream coordinates for crossflow development.

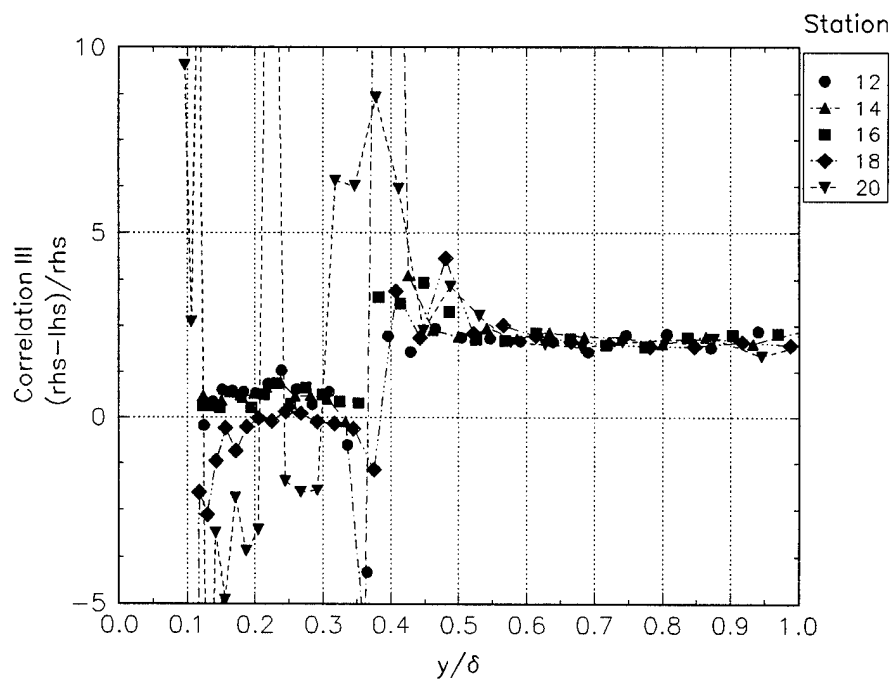


Figure M.12.b Correlation III for Schwarz in free-stream coordinates for crossflow decay.

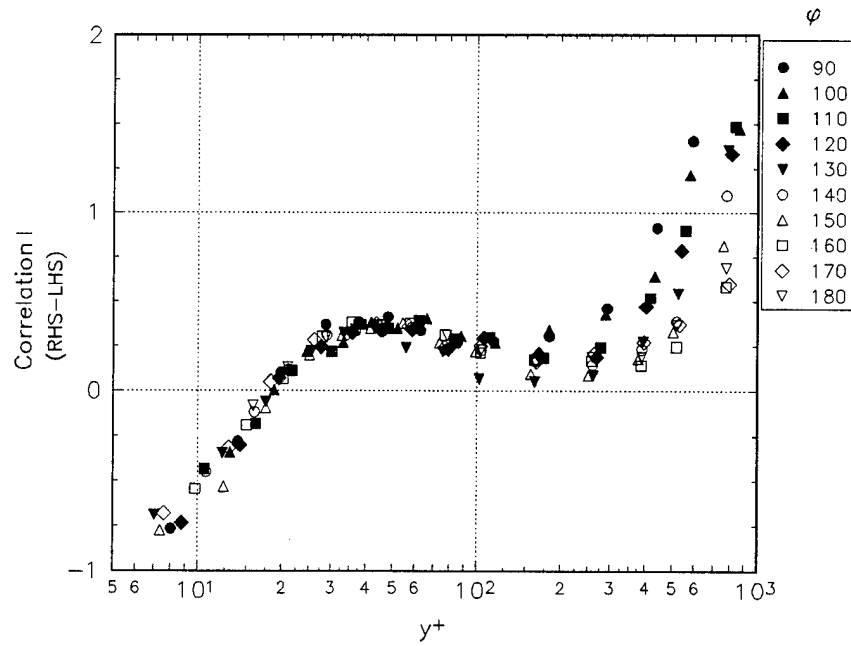


Figure M.13.a Correlation I with the Chesnakas data at  $x/L = 0.40$ .

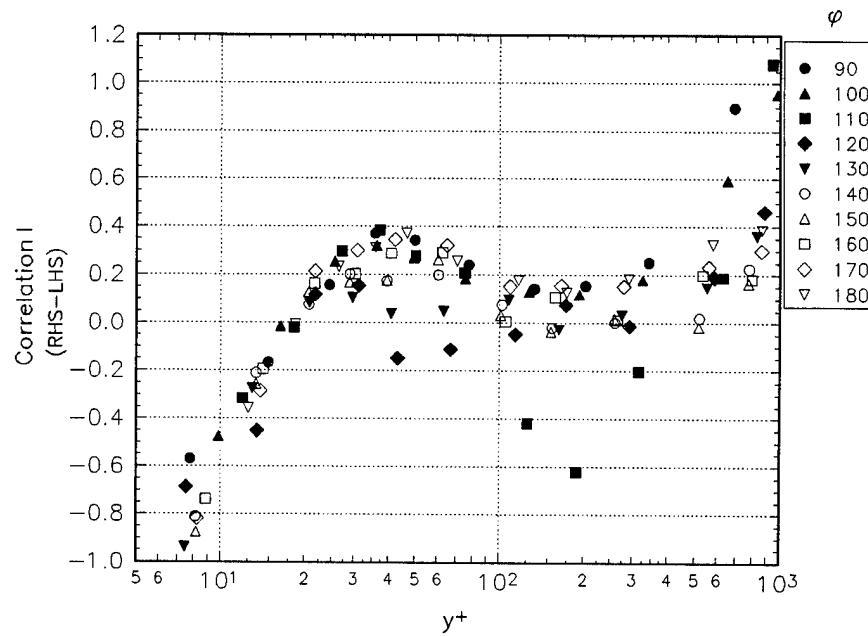


Figure M.13.b Correlation I with the Chesnakas data at  $x/L = 0.60$ .

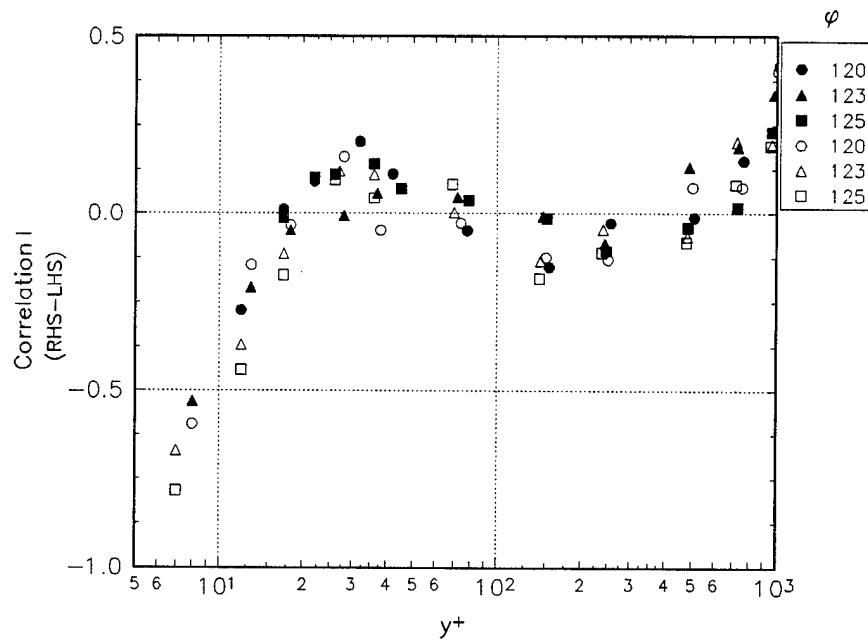


Figure M.13.c Correlation I for Chesnakas, closed symbols for  $x/L = 0.75$  and open for 0.76.

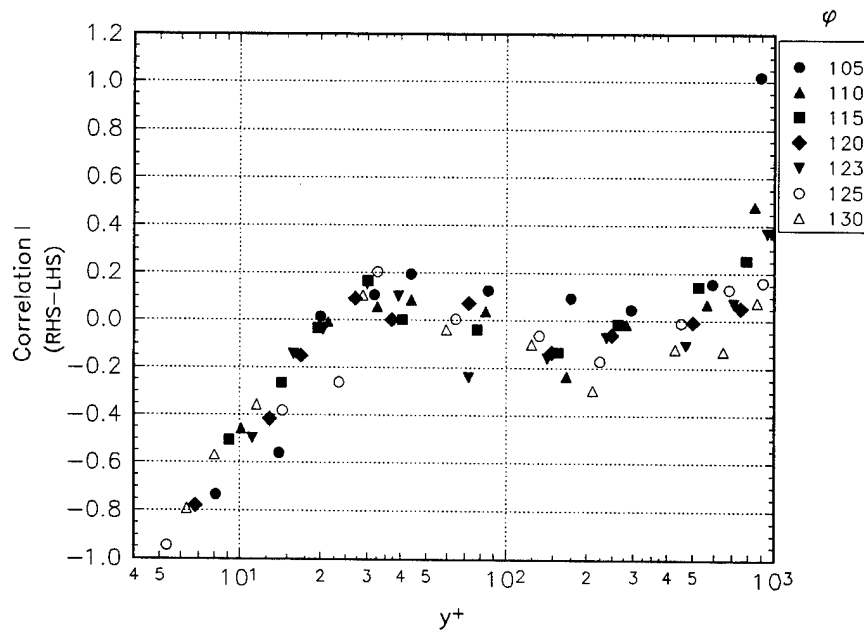


Figure M.13.d Correlation I with the Chesnakas data at  $x/L = 0.77$ .

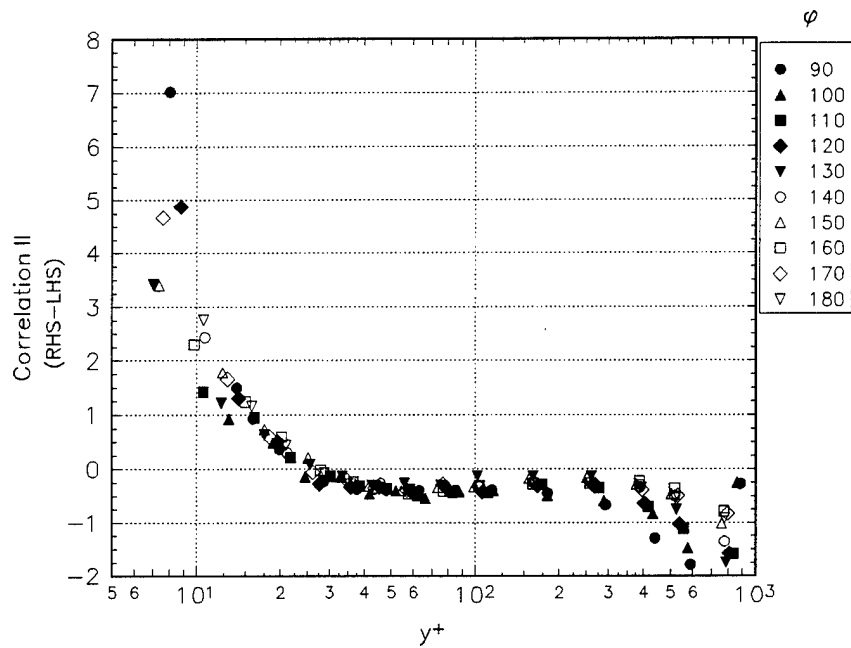


Figure M.14.a Correlation II with the Chesnakas data at  $x/L = 0.40$ .

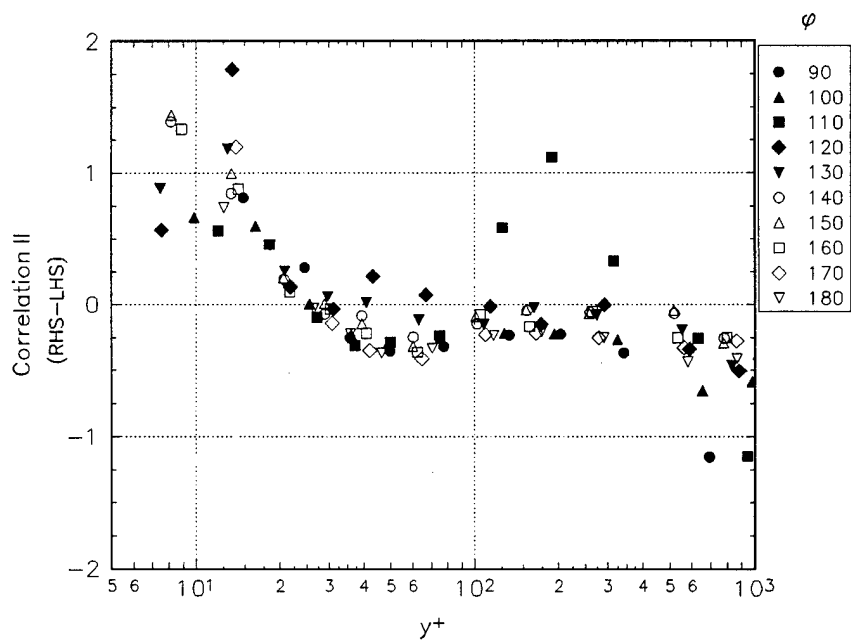


Figure M.14.b Correlation II with the Chesnakas data at  $x/L = 0.60$ .

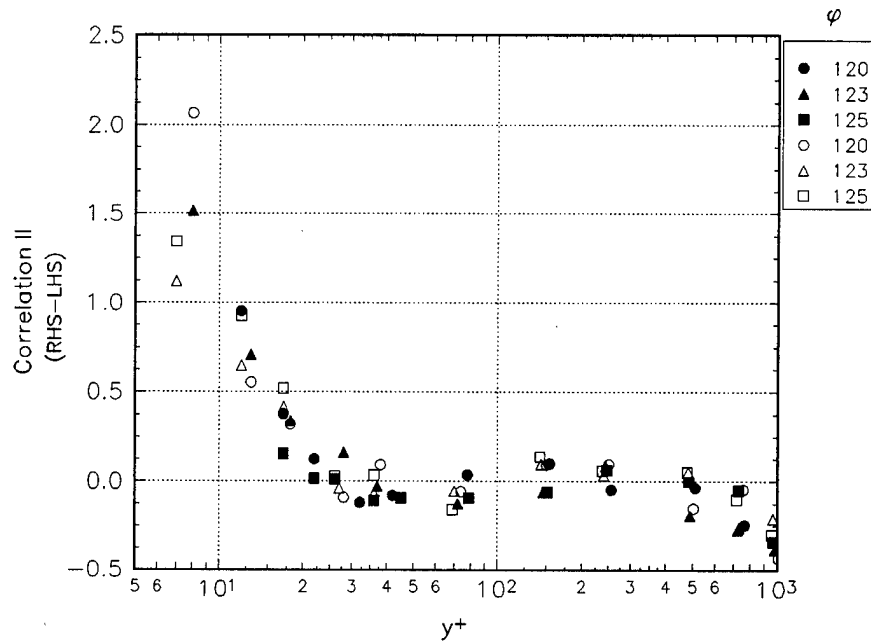


Figure M.14.c Correlation II for Chesnakas, closed symbols for  $x/L = 0.75$  and open for 0.76.

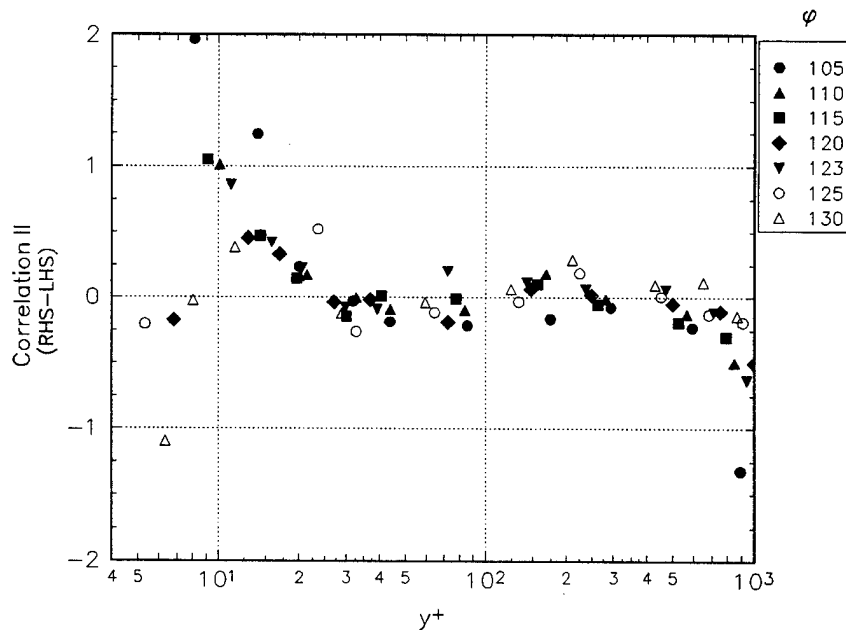


Figure M.14.d Correlation II with the Chesnakas data at  $x/L = 0.77$ .



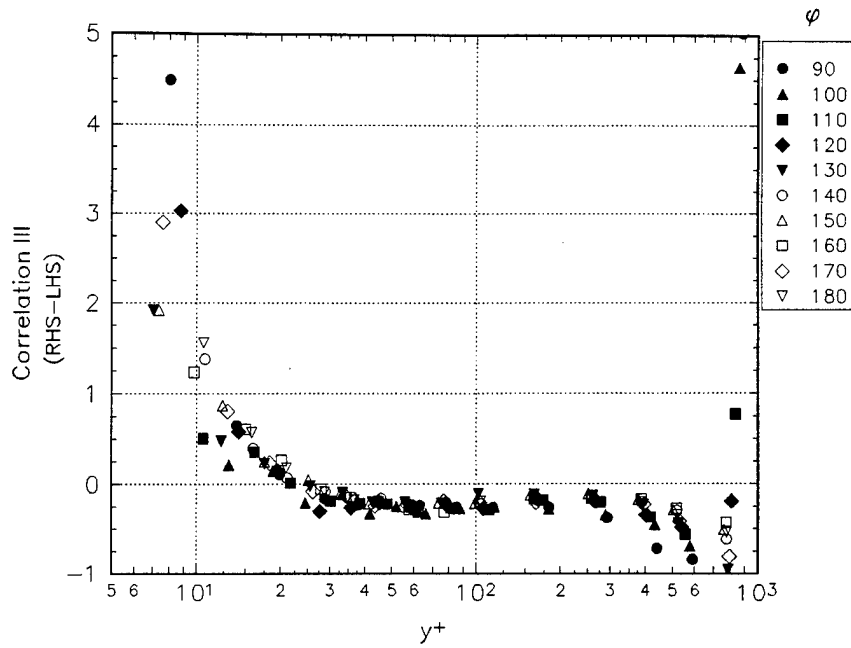


Figure M.15.a Correlation III with the Chesnakas data at  $x/L = 0.40$ .

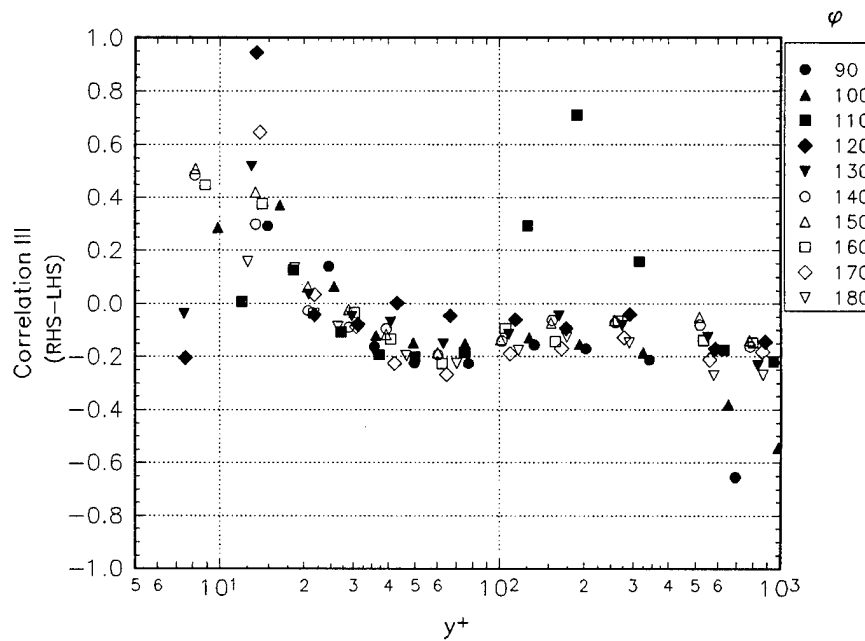


Figure M.15.b Correlation III with the Chesnakas data at  $x/L = 0.60$ .

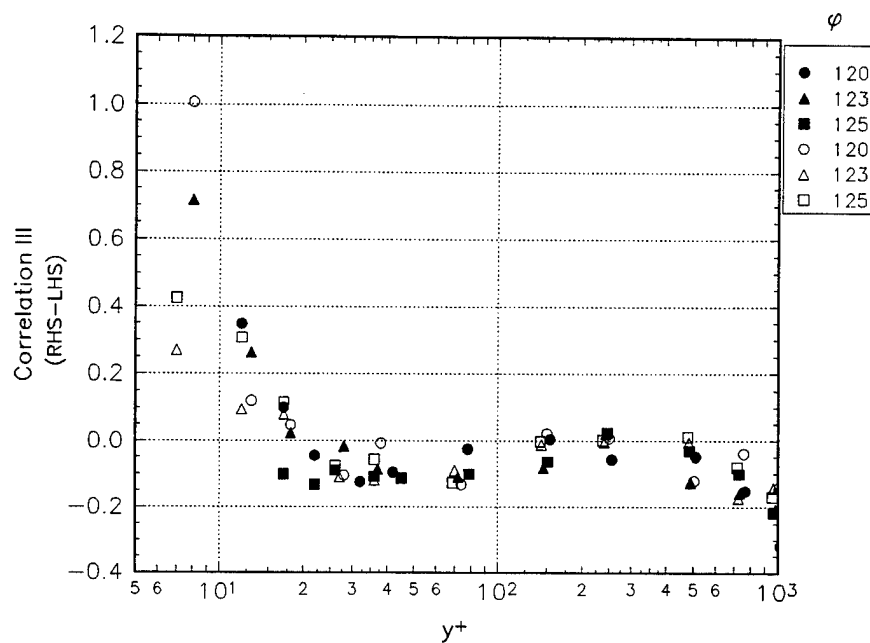


Figure M.15.c Correlation III for Chesnakas, closed symbols for  $x/L = 0.75$  and open for 0.76.

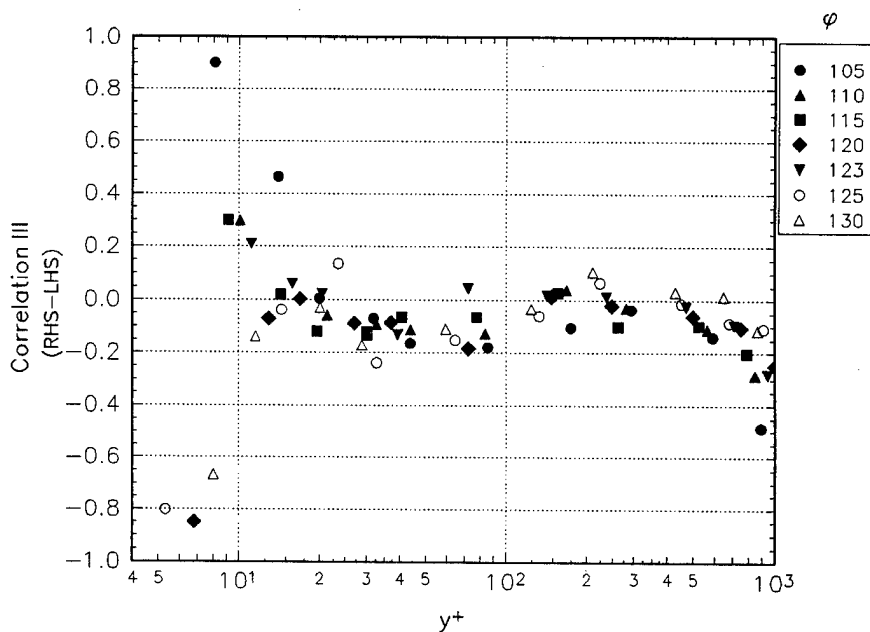


Figure M.15.d Correlation III with the Chesnakas data at  $x/L = 0.77$ .

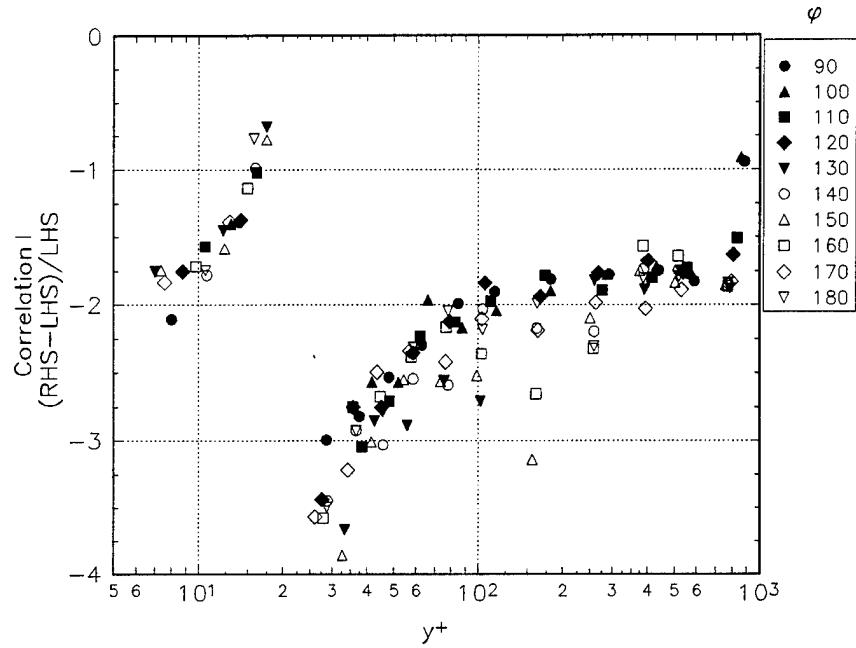


Figure M.16.a Correlation I with the Chesnakas data at  $x/L = 0.40$ .

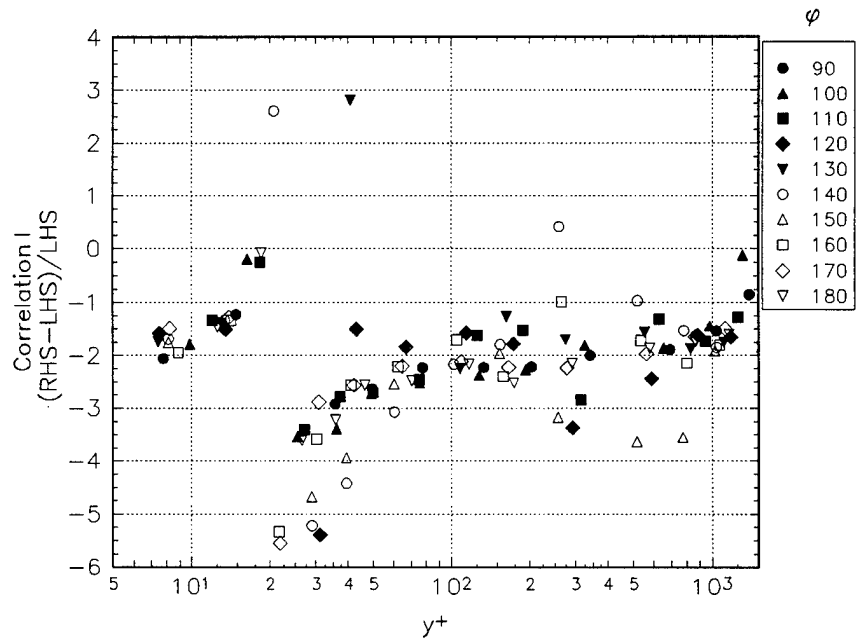


Figure M.16.b Correlation I with the Chesnakas data at  $x/L = 0.60$ .

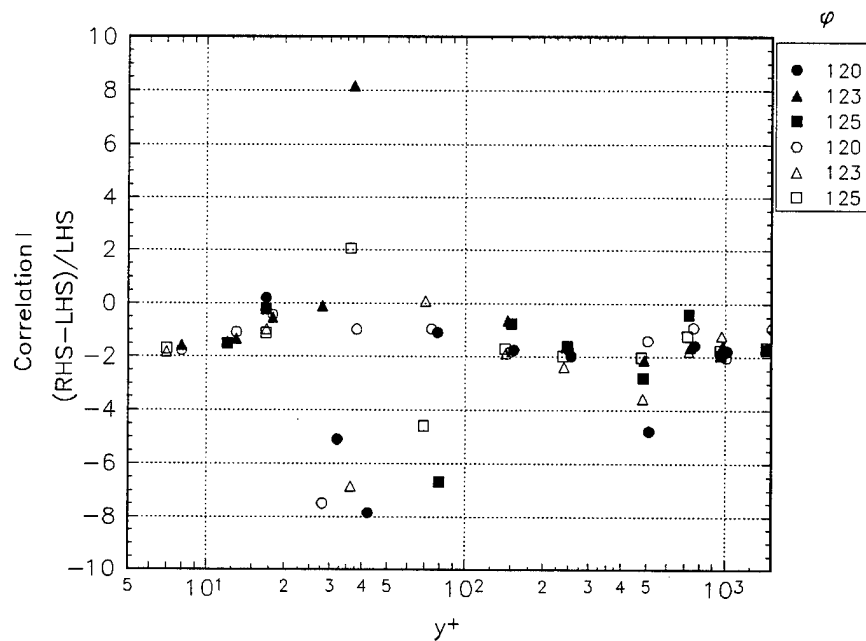


Figure M.16.c Correlation I for Chesnakas, closed symbols for  $x/L = 0.75$  and open for 0.76.

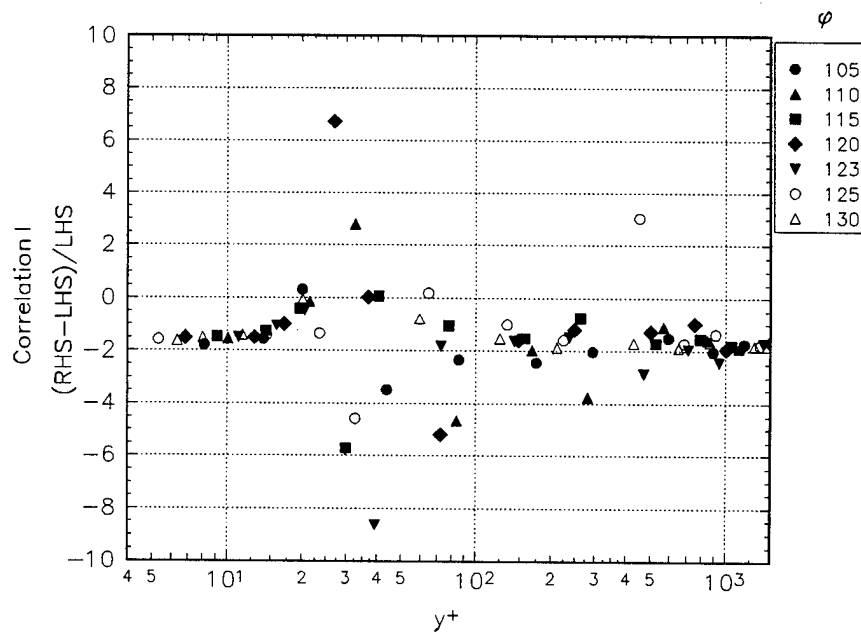


Figure M.16.d Correlation I with the Chesnakas data at  $x/L = 0.77$ .

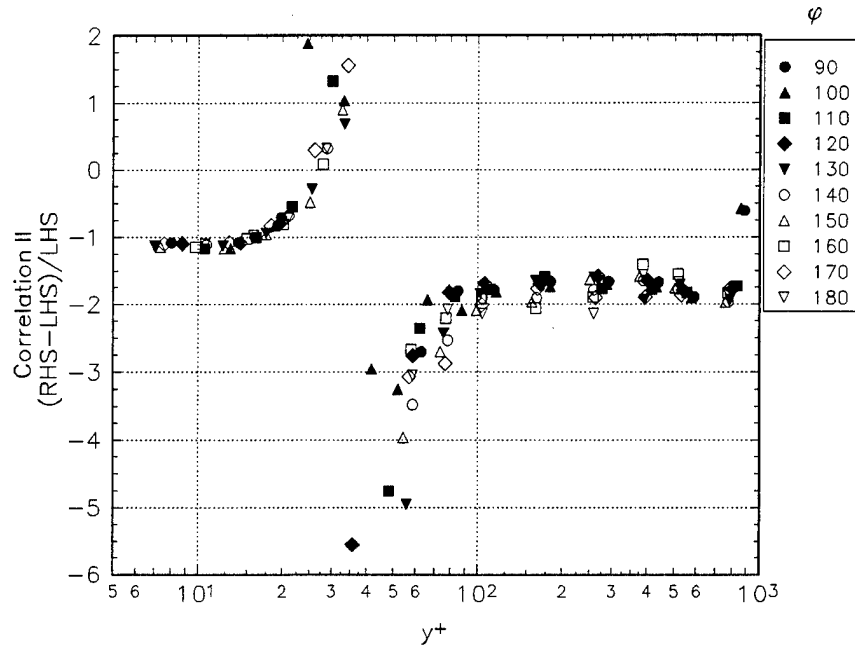


Figure M.17.a Correlation II with the Chesnakas data at  $x/L = 0.40$ .

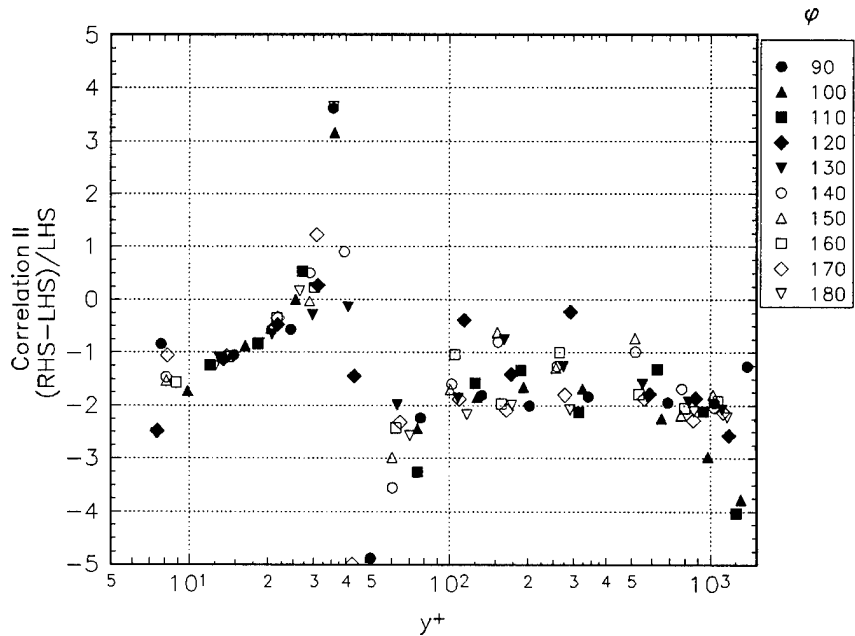


Figure M.17.b Correlation II with the Chesnakas data at  $x/L = 0.60$ .

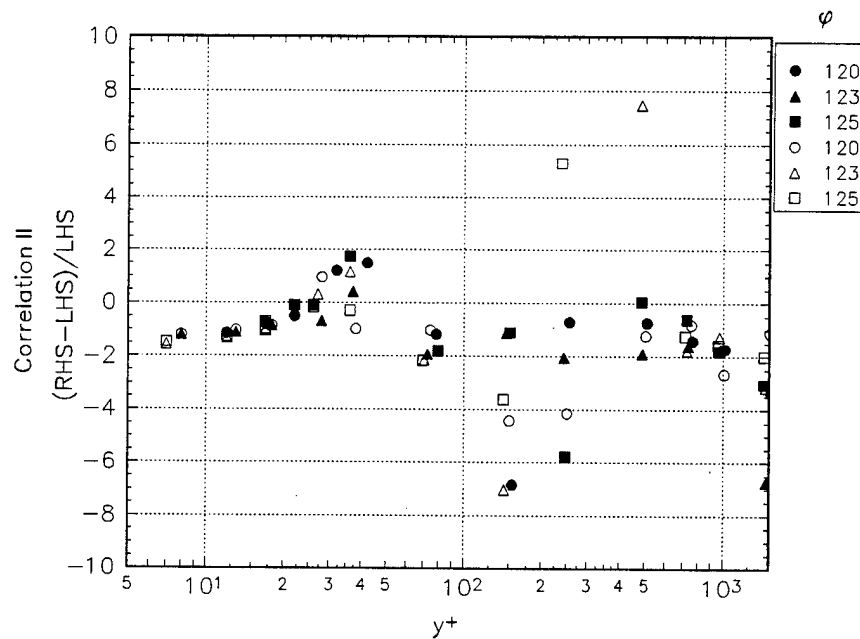


Figure M.17.c Correlation II for Chesnakas, closed symbols for  $x/L = 0.75$  and open for 0.76.

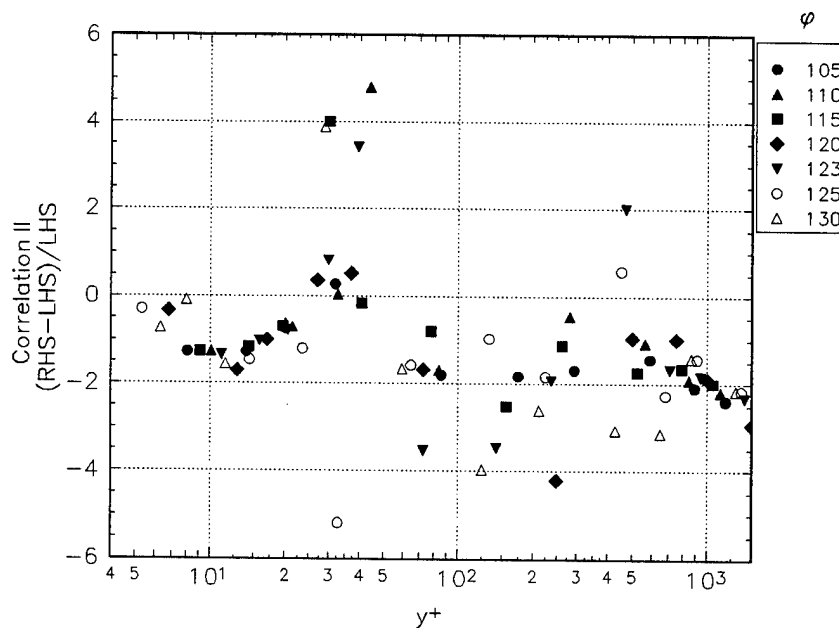


Figure M.17.d Correlation II with the Chesnakas data at  $x/L = 0.77$ .

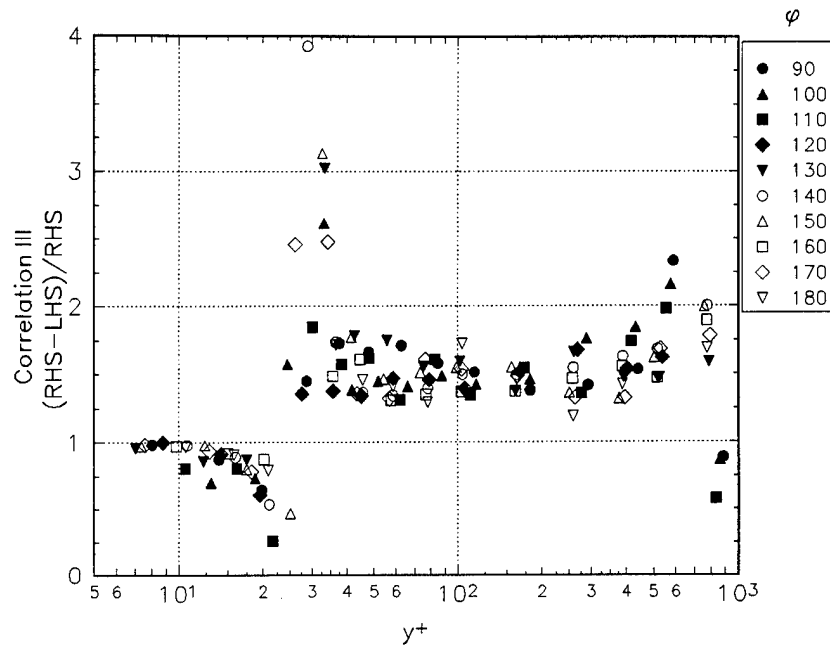


Figure M.18.a Correlation III with the Chesnakas data at  $x/L = 0.40$ .

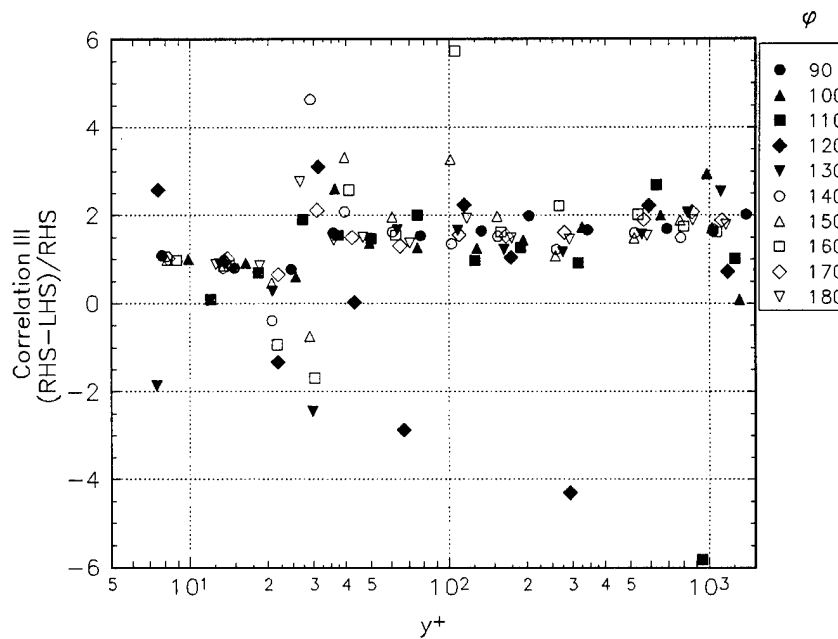


Figure M.18.b Correlation III with the Chesnakas data at  $x/L = 0.60$ .

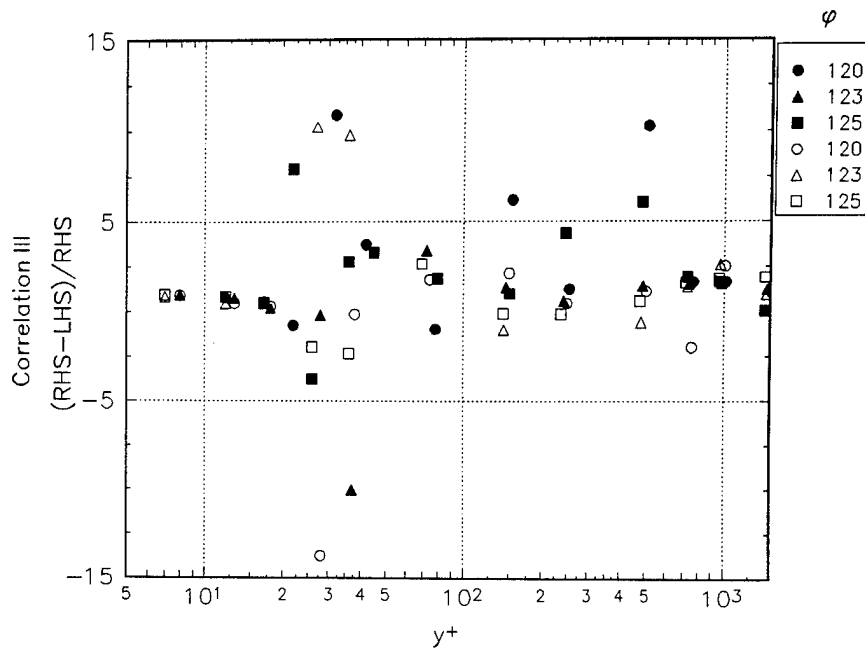


Figure M.18.c Correlation III for Chesnakas, closed symbols for  $x/L = 0.75$  and open for 0.76.

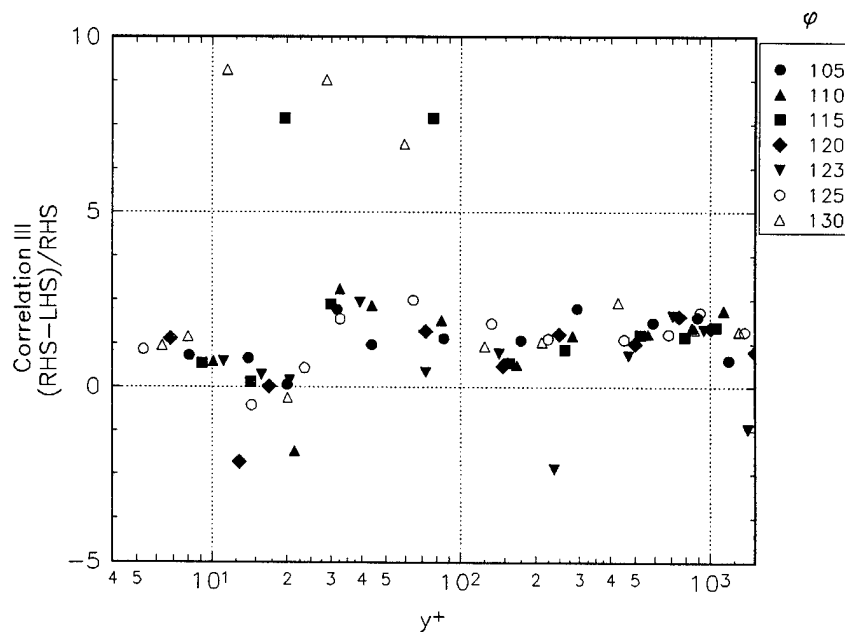


Figure M.18.d Correlation III with the Chesnakas data at  $x/L = 0.77$ .